U.S. Department
of Transportation

**Federal Aviation
Administration**
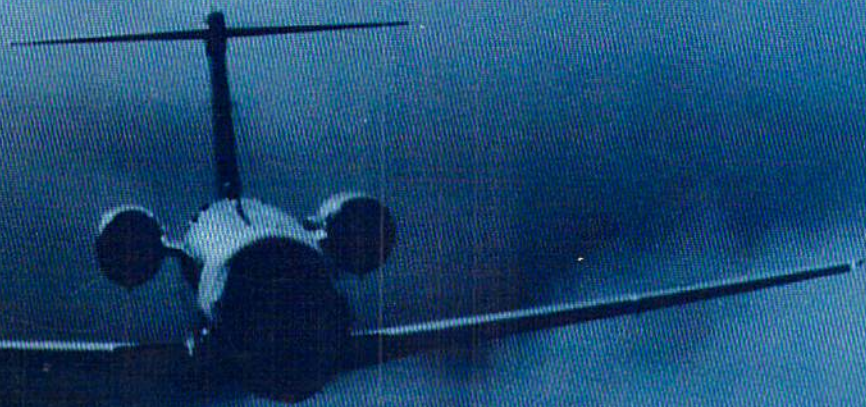
Office of Engineering
and Development
Washington, DC 20591

Proceedings of the
AIRCRAFT
WAKE VORTICES
CONFERENCE - Vol.2

Washington, D.C.
October 29-31, 1991

Cosponsored by:
ALPA, AOCI, AOPA-ASF,
ATA, ATCA, FST, NASA,
NCAR, NOAA and NTSB

REPORT DOCUMENTATION PAGE

Form Approved
OMB No. 0704-0188

Public reporting burden for this collection of information is estimated to average 1 hour per response, including the time for reviewing instructions, searching existing data sources, gathering and maintaining the data needed, and completing and reviewing the collection of information. Send comments regarding this burden estimate or any other aspect of this collection of information, including suggestions for reducing this burden, to Washington Headquarters Services, Directorate for information Operations and Reports, 1215 Jefferson Davis Highway, Suite 1204, Arlington, VA 22202-4302, and to the Office of Management and Budget, Paperwork Reduction Project (0704-0188), Washington, DC 20503.

1. AGENCY USE ONLY (Leave blank)	2. REPORT DATE June 1992	3. REPORT TYPE AND DATES COVERED Final Report

4. TITLE AND SUBTITLE
Proceedings of the Aircraft Wake Vortex Conference
Volume II, Papers 30-55

6. AUTHOR(S)
J.N. Hallock, Ed.

5. FUNDING NUMBERS
A2070/FA227

7. PERFORMING ORGANIZATION NAME(S) AND ADDRESS(ES)
U.S. Department of Transportation
John A. Volpe National Transportation Systems Center
Kendall Square
Cambridge, MA   02142

8. PERFORMING ORGANIZATION REPORT NUMBER
DOT-VNTSC-FAA-92-7.II

9. SPONSORING/MONITORING AGENCY NAME(S) AND ADDRESS(ES)
U.S. Department of Transportation
Federal Aviation Administration
Office of Engineering and Development
Washington, DC   20591

10. SPONSORING/MONITORING AGENCY REPORT NUMBER
DOT/FAA/SD/92-1.II

11. SUPPLEMENTARY NOTES

12a. DISTRIBUTION/AVAILABILITY STATEMENT
This document is available to the public through the National Technical Information Service, Springfield, VA   22161

12b. DISTRIBUTION CODE

13. ABSTRACT (Maximum 200 words)
This volume contains the proceedings of the international conference of Aircraft Wake Vortices held at the Quality Hotel Capitol Hill, Washington, DC, on October 29-31, 1991. The contributed papers discuss technological advances in the knowledge of the phenomenon, its effect on aircraft and airport capacity, detection techniques, and vortex avoidance schemes.

14. SUBJECT TERMS
Aircraft Wake Vortex, Vortices, Vortex hazards, Wake Behavior

15. NUMBER OF PAGES
1138

16. PRICE CODE

17. SECURITY CLASSIFICATION OF REPORT	18. SECURITY CLASSIFICATION OF THIS PAGE	19. SECURITY CLASSIFICATION OF ABSTRACT	20. LIMITATION OF ABSTRACT
Unclassified	Unclassified	Unclassified	Unclassified

NSN 7540-01-280-5500

Standard Form 298 (Rev. 2-89)
Prescribed by ANSI Std. 239-18
298-102

TABLE OF CONTENTS

VOLUME I,

OPERATIONAL CONSIDERATIONS

TRACK A—VORTEX PHYSICS I

TRACK B—OPERATIONAL CONSIDERATIONS II

VOLUME II

FOREWORD

This international conference on aircraft wake vortices was sponsored by the Federal Aviation Administration (FAA) and cosponsored by Air Line Pilots Association (ALPA), Airports Association Council International (AACI, formerly AOCI), Aircraft Owners and Pilots Association - Air Safety Foundation (AOPA-ASF), Air Transport Association (ATA), Air Traffic Control Association (ATCA), Flight Safety Foundation (FSF), National Aeronautics and Space Administration (NASA), National Center for Atmospheric Research (NCAR), National Oceanic and Atmospheric Administration (NOAA), and National Transportation Safety Board (NTSB). The sessions were held in the Quality Hotel Capitol Hill, Washington, DC, on October 29-31, 1991. The purpose of the conference was to discuss wake vortex phenomena and to exchange information which will guide future research and international cooperation in addressing the wake vortex problem.

The papers were presented in 9 sessions. The titles of the sessions and the respective session chairmen were:

o	Opening - Dr. Robert E. Machol
o	National Initiatives - Dr. Robert E. Machol
o	Operational Considerations I - Louis J. Williams
* o	Vortex Physics I - Dr. Steven Crow
o	Operational Considerations II - Hon. J. Lynn Helms
* o	Vortex Physics II - Dr. James N. Hallock
o	Vortex Detection - Edward A. Spitzer
o	Field Measurements - Richard D. Page
o	Hazards and Standards - Siegbert Poritzky

* simultaneous sessions

Editing this compendium consisted of chasing down the authors to get the papers, checking the spelling and punctuation, fixing a few verbs, correcting typographical errors, establishing a standard for the format of the papers (e.g., references), fixing a few misquoted equations, etc. As much as I wanted to rewrite or even change some of the text, I resisted; thus, the papers represent the opinions of the authors.

The diligence of Dr. Robert Machol, the Conference Chairman, was apparent to all in attendance. It has been my pleasure to work with him and to present this written archive of the conference.

James N. Hallock
Editor

LABORATORY AND NUMERICAL STUDIES OF VORTEX EVOLUTION IN IDEAL AND REALISTIC ENVIRONMENTS

Donald P. Delisi
Robert E. Robins
Donald B. Altman
Northwest Research Associates
P.O. Box 3027
Bellevue, WA 98009

ABSTRACT

Laboratory and numerical results are presented for the evolution of aircraft vortices. The laboratory results, for vortices from a rectangular wing towed in a nonstratified, water-filled tank, show that organized vorticity migrates much farther and lasts significantly longer than shown in previous studies. The differences between our results and results from previous studies are attributed to differences in flow visualization techniques. Numerically, we use a 2-D code to simulate full-scale measurements from a Boeing-747 aircraft in ground effect and to investigate the vortex hazard generated by a Boeing-767 aircraft near touchdown on landing. Measured stratification and cross-track winds are included in both numerical simulations. The numerical results show that full-scale measurements can be simulated by numerical codes, and that vortices generated by aircraft in ground effect may last longer than previously thought. It is cautioned that additional research is needed before a credible wake vortex hazard can be estimated from these results.

INTRODUCTION

Aircraft wake vortices pose a potential limit on airport capacity due to the possible hazard to a following aircraft from the vortex system generated from a preceding aircraft. In order to maximize airport capacity and minimize the vortex hazard, we must understand the basic physics underlying the generation and evolution of these vortices.

The wake vortex problem can be broken down into three elements. The first element is vortex generation from the lead aircraft; that is, what are the initial strengths and separations of the vortices comprising the vortex system at some initial location downstream of the trailing edge? These initial conditions appear to depend not only on the weight but also on the aerodynamics of the lead aircraft. The second element is the evolution of this initial vorticity; that is, how does the vortex system evolve in the atmosphere with time? This evolution depends on the

initial vorticity distribution as well as ambient atmospheric conditions such as stratification, turbulence, and shear. Finally, the wake vortex hazard is due to the interaction of a following aircraft with the vortex system at some position downstream of the lead aircraft. This interaction depends on the characteristics of the vortex system at the interaction position as well as the interaction time of the following aircraft in the vortex system and the roll and control characteristics of the following aircraft.

In this paper, we will focus on the evolution problem only. Hence, we are concerned with characterizing the vortex system with time (or distance) behind the lead aircraft. Previous studies have examined this problem in the laboratory, in the field, and numerically. The problem has also been examined both with and without ground effect. In the laboratory and in the field, vortices out of ground effect have been measured using dye (in the laboratory) or smoke (in the field) to track the vortex cores. Examples of laboratory studies are those by Barker and Crow (1977), Tomassian (1979), Sarpkaya (1983), Sarpkaya and Daly (1987), and Liu and Srnsky (1990). In the field, both small and large aircraft have been used (e.g., Condit and Tracy (1971), Tombach (1973), Burnham et al (1978), and Burnham (1982)). Numerically, the interaction of vortices with the ground has been investigated by Bilanin et al (1978). All of the above studies suggested maximum limits on both the vertical migration distance of the vortices and on their lifetimes. We will show below that, at least in the laboratory, the above studies greatly underestimated both the vertical migration distance and the vortex lifetime.

This paper is divided into two parts. In the second section, we present laboratory results on the evolution of a vortex pair far from ground effect in a nonstratified, nonturbulent, nonsheared flow. The importance of the results presented here is that we will show that organized vorticity migrates significantly farther and lasts significantly longer than shown by previous studies. Thus, previous studies underestimated both the height and the time in which there may be a potential vortex hazard. In the third section, Numerical Results, we will show numerical simulations of vortex evolution in ground effect. The results of these simulations also show that a potential vortex hazard may last for a longer time than previously thought. A discussion of the results is presented in the fourth section, Discussion. There we stress that, although our results show that organized vorticity lasts longer than previously thought, these results do not necessarily mean that the vortex wake is hazardous during this time. Thus, we stress the importance of developing models of following aircraft interacting with the vortex system and of further laboratory, numerical, and field measurements to correlate with our findings.

LABORATORY RESULTS

The Experimental Facility

Our experiments were performed in a nonstratified, water-filled towing tank measuring 9.8 m long, 0.9 m wide, and 1.0 m deep. Vortices were generated by towing rectangular lifting wings down the tank, as in Delisi and Greene (1990). For the results presented here, the wings were curved brass plates (0.056 cm thick) with a span of 5.1 or 3.8 cm, a chord of 2.5 or 1.9 cm, and a maximum thickness of 0.28 or 0.22 cm from the baseline. The wings were attached to thin struts, and the struts were attached to a carriage at the top of the tank. The carriage moved down the tank at a speed of 324 cm/sec, yielding a chord Reynolds number of 82,300 for the

5.1 cm span wing and 61,600 for the 3.8 cm span wing. The wings were towed near the water surface, and the resulting vortices propagated downwards towards the floor of the tank.

Flow visualization was performed with fluorescein dye and nearly neutrally buoyant particles. The dye was mixed with Liquitex (Sarpkaya, 1983) and applied to transparent tape which was then attached to the wing tips. This resulted in dyed vortex cores when the wing was towed down the tank. The dyed cores were photographed with a 35-mm camera and videotaped with a camcorder.

Neutrally buoyant particles were also used to visualize the flow (Delisi and Orlanski, 1975; Delisi and Dunkerton, 1989; Delisi and Greene, 1990). In this paper, the particles were placed only in the top layer of the tank, near the surface. When the wing was towed down the tank, the particles were entrained into the vortices. For these experiments, a light sheet was oriented along the path of the wing, from the water surface to the floor, and a 35-mm camera and camcorder looking through the side of the tank recorded the paths of the particles.

Wing lift and towing speed were measured during each run. Lift was measured with a low impedance force transducer and was measured to be certain that we were not near aerodynamic stall. Towing speed was measured by timing the passage of a 10-cm rod, attached to the carriage, to pass by a given point. Velocity was measured at ten positions at or near the test section. For the runs presented here, the average carriage speed through the test section was 324 cm/sec $\pm$ 1 cm/sec.

Results

Figure 1 shows dye observations of nonstratified vortex motions from previous laboratory studies. In this figure, H is the nondimensional vertical migration distance, $H = h/b_0$, where h is the vertical distance the vortex has migrated in time t ($h = 0$ at $t = 0$) and b_0 is the initial vortex separation, and T is the nondimensional vortex time, $T = V_0 t/b_0$, where V_0 is the initial vortex migration velocity. In Figure 1, the plus symbols are from Tomassian (1979), the Xs are from Sarpkaya (1983), the squares are from Liu and Srnsky (1990), and the circles are our dye data from Delisi and Greene (1990). Note that Tomassian (1979) generated two-dimensional vortices while the other studies all generated three-dimensional vortices from wings.

Figure 1 shows that all observations using dye are reasonably consistent, with a maximum H of around 6.5 and a maximum T of around 9. Delisi and Greene (1990) showed that, using neutrally buoyant particles, vortex observations can continue beyond those shown in Figure 1, and can continue to at least $H = 8.5$ and $T = 16$. In their study, Delisi and Greene were unable to determine the maximum vertical migration distance and lifetime of the vortices due to the large wing span used (large b_0) and the finite depth of their facility. In this paper, we use a smaller span wing than that used in Delisi and Greene; hence, we expand on their results here.

Figure 2 shows a series of streak photographs of the particles for one run with the 5.1 cm span wing. (The time exposure for these photographs was 1/2 sec, resulting in particle streaks in those regions where the particles moved during the exposure.) In this figure, the flow is illuminated with a vertical light sheet along the wake centerline, and the view is from the side of

the tank. The wing has moved from left to right near the top of each photograph. In the first two photographs, Figures 2a and 2b at T = 2.8 and 5.3, the trailing wake is a nearly two-dimensional line vortex pair, from left to right, at the bottom edge of the region with particles. Note the downward propagation of the wake with each photograph. Also note that, as the vortices propagate vertically downwards into the tank, some of the particles are transported from near the surface downwards towards the floor. In Figure 2c at T = 7.8, the two-dimensional wake is becoming three-dimensional. In Figure 2d at T = 10.3, three-dimensional ring vortices have formed from the original two-dimensional line vortex pair. The rings are being cut down the center by the light sheet, similar to cutting a doughnut in half. The remaining photographs, Figures 2e to 2h at T = 12.8 to 20.2, show the rings migrating downwards, essentially unchanged, to the bottom of the tank.

Figure 3 shows drawings of the flow fields in Figure 2 at two times in the evolution. For each of the two times, there is a three-dimensional view (a or c) and a side view (b or d). Figures 3a and 3b correspond to Figure 2a or 2b and show the flow at an early time. At this time, the flow is two-dimensional, and the line vortex pair, when viewed from the side in Figure 3b, shows motion only at the bottom of the region containing particles. Figures 3c and 3d correspond to Figures 2d and 2h and show the flow at a later time. By this time, three-dimensional vortex rings have formed from the two-dimensional line vortex pair. The side view, Figure 3d, shows the slice down the centerline and shows one vortex pair associated with each ring. Note that the diameter of each vortex ring, D, is much smaller than the distance between the rings, d. The 2-D to 3-D evolution shown in Figures 2 and 3 is the well-known mutual induction, or Crow, instability which was identified by Scorer (1958) and analyzed by Crow (1970).

Figure 4 is a replot of Figure 1 to show the dyed wake data on the relevant scales. Figure 5, using the same scales as on Figure 4, shows our H vs. T results for the 3.8 cm span wing using particles. Note in Figure 5 that we can follow organized, 3-D vortex structures to H = 22 and T = 100. (Note that these numbers are themselves not the maximum values of H or T since many (but not all) of the vortices in these runs hit the bottom of the tank at H = 26. Thus, the values of H = 22 and T = 100 should not be considered to be the maximum vortex rise heights or the maximum vortex lifetimes.)

As discussed in Delisi and Greene (1990), in additional experiments (not shown), both dye and particles were used in the same run to determine whether both dye and particles were following the same flow. The results showed that both dye and particles followed the vortex motion accurately only for short evolution times, after which the dye diffused rapidly. Only the particles followed the vortex motion for long times.

The comparison of Figures 4 and 5 is significant. From Figure 4, one is left with the impression that the vortex motion has died out by H = 6.5 and T = 9. From Figure 5, however, it is clear that organized vorticity lasts to at least H = 22 and T = 100. Note, also, in Figure 5 that there is little scatter up to H of around 10, but significant scatter beyond H = 10. This scatter is due to differing vertical migration velocities of the 3-D vortices.

Using a small, propeller-driven aircraft, Tombach (1973) observed that Crow instability occurred infrequently and that vortex bursting more often destroyed the vortices before Crow instability

occurred. These aircraft observations were obtained, however, using smoke to track the aircraft wake vortices. In our laboratory experiments, dye in the vortex cores also showed that vortex bursting often occurred before Crow instability. Observations using particles, however, show that vortex bursting does not prevent Crow instability. Rather, Crow instability is always observed to occur, either before or after bursting, and the resulting ring vortices propagate to the floor of the tank.

Note that the differing observations of vortex migration distance, maximum vortex lifetime, and vortex bursting vs. Crow instability between our results and previous results may all be due primarily to the different flow visualization techniques used in the studies and secondarily on other factors. Thus, it may be that, although Tombach (1973) observed Crow instability infrequently, his use of smoke to follow the vortex motions in his study may have yielded misleading results in the same way that the use of dye underestimated vortex rise height and lifetime in the laboratory.

Consequently, we would urge caution in using smoke in full-scale tests for other than early vortex lifetime measurements until it can be shown that the smoke is accurately following the vortex motions for long times. A similar caution should be used with laboratory studies using dye as the sole flow visualization technique.

NUMERICAL RESULTS

Background

In this section of our paper, we report on the results of numerical simulations of how ground interaction and crosswind affect the evolution of an aircraft wake vortex system. Since atmospheric stratification is also known to affect vortex evolution profoundly (Greene, 1986), we have included measured stratification in our aircraft wake vortex simulations. Measured wind profiles were also included in the simulations when available.

Previous studies of vortices in ground effect include the field observations of Pengel and Tetzlaff (1984), Burnham (1982), Tombach et al (1977), and Dee and Nichols (1968). Pengel and Tetzlaff studied the cross-runway transport of wake vortices at Frankfurt Airport where parallel runways are frequently used. They observed that under stable atmospheric conditions, wake vortices were capable of surviving up to 3.5 minutes and traveling about 500 meters perpendicular to the runway when influenced by crosswinds having mean speeds of 3 to 5 meters per second, measured at a height of 10 meters. Among Burnham's findings was the confirmation of Dee and Nichols' earlier findings that wake vortices will separate and rebound upon interacting with the ground. Inviscid theories predict the separation but not the rebound. The study of Tombach et al focused on vortex breakdown during ground interaction, noting that ground contact frequently led to some form of vortex breakdown, and that the particular form of vortex breakdown known as core bursting usually changes the form of a vortex without destroying it.

Laboratory observations of vortices in ground effect include the studies of Delisi et al (1987), Ciffone and Pedley (1979), Barker and Crow (1977), and Harvey and Perry (1971). These

studies all found, in agreement with the field observations of Burnham, and Dee and Nichols, that wake vortices will separate and rebound when they interact with the ground. Delisi et al used a tilting water tank to study stratification and vertical shear[1] effects on the ground interaction with two-dimensional vortices and found that either of these effects will reduce the extent of the rebound. They also found that weak vertical shear will cause the downwind vortex to rebound higher than the upwind vortex, and that the reverse will be true in strong vertical shear. This finding is in agreement with the work of Brashears et al (1975) (see below). Ciffone and Pedley towed 1/25th-scale models of Boeing-747 and DC-10 aircraft in water and found that the ground effect caused distortions in the vortex tangential velocity profiles, but left the maximum tangential velocities unchanged. Barker and Crow generated two-dimensional vortices in a stationary water tank and observed the rebound effect for a free as well as a solid surface. Conducting their experiments with a half-span rectangular wing in a low speed wind tunnel, Harvey and Perry used a moving floor to simulate the ground boundary condition.

Theoretical treatments of a vortex pair in ground effect have been reported by Peace and Riley (1983), Saffman (1979), Bilanin et al (1978), and Brashears et al (1975). Peace and Riley, Saffman, and Bilanin et al, all sought an understanding of the phenomenon of vortex rebound. Taken together, their work cast doubt on the finite core size hypothesis suggested by Barker and Crow (1977), and essentially confirmed the qualitative explanation of Harvey and Perry (1971) that viscous generation of secondary vorticity was the main ingredient responsible for the rebound. Attempting to explain Barker and Crow's observation of a rebound at both free and solid surfaces, Peace and Riley introduced a viscous displacement mechanism which acts in addition to secondary vorticity at a solid surface and a vorticity diffusion mechanism which acts in addition to the other mechanisms at a solid surface and alone at a free surface. Brashears et al, focus on an explanation for the phenomenon of vortex tilting, which they observed in field studies. Their approach was to study the streamlines arising from the combination of vertical shear and a vortex pair. In agreement with the observations, their results showed that weak vertical shear will cause the downwind vortex to rebound higher than the upwind vortex, and that strong vertical shear will have the opposite effect (cf, Delisi et al, 1987).

None of the theoretical treatments described above follow the development of the rebound phenomenon beyond the point of the initial rebound. Some field and laboratory observations (e.g., Burnham, 1982; Delisi et al, 1987; Barker and Crow, 1977) have shown, however, that after rebounding, vortices may continue to separate while maintaining an approximately constant distance from the surface. Other laboratory observations (e.g., Van Heijst and Flor, 1989) have shown that rebounding vortices may relink and even undergo additional rebound. The determining factor appears to be the vortex Reynolds number, $Re = \Gamma/\nu$, where Γ is the vortex circulation and ν is the kinematic viscosity. The vortices that continue to separate after rebound have higher values of Re ($\geq 20{,}000$) than those that relink (Re $\leq 2{,}000$). The universality of this observation is the subject of further investigation.

Since our main interest in this paper is aircraft wake vortices (which have large Re values), we present numerical results which model the higher Re observations of vortex rebound followed

---

1   By vertical shear we mean the change in the crosswind speed as a function of the vertical coordinate.

by continued separation at approximately constant distance from a solid surface. Our approach has been to use a computer code which solves the two-dimensional, time-dependent, incompressible Navier-Stokes equations. The code permits the specification of arbitrary atmospheric stability and wind profiles. For vortices out of ground effect, the code has been validated by means of comparisons with laboratory and field data (see the next paragraph, Numerical Approach). To model the interaction of the vortices with the ground, we have used a mixed no-slip/free-slip boundary condition. When applied to realistic conditions, our simulation results confirm the findings of Pengel and Tetzlaff that vortices generated by large aircraft close to the ground in a crosswind can survive after evolution times and cross-runway transport distances on the order of 3 minutes and 500 meters. Our results suggest that surviving vortices can possess sufficient strength to be a potential hazard to smaller aircraft operating on the same runway or on parallel runways which are downwind of the larger aircraft.[2]

Numerical Approach

The computer code used in our study solves the two-dimensional, time-dependent, incompressible Navier-Stokes equations, expressed in streamfunction-vorticity form. Mean buoyancy and shear effects are included in the equations, and the code permits the specification of arbitrary mean profiles of atmospheric stability and wind. Variations of density in the momentum equations are neglected except where they give rise to buoyancy forces, a simplification known as the Boussinesq approximation. A simple, scale-dependent eddy-viscosity-like damping scheme (greater damping for smaller scales) is used to dissipate energy transferred to small scales of motion.

The model obtains separate solutions for horizontally averaged quantities and for perturbations about these averages. No assumptions are made in the model about the size of the perturbations. The solution method is to represent the horizontal variation of the perturbation quantities in terms of complex exponential series with coefficients depending on the vertical coordinate, z, and time, t. Side boundaries are thus periodic. The top boundary is chosen to be free slip and the bottom boundary is discussed further below. Centered differences are used to approximate vertical derivatives of mean and perturbation quantities, and a leapfrog scheme with periodic averaging of successive time steps is used to advance the solution in time.

The numerical vortices used in the study are specified by means of an initial field of perturbation vorticity. The vorticity distribution for each vortex has Gaussian form, where a separation distance, b_o, a circulation, $2\pi B_o$, and a core radius, r_o, specify the distribution. For a complete description of the numerical approach, including equations, see Robins and Delisi (1990).

---

2   We note that our numerical results neglect the effects of ambient turbulence, which may have significant effects on vortex decay. Nevertheless, as supported by the results of Pengel and Tetzlaff, there may be times when atmospheric turbulence effects are negligible.

The treatment of the bottom, or ground, boundary condition is critical to the successful modeling of the interaction between wake vortices and the ground. The conventional method is to use a no-slip condition, but our simulations with this condition were not successful because the coarseness of our computational grid resulted in an overestimate of the viscous interaction at the ground. The boundary condition we used for the results presented here was a mixed no-slip/free-slip condition, where the vorticity at the ground, η_o, is specified as

$$\eta_o = \alpha\, \eta_N + (1\text{-}\alpha)\, \eta_F$$

where η_N is the no-slip value of η_o, η_F is the free-slip value of η_o, and $0 < \alpha < 1$ where α is what we call the no-slip fraction. As suggested by Roache (1976), we chose

$$\eta_N = -2\psi_1/(\Delta z)^2$$

and we set η_F to η_1, where ψ_1 and η_1 are the values of perturbation streamfunction and vorticity at the first grid point above the ground, and Δz is the vertical grid spacing. The value of α is chosen by comparing numerical results with observations.

The code has been validated in the case of vortex evolution out-of-ground effect by comparing computed vortex trajectories with laboratory and field measurements, and computed average circulation[3] with field measurements. Robins and Delisi (1990) show good agreement between code results and laboratory data for nonstratified and stratified flows, and Delisi et al (1991) show good agreement between code results and laboratory data for a stratified shear flow. We used the measurements of Burnham et al (1978) as the basis for validating the code for the field situation. Figures 6 and 7 show comparisons of code results with vortex trajectory and average circulation data from Run 8 of this data set. Measured vortex parameters b_o, B_o, r_o, and measured atmospheric stability data for this run were used to initialize the code. The comparisons show that the code predicts the trajectory data and the circulation data reasonably well.

Results for Full-Scale Vortices in Ground Effect with Crosswind

To evaluate our computational approach for a ground-effect case, we compared results of numerical simulations with measurements of vortex height, lateral position, and average circulation from a series of Boeing-747 flight tests reported by Burnham (1982). Data from Run 1 at Edwards AFB are shown in Figures 8 and 9. In this case, a crosswind holds one of the vortices at a nearly constant lateral position while causing the other vortex to traverse out of the field of

---

[3]   The average circulation about a vortex, Γ, up to a radius, r, is defined as

$$\Gamma(r) = \frac{1}{r} \int_0^r \Gamma(r')\, dr'$$

where $\Gamma(r')$ is the vortex circulation $2\pi r' V(r')$, r' being the vortex radius and $V(r')$ the tangential velocity profile.

view. From the altitude vs. time data, the visible vortex is seen to undergo a rebound and then remain at a more-or-less fixed distance from the ground.

In order to simulate these observations, several pieces of information were required. Since the test aircraft was in a landing configuration, a vortex pair is not an adequate description of the vortex wake. Instead we used an adaptation of the Betz method to model the distribution of vorticity. The Betz method and its extension to complex load distributions is described by Donaldson et al (1974), and our adaptation is described in the appendix to Robins and Delisi (1991). An estimate of span loading, which is required by this method, was provided by the Boeing Company. The result was four pairs of vortices (which rapidly roll up into one pair).

Vertical profiles of atmospheric stability and wind are also required by the code. These profiles were obtained from an addendum to Burnham's report. Nominal values, at a height of 20 m, for the stability frequency, the vertical wind shear, and the component of wind velocity across the aircraft flight path were 25 cyc/hr, 0.007 sec^{-1}, and 25 cm/sec.

Remaining code requirements are the form of the scale-dependent damping and a value for α to establish the boundary condition at the ground. We initially chose the damping to be the same as for the Boeing-747 validation case, described in Section 3.2. This resulted in too much damping at small scales as determined by comparisons with the circulation data, and we concluded that a modified damping model was required for the ground-effect case. We ultimately chose the damping for the ground-effect case to be identical, for all scales, to the large-scale damping used for the out-of-ground-effect case. Evidently, the dynamics of the ground interaction was sufficiently effective in damping small scales that the additional small-scale damping provided by the code's damping model proved to be excessive.

We empirically fixed α, the no-slip fraction in the mixed no-slip/free-slip condition, to give a reasonable representation of viscous processes occurring at the ground. The value for α was 0.075. Results from the code simulation of Burnham's Run 1 are superimposed as the solid lines on the field data in Figures 8 and 9. Good agreement is seen in Figure 8, and reasonably good agreement is seen in Figure 9. These comparisons are more impressive when one realizes that the initial wake vorticity distribution was not based on observations of b_0, B_0, and r_0, as in the previous case (see Numerical Approach), but on an estimate of the span loading.

Note in Figure 9 that the field measurements decay rapidly for times greater than 160 sec for radii greater than or equal to 10 m. This rapid decay is not modeled well in the calculation. It is not clear, however, whether the rapid decay of the field measurements is due to a physical phenomenon or to measurement error. It is important for airport capacity to determine how long vortices near the ground survive and what their decay mechanisms are. Hence, it is important to determine whether the rapid decay observed in Figure 9 is physically real. Additional full-scale data need to be obtained to determine the physical mechanisms of vortex decay and to provide a data base for additional numerical simulations.

Code Simulation of the Vortex Wake of a Landing Aircraft

In this section, we describe the simulation of the vortex wake of a heavy aircraft on the verge of landing. Our particular interest was to assess the potential hazard to a smaller aircraft operating on a parallel and downwind runway.

For this simulation, we used the same damping model and ground boundary condition as we used for the case in Section 3. 3. For the aircraft, we chose a Boeing-767, and, as in the last section, Results for Full-Scale Vortices in Ground Effect with Crosswind, for a Boeing-747, we used span loading provided by the Boeing Company to specify the initial state of the vortex wake. This time our adaptation of the Betz method led to the specification of five vortex pairs from which one pair rapidly formed.

We chose a starting height for the vortices of 5 meters, which corresponds to a time just seconds before touchdown and loss of lift. Vertical profiles of atmospheric stability and wind were chosen from atmospheric data recorded at a mid-west airport. Nominal values, at a height of 20m, for the stability frequency, the vertical wind shear, and the component of wind velocity across the aircraft flight path were 6 cyc/hr, 0.025 sec^{-1}, and 4 m/sec. The results from this simulation are shown in Figures 10, 11, and 12.

Figure 10 shows the trajectories of the vortices. The effect of the crosswind is clear in the lateral position plot, as both vortices are moved in the same direction away from the position of generation. Note that the effect of the crosswind is not simple advection, as the slope of the lateral position versus time relation is less for the upwind vortex than for the downwind vortex. Also note that due to their low generation height, these vortices are immediately in ground effect and so do not "rebound" as did the vortices whose trajectories were shown in Figure 8. Average circulation at radii of 5, 10, 15, and 20 meters is shown in Figures 11 and 12, for upwind and downwind vortices, respectively. After 3 minutes, the upwind vortex has traversed nearly 500 meters and its average circulation at radii of 15 and 20 meters is in the range 100-150 meters squared per second.

To gauge the effect of this amount of average circulation on a following aircraft, we present a brief summary of an analysis presented by Burnham and Hallock (1982). In their report they present an expression for

$$\Gamma_T \ (b/2) \ ,$$

the "vortex strength hazard threshold," which is the minimum average circulation at a radius of b/2 that a vortex must have to be considered a hazard to a following aircraft of wing span b. As an example, they show for a DC-9 aircraft (b = 30m) that 150 m^2/sec is an extreme upper estimate for this threshold (e.g., average circulation values as low as 75 m^2/sec might also represent a hazard). It follows from Figure 11 that the upwind vortex from our simulation could be considered a potential hazard for a DC-9 aircraft. Similar considerations could be used to show that smaller aircraft are also potentially at risk.

Our results thus imply that the trailing vortices from a Boeing-767 class or larger aircraft which is operating near the ground could potentially pose a hazard for DC-9 or smaller aircraft

operating near the ground and downwind from the larger aircraft. If the crosswind were just strong enough to counteract the cross-runway movement of one vortex and prevent it from traversing away from the runway, then the potential hazard would be to aircraft operating on the same runway.

DISCUSSION

In the second section, Laboratory Results, we presented results that showed that, for a nonstratified flow in the laboratory, organized vortex motion persists for much greater distances and for much longer times than shown by previous studies. We also showed that the vorticity evolves from two-dimensional to three-dimensional structures.

In the third section, Numerical Results, we presented results that showed that, using a 2-D Navier Stokes numerical code, we can predict reasonably well field measurements of vortex motion from a Boeing-747 aircraft in ground effect. We also showed, using the same code, that for a Boeing-767 near landing, the vortices migrate above the generation point and remain potentially hazardous for up to three minutes after generation.

For the aircraft industry, these results suggest the following:

a. The full-scale wake vortex hazard *may* last longer than found with full-scale measurements using smoke to follow the vortex cores. Our results indicate that this statement may be valid both in- and out-of-ground effect.

b. Caution should be used in developing hazard criteria from laboratory experiments which used dye to follow the vortex motion, since dye accurately follows the vortex motion only for early vortex evolution times.

c. Caution should be used in developing hazard criteria from full-scale experiments using smoke to follow the vortex motion until it can be shown that smoke accurately follows the vortices for long times.

d. Atmospheric parameters will most probably have a large effect on vortex evolution. Greene (1986) has shown the significant effects of stratification. In the above numerical simulation, the cross-track wind had an effect on both the transport of the vortex system and on its strength. In other studies by Robins and Delisi (1990) and Delisi et al (1991), it was shown that cross-track shear can enhance the vortex lifetime, as long as ambient stratification is not too great.

Thus, to fully understand vortex evolution in the field, atmospheric parameters need to be measured simultaneously with vortex measurements.

e. More full-scale measurements need to be performed to correlate with our results, and more research needs to be performed to determine how the background affects vortex evolution.

f.   Models of a following aircraft interacting with the vortex wake from a lead aircraft need to be developed for 3-D vortex wakes as well as for 2-D vortex wakes. These models need to account for the vortex evolution from 2-D to 3-D, the nonuniform along-track motions caused by the ambient atmosphere, the interaction time of the following aircraft in the vortex system, and the roll and control characteristics of the following aircraft.

These last two points are particularly important. Our study has shown that there is a great deal about vortex evolution that we do not understand at this time. Our study might also be construed to indicate that the wake vortex hazard lasts for much longer times than currently thought, but we believe this interpretation is not warranted at this time. Our results are from a low Reynolds number laboratory study and 2-D numerical simulations, neither of which have a sufficient amount of corroborating field data. Perhaps more importantly, without good inter-action models, we do not know how to evaluate the wake vortex hazard from our studies even if our results are accurate. Just as importantly, we do not know at this time how the atmosphere affects vortex evolution. (Note that all previous laboratory studies which evaluated the effects of ambient stratification and turbulence used dye to track the vortex motions, and we have shown that dye cannot be used for long-time vortex evolution studies, at least under our flow conditions. Thus, caution is urged in using previous laboratory studies with dye to assess the effects of ambient stratification and turbulence on maximum vortex migration distance and maximum vortex lifetime. Hence, we believe we do not know, at this time, how the atmosphere affects vortex evolution.)

In summary, we believe additional laboratory and numerical studies need to be performed, additional field measurements need to be made, and adequate interaction models need to be developed before we can adequately assess the wake vortex hazard and before adaptive aircraft spacing can be achieved.
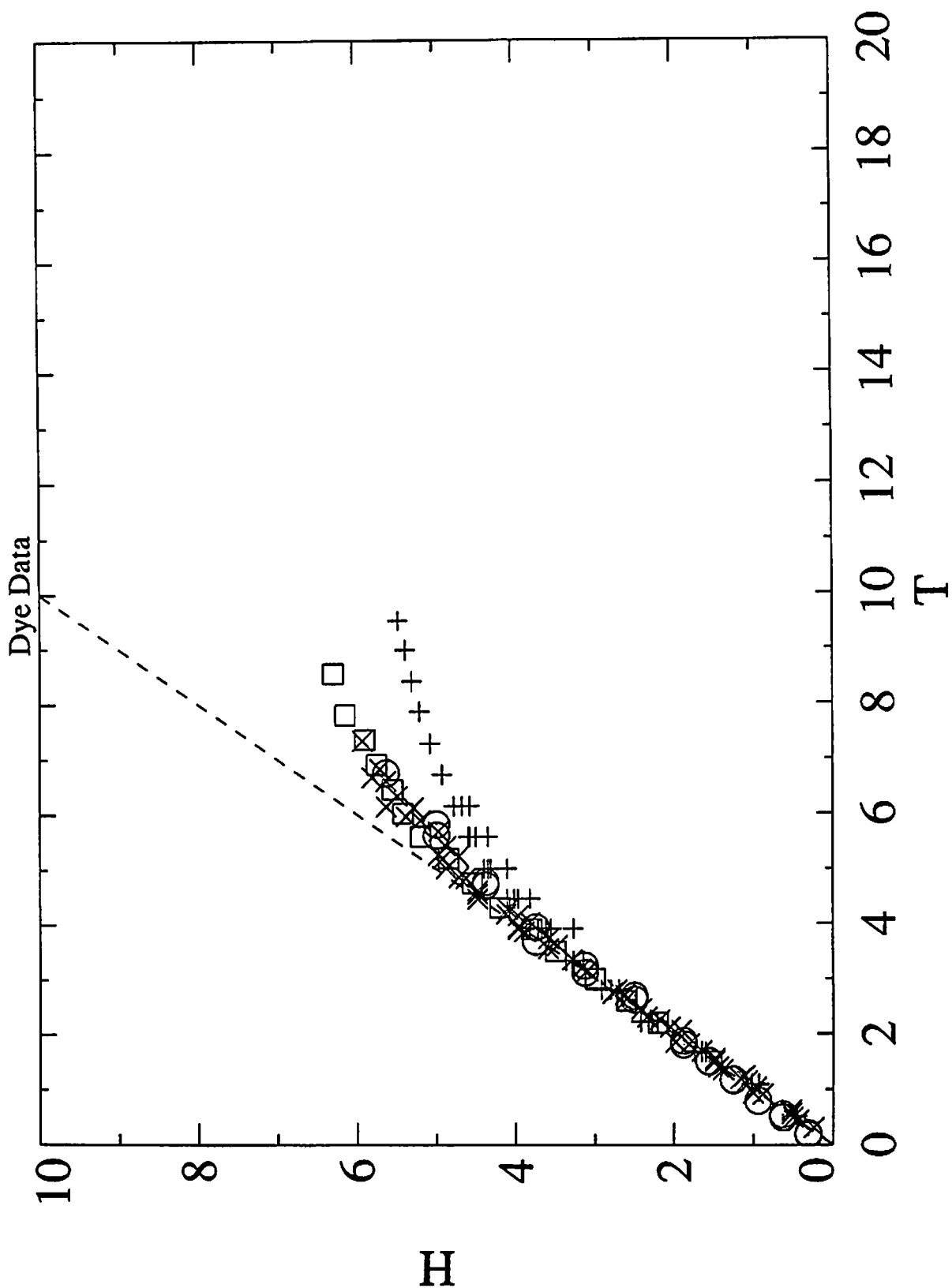
Figure 1. H vs T for nonstratified, dyed vortex laboratory measurements from Tomassian (1979; plus symbols), Sarpkaya (1983; X), Liu and Srnsky (1990; squares), and Delisi and Greene (1990; circles).
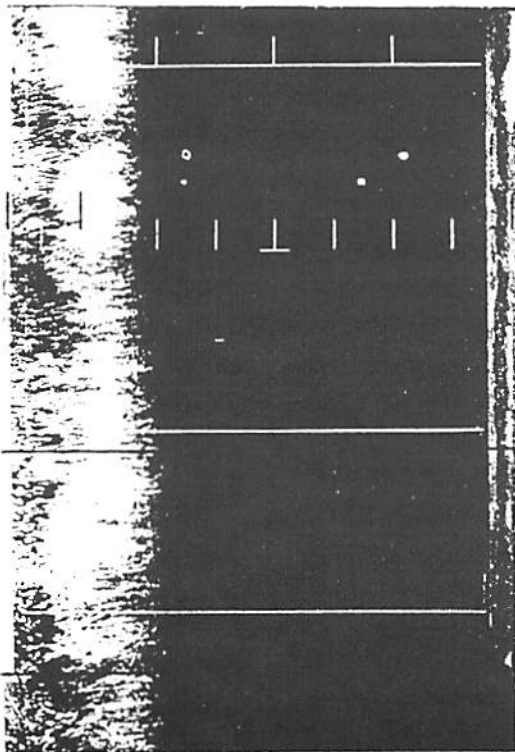
Figure 2b.
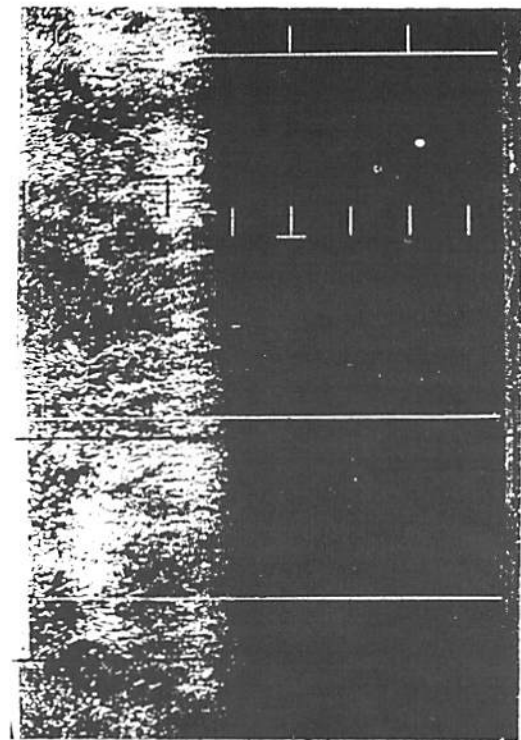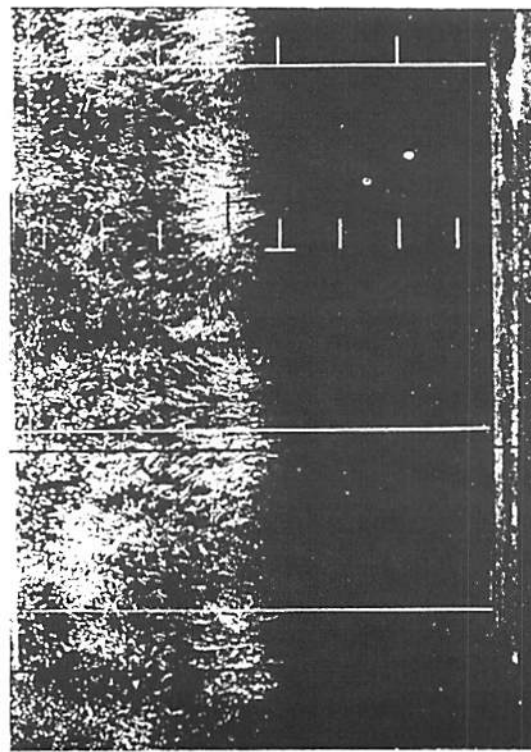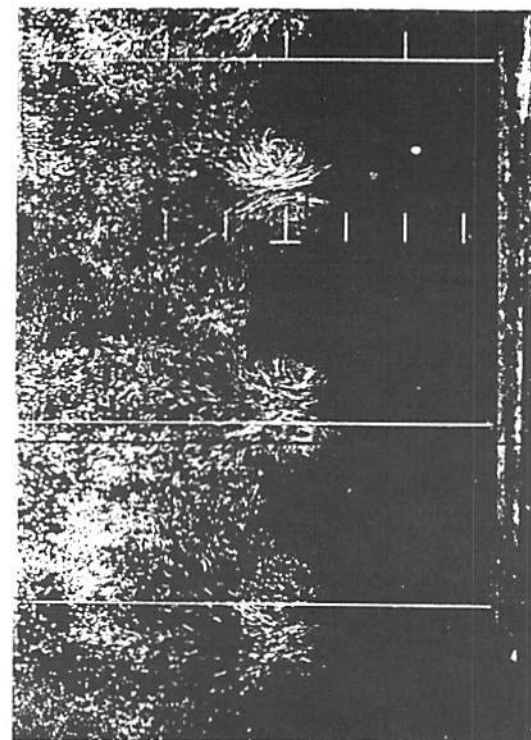
Figure 2d.

Figure 2a.

Figure 2c.

Figure 2. Streak photographs for the 5.1 cm span wing at an angle of 13 deg and a towing speed of 324 cm/sec for T of (a) 2.8, (b) 5.3, (c) 7.8, (d) 10.3, (e) 12.8, (f) 15.3, (g) 17.8, and (h) 20.2.
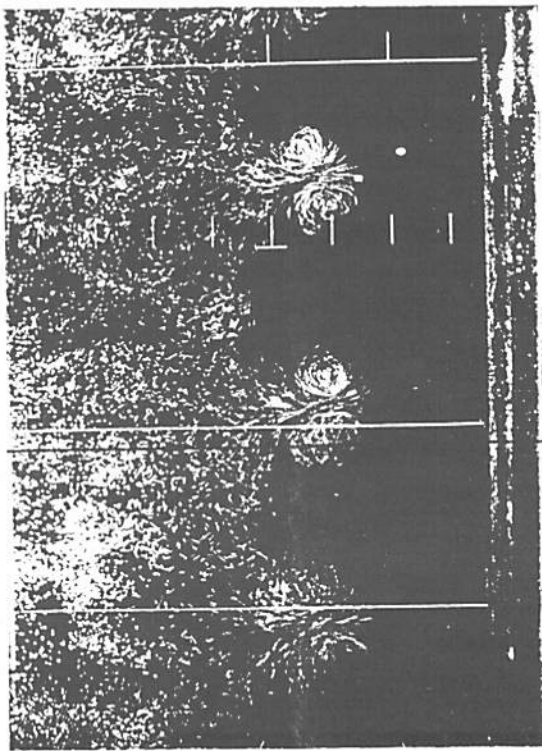
Figure 2f.
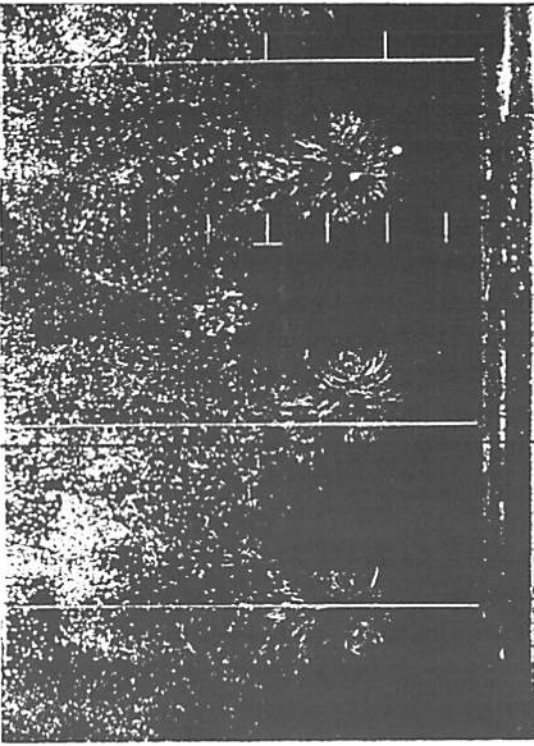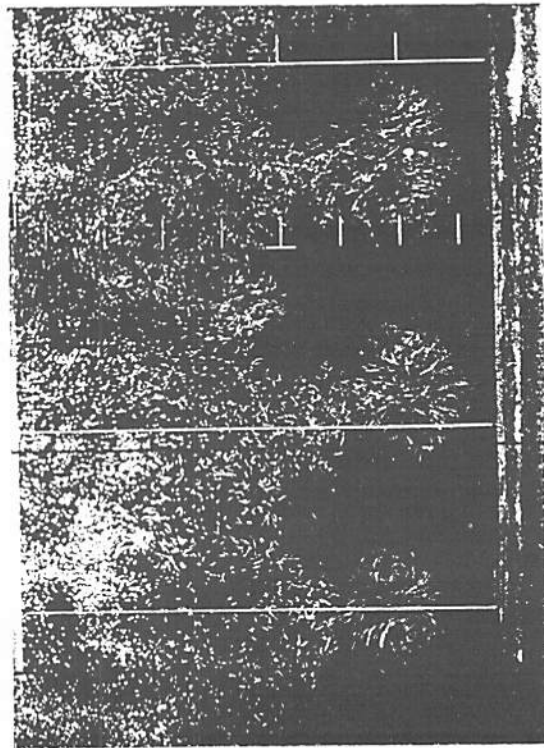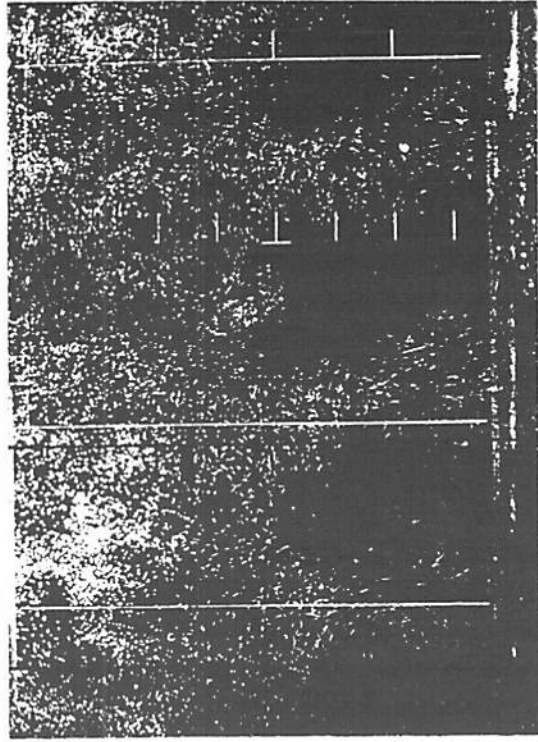
Figure 2h.

Figure 2e.

Figure 2g.

Figure 2. continued.
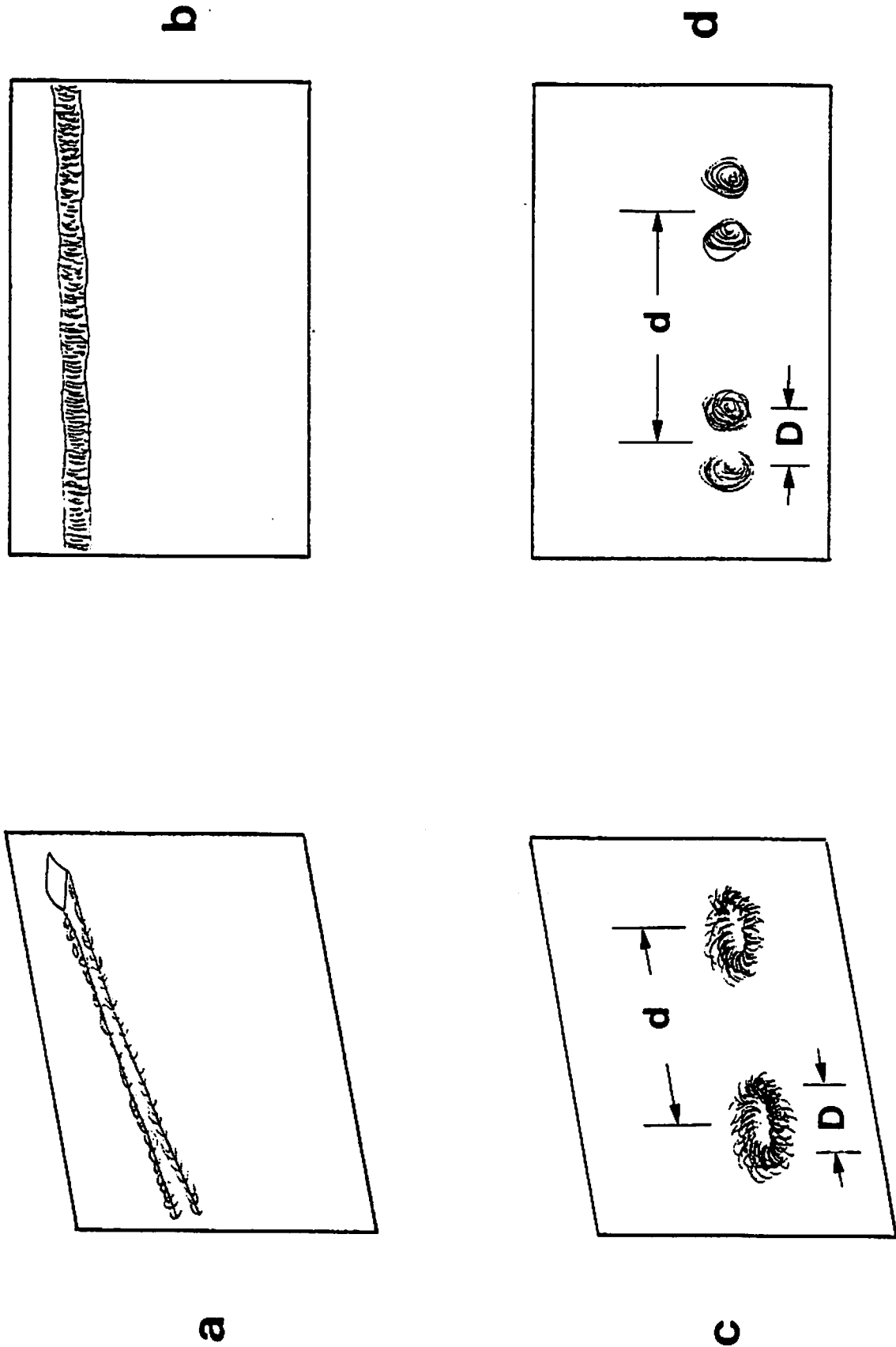
Figure 3. Drawings of the flow field at two times in the evolution of a vortex wake. Figures 3a and 3b show the three dimensional and side view, respectively, of the flow field at an early time, when the wake is two-dimensional. Figures 3c and 3d show the same views at a later time, after the wake has evolved into three-dimensional ring vortices.
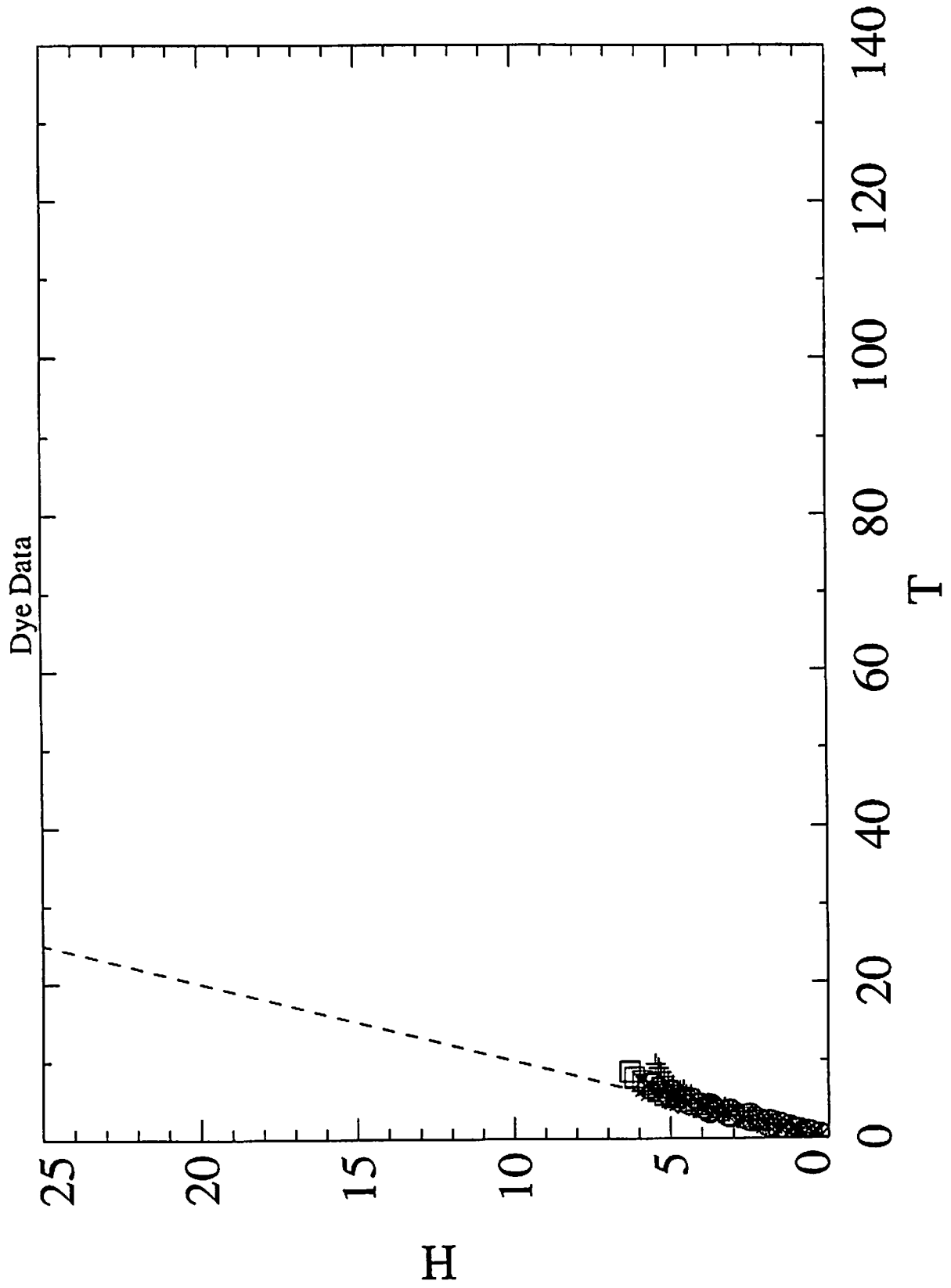
Figure 4. H *vs* T for the dyed vortex data from Figure 1 on scales consistent with Figure 5.
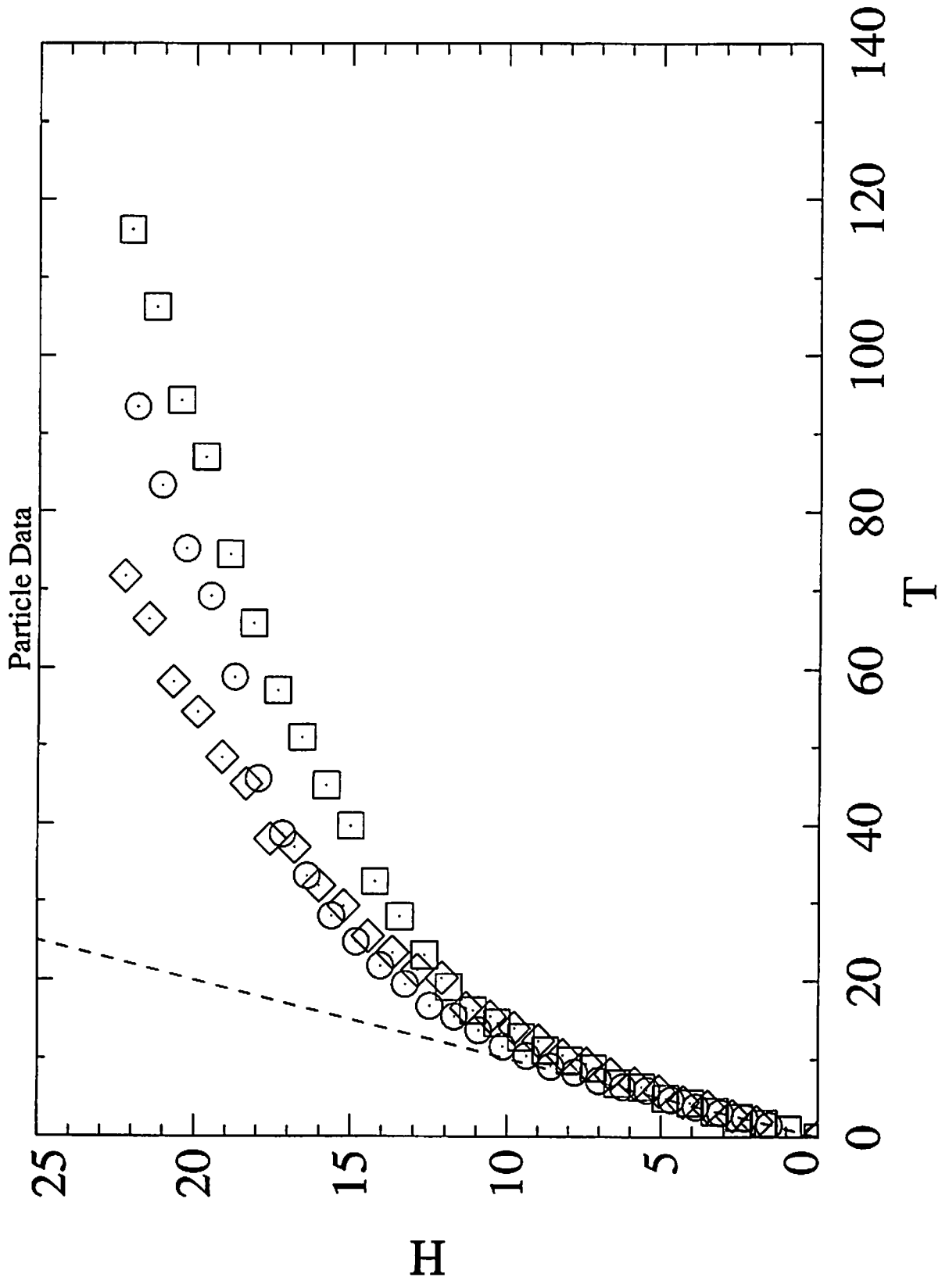
Figure 5. H *vs* T for particle streak vortex measurements using the 3.8 cm span wing.
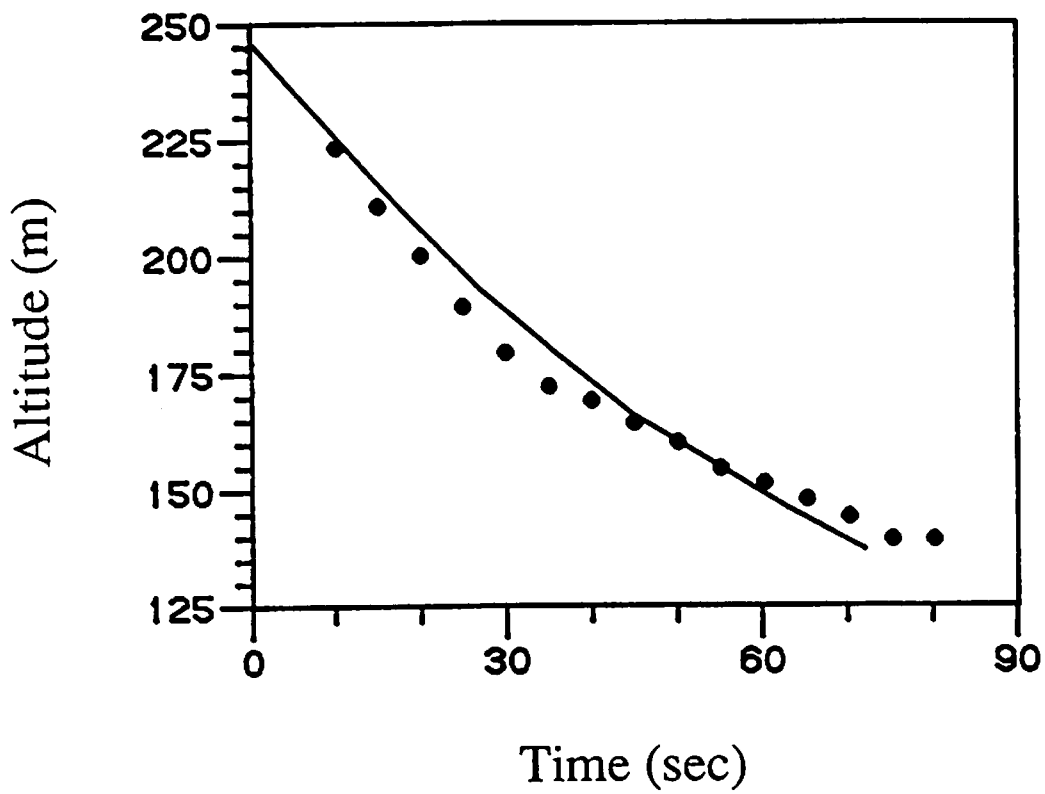
Figure 6. Comparison of our code results (———) with field measurements (●) of
vortex altitude vs time for Run 8 in Burnham et al (1978).
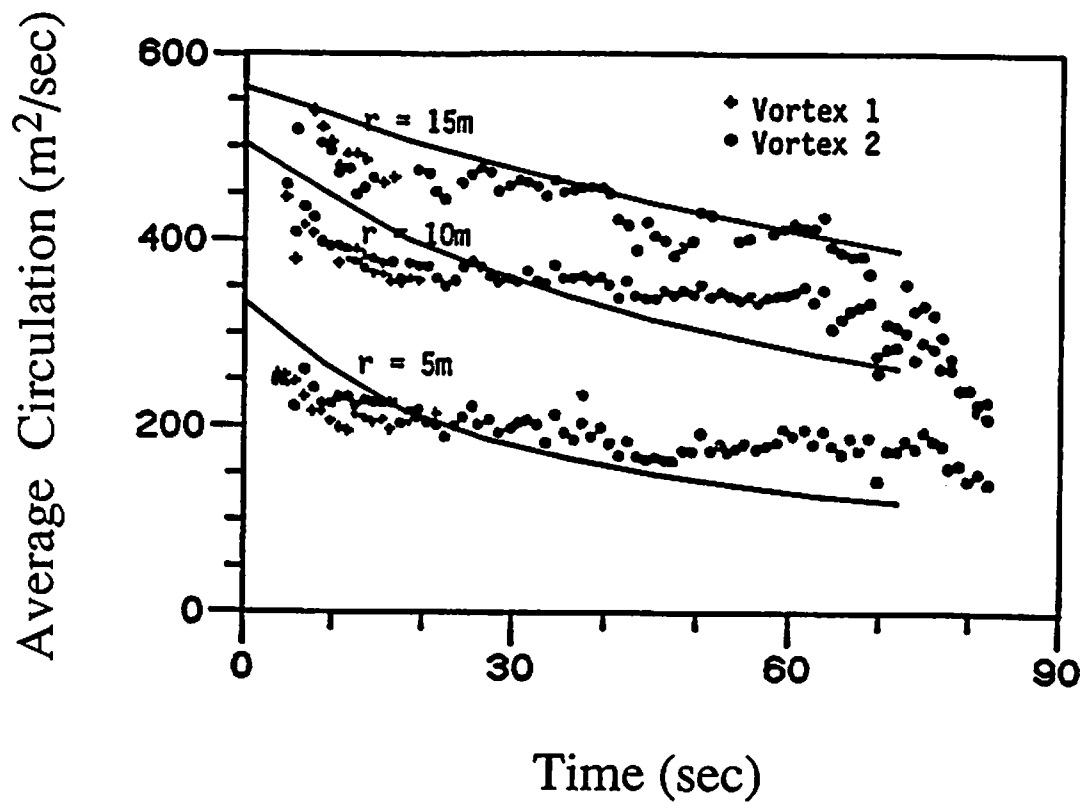
Figure 7. Comparison of our code results (———) with field measurements (+,●) of average circulation for r = 5, 10, 15 m vs time for Run 8 in Burnham et al (1978).
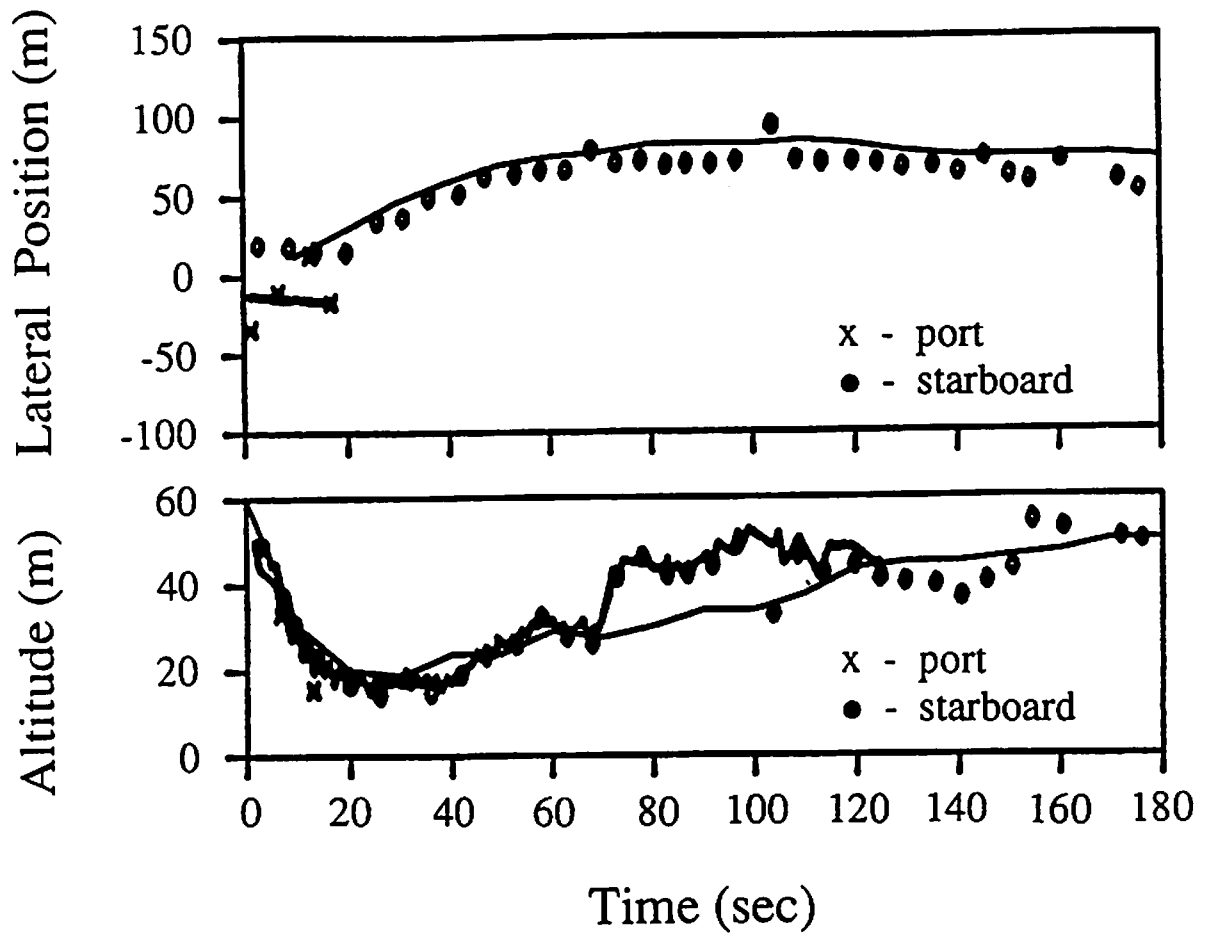
Figure 8. Comparison of our code results (smooth solid lines) with field measurements of (a) lateral and (b) vertical vortex motion from Burnham (1982).
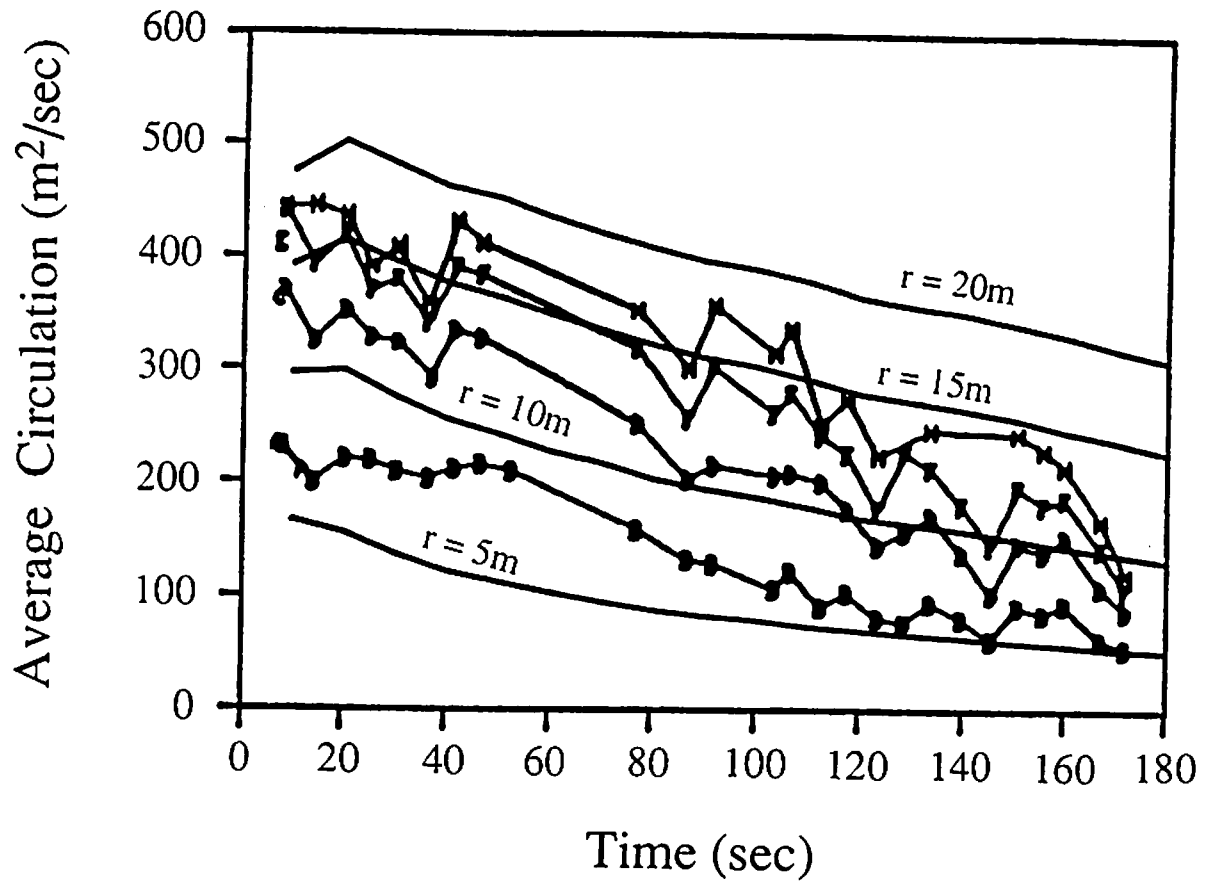
Figure 9. Comparison of our code results (smooth solid lines) with field measurements of average circulation from Burnham (1982) about the vortices whose trajectories are shown in Fig. 8. Results for averaging radii 5, 10, 15, and 20 m are shown.
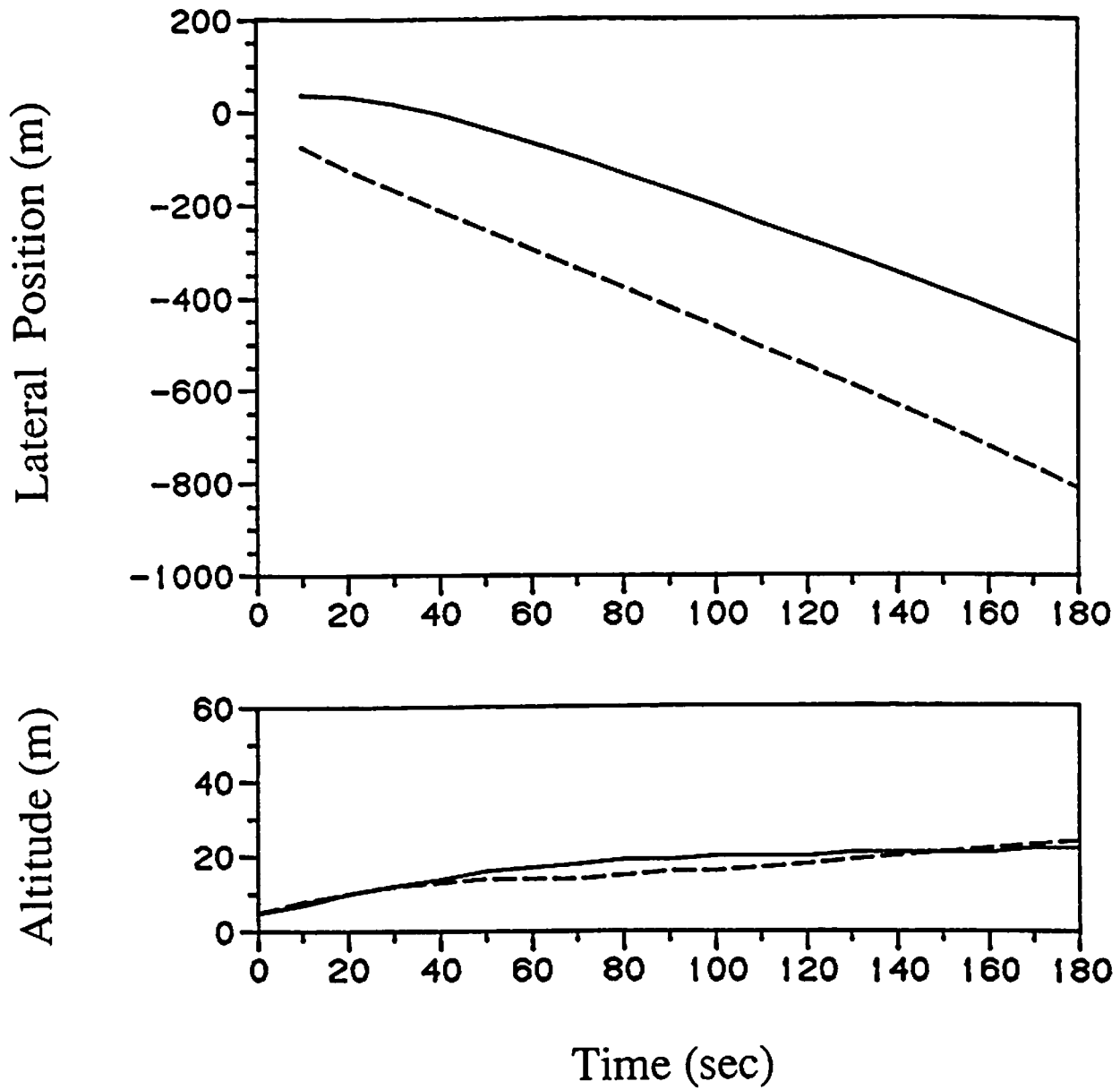
Figure 10. Numerically calculated trajectories of vortices in the wake of a Boeing-767
aircraft landing in the presenceof a crosswind. Lateral position and vertical
altitude of upwind (——) and downwind (—— ——) vortices are shown.
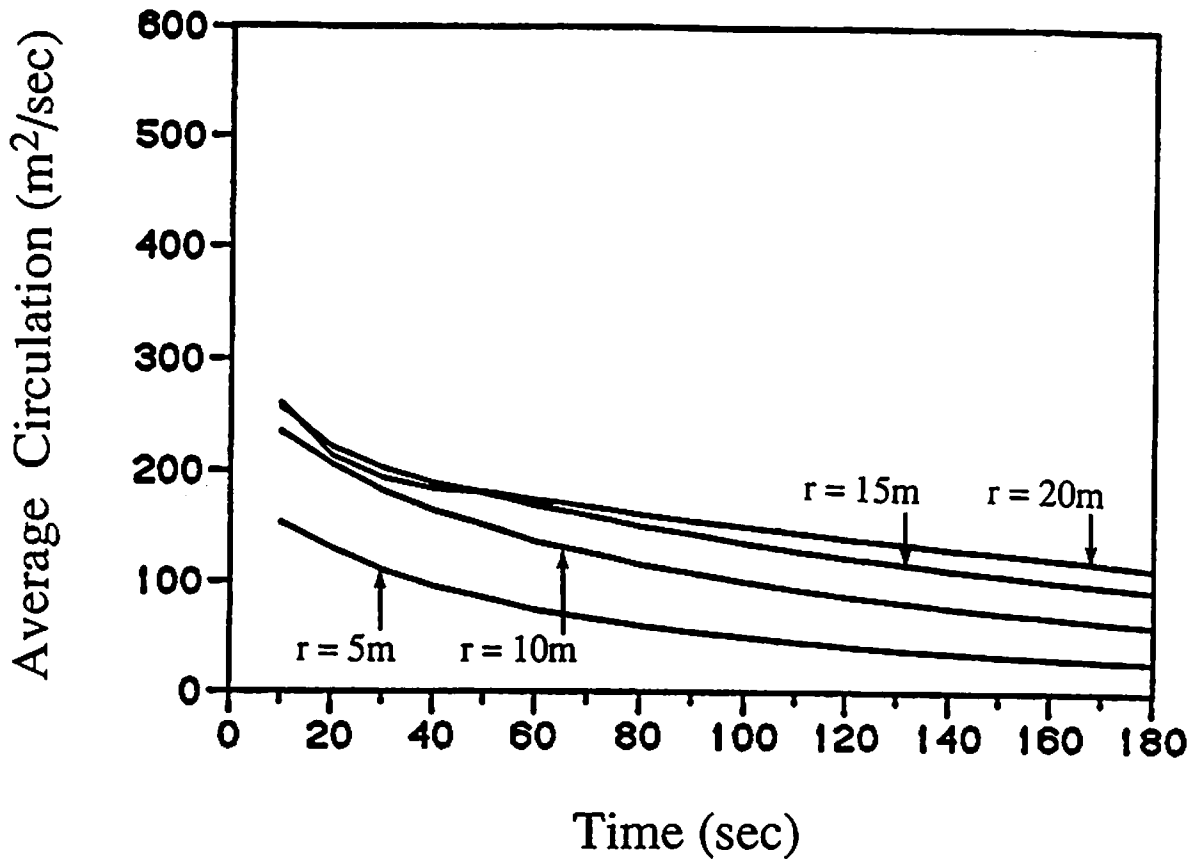
Figure 11. Numerically calculated average circulation about the upwind vortex whose trajectory is presented in Fig. 10. Results for averaging radii 5, 10, 15, and 20 m are shown.
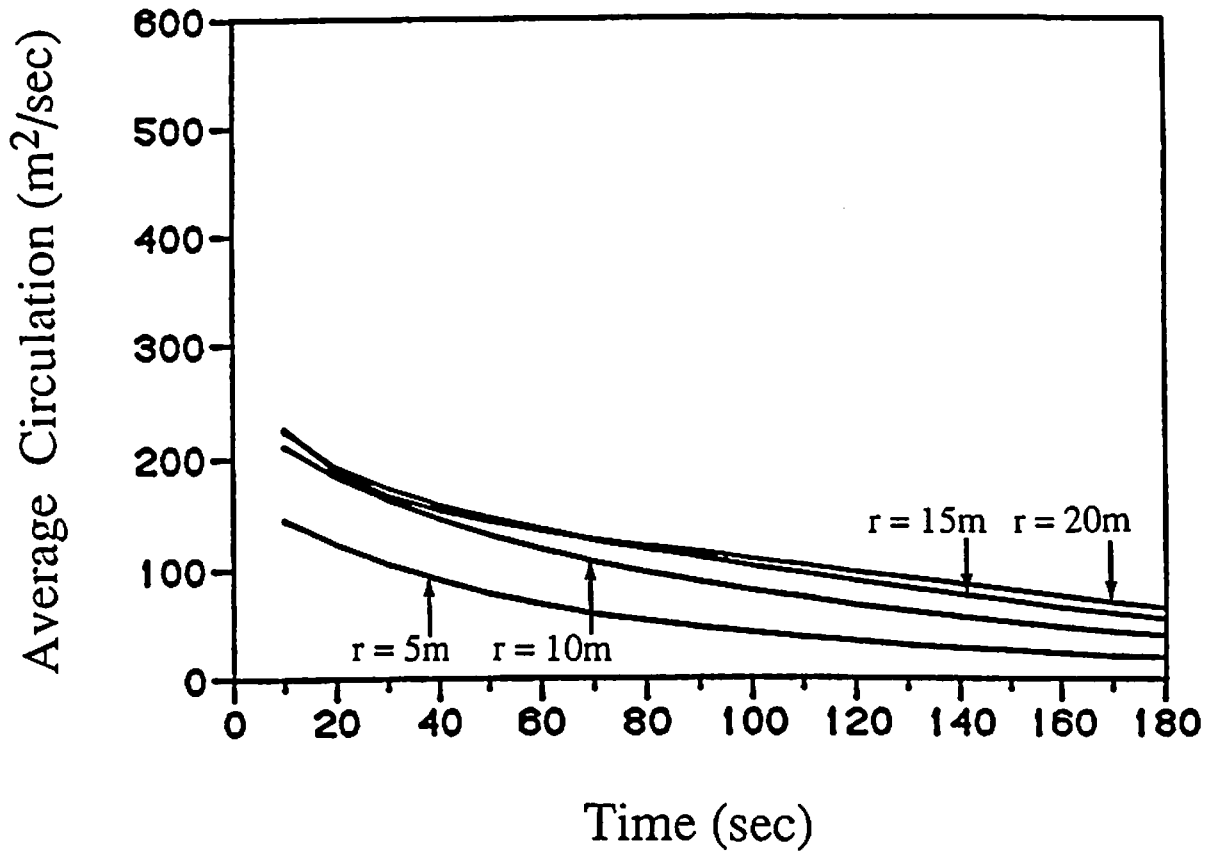
Figure 12. Numerically calculated average circulation about the downwind vortex whose trajectory is presented in Fig. 10. Results for averaging radii 5, 10, 15, and 20 m are shown.

REFERENCES

Barker, S.J. and S.C. Crow (1977), "The Motion of Two-Dimensional Vortex Pairs in a Ground Effect," J. Fluid Mech., 82, pp. 659-671.

Bilanin, A.J., M.E. Teske, and J.E. Hirsh (1978), "Neutral Atmospheric Effects on the Dissipation of Aircraft Vortex Wakes," AIAA Journal, 16, pp. 956-961.

Brashears, M.R., N.A. Logan, and J.N. Hallock (1975), "Effect of Wind Shear and Ground Plane on Aircraft Wake Vortices," J. Aircraft, 12, pp. 830-833.

Burnham, D.C. (1982), "B-747 Vortex Alleviation Flight Tests: Ground-Based Sensor Measurements," U.S. Dept. of Transportation, Federal Aviation Admin. Report DOT-TSC-FAA-81-19.

Burnham, D.C. and J.N. Hallock (1982), "Chicago Monostatic Acoustic Vortex Sensing System, Volume IV: Wake Vortex Decay," U.S. Dept. of Transportation, Federal Aviation Admin. Report DOT-TSC-FAA-79-18.

Burnham, D.C., J.N. Hallock, I.H. Tombach, M.R. Brashears, and M.R. Barber (1978), "Ground-Based Measurements of the Wake Vortex Characteristics of a B-747 Aircraft in Various Configurations," U.S. Dept. of Transportation, Federal Aviation Admin. Report DOT-TSC-FAA-78-28.

Ciffone, D.L., and B. Pedley (1979), "Measured Wake-Vortex Characteristics of Aircraft in Ground Effect," J. Aircraft, 16, pp. 102-109.

Condit, P.M., and P.W. Tracy, (1971), "Results of the Boeing Company Wake Turbulence Test Program," Aircraft Wake Turbulence and Its Detection, ed. J.H. Olsen, A. Goldberg, and M. Rogers, Plenum, New York, pp. 473-508.

Crow, S.C. (1970), "Stability Theory for a Pair of Trailing Vortices," AIAA Journal, 8, pp. 2172-2179.

Dee, F.S. and O.P. Nichols (1968), "Flight Measurement of Wing Tip Vortex Motion Near the Ground," CP 1065, British Aeronautical Research Council.

Delisi, D.P. and T.J. Dunkerton (1989), "Laboratory Observations of Gravity Wave Critical-Layer Flows," Pure and Applied Geophysics, 130, pp. 445-461.

Delisi, D.P., and G.C. Greene (1990), "Measurements and Implication of Vortex Motions Using Two Flow-Visualization Techniques," Journal Aircraft, 27, pp. 968-971.

Delisi, D.P. and I. Orlanski (1975), "On the Role of Density Jumps in the Reflection and Breaking of Internal Gravity Waves," J. Fluid Mech., 69, pp. 445-464.

Delisi, D.P., R.E. Robins, and R.B. Fraser (1987), "The Effects of Stratification and Wind Shear on the Evolution of Aircraft Wake Vortices Near the Ground: Phase I Results," NWRA Report NWRA-87-R006, Northwest Research Associates, Inc., Bellevue, WA.

Delisi, D.P., R.E. Robins, and R.D. Lucas (1991), "Initial Laboratory Observations of the Evolution of a Vortex Pair in a Stratified Shear Flow," in press, Phys. Fluids.

Donaldson, C. DuP., R.S. Snedeker, and R.D. Sullivan (1974), "Calculation of Aircraft Wake Velocity Profiles and Comparison with Experimental Measurements," J. Aircraft, 11, pp. 547-555.

Greene, G.C. (1986), "An Approximate Model of Vortex Decay in the Atmosphere," J. Aircraft, 23, pp. 566-573.

Harvey, J.K., and F.J. Perry (1971), "Flowfield Produced by Trailing Vortices in the Vicinity of the Ground," AIAA Journal, 9, pp. 1659-1660.

Liu, H.-T. and R.A. Srnsky (1990), "Laboratory Investigation of Atmospheric Effects on Vortex Wakes," Flow Research Report No. 497, Flow Research, Inc., Kent, WA.

Peace, A.J., and N. Riley (1983), "A Viscous Vortex Pair in Ground Effect," J. Fluid Mech., 129, pp. 409-426.

Pengel, K. and G. Tetzlaff (1984), "Report of Wake Vortex Measurements with a Ground Wind Vortex Sensing System Using u-v-w Anemometer," Presentation at FAA and NOAA.

Roache, P.J. (1976), Computational Fluid Dynamics, pp. 141 and 145, Hermosa Publishers, Albuquerque, New Mexico.

Robins, R.E. and D.P. Delisi (1991), "The Potential Hazard of Aircraft Wake Vortices in Ground Effect with Crosswind," accepted for publication in J. Aircraft.

Robins, R.E., and D.P. Delisi (1990), "A Numerical Study of Vertical Shear and Stratification Effects on the Evolution of a Vortex Pair," AIAA Journal, 28, pp. 661-669.

Saffman, P.G. (1979), "The Approach of a Vortex Pair to a Plane Surface in Inviscid Fluid," J. Fluid Mech., 92, pp. 497-503.

Sarpkaya, T. (1983), "Trailing Vortices in Homogeneous and Density-Stratified Media," J. Fluid Mech., 136, pp. 85-109.

Sarpkaya, T., and J.J. Daly (1987), "Effect of Ambient Turbulence on Trailing Vortices," J. Aircraft, 24, pp. 399-404.

Scorer, R.S. (1958), Natural Aerodynamics, Pergamon Press, New York.

Tomassian, J.D. (1979), "The Motion of a Vortex Pair in a Stratified Medium," Ph.D. Thesis, Univ. of California, Los Angeles, CA.

Tombach, I.H. (1973), "Observations of Atmospheric Effects of Vortex Wake Behavior," J. Aircraft, 10, pp. 641-647.

Tombach, I., P.B.S. Lissaman, J.B. Mullen, and S.J. Barker (1977), "Aircraft Vortex Wake Decay Near the Ground," U.S. Dept. of Transportation, Federal Aviation Admin. Report DOT-TSC-FAA-77-8.

Van Heijst, G.J.F. and J.B. Flor (1989), Mesoscale/Synoptic Coherent Structures in Geophysical Turbulence, J.C.J. Nihoul and B.M Jouart eds., Elsevier, Amsterdam, pp. 591-608.

VISCOUS EFFECTS ON A VORTEX WAKE IN GROUND EFFECT

Z. Zheng and R. L. Ash
Old Dominion University
Norfolk, VA 23529

ABSTRACT

Wake vortex trajectories and strengths are altered radically by interactions with the ground plane. Prediction of vortex strength and location is especially important in the vicinity of airports. Simple potential flow methods have been found to yield reasonable estimates of vortex descent rates in an otherwise quiescent ambient background, but those techniques cannot be adjusted for more realistic ambient conditions and they fail to provide satisfactory estimates of ground-coupled behavior. The authors have been involved in a systematic study concerned with including viscous effects in a wake-vortex system which is near the ground plane. The study has employed numerical solutions to the Navier-Stokes equations, as well as perturbation techniques to study ground coupling with a descending vortex pair.

Results of a two-dimensional, unsteady numerical-theoretical study are presented in this paper. A time-based perturbation procedure has been developed which permits the use of analytical solutions to an inner and outer flow domain for the initial flowfield. Predictions have been compared with previously reported laminar experimental results. In addition, the influence of stratification and turbulence on vortex behavior near the ground plane has been studied.

INTRODUCTION

It is known that aircraft trailing vortex wakes can cause serious loss of control when following aircraft encounter them. The hazard is more severe near the ground because of the limited time and space available to maneuver the aircraft. Therefore, prediction of wake vortex trajectories and strengths is especially important for effective airport flight control. The work reported here has been focused on the viscous interaction between vortex wakes and the ground plane.

Potential theory representation of a pair of counter-rotating vortex filaments above an infinite plane yields reasonable estimates of wake vortex descent rates in an otherwise quiescent atmosphere, when the wake is sufficiently far from the ground (Saffman, 1979). By assuming the vortices could be treated as small core sized vorticity spots above a very thin ground boundary-layer, Liu and Ting (1987) determined that away from the small cores and the thin boundary-layer region, the flowfield obeyed the Euler equations. From that perspective, it is

very inefficient and expensive to study the trailing vortex problem using Navier-Stokes solvers for the entire flowfield. However, the methods of Liu and Ting (1987) are only valid when the vortical spot is sufficiently far away from the ground relative to the core size, so that vortex-core interactions with the ground-plane boundary layer can be neglected. Hence, Euler equations can be used to model large portions of the computational domain, but that region must be adjusted continuously near the ground plane.

It should be stated that without ground effect, even in more realistic atmospheric conditions, an approximate model developed by Greene (1986) demonstrated surprisingly good agreement with experimental data. That method was based upon empirical engineering approximations. But from the authors' experience, the extension required to include ground effects was not compatible with Greene's model.

Experiments to establish the features of the flowfield induced by a single vortex near the ground were carried out by Harvey and Perry (1971) in a low-speed wind tunnel. The primary objective of those experiments was to explain the cause of the vortex rebound phenomenon which is considered to be a significant feature of the ground effect and which can influence terminal flight conditions. They inferred that rebound was caused by separation of the ground boundary-layer flow underneath the vortex. They argued that boundary-layer separation produces a secondary vortex whose development makes the primary vortex rise. Later Barker and Crow (1977) observed rebound for a vortex pair, generated in water, approaching either a free upper surface or a rigid horizontal plane immersed in the water. They asserted that the phenomenon could be attributed to the effect of finite vortex core size. Recently, experiments were designed by Liu and Srnsky (1990) to minimize the sidewall effects that can mask the ground effects. From their dye visualization results in water, they identified the emergence of secondary, counter-rotating vortices outboard from the vortex wake near ground level. They determined that as soon as the secondary vortex began to form, rebound of the main vortex was initiated. Specifically, the primary and secondary vortices form a vortex pair that moves upward. Those results have confirmed essentially the scenario of secondary vortex generation suggested by Harvey and Perry (1971).

Many theoretical studies of a vortex pair in ground effect have been reported during the last two decades. Research reported by Bilanin, Teske and Hirsh (1978), Saffman (1979) and Peace and Riley (1983) disagreed with the finite core size hypothesis of Barker and Crow (1977). Saffman (1979) showed, within the framework of inviscid theory, that it was not possible to explain the rebound phenomenon by finite core size and that the wallward velocity component cannot change sign. Navier-Stokes computational results for a trailing vortex pair near the ground were performed by Bilanin, Teske and Hirsh (1978) for both laminar and turbulent conditions. They demonstrated that the rebound did not occur unless the viscous, no-slip boundary condition was applied. One of the important conclusions drawn by them was that the proximity of a ground plane reduces the vortex hazard by scrubbing. That is, the vortex pair separates or spreads and interacts viscously with the ground thereby reducing its strength more rapidly. A numerical study of the effects of stratification and wind shear on the evolution of aircraft wake vortices near the ground was also included in the report by Delisi, Robins and Fraser (1987), who found that both effects reduce the extent of vortex rebound. As they stated, turbulence was not included formally in their computational model. But some ad hoc small scale damping was added to the equations included in the numerical model. They thought this simple "turbulence model" was adequate to

predict vortex migration. In addition, a mixed no-slip/slip boundary condition was invoked on the ground plane which needed an empirical adjustment for different flow cases.

In the work which follows, a two-dimensional, unsteady numerical-theoretical study will be reported. A time-dependent double series, asymptotic expansion in terms of Reynolds number and time has been used for the initial flowfield. The computational domain and grid spacing have been chosen carefully to avoid using approximate boundary conditions and to get proper resolution. Subsequently, the influences of stratification and turbulence on vortex behavior near the ground plane have been shown.

COMPUTATIONAL APPROACH

An unsteady vorticity, stream-function formulation has been used in the numerical calculations. Invoking symmetry of the vortex pair permits the computations to be restricted to the first quadrant ($0 \leq x < \infty$, $0 \leq y < \infty$). The system of equations were made dimensionless using the initial vortex half-span, s_0, as the characteristic length and the initial circulation, Γ_0, along with the fluid density, ρ_0, to formulate the other dimensionless variables. The characteristic flow Reynolds number is $Re = \Gamma_0/\nu_0$, where ν_0 is the kinematic viscosity. Characteristic velocity, time and pressure are given by Γ_0/s_0, s_0^2/Γ_0 and $\rho_0\Gamma_0^2/s_0^2$, respectively. Since there is only one component of vorticity, ζ, the governing vorticity and stream-function (ψ) equations are:

$$\frac{\partial \zeta}{\partial t} + (\overline{u} \cdot \overline{\nabla}) \zeta = \frac{1}{Re} \nabla^2 \zeta \qquad (1)$$

and

$$\nabla^2 \psi = -\zeta \qquad (2)$$

respectively. Here

$$\overline{u} = u\,\overline{i} + v\,\overline{j} \qquad (3)$$

and

$$\zeta = \frac{\partial v}{\partial x} - \frac{\partial u}{\partial y}, \text{ with } u = \frac{\partial \psi}{\partial y}, \text{ and } v = \frac{\partial \psi}{\partial x} \qquad (4)$$

The coordinate system is shown in Figure 1.

Since the flow is for the most part inviscid, with an unsteady, viscous ground-plane boundary layer and a small viscous vortex core region, problems were encountered in starting the numerical calculations. The initial velocity field problem has been addressed previously by

Peace and Riley (1983), but they used a single series expansion in time, scaled by Reynolds number (t/Re), to start their asymptotic solution. Limitations of the single series expansion for unsteady boundary-layer flows have been discussed by Nam (1990). Considerable effort was devoted to developing an appropriate initial velocity field which accommodated the ground effect region in the numerical simulation without producing non-physical, numerical start-up transients. A forthcoming contractor report (Ash and Zheng, 1991) contains a more detailed derivation of the asymptotic expansion formulations, but the essential features of the approach are developed below. In addition, the computational domain transformation procedure and boundary condition specifications are discussed.

FLOWFIELD INITIALIZATION

Since a goal of this study was to extend the Reynolds number range over which vortex-ground plane interactions could be modeled, viscous effects were anticipated in both the vortex core and boundary layer regions long before any interactions between the vortex core(s) and boundary layer occurred. Furthermore, a fine numerical grid was required for both the vortex region, including its path of descent, and the ground-plane boundary layer. Both requirements demanded an initial velocity field which was free of anomalous velocity gradients.

The Oseen (1911) vortex is an exact solution to the Navier-Stokes equations for the diffusion of a vortex filament into a viscous region of infinite extent. For any time greater than zero, the Oseen vortex includes viscosity, while at $t = 0$, it is an inviscid point vortex. Hence, placing a pair of those vortices at $\pm x_0$, y_0 at $t = 0$, is equivalent to placing a pair of potential vortices at those locations, but then allowing viscous effects to occur immediately after placement. Oseen vortex solutions do not include either non-linear coupling of the vortex pair or the viscous influence of a ground plane. Adding a mirror image pair of Oseen vortices (at $\pm x_0$, $-y_0$) can be used to initiate a ground plane interaction. Since those vortices proceed immediately to viscous flows, they appear to be a more realistic starting flow than that of a pair of potential vortices in any practical numerical grid. Hence, analytic perturbation methods can be used to predict the flow during the initial time interval when local velocity gradients create severe problems for numerical techniques.

In the ground plane boundary-layer region, the initial stream-function $\psi(x,y,t)$ is assumed to take the form:

$$\psi(x,y,t) = 2\epsilon \left[\psi_1(x,\eta,t) + \epsilon\psi_2(x,\eta,t) + ... \right] \tag{5}$$

where $\epsilon = \sqrt{t/Re}$ and $\eta = y/2\epsilon$, with

$$\psi_i(x,\eta,t) = \sum_{p=0}^{\infty} t^p \phi_p^i(x,\eta,t) \tag{6}$$

31-4

This stream-function must satisfy the no-slip boundary conditions.

In the outer flow, it is assumed that the stream-function can be represented initially by

$$\psi(x,y,t) = \psi_0(x,y,t) + \epsilon\psi_1(x,y,t) +... \tag{7}$$

This stream-function must satisfy the initial potential vortex requirements of both a symmetry plane and a ground plane. Application of the two-dimensional, incompressible Navier-Stokes equations to the two stream-function series and matching the expansions using van Dyke (1976) type matching procedures yields

$$\psi = 2\epsilon(\psi_1 +\epsilon\psi_2) + O\left[\epsilon^3\right] \tag{8}$$

where

$$\psi_1 = U_0\ f_{01} + t\ \left[\frac{\partial U_0}{\partial t}f_{11} + U_0\frac{\partial U_0}{\partial x}f_{12}\right] + O[t^2] \tag{9}$$

$$\psi_2 = U_1 g_{01} + t\ \left[\frac{\partial U_1}{\partial t}g_{11} + U_0\frac{\partial U_1}{\partial x}g_{12} + U_1\frac{\partial U_0}{\partial x}g_{13}\right] + O[t^2] \tag{10}$$

$$f_{01} = \eta\ \mathrm{erf}(\eta) + \frac{1}{\pi^{1/2}}\ e^{-\eta^2} - \frac{1}{\pi^{1/2}} \tag{11}$$

$$f_{11} = \frac{1}{3\pi^{1/2}}\ (1 - e^{-\eta^2}) - \frac{2}{3}\ \eta^3\ \mathrm{erfc}(\eta) + \frac{2}{3\pi^{1/2}}\ \eta^2\ e^{-\eta^2} \tag{12}$$

31-5

$$f_{12} = -\frac{11}{6\pi^{1/2}} \left(1 - e^{-\eta^2} \text{erfc}(\eta)\right) + \frac{8}{3\sqrt{2}\,\pi^{1/2}} \text{erf}\left(\sqrt{2}\,\eta\right) - \frac{1}{3}\left[2 + \frac{4}{3\pi}\right]\eta^3\,\text{erfc}(\eta)$$

$$-\frac{2}{3\pi^{1/2}}\,\eta^2\,e^{-\eta^2}\,\text{erfc}(\eta) + \frac{1}{3\pi}\eta e^{-2\eta^2} - \frac{1}{2}\eta\,\text{erfc}^3(\eta) + \left[\frac{3}{2\pi^{1/2}} - \frac{4}{9\pi^{3/2}}\right]\left(1 - e^{-\eta^2}\right) \tag{13}$$

$$+ \left[\frac{1}{2} - \frac{2}{3\pi}\right]\eta\,\text{erfc}(\eta) - \frac{2}{3\pi^{1/2}}\,\text{erf}(\eta) + \left[\frac{1}{\pi^{1/2}} + \frac{4}{9\pi^{3/2}}\right]\eta^2 e^{-\eta^2}$$

$$g_{01} = \eta + \frac{1}{2}\pi^{1/2}\eta^2\,\text{erfc}(\eta) - \frac{1}{2}\eta e^{-\eta^2} - \frac{1}{4}\pi^{1/2}\,\text{erf}(\eta) \tag{14}$$

$$g_{11} = \frac{\pi^{1/2}}{4}(\eta^3 + \eta^4)\,\text{erfc}(\eta) + \frac{1}{2}\int_0^\eta (-\eta^2 + \eta^4)e^{-\eta^2}d\eta \tag{15}$$

$$g_{12} = \int_0^\eta \left\{ \frac{7}{6}\pi^{1/2}\left[\eta + \frac{2}{3}\eta^3\right] - \frac{\pi^{1/2}}{4}\left[\left(\eta + \frac{2}{3}\eta^3\right)\text{erf}(\eta) + \frac{2}{3\pi^{1/2}}(1 + \eta^2)e^{-\eta^2}\right]\right.$$

$$+ \pi^{1/2}\left[-\frac{1}{2}\eta - \eta^3\right](\text{erf}(\eta))^2 + \left[-\frac{1}{2} - 2\eta^2\right]e^{-\eta^2}\text{erf}(\eta) - \frac{1}{8}\eta e^{-2\eta^2} \tag{16}$$

$$\left. - \pi^{1/2}\eta\,\text{erf}(\eta) - \frac{2}{3}\text{erf}(\eta) + \frac{2}{3} - \frac{1}{2}e^{-\eta^2}\right\}\,d\eta$$

$$\tag{16}$$

$$g_{13} = \frac{3}{8}\pi^{1/2}\left[\eta^2 + \frac{1}{3}\eta^4\right]\text{erfc}(\eta) + \frac{1}{2}\int_0^\eta \left[\eta^2 + \frac{1}{3}\eta^4\right]e^{-\eta^2}d\eta \tag{17}$$

It is noted that $U_0(x,t)$ and $U_1(x,t)$ are the outer flow representations of the vortices along the ground plane $(y = 0)$. These solutions are restricted to small times and are given by

$$U_0(x,t) = \frac{4}{\pi} \ \frac{y_0 x}{\left[(x-1)^2 + y_0^2\right]\left[(x+1)^2 + y_0^2\right]} \tag{18}$$

and

$$U_1(x,t) = \frac{2}{\pi^{3/2}} \int_0^\infty \frac{\partial U_0}{\partial x} \Big|_{x=\xi} \ \frac{d\xi}{x-\xi} \tag{19}$$

which are the same forms used by Peace and Riley (1983).

In effect, four Oseen vortex solutions, with Cartesian velocity components given by

$$\begin{aligned}
U_c(x,y,t) &= (y - y_0)[\Phi(x,y,t; -1, y_0) - \Phi(x,y,t; 1,y_0)] \\
&\quad + (y + y_0)\left[\Phi(x,y,t;1, - y_0) - \Phi(x,y,t; - 1, - y_0)\right]
\end{aligned} \tag{20}$$

and

$$\begin{aligned}
V_c(x,y,t) &= (x - 1)[\Phi(x,y,t;1,y_0) - \Phi(x,y,t; 1, - y_0)] \\
&\quad + (x+1)[\Phi(x,y,t; - 1, - y_0) - \Phi(x,y,t; - 1, y_0)]
\end{aligned} \tag{21}$$

where

$$\Phi(x,y,t;\alpha,\beta) = \frac{1}{2\pi} \ \frac{1 - e^{-R_c[(x-\alpha)^2+(y-\beta)^2]/4t}}{(x-\alpha)^2+(y-\beta)^2} \tag{22}$$

have been employed in the outer flow, in the vicinity of $x = 1$, $y = y_0$. Again, these functions are restricted to small times, where they do not alter the asymptotic matching conditions.

To summarize, the asymptotically generated velocity field, which constitutes the initial velocity distribution in the numerical scheme, is a combination of solutions (7), (8), (20) and (21). Small values of time, compared to the Reynolds number, have been employed. The asymptotic solution time level selected to generate the initial velocity field depended on the circulation Reynolds number, but it was the maximum time allowable by the finite term approximations to the infinite series expansions. The asymptotic solutions were thus used to produce an initial velocity field whose local gradients could be handled by the numerical grid, but whose series representations did not represent a significant amount of computational overhead.

DOMAIN TRANSFORMATION AND BOUNDARY CONDITIONS

A moving grid was considered for this study but was discarded subsequently, due to the complexity of the vortex trajectory in ground effect and to uncertainty in the viscous zones requiring fine grid resolution. It was deemed more reasonable to pack grid points adjacent to the symmetry- and ground-planes and allow the vortex system to move with respect to the grid. This was possible because the nominal regions where viscous effects occurred were known to a first order approximation. It is noted further that the elliptic character of the incompressible flowfield mandates enforcing the boundary conditions at the infinite limits of x and y or alternatively-developing rigorous boundary condition approximations within a finite domain.

Bilanin et al (1977) and Ting (1983) studied the far field boundary condition problem. They used the far field expansions of Poisson integrals which could be employed in a finite subdomain of an unbounded fluid. The exponential decay laws for vorticity distributions were required for the convergence of the far field expansions (Ting, 1983). The expansions were developed further by Ting (1983) using integral invariants. Unfortunately, neither the decay laws nor the integral invariants exist when a no-slip boundary is present because the vorticity distribution in the viscous ground-plane boundary layer cannot be estimated *a priori*. Here a coordinate mapping has been used, employing a simple exponential transformation which yields densely packed grid points near the ground plane and stretches the grid as the infinite limits are approached. The mapping

$$X = a \left(1 - e^{-bx}\right)$$
$$Y = c \left(1 - e^{-dy}\right) \tag{23}$$

transforms $0 \leq x < \infty$, $0 \leq y < \infty$ into the finite domain $0 \leq X < a$, $0 \leq Y < c$. The corresponding spacing intervals are

$$\Delta X \approx abe^{-bx} \Delta x$$
$$\Delta Y \approx cde^{-dy} \Delta y \tag{24}$$

Hence the boundary-layer and vortex core resolution can be controlled by adjusting the arbitrary constants a, b, c and d.

Since the ground plane spacing is compressed automatically via the coordinate mapping, resolution requirements are more severe in the far field. In addition, vortex core resolution in the vertical direction is most sensitive at start-up ($y = y_0$), while horizontal resolution is least accurate at the end of the numerical simulation (when the vortex core is at the greatest horizontal distance from the symmetry plane) -- say x_1. Since the vortex dilates as time increases, selecting an appropriate grid spacing initially produces a conservative spacing level at later times.

As an example, if the initial vortex core radius is $r_c = 0.2$, then we would require that $\Delta y_{max} = 0.02$ ($= r_c/10$) at y_0, and that $\Delta x_{max} = 0.1$ ($= r_c/2$) at x_1. The Δx_{max} spacing will be more

compact relative to the vortex core due to dilation beginning from $t = 0$. However, the spacing interval is given by:

$$\Delta X \leq 0.1 \, abe^{-bx_1} \tag{25}$$

and

$$\Delta Y \leq 0.01 \, cde^{-xy_*} \tag{25}$$

Since the number of grid increments in the X-direction must satisfy $M\Delta X = a$, while $N\Delta Y = c$,

$$M \geq \frac{10e^{bx_1}}{b}$$

and

$$N \geq \frac{50e^{dy_*}}{d} \tag{26}$$

The minimum number of grid points for acceptable resolution occurs when $b = 1/x_1$, and $d = 1/y_0$ and is given by

$$M \geq 10x_1 e$$

and

$$N \geq 50y_0 e \tag{27}$$

The boundary conditions in the transformed domain are:

$$\zeta(0,Y,t) = 0, \quad \psi(0,Y,t) = 0, \tag{28}$$

$$\zeta(a,Y,t) = 0, \quad \psi(a,Y,t) = 0, \tag{29}$$

$$\varsigma(X,0,t) = -c^2 d^2 \frac{\partial^2 \psi}{\partial Y^2} (X,0,t), \qquad (30)$$

$$\varsigma(X,c,t) = 0, \text{ and } \psi (X,c,t) = 0. \qquad (32)$$

The discretized expression for the ground-plane vorticity, Eq. (30), was developed by Roache (1972), and is given by

$$\varsigma(X,0,t) \approx - 2\psi_n c^2 d^2 / \Delta Y^2 \qquad (33)$$

where the subscript, n, indicates the grid locations adjacent to the ground plane.

In this study, the vertical grid spacing was fine enough to permit implementation of the no-slip boundary condition on the ground plane without exaggerating numerically the viscous interaction encountered previously by Delisi, Robins and Fraser (1987).

While the velocity boundary conditions appear to be overspecified (Anderson, 1986), they are compatible with the velocity components in the transformed domain, given by

$$u = \frac{\partial \psi}{\partial Y} d (c - Y)$$

$$v = - \frac{\partial \psi}{\partial X} b (a - X) \qquad (34)$$

which can be easily verified. These boundary conditions also satisfy the integral conditions developed by Anderson (1986).

An alternating-direction implicit (ADI) scheme was used to solve the vorticity transport equation (1), with the upwind flux-splitting method applied to the convection terms and central-differencing for diffusion terms. An efficient Poisson solver (Swarztrauber and Sweet, 1979) was used to solve Eq.(2). Viscous flow in a driven cavity was chosen as a test problem for that computational scheme to explore the capability of capturing the secondary-vortex evolution phenomena at high Reynolds number. The systematic numerical studies of this problem are well-documented in Bozeman and Dalton (1973) and Rubin and Harris (1975).

STRATIFICATION EFFECTS

The present analysis has employed the Boussinesq approximations to model buoyancy effects. Specifically, the local density has been assumed related linearly to temperature via

$$\rho = \rho_0 \left[1 - \alpha \left(T - T_0 \right) \right] \tag{35}$$

where α is the volumetric coefficient of thermal expansion and $\alpha \ll 1$. Hence, the density departure from the reference value can be represented in dimensionless form as

$$\tilde{\rho} = \left(\rho - \rho_0 \right)/\rho_0 = -\alpha \left(T - T_0 \right) \tag{36}$$

The complete Boussinesq model neglects all density variation effects except the body force term in the momentum equation so that the conservation of momentum equations results in the modified vorticity transport equation:

$$\frac{\partial \zeta}{\partial t} + \left(\vec{u} \cdot \vec{\nabla} \right) \zeta = -\frac{1}{F_v^2} \frac{\partial \tilde{\rho}}{\partial x} + \frac{1}{Re} \nabla^2 \zeta \tag{37}$$

where

$$F_v^2 = \Gamma_0^2 / g s_0^3 \tag{38}$$

For the case of a linearly stratified ambient fluid, the dimensionless temperature, θ, defined by

$$\theta \equiv (T - T_0)/T_0 \tag{39}$$

is assumed given in the quiescent, ambient state as

$$\theta = \beta y \tag{40}$$

Hence, the ambient density departure is given by

$$\bar{\rho} = -\alpha \beta y T_0 \tag{41}$$

or

$$\bar{\theta} = -\bar{\rho}/\alpha T_0 \tag{42}$$

31-11

Similarly, the density and temperature fluctuations are related such that

$$\rho' = \tilde{\rho} - \bar{\rho}$$
$$\theta' = \theta - \bar{\theta}$$

(43)

and

$$\rho' = -\alpha T_0 \theta'$$

(44)

Neglecting viscous dissipation, the appropriate conservation of energy equation, invoking the Boussinesq approximation is:

$$\frac{\partial \theta}{\partial t} + (\vec{u} . \vec{\nabla})\theta = \frac{1}{RePr} \nabla^2 \theta,$$

(45)

which can be written in terms of the density fluctuations (through Eq. (44)) for the stably stratified case as

$$\frac{\partial \rho'}{\partial t} + u\frac{\partial \rho'}{\partial x} + v\frac{\partial \rho'}{\partial y} + v\frac{d\bar{\rho}}{dy} = \frac{1}{RePr}\nabla^2 \rho'$$

(46)

Restricting attention to cases where $RePr \gg 1$, we can neglect the diffusion terms and the conservation of energy equation becomes:

$$\frac{\partial \rho'}{\partial t} + (\vec{u} . \vec{\nabla})\rho' = -v\frac{d\bar{\rho}}{dy} .$$

(47)

Alternatively, buoyancy effects could have been introduced through the compressible conservation of mass equation. By expanding the conservation of mass equation in terms of the volumetric coefficient of thermal expansion, α, the incompressible continuity equation and Eq. (46) evolve from the zeroth and first order groupings in the α expansion. Hence, the numerical simulation is modified via Eqs. (37), (41) and (47) when stratification effects are included. The computational scheme was easily modified to include stratification since the same grid was used and the density fluctuation equation could be implemented using the same procedures employed for the vorticity transport equation.

It is noted that the dimensionless parameter, F_v, which appears in the vorticity transport Eq. (37), is related to the Brunt-Vaisala frequency. That is, if the dimensionless density gradient is defined by

then the Brunt-Vaisala frequency, N, is given by

$$n^2 \equiv - \frac{d\bar{\rho}}{dy} \qquad (48)$$

$$N^2 = - \frac{g}{s_o} \frac{d\bar{\rho}}{dy} = \frac{\Gamma_0^2 n^2}{s_0^4 F_v^2} \qquad (49)$$

Stratification effects represent additional difficulties because of the characteristic time introduced via Brunt-Vaisala or density induced oscillations. If $s_0^2 N / \Gamma_0 \ (=n/F_v) \gg 1$, buoyancy effects are significant and the characteristic time $\left(s_0^2/\Gamma_0 \right)$ is large compared with the time interval over which density induced oscillations occur. The complication arising from these two characteristic times has been examined in detail by Hirsh (1985). For more realistic physical problems, F_v is typically quite large and the stratified density gradient (through n) is not large enough to result in large values of $s_0^2 N / \Gamma_0$. Consequently, a limiting test case is when the two time scales are equivalent $\left(s_0^2 N / \Gamma_0 \approx 1 \right)$.

Simulations were run with $s_0^2 N / \Gamma_0 = 1$, but the density effects were so large that major vortices of opposite sign were generated very rapidly and the flow quickly became unstable numerically.

AMBIENT TURBULENCE

Inclusion of turbulent effects is an important element of this study. However, due to the approximate nature of turbulence models, initial work has restricted attention to limited types of turbulent processes and simple models. It is assumed here that atmospheric turbulence is being generated by axial (z-direction) wind shear. Since stratification effects are under investigation, it should be noted that buoyancy induced turbulence effects are usually small in the immediate vicinity of the ground, when compared to wind-driven fluctuations and have been neglected. However, some very important types of buoyancy-driven turbulence phenomena are known to occur with potentially serious consequences (e.g., microbursts), but those processes are too complicated to be modelled reliably at this time. These catastrophic-type, buoyancy-driven turbulence effects supercede wake-vortex prediction requirements and should be investigated separately. In addition, turbulence is generated by the wake vortex structures themselves. Those turbulence generation processes are also outside of the turbulence modelling capabilities employed in the present study.

The dimensionless vorticity transport equation can be written in index notation as

$$\frac{D\Omega_i}{Dt} - \Omega_j \frac{\partial u_i}{\partial x_j} = \frac{1}{R_e} \nabla^2 \Omega_i \tag{50}$$

By assuming that the vorticity components can be decomposed into (slowly varying) time mean and (rapidly varying) unsteady parts, i.e.,

$$\Omega_i = \overline{\Omega}_i + \Omega_i' \tag{51}$$

with

$$u_i = \overline{u}_i + u_i'$$

then the Reynolds averaged vorticity transport equation can be written:

$$\frac{\partial \overline{\Omega}_i}{\partial t} + \frac{\partial}{\partial x_j} \left(\overline{\Omega}_i \overline{u}_j \right) - \overline{\Omega}_j \frac{\partial \overline{u}_i}{\partial x_j} = \frac{1}{R_e} \nabla^2 \overline{\Omega}_i + \frac{\partial}{\partial x_j} \left(\overline{\Omega_j' u_i'} \right)$$

$$- \frac{\partial}{\partial x_j} \left(\overline{u_j' \Omega_i'} \right) \tag{52}$$

Here, we restrict attention to mean flows which are steady and parallel in the z-direction, i.e., $\overline{w} = \overline{w}(y)$ so that

$$\overline{u} = \overline{u}(x,y,t) \tag{53}$$

and

$$\overline{v} = \overline{v}(x,y,t)$$

These are essentially two-dimensional flows, but permit the existence of two mean vorticity components. That is,

$$\overline{\Omega}_1 = \frac{d\overline{w}}{dy} = \overline{\Omega}_1(y)$$

and

31-14

$$\bar{\Omega}_3 = \bar{\zeta}(x,y,t), \tag{54}$$

with

$$\bar{\Omega}_2 = 0$$

Consequently, the governing equation on $\bar{\zeta}$ becomes:

$$\frac{\partial \bar{\zeta}}{\partial t} + \frac{\partial}{\partial x}(\bar{u}\,\bar{\zeta}) + \frac{\partial}{\partial y}(\bar{v}\,\bar{\zeta}) = \frac{1}{R_e}\nabla^2\bar{\zeta} - \frac{\partial}{\partial x}\overline{u'\Omega'_3} - \frac{\partial}{\partial y}\left(\overline{v'\Omega'_3}\right)$$
$$+ \frac{\partial}{\partial x}\left(\overline{w'\Omega'_1}\right) + \frac{\partial}{\partial y}\left(\overline{w'\Omega'_2}\right) \tag{55}$$

where the $\overline{u'_i\Omega'_j}$ terms are the terms which must be modelled.

We have already stated that atmospheric turbulence has not been coupled with vortex-generated turbulence in this study. Essentially, it is assumed that the aircraft vorticity field behaves like a passive scalar, immersed in atmospheric turbulence. In that context, we have assumed that

$$\overline{\Omega'_i u'_j} = -c_1 q \Lambda \frac{\partial \bar{\Omega}_i}{\partial x_j} \tag{56}$$

where q^2 is the local turbulent kinetic energy,

$$q^2 = \frac{1}{2}\overline{u'_k u'_k}, \tag{57}$$

while Λ is a turbulent length scale and c_1 is the turbulence modelling constant. It is assumed that q and Λ are not altered by vortex interactions.

In order to utilize Eq. (56), it is necessary to model q and Λ. Bilanin, Teske and Hirsh (1978) have employed a second order closure model, using similar nomenclature, to study vortex wake decay. When the wake vortex velocity field did not contribute to the turbulence, it was possible to show that q was constant both near the ground plane and in the far field. In addition, the von Karman constant, κ, can be used to model the characteristic turbulent length scale near the ground as

$$\Lambda \approx \kappa y. \tag{58}$$

Since Λ should be constant away from the ground, it was necessary to model the intermediate zone. Here, we have assumed that

$$\Lambda \approx c_2\left(1-e^{-\kappa y/c_2}\right) \tag{59}$$

which matches Eq. (58) for small y. von Karman's constant has been taken as 0.4 in this study, leaving c_2 as the remaining arbitrary constant.

Employing Eq. (56) in Eq. (55) yields:

$$\frac{\partial \bar{\zeta}}{\partial t} + \frac{\partial}{\partial x}\left(\bar{u}\ \bar{\zeta}\right) + \frac{\partial}{\partial y}\left(\bar{v}\ \bar{\zeta}\right) = \frac{1}{R_e}\Delta^2\bar{\zeta} + c_1 q\Lambda\ \frac{\partial^2\bar{\zeta}}{\partial x^2} \\
+ c_1 q\frac{\partial}{\partial y}\ \left[\Lambda\frac{\partial\bar{\zeta}}{\partial y}\right] \tag{60}$$

where Λ is given by Eqs. (58) and (60) and c_1, c_2 and q are evaluated using experimental data.

RESULTS

Based upon previous numerical studies, it was determined that the vortex core centers could be placed at $x_o = 1$, $y_o = 2$ (and $x_o = -1$, $y_o = 2$, from symmetry) to start the simulations. That vertical distance $y_o=2$ was deemed close enough to the ground plane to produce detectable coupling effects after moderate time intervals after start-up, but it was also far enough from the ground plane to enable the vortex flowfield to establish itself prior to strong ground-plane interactions. The initial vortex core was assumed to have a core radius, r_c , of 0.2 and a 150 x 300 grid was employed in the numerical simulations reported herein. Calculations were performed using a Cray II computer at NASA Langley Research Center.

Limited experimental data were available for numerical validation studies. Only the experiments of Liu and Srnsky (1990) were used. Their vortex flows were produced using an NACA 0012 wing model and the estimated circulation based Reynolds number (Γ_o/ν) was 7,650. Their experiments did not investigate stratification effects near a ground plane.

For the unstratified, validation studies, circulation Reynolds numbers of 1000, 7,650 and 75,000 were simulated. Figure 2(a) represents the trajectories (x(t), y(t)) followed by the three simulated vortices, along with the measured trajectory of Liu and Srnsky (1990). The time histories of x(t) and y(t) for the four vortex cases are shown in Figures 2(b) and (c), respectively. The agreement between the numerical simulation and the experiment is quite good.

In order to assess the influence of Reynolds number, stratification and turbulence on the vortex hazard, some measure of hazard strength was required. However, since the computational

31-16

domain is an unbounded quadrant, overall or global measures of circulation or velocity levels appeared to be of little value. It was finally decided that circulation and kinetic energy histories in the aircraft approach zone would be meaningful. The zone was selected somewhat arbitrarily to be the area bounded by $-2 < x < 2$ and $0 < y < 3$, which would span a typical runway entrance. The velocity components and vorticity were computed at each grid point within the right half of that area ($0 < x < 2$, $0 < y < 3$) at each time level. Subsequently, zonal circulation, $\Gamma(2\text{x}3)$, was calculated by integrating the vorticity over the half area and the instantaneous kinetic energy within the zone, $E(2\text{x}3)$, was computed by a similar integration of

$(u^2+v^2)/2$. Those histories are shown in Figure 3 for the extreme Reynolds number cases (1000 and 75,000). The experiments of Liu and Srnsky did not report circulation and energy history data of this type.

Data were not available for comparison between simulated vortex flows in a stably stratified ambient environment with ground effect. Stratification effects were tested for a circulation-based Reynolds number of 1000, at dimensionless Brunt-Vaisala frequencies (n/F_v) of $N = 0.05$ and $N = 0.1$. The predicted results for this laminar flow case are displayed in Figure 4, along with the unstratified case ($N = 0$), for comparison. The trajectories, lateral and vertical position histories, along with circulation strength $\Gamma(2 \times 3)$ and kinetic energy $E(2 \times 3)$ histories are displayed in Figures 4(a) through (e), respectively.

The background turbulence model, discussed in the previous section, was incorporated in the simulations for a circulation-based Reynolds number of 75,000. A global turbulence constant, C, defined by

$$C \equiv c_1 c_2 q$$

is all that is required to model this eddy-viscosity type turbulence (since c_2 was chosen as 0.5) and values of $C = 0.001$ and 0.1 were employed in the simulations. The combined effects of Reynolds number, turbulence and ground effect on vortex motion and strength are shown in Figure 5.

DISCUSSION

While the laminar flow simulations (Re = 1000) are less realistic, in terms of aircraft vortices, they are less ambiguous, in terms of effects of turbulence models and numerical uncertainties. Consequently, vortex rebound and stratification effects derived from fundamental phenomena can be discussed with more certainty for those flow cases. Thus stratification effects in the vicinity of the ground plane have altered vortex trajectories rather remarkably, as shown in Figure 4.

Referring to Figure 4, it can be seen that the vortex appears to literally try to "fall back down hill" in both stratified cases, even though the initial descent and rebound trajectories nearly coincide with the unstratified case. The mechanism which is responsible for that effect can best be explained by comparing the computational flow visualization results from the unstratified case ($N = 0$) with the stratified case ($N = 0.1$).

Figures 6 and 7 are color panels comparing the vorticity distributions at four time levels for an unstratified flow (Figure 6) and a stratified flow (Figure 7). Streamfunction contours are compared in Figures 8 and 9.

The stratification effect on vortex trajectory is most easily understood by looking at the density distribution. Figure 10 shows density departure contours (from Eq. 41, via V8,35 via ρ' given in Eq. 43) at four different times. There, it can be seen that relatively higher density fluid is pulled from the ground plane around the primary vortex, where it tends simultaneously to compress the vortex and cause more rapid vortex deceleration due to increased inertia. While the vortex doesn't actually roll back toward the ground by reversing itself like a wheel, the density distributions show that the body forces actually push the primary vortex back toward the ground plane and the lateral density variations even push the vortex toward the symmetry plane. Clearly, density stratification can confine then destroy trailing line vortices much more rapidly than any other process considered in this study.

CONCLUSIONS

This study has shown that trailing line vortex flows can be resolved in the vicinity of a ground plane. Vortex trajectory comparisons with the experimental measurements of Liu and Srnsky are in quite good agreement. The preliminary inclusion of modelled turbulence effects has not produced any startling results. On the other hand, density stratification can have a very pronounced effect on vortex trajectories. At the admittedly high stratification levels considered here, we have shown that vortex hazard alleviation could be facilitated by density stratification effects within the immediate vicinity of airport runways.

ACKNOWLEDGEMENT
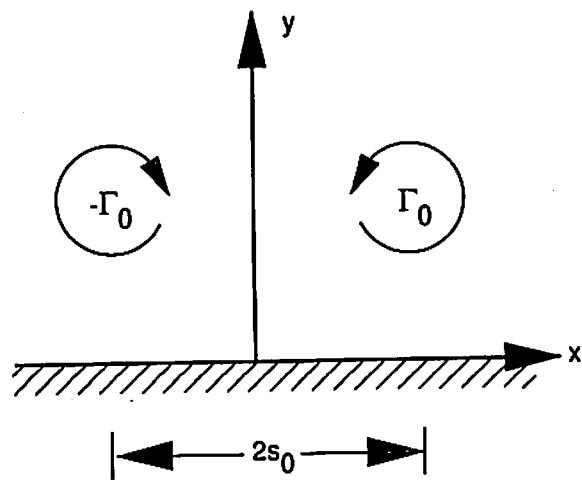
Figure 1. Coordinate system employed in this study.
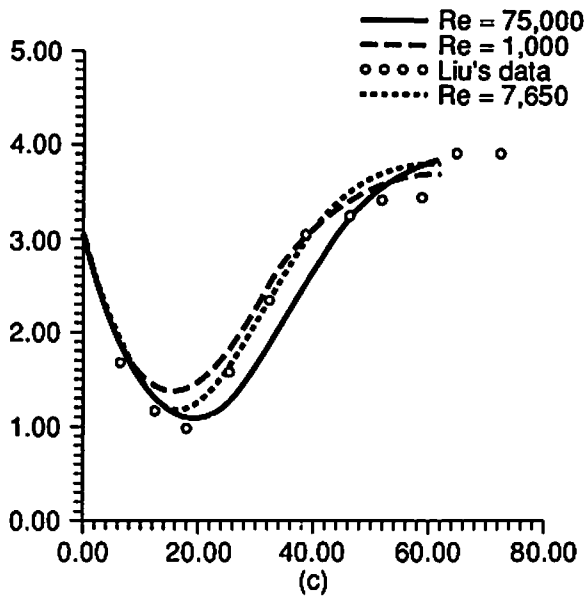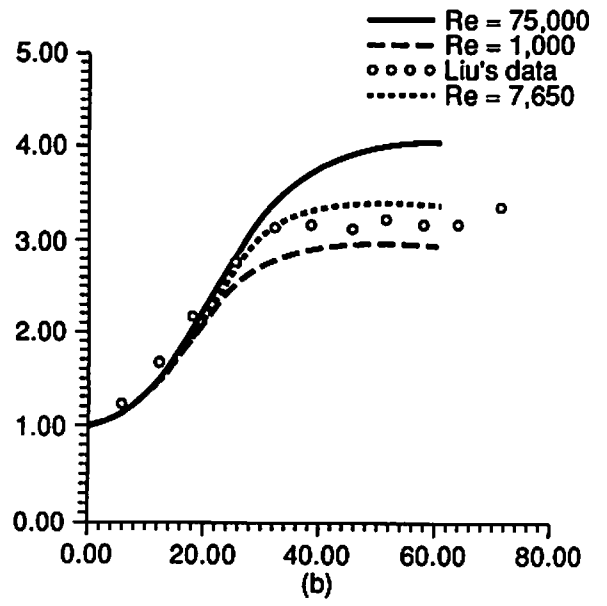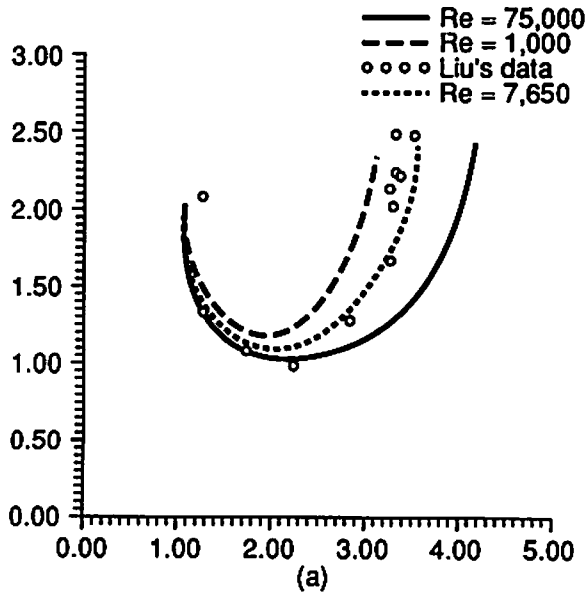
Figure 2. Comparison between computed and measured (a) vortex trajectories,
(b) lateral vortex position histories, (c) vortex elevation histories,
at various Reynolds numbers.
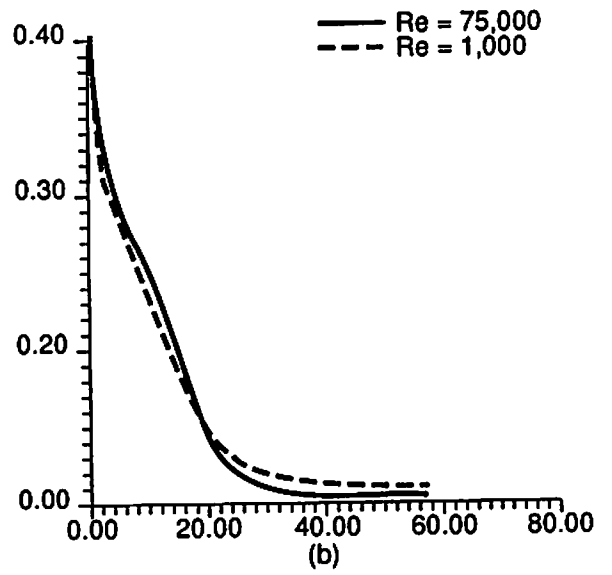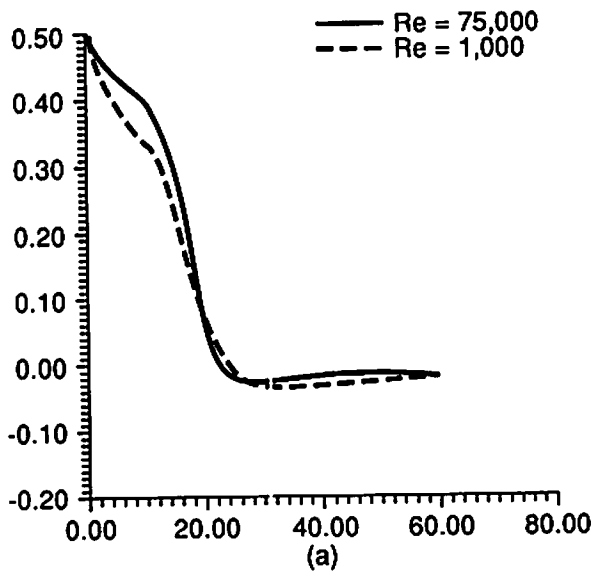
Figure 3. Predicted variation of (a) circulation (23), (b) kinetic energy E(23), with time for various Reynolds numbers.
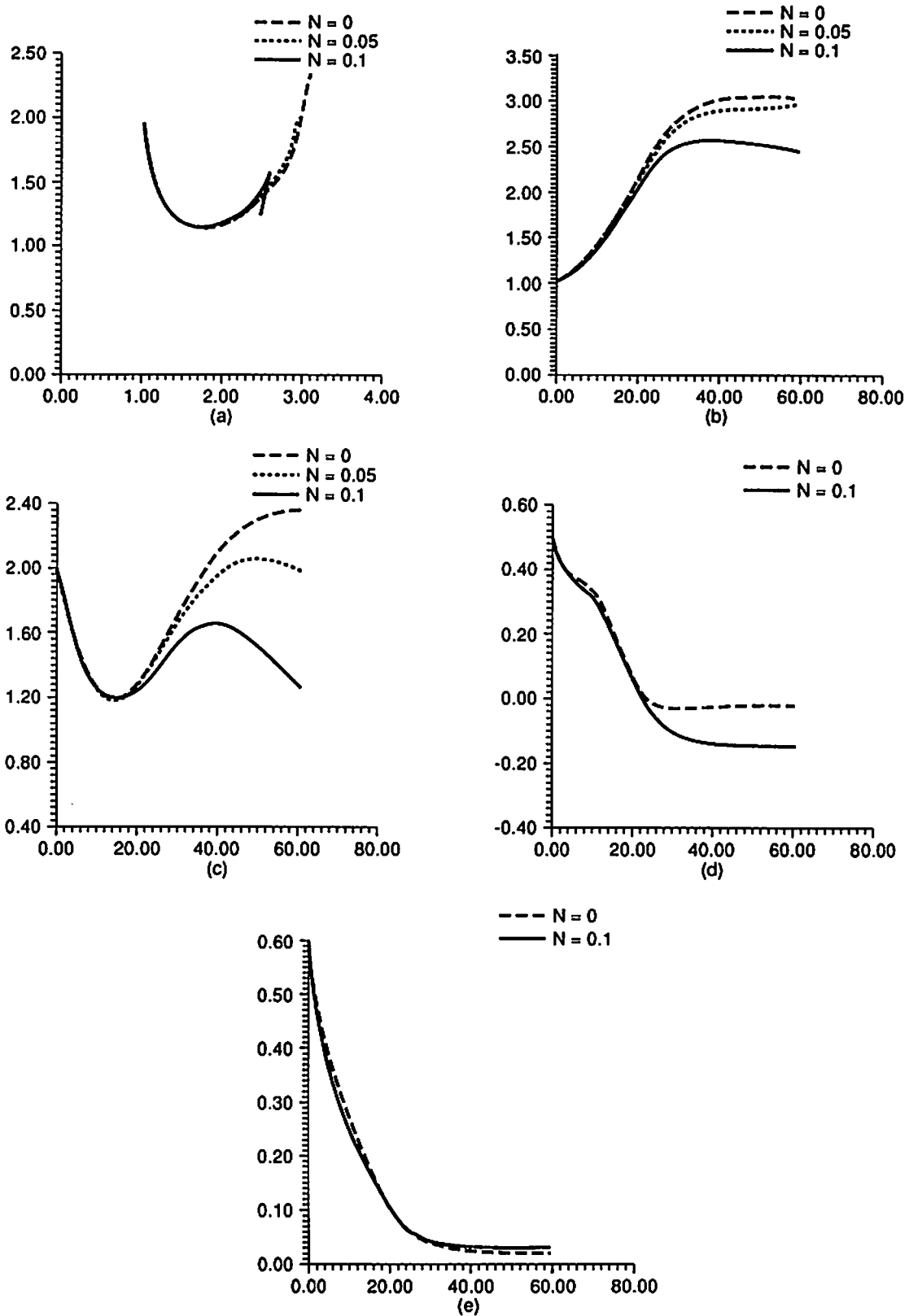
Figure 4. Influence of stratification on predicted (a) vortex trajectories, (b) lateral vortex position histories, (c) elevation histories, (d) circulation Γ(2×3), (e) kinetic energy E(2×3), Re=1000.
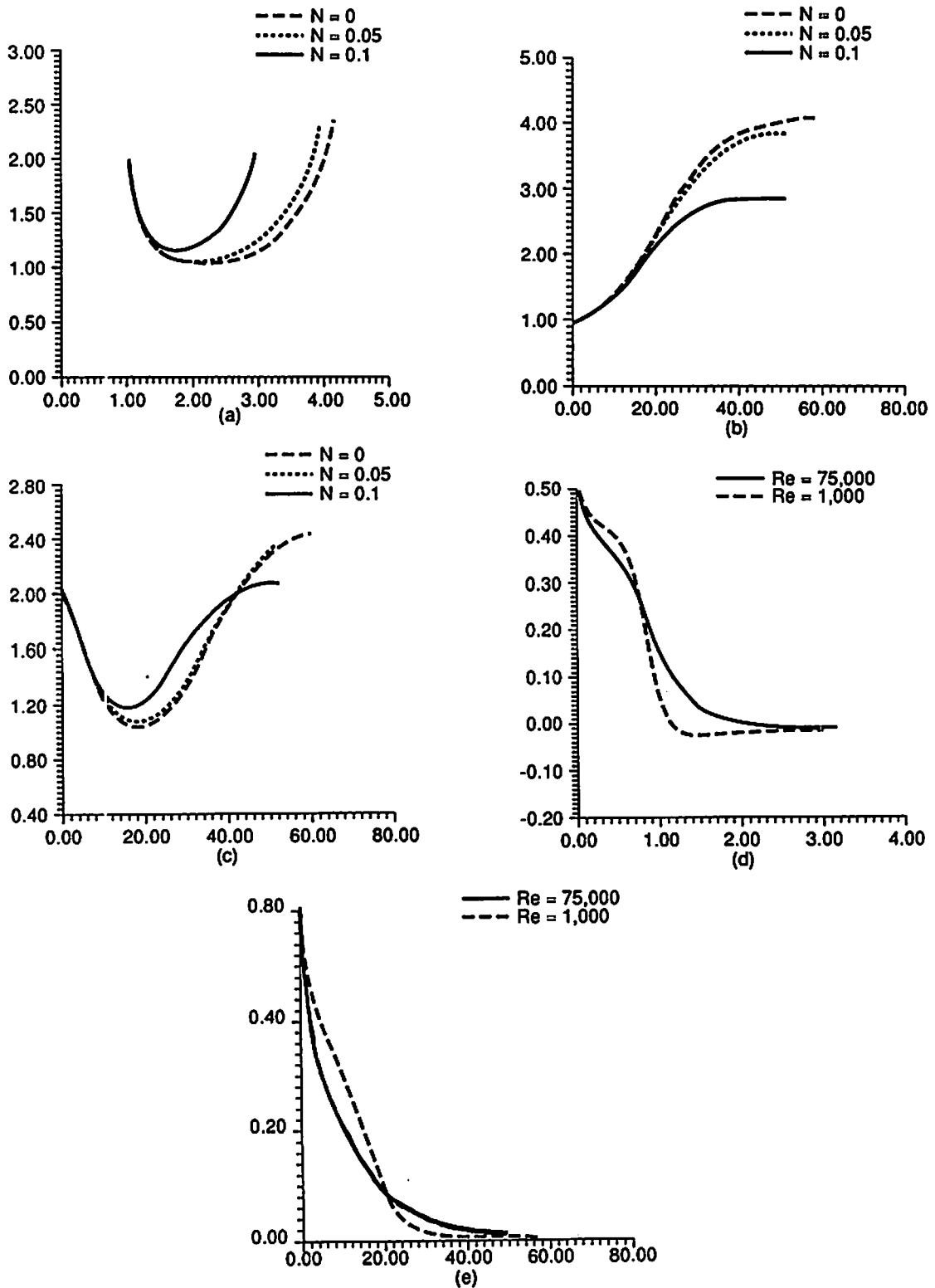
Figure 5. Influence of turbulence on predicted (a) vortex trajectories, (b) lateral vortex position histories, (c) elevation histories, (d) circulation Γ(2×3), (e) kinetic energy E(2×3), Re=1000.

31-23
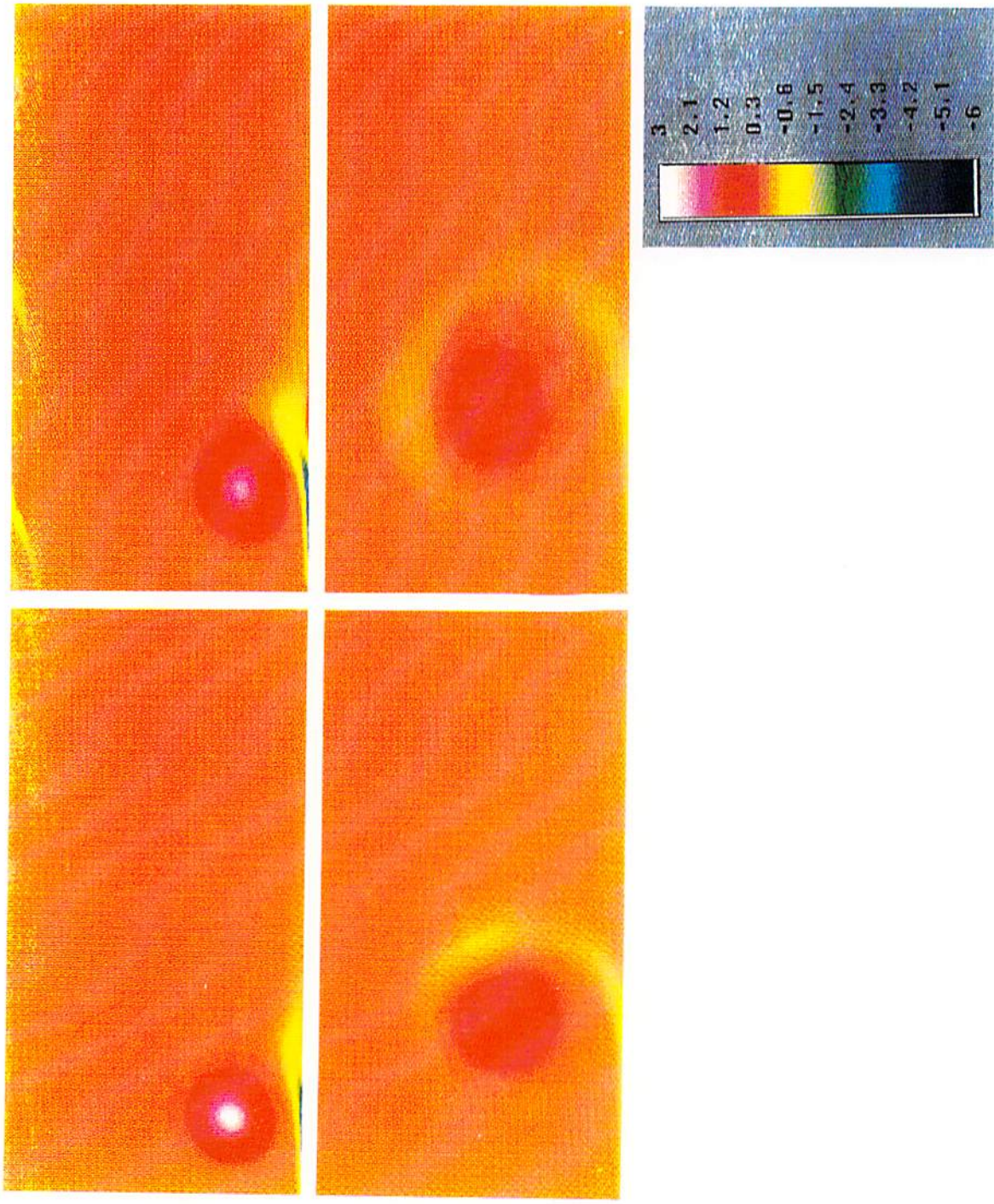
Figure 6. Vorticity distributions at t=10, 14, 40, 60 for an unstratified flow, Re=1000.
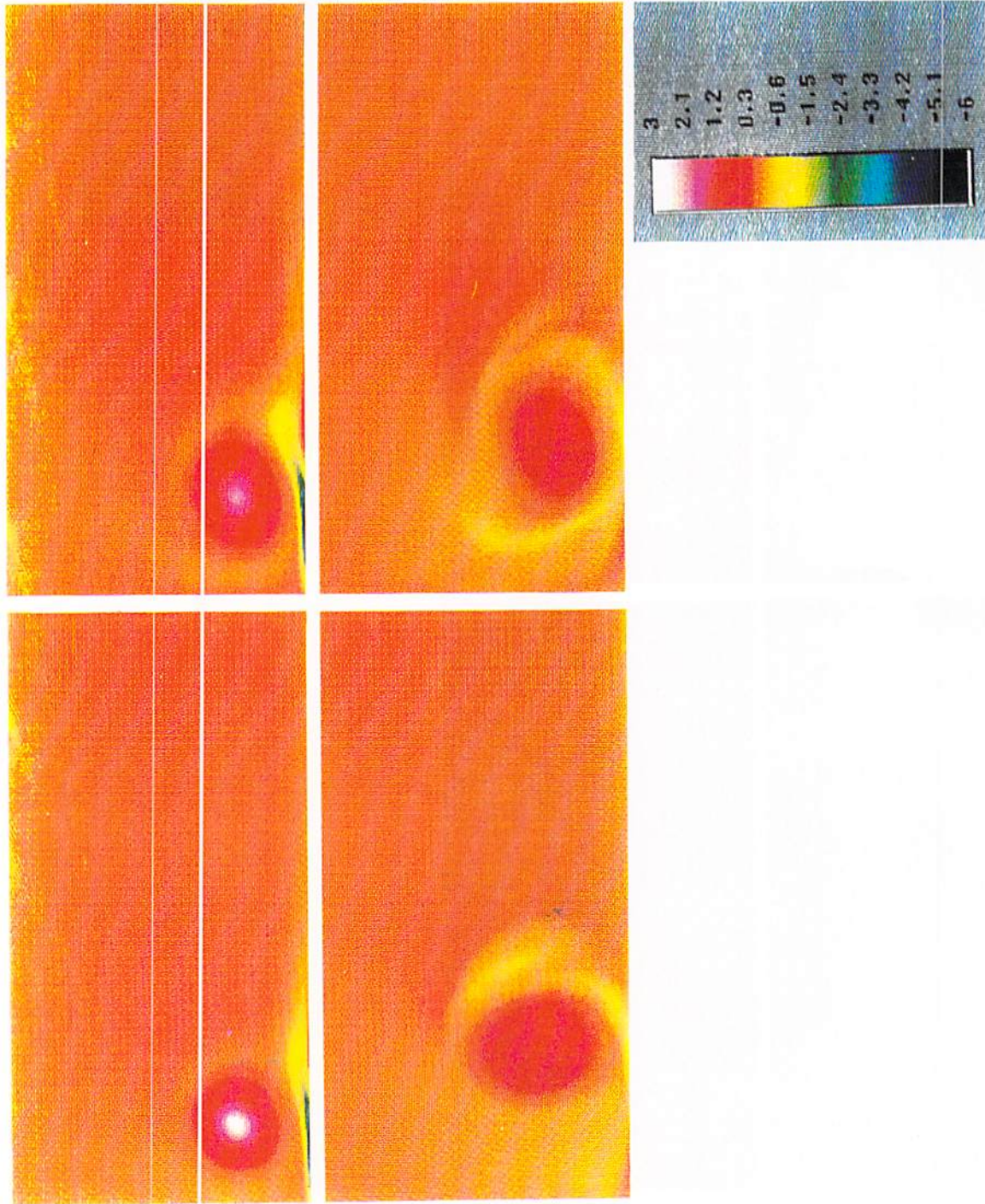
Figure 7. Vorticity distributions at t=10, 14, 40, 60 for a stratified flow, Re=1000, N=0.1.
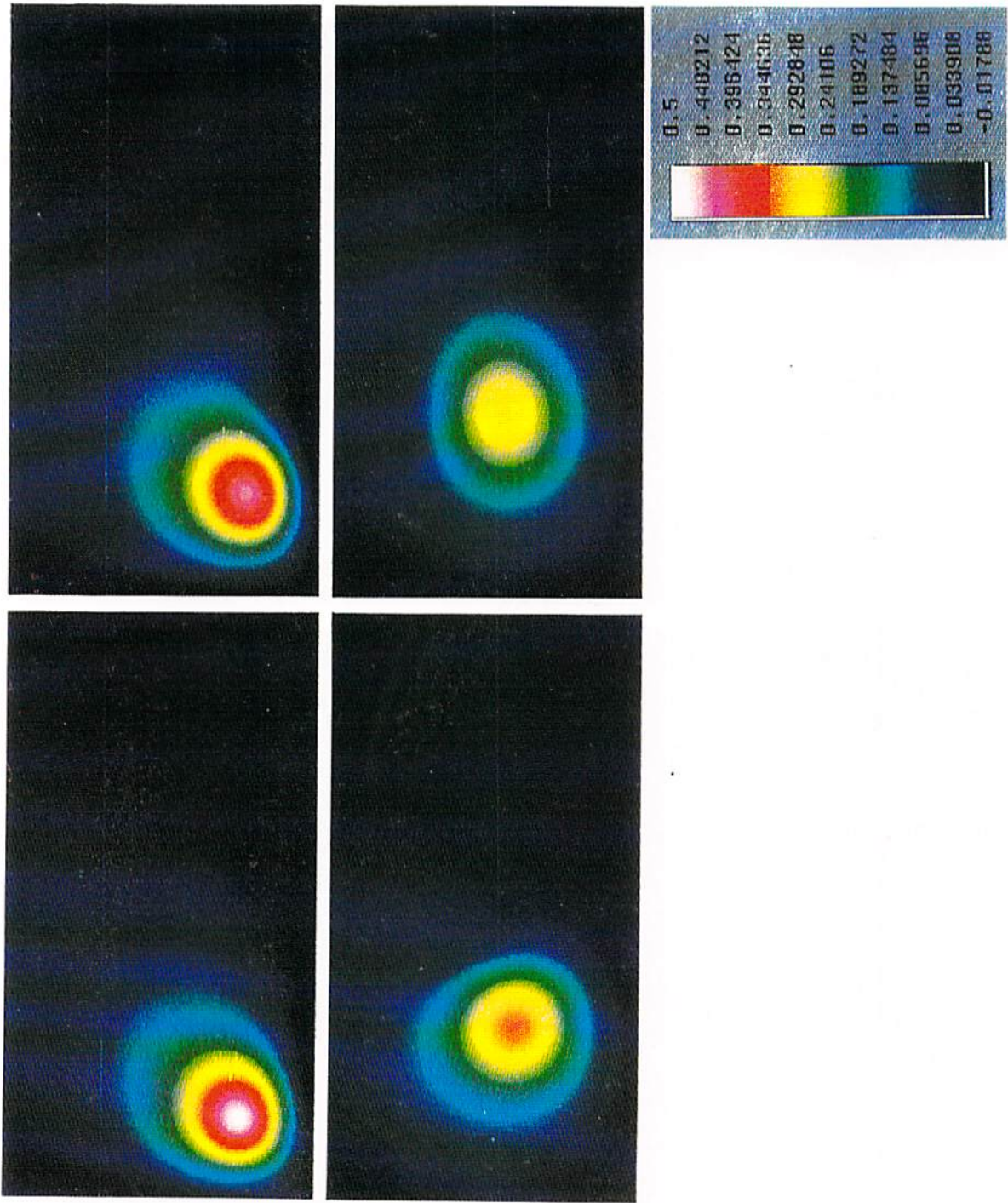
Figure 8. Streamfunction contours at t=10, 14, 40, 60 for an unstratified flow, Re=1000.
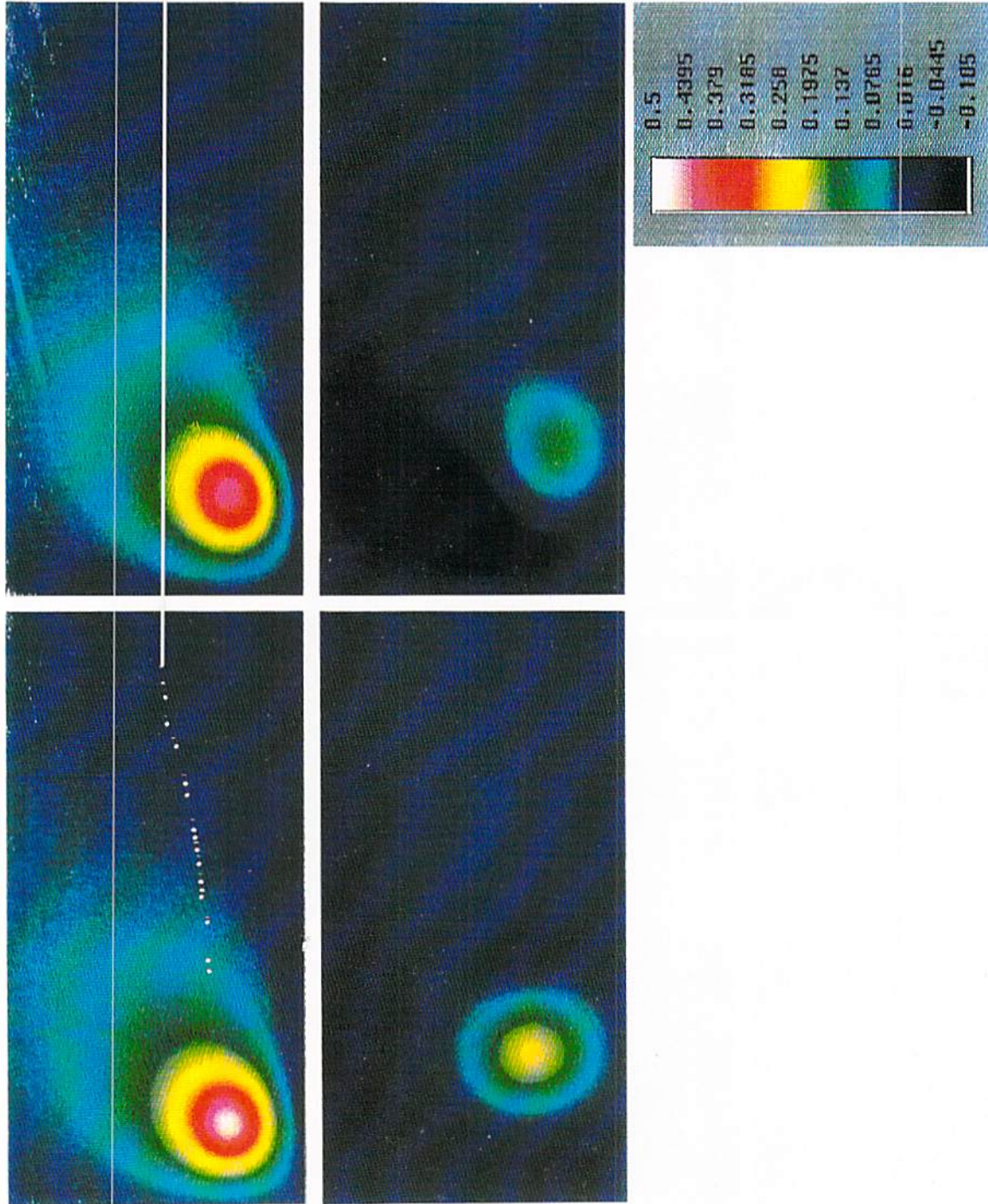
Figure 9. Streamfunction contours at t=10, 14, 40, 60 for a stratified flow, Re=1000, N=0.1.
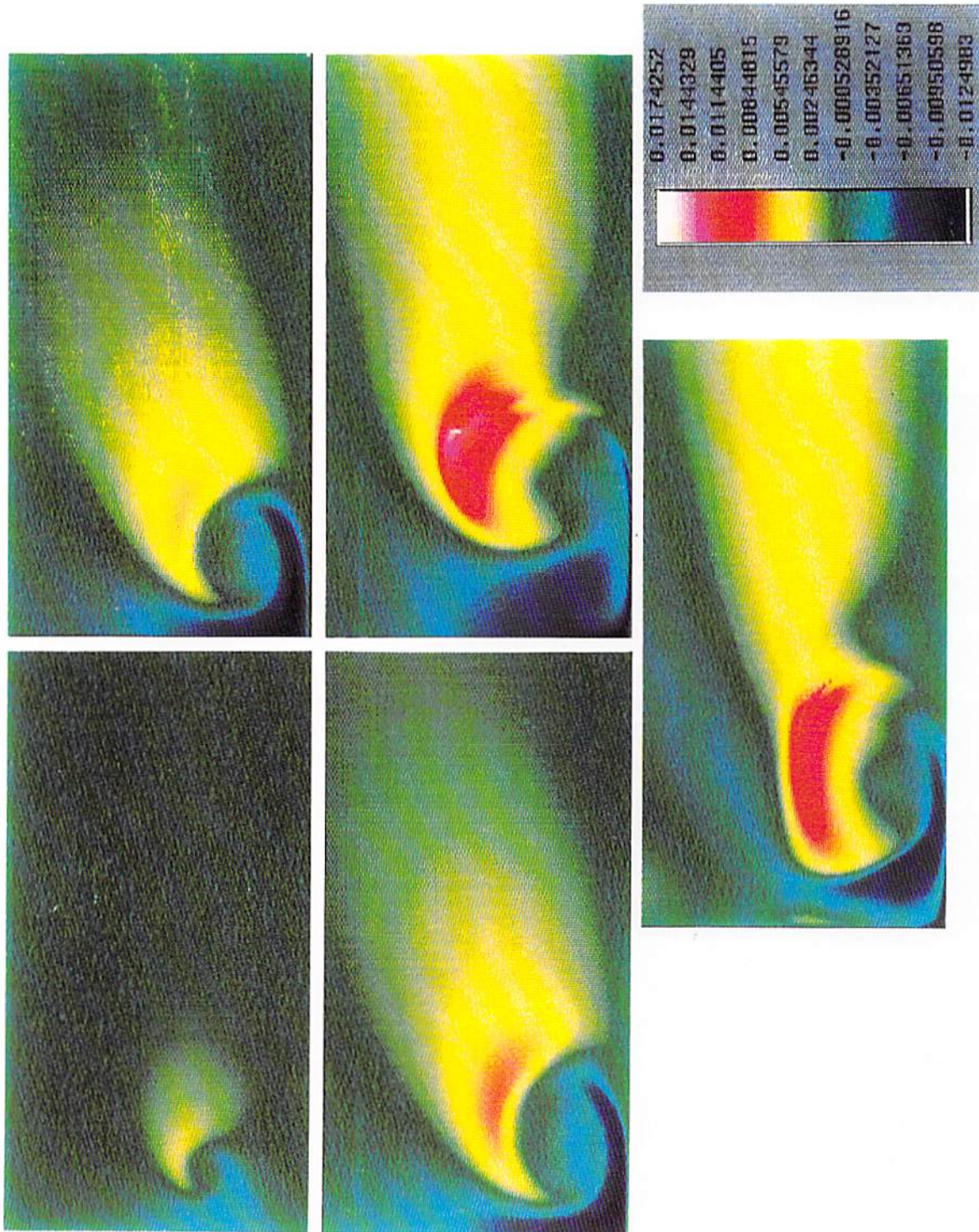
Figure 10. Density departure contours at t=2, 10, 40, 60, for a stratified flow, Re=1000, N=0.1.

The legend shows the following values:

0.0174252
0.0144329
0.0114405
0.00844815
0.00545579
0.00246344
-0.0005288916
-0.00352127
-0.00651363
-0.00950598
-0.0124983

REFERENCES

Anderson, C. R. 1986 On vorticity boundary conditions. Center for Large Scale Scientific Computation, Stanford University, Report Classic 86-14.

Ash, R. L. and Zheng, Z. 1991. NASA Contractor Report.

Baker, S. J. and Crow, S. C. 1977 The motion of two-dimensional vortex pairs in ground effect. J. Fluid Mech. 82, pp. 659-671.

Bilanin, A. J., Teske, M. E., Donaldson, C. duP. and Williamson, G. G. 1977 Vortex interactions and decay in aircraft wakes. NASA Contractor Report, NASA CR-2870.

Bilanin, A.J., Teske, M.E. and Hirsh, J.E. 1978 Neutral atmospheric effects on the dissipation of aircraft vortex wakes. AIAA J. 16, pp. 956-961.

Bozeman, J.D. and Dalton, C. 1973 Numerical study of viscous flow in a cavity. *J. Computational Physics* 12, pp. 348-363.

Delisi, D.P., Robins, R.E. and Fraser, R.B. 1987 The effects of stratification and wind shear on the evolution of aircraft wake vortices near the ground: Phase I Results. Northwest Research Associates, Inc. NWRA-87-R006.

Greene, G.C. 1986 An approximate model of vortex decay in the atmosphere. *J. Aircraft* 23, pp. 566-573.

Harvey, J.K. and Perry, F.J. 1971 Flowfield produced by trailing vortices in the vicinity of the ground. AIAA J. 9, pp. 1659-1660.

Hirsh, R.S. 1985 A numerical simulation of vortex motion in a stratified environment and comparison with experiments. Johns Hopkins APL Technical Digest, 6, pp. 203-210.

Liu, C.H. and Ting, L. 1987 Interaction of decaying trailing vortices in spanwise shear flow. *Computers & Fluids* 15, pp. 77-92.

Liu, H.T. and Srnsky R.A. 1990 Laboratory investigation of atmospheric effects on vortex wakes. Flow Research Inc. Technical Report No. 497.

Oseen, C.W. 1911 Uber wirbelbewegung in einer meibenden flüssigkeit. Arkiv För Matematic, Astronomi Och Fysik 7, pp. 1-13.

Peace, A.J. and Riley, N. 1983 A viscous vortex pair in ground effect. J. Fluid Mech. 129, pp. 409-426.

Roach, P.J. 1972 *Computational Fluid Dynamics*, Hermosa Pub.

Rubin, S.G. and Harris, J.E. 1975 Numerical studies of incompressible viscous flow in a driven cavity. NASA SP-378.

Saffman, P.G. 1979 The approach of a vortex pair to a plane surface in inviscid fluid. *J. Fluid Mech.* 92,
pp. 497-503.

Swarztrauber, P.N. and Sweet, R.A. 1979 Algorithm 541, Efficient FORTRAN subprograms for the solution of separable elliptic partial differential equations [D3]. ACM Trans. on Math. Software 5, pp. 352-364.

Ting, L. 1983 On the application of the integral invariants and decay laws of vorticity distributions. *J. Fluid Mech.* 127, pp. 497-506.

TOW-TANK SIMULATION OF VORTEX WAKE DYNAMICS

H.-T. Liu
QUEST Integrated, Inc.,
(formerly Flow Research, Inc.)
Kent, Washington

ABSTRACT

Towing tank experiments were conducted to investigate ambient and ground effects on vortex wakes. Two methods were used to generate the vortex wakes: a towed NACA 0012 wing with a chord Reynolds number of 20,400 and a slotted-jet vortex generator. The ambient turbulence was generated by towing upstream of the wing three grids of different meshes. Turbulence parameters were measured with crossed hot-film probes. The trailing vortex wake, tagged with a fluorescent dye, was visualized and its evolution was derived from 16-mm movie records. For weak turbulence with large integral scales compared with the vortex separation, vortex linking is the dominant mode of instability. The dominant wavelength of the linking decreases with increasing turbulence intensity or dissipation rate. As the turbulence intensity increases, vortex bursting appears and eventually replaces linking as the dominant mode of instability. For turbulence with a small integral scale as compared with the vortex separation, vortex instability is predominantly of the bursting type.

Trajectories derived from trailing vortex wakes near a simulated ground surface have confirmed the inadequacy of the two-dimensional inviscid solution. The generation of a relatively weak secondary vortex causes the primary vortex to rebound from the surface as a result of unsteady separation. For the slotted-jet vortex generator, the introduction of a rigid surface close to the jet exit results in the formation of relatively strong and persistent secondary vortices at the ground outboard of the primary vortices. A simple modification of the two-dimensional inviscid theory -- namely, adding a secondary vortex to the system -- recreates the rebound phenomenon, which agrees qualitatively with the trend seen in the experiments.

INTRODUCTION

Studies have demonstrated that atmospheric disturbances such as stratification, wind shear, and turbulence have a strong influence on the evolution of aircraft vortices.[1-3] However, systematic investigation of these processes is hampered by difficulties in controlling the test conditions and in collecting quantitative results during full-scale flight tests. On the other hand, wind tunnel

testing is limited for studying the wake evolution process because the vortex wake is quickly swept downwind of the working section. Although empirical, analytical, and numerical models have been developed to investigate the vortex wake phenomenon, these models have not been subjected to thorough verification due to the lack of quantitative field or laboratory data.[2-6] An operational analytical/numerical model that takes into consideration all the important atmospheric disturbances does not currently exist.

As soon as a vortex wake is formed, the aging process begins as a consequence of turbulence diffusion, entrainment, and dissipation. In a quiescent background, de-intensification of vortex pairing results from sinusoidal instability[7] and from vortex breakdown.[8,9] Sinusoidal instability is a convective instability that arises by balancing the self-induced rotation of a sinusoidally deformed vortex with the velocity induced at this vortex by the deformed opposite vortex.[7] The amplification rate of the instability is exponential in time and depends on the vortex core structure.[10] As a result of the sinusoidal instability, linking of the two trailing vortices occurs at the position of minimum separation and leads to the formation of a series of vortex rings.

Vortex breakdown or bursting may be described as the abrupt structural change of the tube of a vortex that is precipitated in a smooth flow seemingly for no reason. The exact cause of vortex breakdown is not yet thoroughly understood, although simplified theories have been developed in an attempt to explain the breakdown phenomenon.[11] Vortex breakdown manifests itself as a localized bursting phenomenon, or a sudden increase in the diameter of a single vortex core, and often results in a very turbulent flow.

In a turbulent environment, the aging of vortex wakes becomes a complicated process. Several investigators have studied the effects of ambient turbulence through numerical simulation. Bilanin et al.[3] studied numerically the dissipation of a 2-D vortex wake in the presence of ambient turbulence. A second-order closure model was used to represent the turbulence. The numerical results show that the circulation drop-off as a function of time changes from $t^{\frac{1}{2}}$ with no ambient turbulence to t^2 with turbulence. However, the 2-D model is incapable of addressing the behavior of sinusoidal instability and of vortex bursting because these phenomena are inherently three-dimensional.

Assuming that the integral scale of the ambient turbulence is large compared with the vortex separation, Crow and Bate[2] derived the following expression to predict the lifespan of a trailing vortex pair or the time at which the two vortices touch due to linking instability:

$$t_t^{*1/4}e^{-0.83t^*} = 1.15\,\epsilon^*, \qquad \epsilon^* < 0.3 \tag{1a}$$

and

$$t_t^* = 0.41\,\epsilon^{*-1}, \qquad \epsilon^* > 0.3 \tag{1b}$$

where $\epsilon^* = (\epsilon b_o/W_o^3)^{1/3}$ and $t_f^* = W_o t_f/b_o$. Here, $b_o = S\pi/4$ is the vortex separation, t_f is the lifespan, W_o is the initial vortex downwash velocity, and ϵ is the turbulence dissipation rate. The two parts of Eq. (1) are matched at $\epsilon^* = 0.3$.

Using a light Cessna 170 airplane with a wingspan of about 11 m, Tombach[1] conducted a series of experiments in the atmospheric boundary layer under a wide range of stability conditions. He estimated the lifespan of the vortex pair from the visual records and found that the data may be enveloped by two lines:

$$t = 15 \ \epsilon^{1/3} \tag{2a}$$

and

$$t = 70 \ \epsilon^{1/3} \tag{2b}$$

where t is the time. For the cases where linking of the vortex pair was observed, the lifespan agrees fairly well with the predictions of Crow and Bate,[2] i.e., Eq. (1). One finding of particular interest is that at any level of turbulence the lifespan tends to be the same, regardless of whether the instability is bursting or linking. This suggests that, at least to first order, $\epsilon^* = (\epsilon b_o/W_o^3)^{1/3}$ may be the only dimensionless parameter required to determine the effects of ambient turbulence on the lifespan of vortex wakes. For isotropic turbulence,[12] the following relationship holds:

$$\epsilon = Kq^2/L_f \quad \text{with} \quad K = 0.25 \tag{3}$$

where q^2 is the total turbulence kinetic energy and L_f is the integral scale of the turbulence. If Eq. (3) is proven sufficient to specify the ambient turbulence, all we need to measure is q^2. Note that the ground effects, with the length scale of atmospheric turbulence proportional to the height above ground, have not been incorporated in Eq. (3).

The greatest impact of the vortex wake of a large aircraft on smaller followers is near ground level (< 60 m), where the smaller aircraft may not have sufficient time or space to recover from the influence of the swirl in the wake. Also, the ground plays an important role in modifying the trajectory of the vortex wake during takeoff and landing. The ground surface acts as a reflection plane, and the motion of the vortex pair is determined not only by the mutual induction of the vortices but also by the image vortex pair below the ground surface. In other words, the trajectory of the ideal vortices is determined by the mutual induction of four vortices.

In an attempt to explain the above phenomenon, Harvey and Perry[13] conducted an experiment using a half-span wing to generate a single vortex passing over a moving floor in a wind tunnel. They reported that the passage of the primary vortex induces a cross-flow on the ground with

an attendant suction peak beneath the vortex core. Consequently, the cross-flow boundary layer has to negotiate an adverse pressure gradient once it has passed under the vortex. When the vortex is sufficiently near the ground, the adverse pressure gradient is strong enough for separation from the boundary layer to occur, and a separation bubble forms containing vorticity opposite to that of the main vortex. The bubble grows rapidly and finally detaches from the ground forming a secondary vortex, which remains outboard of the primary vortex. One of the effects of the secondary vortex is to induce an upward movement of the primary vortex.

In another study, Bilanin et al.[14] incorporated a viscous ground plane in a second-order closure turbulence model to simulate the ground/vortex interaction. The numerical solution demonstrated the growth and separation of the boundary layer beneath the approaching vortex, resulting in a counterrotating secondary vortex. The secondary vortex induces an upward and outward motion on the approaching vortex, leading to the rebounding phenomenon. One of the most important findings is that the rebounding phenomenon does not occur unless the viscous boundary layer condition is applied. Didden and Ho[15] investigated experimentally the impingement of a jet on a flat plate. The vorticity in the shear layer combines to form a secondary vortex and protrudes into the inviscid region, leading to unsteady separation. The generation of the secondary vortex has been confirmed computationally using the method of large-eddy simulations.[16]

This paper is an excerpt from two papers.[17,18] It presents the results of several series of towing tank experiments with emphasis on the effects of ambient turbulence on the vortex wake and the rebound of primary vortices due to ground effect.

TECHNICAL APPROACH AND EXPERIMENTAL METHODS

The use of a towing tank has been demonstrated to be most suitable for studying the evolution of vortex wakes.[2,19] The simulated vortex phenomenon has the same spatial and temporal references as those of airplane wakes, and the turbulence and ground effects on the vortex evolution may be easily simulated under different atmospheric conditions.

The towing tank system used in this study is 18.3 m long, 1.2 m wide, and 0.91 m high. It has glass sidewalls and a glass floor to permit visualization from all directions. A description of the towing tank system for physically modeling vortex phenomena is given elsewhere.[17]

Vortex wakes were generated using two different methods: a rectangular wing model (NACA 0012) towed along the axis of the tank and a slotted-jet vortex generator (for studying the ground effects only) with its axis perpendicular to that of the tank. The NACA 0012 wing model has a 10.2-cm span and a 5.1-cm chord. For a towing speed of 40 cm/s, the chord Reynolds number is 20,400. The wing was set at - 10° for all the runs. Instead of using a strut or sting, a special mounting technique was used to suspend the wing with three thin, stainless-steel wires (0.008 to 0.013 cm in diameter). This eliminated any flow interference by the strut or sting, which would interact with and possibly contaminate the vortex wake during its evolution. For a detailed description of the wing and its performance, such as its stability during tow, refer to Liu.[17]

Ambient turbulence was generated by towing three grids, with square meshes of 1.45, 10.2, and 20.3 cm and corresponding solidities of 0.3, 0.2, and 0.1, through the tank. The small grid, made of plastic, had elements with cross sections of 0.35 x 0.96 cm² with the long side oriented in the streamwise direction. The medium and large grids had square elements with a cross section of 1.27 x 1.27 cm²; the large grid had the same frame as the medium one with half of elements removed. The theoretical prediction of the vortex lifespan due to the onset of linking instability [Eq. (1)] was derived under the assumption that L_f is large compared with the vortex separation. The medium and large grids were selected to generate ambient turbulence with integral scales comparable to or larger than the vortex separation in order to meet the above assumption.

The characteristics of the grid-generated turbulence in terms of turbulence intensity, dissipation rate, and integral scale were measured with an array of four to five quartz-coated hot-film probes (TSI 1248Y) driven by a TSI constant-temperature anemometer (Model 1053B). The probes were mounted on a stainless-steel strut (1.3 cm thick and 15 cm wide), with tapered leading and trailing edges, and towed behind the grid at the same speed as the grid. Three of the probes were oriented to measure the longitudinal (U) and vertical (W) velocity components, and at least one probe was rotated 90° to measure the longitudinal and lateral velocity components. The hot-film probes were calibrated by towing them (with no grid) at several speeds in a quiescent fluid. The tow speeds and the corresponding voltage outputs of the two film elements were fitted with second-degree polynomials. The two velocity components were derived from the outputs of the two elements using the cosine law.

The ambient water usually returns to a quiescent state in about one and a half hours after a run. We consider the ambient to be quiescent when the maximum residue motion in the tank is less than 0.08 cm/s. The motion in the tank is monitored by tracking purple streaks left behind fine potassium permanganate crystals released into the water column. For a reference run without the grid, we wait until the tank is indeed quiescent.

From the experimental data, we can estimate the dissipation rate, ϵ, according to the formula derived for locally isotropic turbulence[20]:

$$\epsilon = 15 \ \nu \ \overline{(\partial u/\partial x)^2} \qquad (4a)$$

or

$$\epsilon = 15 \ \nu \ \overline{(\partial u/\partial t)^2} \ /\bar{U} \qquad (4b)$$

using Taylor's hypothesis, where ν is the kinematic viscosity, and u and $\bar{U}$ are the fluctuating and mean velocity component along the x axis coincident with the tow direction. Therefore, we can estimate the dissipation rate from the mean square of the time derivatives of the longitudinal turbulence velocity fluctuations, with the noise subtracted from the signals.[17]

Ground effects on the vortex trajectories were simulated by placing the NACA 0012 wing below the water surface at -10° incidence; several depths were tested. This setup corresponds to an

inverted model of a vortex wake generated by an aircraft flying near the ground at a constant altitude. To simulate a rigid surface in the towing tank, the water surface was covered with rigid foam sheets, leaving a narrow gap (10 to 15 cm or $1.25b_o$ to $1.9b_o$ wide) directly above the wing to clear the suspension wires. From the visual records, it can be seen that the vortices quickly separate beyond the width of the gap, so the gap has little effect on the rebound process. In a few cases, the water was left free to enable visualization of both the top and end views of the vortex wake. These tests also allow comparison of differences in ground effects that are attributable to different surface types.

The second vortex-generation method used in this study is a slotted-jet vortex generator that operates by ejecting fluid out of a box through a narrow slot. This vortex generator consists of a sealed box with a slot 5.7 cm wide and 120 cm long (the same as the tank width) on its bottom side; the edges of the slot have a 45° bevel. The box is made of aluminum with dimensions of 18 cm (width) by 32 cm (depth). The bottom of the box is submerged below the water surface, and the vortex pair is formed and exits from the slot. The water level in the box is lifted by means of a vacuum pump. Compressed air is supplied by a large shop compressor. A pressure line is connected to a paint tank that is partially filled with water; a separate pressure line connects the paint tank and the generator box. The volume of water in the tank is inversely proportional to the pressure used to drive the vortex generator. The generator was specifically designed to introduce a "soft stop" at the end of the stroke to prevent the generation of the counterrotating vortex pair which quickly annihilates the primary vortex pair.

Fluorescent dye illuminated by a laser sheet was used to trace the vortex wakes.[17] In the towed wing experiments, a thin paste of fluorescent dye (e.g., fluorescein disodium salt) mixed in corn syrup was spread onto the side edges of the wing. For the slotted-jet vortex pair, a neutrally buoyant fluorescent dye solution was suspended in the vortex generator just above the slot. The dye was carried into the vortex pair to serve as the tracer for visualization. For the trailing vortex wake, visualization of the end view was achieved by illuminating a plane perpendicular to the axis of the tank with a sheet of laser light (5-W argon laser) generated by projecting the laser beam onto an oscillating mirror. Cameras were placed outside the tank at about 30 from the tank axis. Corrections were applied to measurements of the vortex trajectories to account for any distortion due to the perspective angle.

<center>RESULTS</center>

<center>Ambient Turbulence</center>

From the time series of the velocity components, we derived the turbulence intensity, the dissipation rate, and the integral scale.[17] Dimensionless parameters were formed by using M or b_o and $\bar{U}$ or W_o as the length and velocity scales, respectively.

Figure 1 shows the decay of the dimensionless dissipation rate, ϵ^*, derived from the time series of the longitudinal velocity components. Here the noise is subtracted from the signals.[17] For the three grids, the dissipation rates follow $(x/b_o)^{-0.77}$, as indicated by the straight lines fairing through the individual data sets. The lines may be represented by

$$\epsilon^{\ast} = 9.07 \, (x/b_o)^{-0.77} \quad \text{for M = 1.45 cm} \tag{5a}$$

and

$$\epsilon^{\ast} = 28.2 \, (x/b_o)^{-0.77} \quad \text{for M = 10.2 and 20.3 cm} \tag{5b}$$

The above equations were used to design the experiments for investigating the effects of ambient turbulence on the vortex instability. For large distances $x/M > 200$ at which the signal-to-noise ratio is too low to provide meaningful measurements, the dissipation rates were extrapolated according to these equations. The integral scale of the ambient turbulence, L_f, generated by the three grids is estimated from the integration of the autocorrelation coefficient of the longitudinal velocity component.[18,20] The trend of increasing L_f/b_o with the increase in x/b_o is established. The results show that the L_f generated by the small grid is small compared with b_o, whereas that generated by the medium and large grids is about the same as or larger than b_o. For large distances downstream of the grid (i.e., $x/M > 200$), L_f is at least as large as b_o.

From the equations for the total turbulence kinetic energy, the dissipation rate, and the integral scale,[17] we derive the dissipation rate in the form

$$\epsilon = 0.18 \, q^2/L_f$$

which is in the same form as Eq. (3) except that the constant is different as the result of anisotropy. The above equation is a convenient alternative for estimating the dissipation rate.

Visualization of Effects of Turbulence

Figure 2 is a top view of a trailing vortex wake in a quiescent fluid at several time intervals after its generation. Initially, the trailing vortex pair manifests itself as two parallel straight lines representing the thin cores. It is evident in this figure that vortex linking is the sole mode of instability. The first linking is observed at $t_t^{\ast} \approx 5$. The wavelengths of the linking range from $5b_o$ to $9b_o$. The linking may best be described as a deterministic process superimposed with a certain degree of randomness, where randomness refers to the discrete locations at which linking takes place. Here, the coherent vortex motion disappears soon after the linking occurs; at others, the coherent vortex may persist for quite some time. As measured from the movie records, the first and subsequent linkings are observed between $t_t^{\ast} = 4.3$ to 6.6.

Figure 3 shows a top view of a trailing vortex wake in the presence of ambient turbulence generated by the large grid at $x/b_o = 355$ ($\epsilon^{\ast} \approx 0.2$). Linking is still the predominant mode of vortex instability, with only a few bursting events observed prior to and during linking. There are considerable spatial and temporal variations in the linking process. For the same time after passage of the wing, the two vortex trails show more distortion and diffusion than their

nonturbulent counterparts (Fig. 2). As a result, linkings are observed between $t_l{}^* \approx 2$ and 4, depending on where the linking occurs. The dominant wavelength of the linking taking place in the middle of the area shown in the figure does not differ much from that of the reference case. These visual results have demonstrated that the lifespan decreases with decreasing the separation distance between the wing and the grid, x/b_o, as anticipated. Here, the lifespan has been generalized to include the time at which local bursting takes place, which is not modeled in Eq. (1).

Figure 4 is a close-up view of the development of a vortex wake that is exposed to relatively stronger ambient turbulence ($\epsilon^* = 0.4$) than that shown in Fig. 3 using the same large grid. It can clearly be seen that both linking and bursting take place in relatively strong ambient turbulence. The dominant wavelength of the linking is about 3 times the vortex separation, which is considerably shorter than that in a quiescent ambient (see Fig. 2). With further increase in the turbulence intensity ($\epsilon^* \approx 0.5$), bursting becomes the dominant mode that destroys the vortex wake, as observed in Fig. 5. There is no sign of any linking development in the short duration before the vortex wake is completely destroyed by bursting.

Careful examination of the visual results has led to the identification of several trends. In the wake of the medium and large grids, the onset of instability is predominantly of the linking type for small ϵ^* but shifts to the bursting type as ϵ^* increases. In the wake of the small grid, the induced instability is of the bursting type. It is important to point out that vortex instability is an extremely localized phenomenon, as is evident from the visual results. The vortex motion is highly organized and potentially hazardous to followers except at discrete locations at which the first and subsequent linking or bursting events take place. This must be kept in mind when optimizing aircraft spacing using laboratory and field results.

From the visual records, we measured the dominant wavelength of vortex linking, L_l, in the wakes of the medium and large grids. The trend of inverse proportionality of L_l/b_o with ϵ is clearly established. Note that ϵ is proportional to q^2/L_f [Eq. (6)]. The above trend indicates that L_l/b_o increases with $q^2/\bar{U}_2$ and $(L_f/b_o)^{-1}$, which is consistent with the visual observations.

Effects of Dissipation Rate on Lifespan

The visualization results were used to derive the lifespan of the vortex wake as a function of the dissipation rate. Attempts were made to verify the theory developed by Crow and Bate[2] [Eq. (1)], which has been subjected to limited verification via field experiments.[1] For consistency with the theory, we select only the first linking or bursting as observed from the visual records (top view). To account for the decaying turbulence field, the dissipation rate is defined as the average of the dissipation rates measured at the time of vortex generation and at the time of the linking or bursting.

In Fig. 6, we plot the dimensionless lifespan $t_l{}^* = W_o t_l/b_o$ versus the dimensionless dissipation rate $\epsilon^* = (\epsilon b_o/W_o{}^3)^{1/3}$. The solid and dashed curves correspond to the theory of Crow and Bate[2] [Eq. (1)] and to the envelope of Tombach's field data[1] [Eq. (2)]. The various symbols represent our laboratory results derived from the visual records (see legend). The solid symbols represent the lifespans at which the first linking or bursting event takes place.

Also included in Fig. 6 are the results in a quiescent environment under neutral and weakly stable conditions, with the values of ϵ^* are estimated to be 0.01 and 0.005, respectively.[18] For the stable cases, the water in the tank was thermally stratified with a Brunt-Vaisala frequency less than 0.02 rad/s. In the nearly quiescent environment, Eq. (1) (solid curve) predicts only small changes of t_ℓ^* with ϵ^*, and errors resulting from an inaccurate estimate of ϵ^* are relatively small. Except for runs under quiescent ambient conditions, most of the data points are above the solid curve, which is consistent with the trend seen in the field experiments.[1] This indicates that Eq. (1) tends to underpredict the lifespan of the vortex wake in a turbulent environment. For practical applications, one must keep in mind that vortex linking is localized phenomena, particularly at their onset. Except at discrete places where linking or bursting takes place, the vortex motion is largely coherent, and the potential hazard remains even after the onset of vortex instability (see Figs. 3 and 4).

In Ref. 17, it is demonstrated that the lifespan due to vortex bursting induced by the small grid is shorter than that due to linking in relatively weak turbulence. For example, the former is about three to four times shorter than the latter at $\epsilon^* \approx 0.1$.

GROUND EFFECTS

Visualization

Figure 7 is a series of photographs excerpted from a movie record showing the end view of a trailing vortex wake approaching and rebounding from a covered surface $1.9b_o$ above the wing; refer to Ref. 18 for a comparison of the visual results in the absence of ground effects. The dimensionless time $W_o t/b_o$ is shown on the side of each photograph; the initial nondimensional depth h_s/b_o was 1.9, where h_s is the initial release depth of the vortex pair. The appearance of the vortex elements at any instant and location may vary depending on how much dye was entrained to track the cores and recirculation regions. The covered surface is identified by a bright line above the vortices. In the photograph series, the evolution of the secondary vortex from the primary vortex can be seen most distinctly in the right-hand-side primary vortex, which shows a relatively clear pattern.

At $W_o t/b_o = 0$, the vortex pair appears as two tightly wound thin cores that expand as the dye diffuses into the recirculation region. As the vortex pair moves upward, the vortex separation begins to increase ($W_o t/b_o > 1$) as the water surface is felt. In the absence of dye outside the primary vortex, the initial generation of a secondary vortex at the water surface outboard of the primary vortex is not visible. The secondary vortex only becomes identifiable after dye from the primary vortex is entrained into the newly formed recirculation cell (but not the cores) and outlines the structure. The generation and evolution of the secondary vortex is convincingly illustrated for the slotted-jet vortex pair as shall be seen. At $W_o t/b_o = 2$, the secondary vortex is barely identifiable outboard to the right of the primary vortex. Subsequently, the secondary vortex is outlined by the dye spirals around the primary vortex ($2 < W_o t/b_o < 4$) and finally turns into a turbulent patch that separates further from the primary vortex ($W_o t/b_o > 4$) and disintegrates. This action indicates that the secondary vortex is weaker in strength than its

primary counterpart. Similar evolution patterns are observed in a test run with a free water surface.[18] The strength of the secondary vortices is comparable for the two runs. As demonstrated by Bernal et al.,[21] surface contamination causes the free surface to act like a rigid surface.

These visual results confirm the scenario inferred by Harvey and Perry.[13] The same phenomenon has also been seen in the results of experimental and numerical modeling studies of a jet impinging onto a fixed wall.[15,16] The authors of these studies attributed the formation of the secondary vortices to the unsteady separation of the wall boundary layer caused by an adverse pressure gradient, again reinforcing the visual results presented here.

In an attempt to demonstrate the rebound phenomenon convincingly, the slotted-jet vortex generator was used with a rigid plate made of Plexiglass (1.2 m x 3.2 m) placed below the exit slot to simulate the ground. Fig. 8 illustrates the evolution of the slotted-jet vortex pair in ground effect with $h_s/b_o = 1.78$. The vortex separation increases as the vortex pair approaches the surface. The bottom of the oval contacts the surface between $W_o t/b_o = 0.54$ and 0.81. The formation of a counterrotating secondary vortex beneath and outboard of the right primary vortex becomes evident at $W_o t/b_o = 0.81$.

Again, the secondary vortex is not visible in the absence of dye outboard of the primary vortex. The secondary vortex can be identified after dye from the primary vortex is entrained into the recirculation region of the new formation. As soon as the secondary vortex begins to form, rebound of the primary vortex is initiated. The primary and secondary vortices form a vortex pair that moves upward. The top of the oval contacts the bottom of the exit plate of the vortex generator between $W_o t/b_o = 1.2$ and 1.6. Now, a tertiary vortex is generated outboard and above the secondary vortex. These vortices form another vortex pair that moves away from the primary vortex, which is rapidly disintegrating. Tipping of the vortex pair is clearly observed as it moves away from the bounded region between the two plates (the top plate is only $2.2b_o$ beyond the slot of the generator).

Vortex Trajectories

Figure 9 illustrates the trailing vortex trajectories in a vertical plane perpendicular to the vortex axis. The coordinates of the trajectories y and z are derived from the measurements of h and b, where h is depth of vortex cores to the mean water surface.[18] To conform with classical theory by Lamb,[18,22] the coordinates are nondimensionalized with b_∞, the asymptotic vortex separation for y and z approaching infinity. The symbols represent the experimental results, and the solid curve represents the corresponding theoretical values of a parabola.[22] For $h_s/b_o = 8.2$, the presence of the surface has little influence over the vortex wake before it is disintegrated due to the linking instability. In fact, the evolution of the linking instability results in a relatively large discrepancy between the measured and predicted trajectories. The rest of the experimental results appear to collapse onto a single curve close to the hyperbolic trajectory for $y/b_\infty < 1$ and then branch out into two distinctive groups, $h_s/b_o = 1.3$ to 3.2 and $h_s/b_o = 0.64$, when $y/b_\infty > 1$.

For $y/b_\infty < 1$, a slight discrepancy is anticipated in the theory due to the idealized representation of trailing vortex wakes by two parallel line vortices. Note that the initial separation measured from the visual results is equal to the span of the wing, which is a factor of $4/\pi$ larger than b_o. The experimental results tend to be above and to the right of the theoretical curve, indicating that the primary vortex is less penetrative than predicted by the two-dimensional theory.

For $y/b_\infty > 1$, the inadequacy of the classical theory in accounting for the rebound of the primary vortex is evident. For $h_s/b_o = 0.64$, the trajectory is seen to deviate considerably from those at larger h_s/b_o. As shown in Ref. 18, b/b_o begins to increase immediately after the wake is released, which differs from the trend of the others with larger h_s/b_o. The close proximity of the surface could have resulted in a strong impingement of the vortex pair onto the surface, which may alter the strength of the secondary vortex.

An attempt is made in this section to examine the effects of the secondary vortex on the rebound of the primary vortex. The classical two-dimensional theory is modified by adding a line vortex to account for the secondary vortex. Because the velocity induced by a vortex is inversely proportional to the square of the distance traveled, it is assumed that to a first-order approximation, the modification of the trajectory of the primary vortex is due to the effect of the nearest secondary vortex. The total induced velocity of the primary vortex becomes

$$\frac{dy}{dt} = \frac{-\kappa y^2}{4\pi r^2 z} + \frac{\kappa' \cos \theta'}{2\pi r'} \tag{7}$$

where κ and κ' are the circulation strength of the primary and secondary vortices, r the instantaneous distance of vortex center from the origin, r' the distance between the primary and secondary vortices, θ' the rotation angle of the primary and secondary vortice, y the horizontal axis perpendicular to the flight path, and t the time.

$$\frac{dz}{dt} = \frac{-\kappa z^2}{4\pi r^2 y} + \frac{\kappa' \sin \theta'}{2\pi r'} \tag{8}$$

where z is the vertical distance.

Eqs. (7) and (8) therefore describe the superposition of a translational velocity due to the four primary vortices (of which two are the mirror image) and the rotational motion induced by the nearest secondary vortex. The differential equation describing the trajectory of the primary vortex is modified to

Note that three additional unknown parameters, κ', r', and θ', were introduced. The angle of rotation of the primary and secondary vortex pair can be expressed as[1]

$$\frac{dz}{dy} + \frac{-\dfrac{z^2}{yr^2} + 2\,\dfrac{\kappa'}{\kappa}\,\dfrac{1}{r'}\,\sin\theta'}{-\dfrac{y^2}{zr^2} + 2\,\dfrac{\kappa'}{\kappa}\,\dfrac{1}{r'}\,\cos\theta'} \tag{9}$$

$$\frac{d\theta'}{dt} = \frac{(\kappa - \kappa')}{2\pi r'^2} \tag{10}$$

Assuming that the secondary vortex is induced at the ground surface, and that the distance r' and vortex strength κ and κ' remain constant, the system of Eqs. (7), (8), and (9) can be numerically computed using the second- and third-order Runge-Kutta algorithm. Four curves corresponding to the conditions $\kappa'/\kappa = 0.3, 0.7, 0.8$, and 0.9 are shown in Fig. 10. In these computations $r' = b_\infty/2$ is assumed. The secondary vortex was assumed to be induced at the matching position when $y/b_\infty = 1.0$ and $z/b_\infty = 0.577$. In the figure, the trajectory given by the classical theory is shown as a solid curve.[22] Note that the trajectories for $\kappa'/\kappa = 0$ and 1 are identical to those computed from the classical theory.

From the comparison of the classical and modified theories in Fig. 10, several interesting features of the vortex system are observed. First, the incorporation of the secondary vortices has brought about the rebound of the primary vortex, which agrees qualitatively with the present experimental results. The trajectories derived from the modified theory show that the rebound motion is periodic; the amplitude and the wavelength depend on the κ'/κ ratio. The periodicity results in momentary arrest of the vortex separation, which is observed experimentally (Ref. 18; see also Ref. 13). The modified theoretical results are in agreement with more elaborate numerical models (e.g., Refs. 13, 23 and 24). It should be emphasized that the theory considers two idealized line vortices. In reality, disintensification of the vortex core as a result of diffusion and turbulent mixing would smear the appearance of the periodicity, even if it is present.

The visual results of the trailing vortex pair (Fig. 7) show that the strength of the secondary vortices is weaker than that of the primary vortices. Therefore, we expect the ratio of κ'/κ to be less than unity. Intuitively, κ'/κ should decrease with increasing h_*/b_0, as the primary vortex disintensifies greatly with the long travel time accompanied by a large h_*/b_0 before impinging onto the ground and initiating the secondary vortex. For the extreme case, the vortex pair released at $h_*/b_0 = 8.5$ does not feel the presence of the ground before it disintegrates. This is consistent with the trend shown in Figs. 9 and 10, except that the periodicity in the solution of the modified theory causes the trajectory for $\kappa'/\kappa = 0.3$ to reverse after a strong initial rebound. Visual results show that the vortex separation between the secondary and primary vortices increases with time as the former spirals around the latter. This also suggests that the periodicity would not be observed in the real fluid.

The good qualitative agreement between the prediction by the modified theory and the experimental results indicates that the inception of the secondary vortices provides the essential physical mechanism to effect the rebound phenomenon. Accurate prediction must rely on more

sophisticated numerical models capable of realistically simulating the viscous-inviscid interaction near the boundary.

CONCLUSIONS

Several series of towing tank experiments were conducted to investigate the ambient turbulence and ground effects on vortex wakes. Fluorescent dye was used as a tracer to visualize the evolution of the vortex wakes generated by a towed NACA 0012 wing and by a slotted-jet vortex generator. The important findings from the laboratory experiments are summarized below.

(1)   In a quiescent environment ($\epsilon^* < 0.01$), linking is the dominant mode of vortex instability. Ambient turbulence with integral scales comparable to or larger than the vortex separation promotes linking instability, shortening both the lifespan and the dominant wavelength of the linking. As the dimensionless dissipation rate increases ($\epsilon^* < 0.2$), vortex bursting emerges at various places along the sinuously distorted vortex wake. In strong turbulence ($\epsilon^* > 0.4$), vortex bursting becomes the dominant mode of vortex instability.

(2)   Turbulence generated by the small grid, which has integral scales smaller than the vortex separation, promotes predominantly vortex bursting. For relatively weak turbulence ($\epsilon^* \approx 0.1$), the lifespan is much shorter (by as much as a factor of 4) than that due to linking/bursting induced by turbulence generated with the medium and large grids.

(3)   With the exclusion of the results of the small grid, the laboratory measurements compare reasonably well with the theory[2] and with field measurements,[1] especially when the lifespan of the first link or burst is used in the comparison. For practical consideration, t_f^* depends solely on ϵ^* for both linking and bursting. The vortex motion is highly coherent except at discrete points of the first or subsequent vortex linking or bursting events. We recommend the adaptation of an equation for the dimensionless separation time between takeoffs/landings for small followers by multiplying Eq. (1) by a safety factor of 2, which may be adjusted according to the classes of larger follows.

(4)   The generation of a secondary vortex outboard of the primary vortex leads to the rebound of the latter from either a free or rigid surface as demonstrated through visual experiments. The vortex separation between the secondary and primary vortices increases with time. The secondary vortex generated by a slotted-jet vortex pair is higher in strength and longer in persistence than that generated by the trailing vortex wake.

(5)   Our results have confirmed the scenario inferred by Harvey and Perry[13] where the secondary vortex is due to unsteady separation of the boundary layer in which the flow has to negotiate an adverse pressure gradient created by the impingement of the primary vortex.

(6) A simple modification of the two-dimensional inviscid theory -- namely, adding a second vortex to the system -- essentially recreates the rebound of the primary vortex, which agrees qualitatively with the experimental results. The rebound curvature appears to reach an asymptotic magnitude when the initial release is sufficiently far from the ground surface. The critical dimensionless distance is approximately one ($h_*/b_o = 1$).

ACKNOWLEDGEMENTS
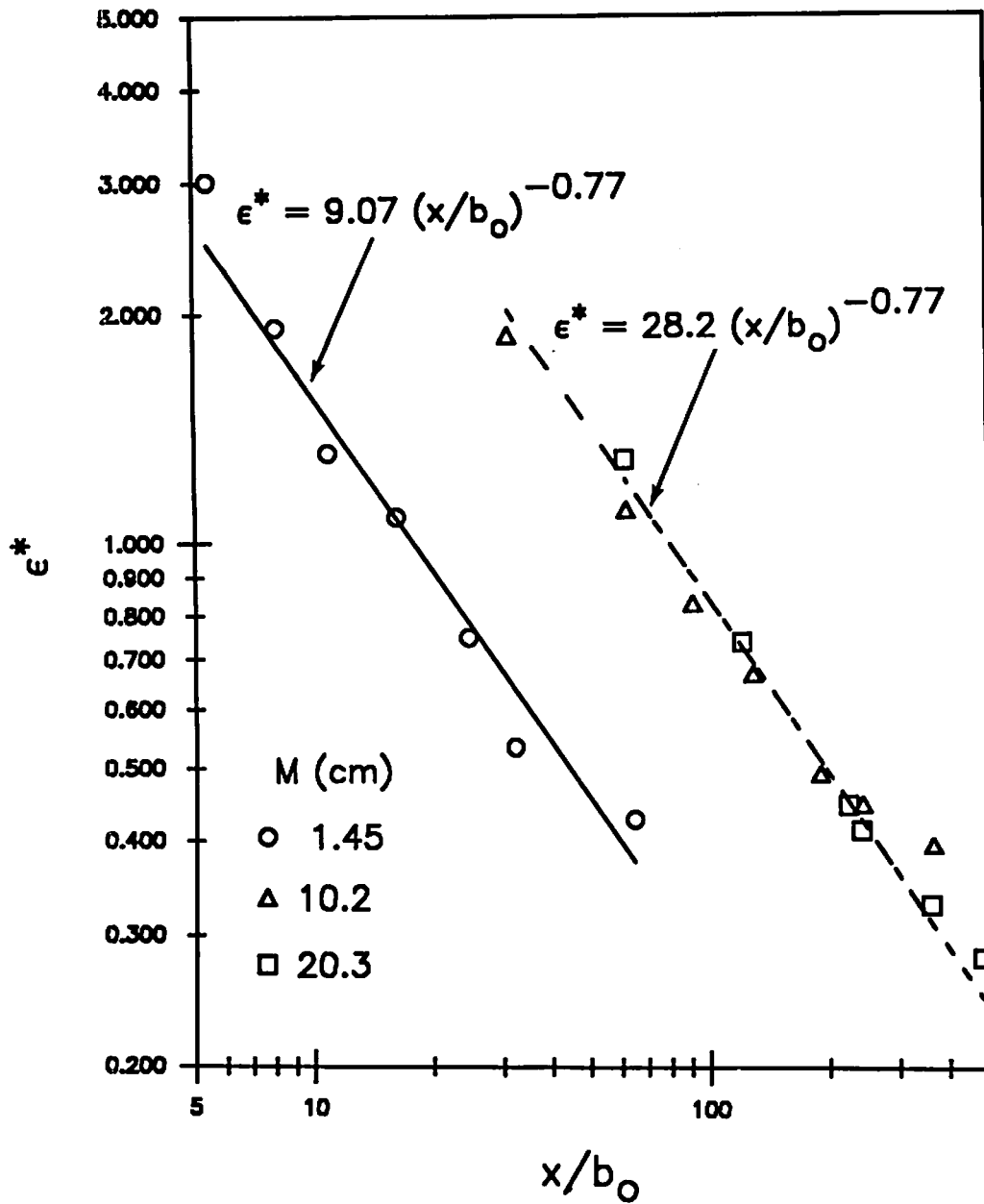
Figure 1. Decay of dissipation rate in grid turbulence.
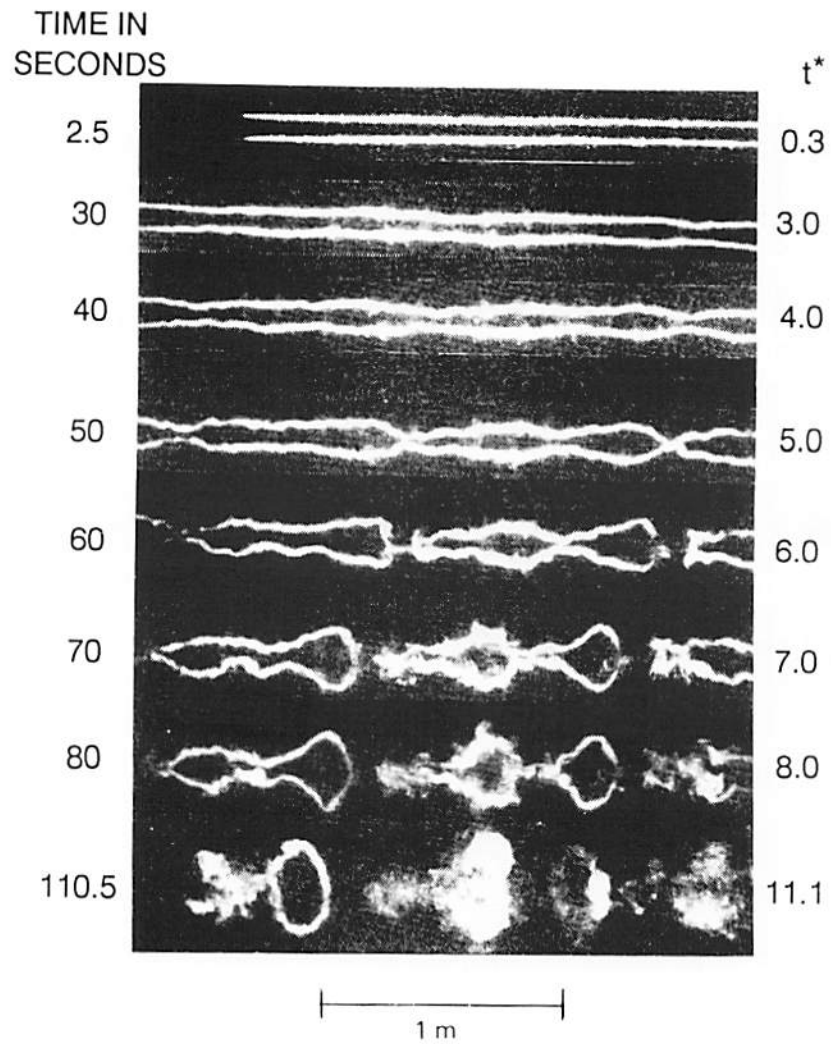
Figure 2. Development of a linking instability in a quiescent, neutrally stable environment.
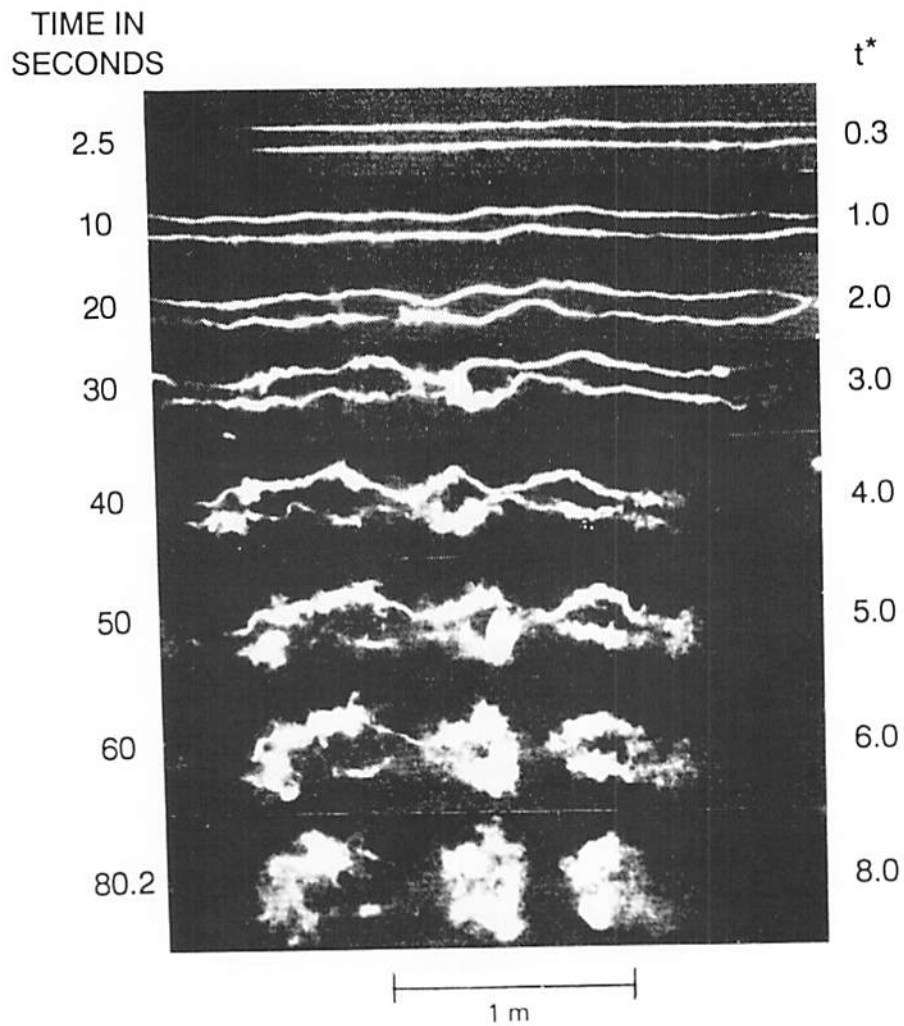
Figure 3. Evolution of a trailing vortex wake in grid turbulence-
$\epsilon^* \approx 0.2$ and M = 20.3 cm.
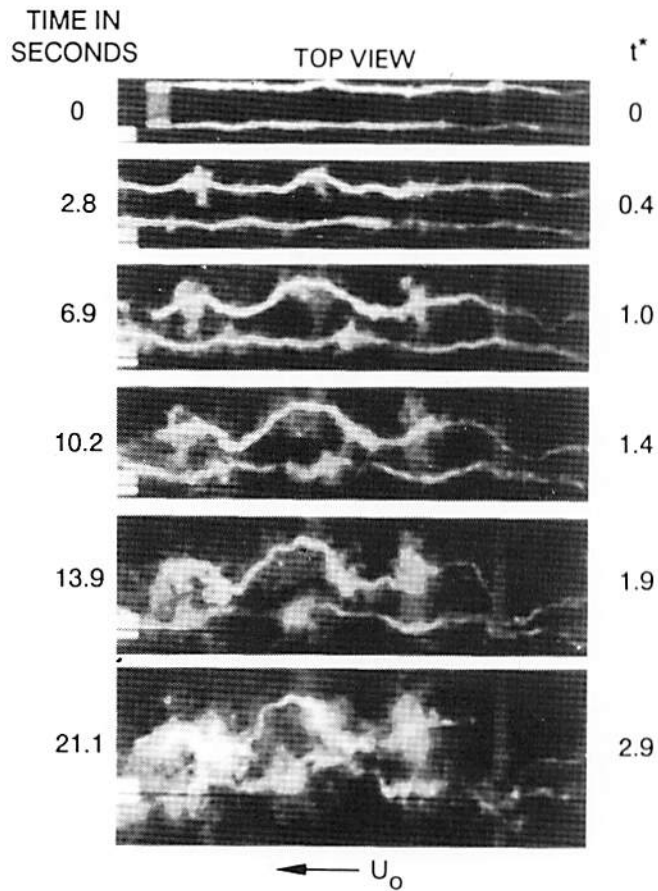
Figure 4. Simultaneous development of vortex linking and bursting in grid turbulence- $\epsilon^* \approx 0.4$ and M = 20.3 cm.
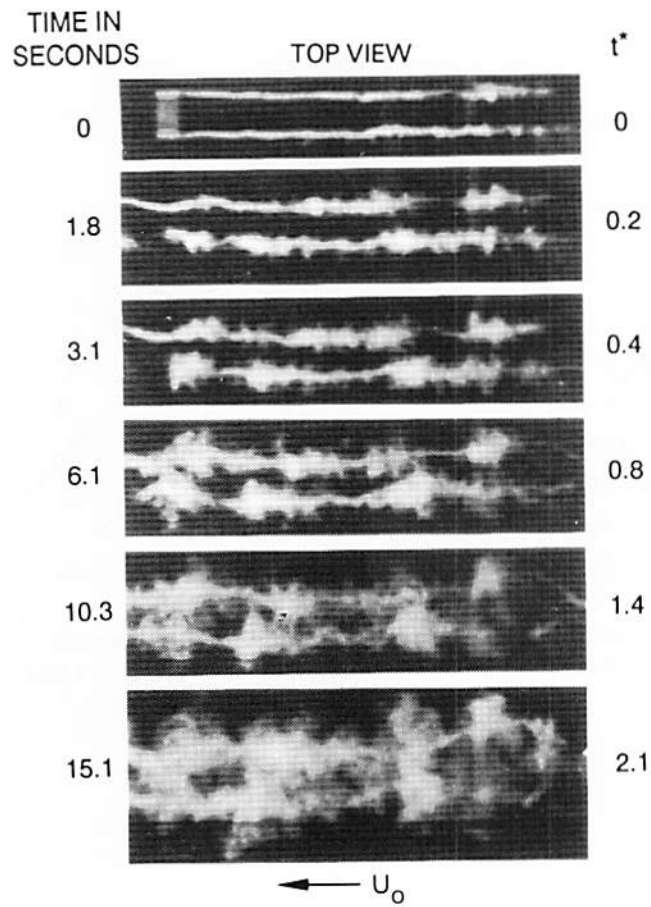
Figure 5. Bursting shown as the dominant mode of vortex instability in grid turbulence- $\epsilon^* \approx 0.5$ and M = 20.3 cm.
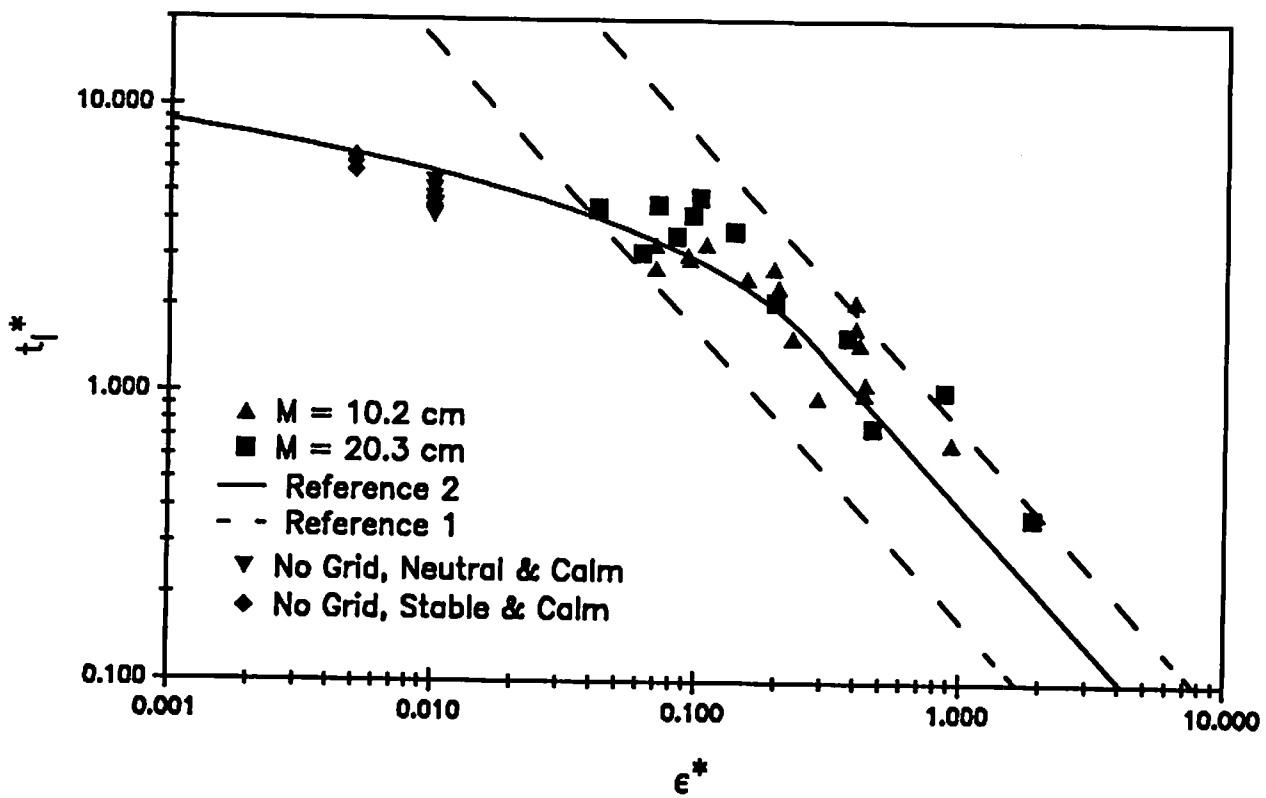
Figure 6. Lifespan of a trailing vortex wake as a function of the dissapation rate with the result of the dissapation rate with the results of the small grid excluded, first linking and bursting only.
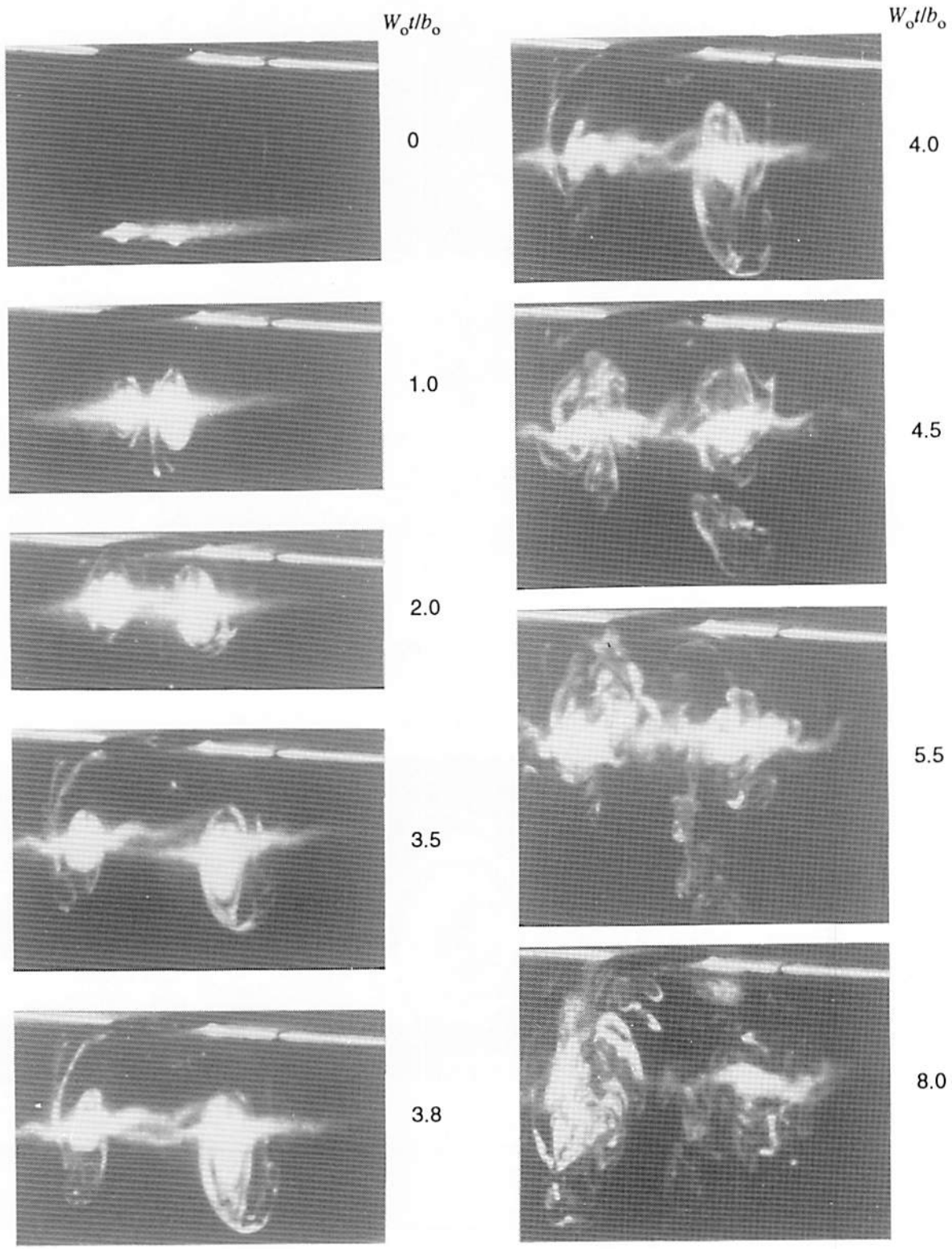
Figure 7. Visual results of a trailing vortex pair released close to a covered water surface (white line), $h_s/b_o = 1.9$.
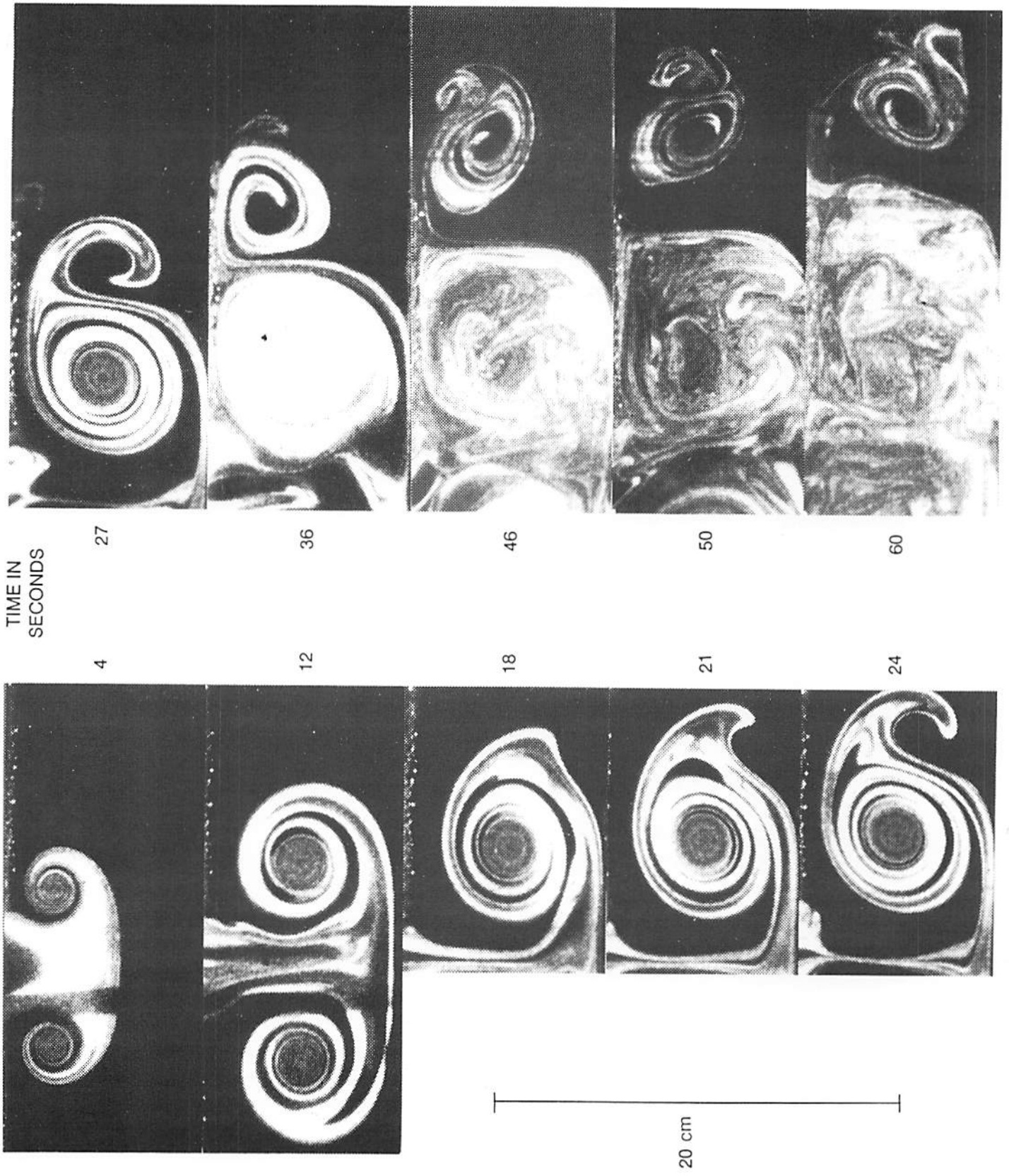
Figure 8. Comparison of vortex trajectories in ground effect as derived from visual results and classical Theory.[22]

TIME IN SECONDS

4   12   18   21   24

27   36   46   50   60

20 cm
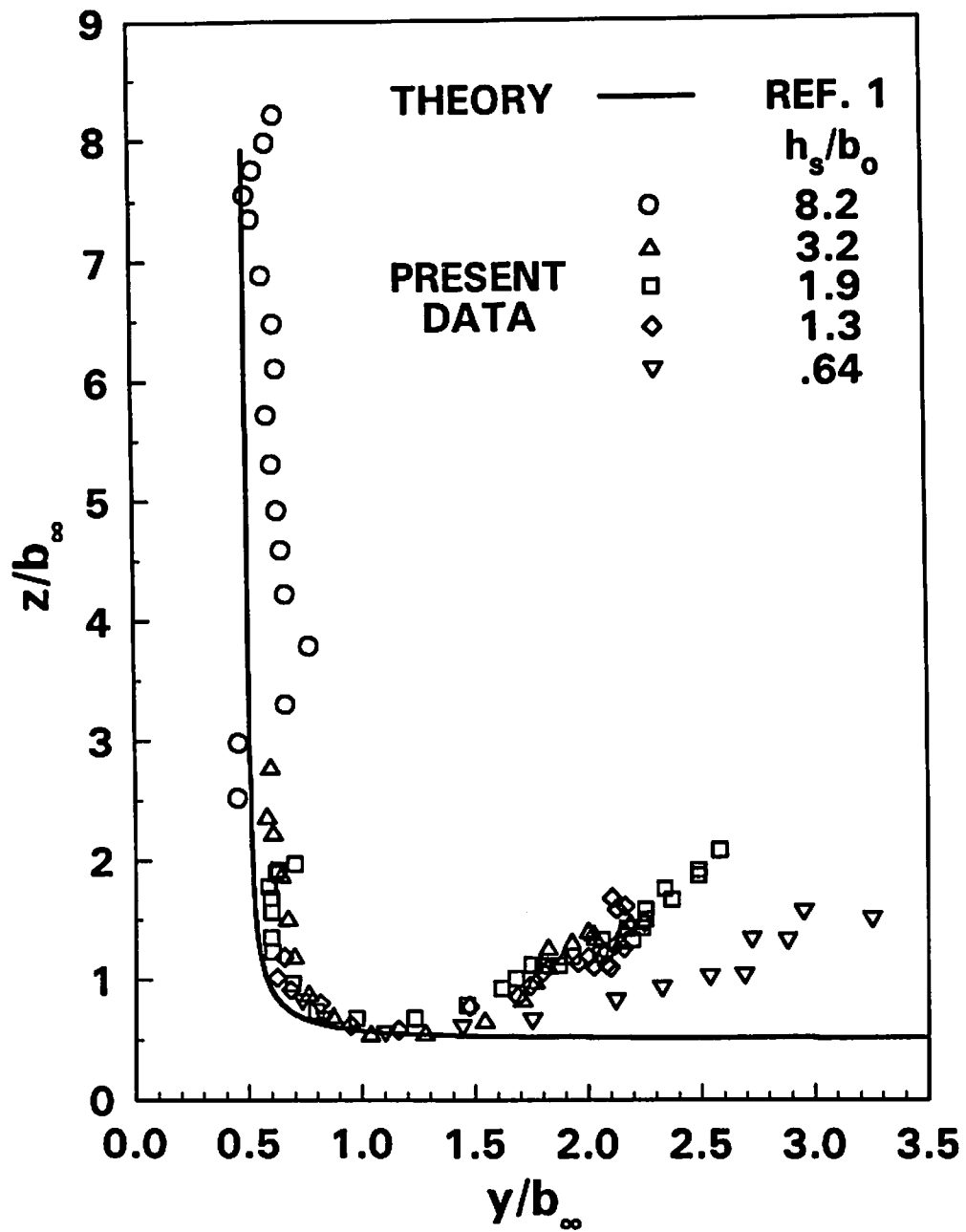
Figure 9. Generation of secondary vortices and the rebound of the primary slotted-jet vortices, $h_s/b_o = 1.78$.
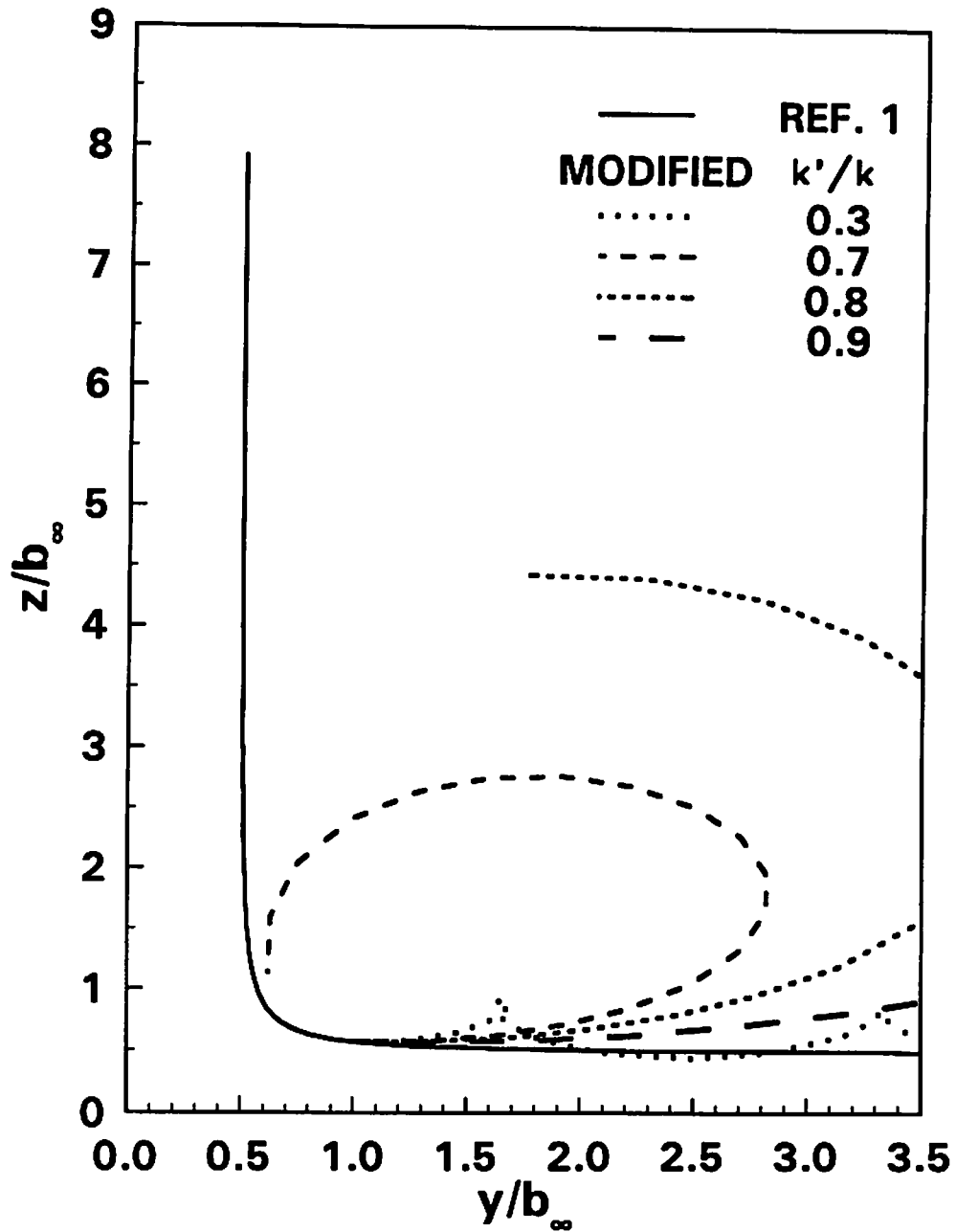
Figure 10. Comparison of vortex trajectories in ground effect
as derived from classical[22] and modified theories.

REFERENCES

1. Tombach, I., "Observations of Atmospheric Effects of Vortex Wake Behavior," Journal of Aircraft, Vol. 10, 1973, pp. 641-647.

2. Crow, S. C., and Bate, E. R. Jr., "Lifespan of Trailing Vortices in a Turbulent Atmosphere," Journal of Aircraft, Vol. 13, No. 7, 1976, pp. 476-482.

3. Bilanin, A. J., Teske, M. E., and Hirsh, J. E., "Neutral Atmospheric Effects on the Dissipation of Aircraft Vortex Wakes," AIAA Journal, Vol. 16, No. 9, 1978, pp. 956-961.

4. Saffman, P. G., "The Motion of a Vortex Pair in a Stratified Atmosphere," Studies in Applied Mathematics, Vol. LI, No. 2, 1972, pp. 107-119.

5. Hirsh, R. S., "A Numerical Simulation of Vortex Motion in a Stratified Environment and Comparison with Experiments," Johns Hopkins APL Technical Digest, Vol. 6, No. 3, 1985, pp. 203-210.

6. Greene, G. C., "An Approximate Model of Vortex Decay in the Atmosphere," Journal of Aircraft, Vol. 23, No. 7, 1986, pp. 566-573.

7. Crow, S. C., "Stability Theory for a Pair of Trailing Vortices," AIAA Paper No. 70-53, 1970.

8. Hall, M. G., "Vortex Breakdown," *Annual Review of Fluid Mechanics*, Vol. 4, 1972, pp. 195-218.

9. Bilanin, A. J., and Widnall, S. E., "Aircraft Wake Dissipation by Sinusoidal Instability and Vortex Breakdown," AIAA Paper No. 73-107, 1973.

10. Widnall, S. E., Bliss, D. B., and Zalay, A., "Theoretical and Experimental Study of the Stability of a Vortex Pair," *Aircraft Wake Turbulence and Its Detection* (Olsen, J. H., Goldburg, A., and Rogers, M., Eds.), New York, Plenum Press, 1971, pp. 305-329.

11. Leibovich, S., "The Structure of Vortex Breakdown," *Annual Review of Fluid Mechanics*, Vol. 10, 1978, pp. 221-246.

12. Batchelor, G. K., *The Theory of Homogeneous Turbulence*, Cambridge University Press, 1953, 106 pp.

13. Harvey, J. K., and Perry, F. J., "Flowfield Produced by Trailing Vortices in the Vicinity of the Ground," AIAA Journal, Vol. 9, 1971, pp. 1659-1660.

14. Bilanin, A. J., Teske, M. E., and Hirsh, J. E., "Neutral Atmospheric Effects on the Dissipation of Aircraft Vortex Wakes," AIAA Journal, Vol. 16, No. 9, 1978, pp. 956-961.

15. Didden, N., and Ho, C.-M., "Unsteady Separation on a Boundary Layer Produced by an Impinging Jet," Journal of Fluid Mechanics, Vol. 160, 1985, pp. 235-256.

16. Rizk, M. H., and Menon, S., "Large-Eddy Simulation of Axisymmetric Excitation Effects on a Row of Impinging Jets," Physics of Fluids, Vol. 31, No. 7, 1988, pp. 1892-1903.

17. Liu, H.-T., "Effects of Ambient Turbulence on the Decay of a Trailing Vortex Wake," QUEST Technical Paper No. 268, 1992 (to appear in AIAA Journal of Aircraft Vol. 29, No. 2).

18. Liu, H.-T., P. A. Hwang, and R. A. Smsky (1992) "Physical Modeling of Ground Effects on Vortex Wakes," QUEST Technical Paper No. 274, 1992 (to appear in AIAA Journal of Aircraft Vol. 29, No. 3).

19. Sarpkaya, T., "Trailing Vortices in Homogeneous and Density-Stratified Media," Journal of Fluid Mechanics, Vol. 136, 1983, pp. 65-109.

20. Hinze, J. O., *Turbulence*, McGraw-Hill, Inc., New York, 1959.

21. Bernal, L. P., Hirst, A., Kwon, J. T., and Wilmarth, W. W., "On the Interaction of Vortex Rings and Pairs with a Free Surface for Varying Amounts of Surface Active Agent," Physics of Fluids, Vol. A1, No. 12, 1989, pp. 2001-2004.

22. Lamb, H., *Hydrodynamics*, 6th ed., Dover, New York, 1945, pp. 221-224.

23. Ohring, S., and H. J. Lugt, "Interaction of a Viscous Vortex Pair with a Free Surface," Journal of Fluid Mechanics, Vol. 227, 1991, pp. 47-70.

24. Walker, J. D. A., C. R. Smith, A. W. Cerra, and T. L. Doligalski, "The Impact of a Vortex Ring on a Wall," Journal of Fluid Mechanics, Vol. 181, 1989, pp. 99-141.

VORTEX ROLL-UP, MERGING AND DECAY
WITH THE UNIWAKE COMPUTER PROGRAM

Milton E. Teske, Todd R. Quackenbush, Alan J. Bilanin and Daniel A. Wachspress
Continuum Dynamics, Inc.
P.O. Box 3073
Princeton, New Jersey 08543

ABSTRACT

The numerical simulation of vortex merging and decay, particularly behind large commercial aircraft, was initially made possible by the NASA WAKE code developed in 1975. Significant enhancements to that code were achieved in the last three years with the development of the UNIWAKE code for the Department of Transportation. This code combines four elements of the merging process: (1) a vortex lattice model patterned after the work of Margason and Lamar to determine the wing loading; (2) a Betz roll-up model of the load distribution, including axial velocity effects; (3) a turbulent transport finite difference model extending the previous WAKE solution scheme to fourth-order accuracy; and (4) a three-dimensional unsteady analysis replacing the merged vortices by curved vortex elements, leading to vortex linking and pinch-off. This paper summarizes each model stage, and examines extensions for solution improvement.

INTRODUCTION

Airport capacity is intimately related to FAA regulated separation standards between landing and taking-off aircraft. Current separation standards were determined after an extensive *in situ* measurement program undertaken by the Federal Aviation Administration of the U. S. Department of Transportation. Subsequent measurement programs identified that, among other aircraft parameters, wake intensity is a function of engine placement (Hallock and Eberle 1977). Although aircraft wake research has been active for more than fifteen years, an analytical methodology has, to this point, not been developed to assess wake intensity prior to the testing of the prototype. Due to the complex interactions of the vortex wake with engine exhaust and the atmosphere, this methodology must necessarily be a computer simulation of wake evolution. If such a tool could be developed and validated, aircraft designers would be able to factor wake intensity into future generation commercial jet liner designs. In addition, government FAA regulators would have an additional tool (besides direct measurement) to assess wake intensities of current operational and future jet liners.

UNIWAKE is such a tool, developed to evaluate the vortex wake intensity behind current and future generation jet liners. The UNIWAKE technology incorporates the wake mitigating effects of propulsion wash, profile drag and atmospheric turbulence diffusion in a relatively "easy-to-use" computer code. The software does not introduce any new physics into understanding the dynamics of the evolution and decay of aircraft vortex wakes, but rather assembles known technologies to provide a software product which is reliable, accurate and cost effective. This computer code should permit direct prediction of wake intensity behind jet liners operating under similar conditions, and lead to a consistent interpretation of wake hazard.

OVERVIEW

UNIWAKE (UNIfied WAKE analysis) is a collection of FORTRAN computer programs that can be used to investigate the downstream behavior of aircraft vortices generated at an aircraft wing. The calculation procedure is supervised by a master oversight program that interactively permits the user to proceed through the computational steps desired (or to begin and end within the computational stream) from aircraft planform lift and drag, to vortex linking, as summarized in Figure 1. These steps include the following operations:

a) Calculation of the lift circulation distribution on the aircraft wing planform by vortex lattice. The vortex lattice computation develops the wing lift circulation distribution from user-specified aircraft characteristics (planform shape, twist and camber of wing, assumed distribution of horseshoe vortices) and operational characteristics (aircraft weight and speed).

b) Roll-up of the lift circulation distribution and profile drag distribution into distinct trailing edge vortices by the Betz methodology. Betz roll-up computation identifies the discrete vortical structure (location, strength and core size of swirling and axial velocities) given the computed wing lift circulation distribution and user-specified sectional profile drag characteristics.

c) Initialization and subsequent integration of turbulent merging and decay of these vortices, with jet engine exhaust, by a fourth-order accurate solution of the modeled incompressible Navier-Stokes equations of motion, including second-order closure of the turbulence. Wake turbulent merging and decay computation evolves from the vortical structure and the modeling of aircraft engine effects.

d) Inviscid line vortex filament interaction of the merged vortices to pinching, utilizing curved vortex elements. Line filament sinusoidal instability computation continues from the merged wake vorticity distribution, and leads to pinching and wake destruction.

These steps are not a new and revolutionary way of numerically assessing wake intensity for existing and future commercial jet liners. Rather, they are seen to be the application of available, proven numerical models to this problem area. The above discrete (and solvable) steps are a natural extension of previous work in this area.

Because of the several fluid dynamic and aerodynamic disciplines incorporated in these four steps (Donaldson and Bilanin 1975), the resulting computer code will be useful only if it possesses the following attributes:

1. It must be easy to use. There is no reason to assemble numerical models that approximate reality if they are so difficult to understand or so cumbersome (or subtle) to operate that no one will take the time to learn how to use them.

2. The numerical models should certainly be validated, either by comparison with available data (in most cases a qualitative test), or by the successful application of the same technique to situations beyond the immediate scope of this research.

3. The collected models must, in each of their parts, be cost effective and computationally efficient. It may be the easiest software to use and be verified by everyone connected with the subject area, but if it takes enormous computer resources then it will not be used.

4. The structure of the overall package must be easily modified as new techniques, new interpretations and new approaches become available.

5. The computational product must be well-documented. It may contain all four of the previous attributes, but if its operational instructions are incomprehensible, then it will simply not be used.

UNIWAKE builds these elements into a single computer product, controlled by a master oversight program that interacts with the code user through the schematic shown in Figure 2. The four existing code modules are briefly discussed below.

Wing Lift and Drag Distribution

The first step in the computational process of analyzing wake effects behind large aircraft is the development of the load distribution on the wing planform. This task is accomplished by a well-documented, extensively embraced and employed technique known as vortex lattice. This method, in all of its numerous incarnations, is an extension of the finite step lifting-line method described by Glauert (1948) and applied by Campbell (1951). This method assumes that flow over the wing planform is steady, irrotational, inviscid, incompressible and attached (compressibility is modeled by the Prandtl-Glauert similarity rule). The Biot-Savart law is used to represent disturbances created in the flowfield by the load distribution on the planform. In essence, the planform is divided into many elemental panels. Each panel is replaced by a horseshoe vortex made up of three filaments: a vortex filament across the quarter chord of the panel and two vortex filaments in the streamwise direction, one on each side of the panel (starting at the quarter chord position) and trailing downstream in the freestream direction to infinity. The boundary condition for each horseshoe vortex is satisfied by requiring that the local fluid flow over the panel be parallel to the planform surface at the three-quarter chord point of the panel. The load distribution required to satisfy this tangency condition at every elemental panel is then determined by the solution of a matrix equation. Finally, the Kutta-Joukowski

theorem is used to determine elemental lift on each panel, and, from these analyses, other fundamental aerodynamic quantities of the assumed wing planform.

Many codes exist in the open literature (and presumably others are commercially proprietary) to estimate lift and induced drag on wing planforms using vortex lattice. It is assumed that this technology is reliable and will be utilized directly. Margason and Lamer (1971) developed a vortex lattice code that has enjoyed wide usage, particularly at NASA Langley Research Center. One version of this code has been implemented as the first computational step in UNIWAKE. The interested user is referred to Margason and Lamar for details on the development and implementation of the vortex lattice method.

The results of applying vortex lattice to a specified wing planform is the lift circulation distribution as a function of semispan from the wing root to tip. This result depends not only on wing geometry and wing twist and camber, but also on the aircraft operating conditions (such as estimated aircraft weight and flight speed). Additionally, vortex lattice codes predict induced drag distributions but do not have the capability of predicting profile drag distributions. Profile drag is an additional input that must be assembled by the user from the known wing planform sectional characteristics.

Vortex lattice methods are in general use in the aircraft industry, and have been shown to well represent the lift distributions measured on wing planforms. The Margason model employs a matrix solution technique known as successive orthogonalization (Purcell 1953). Introductory textbooks on aerodynamics generally devote a chapter to the development of this topic, and include guidelines for the selection of spanwise and chordwise quantities of horseshoe vortices. Additionally, Margason and Lamar include their own suggestions for acceptable horseshoe vortex arrangements, and the technical literature frequently includes a re-examination of this technique (Hough 1973). Vortex lattice is an accepted technique for determining planform characteristics.

Betz Roll-Up

The second step in the computational process involves taking the lift and drag distributions developed for the wing planform and identifying the number, strength, location and structure of vortices which form the rolled-up wake downstream of the wing trailing edge. In the roll-up region discrete vortices may be evaluated from inviscid models motivated by the work of Betz (1932) and rediscovered by Donaldson (1971). This approach has been the starting point for numerous inviscid wake models (Brown 1973; Rossow 1973; Jordan 1973 and Donaldson et al. 1974) applied to the two-dimensional case. A way to extend the Betz methodology to three

dimensions was first proposed by Bilanin and Donaldson (1975), and forms the basis of the Betz model programmed in UNIWAKE.

The Betz approach was originally applied to the roll-up of an initially flat two-dimensional vortex sheet. The roll-up process is assumed to conserve the centroid, circulation and angular momentum of the vortex sheet on a station-by-station basis. In other words, each incremental distance along the span of the vortex sheet is assumed to satisfy the postulated conservation laws.

Because this approach is applied at each finite subinterval along the sheet, a detailed swirl distribution is obtained for the final vortex core in terms of the initial circulation distribution of the sheet. This approach, although approximate, is particularly attractive here because the spanwise circulation distribution is a principle result of vortex lattice theory applied to the assumed wing planform shape.

The important feature of the three-dimensional extension proposed by Bilanin and Donaldson is the assertion that angular momentum flux should also be conserved. The torque applied by each subinterval of the wing is equated to the net angular momentum flux within the corresponding radius of the fully formed vortex core. In this way the axial velocity generated during three-dimensional roll-up may be obtained. By following specific rules established for discretizing the lift distribution on the wing, multiple vortices may be identified and resolved. Details on the inviscid roll-up procedure for tip vortices may be found in Bliss (1987).

Viscous/Turbulent Merging Analysis

The third step in the computational process involves initializing a two-dimensional grid with the vorticity and axial velocity profiles developed for each vortex from the Betz methodology, adding additional axial velocity and temperature profiles to simulate jet engines and drag effects, and solving for the turbulent merging and decay that follow. This step encompasses the cornerstone of the UNIWAKE code. While earlier computer codes have been developed to examine this problem (Teske 1976), and such codes have been used extensively to perform vortex merging and decay calculations (Bilanin et al. 1977, 1978), they all suffer from limited accuracy and nearly unlimited computer resource demands.

It was judged imperative that the latest, most accurate techniques be applied to solve the system of partial differential equations governing this part of the flow- field. The goal here was to replace the computer tools of 1976 with more recent solution techniques. Also, whereas the earlier codes used brute-force to solve all the needed turbulence correlation equations, recent modeling work suggests that relatively simple, straight-forward models may be substituted with confidence.

The merging region is viscous and involves turbulent transport. It is a flow- field, moreover, which is slowly varying downstream and, therefore, the equations of motion may be simplified by making a parabolic approximation, i.e., by neglecting second derivatives in the streamwise direction. The effects of turbulence are included by closing the Reynolds stress equations at the second order with an invariant model (Sykes et al. 1986).

In UNIWAKE a fourth-order accurate, compact differencing technique employing an alternating direction implicit (ADI) scheme has been programmed to solve the resulting partial differential equations (Hirsh 1983). Each of the dependent variables (turbulence, axial velocity, temperature and vorticity) is solved at each grid point in each downstream marching step with its first and second derivatives on a three-point mesh. While this technique requires the solution at every grid point of a three-by-three matrix inversion, the increased accuracy inherent in the scheme permits a factor of four or five fewer grid points *in each direction* than the previous second-order technique (for the same accuracy). Initial conditions are entered as Gaussians of

the variable, giving the magnitude, standard deviation and location on the uniform mesh. Solution proceeds until merging of vortices occur.

3D Inviscid, Unsteady Vortex Interaction

The fourth step in the computational process involves replacing the merged vortical structure from the wake solution by a pair of vortex filaments undergoing sinusoidal instability.

Once merging has been achieved, wake decay will be very slow, since diffusion of vorticity across the wake centerline proceeds from turbulence generated in the wake itself. It is therefore prudent to interpret the results of the wake code as appropriate initial conditions for a three-dimensional unsteady code developed for the filament pinching process.

Sinusoidal instability of three-dimensional vortex pairs was first studied by Crow (1970). It involves a balance between the mutual interaction of the deformed vortices and the self-induced motion due to the curvature of the vortex elements (Bliss 1982). A recent code developed by Continuum Dynamics, Inc. (Bliss et al. 1987) incorporates curved vortex elements to define the three-dimensional filament structure and solve for the evolution of the filament geometry with the Biot-Savart law. This code has been adapted to the pinching problem.

This instability is begun by a small sinusoidal variation down one modeled period of the filament (all other periods are replicates of the modeled period). This initialization is representative of the actual behavior of trailing vortices. The sinusoidal instability then grows until the cores of the two vortices come into contact, often causing the pattern to break into a ring-like structure. It is at this point that the pinching model is complete. The time taken to pinch is a good representation of the time it would take the vortex sheet behind a wing planform to pinch off and dissipate. That number may then be interpreted and compared with results produced by other possible wing planform shapes.

DATA COMPARISONS

Extensive tower fly-by data (Garodz et al. 1974) and laser Doppler velocimeter wake measurements (Burnham et al. 1978) exist for the B747 aircraft. These experiments provide a data base with which to compare predictions of the numerical models developed for the unified vortex wake analysis.

The Betz roll-up model provides the solution approach to rolling-up the lift distributions on the B747 for the conditions detailed in Garodz and 'produces' or 'predicts' the representative swirl velocity profiles as a function of radius. Selected results for take-off, holding and landing are shown in Figures 3, 4 and 5, respectively. The near-inviscid behavior for take-off and holding (a regime dominated by a strong tip vortex) cannot be completely represented by the viscous vortex equivalent profiles developed here; however, in landing the vortex behavior is nearly identical to the data. All other B747 data exhibit these same trends.

The laser Doppler velocimeter experiments of Burnham provide details on the circulation decay and vortex structure of one run, specifically their Run 5. In the corresponding turbulent merging calculation, it was assumed that the several discrete vortices generated from the B747 planform had quickly merged, forming one compact vortex near the aircraft wing tip. The resulting vortex pair was then solved by the merging code with the tight vortex core predicted by Betz roll-up. The resulting decay of average circulation may be seen in Figure 6 where code predictions are in excellent agreement with experimental data for all four of the experimental averaging radii. In this study the initial circulation level in the vortex was assumed to be 542 sq m/sec, consistent with the level assumed in the data report. That this level is probably correct may be seen by the vortex velocity profile comparison shown in Figure 7 at the reported time of 9.8 seconds after aircraft passage. The turbulent merging code predicts the core size and the maximum velocity remarkably well.

PROGRAM EXTENTIONS

A variety of extensions to the existing analysis have been proposed or are currently being undertaken:

-inclusion of atmospheric refraction (for data correlation)

-simple turbulent scale equation

-multiple-scale vortex cores

-stratification effects (wave trapping at computational boundaries)

-viscous ground plane interaction

-full 3D vortex wake evolution to replace Betz roll-up

Some of these features have already been examined (Teske 1989) and others are contemplated. The multiple-scale vortex cores approach would replace the Betz solution representation of a single Gaussian profile

$$V = \frac{\Gamma}{2\pi r}\left[1 - \exp\left(-\frac{r^2}{2\sigma^2}\right)\right]$$

by a two-scale model

$$V = \frac{\Gamma}{2\pi r}\left[1-\exp\left(-\frac{1}{2}\left[\frac{r}{r_c}\right]^{1/2}\right)\right]\left[1 - \exp\left(-\frac{1}{2}\left[\frac{r}{r_b}\right]^{3/2}\right)\right]$$

33-7

This approach captures velocity linear with radius for small radius, velocity following a square root behavior for intermediate radius $r_b > r_c$, and velocity behaving inversely with radius for large radius.

Other possible improvements to the present Betz roll-up model include implementation of a direct computation of 3D vortex wake evolution. Recent work in vortex dynamics for rotorcraft applications has led to the development of a novel solution method for free vortex wake geometries. This wake solution method discretizes the wake into filamentary vortices that trail from each blade. The vortex filaments consist of parabolic curved vortex elements, and a robust relaxation method is used to compute the free distortion of the resulting vortical wake using Biot-Savart integration. Thus a fully 3D inviscid calculation of the wing wake may be carried out, replacing the instantaneous Betz roll-up model presently in the UNIWAKE code. Details of this replacement approach follow below.

Such a modification is desirable because the current Betz implementation was designed as a convenient engineering tool that would model rather than explicitly compute the behavior of the wake. The present implementation assumes that the angular momentum balance that is used to compute the velocity distributions in the rolled-up vortices can be applied piecewise in the case of multiple trailers. This approximation becomes increasingly inaccurate as more and more vortex trailers are added, and so constitutes a significant limitation to the analysis of aircraft in landing configuration with multiple flap vortices. Also, there remains the fundamental limitation of any such analytical model with respect to wakes of wings at high lift coefficient and low speed. For such conditions, the nonlinear deflection of the wake may become important, and it is desirable to use a wake model that can accommodate such flight conditions.

Though the formation of the vortex wake in the vicinity of the side and trailing edges of the wing is fundamentally a viscous process, the effects of viscosity are restricted to a very small region; the same is true of the wake roll-up process for the first several wingspans downstream, and so this part of the roll-up process is well approximated by an inviscid computation.

Unsteady 3D vortex wake calculations can be accomplished by extending the vortex lattice used for the computation of wing loading into the near wake and discretizing the free portion downstream of the trailing edge into vortex elements that are then convected through application of the Biot-Savart law. Computations of this type have in fact been undertaken (Evans and Hackett 1976), but these early approaches can be improved in several important respects. First, such calculations have typically used straight vortex elements in the discretization of the trailing filaments. However, work over the past several years (Bliss et al. 1987) has shown that using parabolic curved vortex elements offers a better combination of accuracy and efficiency for any application involving freely distorting vortex elements. Second, the time-marching scheme used in such models inevitably encounters fundamental instabilities in the course of the calculations. Such problems can be bypassed by using a non-time-marching relaxation scheme for the wake geometry. This approach solves for the free vortex geometry while circumventing the well-documented convergence problems associated with time-marching simulations through the use of an influence coefficient approach (Quackenbush et al. 1989, 1990). The EHPIC (Evaluation of Hover Performance using Influence Coefficients) code that incorporates this approach has produced accurate performance predictions for a wide variety of rotor systems in hover, and has proved to be flexible and robust. Recent extensions of the methods described

in these references have allowed the computation of the inviscid roll-up of rotor tip vortices (Figure 8). The application of this model to the fixed wing case is conceptually straight-forward.

Along with the computation of loads and bound circulation on the blades, implementation of this approach in the revised code will track the natural evolution of the vortex wake in three dimensions downstream of the wing. No restrictions need be placed on vertical deflection of the wake, nor need there be preconceived numbers or locations of rolling-up trailers; concentrations of vorticity will arise naturally out of the mutual interaction of the wake filaments. Of course, since 3D vortex elements and a finite span wing will be used, the approximations involved in 2D unsteady vortex calculations will also be avoided. Also, because an Eulerian reference frame that moves with the wing will be used, the curved elements that make up the trailing filaments need not all be of the same length; small elements may be used in regions of rapid roll-up, while larger ones may be used in other regions to save computation time. Finally, because no convective washout of the wake geometry is needed (unlike a time-domain computation) the configuration of wing wakes at adjacent flight conditions (slightly different values of flight speed or wing lift) may be computed very rapidly by suitably perturbing the baseline result.

One very useful capability of the revised code will be the ability to directly compute the centroids and higher moments of vorticity in various crossflow planes in the wake. These results may then be compared to the predictions made by the Betz roll-up model to quantify the strengths and weaknesses of the current Betz approach, and to imitate the vortex merging portion of UNIWAKE.

SUMMARY

In summary, then, UNIWAKE

-is the only front-to-back wing wake code currently available

-does well in comparison with field data

-is modular and can include improvements as technology improves (such as the modifications proposed here).

ACKNOWLEDGEMENT

Figure 1. Module regions comprising the unified vortex wake predictive model.
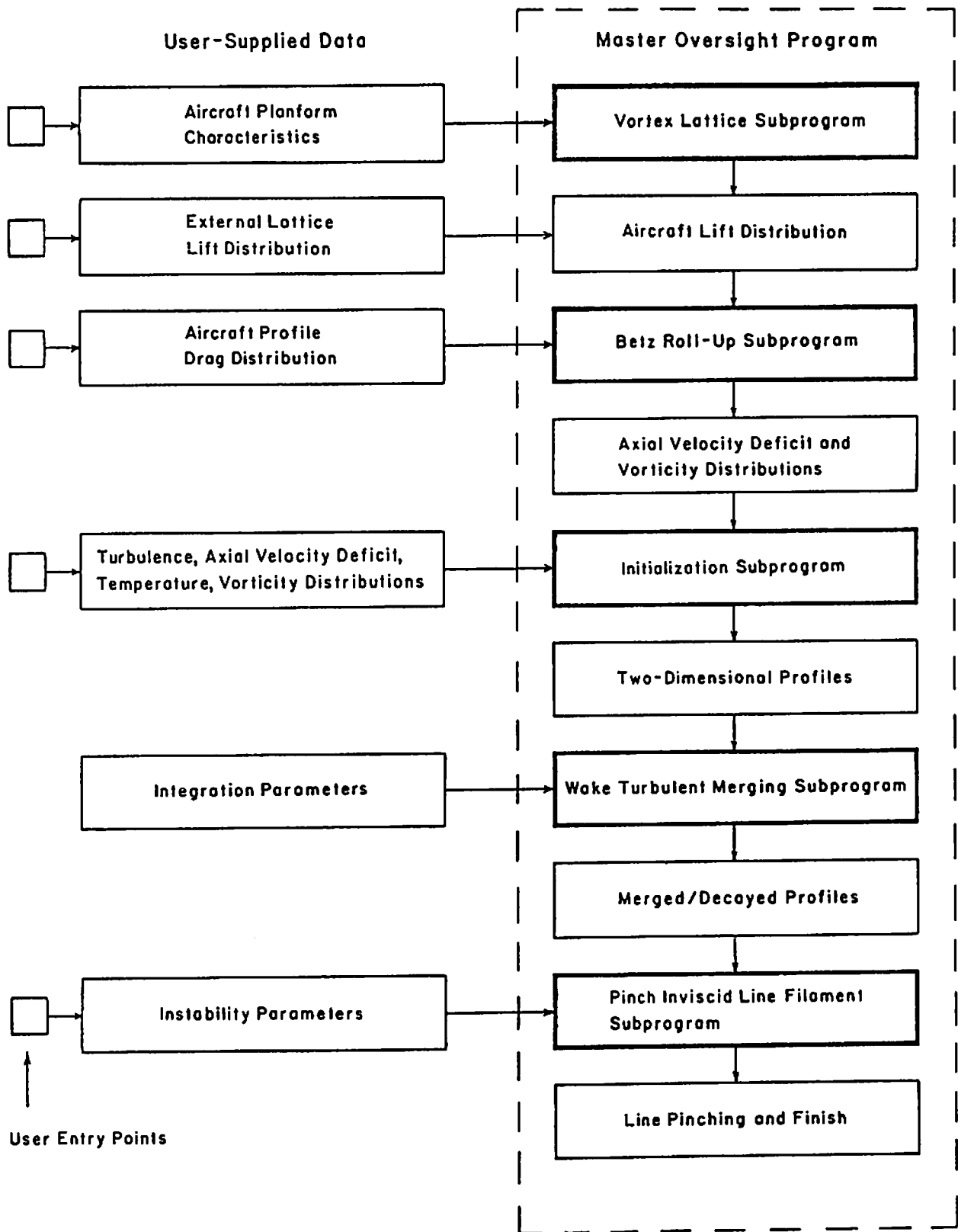
Figure 2. UNIWAKE program flowchart.
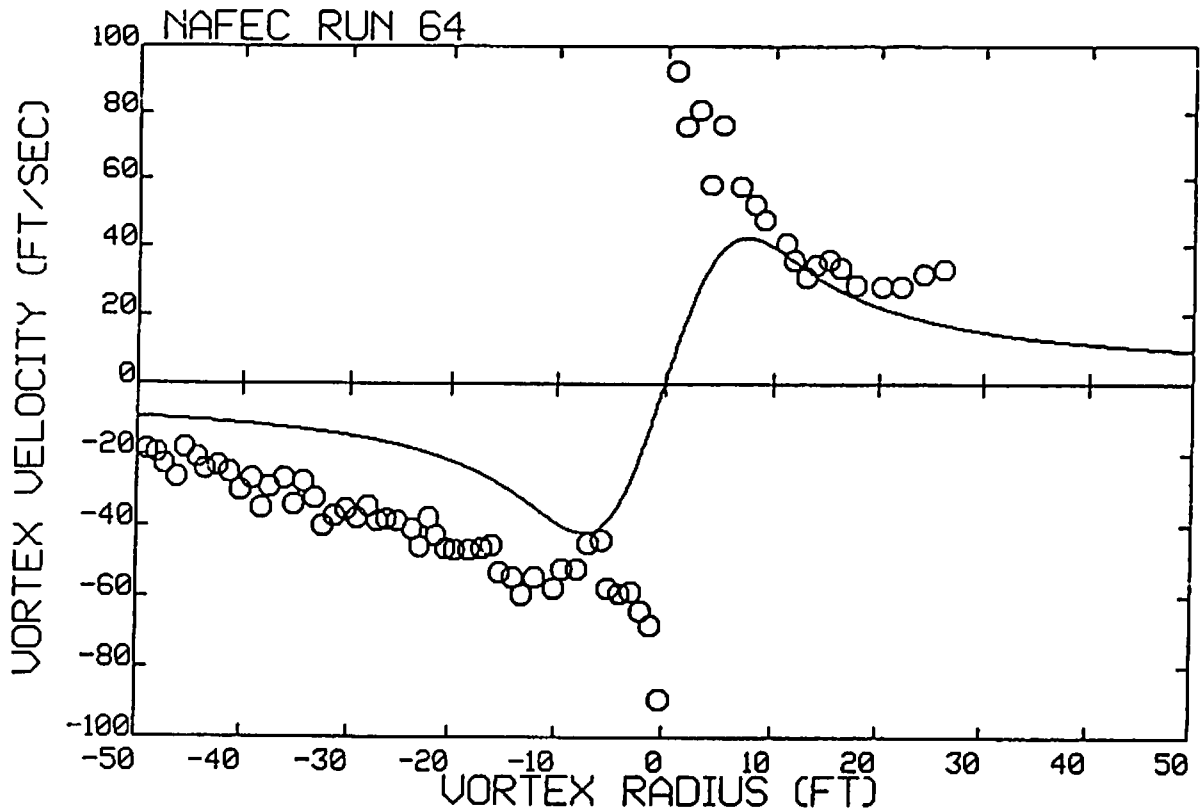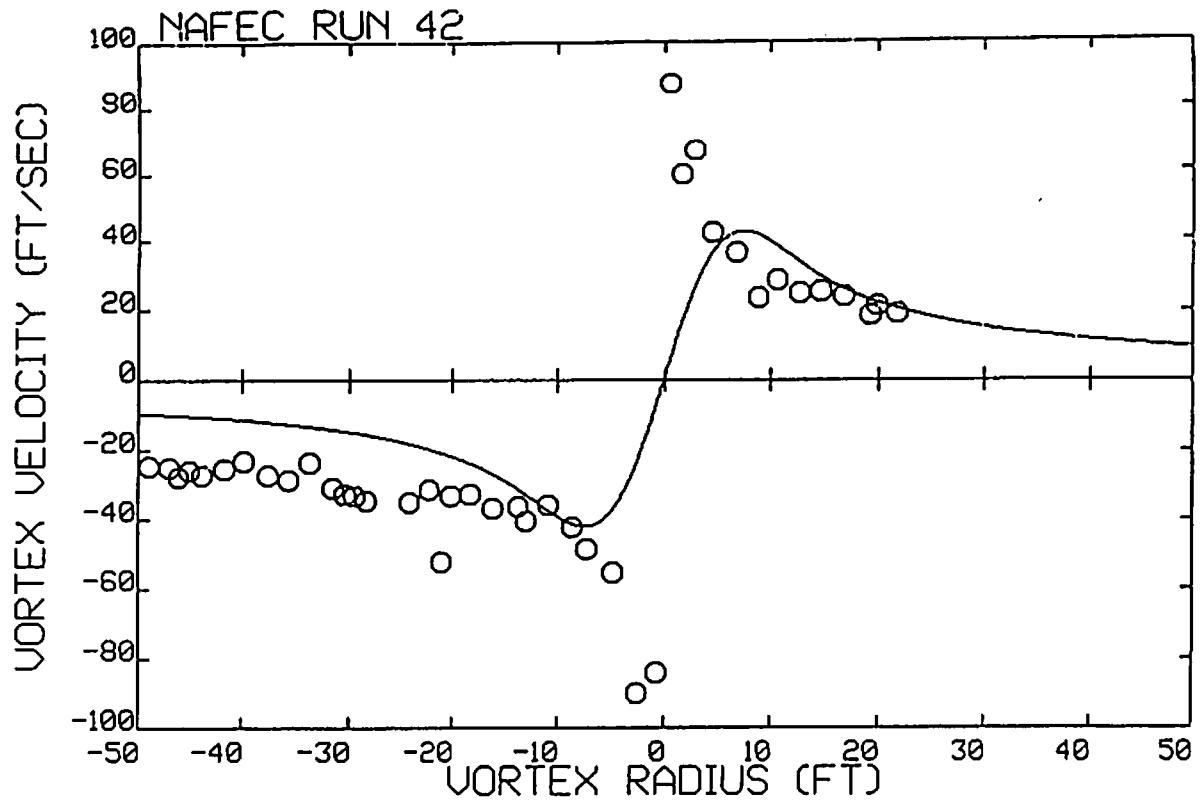
Figure 3. Comparison of measured (circles) and predicted (curve) swirl velocity profiles for a B747 in take-off configuration. Top: NAFEC Run 42; Bottom: NAFEC Run 64. Data from Garodz et al. (1974).
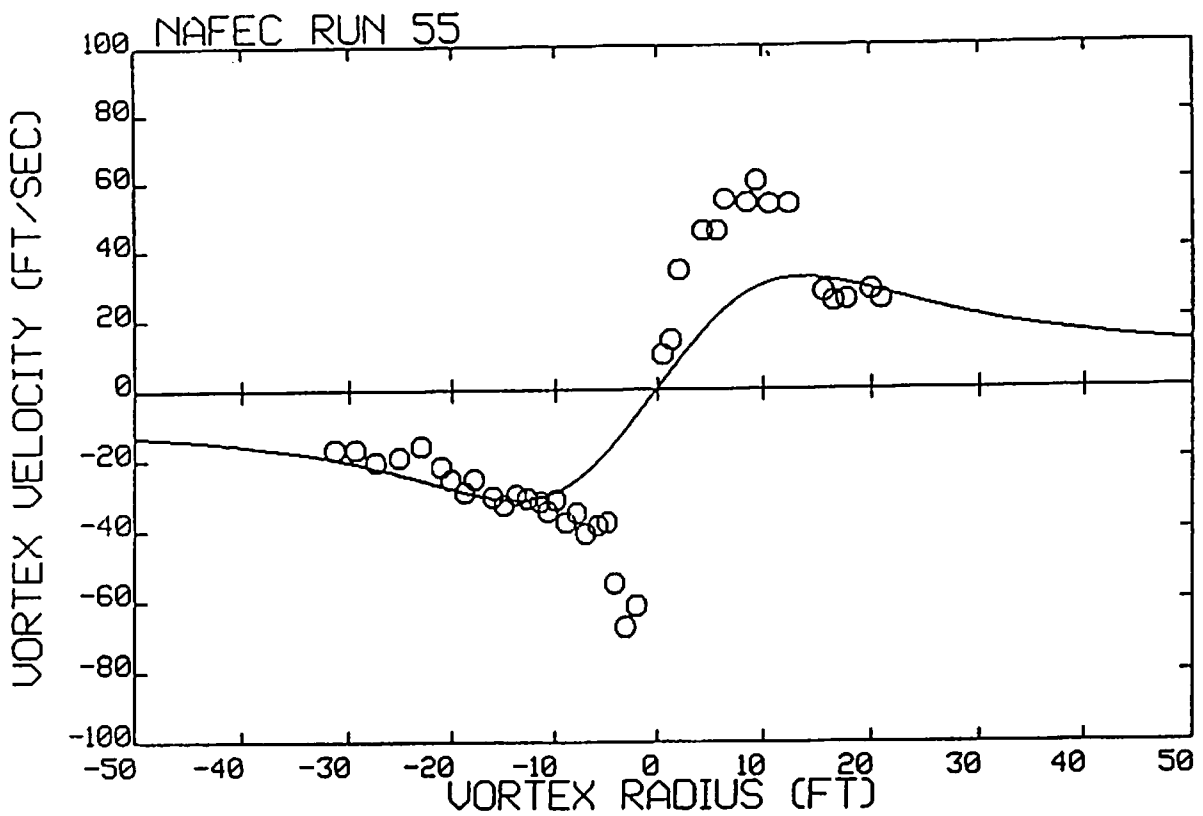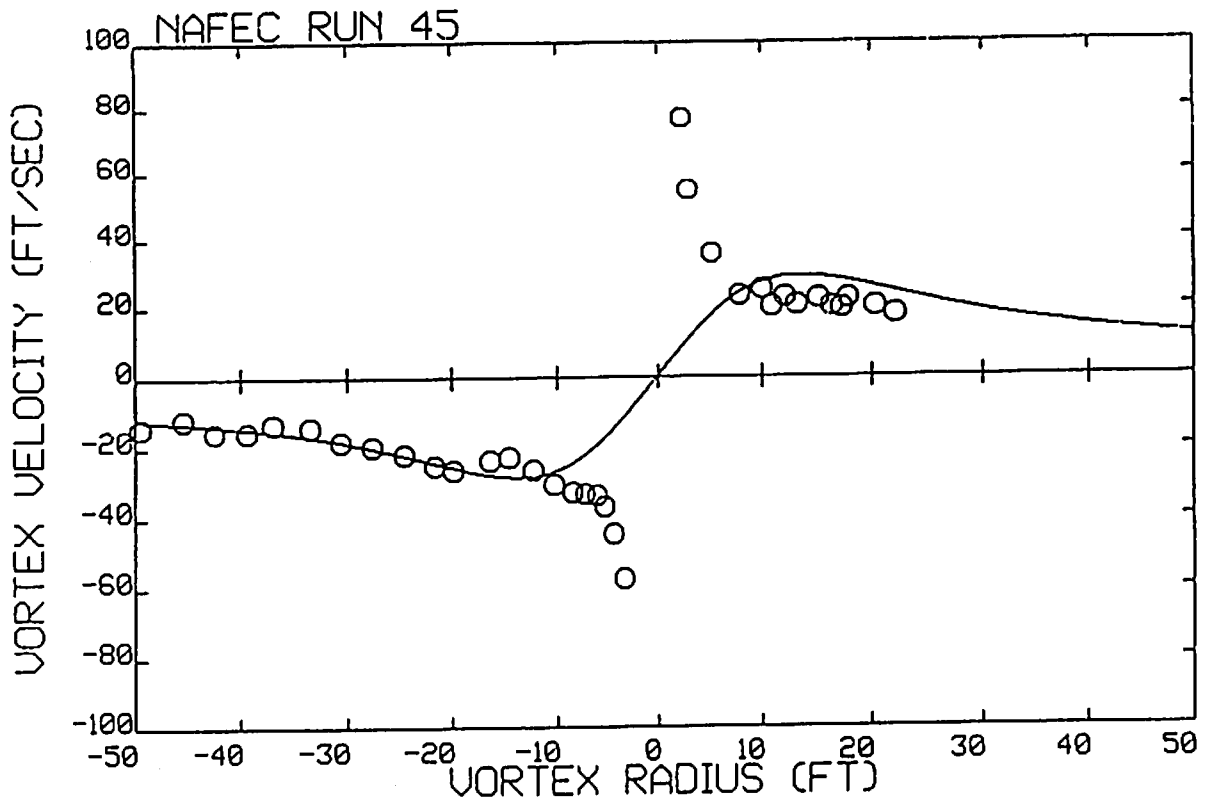
Figure 4. Comparison of measured (circles) and predicted (curve) swirl velocity
profiles for a B747 in holding configuration. Top: NAFEC Run 45;
Bottom: NAFEC Run 55. Data from Garodz et al. (1974).
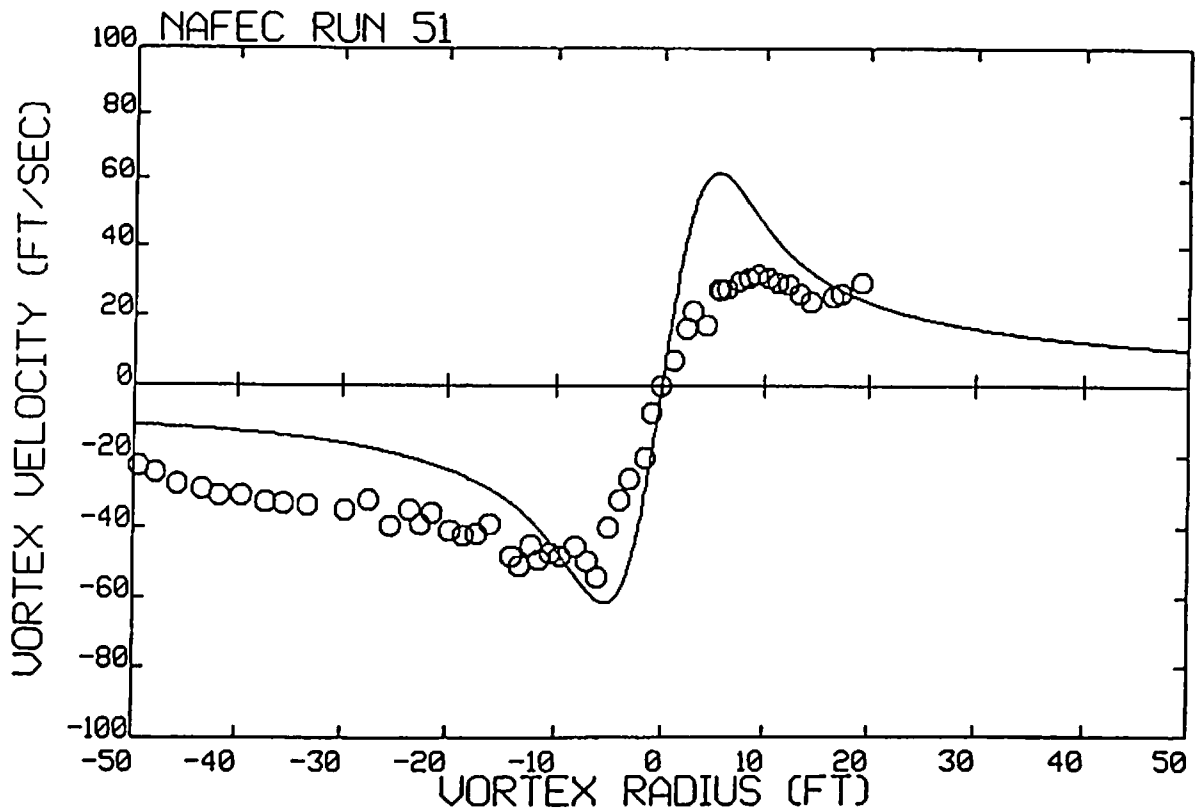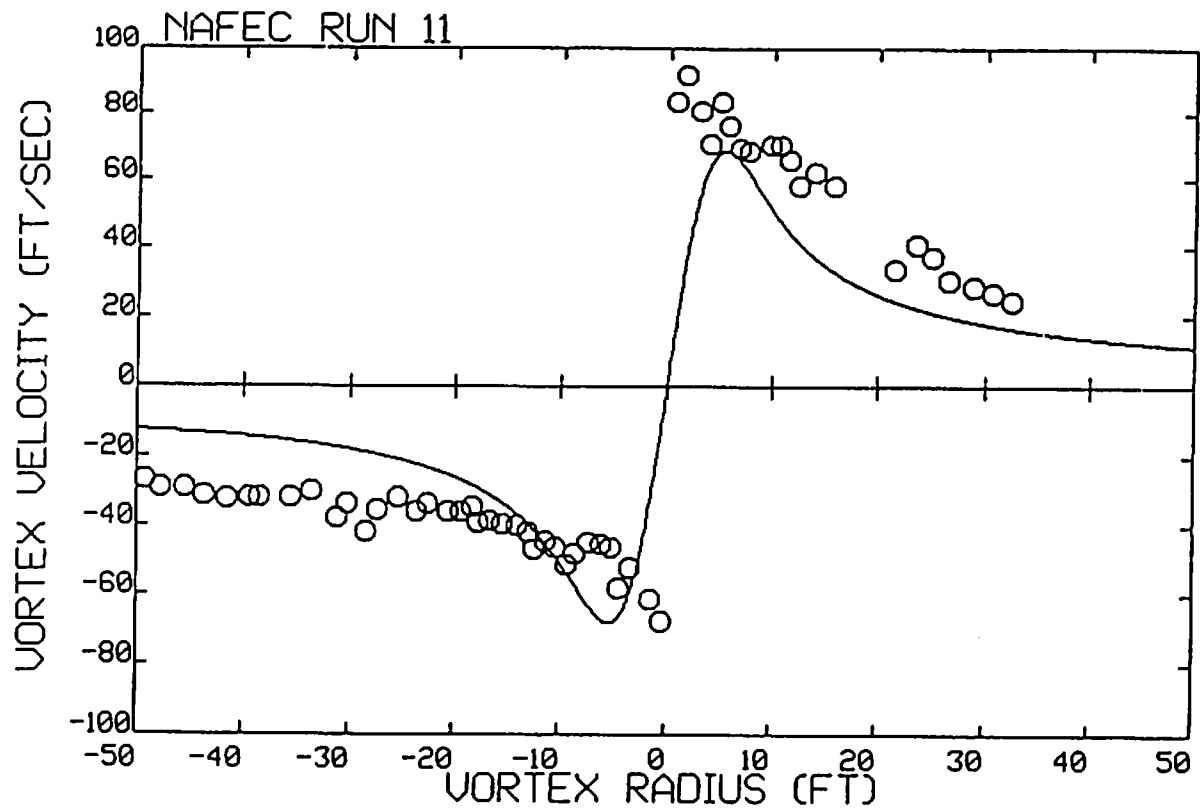
Figure 5. Comparison of measured (circles) and predicted (curve) swirl velocity profiles for a B747 in landing configuration. Top: NAFEC Run 11; Bottom: NAFEC Run 51. Data from Garodz et al. (1974).
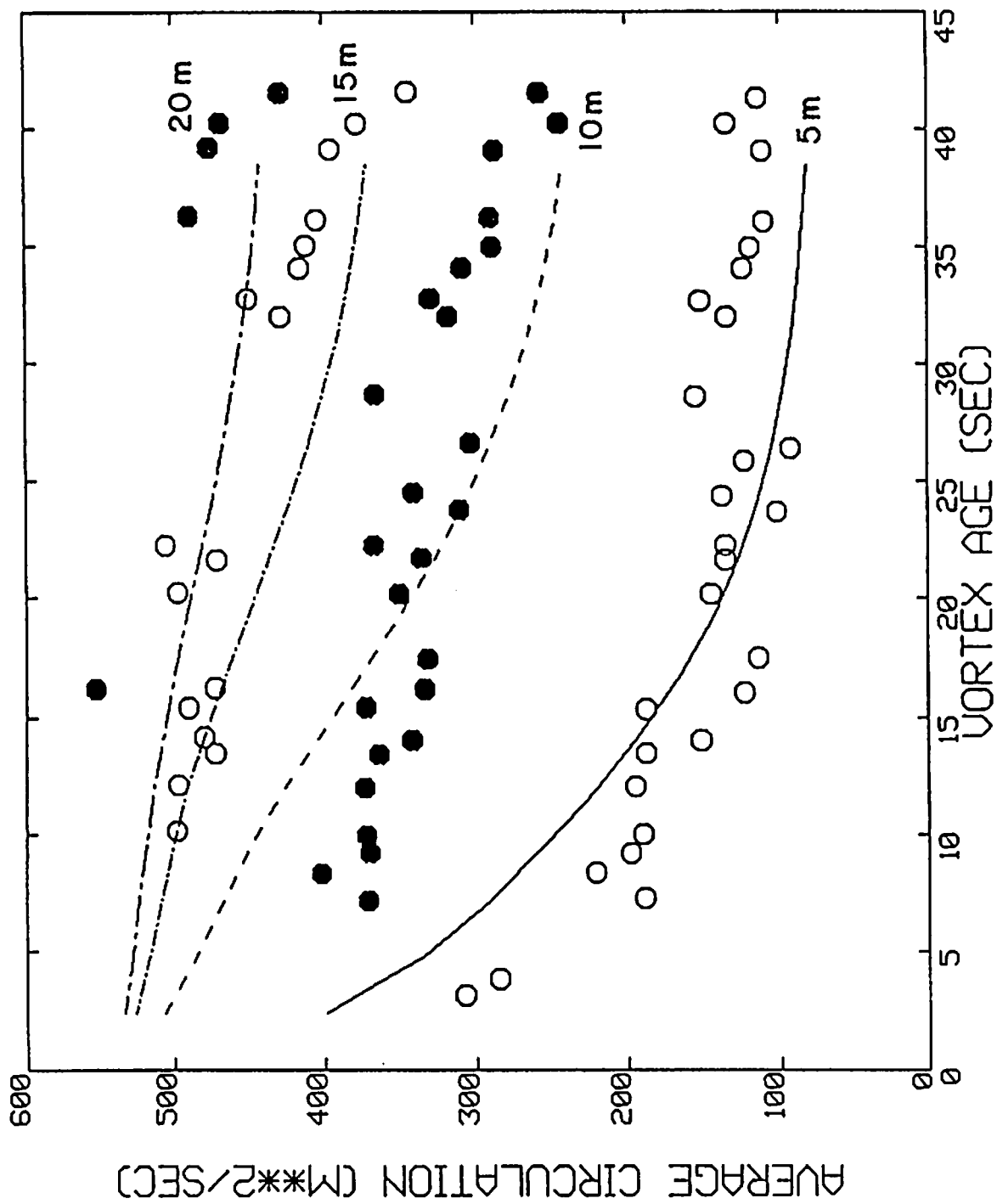
Figure 6. Comparison of measured (circles) and predicted (curves) average circulation in the wake of a B747 in a landing configuration, Run 5 (Burnham et al. 1978). The averaging radii are 5, 10, 15 and 20 meters around the center of the vortex.
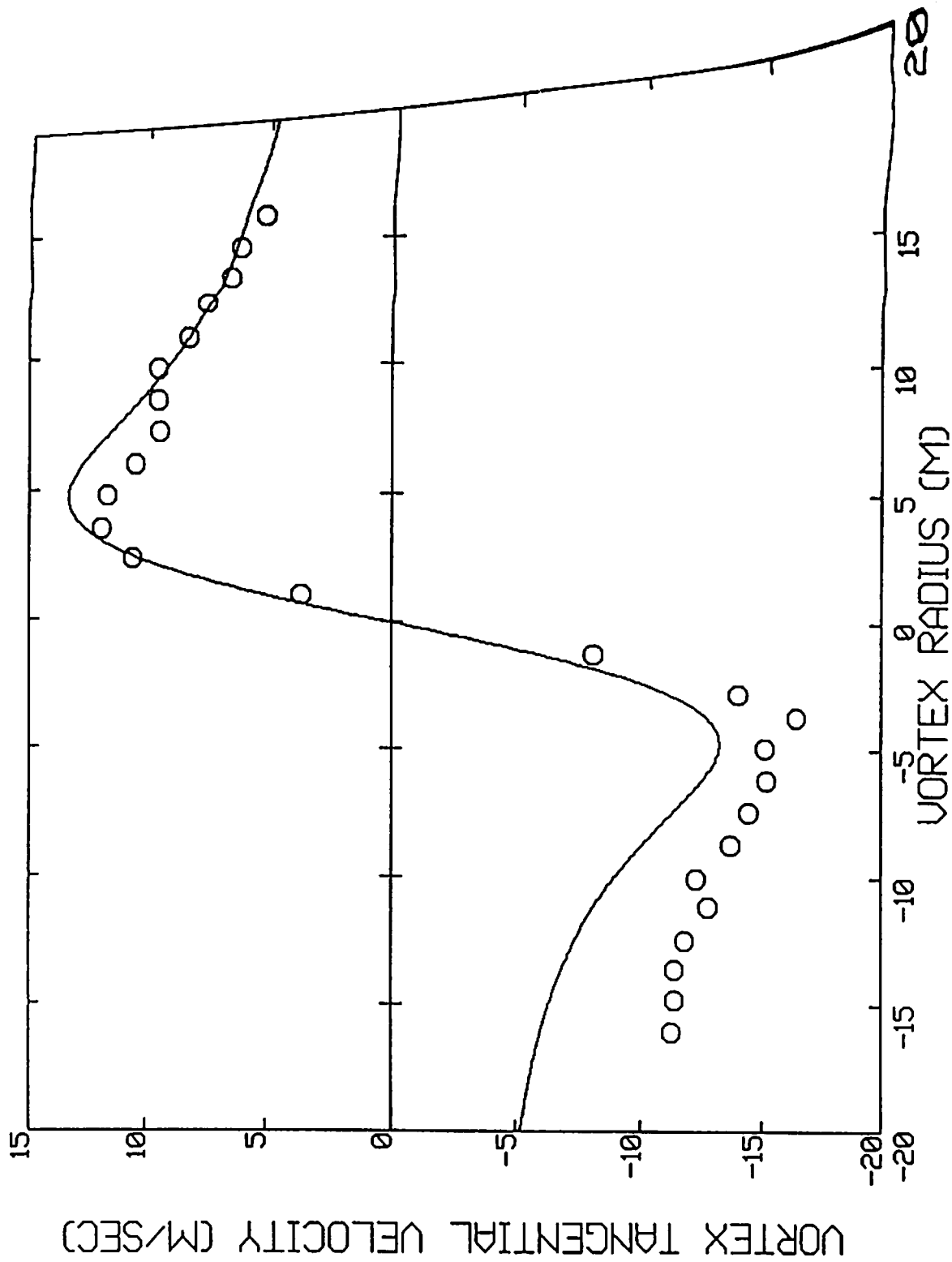
Figure 7. Comparison of measured (circles) and predicted (curve) vortex velocity in the wake of a B747 in a landing configuration, Run 5 (Burnham et al. 1978). The vortex has aged 9.8 seconds after aircraft fly-by.
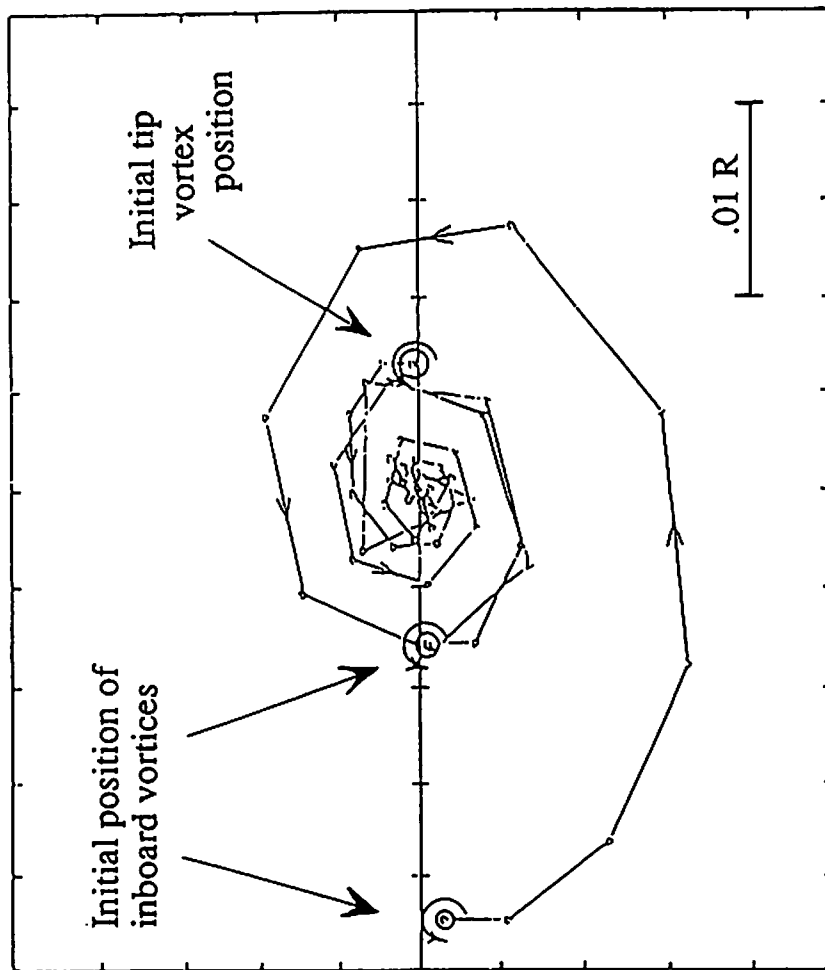
Figure 8. Three vortices rolling up into a single vortex; viewed in a reference frame moving with the centroid of vorticity.

REFERENCES

Betz, A. 1932: "Behavior of Vortex Systems," Zeitschrift fur Angewandte Mathematik und Mechank, Vol. 12, also NASA TM 713.

Bilanin, A. J. and Donaldson, C. duP. 1975: "Estimation of Velocities and Roll-Up in Aircraft Vortex Wakes," Journal of Aircraft, Vol. 12, pp. 578-585.

Bilanin, A. J. and Teske, M. E. 1988: "Unified Wake Analysis," C.D.I. Report No. 88-06, prepared for the U. S. Department of Transportation SBIR Program Contract No. DTRS-57-85-C-00134.

Bilanin, A. J., Teske, M. E. and Hirsh, J. E. 1978: "Neutral Atmospheric Effects on the Dissipation of Aircraft Vortex Wakes," AIAA Journal, Vol. 16, pp. 956-961.

Bilanin, A. J., Teske, M. E. and Williamson, G. E. 1977: "Vortex Interactions and Decay in Aircraft Wakes," AIAA Journal, Vol. 15, pp. 250-260.

Bliss, D. B. 1982: "Effect of Unsteady Forcing on the Sinusoidal Instability of Vortex Wakes," Journal of Aircraft, Vol. 19, pp. 713-721.

Bliss, D. B. 1987: "Analysis of Tip Vortex Self-Induced Motion," NASA Contractor Report No. 177439.

Bliss, D. B., Teske, M. E. and Quackenbush, T. R. 1987: "A New Methodology for Free Wake Analysis Using Curved Vortex Elements," NASA Contractor Report No. 3958.

Brown, C. E. 1973: "Aerodynamics of Wake Vortices," AIAA Journal, Vol. 11, pp. 531-536.

Burnham, D. C., Hallock, J. N., Tombach, I. H., Brashears, M. R. and Barber, M. R. 1978: "Ground-Based Measurements of the Wake Vortex Characteristics of a B-747 Aircraft in Various Configurations," FAA-RD-78-146.

Campbell, G. S. 1951: "A Finite-Step Method for the Calculation of Span Loadings of Unusual Planforms," NACA RM L50L13.

Crow, S. C. 1970: "Stability Theory for a Pair of Trailing Vortices," AIAA Journal, Vol. 8, pp. 2172-2179.

Donaldson, C. duP. 1971: "A Brief Review of the Aircraft Trailing Vortex Problem," AFOSR-TR-71-1910.

Donaldson, C. duP. and Bilanin, A. J. 1975: "Vortex Wakes of Conventional Aircraft," AGARDograph No. 204.

Donaldson, C. duP., Snedeker, R. S. and Sullivan, R. D. 1974: "A Method of Calculating Aircraft Wake Velocity Profiles and Comparison with Full-Scale Experimental Measurements," Journal of Aircraft, Vol. 11, pp. 547-555.

Evans, P. F. and Hackett, J. E. 1976: "Numerical Studies of Three-Dimensional Breakdown in Trailing Vortex Wakes," NASA CR-137888.

Garodz, L. J., Lawrence, D. and Miller, N. J. 1974: "The Measurement of the Boeing 747 Trailing Vortex System Using the Tower Fly-By Technique," DOT/FAA Report No. FAA-RD-73-156.

Glauert, H. 1948: *The Elements of Aerofoil and Airscrew Theory*, Second Edition, Cambridge University Press.

Hallock, J. N. and Eberle, W. R. 1977: "Aircraft Wake Vortices: A State-of-the-Art Review of the United States R&D Program," FAA-RD-77-23.

Hirsh, R. S. 1983: "Higher Order Approximations in Fluid Dynamics - Compact to Spectral," von Karman Institute Lecture Series 1983-84.

Hough, G. R. 1973: "Remarks on Vortex-lattice Methods," Journal of Aircraft, Vol. 10, pp. 314-317.

Jordan, P. F. 1973: "Structure of Betz Vortex Cores," Journal of Aircraft, Vol. 10, pp. 691-693.

Margason, R. J. and Lamar, J. E. 1971: "Vortex Lattice FORTRAN Program for Estimating Subsonic Aerodynamic Characteristics of Complex Planforms," NASA TN D-6142.

Purcell, E. W. 1953: "The Vector Method of Solving Simultaneous Linear Equations," Journal of Mathematics and Physics, Vol. 32, pp. 180-183.

Quackenbush, T. R., Bliss, D. B. and Wachspress, D. A. 1989: "New Free Wake Analysis of Rotorcraft Hover Performance Using Influence Coefficients," Journal of Aircraft, Vol. 26, pp. 1090-1097.

Quackenbush, T. R., Bliss, D. B., Wachspress, D. A. and Ong, C. C. 1990: "Free Wake Analysis of Hover Performance Using a New Influence Coefficient Method," NASA CR 4309.

Rossow, V. J. 1973: "On the Inviscid Rolled-Up Structure of Lift-Generated Vortices," Journal of Aircraft, Vol. 10, pp. 647-650.

Sykes, R. I., Lewellen, W. S. and Parker, S. F. 1986: "On the Vorticity Dynamics of a Turbulent Jet in a Crossflow," Journal of Fluid Mechanics, Vol. 168, pp. 393-413.

Teske, M. E. 1976: "Vortex Interactions and Decay in Aircraft Wakes. II: The Vortex Wake Computer Program User Manual. III: The Vortex Wake Computer Program Programmer Manual," Aeronautical Research Associates of Princeton, Inc. Report No. 271.

Teske, M. E. 1989: "Unified Wake Analysis User Manual Supplement," C.D.I. Technical Note No. 89-20.

VORTEX INTERACTIONS WITH A FREE-SURFACE

Edwin P. Rood
Fluid Dynamics Program (1132F)
Office of Naval Research
Arlington, VA 22217

Free-surface phenomena are characterized by viscous processes that produce vortices of all scales. Although the processes are similar to those associated with solid wall boundary layers, the quite different boundary conditions distinguish the two types of flow. Recent advances in capabilities for both physical and numerical experiments as well as analytic investigations of boundary conditions have provided the means to comprehensively investigate the detailed dynamics of vortices interacting with the free-surface. Naval scientific curiosity in this area is driven by the need to understand the air-sea interface and to predict and control marine vehicle signatures. An understanding of the three-dimensional interactions is also important for interpreting results of laboratory scale aircraft wake studies in which an air-water free-surface is employed as a ground plane.

In this paper the physical problem is the interaction between vortices in water and an air-water interface. The term "free-surface" denotes the interface between water and air on which the shear stresses caused by the motions of the air are insignificant compared to those caused by the motion of the water. Surface contamination, when present, produces a gradient in the surface tension that results in a stress on the water. Specifics about the surfactant and its dispersion are not addressed, nor required, since the focus of this paper is on the qualitative mechanisms underlying the observed interactions between vorticity and the free-surface.

The boundary condition at the free-surface is derived from stress equilibrium. Therefore the boundary condition is on gradients of the velocity as well as on the pressure. These conditions are different than that for a solid body boundary in which case the boundary condition is on the velocity.

This paper is concerned with the description of the mechanisms underlying interactions between vortices and the free-surface. Therefore the flow is discussed in the context of distributed vorticity. The fluid is essentially incompressible, and the governing equations are derived from the conservation of mass and the conservation of momentum. These conservation equations express the evolution of the pressure and the velocity (as well as the distribution of the density even for incompressible flow). The vorticity is defined to be the curl of the velocity, and is a kinematic variable (Morton, 1984). The vorticity is a special variable that has an evolution field

equation that resembles the equation for conservation of momentum. However, the vorticity obeys mathematical laws defined by vector operations and is not governed by a conservation statement. Some aspects of vorticity/free-surface interactions are best explained by erasing notions that vorticity is angular momentum. Examination of the boundary conditions on vorticity shows that tangential vorticity can flux into or out of the free-surface. A special case occurs when the vorticity entirely disappears from the flow.

Lugt (1987) shows that the zero-stress condition at the free-surface leads to a boundary condition relating the flux (through the free-surface), of the tangential vorticity, to the gradient of the fluid velocity in the free-surface plane. Although Lugt considered steady flows, the inclusion of time dependence in the flow for a time-independent free-surface, such as a flat surface, adds an additional term proportional to the local fluid acceleration in the plane of the interface. These boundary conditions lead to the observation that flat free-surfaces have nonzero tangential vorticity flux in the presence of vortices.

This analysis demonstrates the essential distinction between fixed rigid body boundary conditions and flat free-surface boundary conditions. For a fixed rigid body boundary, the flux of vorticity is proportional to the pressure gradient on the no-slip surface. On the other hand, the flux of vorticity for a full slip (zero stress) free-surface is proportional to the local accelerations of the fluid in the interface. This distinction is made apparent in the following example (Anthony, 1991). Consider the two-dimensional flow between two parallel plates, initially at rest but with one plate suddenly imparted a constant velocity. The flow approaches a state of constant vorticity with a linear distribution of velocity between the plates. The vorticity generated at the instant of acceleration of the moving plate diffuses into the flow interior. Now consider the response if the nonmoving plate is replaced with a free surface. The flow again approaches a state of constant vorticity but the value is zero. This is because the vorticity produced by the accelerated plate diffuses through the flow and fluxes out through the free surface. Coincidentally the free surface, and in fact the entire flow, is accelerated as the vorticity fluxes out of the field. In this second example vorticity has "disappeared" from the flow, but no conservation principle has been violated because mass and momentum are conserved.

The feature that vorticity can disappear from the fluid interior is an essential consideration for explaining observations of interactions between vorticity and the free-surface. Numerical predictions of the interaction demonstrate this feature quite clearly. Ohring & Lugt (1991) have performed fully nonlinear predictions of the interaction for a pair of two-dimensional vortex tubes approaching the free-surface. Their results clearly show a dissipation of the vorticity as it contacts the free-surface. Interpretations of their data requires one additional piece of information: that the boundary value of the vorticity at a curved free-surface is fixed by the fluid velocity in the interface and the radius of curvature of the interface. Hence the interaction of the vortex tube with the free-surface is complicated by the appearance of countersign vorticity in regions of negative interface curvature. This vorticity cancels with primary vorticity. However, the predictions clearly show the relatively small amount of generated countersign vorticity, leading to the conclusion that the primary loss of vorticity is to the flux through the free-surface.

The predictions verify what the analytic boundary conditions state must be the condition on the interaction. This knowledge can be applied to interpretations of physical experiments in which vortex tube pairs interact with the free surface. The famous experiments of Barker & Crow (1977) showed apparent rebound of the vortices from the free-surface. This reaction is what is observed when vortices interact with a rigid no-slip boundary where secondary boundary layer vorticity induces the primary vorticity away from the wall. One explanation for the rebound in the presence of a free-surface, not discussed in the literature, is that a small surface tension gradient resulted in countersign vorticity. For the moment this explanation will be ignored, but will be taken up later in this paper. A subsequent numerical experiment by Peace & Riley (1983) also showed a rebound of the vortex. In the numerical experiment the center of the diffusing vortex was defined to be the location of maximum vorticity. An explanation for the rebound can be found in the above description of vorticity flux through the free-surface. As the primary vortex approaches the free-surface and deforms, the gradient of the vorticity acts to drive vorticity to the interface, where it fluxes out of the field. Saffman (1991) rigorously shows that the location of the centroid of maximum vorticity then moves away from the free-surface. The centroid is not a Lagrangian quantity and hence fluid particles associated with the vortex move toward the free surface and the vortex does not rebound! In fact, one could expect most of the vorticity to eventually diffuse through the free-surface, which must be maintained at zero vorticity if it is flat and shear-free. In this case the resulting flow would be irrotational and would have acquired a velocity in the interface consistent with the flux of vorticity through the interface.

Vortex tube pairs are of naval interest because they are generated by marine vehicles and leave signatures on the free-surface. An understanding of the evolution of nominally two-dimensional pairs is hence important. It is observed with both physical and numerical experiments that three-dimensionality sets in very quickly with nominally two-dimensional vortices. Sarpkaya (1986) shows with physical experiments that small scale three-dimensional features, called striations, appear soon after the pair is formed. At later time, large-scale instabilities such as Crow instabilities appear. For this paper, the focus is on the small-scale instabilities.

Sarpkaya (1986) also shows "whirls" appearing at the edges of the free-surface depressions ("scars") paralleling the primary vortex axes. The nominally two-dimensional vortex pair is then manifested on the free-surface by cross-axis striations and normal (to the free-surface) eddies. These features are believed to result from short wave instabilities and from surface tension gradients on the free-surface, both of which are discussed in the remainder of this paper.

Short wave instabilities of a vortex pair have been numerically investigated by Dommermuth & Yue (1990) using a finite difference technique. Linearization of the free-surface boundary conditions restricts the method to low Froude numbers. Nevertheless, the basic dynamics of the short-wave instabilities, including interactions with the free-surface boundary layer, are revealed. The numerical experiment was conducted in a periodic domain of spatial period less than that required for Crow instability. Secondary vorticity was observed to reconnect to the free-surface to produce the dimples observed by Sarpkaya (1986). The striations are produced by helical vorticity stripped from the primary vortex and pulled away by induction of the other primary vortex. In this description, both the striations and the dimples are produced by the same mechanism. The helical instabilities produce U-shaped vortex loops hanging from the primary vortex. This U-shaped vortex is accelerated by the mutual induction of the vortex pair, and

interacts with the boundary layer vorticity produced by the deformed free-surface. In a complicated process the U-shaped vorticity is stretched and reconnected to the free-surface to produce the dimples.

Stacking of the Dommermuth & Yue (1990) periodic solutions of the vortex pair interaction with the free-surface produces a vorticity field that very much looks like the photographs obtained by Sarpkaya (1986). This feature of vortex reconnection at the free-surface is vividly depicted by Sarpkaya (1990) with a two-dimensional experiment at very high Froude number. In this case, the vortex momentum is sufficient to greatly deform the free-surface and clearly show the striations and the dimples.

The so-called "reconnection" of vortex loops at the free-surface is explained using the analytic description of the boundary conditions at the beginning of this paper. As the vortex loop approaches the free-surface, the core is deformed against the free-surface leading to large vorticity gradients. The free-surface vorticity is required to be a value determined by the curvature of the free surface and the fluid velocity in the free-surface. For linearized free-surface conditions the free-surface value for the vorticity is nearly zero, such as for the numerical predictions by Dommermuth & Yue (1990). For the physical experiments of Sarpkaya (1990) the peak value is nonzero, but nevertheless fixed by kinematics in the interface. The vorticity in the vortex loop will rapidly diffuse to the free-surface, and in fact will flux out of the field. This mechanism is not to be confused with "breaking" of vortex lines, and is instead a process by which the apex of the loop simply fluxes out to the field at the boundary leaving only normal vorticity (for a flat surface). For a deformed free-surface the results are complicated by the free-surface vorticity condition, but the concept, of course, remains identical.

The presence of surfactant and indirect evidence of surface tension gradients also produces secondary vorticity leading to dimples on the free-surface. Willmarth, et al. (1989) conducted an experiment identifying the features attributed to the presence of surfactant on the free-surface. A towed delta wing produced a vortex pair interacting with the free-surface. With careful attention to detail, the Reynolds ridge in the region of the dimples at the edge of the primary vortex scar was isolated. The Reynolds ridge is a phenomena that has received attention numerous times in the literature (Scott, 1982). It appears when the interacting vortices sweep the free-surface contaminants to the side. Replenishment of the free-surface with cleaner fluid leads to a surface tension gradient at the edge of the surfactant, the Reynolds ridge. The surface tension gradient produces an acceleration of the fluid that is balanced by viscous stresses resulting in a boundary layer originating at the Reynolds ridge similar to the origination of a boundary layer at the leading edge of a flat plate. That secondary vorticity separates to produce vortical structures that then reconnect to the free-surface. The result is primary vortices laced with cross-vorticity striations, accompanied by vortex loops hanging down from the free-surface at the edge of the scars produced by the primary vortices.

In summary, vortex interactions with a free-surface are characterized by vorticity flux through the interface with coincident flow acceleration, three-dimensional instabilities of many scales, and secondary shear layers produced by interface curvature and surface tension gradient.

REFERENCES

Anthony, D. (1991). Private communication.

Barker, S.J. & Crow, S.C. (1977). "The Motion of Two-Dimensional Vortex Pair in a Ground Effect," *Journal of Fluid Mechanics*, 82.

Dommermuth, D.G. and Yue, D.K.P. (1990). "A Numerical Study of Three-Dimensional Viscous Interactions of Vortices with a Free Surface," *Eighteenth Symposium on Naval Hydrodynamics*, Ann Arbor, Michigan, National Academy of Sciences.

Lugt, H.J. (1987). "Local Flow Properties at a Viscous Free Surface," *Physics of Fluids*, 30, Dec.

Morton, B.R. (1984). "The Generation and Decay of Vorticity," *Geophysical and Astrophysical Fluid Dynamics*, Vol. 28.

Ohring, S. & Lugt, H.J. (1991). "Interaction of a Viscous Vortex Pair with a Free Surface," *Journal of Fluid Mechanics*, 127.

Peace, A.J. & Riley, N. (1983). "A Viscous Vortex Pair in Ground Effect," *Journal of Fluid Mechanics*, 125.

Saffman, P.G. (1991). "Approach of a Vortex Pair to a Rigid Free Surface in Viscous Fluid," *Physics of Fluids A*, 3, May.

Sarpkaya, T. (1986). "Trailing-Vortex Wakes on the Free Surface," *Sixteenth Symposium on Naval Hydrodynamics*, University of California, Berkeley, William C. Webster (ed.)

Sarpkaya, T. & Suthon, P.B. (1990). "Scarred and Striated Signature of a Vortex Pair on the Free Surface," *Eighteenth Symposium on Naval Hydrodynamics*, Ann Arbor, MI, National Academy of Sciences.

Scott, J.C. (1982). "Flow Beneath a Stagnant Film on Water: The Reynolds Ridge," *Journal of Fluid Mechanics*, 116.

Willmarth, W.W., Tryggvason, G., Hirsa, A., & Yu, D. (1989). "Vortex Pair Generation and Interaction With a Free Surface," *Physics of Fluids A*, 2, Feb.

INITIAL ROLL-UP OF A WINGTIP VORTEX

Jim S. Chow, Greg G. Zilliac, Peter Bradshaw
Ames Research Center, Moffett Field, CA 94035, and
Mechanical Engineering Department
Stanford University
Stanford, CA 94305

ABSTRACT

The roll-up of a wingtip vortex, at high Reynolds number, was studied with an emphasis on suction side and near wake measurements. Research was conducted in the 32 in x 48 in low-speed wind tunnel at the Fluid Mechanics Laboratory of NASA Ames Research Center. The half-wing model has a 3-ft semispan and 4-ft chord, with a NACA 0012 airfoil section and rounded tip. Angle of attack of the wing was set at 10° and the Reynolds number based upon chord was 4.6 million.

Flow visualization studies using surface oil flow and laser smoke flow techniques were conducted, showing the highly three-dimensional nature of the flow around the wingtip and illuminating the formation of the feeding sheet and the viscous core region of the vortex. Airfoil surface pressure measurements, taken at over 450 locations on the upper and lower surface of the wing, clearly showed a suction peak associated with the development of the primary vortex. Seven-hole pressure probe measurements of the velocity field surrounding the wingtip showed an axial core velocity magnitude of approximately 1.7 U_∞. This level of axial velocity is not currently being computed correctly by Navier Stokes codes.

NOMENCLATURE

x,y,z	wing model fixed coordinate system
x',y',z'	wind tunnel fixed coordinate system
u	x'-component of velocity
U_∞	freestream velocity
$|U|$	magnitude of the local velocity vector
c	wing model chord
b	wing span of model including tip
w	wing span of constant chord section
C_p	pressure coefficient

Re$_c$	Reynolds number based on chord
α	angle of attack
γ	tip circumferential angle measured from mean chord centerline
ρ	density
P	static pressure
P$_\infty$	freestream static pressure

INTRODUCTION

The wingtip vortex flow is one of great importance because of its effect on practical problems such as landing separation distances for aircraft, blade/vortex interactions on helicopter blades, and propeller cavitation on ships. It also continues to be a perplexing problem for the computational scientist because of the presence of large gradients of velocity and pressure in all three dimensions, especially in the near field at high Reynolds number. In the case of wings with nearly-elliptic loading, a discrete vortex forms at the tip (Figure 1), fed by vorticity from the tip boundary layer. As the vortex moves downstream, it rolls up more and more of the wing wake until its circulation is nominally equal to that of the wing. The rollup distance is small compared to the separation of aircraft on the approach path, but not necessarily small compared to the distance between the interacting lifting surfaces, such as the strake or foreplane and the main wing on a close-coupled fighter. The flow in the near-field rollup region is therefore important in its own right as well as in providing a possible means of control of the far-field vortex.

The state-of-the-art computational work by Srinivasan et al. (1988), on a helicopter wingtip, shows good qualitative comparisons with experimental work done by Spivey (1968), but the resolution of the viscous wake and the surface pressure suction peak, due to the vortex, was poor. Analytical studies by Hoffmann & Joubert (1963), Batchelor (1964), Squire (1965), and Moore & Saffman (1973) have investigated fully-rolled-up laminar trailing vortices; however, at the Reynolds numbers found in most practical applications, trailing vortices are turbulent. Quite apart from possible transition in the vortex itself, or transition due to a strong adverse gradient, which can occur at relatively low Reynolds number, surface roughness due to rivet heads, dirt or impact damage is likely to cause transition of the tip boundary layer upstream of the start of vortex formation. Govindaraju & Saffman (1971) and Phillips (1981) analysed the turbulent trailing vortex, but focused on the vortex flow relatively far downstream of the trailing edge of the wing, where flow self-similarity can be observed. Ikohagi et al. (1986) developed a model for the turbulent vortex in the near field. It was based partially upon data taken from an elliptically loaded hydrofoil at low Reynolds number and therefore its applications may be limited. There have, of course, been many theoretical studies of the formation and rollup of delta-wing vortices, based on inviscid models, but these are not very relevant to the vortex from a rounded tip where the separation line is not defined by a sharp edge.

There have been several experimental studies of the fully developed vortex far downstream of the wing tip, parametric studies of various tip shapes (Spivey, 1968) and studies where devices were used to alleviate the tip vortex (Carlin et al., 1989). The latter studies, which in the last few years have usually been related to helicopter blades rather than fixed wings, have generally concluded that tip shape can substantially affect the way the vorticity in the tip vortex is

concentrated. However, trade-offs with drag make more experimental work necessary before reliable modifications can be made.

Other experimental work on the flow over the tip and in the rollup region, e.g., Spivey & Morehouse (1970) and the related work by Chigier & Corsiglia (1971), show a characteristic surface-pressure suction peak near the tip, denoting the approximate location of the tip vortex as it develops on the top surface of the wing. Other features Chigier noted were a relatively high axial velocity in the core of the vortex in the near field ($u/U_\infty = 1.1$ to 1.4 at $\alpha = 12°$) and a secondary vortex with the same sense of rotation as the main vortex located in between the main vortex and the wingtip.

Recently, Bandyopadhyay, Stead, & Ash (1990) investigated the turbulence structure in a turbulent trailing vortex and concluded that for their range of test conditions, the Rossby number (axial velocity defect/maximum tangential velocity) was the controlling parameter for the turbulence structure, not the vortex Reynolds number (circulation/viscosity). They also concluded that the inner core is not, as thought previously, a region in solid-body rotation that does not interact with the outer vortex region, but a relaminarizing region where patches of turbulent fluid are intermittently brought in from the outer region. However, their vortex was created by a double-wing vortex generator, and their measurements were taken far downstream of the trailing edge so that they may not be quantitatively representative of the near-field rollup region of a wingtip vortex.

There seems to have been no study of the tip flow and near-field vortex rollup process detailed enough to be used in developing or testing a prediction method or for putting the design of tip modifications on a firm fundamental basis. The present experimental study focuses on the initial roll-up region of the turbulent vortex from a generic wingtip at high Reynolds number. The approach is first to reach a basic understanding of the physics involved in the flow near the wingtip, supported by detailed measurements of turbulence structure, before proceeding to development of prediction methods or tip modifications, although both are in our program.

In our experiment, surface oil-flow visualization, laser-illuminated smoke visualization, surface pressure measurements, and velocity-field measurements by use of a 7-hole pressure-probe (Zilliac, 1989) have been completed for the flow over a rectangular wing with rounded tip as far as a half chord downstream of the trailing edge. The Reynolds number based on chord was 4.6 million. Given the trade-off between taking extensive measurements at one flow condition or taking fewer measurements at several flow conditions, the former option was chosen because measurements at closely spaced points are needed to resolve the large spatial gradients in the thin tip boundary layer and the rollup region, and because it would give the computational scientist a solid test case to compare with his/her results.

From the results acquired to date, we have been able to build up a detailed qualitative and quantitative picture of the process by which the tip boundary layer separates and rolls up into a vortex.

EXPERIMENTAL PROCEDURE

The measurements were performed in the 32 in. x 48 in. low speed wind tunnel (Figure 2) at the Fluid Mechanics Laboratory (FML) of NASA Ames Research Center. Maximum freestream turbulence in the wind tunnel, as measured by hot wire anemometer, is 0.15%. A half-wing model of 4-ft chord, 3-ft semi-span, rounded (body of revolution) wingtip, and NACA 0012 wing section was used, as shown in Figure 3. The two coordinate systems used to describe the physical locations of the experiment are also shown in Figure 3. During the design phase of this study, the decision was made to use as large a model as possible to avoid severe "viscous" tunnel interference due to excessive growth or separation of the tunnel wall boundary layers. "Inviscid" tunnel interference is, of course, very large and any computations would have to take into account the presence of tunnel walls. This could be done by using slip boundary conditions and imposing a small transpiration velocity through the walls to simulate the displacement thickness of the boundary layer. A similar approach was taken in the European GARTEUR swept-wing experiment (van den Berg, 1989).

The model was constructed out of aluminum with a skin thickness of 1/4 in and precision machining of the surface contour ($\pm$ 0.0005 in). The angle of attack setting of the model could be varied from $\pm 16°$ angle of attack by rotating the model about its quarter chord, although, as stated previously, the only test case of interest in the present study was at $+10°$ angle of attack. The quarter chord point was located in the vertical center of the test section so that geometries at positive and negative angles of attack would be identical.

A trip was used to fix transition near the leading edge. Roughness elements of 0.017 in diameter were packed closely together to form a 1/8 in wide strip. The strip was placed across the span of the wing at a surface distance of 2.0 in from the leading edge. The trip extended around the tip and along the bottom surface of the wing. Napthalene sublimation and microphone techniques were used to confirm that the boundary layers were turbulent after the trip.

On the upper half of the wing model surface, 222 static pressure taps are located in 12 chordwise rows at the constant chord spanwise locations of $z/w = 0.181, 0.362, 0.725, 0.845, 0.906, 0.936$, and 0.966 and at the tip spanwise locations of $\gamma = 0.0°, 22.5°, 45.0°, 67.5°$, and $80.0°$. The tubing to the taps is connected to a six-cap Scanivalve (40 barrels/cap) which in turn was connected to a MKS 223B pressure transducer. All measurements on the pressure side of the wing were made by rotating the model to negative angle of attack.

Traversing was done using custom built rails and slides driven by Compumotor microstepping motors and controllers (25,000 microsteps/rev). The five-degree-of-freedom traversing system had the capability of translation in three directions, and of pitching and yawing the probe. Probe position and orientation was derived from optical encoders on all axes (not from motor step counts). Absolute positioning accuracy of a probe (relative to wing model surface) was within .02 inches. Incremental positioning accuracy was determined to be within .001 inches for translation, 0.2° for pitch, and 0.1° for yaw.

To get a qualitative picture of the skin friction lines on the wing, surface-oil flow visualization was done using a mixture of titanium oxide, oleic acid, kerosene, 10 weight oil, and fluorescent

powder and photographed using a 2 by 2 in large format still camera. An ultraviolet lamp was used to illuminate the mixture. Laser-illuminated smoke flow visualization using a Rosco 1500 smoke generator and a 5 Watt Lexel argon-ion laser, was videotaped with a Sony DXC-M3A video camera and also a 35 mm camera.

Flowfield data were taken at the following cross-flow planes: x'/c = -0.40, 0.15, 0.35, 0.44, 0.54, 0.63, 0.73 (approximately at T.E.), 0.74, 0.99, 1.19, and 1.42. Data planes taken in the wake and in front of the wing model had 20 x 29 data points (23.0 in vertical, 28.0 in span). The boundaries of the data planes were at z/w = 0.36, z/w = 1.20, y'/c = -0.24, and y'/c = 0.24. Data planes taken above the surface of the wing had 11 x 29 data points. These planes were, in essence, half-planes, since they extended exactly half way around the tip, but did not include any points below that line. For data points near the wing surface, an electronic touch sensor was used to find the surface of the model. The first vertical data point above the surface was taken 0.10 inches above the location found by the touch sensor. An additional cross-flow plane, with concentrated grid spacing (15 x 29 data points, 4.0 in span) focusing on a smaller region, was taken at x'/c = 0.53.

A 7-hole pressure probe was used to measure static pressure and the velocity vector. Calibration of the probe was done in-situ, prior to installation of the model. The procedure for the calibration is described by Zilliac (1989). Data rate of the probe measurement system was maximized by use of simultaneous sampling of the eight required pressure measurements at each measurement location (seven for the probe and one for tunnel static) with the use of eight separate MKS 223B pressure transducers. For high flow angles (> 30°), flow angle measurement uncertainty for the 7-hole probe is within 1° while velocity magnitude uncertainty is within 1.1% of freestream velocity. For low flow angles (< 30°), flow angle uncertainty is within 0.5° while velocity magnitude uncertainty is within 0.8%.

Like all probe based measurements, velocity gradients can lead to additional error. The effect of flow gradients on the axial-core-velocity magnitude is of particular interest. An estimation of the additional error, due to flow gradients in the core, can be made by considering a vortex with a core radius of 1.5 in (a characteristic size for our present case) and a maximum tangential velocity of 1.0 U_∞. A simple calculation shows that the worst case tangential-velocity variation across the face of the probe (0.1 inches diameter) would be 0.066 U_∞. This leads to an estimation of a possible flow angle measurement error of 2.2 degrees. In the core, the streamwise pressure gradient variation is negligible, thus the maximum error in core-axial-velocity magnitude measurement is 0.1% above the 1.1% estimated velocity magnitude uncertainty.

Data acquisition was done using a 32-bit DEC μVAX II computer to control a 15-bit Tustin X-2100 A/D. Measurement error due to A/D resolution was negligible compared to instrument error.

RESULTS AND DISCUSSION

Streamwise development of the tip vortex is shown by laser-illuminated smoke flow photos in Figure 4. Each frame visualizes the crossflow plane perpendicular to the x' axis. Still

photographs of crossflow planes were taken at the following locations: x'/c = 0.36, 0.49, 0.61, 0.74, 0.86, 0.99, 1.11, 1.24. The spanwise location of the vortex core is nearly constant at a z/w = 0.97. The perpendicular distance to the core from the wing surface increases with chord. At a x'/c = 0.36, the vortex core is located about 0.4 inches above the wing surface, while at the trailing edge (x'/c = 0.74), the vortex core "sits" approximately 1.5 inches above the wing surface. The first signs of the tip vortex can be seen in the first photo at x'/c = 0.36.

Surface oil flow results on the lower surface of the model (Figure 5a, freestream from left to right) show the highly three-dimensional nature of the flow near the tip region. In the tip region, the effect of the spanwise pressure gradient causes the skin friction lines to become skewed outboard. Figure 5b shows the tip region skin friction patterns (freestream velocity flows from top to bottom). Again, the general action of flow wrapping around the tip from the lower surface to the upper surface is evident. The dominant feature, in Figure 5, is a line where other skin friction lines converge, starting at about 55% chord. The properties of this "convergence line" are hard to quantify. Unlike classical two-dimensional separation, the skin friction magnitude is non-zero along this line (owing to the presence of a streamwise component). In the literature, this line is often described as indicative of "local separation" or "open separation." The salient characteristic of this type of separation is that there are no singular points in the skin-friction line topology. Additionally, there is no zone of stagnant fluid or reversed flow which typically occurs in flows which are "globally separated" (for more detail, see Zilliac 1989). The convergence line is indicative of the departure of the shear layer from the surface. This lifting off of vorticity occurs due to the adverse pressure gradient encountered by the cross flow velocities which wrap the flow around the tip. Figure 5c shows the upper-surface-skin-friction patterns. The effect of the tip vortex is apparent near the trailing edge of the tip region. Directly beneath the tip vortex, the skin friction lines get swept outboards. Additional converging skin friction lines (two of them) can be seen adjacent to the main line of converging skin friction mentioned previously. These correspond to secondary and tertiary vortices formed by local separation of the crossflow induced by the primary and secondary vortices respectively.

The flow phenomenon described in the oil-flow results are also evident in the surface pressure measurements (Figure 6). Here, surface pressure coefficient contours ($C_p \equiv (P - P_\infty)/ .5 \rho U^2_\infty$) are plotted on the upper and lower surface of the wing. The lower wing surface contours show the stagnation line which is nearly straight, across most of the wing, at an average arc distance from the leading edge of s = 0.01 c. Away from the tip of the wing, the flow approaches two-dimensional behavior, and the pressure gradient in the x-direction is favorable, for 60% of the chord, only to become slightly adverse for the remaining part of the wing. Near the tip of the wing, the flow and the pressure gradients become highly three-dimensional. The pressure gradients induce large cross flow velocities around the tip. The large aqua-colored region on the lower rear part of the tip corresponds to very high velocity air whipping around the tip, only to encounter an adverse pressure gradient after circumventing about half way around the tip. This region corresponds to the main converging-skin-friction line seen in the oil flow photo. In a two-dimensional sense, the flow in this region is similar to crossflow past a circular cylinder, where the shear layer detaches shortly after the onset of an adverse pressure gradient.

The pressure-coefficient contours on the upper surface of the wing are fairly two-dimensional on the inboard third of the wing. The leading edge suction peak is evident, and the minimum

surface pressure coefficient found here was -2.64. Nearer the tip, in the pre-tip-vortex developing portion of the flow, the surface pressures taper off to gradually equalize themselves with the pressures on the lower surface of the wing. The suction peak, due to the main tip vortex, is also evident and a minimum C_p of -1.30 was found in this region. The footprint of the main tip vortex lies at approximately $z/w = 0.97$, assuming the core of the vortex lies directly above the surface of minimum pressure coefficient), and the crossflow pressure gradient becomes adverse as one traverses outboard of this core footprint. This adverse-crossflow-pressure gradient occurs slightly inboard of the secondary converging skin friction line shown in Figure 5c. It is believed that the vorticity sheet lifting off from this secondary converging skin friction line forms a secondary vortex of the opposite sense to the primary vortex. This belief is corroborated by seven-hole pressure probe data shown later. The surface pressure data could not confirm the existence of a suction peak due to this secondary vortex or a tertiary vortex because of resolution limitations.

The surface pressure distribution was numerically integrated to find the lift of the wing ($C_L = 0.51$, consistent with Prandtl's results for a rectangular wing with low aspect ratio). The inboard portion of the wing (where pressure taps are not present) was included in the computation by extrapolating the nearly two-dimensional behavior of the pressure distribution inboard.

Figure 7 displays normalized crossflow velocity magnitude at various crossflow planes as measured by seven-hole pressure probe. The freestream velocity direction is coming out of the page and the wingtip is on the left side of the plots. The crossflow planes are displayed in conjunction with the wing-surface-pressure-coefficient contours. Black dots represent measurement locations. Bad data points at $x'/c = 0.74$ (a green rectangular region) and a single bad data point at $x'/c = 1.42$ occur near the core of the vortex. It is believed that these points were erroneous due to flow gradient/probe volume problems. At $x'/c = 0.15$, high crossflow velocity circumventing the tip can be seen, but no tip vortex is evident yet. As the axial progression of data planes is made down the chord of the wing, the region of high crossflow velocity increases (both in area and magnitude) as the tip vortex gains strength from the feeding sheet of boundary layer vorticity. Note how the location of the vortex matches up with the pressure suction peak on the surface of the wing. Small blue patches can be seen in between the feeding sheet and the main vortex, corresponding to the approximate location of the secondary line of converging skin friction. These patches of low-crossflow-velocity air are not readily observable in data planes taken in the wake ($x'/c > 0.74$). Planes in the wake also show the crossflow velocity approaching zero as the core of the vortex is approached. Maximum crossflow velocity (on the order of the freestream velocity) is found on the viscous/inviscid boundary of the vortex.

Figure 8 shows normalized velocity magnitude and surface pressure coefficient at the exact same locations and with the same perspective as data shown in Figure 7. Again, the axial development of the tip vortex is apparent when looking at the progression of data planes. The velocity magnitude in the core of the vortex increases as one progresses down the chord of the wing. A maximum velocity magnitude of $|U|/U_\infty = 1.77$ was obtained at $x'/c = 0.74$ (right after the T.E.). This point of maximum velocity magnitude occurred in the core region of the tip vortex where the crossflow velocity was low, implying very high axial velocity. Chigier noted a maximum axial velocity in the core right before the trailing edge of about u/U_∞

= 1.4 (NACA 0015, at $\alpha = 12.0°$, $Re_c = 953,000$). Immediately after the trailing edge in the wake, the axial velocity in the core, he observed, decreased to $u/U_\infty = 1.1$. In the present study, the velocity-magnitude maxima very slowly decreases in the wake to a value of $|U|/U_\infty = 1.69$, a marked difference from the results of Chigier.

The growth of the boundary layer thickness (green-blue area nearly spanning the wing) with chord, and its development into the wake, are quite vivid. An interesting development is the apparent dip in the boundary layer thickness in between the main tip vortex and the nearly-two-dimensional section of the flow. As one progresses down the chord, the span of this boundary layer "dip" increases. The crossflow velocity in this region is dominated by v-velocity (a downward component towards the surface). It is believed that the tip vortex induces a flow such that the low momentum fluid in the boundary layer is "pushed aside" and replaced by higher momentum fluid, thus thinning the effective boundary layer thickness. The "dip" in the boundary layer is convected into the wake and at an x'/c of 0.99, it seems that the "dip" part of the wake has separated from the main part of the wake. In subsequent crossflow planes, this low momentum fluid is wrapped into the tip vortex.

A concentrated grid of data, taken by seven-hole pressure probe at a x'/c of 0.53 is shown in Figure 9. Displayed are x' component of vorticity (normalized by U_∞, resulting units are 1/length), crossflow velocity magnitude, and velocity magnitude contours overlayed with normalized velocity vectors for this data plane. The x'-vorticity contour shows an absolute maximum of -8.8 in the feeding sheet and a value of about -3.2 in the core of the main vortex. The resolution of the concentrated grid allows the core of the secondary vortex to be easily visible and the value of the x'-vorticity, in this core, was about 3.5. The absolute accuracy of these numbers can be questioned due to insufficient grid resolution, but the general trends of positive and negative values of vorticity (clockwise and counterclockwise vortices) are certainly adequately resolved. The superimposed velocity vectors confirm that the rotational sense of the secondary vortex is opposite that of the main tip vortex and they suggest the location of a tertiary vortex further outboard of the secondary vortex with the same sense as the main vortex.

The radius of the viscous core of the main tip vortex at a $x'/c = 0.53$ was found to be about 1.0 inch. The core radius was estimated by determining the distance from the point of minimum crossflow velocity in the core to the point of maximum crossflow velocity. Admittedly for a tip vortex that is still developing, this definition is a bit arbitrary, but adequate as a general descriptor.

The nondimensional circulation of the vortex $\left[\Gamma' \equiv \dfrac{\gamma}{[U_\infty \times \text{Chord}]} \right]$ was found by taking the line integral of the velocity vector over a closed path, in a crossflow plane. The enclosed area formed by this path included 75% of the span, so that much of the vorticity shed by the viscous wake of the wing is included in this calculation. The value was found to be $\Gamma' = 0.33$ at an $x'/c = 0.74$.

CONCLUSIONS

The experimental results to date, on the near-field flow of a wingtip vortex at high Reynolds number, have demonstrated the highly three-dimensional nature of the flow. The initial roll-up process of the tip vortex has been observed and quantified (in a mean sense). As a result, a good qualitative understanding of how the vorticity from the "local separation" of the free shear layers is wrapped into the tip vortex was found. The presence of a secondary vortex of the opposite sense to the primary tip vortex was located and the possibility of a tertiary vortex is suspected. Extremely high axial velocity in the vortex core was measured. The details of these flow phenomena have not been predicted by computational studies as of yet.

In the near future, all six components of the Reynolds stresses will be measured at the same data locations as the seven-hole pressure probe by use of cross-wire probes, and LDV equipment will be used to survey the core of the tip vortex. In combination with the mean flow data, this database will be used to further computational models.
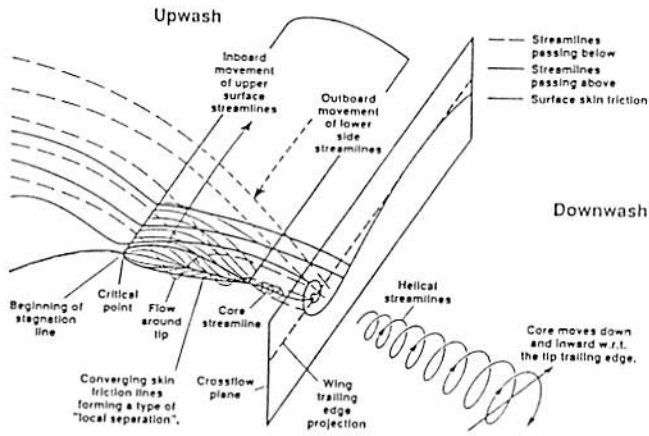
ACKNOWLEDGEMENTS
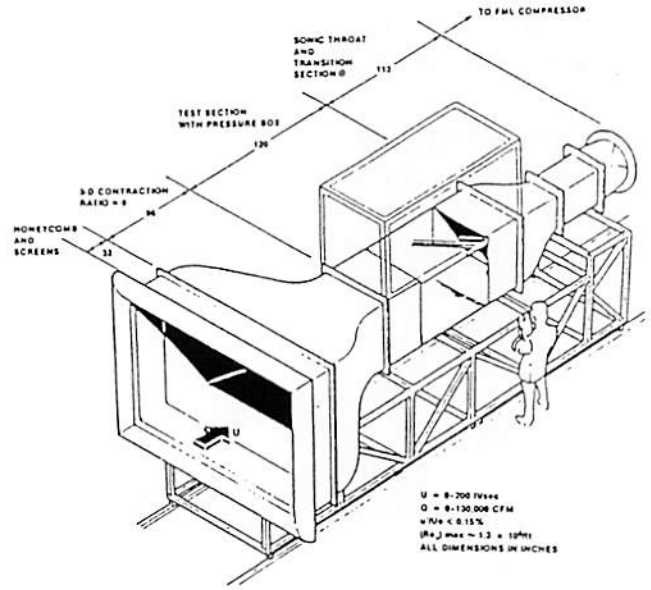
Figure 1. Schematic representation of wingtip vortex flowfield.
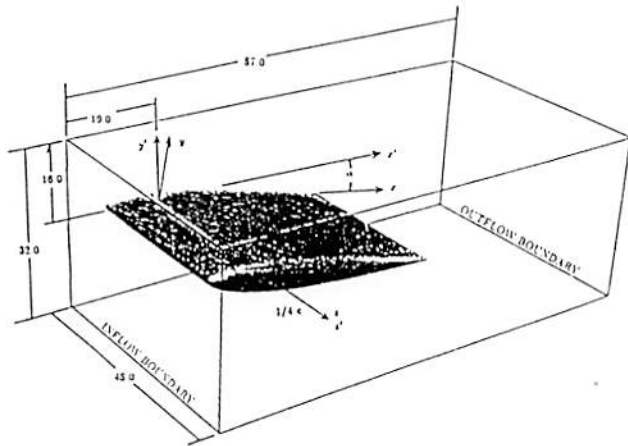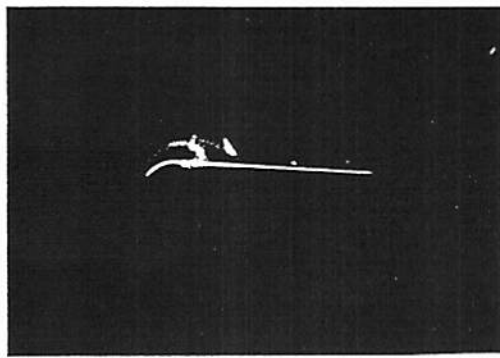

Figure 2. The 32x48-inch low turbulence wind tunnel.

Figure 3. Wingtip model and coordinate systems.

$x'/c = 0.36$
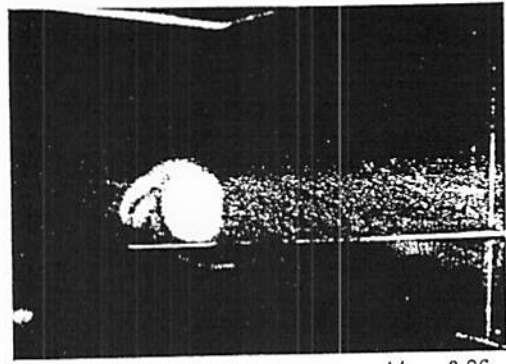
$x'/c = 0.86$
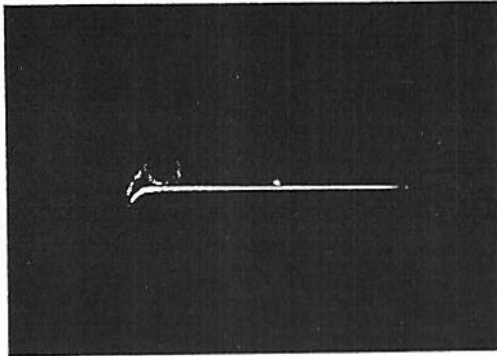
$x'/c = 0.49$
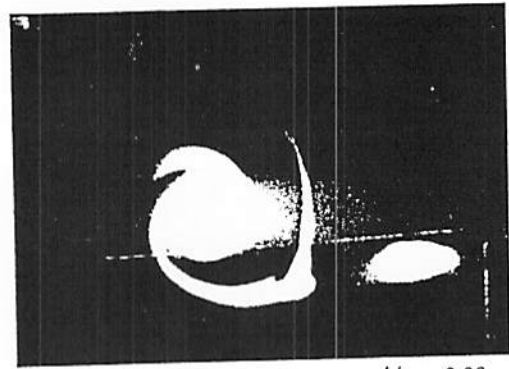
$x'/c = 0.99$
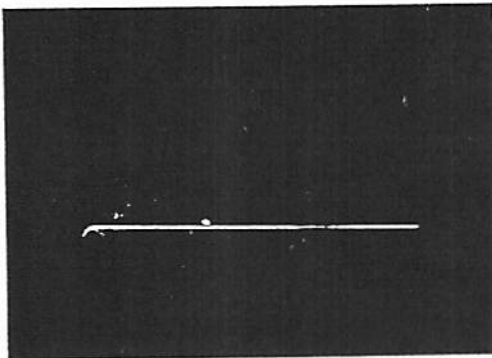
$x'/c = 0.61$
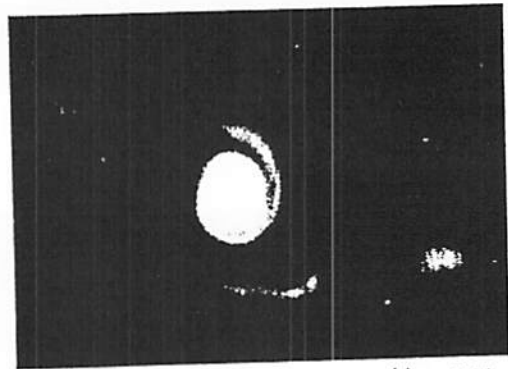
$x'/c = 1.11$
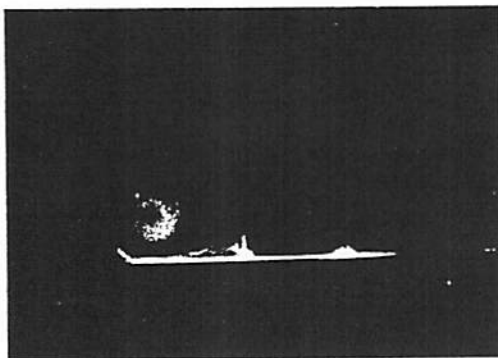
$x'/c = 0.74$
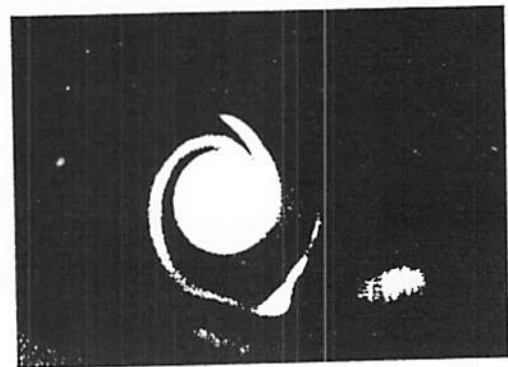
$x'/c = 1.24$

Figure 4. Laser-smoke flow visualization of the tip vortex.
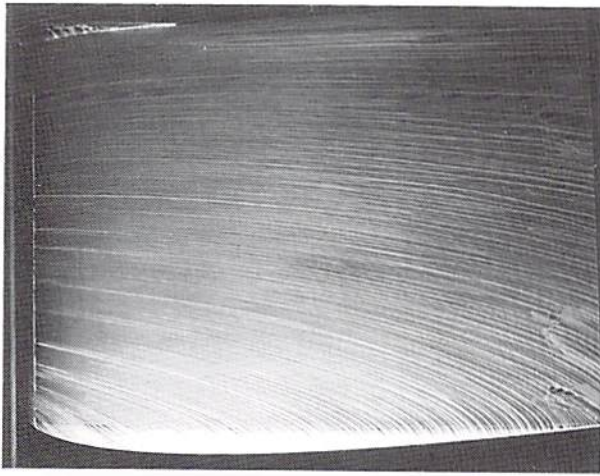
(a) Pressure side
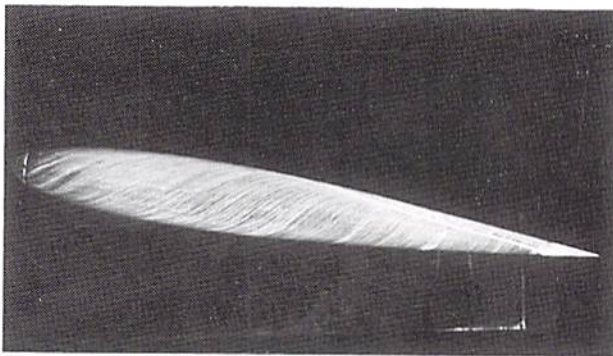
(b) Tip view

(c) Suction side

Figure 5. Wingtip surface oil flow.
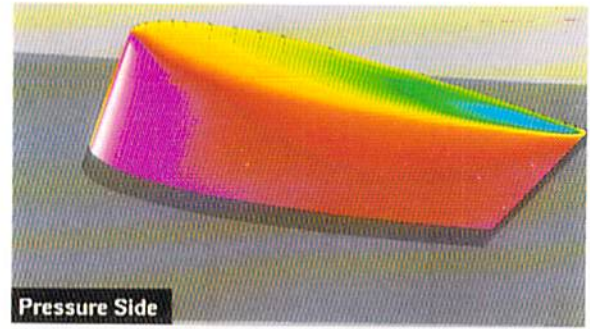
Pressure Side
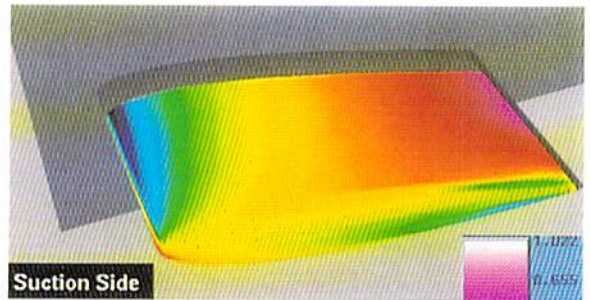
Suction Side
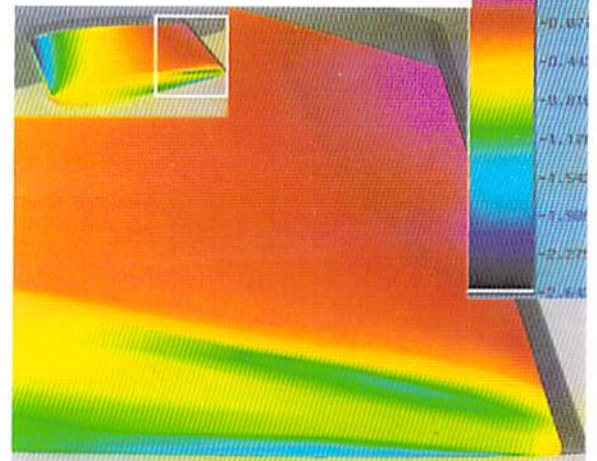
Figure 6. Surface pressure coefficient.
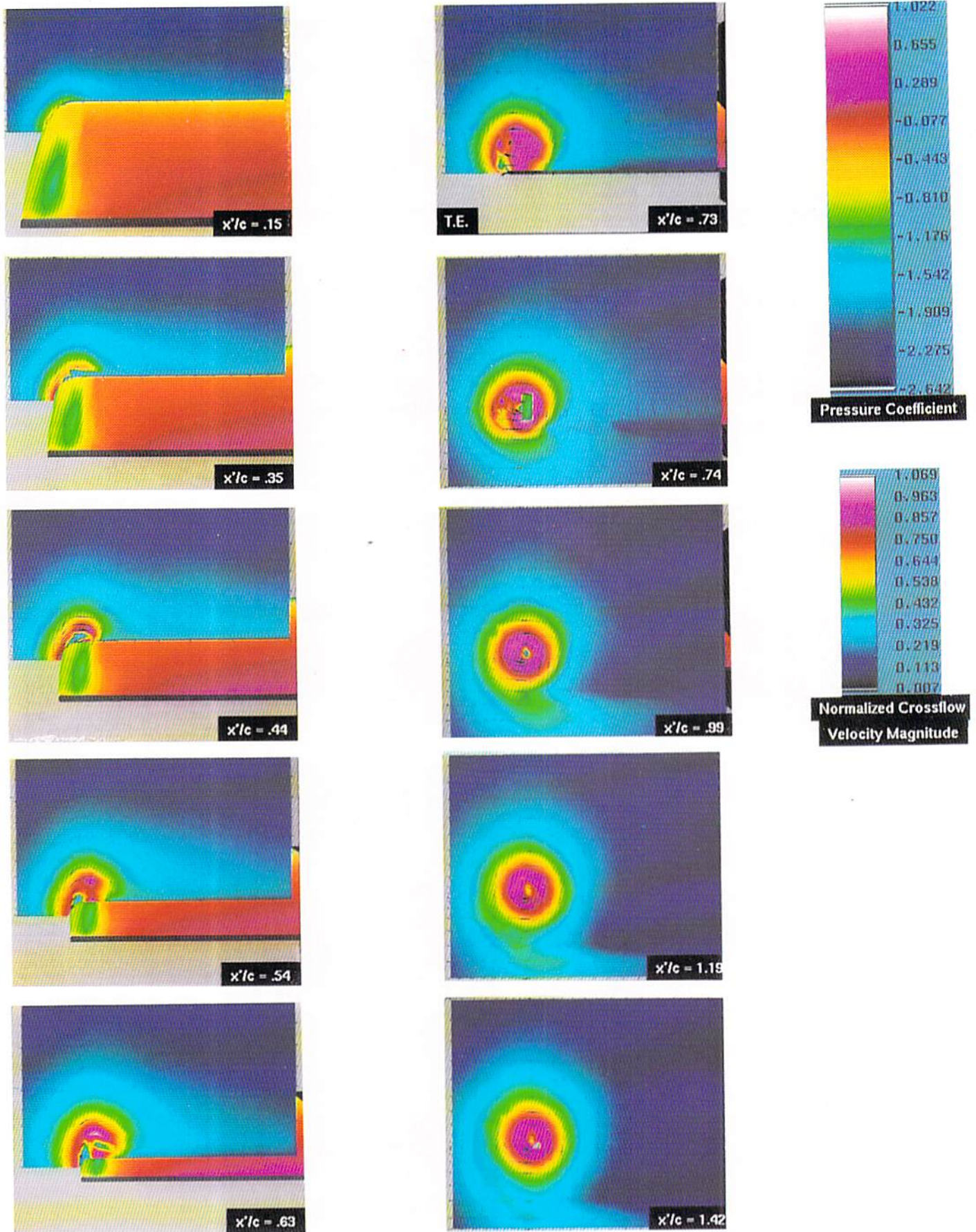
Figure 7. Crossflow velocity magnitude and surface pressure coefficient.
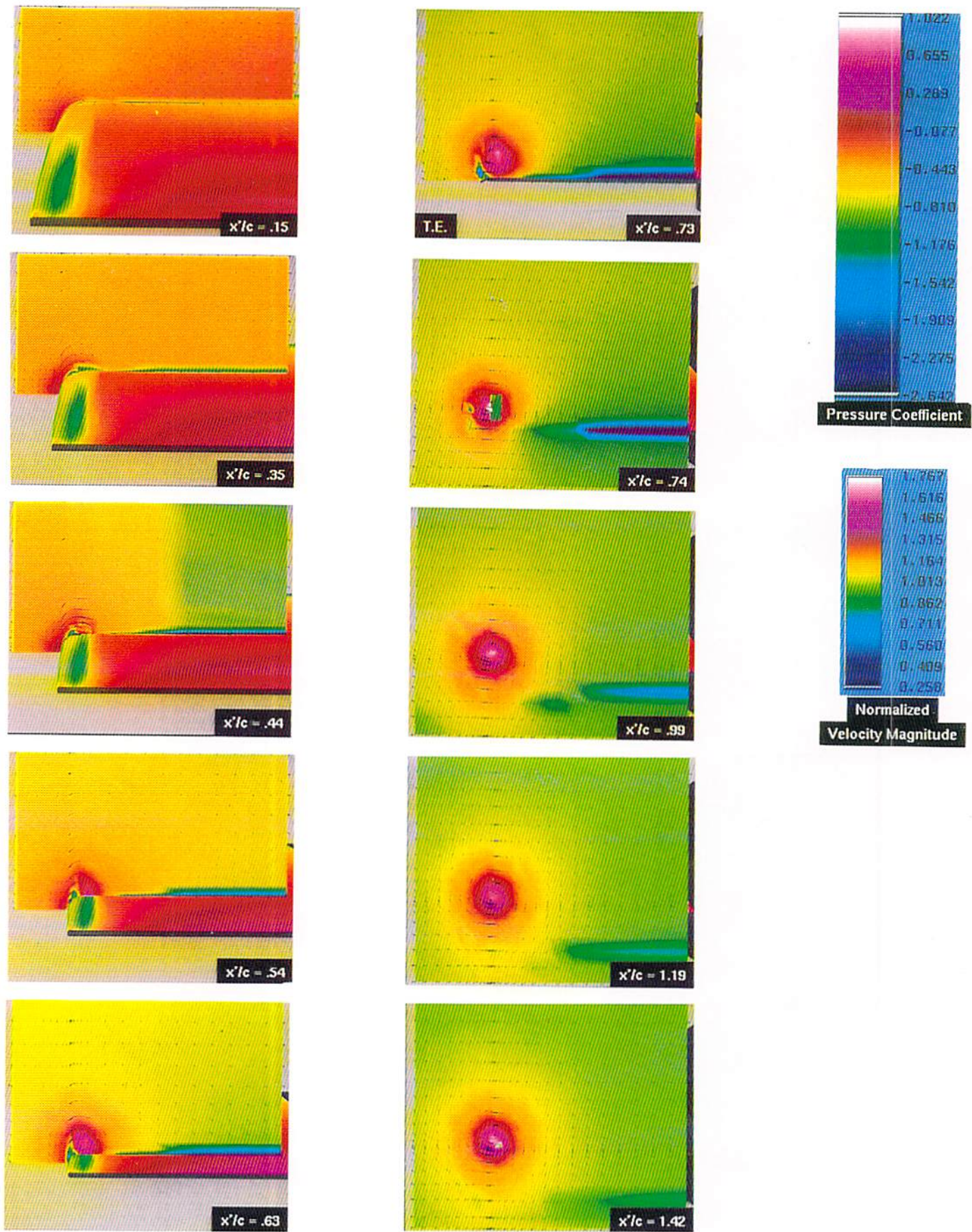
Figure 8. Velocity magnitude and surface pressure coefficient.

35-14
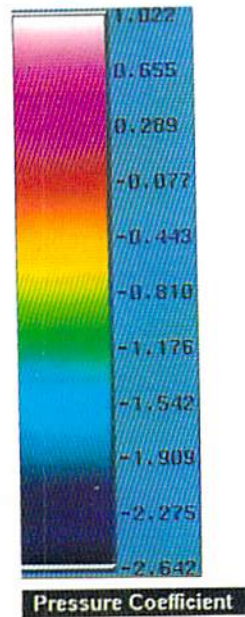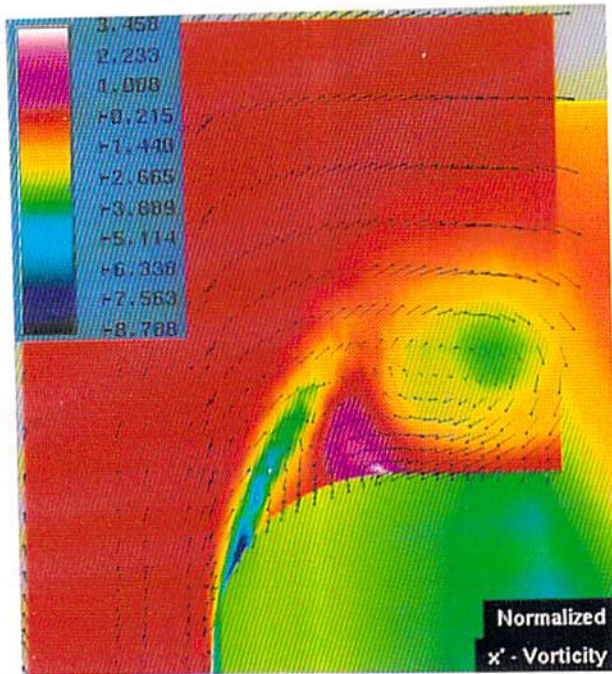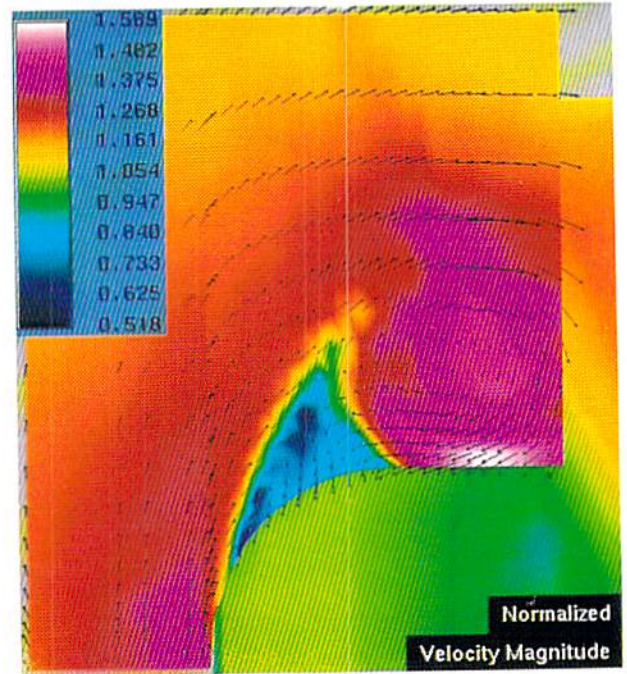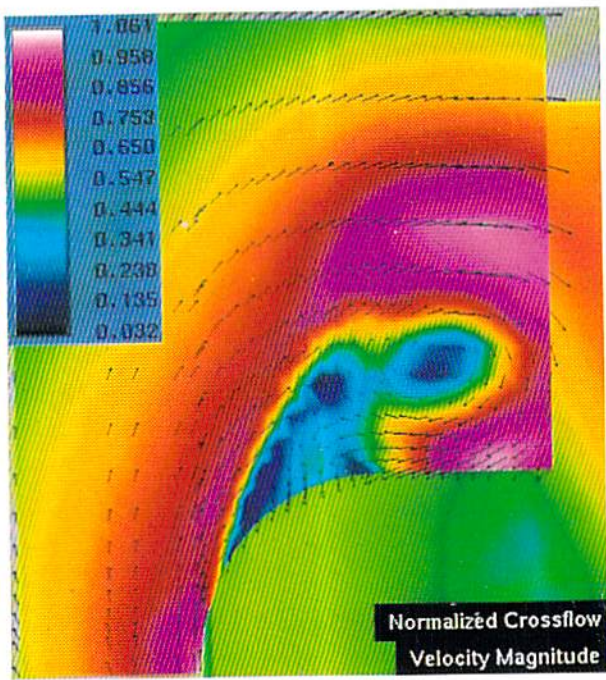
Figure 9. High-resolution crossflow plane at x'/c=0.53.

REFERENCES

Bandyopadhyay, P.R., Stead, D.J., Ash, R.L., "The Organized Nature of a Turbulent Trailing Vortex," 21st Fluid Dynamics, Plasma Dynamics and Lasers Conference, June 18-20, 1990, Seattle, WA.

Batchelor, G.K., "Axial Flow in Trailing Line Vortices," *Journal of Fluid Mechanics*, Vol. 20, Part 4, 1964, pp. 645-658.

Carlin, G., Dadone, L., Spencer, R., "Results of an Experimental Investigation of Blade Tip Vortex Modification Devices," NASA CR-181853, 1989.

Chigier, N.A., Corsiglia, V.R., "Tip Vortices - Velocity Distributions," NASA TM X-62,087, September 1971.

Govindaraju, S.P., Saffman, P.G., "Flow in a Turbulent Trailing Vortex," *Physics of Fluids*, Vol. 14, Number 10, October 1971, pp. 2074-2080.

Hoffman, E.R., Joubert, J., "Turbulent Line Vortices," *Journal of Fluid Mechanics*, Vol. 16, 1963, pp. 395-411.

Ikohagi, T., Higuchi, H., Arndt, R.E.A., "The Structure of Trailing Vortices," in Advancement in Aerodynamics, Fluid Mechanics and Hydraulics, Joint AIAA, ASME and ASCE Symposium, Univ. of Minnesota, June 1986.

Moore, D.W., Saffman, P.G., "Axial Flow in Laminar Trailing Vortices," Proceedings Royal Society London, Vol. 333, June 1973, pp. 491-508.

Phillips, W., "Turbulent Trailing Vortex During Roll-Up," *Journal of Fluid Mechanics*, 1981, Vol. 105, pp. 451-467.

Spivey, R.F., "Blade Tip Aerodynamics, Profile and Planform Effects," 24th Annual National Forum of the American Helicopter Society, May 1968.

Spivey, W.A., Morehouse, G.G., "New Insights Into the Design of Swept-Tip Rotor Blades," 26th Annual National Forum of the American Helicopter Society, June 1970.

Squire, H.B., "The Growth of a Vortex in Turbulent Flow," *The Aeronautical Quarterly*, Vol. 16, Part 3, August 1965, pp. 302-306.

Srinivasan, G.R., McCroskey, W.J., Baeder, J.D., Edwards, T.A., "Numerical Simulation of Tip Vortices of Wings in Subsonic and Transonic Flows," *AIAA Journal*, Vol. 26, Number 10, October 1988, pp. 1153-1162.

van den Berg, B., "A European Collaborative Investigation of the Three-Dimensional Turbulent Shear Layers of a Swept Wing," AGARD-CP-438, 25, 1989.

Zilliac, G., "Calibration of Seven-Hole Pressure Probes for Use in Fluid Flows with Large Angularity," NASA TM 102200, December 1989.

Zilliac, G., "Computational/Experimental Study of the Flowfield on a Body of Revolution at Incidence," *AIAA Journal*, Vol. 27, No. 8. pp. 1008-1016, 1989.

ANALYSIS AND COMPUTATION OF TRAILING VORTICES AND THEIR HAZARDOUS EFFECTS

Osama A. Kandil, Tin-Chee Wong
Department of Mechanical Engineering and Mechanics
Old Dominion University, Norfolk, VA 23529

C. H. Liu
Theoretical Flow Physics Branch
NASA Langley Research Center, Hampton, VA 23665

ABSTRACT

The thin-layer, Reynolds-averaged, Navier-Stokes equations along with an implicit, upwind, flux-difference splitting, finite-volume scheme are used to compute the vortex wake of a large-aspect-ratio wing. A C-O grid with grid stretching at the wing leading, trailing and side edges is used to solve for the wing and its near-vortex wake flows. The computed surface-pressure distribution is validated by comparison with a set of experimental data. Next, a relatively small trailing wing, in comparison with the leading wing, having a large aspect ratio is introduced in the near-vortex wake of the leading wing. The trailing wing grid has also been stretched at critical interference locations. The interacting-wing problem is recomputed using the solution of the previous isolated-wing problem as the initial condition. Fixing the downstream separation distance, the spanwise location of the trailing wing is varied to simulate two flow interference problems. The first problem is called the "along-track penetration through vortex center" and the second is called the "along-track penetration between vortices."

INTRODUCTION

Since the introduction of wide-body and jumbo jets for civil air transport in the early '70s, the problem of hazardous effect of wake vortices trailing behind these aircraft on the smaller trailing aircraft has received significant research efforts. The vortex trails are characterized with high intensity and turbulence, and may produce high rolling moments on trailing aircraft which could exceed the available roll control of the trailing aircraft. Moreover, the trailing aircraft, under the influence of these vortex trails, could suffer a loss of altitude or climb rate in addition to structural damages (Figure 1). These vortex trails may persist up to several miles and for long periods of time before their decay, and therefore they play a major role in sequencing landing and take-off operations at busy airports. For example, a minimum safe-separation distance between aircraft needs to be specified which depends on the vortex intensity, wind shear, atmospheric turbulence and temperature gradient; among others.

The literature shows a few experimental and computational investigations that attempt to model and analyze vortex wake interaction, merging, decay and their hazardous effects on trailing aircraft. Hallock and Eberle[1] presented a review of the state of the art of aircraft wake vortices covering the research efforts in the United States until the mid-seventies. Experimental wind tunnel and airport measurements of the vortex wakes were conducted by Dee and Nicholas[2], Harvey and Perry[3], El-Ramly[4], Wood and McWilliams[5], Garodz[6], Cliffone and Lonzo[7], and Olwi and Ghazi[8].

Mathematical models and computational schemes were developed using inviscid analysis by Chorin and Bernard[9], Hacket and Evans[10], Yates[11], Iversen and Bernstein[12], and Rossow[13]. Although an inviscid model cannot describe the wake aging including its diffusion, it is still capable of producing the wake shape and its dynamics. The mathematical modeling used in the above references was based on the use of the point vortex method to compute the motion of a finite number of point vortices which model the vorticity behind a wing. The first three-dimensional inviscid model was introduced by Kandil, et al.[14], where the nonlinear vortex-lattice, which was also developed by Kandil, et al.[15], was used to compute the interference flow between wings and the vortex wake hazardous effects.

Viscous modeling of trailing vortices was first introduced by McCormick, et al.[16]. Viscous interactions in vortex wakes and the effects of background turbulence, wind shear and ground on two-dimensional vortex pairs were presented by Bilanin, et al.[17,18]. Liu and his co-workers[19-21] studied the interaction, merging and decay of vortices in two-dimensional space and of three-dimensional vortex filaments. For the two-dimensional flow simulation, the incompressible Navier-Stokes equations, expressed in terms of vorticity-stream function formulation, were used. For the three-dimensional flow simulation, the incompressible Navier-Stokes equations, expressed in terms of the vorticity-velocity vector potential formulation, were used. An extensive review of this work is given in Ref. 22. To estimate the effects of density stratification, turbulence and Reynolds number on vortex wakes, an approximate model was recently developed by Greene[23]. Later on, Greene and his co-workers[24] presented selected results of aircraft vortices which include a juncture vortex, a lifting-wing vortex and a wake vortex.

It is concluded from the above brief literature survey that the problem contains several vortex flow regions along with several critical parameters influencing the vortex wake flows. The vortex wake flow of interacting-wing problems can be divided into three regions. The first region includes the leading wing and its near-wake flow. The second region includes the interacting vortices in the wake. The third region includes the far-wake flow along with the trailing-wing flow. The leading-wing shape including its deflected control surfaces, flow unsteadiness due to nonsteady motion of the wing, angle of attack and Reynolds number of the flow and presence of wind shear and temperature gradients in the flowfield are some of the critical dominant parameters of the first region. In the second region, the flow Reynolds number, background turbulence, wind shear and temperature distribution are some of the critical dominant parameters. In the third region, the flow Reynolds number, angle of attack, shape of the trailing wing and the path of the trailing wing are some of the critical dominant parameters.

In this paper, we only focus on the steady leading-wing flow and its near-wake region. Moreover, a trailing wing is introduced in the near-wake region in order to study the vortex wake effects on the trailing wing. The isolated-wing and interacting-wing problems are solved using the unsteady, compressible, thin-layer, Reynolds-averaged, Navier-Stokes equations along with an implicit, upwind, flux-difference splitting, finite-volume scheme. The turbulent viscosity is modeled using the modified Baldwin-Lomax algebraic equations. No wind shear or temperature gradients are assumed to exist in the flowfield.

Formulation

Thin-Layer Navier-Stokes Equations

The conservative form of the dimensionless, unsteady, compressible, thin-layer Navier-Stokes equations in terms of time-independent, body-conformed coordinates ξ^1, ξ^2 and ξ^3 is given by

$$\frac{\partial \bar{Q}}{\partial t} + \frac{\partial \bar{E}_s}{\partial \xi^s} - \frac{\partial (\bar{E}_v)_2}{\partial \xi^2} = 0; \quad s=1-3 \tag{1}$$

where

$$\xi^m = \xi^m(x_1, x_2, x_3) \tag{2}$$

$$\bar{Q} = \frac{\hat{q}}{J} = \frac{1}{J} [\rho, \rho u_1, \rho u_2, \rho u_3, \rho e]^t \tag{3}$$

$$\bar{E}_m \equiv \text{inviscid flux} = \frac{1}{J} \left[\partial_k \xi^m \hat{E}_k \right]^t = \frac{1}{J} \left[\rho U_m, \rho u_1 U_m + \partial_1 \xi^m p, \rho u_2 U_m \right.$$

$$\left. + \partial_2 \xi^m p, \rho u_3 U_m + \partial_3 \xi^m p, (\rho e + p) U_m \right]^t \tag{4}$$

$$U_m = \partial_k \xi^m u_k \tag{6}$$

$(\bar{E}_v)_2 \equiv$ viscous and heat–conduction flux in ξ^2 direction

$$= \frac{1}{J} \left[0, \partial_k \xi^2, \tau_{k1}, \partial_k \xi^2 \tau_{k2}, \partial_k \xi^2 \tau_{k3}, \right. \tag{5}$$

$$\left. \partial_k \xi^2 (u_n \tau_{kn} - q_k) \right]^t; \quad k = 1 - 3, \; n = 1 - 3$$

The first element of the three momentum elements of Eq. (5) is given by

$$\partial_k \xi^1 \tau_{k1} \equiv \frac{M_\infty \mu}{Re} \left[\psi \partial_1 \xi^2 + \phi \frac{\partial u_1}{\partial \xi^2} \right] \tag{7}$$

The second and third elements of the momentum elements are obtained by replacing the subscript 1, everywhere in Eq. (7), with 2 and 3, respectively. The last element of Eq. (5) is given by

$$\partial_k \xi^2 (u_n \tau_{kn} - q_k) \equiv \frac{M_\infty \mu}{Re} \left\{ \psi W + \phi \left[\frac{1}{2} \frac{\partial}{\partial \xi^2} (u_p u_p) + \frac{1}{(\gamma - 1) Pr} \frac{\partial (a^2)}{\partial \xi^2} \right] \right\} ; \; p = 1 - 3 \tag{8}$$

where

$$\phi = \partial_k \xi^2 \partial_k \xi^2, \psi = \frac{1}{3} \partial_k \xi^2 \frac{\partial u_k}{\partial \xi^2}, \; W = \partial_n \xi^2 u_n \tag{9}$$

In Eqs. (1)-(9), the dimensionless variables are referenced to their appropriate freestream values. The dimensionless density ρ, Cartesian velocity components u_1, u_2 and u_3, total energy per unit mass e, dynamic viscosity μ, and speed of sound a, are defined as the ratio of the corresponding physical quantities to those of the freestream; namely, ρ_∞^2, a_∞, ρ_∞, a_∞^2, μ_∞, and a_∞; respectively. The pressure, p, is nondimensionalized by $\rho_\infty a_\infty^2$ and is related to the total energy for a perfect gas by the equation of state

$$p = (\gamma - 1)\rho \left[e - \frac{1}{2} u_j u_j \right] ; \; j = 1 - 3 \tag{10}$$

where γ is the ratio of specific heats and its value is 1.4. The viscosity, μ, is calculated from the Sutherland's law

$$\mu = T^{3/2} \left[\frac{1 + c}{T + c} \right] \, , \ c = 0.4317 \tag{11}$$

where T is the temperature which is nondimensionalized by T_∞. The Prandtl number, P_r is fixed at 0.72. The Reynolds number is defined as $R_e = \rho_\infty U_\infty L / \mu_\infty$ and the characteristic length, L, is chosen as the root chord of the leading wing.

In Eqs. (1)-(10), the identical notation is used for convenience. The subscripts k, n, p and j are summation indices, the superscript or subscript s is a summation index and the superscript or subscript m is a free index. The partial derivative $\partial / \partial X_k$ is referred to by ∂_k.

Turbulent Flow

For the turbulent flow, the thin-layer, Navier-Stokes equations are transformed to the Reynolds-averaged equations by replacing the coefficient of molecular viscosity, μ, and the coefficient of thermal conductivity, k, with

$$\mu_e = \mu + \mu_t = \mu \, (1 + \mu_t / \mu) \tag{12}$$

$$k_e = k + k_t = \frac{\mu C_p}{P_r} \left[1 + \frac{\mu_t}{\mu} \frac{P_r}{P_{r_t}} \right] \tag{13}$$

where μ_e is the effective viscosity, k_e the effective thermal conductivity, μ_t the turbulent viscosity, P_r the laminar Prandtl number, P_{r_t} the turbulent Prandtl number and C_p the specific heat under constant pressure. The turbulent viscosity μ_t is obtained by using the two-layer algebraic eddy viscosity model which was first developed by Cebeci[25] for the boundary-layer equations and modified later by Baldwin and Lomax[26] for the Navier-Stokes equations. The details of the turbulent model is given in Ref. 27 by Wong, Kandil and Liu.

Boundary and Initial Conditions

Boundary conditions are explicitly implemented. They include the inflow-outflow conditions and the solid-boundary conditions. At the plane of geometric symmetry, periodic conditions are used. The inflow-outflow boundary conditions are implemented using the one-dimensional Riemann-invariant conditions normal to these boundaries. On the solid boundaries, the no-slip and no-penetration conditions are enforced; $u_1 = u_2 = u_3 = 0$, and the normal pressure gradient

is set equal to zero. For the temperature, the adiabatic boundary condition is enforced at the solid boundaries.

The initial conditions correspond to the freestream conditions with $u_1 = u_2 = u_3 = 0$ on the solid boundaries. The freestream conditions are given by

$$\rho_\infty = a_\infty = T_\infty = 1,$$

$$u_{1\infty} = M_\infty \cos \alpha,$$

$$u_{2\infty} = M_\infty \sin \alpha,$$

$$u_{3\infty} = 0,$$

$$p_\infty = 1/\gamma, e_\infty = \frac{1}{\gamma(\gamma-1)} + \frac{M_\infty^2}{2}$$

(14)

where α is the angle of attack.

Computational Scheme

The implicit, upwind, flux-difference splitting, finite-volume scheme is used to solve the unsteady, compressible, thin-layer, Reynolds-averaged, Navier-Stokes equations. The scheme uses the flux-difference splitting scheme of Roe which is based on the solution of the approximate Riemann problem. In the Roe scheme, the inviscid flux difference at the interface of computational cells is split into two parts; left and right flux differences. The splitting is accomplished according to the signs of the eigenvalues of the Roe averaged-Jacobian matrix of the inviscid fluxes at the cell interface. The smooth flux limiter is used to eliminate oscillations at locations of large flow gradients. The viscous- and heat-flux terms are linearized and the cross-derivative terms are eliminated in the implicit operator. The viscous terms are differenced using a second-order accurate central differencing. The resulting difference equation is approximately factored and is solved in three sweeps in the ξ^1, ξ^2, and ξ^3 directions. The computational scheme is coded in the computer program "CFL3D".

Computational Applications

We consider a large-aspect-ratio rectangular wing of $AR_1 = 5.9$ and a NACA 0012 chordal section, at an angle of attack of $\alpha_1 = 4.64°$. The flow Reynolds number, Re_∞ is 3.2×10^6 (which is based on the root-chord length) and the freestream Mach number, M_∞ is 0.3. The computational domain consists of a hemispherical boundary which is followed by a cylindrical boundary. The hemisphere center is located on the root-chord of the wing at the trailing edge. Its radius is 15 chords ($C_{r1} = 1$) and the cylindrical boundary extends 15 chords in the downstream direction beyond the wing trailing edge. A C-O grid of 201x59x53 grid points in the axial wrap-around, spanwise wrap-around and normal directions, respectively, is used. The

36-6

minimum grid size normal to the wing is 10^{-5}. The flow is considered to be laminar until the chord station of 0.05 from the wing leading edge. Thereafter, the turbulent model is turned on to mimic the transition to turbulent flow. This location of the transitional flow has been experimentally determined by Yip and Shubert[28].

Isolated Wing and Near-Vortex-Wake Flow

Figures 2-5 show the computed results of this flow case. Figure 2 shows the history of the residual error, the total lift and drag coefficients over 12,100 iteration steps. Figure 3 shows a comparison of the present computed surface-pressure-coefficient distribution in the chordwise direction at different spanwise stations with the experimental data of Ref. 28. The present results are in good agreement with the experimental data with the exception of the peak suction pressure at the wing leading edge. This is attributed to the improper modeling of the transitional flow at this location. The evolution of the vortex wake, depicted in terms of the total-pressure-loss contours, from the chord station of $x/c_{r1} = 0.95$ to the chord station of $x/c_{r1} = 7.0$ is given in Figure 4. Figure 5 shows a three-dimensional view of the wing and wake vortex evolution in terms of the total pressure loss.

The total-pressure-loss contours show that the tip vortex reaches its maximum strength at about 0.5 chord length from the wing trailing edge. Thereafter, the tip-vortex core expands due to the viscous diffusion and grows to almost double of its original size after two chords from the wing trailing edge ($x/c_{r1} = 3.0$). It is also noticed that at the same location the wake thickness increases to almost double of its original thickness.

Leading/Trailing Wing Interaction (Along-Track Penetration Through Vortex Center)

A rectangular wing of aspect ratio of $AR_2 = 3.3$ (trailing wing) is introduced in the vortex wake of the leading wing. The trailing-wing leading edge is located at one chord length in the chordwise direction from the trailing edge of the leading wing. The centerline of the trailing wing is located along the leading-wing tip in the spanwise direction. The chord length of the trailing wing is 0.5 that of the leading wing and has the same angle of attack as that of the leading wing. The grid of the trailing wing is stretched at its leading and trailing edges. This leading/trailing wing interaction problem is usually known as the "along-track penetration through vortex center" case. A typical grid for the interaction problem is given in Figure 6. In Figure 7, the snapshots of total-pressure-loss contours show the evolution of the vortex wake including that of the trailing wing up to the chord station $x/c_{r1} = 7.0$. Figure 8 shows the spanwise distribution of the C_p for the trailing wing at the chord stations of 2.1, 2.2, 2.3, 2.4 and 2.5. We also show in Figure 8 the corresponding cross-flow streamlines of the flow around the trailing wing. Figure 9 shows a three-dimensional view of the total-pressure-loss contours of the flow of interacting wings.

Figures 7-9 clearly show the effects of tip vortex and wake of the leading wing on the tip vortex of the trailing wing in the range from $x/c_{r1} = 2.0$ to $x/c_{r1} = 2.5$ (chord-length range of the trailing wing). The left tip vortex of the leading-wing is located to the right from the trailing-wing centerline (C_L). The right tip vortex of the trailing wing vanished (Figure 7), and it is noticed that a saddle point appears in the flow to the right of the leading-wing tip vortex (Figure

8). This is expected since the leading-wing tip vortex is of large size and strength as compared to those of a smaller wing size. Moreover, its vorticity is of opposite sign to that of the right-side tip vorticity of the trailing wing. On the left-side of the trailing wing (Figure 7), its tip vortex grows in size and strength and moves outboards in the downstream direction. Beyond the trailing edge of the trailing wing, two strong tip vortices of the same vorticity sign exist along with a kinked wake. The left tip vortex of the leading wing feeds the left tip vortex of the trailing wing. The reason behind the kink in the trailing wake is that the vorticity of wake of the right side of the trailing wing is of opposite sign to that of the left side of the leading wing. Hence, the resultant vorticity of the kinked part of the wake will be smaller than that of the remainder of the wake. In the downstream direction, the tip vortices and the wake increase in size due to the viscous effects. The snapshots of the pressure distribution depicted in Figure 8 show the serious hazardous effect of the leading-wing tip vortex on the trailing wing loading. The spanwise surface-pressure distribution is strongly asymmetric, due to the disappearance of the right tip vortex of the trailing wing, resulting in a substantial clockwise rolling-moment coefficient.

Leading/Trailing Wing Interaction (Along-Track Penetration Between Vortices)

Next, the trailing wing centerline is moved to the 1/2 semispan location of the leading wing. The chordwise separation distance is kept fixed as that of the previous case. Also, the trailing-wing angle of attack, α_2, is kept fixed. This leading/trailing wing interaction problem is usually known as the "along-track penetration between vortices" case. Figures 10-12 show the results of this flow case.

In Figure 10, the snapshots of the total-pressure-loss contours show the evolution of the vortex wake including that of the trailing wing up to the chord station $x/c_{r1} = 7.0$. Figure 11 shows the spanwise distribution of C_p for the trailing wing at the chord stations of 2.1, 2.2, 2.3, 2.4 and 2.5. Figure 12 shows a three-dimensional view of the total-pressure-loss contours of the flow of interacting wings.

Figure 10 shows that the left tip vortex of the leading wing is located to the left of the trailing wing. The snapshots, in the downstream direction, show that the right tip vortex of the trailing wing disappears while its left tip vortex grows and feeds the left tip vortex of the leading wing. Beyond the trailing edge of the trailing wing, the left tip vortex of the leading wing grows in size until it is shed in the flowfield at the chord station $x/c_{r1}, = 7.0$. Again, we notice that the wake shape is kinked. The spanwise distributions of C_p of the trailing wing (Figure 11) show that the shape of the pressure-coefficient curve of the right side of wing is symmetric around $C_p = 0$. Around $y/c_{r1} = 1.475$ (location of C_L of trailing wing), there is a small asymmetry in the C_p distribution which produces a small counterclockwise rolling moment. The magnitude of this rolling moment is substantially smaller than that of the clockwise rolling moment of the previous case. By comparing the C_p levels of this case (Figure 11) with the previous case (Figure 8), it is concluded that the lift coefficient of the present case is smaller than that of the previous case.

Thus, the hazardous aerodynamic effects of the "along-track penetration through vortex center" case are much more serious than those of the "along-track penetration between vortices" case.

CONCLUDING REMARKS

The unsteady, compressible, thin-layer, Reynolds-averaged, Navier-Stokes equations are used to compute and analyze vortex wake flows of isolated and interacting wings. An implicit, upwind, flux-difference splitting, finite-volume scheme is used to compute these flows. A C-O grid has been used to carry out the computations with a computational domain that extends 15 chords behind the leading wing. The emphasis of this paper is to study the effects of the near-vortex-wake flow on a small trailing wing for two vortex wake interference cases. The first flow-interference case is called the "along-track penetration through vortex center" and the second flow-interference case is called the "along-track penetration between vortices." The present computations show that the first flow-interference case is much more hazardous to the trailing wing in comparison with the second flow-interference case. It has been demonstrated that the trailing wing experiences large rolling moments if the trailing wing is along-track penetration through vortex center.

The present research work is the first attempt to address this problem using the CFD and Navier-Stokes equations. There are still several computational issues to be addressed. The first issue is the level of grid fineness and its distribution in order to obtain accurate near-vortex-wake results. The second issue is the level of grid fineness and its type for the trailing wing to obtain accurate vortex wake flows of the interaction problems. The third issue is how efficiently and accurately the computations can be implemented in order to compute the farfield vortex wake flows. A serious computational problem with this type of long-distance vortical flow is the effect of the numerical dissipation of the scheme on the diffusion of these vortices. Currently, we are addressing these computational issues along with other physical flow issues. The physical flow issues include the level of the turbulent model; the effects of several parameters such as the relative angle of attack, relative vertical and horizontal separation distances, relative sizes of the wings and existence of deflected control surfaces, the unsteady climb rate of the wing and the presence of wind shear, temperature gradient and background turbulence in the flowfield.

ACKNOWLEDGEMENT
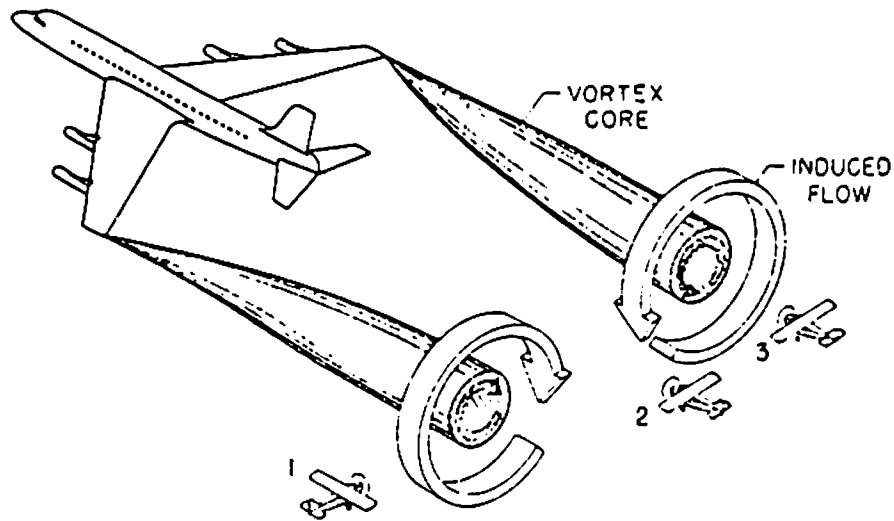
Figure 1. Trailing vortex wake and types of interference, (1) cross-track penetration,(2) along-track penetration between vortices, (3) along-track penetration through vortex center.
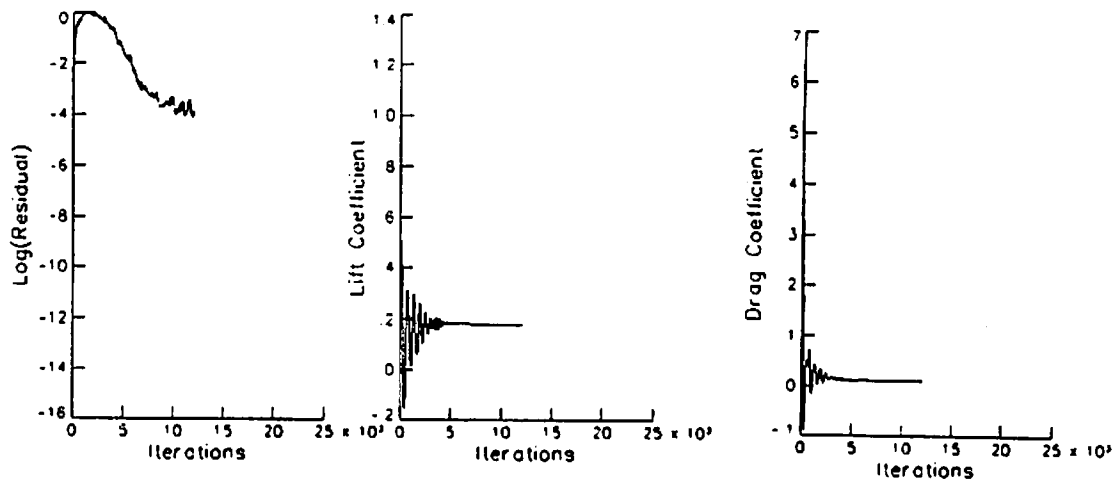
Figure 2. Iteration history of residual error, lift coefficient and drag coefficient.
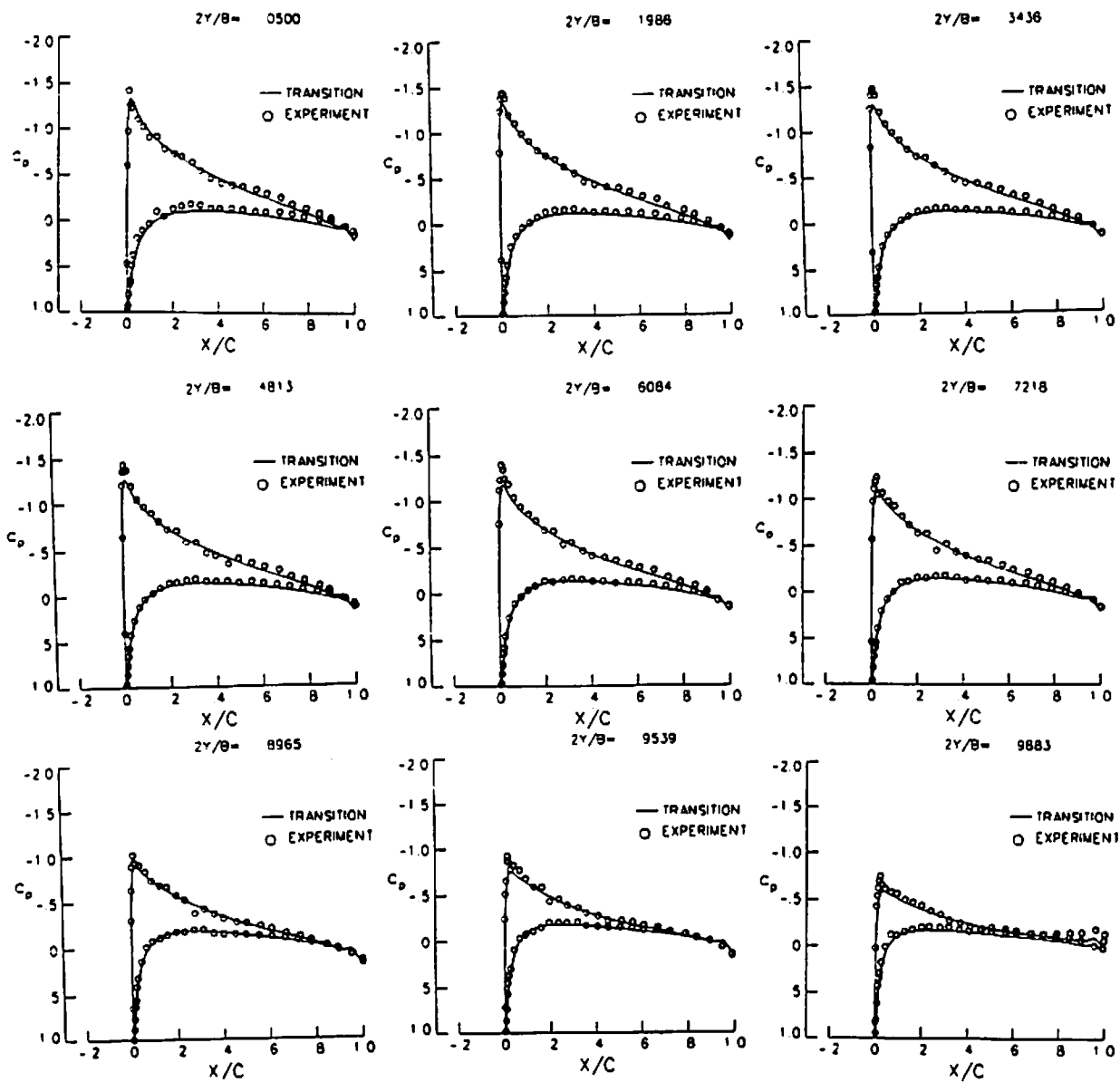
Figure 3. Chrowise surface pressure distribution at spanwise stations
for an isolated wing and comparison of experimental data, $AR_1 = 5.9$,
$\alpha_1 = 4.64°$, $R_e = 3.2x10_6$, $M_\infty = 0.3$.
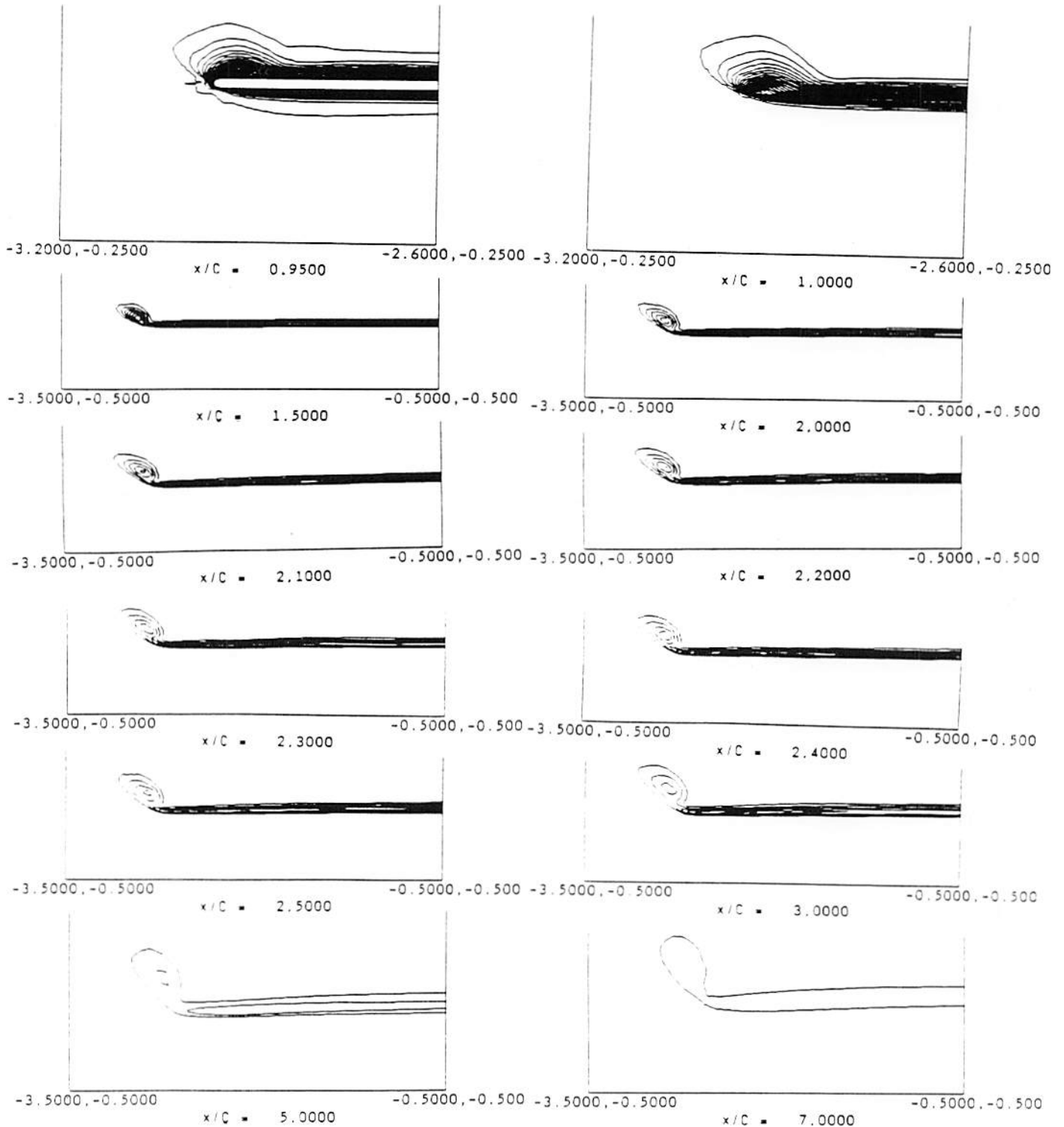
Figure 4. Total-pressure-loss contours at chordwise stations
in the vortex wake of an isolated wing, range 0.0-0.1,
$AR_1 = 5.9$, $\alpha_1 = 4.64°$, $R_c = 3.2 \times 10_6$, $M_\infty = 0.3$.
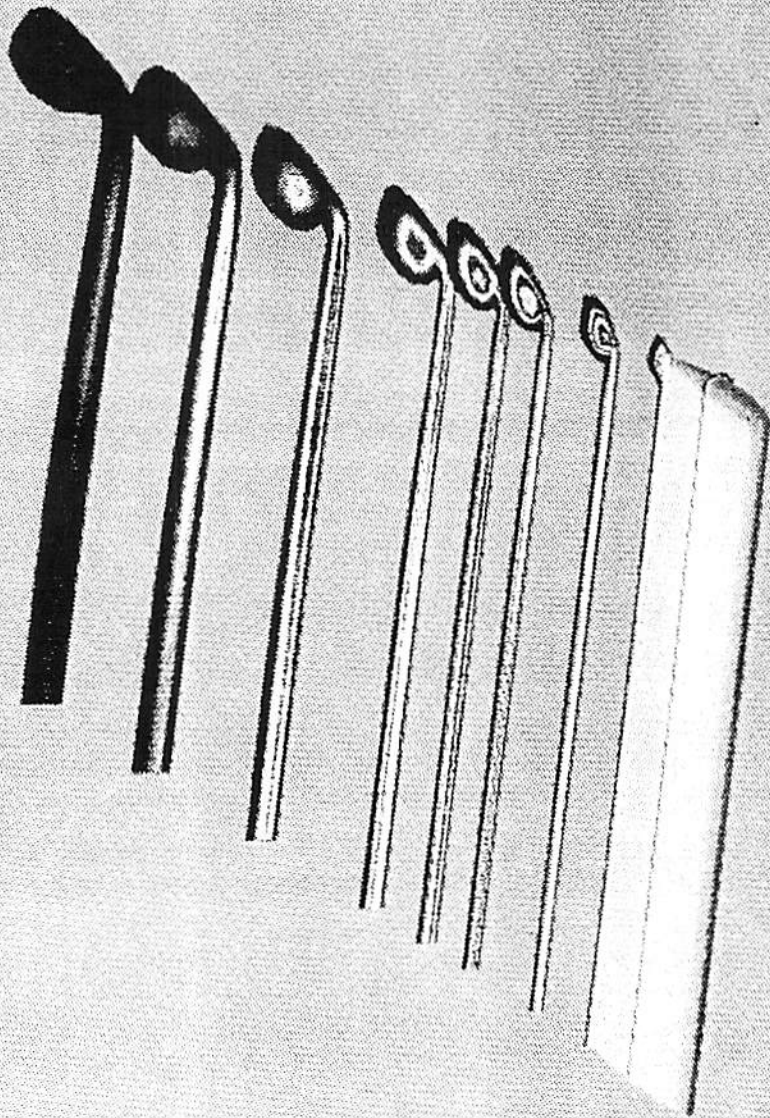
Figure 5. Three-dimensional view of the vortex wake interaction of an isolated wing.
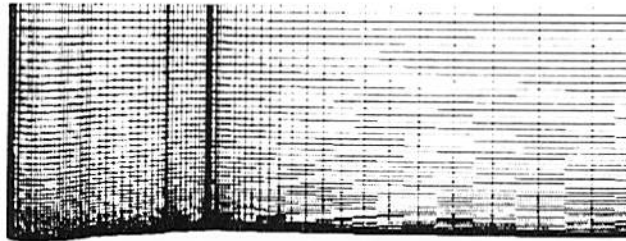
Figure 6. Typical C-O grid for the leading/trailing wing interaction problems.
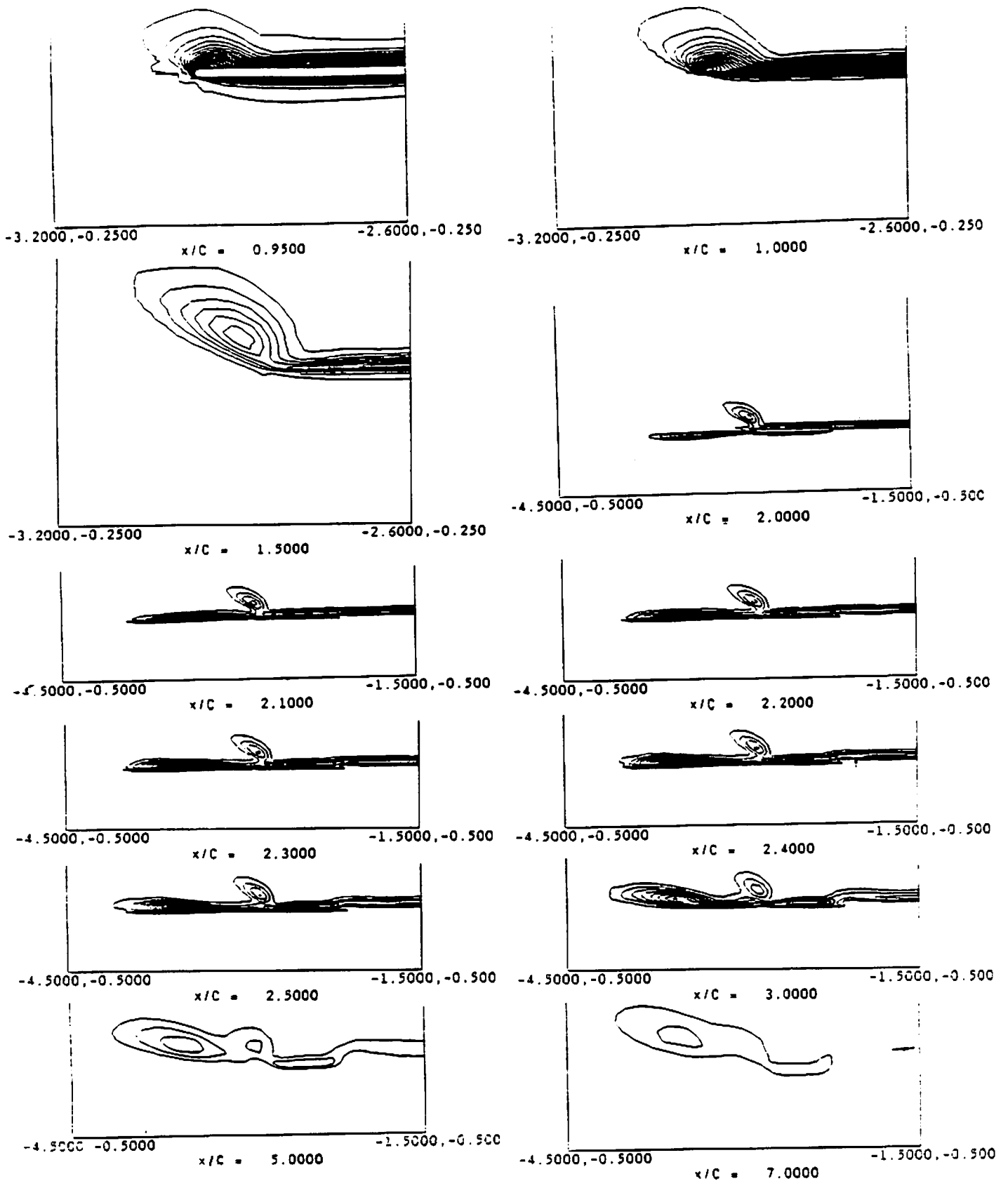
Figure 7. Total-pressure-loss contours at chordwise stations in the vortex wake of leading/trailing wing interaction, $AR_1 = 5.9$, $AR_2 = 3.3$, $C_{r2} = 0.5\ C_{r1}$, $\alpha_{1,2} = 4.64°$, $R_c = 3.2\text{x}10^6$, $M_\infty = 0.3$ (along-track penetration through vortex center).
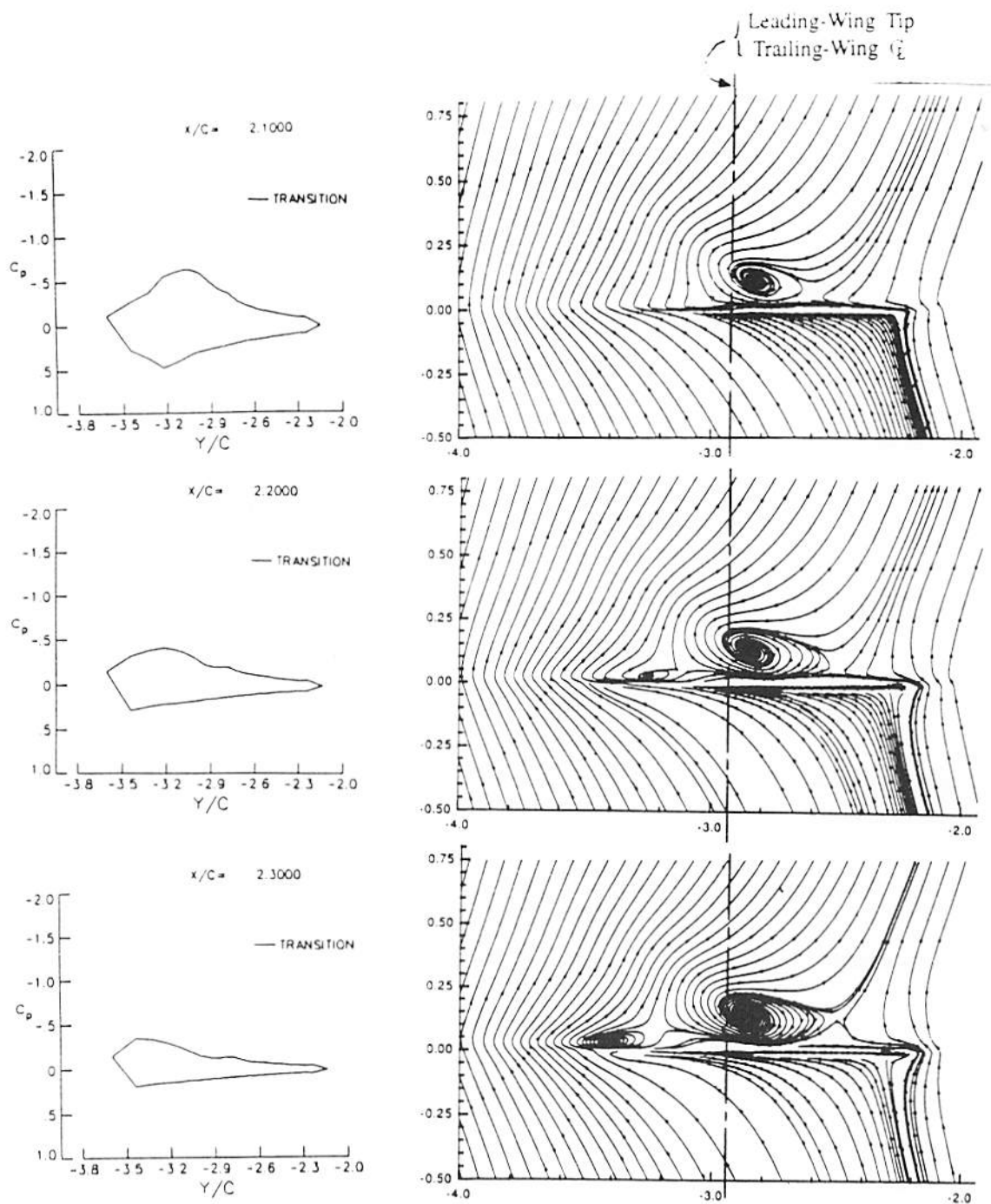
Figure 8. Spanwise surface-pressure distribution at chordwise stations of the trailing wing and the corresponding cross-flow streamlines, along-track penetration through vortex center.

36-16
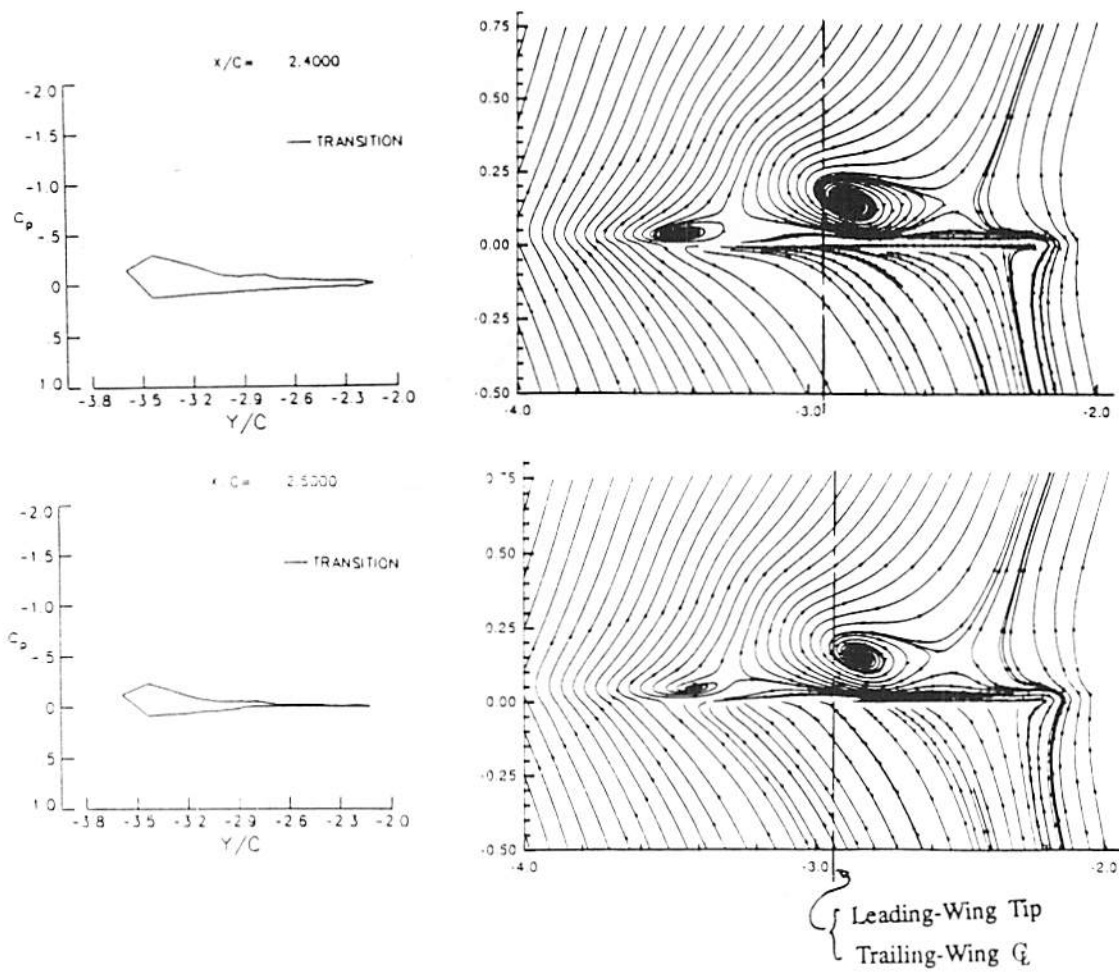
Figure 8. (continued) Spanwise surface-pressure distribution at chordwise stations of the trailing wing and the corresponding cross-flow streamlines, along-track penetration through vortex center.
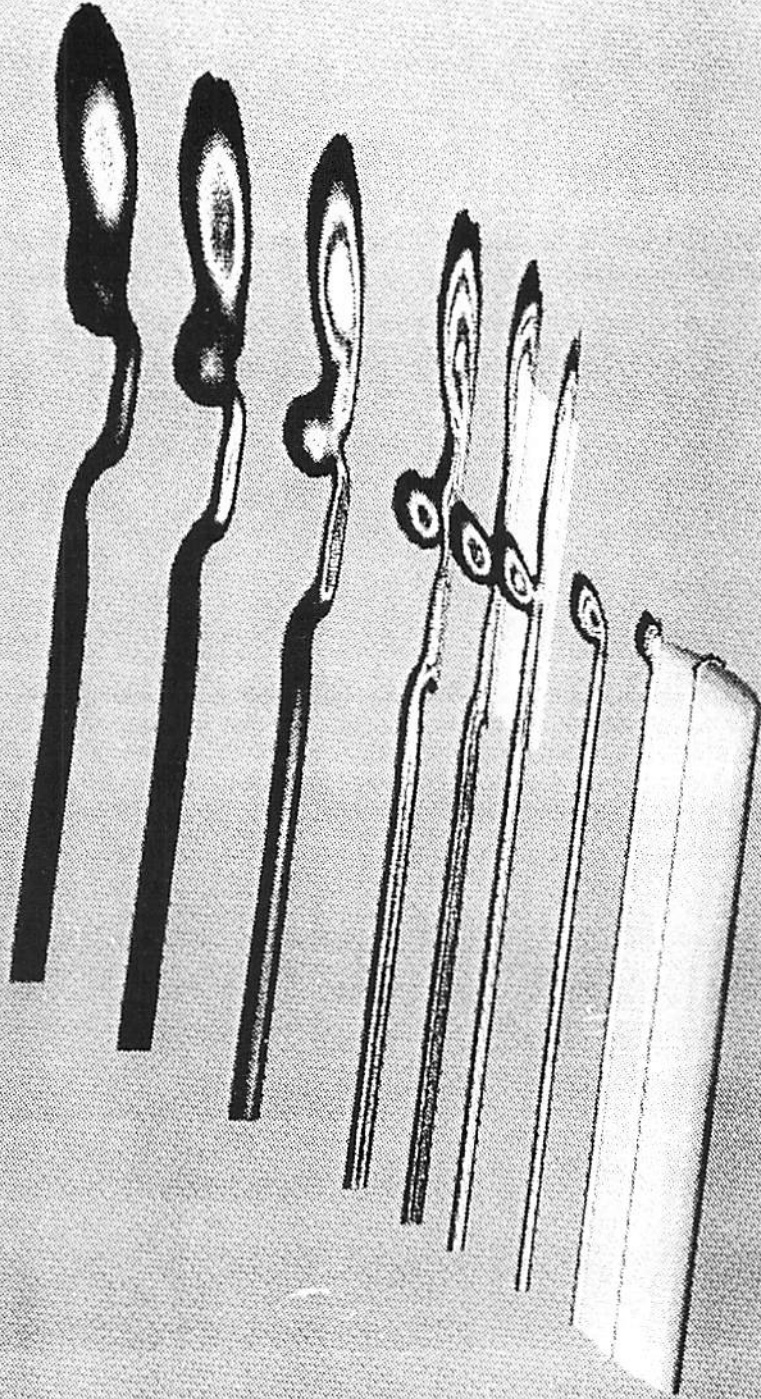
Figure 9. Three-dimensional view of the leading/trailing wing interaction, along-track penetration through vortex center.
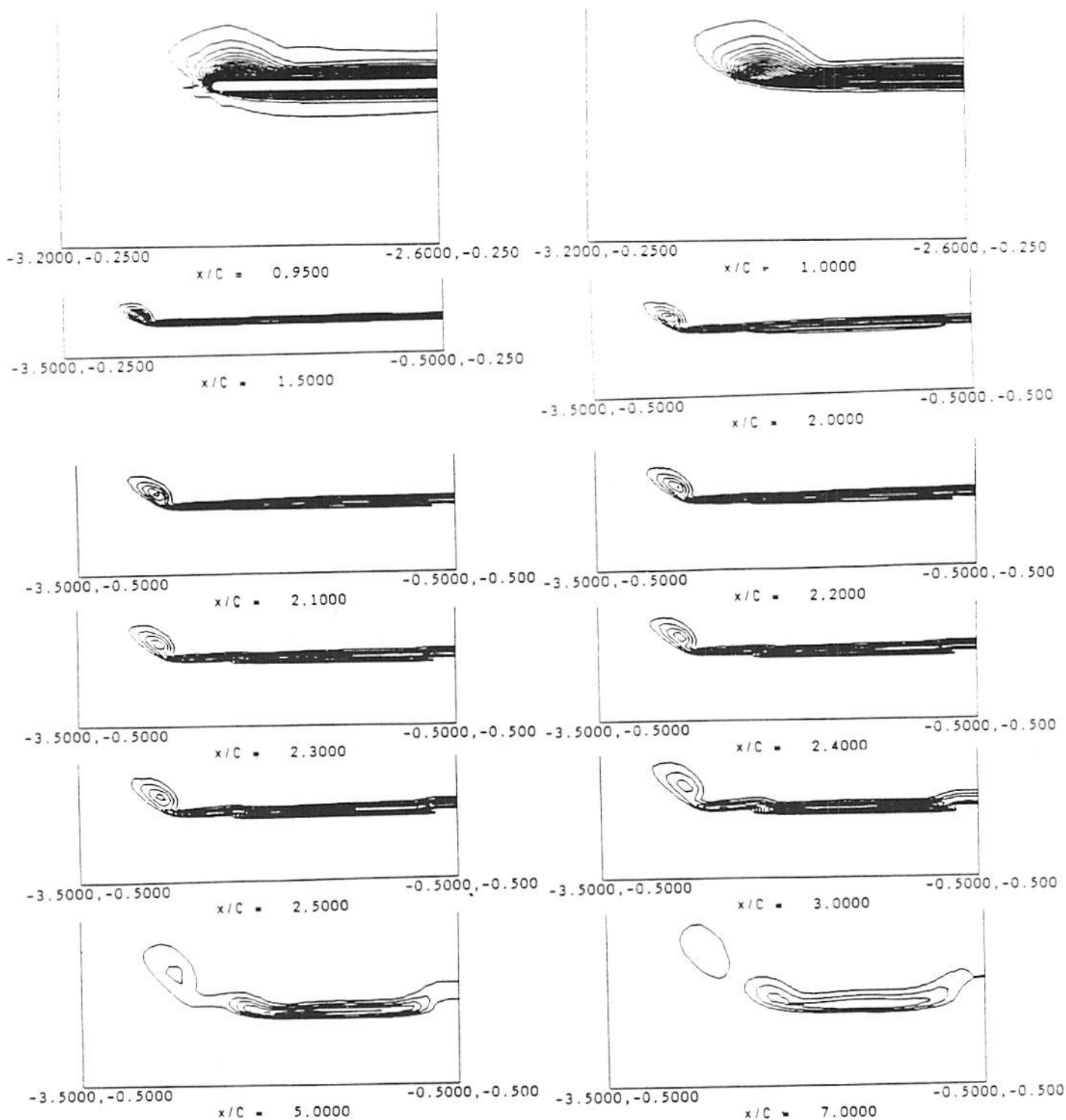
Figure 10. Total-pressure-loss contours at chordwise stations in the
vortex wake of leading/trailing wing interaction, $AR_1 = 5.9$,
$AR_2 = 3.3$, $C_{r2} = 0.5\ C_{r1}$, $\alpha_{1,2} = 4.64°$, $R_e = 3.2 \times 10^6$,
$M_\infty = 0.3$ (along-track penetration through vortex center).
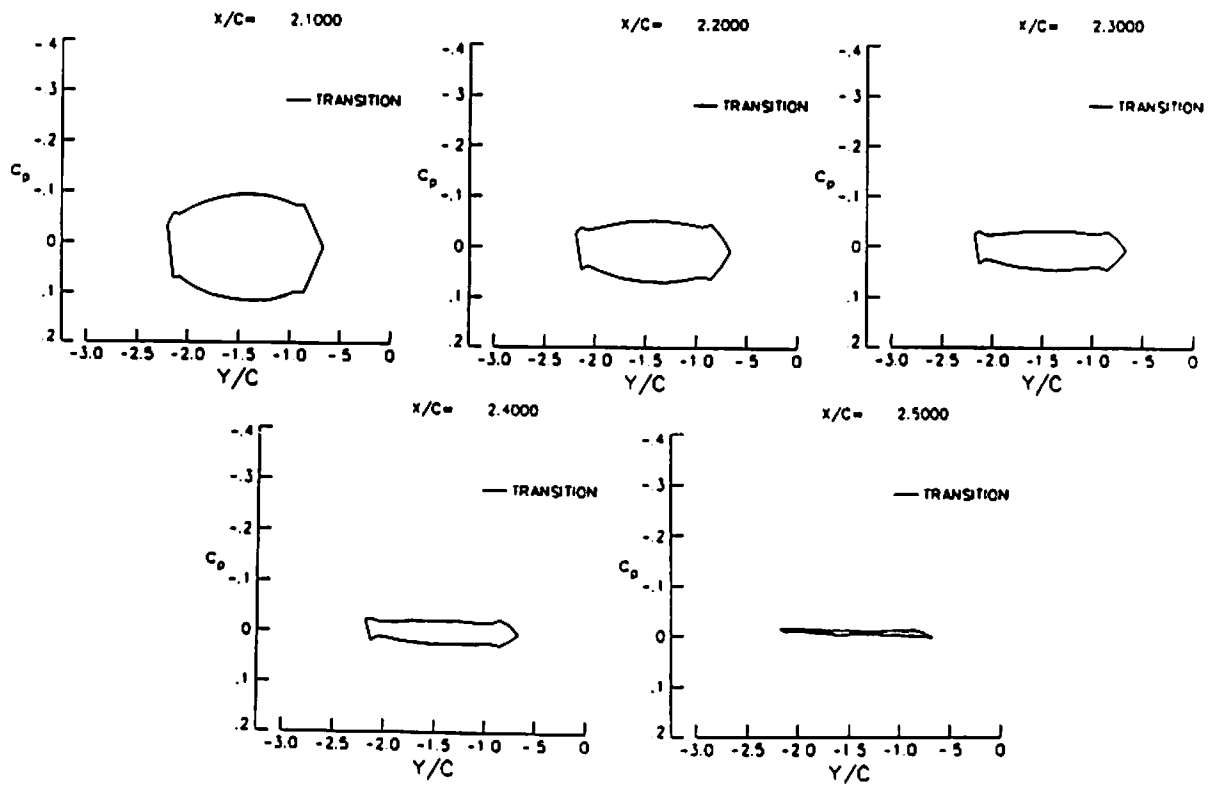
Figure 11. Spanwise surface-pressure distribution at chordwise stations of the trailing wing, along-track penetration between vortices.
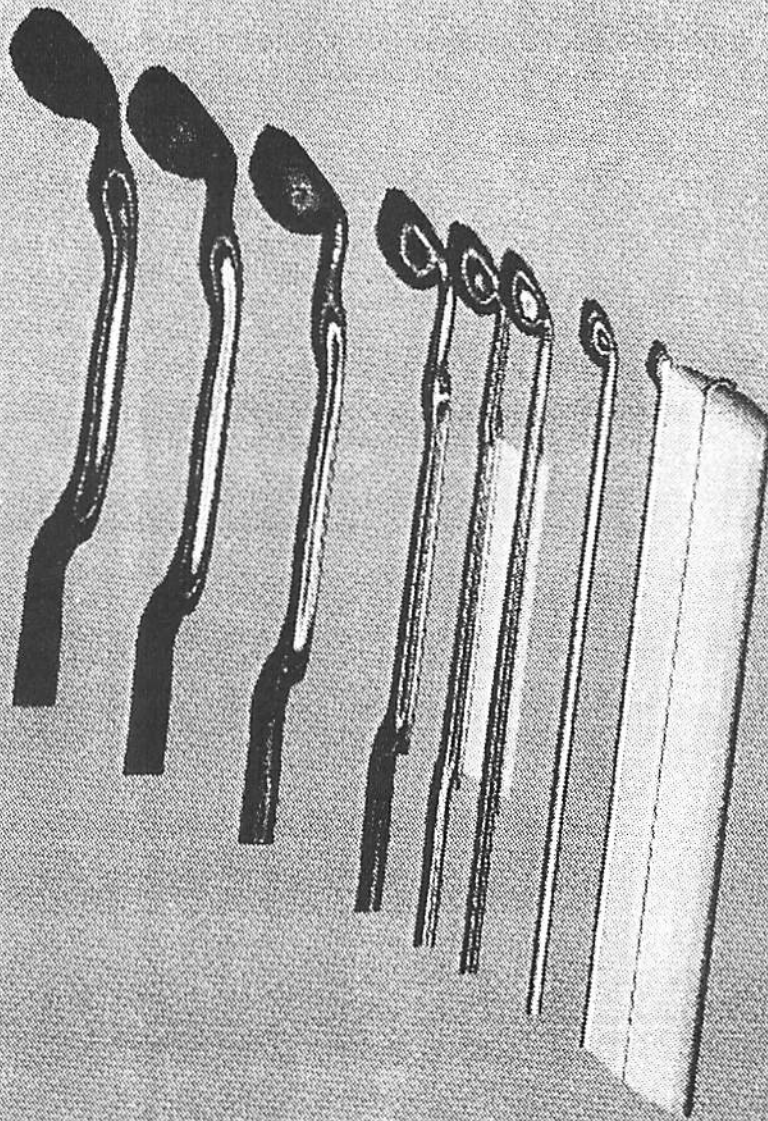
Figure 12. Three-dimensional view of the leading wing interation, along-track penetration between vortices.

REFERENCES

1. Hallock, J.N. and Eberle, W.R., "Aircraft Wake Vortices: A State-of-the-Art Review of the United States R&D Program," FAA Rept. FAA-RD-77-23, February 1977.

2. Dee, F.W. and Nicholas, O.P., "Flight Measurements of Wing Tip Vortex Motion Near the Ground," CF 1065, British Aeronautical Research Council, London, 1968.

3. Harvey, J.K. and Perry, F.J., "Flowfield Produced by Trailing Vortices in the Vicinity of the Ground," AIAA Journal, Vol. 9, Aug. 1977, pp. 1659-1660.

4. El-Ramly, Z., "Induced Rolling Moment on Trailing Wings," AIAA 10th Fluid & Plasmadynamics Conference, Albuquerque, NM, June 1977.

5. Wood, W.D. and McWilliams, T.G., "Wake Turbulence Detection and Economic Impact of Proposed Improvements," SAE Air Transportation Meeting, Washington, D.C., May 1977.

6. Garodz, L.J., "Federal Aviation Administration Full-Scale Aircraft Vortex Wake Turbulence Flight Test Investigations: Past, Present, Future," AIAA Paper No. 71-97, January 1971.

7. Cliffone, D.L. and Lonzo, C., Jr., "Flow Visualization of Vortex Interactions in Multiple Vortex Wakes Behind Aircraft," NASA TMX 62, 459, June 1975.

8. Olwi, I.A. and Ghazi, M.A., "An Experimental Investigation of the Turbulence Effect of a Leading Wing on a Trailing Aircraft," AIAA 91-3309-CP, AIAA 10th Applied Aerodynamics Conference, September 1991, pp. 830-837.

9. Chorin, A.J. and Bernard, P.S., "Discretization of a Vortex Sheet, with an Example of Roll-Up," Journal of Computational Physics, Vol. 13, November 1973, pp. 423-429.

10. Hackett, J.E. and Evans, M.R., "Vortex Wakes Behind High Lift Wings," Journal of Aircraft, Vol. 8, May 1971, pp. 334-340.

11. Yates, J.E., "Calculation of Initial Vortex Roll-Up in Aircraft Wakes," Journal of Aircraft, Vol. 11, July 1974, pp. 397-400.

12. Iversen, J.D. and Bernstein, S., "Trailing Vortex Effects on Following Aircraft," Journal of Aircraft, Vol. 11, January 1974, pp. 60-61.

13. Rossow, V.J., "Inviscid Modeling of Aircraft Trailing Vortices," Proceedings of NASA Symposium on Wake Vortex Minimization," Washington, D.C., February 1976, pp. 4-54.

14. Kandil, O.A., Mook, D.T. and Nayfeh, A.H., "Application of the Nonlinear Vortex-Lattice Concept to Aircraft-Interference Problems," Advances in Engineering Science, NASA CP-2001, Vol. 4, November 1976, pp. 1321-1326.

15. Kandil, O.A., Mook, D.T. and Nayfeh, A.H., "Nonlinear Prediction of the Aerodynamics Loads on Lifting Surface," Journal of Aircraft, Vol. 13, No. 1, January 1976, pp. 22-28.

16. McCormick, B.W., Tangler, J.L. and Sherrieb, H.E., "Structure of Trailing Vortices," Journal of Aircraft, Vol. 5, No. 3, May-June 1968, pp. 260-267.

17. Bilanin, A.J., Teske, M.E. and Williamson, G.G., "Vortex Interactions and Decay in Aircraft Wakes," AIAA Journal, Vol. 15, No. 2, Feb. 1977, pp. 250-260.

18. Bilanin, A.J., Teske, M.E. and Hirsh, J.E., "Neutral Atmospheric Effects on the Dissipation of Aircraft Vortex Wakes," AIAA Journal, Vol. 16, No. 9, September 1978, pp. 956-961.

19. Liu, C.H. and Ting, L., "Interaction of Decaying Trailing Vortices in Spanwise Shear Flow," Computer and Fluids, Vol. 15, No. 1, 1987, pp. 77-92.

20. Weston, R.P., Ting, L. and Liu, C.H., "Numerical Studies of the Merging Vortices," AIAA 86-0557, January 1986.

21. Liu, C.H., Tavantzis, J. and Ting, L., "Numerical Studies of Motion and Decay of Vortex Filaments," AIAA Journal, Vol. 24, No. 8, August 1986, pp. 1290-1297.

22. Liu, C.H., Krause, E. and Ting, L., "Vortex-Dominated Flow with Viscous Core Structure," AIAA 85-1556, invited paper, July 1985.

23. Greene, G.C., "An Approximate Model of Vortex Decay in the Atmosphere," Journal of Aircraft, Vol. 23, No. 7, July 1986, pp. 566-573.

24. Greene, G.C., Lamar, J.E. and Kubendran, L.R., "Aircraft Vortices: Juncture, Wing and Wake," AIAA 88-3743, July 1988.

25. Cebeci, T., "Calculation of Compressible Turbulent Boundary Layers with Heat and Mass Transfer," AIAA Paper 70-741, June 1970.

26. Baldwin, B.S. and Lomax, H., "Thin-Layer Approximation and Algebraic Model for Separated Turbulent Flows," AIAA Paper 78-257, January 1978.

27. Wong, T.C., Kandil, O.A. and Liu, C.H., "Navier-Stokes Computations of Separated Vortical Flows Past Prolate Spheroid at Incidence," AIAA 89-0553, January 1989.

28. Yip, L.P. and Shubert, G.L., "Pressure Distributions on a 1-By 3-Meter Semispan Wing at Sweep Angles from 0°-40° in Subsonic Flow," NASA TN D-8307, December 1976.

DOPPLER RADAR DETECTION OF VORTEX HAZARD INDICATORS

J.D. Nespor, B. Hudson, R.L. Stegall and J.E. Freedman
Government Electronic Systems Division
General Electric Company, MS 108-102
Moorestown, NJ 08057

ABSTRACT

Wake vortex experiments were conducted at White Sands Missile Range, NM using the AN/MPS-39 Multiple Object Tracking Radar (MOTR). The purpose of these experiments was twofold. The first objective was to verify that radar returns from wake vortex are observed for some time after the passage of an aircraft. The second objective was to verify that other vortex hazard indicators such as ambient wind speed and direction could also be detected. The present study addresses the Doppler characteristics of wake vortex and clear air returns based upon measurements employing MOTR, a very sensitive C-Band phased array radar. In this regard, the experiment was conducted so that the spectral characteristics could be determined on a dwell-to-dwell basis. Results are presented from measurements of the backscattered power, velocity and spectral width when the aircraft flies transverse and axial to the radar beam. The statistics of the backscattered power and spectral width for each case are given. In addition, the scan strategy, experimental test procedure and radar parameters are presented.

INTRODUCTION

The need to provide protection against wake vortex-induced turbulence hazards necessitates imposing large separations between heavy jets and other aircraft, resulting in a major constraint on ATC system capacity. In truth, an actual wake vortex hazard is rarely present--occurring only when ambient winds along the approach path are too weak to rapidly dissipate the vortices. Since today's ATC system lacks a sensor system that can indicate presence or absence of the wake vortex hazard, it must always be assumed that the hazard is present and the cost of reduced capacity is borne in the interest of safety. Previous research with microwave doppler radar has suggested the potential of this technology to monitor the winds and detect turbulence even in clear air conditions. This capability, if combined with the flexibility produced by the beam agility of phased array antennas, offers hope for an operational sensor system that can support an all-weather fail-safe solution of the vortex problem. This solution could be accomplished in the following three ways. First, radar can provide doppler wind field measurements covering the terminal area which, when combined with data from other meteorological sensors present, can enable highly accurate mesoscale, short-term wind condition forecasts. These forecasts

looking 20 to 30 minutes ahead provide the lead time needed for air traffic controllers to adjust traffic separations to the vortex hazard as indicated by forecasted wind speed and direction in the final approach corridor. Second, the radar could perform continuous real-time monitoring of the wind conditions actually occurring along the final approach path, providing a means for verifying the forecasted hazard level and if necessary alerting the controller to increase separations. Third, for ultimate protection, the radar could provide a means for actually detecting the vortices and determining decay rate and motion and, if necessary, alerting the controller to wave-off the approaching aircraft.

The above described possibilities have stimulated interest in including wake vortex protection as a functional requirement for the FAA's recently announced Terminal Area Surveillance System (TASS). Encouraged by such interest, the General Electric Co., over the past year, has conducted an informal series of cooperative experiments with the White Sands Missile Range (WSMR) exploring the feasibility of including vortex protection functionality in an advanced multifunction terminal radar as envisaged for TASS. The aircraft test vehicles were limited to small jet aircraft (A-7), as heavier aircraft were not available. The sensor used was the AN/MPS-39, a C-Band pulse doppler phased array radar originally developed by GE for the WSMR range instrumentation complex. The AN/MPS-39 is an excellent tool for exploring how beam agility can be exploited to provide prediction, detection and location of vortex hazards for a multifunction airport radar. This paper reports on the experimental results. It first reviews the physical basis underlying the application of microwave radar to the vortex problem, then describes the test radar and the experimental setup. It then goes on to present results, recommendations for further work, and finally conclusions.

WAKE VORTEX AND OPTICALLY CLEAR AIR PHENOMENOLOGY

Scattering from fluctuations in the refractive index of the atmosphere has provided a very powerful tool in the application of radars to clear air turbulence (CAT) investigations. It has been clearly established [1] [2] and widely accepted that high powered, very sensitive microwave radars can detect echoes caused by backscattering from inhomogeneities of the refractive index in the atmosphere. The backscattered power is related to the intensity of the fluctuations in the refractive index within a narrow range of turbulent eddy sizes centered at one-half the radar wavelength. This region is known as the inertial subrange of the turbulence.

The theory of scattering of electromagnetic waves from refractive index in homogeneities has been developed by Tartarski. [3] For homogeneous and isotropic turbulence, Tartarski has shown

$$D_n^{(r)} = C_n^2 \, r^{2/3}$$

that the structure constant can be expressed as   . The scattering mechanism from homogeneous and isotropic turbulent media is similar to Bragg scatter in that a radar of wavelength λ scatters from a particular component of turbulence with eddy sizes equal to $\lambda/2$. [4] Ottersten [5] has derived the following expression relating volumetric reflectivity to the intensity of refractive index variations:

$$n = 0.38 \, C_n^2 \, \lambda^{-1/3} \tag{1}$$

where C_n^2 is the structure constant and is a measure of the intensity of the refractive index fluctuations, and λ is the radar wavelength. It has been established by Chadwick [6] et al. that the scattering model for clear air turbulence is applicable to scattering from wake vortex induced turbulence. In other words, the vortex induced turbulence is created at scale sizes of 5-10 meters during the wingtip roll-up process and then fractures to smaller sizes as the vortex dissipates. When the vortex induced turbulent scale size dissipates to the point where it becomes on the order of half the radar wavelength, the radar backscattered power then becomes proportional to the refractive index fluctuations.

For turbulence associated with wake vortices, the characteristics of the vortex are generated primarily by a discontinuity in the air flow traversing the wings. This causes a vortex flow to be shed along the wing tips. The velocity gradients that are generated across the width of the vortex core are the primary contributor to the refractive index fluctuations. The entrainment of the heat emissions and water vapor from the engines leads to increased fluctuations in the refractive index of the vortex as it propagates through the atmosphere behind the aircraft producing it. [7]

Continuous real-time monitoring of the low-altitude wind speed and direction has been demonstrated with the AN/MPS-39 radar. We believe the sensitivity of this radar to monitoring wind speed and direction results from refractive index inhomogeneities caused by convective cells produced by the heating of the earth's surface, as well as particulate scatter from small millimeter sized particles such as dust and insects which may be lifted by buoyant air parcels rising from the heated surface of the earth. Due to the size and nature of these particles, they are accurate tracers of air motion up to the boundary layer. It should be noted that there may be seasonal and geographical variations in the scattering mechanisms that produce the radar echoes for mapping the low altitude winds. This is an area that needs to be investigated further.

DESCRIPTION OF MULTIPLE OBJECT TRACKING RADAR (MOTR)

Background

The AN/MPS-39 Multiple Object Tracking Radar (MOTR) is a new precision instrumentation system designed to support range safety, weapon development, operational test and evaluation, and training exercises involving multiple participants. The first MOTR was delivered to the U.S. Army's White Sands Missile Range (WSMR) in May 1988 where it underwent extensive field testing culminating in final government acceptance in December of that year. Since then two other MOTR radars have been delivered to various DoD test ranges around the country. A fourth MOTR unit is now being tested by GE at its Moorestown, New Jersey, location for the U.S. Air Force Western Space and Missile Center. A photograph of the radar is shown in Figure 1.

The MOTR's transmission lens phased array antenna, mounted on an elevation over azimuth pedestal, enables it to accurately track up to ten targets while simultaneously processing two surveillance beams. Accuracies better than 0.2 mil RMS angle and 1.0 yd RMS range are achieved while tracking a 20 dB or greater signal-to-noise ratio target. A 5.0 dB or better signal-to-noise ratio is obtained while tracking a 6-inch diameter sphere with a 1.0 micro-second pulse width at 100 kiloyard range. MOTR is fully coherent and has built-in clutter suppression capability. The radar is mobile, and its design is based on Inter-Range Instrumentation Group (IRIG) timing, transponder, and frequency standards. Table 1 lists important MOTR system parameters.

As can be seen from Table 1, the radar has the following unique features that make it very well suited for vortex detection experiments:

1) High peak transmit power of 1 MW for high sensitivity.

2) Antenna beamwidth of 1° for good angular resolution of targets.

3) Very low antenna sidelobes -35 dB rms for reduced sidelobe clutter contamination.

4) Variable pulsewidth between 0.25 μsec and 1 μsec. This corresponds to range resolutions of between 37.5 meters to 150 meters.

5) The ability to electronically steer the beam reduces ground clutter contamination.

6) High system stability for high doppler resolution.

Modifications

MOTR software was extensively modified to support the wake vortex experiments and these changes have permanently been made part of all existing systems. MOTR additions consisted of a new mode to enable disk recording of 36 range gates of coherent in-phase and quadrature sum channel data and angle scan modifications to permit dwells of up to 256 pulse repetition intervals.

WSMR WAKE VORTEX EXPERIMENTAL OVERVIEW

During January-February of 1991, the AN/MPS-39 MOTR at WSMR, NM was used to conduct wake vortex detection experiments. Weather conditions during this time were characterized by mild daytime temperatures, rising to 55-60 degrees Fahrenheit on the average, with generally light winds. In general, during the winter months, the two dominant type air masses influencing WSMR weather are modified Maritime Polar and Modified Continental Arctic. The modified Maritime Polar was the system that dominated the weather patterns during this time. No precipitation in the region occurred during the days when fly-bys were being conducted.

Experiments were conducted using A-7 fighter aircraft flying out of Holloman, Air Force Base. Figure 2 is an elevation view of the geometry of the experiment. Figure 3 shows the location of the two space points that the aircraft flew through relative to the radar. Space Point 1 was located 3 kyds directly north of the radar, and space point 2 was located 3 kyds directly west of the radar. The aircraft flew a clockwise racetrack flight pattern and was vectored to the appropriate space point and altitude by the WSMR control tower. The experiment was set up such that the radar looked axially behind the aircraft for vortices as it flew through space point 2, and looked transverse to the aircraft flight direction as it flew through space point 1. The aircraft flew at an approximate speed of 180 knots with both flaps and landing gear down to simulate as close as possible a landing configuration. Each mission was composed of three separate data collection modes. These consisted of a pre-mission, target mission, and post-mission data collection mode. The pre-mission data collection mode was performed approximately 15 minutes before the aircraft arrival. The intent was to record data on clear air returns prior to the aircraft's arrival. Data was then collected for at least 30 seconds immediately before the aircraft flew through the beam and for at least one minute after the aircraft flew through the beam. Another post-mission data collection mode was then taken for two minutes to determine the ambient wind conditions after the fly-by. Before and after each mission, a call was placed to the WSMR weather station located a half mile from the radar so that the temperature, humidity, pressure, wind speed and direction both at the surface and aircraft altitude could be monitored and used in subsequent data analysis. Visual observations were made of the two space points with personnel using binoculars during the entire mission. Two observers were employed; one monitored space point 1 and the other space point 2 for birds, insects, etc., flying through or around the beam.

Figure 4 shows the scan pattern employed by the radar for the axial passes (looking due west to space point 2). The radar electronically scanned a 3x3 array, the aircraft was vectored through the top middle beam. This scan strategy facilitated vortex detection even when the cross winds were strong enough to blow the vortex into the adjacent beams or, as it sank into the lower beams, when the wind conditions were calm. Figure 5 shows the scan pattern employed by the radar for the transverse pass when the radar was looking due north to space point 1. For this scan, the radar electronically scanned a 1x7 array. The aircraft flew through the third beam from the top. This allowed for some uncertainty in the aircraft's altitude as it flew through the beam, and also allowed the vortex to be detected as it sank into the lower beams.

Data collection modes for clear air mapping were very similar to the vortex scan modes discussed above except the tests were conducted without an aircraft fly-by. Data was collected for up to three minutes in this mode at space points 1 and 2.

DATA ANALYSIS AND RESULTS

Table 2 compares the vortex characteristics of the A-7 aircraft used for this experiment against other well known aircraft types. As Table 2 indicates, the circulation strength of the vortex produced by the A-7 is significantly less than all the other aircraft presented. This is primarily a function of the lighter weight of the A-7 aircraft. With this in mind, this section presents the spectral characteristics of what is believed to be a vortex detected when the A-7 aircraft flew

through space point 2 (axial to the beam). While several passes were conducted on this day with the A-7 aircraft, the pass presented herein represents the only data set collected to date that has been usable. This is because of experimental problems that occurred on the other passes on this day. Subsequently, constraints on range or aircraft availability have prevented us from reproducing these results. In addition, spectral characteristics from a very windy and a calm clear air day are presented.

Wake Vortex Spectral Processing

The experiment was set up such that 36 range gates were spread out over a 2 kyd range interval. Essentially, there were 18 range gates on either side of the designated space point. The radar was operating with a 1 microsecond pulse and a 1280 Hz pulse repetition frequency. For each range gate, 128 I & Q samples were recorded for each of the nine or seven beams at a given space point. Thus, the dwell time for each beam was 0.1 seconds, and each beam was revisited every 0.9 seconds over the course of a given data collection period. A 256 point FFT was then performed for each of the 36 range gates for all nine beams over the entire data collection interval. The time series data was weighted by minimum three-term Blackman-Harris weights to push the sidelobes below -70 dB. The periodogram at each range gate was then used to estimate the first three central moments such that

$$\hat{p} = \sum_{i=1}^{N} S(v_i) \tag{2}$$

where $\hat{p}$ is the estimate of backscattered power and N is the number of spectral lines. The

backscattered power in dBsm was then converted to an equivalent structure constant C_n^2.

$$\hat{v} = \frac{\sum_{i=1}^{N} v_i \, S(v_i)}{\sum_{i=1}^{N} S(v_i)} \tag{3}$$

where $\hat{v}$ is the mean velocity estimate and N is the number of spectral lines.

where $\hat{w}^2$ is the spectrum width estimate, $\hat{v}$ is the mean velocity estimate and N is the number of spectral lines.

$$\hat{w}^2 = \frac{\sum\limits_{i=1}^{N} (v_i - v)^2 \, S(v_i)}{\sum\limits_{i=1}^{N} S(v_i)} \tag{4}$$

It should be noted that care was taken to remove the undesired ground clutter spectral components before each of the first three central moments were computed. This was accomplished by removing four spectral lines on either side of the zero velocity component.

Figures 6(a) through 6(c) show "waterfall" or Doppler history plots of a vortex produced by the A-7 aircraft as it was flying axially through the top left radar beam. These plots consist of the time history of the spectral characteristics for three range gates. For these plots, negative velocities represent motion toward the radar and positive velocities represent motion away from the radar. Time increments between each spectrum are 0.9 second. On this day at the time of this mission, it was exceptionally calm at the surface and winds were reported between 1 - 2 knots at 800 feet, the approximate altitude of the aircraft. There were no birds or insect swarms reported from the visual observations made during the course of this mission. Figure 6(a) shows no vortex in range gate 14, but it does show the target saturating the receiver as it goes through the beam at this range gate. This figure also substantiates the wind conditions reported by the WSMR meteorological station. Also note that there were approximately 10 seconds of data collected before the aircraft flew through the beam. No spectra induced by vortices shed by the A-7 are evident after the aircraft flies through the beam for this range gate. The dark narrow spectral lines centered around zero velocity are ground clutter. However, for Figure 6(b) which is a spectral history for adjacent range gate 15, vortex induced spectra appear about 8 seconds after the aircraft leaves the beam at 18:07:22 GMT. Figure 6(c) which is the spectral history for range gate 16, shows a larger amplitude in the spectra and again no wind induced spectra before the aircraft flies through this gate. It appears that the vortex is in this gate for approximately 10 seconds. The two spectra, one on each side of the zero doppler, may be evidence of the vortex breaking up as it decays, but it does definitely show two different velocity components of the vortex. However, we reiterate that relating the very complex vortex physics to the spectral characteristics is difficult. The spectra produced by the vortices appear in the succeeding range gates 17 and 18 as well for this upper beam.

Figures 7(a) through 7(e) show Doppler History plots for the beam directly below the upper left beam considered above. The first range gate where the vortex induced spectral characteristic occurs is number 13. We believe the vortex produced by the A-7 aircraft is sinking into the lower beams and into the closer-in range gates. This is consistent with results reported by other investigators [8] [9]. For Figure 7(a), the first evidence of vortex induced spectra occurs at 18:07:43 GMT approximately 21 seconds after the time the vortex appears in the upper beam. It should also be noted that the target returns shown in the plots for this beam are caused by the aircraft flying in the angular sidelobes of the antenna. For adjacent range gate 14 in Figure 7(b), the spectral amplitude is larger. In range gate 15 in Figure 7(c), two sets of spectra occur. The new spectra occur at approximately 18:07:26 GMT. The exact nature of the spectra occurring earlier in time at the farther out gates is not well understood. This is probably the result of the different velocity components of the vorticity distribution manifesting themselves

at different times over the vortex lifetime as it decays. In range gate 16 in Figure 7(d), the spectra occurring at the later time begins to decay while the spectra occurring earlier in time but at farther out range gates begins to grow. At range gate 17 in Figure 7(e), the spectra occurring later in time are almost fully dissipated while the spectra occurring earlier is larger in amplitude. By range gate 19, the spectra occurring earlier dissipates as well. Both sets of spectra lasted for about 10 seconds.

Figures 8(a) and 8(b) are Doppler History plots for the lowest beam. The first gate where vortex induced spectra occur is in range gate 12. The time associated with this spectra is approximately 18:07:45 GMT which is about the same time that was observed for the spectra in the beam above. This could mean that the vortex had a large enough spatial extent to straddle both beams as it sank. In fact, the vortex might have grown in spatial extent as it sank and dissipated. This might account for both sets of spectra appearing in both lower beams at about the same time.

Figure 8(b) shows the spectra getting larger in amplitude and width, which is indicative of increased backscattered power for that gate. The spectra last for about 12 seconds and are spread out spatially over range gates 12 to 17. The apparent radar cross sections of the vortices presented for each of the three beams ranged from -65 dBsm to -80 dBsm. The equivalent

structure constant, C_n^2 ranged from -116.7 to -135.4 dB. The apparent cross sections tended

to increase as the vortex dropped into the lower beams. This might mean that the vortex grows spatially as it decays and occupies more of the pulse volume as it dissipates with time. This could possibly lead to more refractive index fluctuations spread out over a greater area within the pulse volume and thus the larger apparent cross sections in the lower beams.

The mean velocities tended to range from 1.1 m/s to 4.5 m/s. Spectral width tended to stay relatively constant and ranged from 2.75 to 3.7 m/s. We believe the data presented for this A-7 axial case to be consistent with what has been generally reported about vortex characteristics. However, specific radar data sets of axial looks at aircraft are nonexistent to the best of our knowledge. This makes making definitive statements difficult.

Clear Air Spectral Processing

Figures 9(a) through 9(c) show Doppler History plots of data collected on a very windy day on 5 May 1991. The wind direction at the surface was from the west at 270 and the wind speed was 15 knots with gusts reported to 25 knots by the WSMR meteorological station. At 800 ft., the wind speed was reported at 25 knots with gusts to 30 knots. The radar was pointed due east and scanning a 3 x 3 pattern. The radial wind velocities of each of the three time history plots correlate very well with the speed and direction reported by the WSMR meteorological station. The plots show that the winds are moving away from the radar as one would expect with the prevailing westerly winds and the radar scanning due east. In addition, Figures 10(a) through 10(c) show the histograms of the first three central moments for the data collected that day. Figure 10(b) shows the average radial velocity to be at -428.04 Hz which corresponds to a wind speed of 23 knots moving away from the radar. This again correlates quite well with the

meteorological station's report. Figure 10(a) shows the average structure constant to be -139 dB for this very windy day. In addition Figure 11(c) shows the average spectral width was 91.5 Hz which corresponds to 2.5 m/s or 5 knots.

Figures 11(a) through 11(c) show Doppler History plots of the data collected on a relatively calm morning on 6 May 1991. The wind direction at the surface was from the south at 190 and the wind speed was 5 knots. At 800 ft., the wind speed was reported at 8-10 kts. The radar was pointed due north to space point 1 and was scanning a 1 x 7 pattern. The Doppler History plots show very little activity for the three highest beams except for occasional gusts. Figures 12(a) through 12(c) show histograms of the first three spectral moments for the data collected on that day. Figure 12(b) shows the average radial velocity to be at -103.9 Hz which corresponds to 5 knots away from the radar. Figure 12(a) shows the average structure constant to be -143.5 dB, and Figure 12(c) shows the average spectral width to be 95 Hz which corresponds to 5.2 knots.

DART Plot Description

The Doppler History Plot was cumbersome to use when initially examining the data since it only provided information on one small segment of the scan volume. Several additional data representations were tried for visualizing over a larger volume. We learned that one of the dimensions that was necessary to include was time. We finally settled on a representation we called a DART (Doppler-Amplitude-Range-Time) plot. Figure 13 shows this plot. Using three axes and color, variations in amplitude and frequency of the spectral peak over range and time are easily seen allowing quicker identification of a potential vortex for more detailed analysis and a visualization of clear air phenomenon. Color indicates the doppler bin that the peak of the power spectrum occurs in. If the velocity is unambiguous, motion toward the radar is indicated by blue, motion away from the radar is indicated by red, and near zero velocity is indicated by green. The vertical axis is the amplitude of the peak of the power spectrum expressed in dBsm/doppler bin, i.e., the received energy is referenced back to the scatterer. Time is shown on the horizontal axis and the 36 range bins are shown on the axis coming out of the page. When an aircraft flies through a beam it shows up on the DART plot as a high amplitude ridge. The order that the range bins is shown can be reversed so that both sides of the ridge can be seen. The DART plot is generated by estimating the power spectrum, as in the Doppler History plot, for each range gate. The doppler bin with the peak amplitude is located and the doppler bin is color coded. A varying color line is then drawn connecting the peak amplitudes of the 36 range bins with values less than -100 dBsm being shown at -100 dBsm in black. The processes are repeated for each time sample. Figure 14 shows a typical DART plot for clear air returns. Unfortunately, color coding of the velocity could not be demonstrated because a color printer was not available. However, this plotting scheme is a very powerful tool for assessing and analyzing our data because of the four dimensions of data displayed simultaneously.

RECOMMENDATIONS FOR FUTURE EXPERIMENTS

In the course of this experiment, it has become clear that there are a number of useful areas for continued investigation. The effort thus far has demonstrated the highly variable and dynamic characteristics of vortex induced turbulence and optically clear air returns. We recommend the following areas for future investigation:

1) Carry out a series of experiments that insure the repeatability of the radar vortex returns presented in this paper and extend the experiments to include the more representative heavy commercial aircraft such as an MD-11 or Boeing 747.

2) Carry out experiments that will identify wake vortex signatures of heavy commercial aircraft and distinguish them from ambient winds.

3) Establish the reliability of monitoring wind speed and direction from ambient winds so that the conditions for wake vortices stalling can be predicted. A long-term investigation for determining wind speed and direction at low altitudes by microwave radar should be compared to a meteorological network of wind sensors to validate the reliability of monitoring winds.

4) The maximum range of detection should be established for heavy commercial aircraft.

5) A thorough study should be carried out to determine how well microwave radars detect vortices in rain, fog and other kinds of precipitation.

SUMMARY AND CONCLUSIONS

The experiments reported herein were an exploratory, limited scale feasibility investigation. They were performed by piggybacking on other scheduled WSMR missions so that resources could be obtained inexpensively. As such, we had to use aircraft that were already at WSMR which limited the aircraft population to A-7 jet fighters. Access to a heavy jet capable of producing the hoped-for very strong vortex radar echoes could not be provided without a formal testing program. Nevertheless, the tests did show definite evidence of detection of weak vortex echoes on an axial view for even the small A-7 aircraft which has an expected vortex backscatter cross section two orders of magnitude less than a heavy jet such as a MD-11 or Boeing 747. Also, the ability of microwave pulse doppler phased array radar to efficiently monitor low-level wind conditions in clear air was demonstrated. We find that these results point toward the feasibility of a multifunction radar playing an important role in TASS as a wide area indicator of wake vortex hazards. We believe the evidence and ultimate benefits to be substantial enough to warrant a serious FAA testing program that would: 1) validate and develop further the role

of microwave radar as a vortex hazard indicator, and 2) establish appropriate operational concepts.

ACKNOWLEDGMENTS

Table 1. MOTR System Parameters

Parameters	Value
Radar Frequency	C-Band (5.4 to 5.9 GHz)
Antenna:	
Directive Gain	45.9 dB
Beamwidth	1.05°
Scan Volume	60° cone plus cusps
Transmitter Power:	
Peak	1.0 MW
Average	5.0 kW
Range	0.5 to 8192 kyd
System PRF (Selectable)	80, 160, 320, 640, 1280 Hz
Object PRF (Selectable)	20, 40, 80, 160, 320, 640, 1280 Hz
Pulsewidth (Selectable):	
Non-Chirp	0.25, 0.5, 1.0 μs
Chirp (Expanded)	3.125, 12.5, 50 μs
Chirp (Compressed)	0.25 μs
Pedestal Servo:	
Position Servo	Rate-aided Type 2
Maximum Rate:	
Azimuth	800 mils/s
Elevation	300 mils/s
Maximum Acceleration	200 mils/s/s
Tracking Filters:	
Coordinates	Cartesian (XYZ)
Types	Alpha-Beta, Alpha-Beta-Gamma
Bandwidth	PRF/2 to 0.1 Hz

Table 2. Aircraft and Vortex Characteristics

	AIRCRAFT CHARACTERISTICS							VORTEX CHARACTERISTICS			
Aircraft	Engine Location and Number/Wing	Weight Lbs.	Wing Span Ft.	Area Ft.^{2}	Aspect Ratio	Take-off Speed MPH	Landing Speed MPH	Γ Vortex Strength Ft.^{2}/sec	Vortex Diameter Ft.	V_θ Tangential Velocity Ft./sec	Vortex Rate of Descent Ft./sec
B-707	Wings 2	258,000	145.75	2892	7.36	195	157	4165	10.0	132.4	5.4
B-727	Rear 3	169,000	108	1650	7.67	159	152	3309	5.3	200x	4.9
B-747	Wings 2	710,000	195.6	5500	6.95	195	163	7700	20.0s	122c	6.6
DC-9	Rear 2	108,000	89.3	914	7.40	165	154	2500	4.0c	200x	4.5
DC-10	Wings 1 and Rear 1	410,000	155	3550	6.8			5595	9.4c	190x	5.8
L-C5A	Wings 2	764,000	222.7	6200	7.20	161	150	7260	20.0c	115x	5.1
L-1011	Wings 1 and Rear 1	409,000	155	1755	6.4			5581	7.9c	225x	5.7
A-7	2	22,000	38.9			200	180	958	2.5c	37.7	2.25
C130	2	80,000	132.0				250	1353			

x = experimentally recorded maximum tangential velocity in tower fly-by at NAFEC

c = calculated parameter

s = estimated parameter

37-13
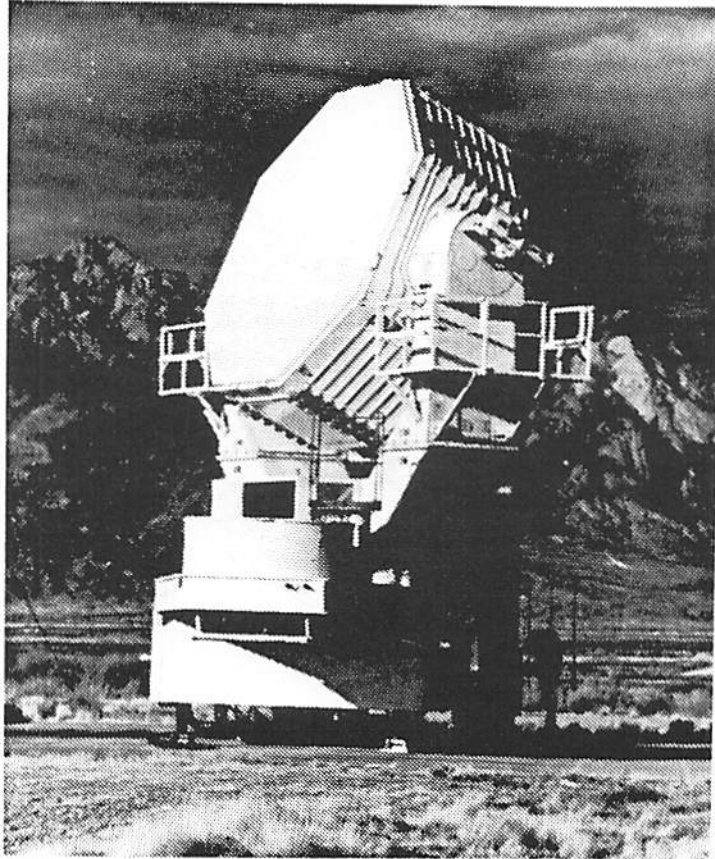
Figure 1. MOTR in operation (US Army photograph).

Elevation View

Aircraft

Pulse
Volume

MOTR
Radar

3°

5 YDS

260 YDS

3 KYDS

Ground
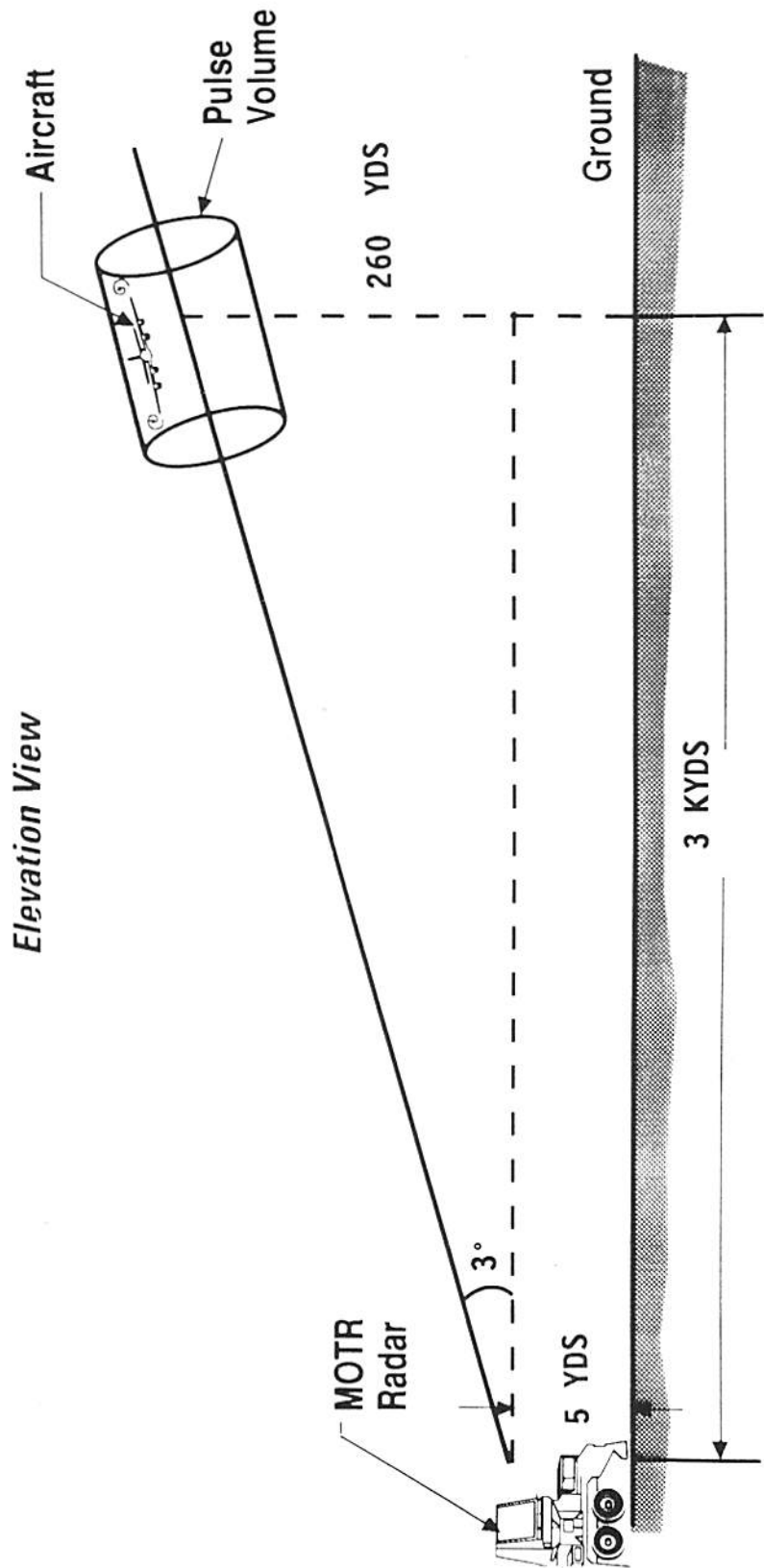
Figure 2. Test site configuration
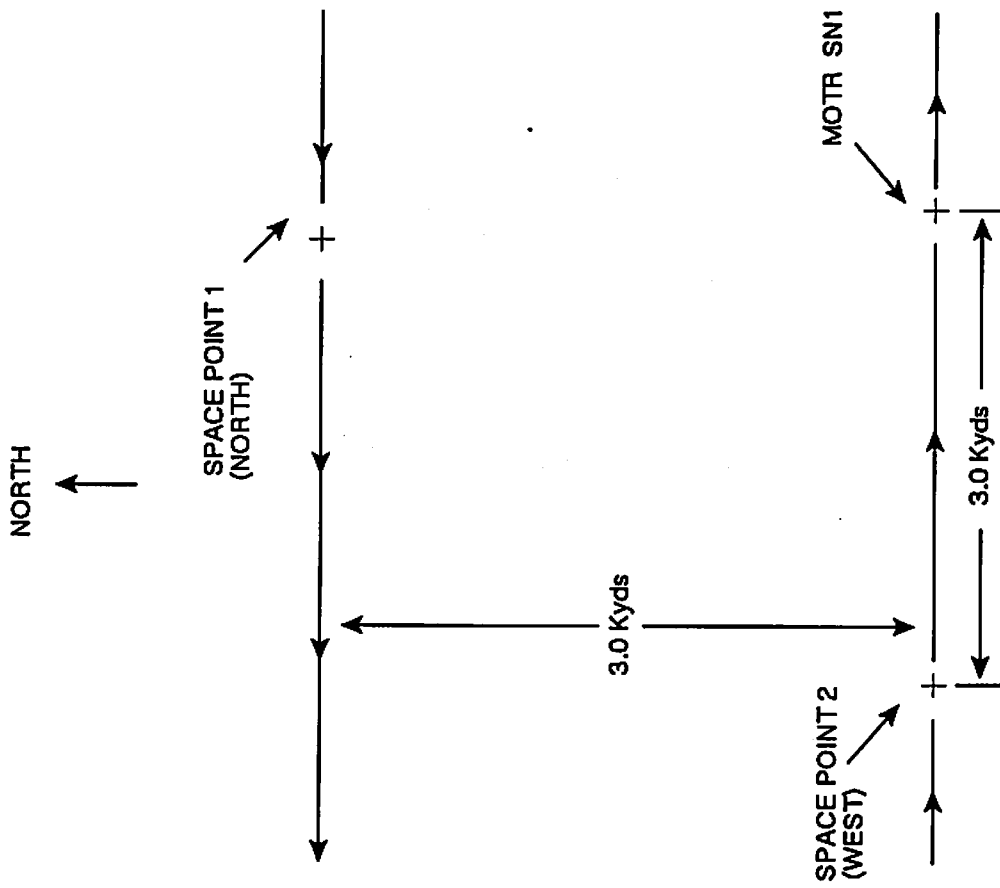
Figure 3. Wake vortex test site layout.
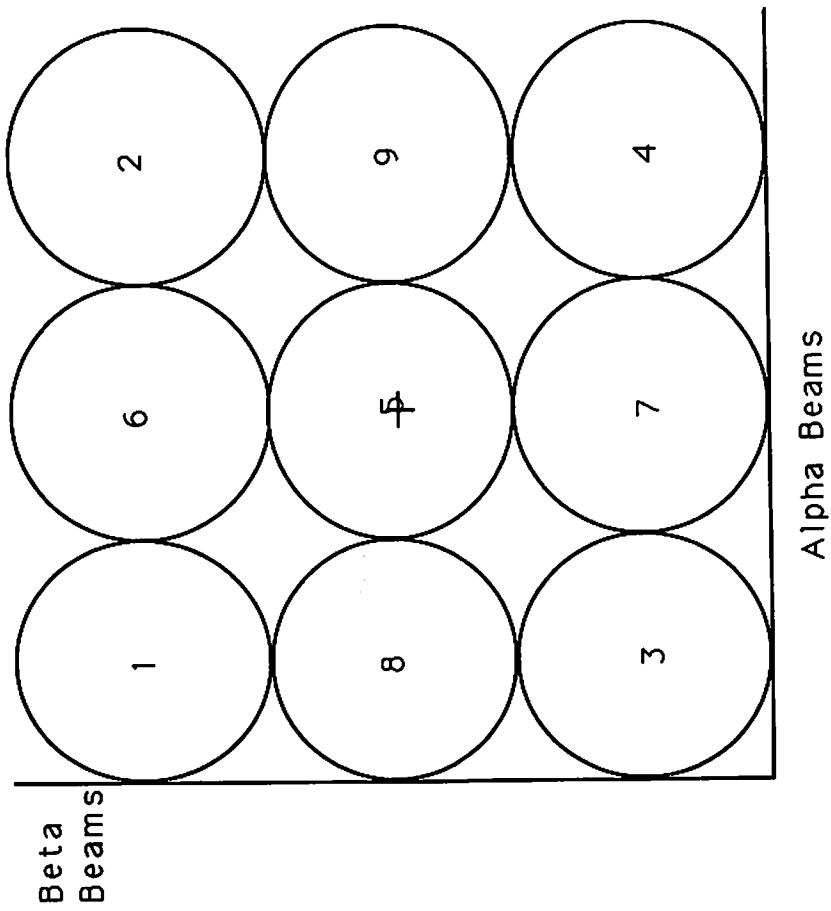
Figure 4. 3x3 scan pattern used for axial passes.
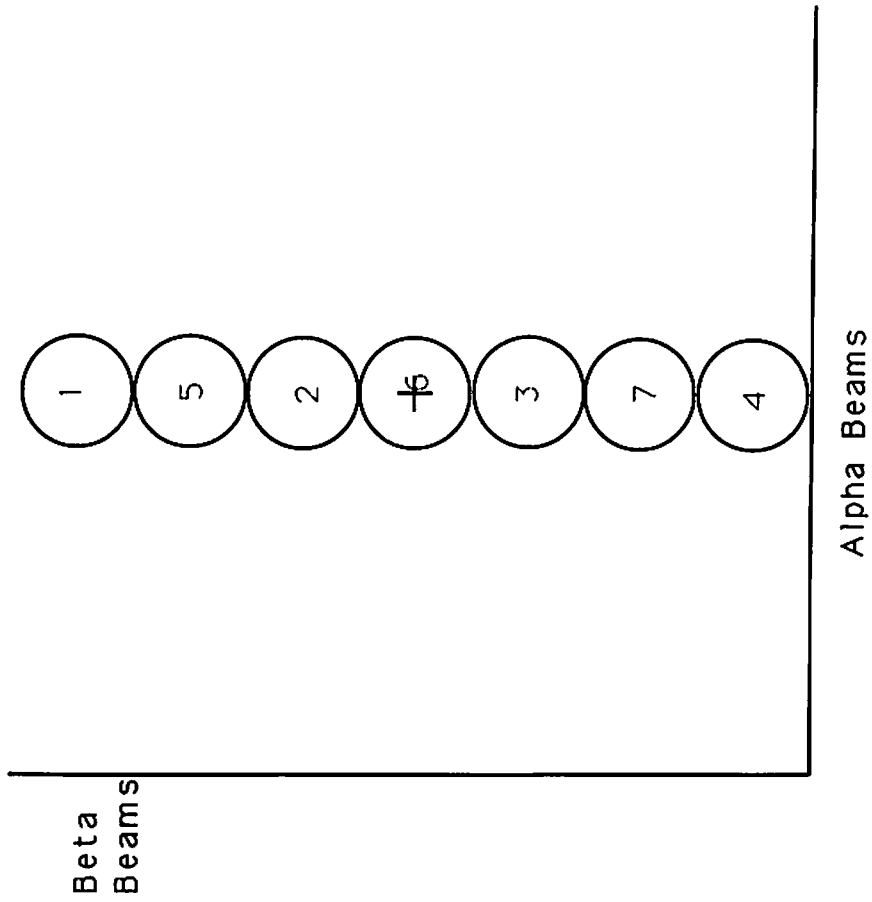
Figure 5. 1x7 scan pattern used for transverse passes.

Figure 6(A). Doppler time history plot for A-7 fly-by, upper beam, range gate 14, axial case.

Figure 6(B). Doppler time history plot for A-7 fly-by, upper beam, range gate 15, axial case.

Figure 6(C). Doppler time history plot for A-7 fly-by, upper beam, range gate 16, axial case.

Plot: Uncomp. Doppler

FFT Samples: 128

Weight: Blackman-Harris

Dynamic Range (dB): 32

Ambiguous Vel. (yd/s) = 36.8968
Spread(Hz)   =   10.01
Peak Spread(Hz)   =   415.22
P.S. Time: 18:07:06.30

Range Bin = 13
UBeams   = -2
VBeams   = 0

Signal Peak   =-63.24   dBsm/Hz
Display Ceiling =-70.00   dBsm/Hz

PRF   = 1280.6917   Hz
Frequency = 5690.0 MHz
Mission: 2/ 6/91   18:06
Analysis: 10/23/91   13:59

Figure 7(A). Doppler time history plot for A-7 fly-by, middle beam, range gate 13, axial case.

Plot: Uncomp. Doppler

FFT Samples: 128

Weight: Blackman-Harris

Dynamic Range (dB): 32

Ambiguous Vel. (yd/s) = 36.8968
Spread(Hz)   = 10.01
Peak Spread(Hz)   = 15.01
P.S. Time: 18:07:09.00

Range Bin = 14
UBeams   = -2
VBeams   = 0

Signal Peak   =-57.27   dBsm/Hz
Display Ceiling =-70.00   dBsm/Hz

PRF   = 1280.6917 Hz
Frequency = 5690.0 MHz
Mission: 2/ 6/91   18:06
Analysis: 10/23/91   14:07

Time

18:08:02.97

18:07:53.98

18:07:44.98

18:07:35.99

18:07:26.99

18:07:17.***

18:07:09.00

-640.   -320.   0.   320.   640.
                      Frequency - Hz
0.5   0.25   0.   -0.25   -0.5
                      Velocity Fraction

Figure 7(B). Doppler time history plot for A-7 fly-by,
middle beam, range gate 14, axial case.
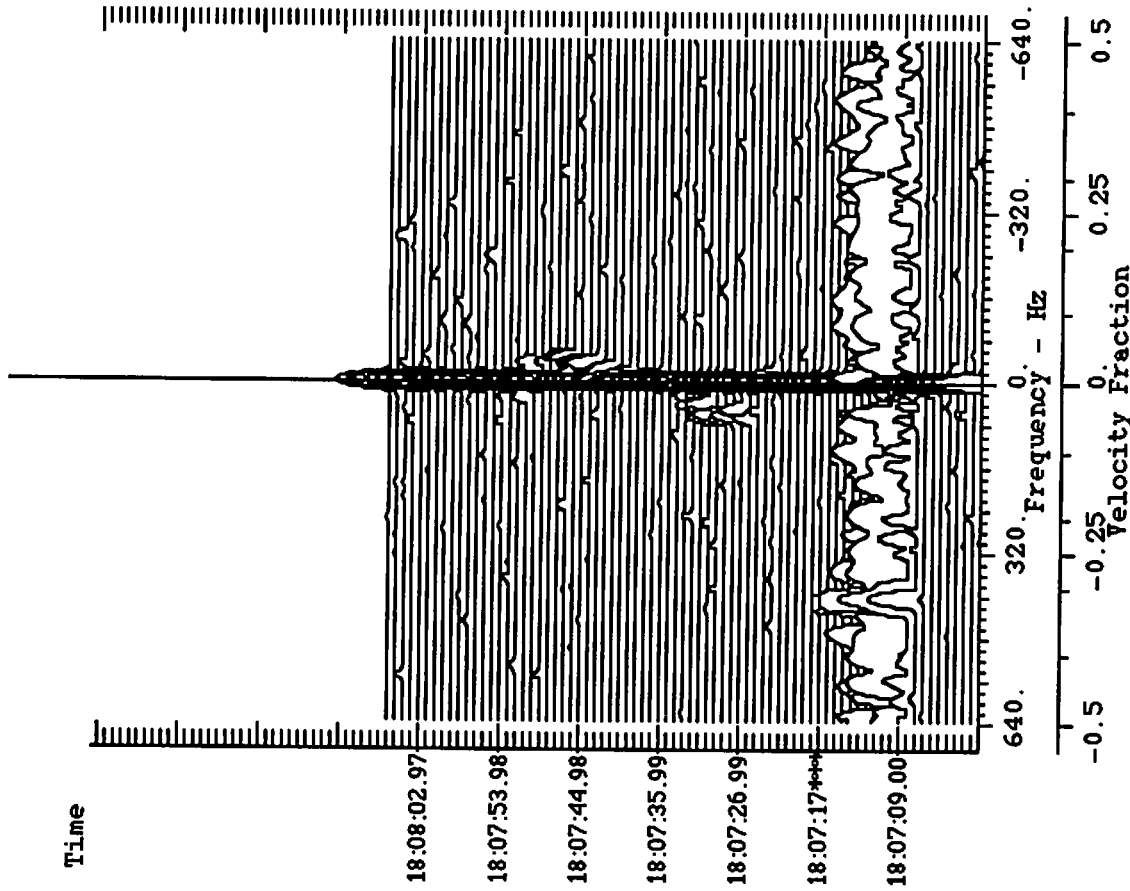
Figure 7(C). Doppler time history plot for A-7 fly-by, middle beam, range gate 15, axial case.
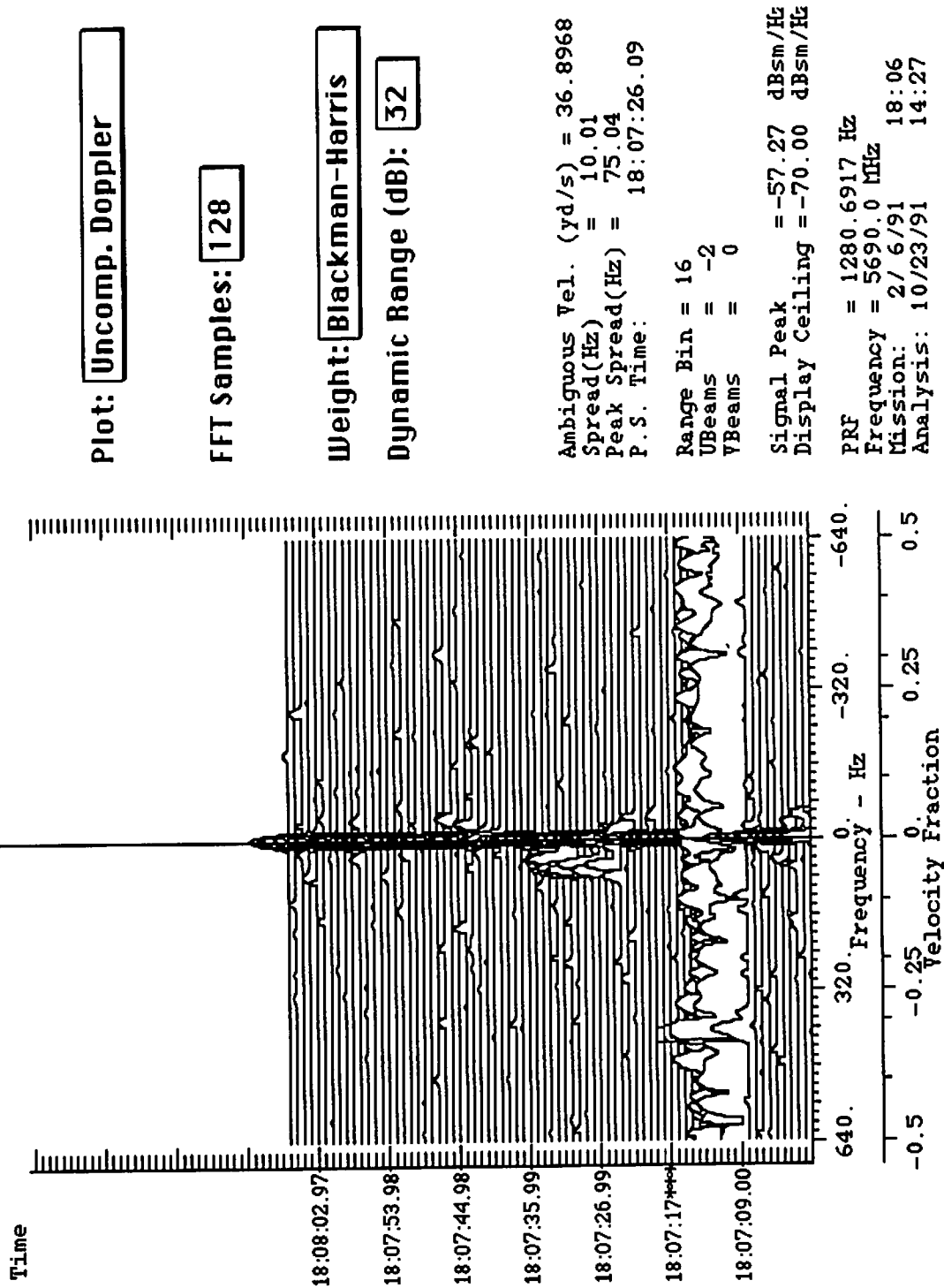
Figure 7(D). Doppler time history plot for A-7 fly-by, middle beam, range gate 16, axial case.
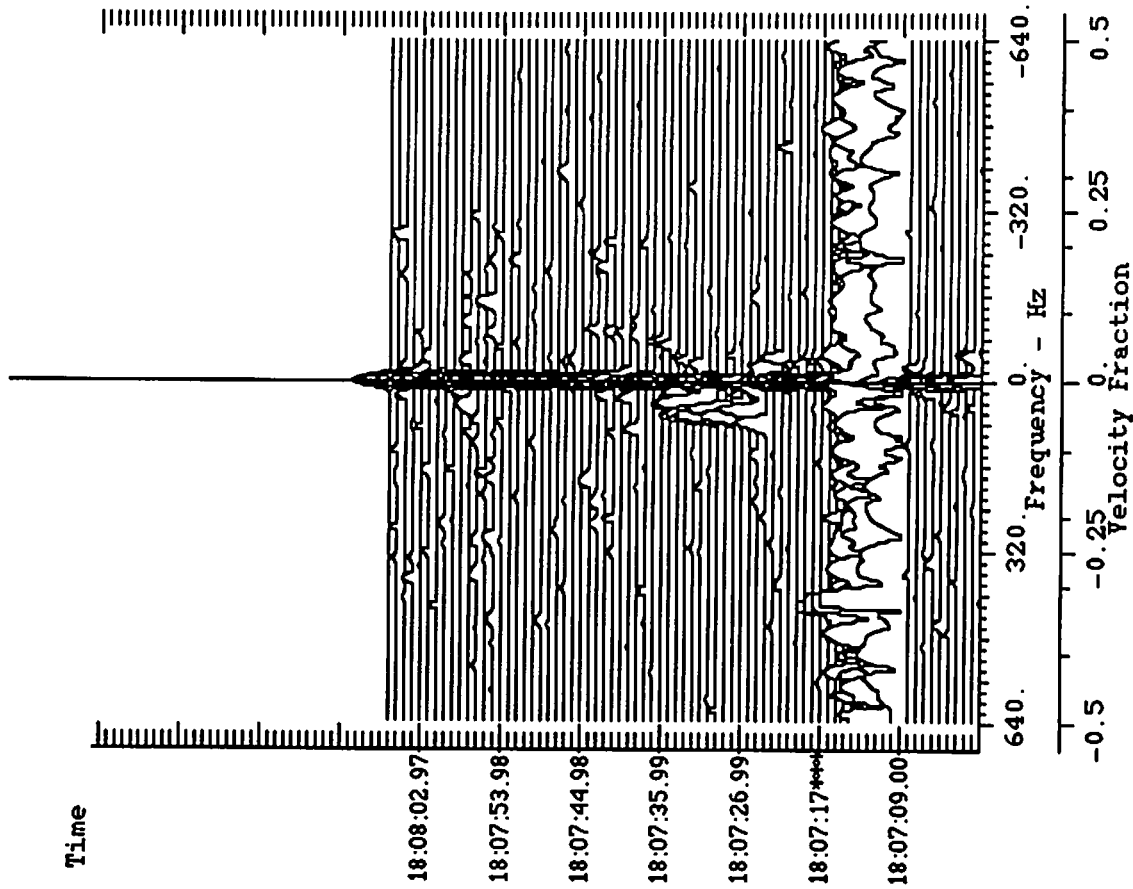
Plot: Uncomp. Doppler

FFT Samples: 128

Weight: Blackman-Harris

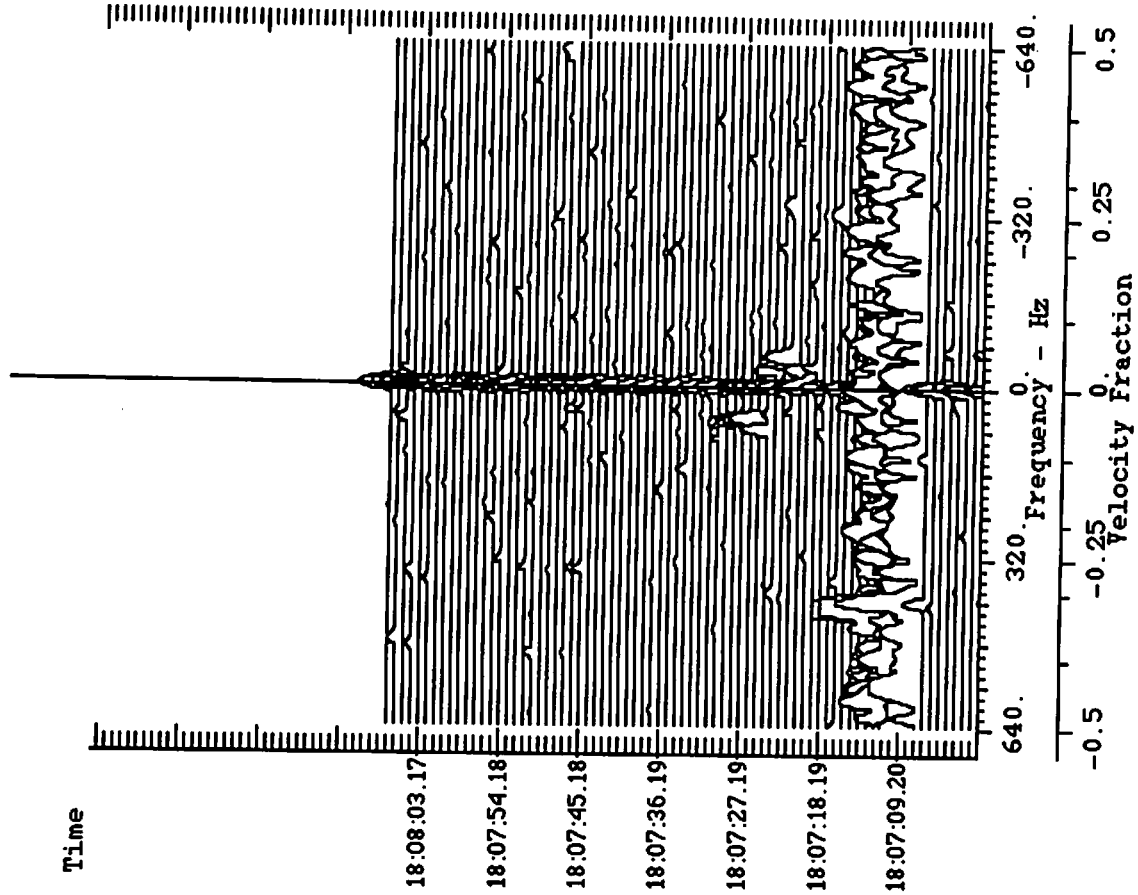Dynamic Range (dB): 32

Ambiguous Vel. (yd/s) = 36.8968
Spread(Hz)   = 10.01
Peak Spread(Hz)   = 65.04
P.S. Time: = 18:07:25.19

Range Bin = 17
UBeams   = -2
VBeams   = 0

Signal Peak   =-57.53 dBsm/Hz
Display Ceiling =-70.00 dBsm/Hz

PRF   = 1280.6917 Hz
Frequency = 5690.0 MHz
Mission: 2/ 6/91   18:06
Analysis: 10/23/91   14:33

Figure 7(E). Doppler time history plot for A-7 fly-by,
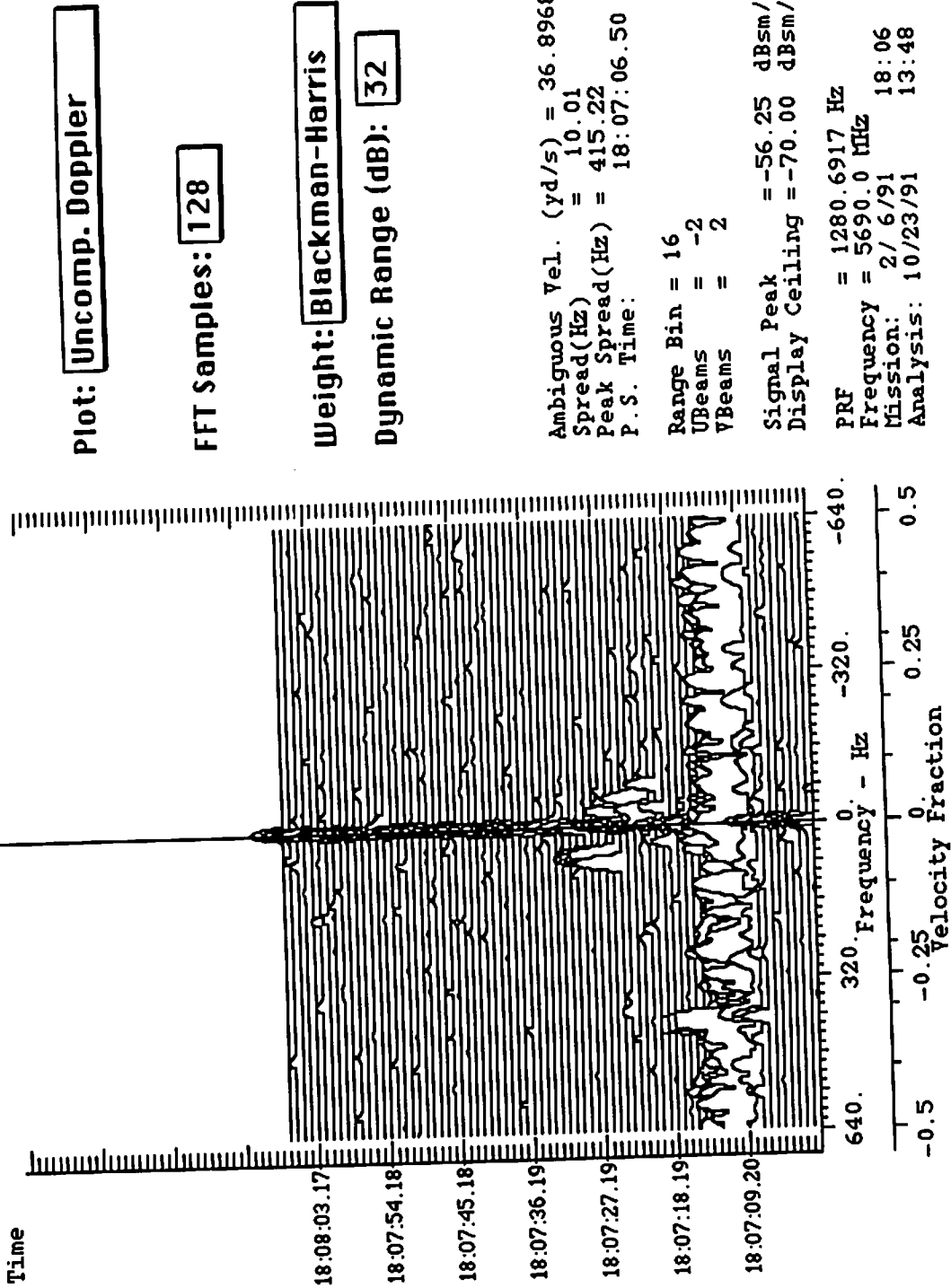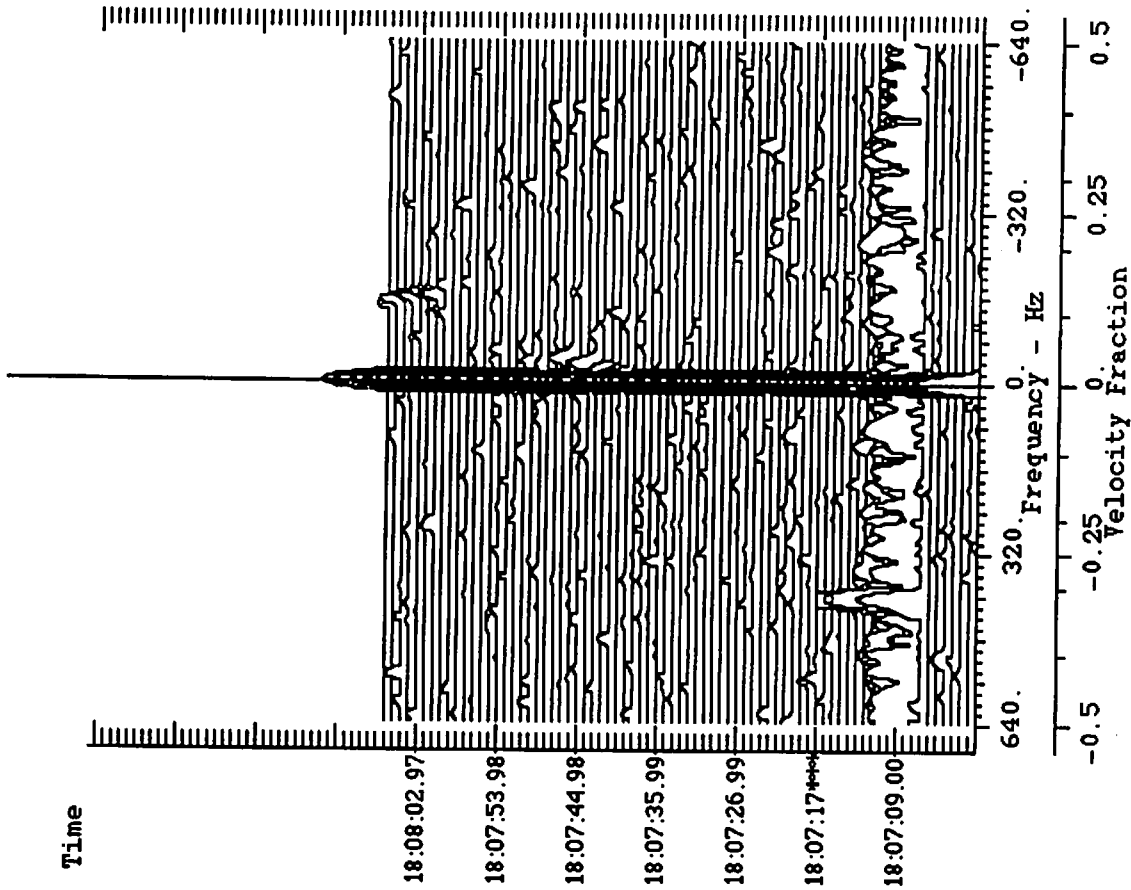middle beam, range gate 17, axial case.

Plot: Uncomp. Doppler

FFT Samples: 128

Weight: Blackman-Harris

Dynamic Range (dB): 32

```
Ambiguous Vel. (yd/s) =  36.8968
Spread(Hz)            =  10.01
Peak Spread(Hz)       = 415.22
P.S. Time:              18:07:08.50

Range Bin = 12
UBeams    = -2
VBeams    = -2

Signal Peak    =-68.83  dBsm/Hz
Display Ceiling =-70.00  dBsm/Hz

PRF       = 1280.6917 Hz
Frequency = 5690.0 MHz
Mission:    2/ 6/91      18:06
Analysis: 10/23/91       14:48
```

Time

18:08:02.47
18:07:53.48
18:07:44.48
18:07:35.49
18:07:26.49
18:07:17.50
18:07:08.50

-640.   -320.   0.   320.   640.

0.5   0.25   0.   -0.25   -0.5

Frequency – Hz

Velocity Fraction

Figure 8(A). Doppler time history plot for A-7 fly-by, lower beam, range gate 12, axial case.

Figure 8(B). Doppler time history plot for A-7 fly-by, lower beam, range gate 13, axial case.

Figure 9(A). Doppler time history plot for a windy day, upper beam, range gate 13, east look.
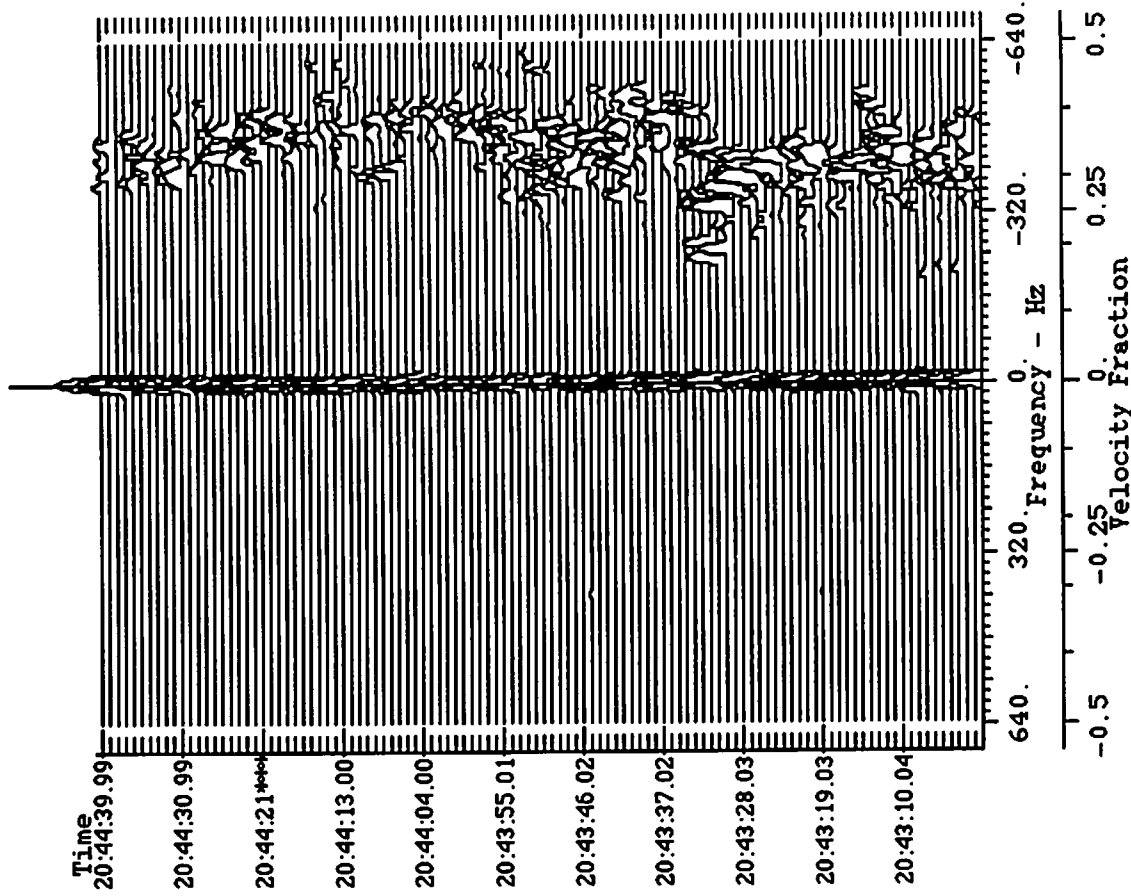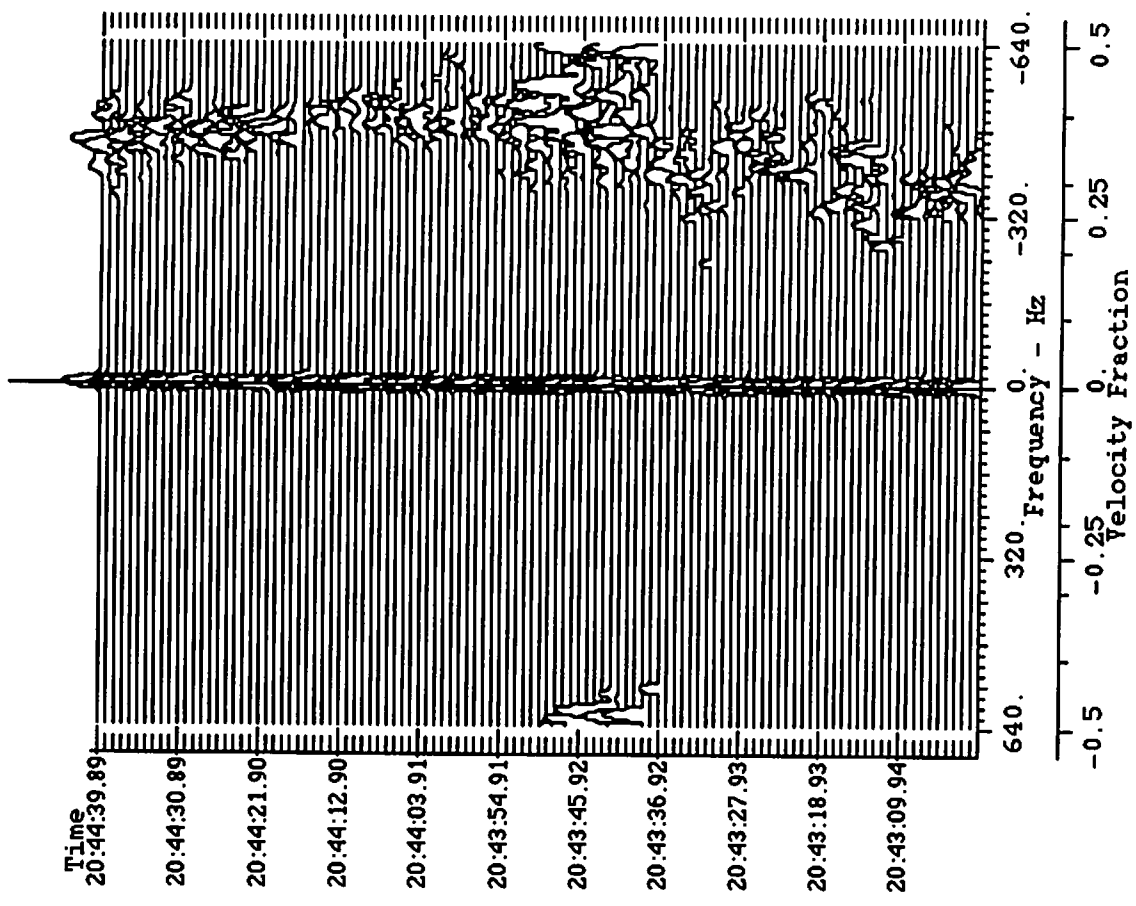
Plot: Uncomp. Doppler

FFT Samples: 128

Weight: Hamming
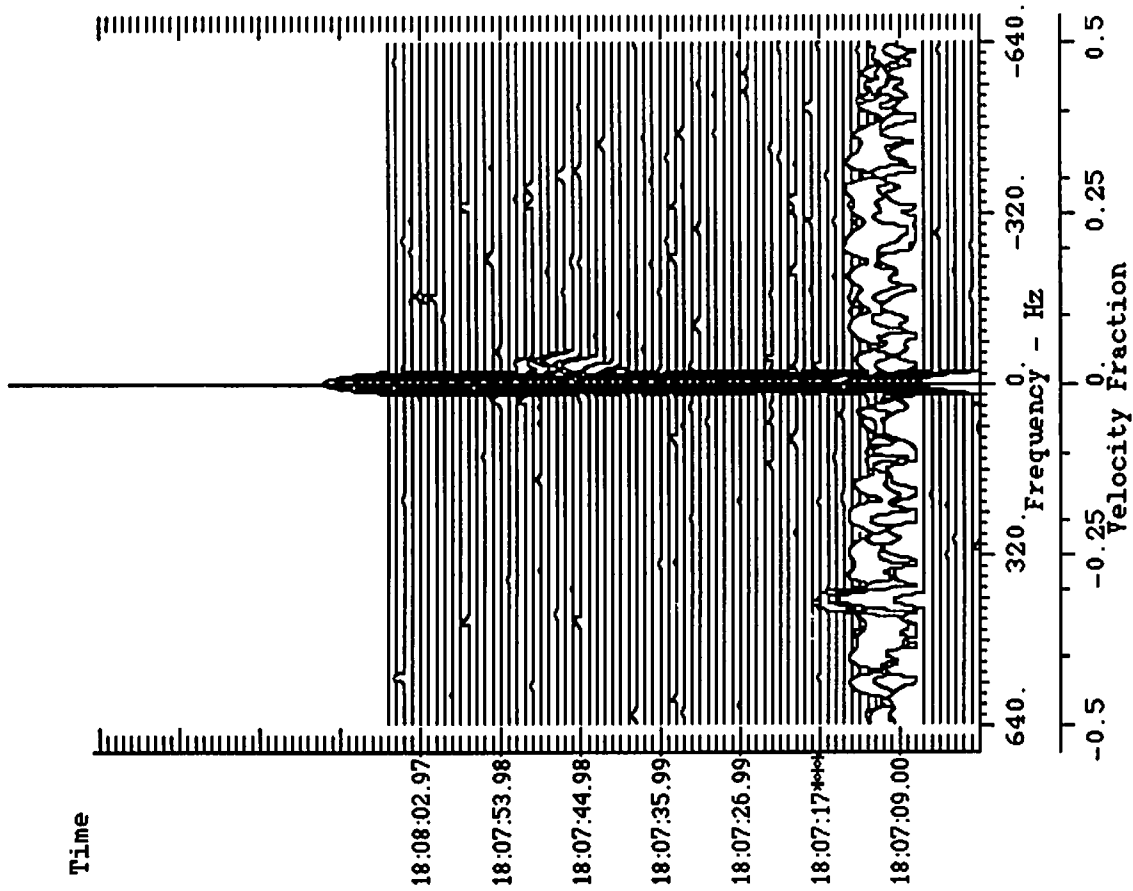
Dynamic Range (dB): 40

Ambiguous Vel. (yd/s) = 36.8968
Spread(Hz)   = 460.25
Peak Spread(Hz)   = ******
P.S. Time: 20:43:45.02

Range Bin = 13
UBeams   = 0
VBeams   = 0

Signal Peak   =-77.33   dBsm/Hz
Display Ceiling =-70.00   dBsm/Hz

PRF   = 1280.6917 Hz
Frequency = 5690.0 MHz
Mission: 5/ 2/91   20:43
Analysis: 10/22/91   10:41

Figure 9(B). Doppler time history plot for a windy day,
middle beam, range gate 13, east look.

Figure 9(C). Doppler time history plot for a windy day, lower beam, range gate 13, east look.

Figure 10(A). Historgram of structure constant for windy day.

40422 samples
Average = -139.609
Std. Dev. = 4.66544

Structure Constant (dB)

Number of occurances

40422 samples
average = -428.04
Std. Dev. = 82.0818

Spectrum First Moment (Hz)

Number of occurrances

Figure 10(B). Historgram of radial velocity for windy day.
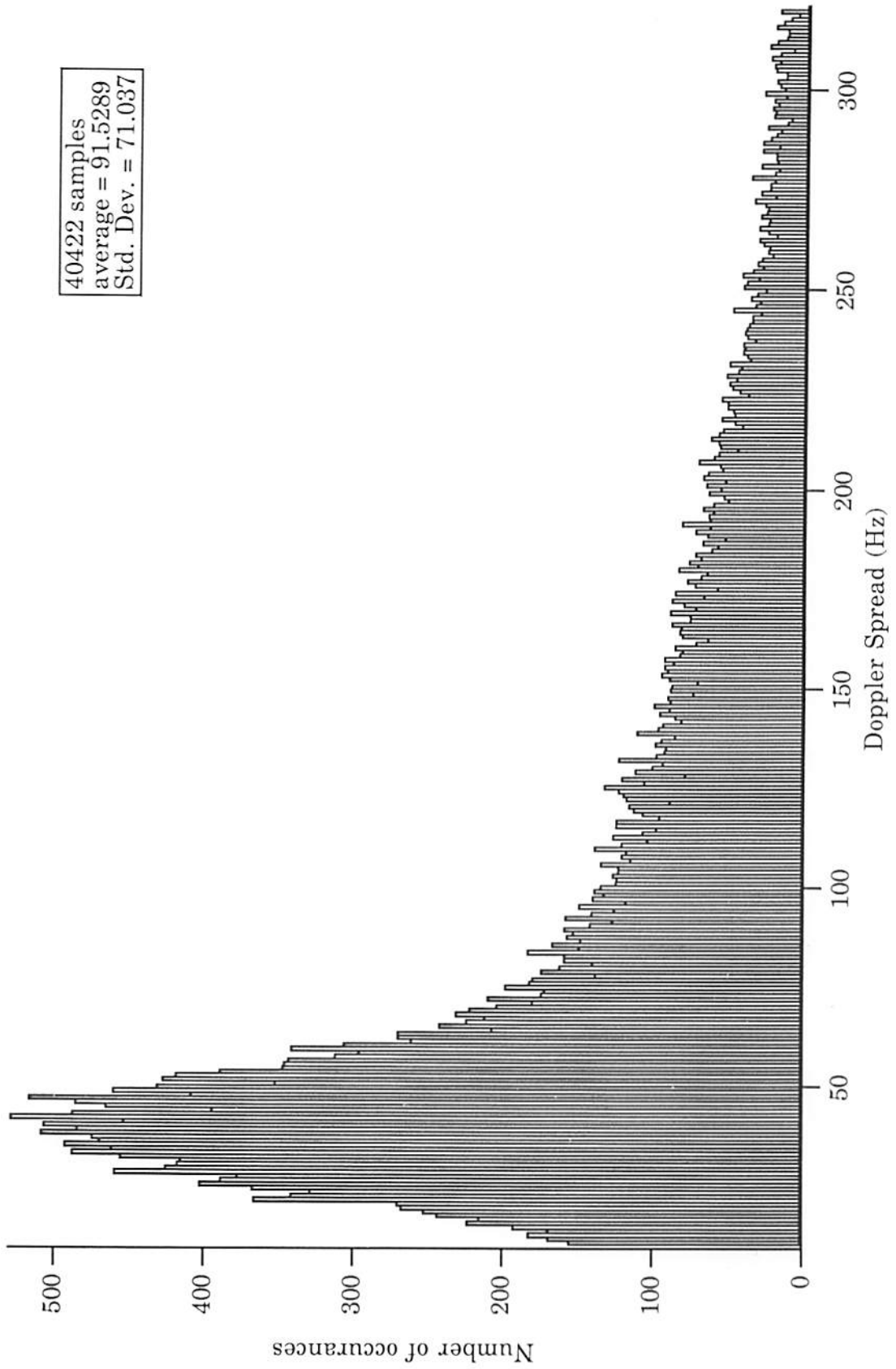
Figure 10(C). Historgram of spectral width for windy day.

40422 samples
average = 91.5289
Std. Dev. = 71.037

Doppler Spread (Hz)

Number of occurances

Figure 11(A). Doppler time history plot for calm day, upper beam, range gate 28, north look.

Figure 11(B). Doppler time history plot for calm day, middle beam, range gate 28, north look

Figure 11(C). Doppler time history plot for calm day, lower beam, range gate 28, north look
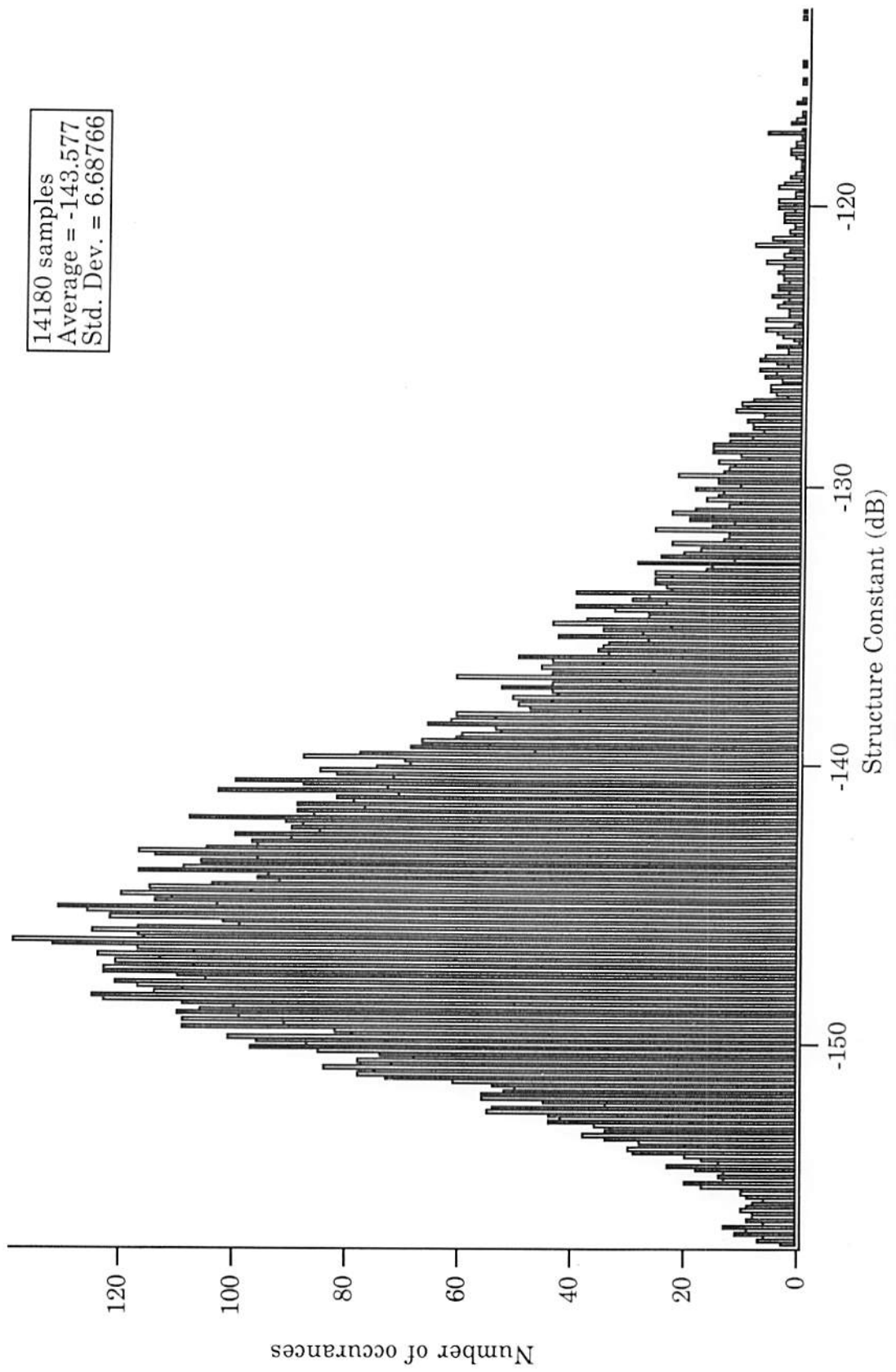
Figure 12(A). Histogram of structure constant for calm day.

14180 samples
Average = -143.577
Std. Dev. = 6.68766

Structure Constant (dB)

Number of occurrances
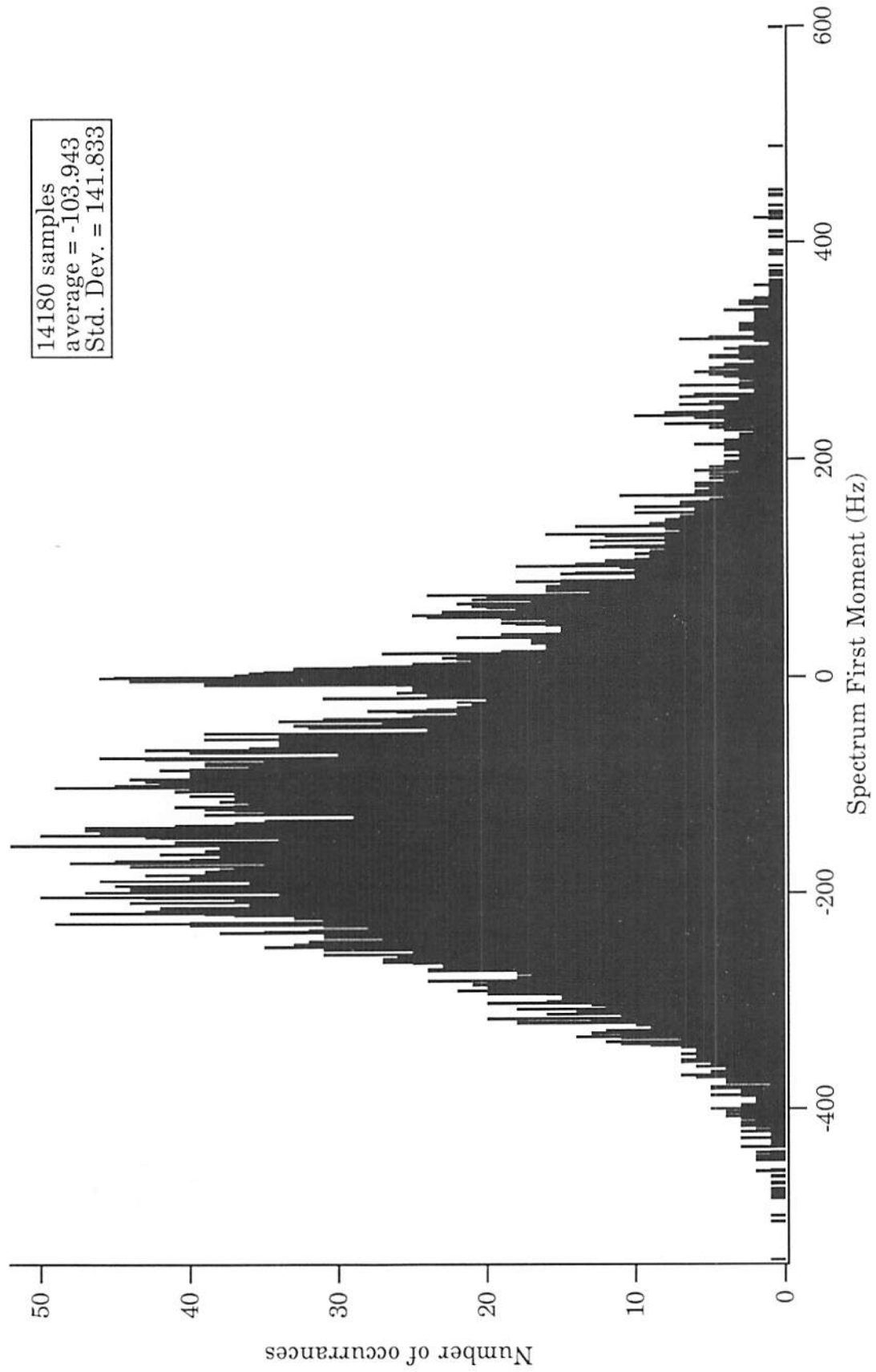
Figure 12(B). Histogram of radial velocity for calm day.

14180 samples
average = -103.943
Std. Dev. = 141.833

Spectrum First Moment (Hz)

Number of occurrances
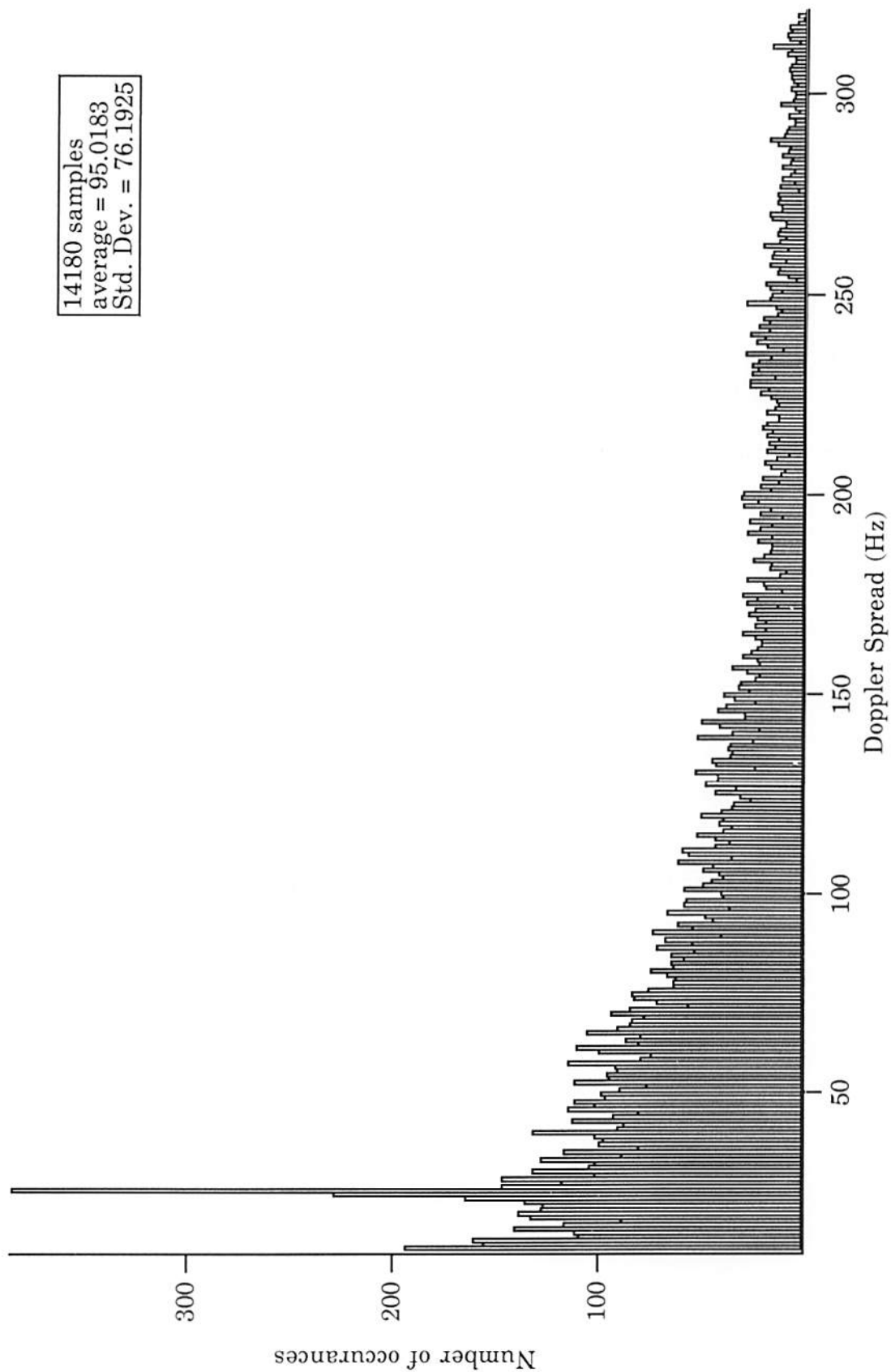
Figure 12(C). Histogram of spectral width for calm day.

14180 samples
average = 95.0183
Std. Dev. = 76.1925

Number of occurances

Doppler Spread (Hz)

Point information

Time:
RangeBin:
Amplitude:
Location in Ambiguity
Interval:

GO

Pause

16:07:34

16:07:25

16:07:16

16:07:07

16:06:58

16:06:49

16:06:40

16:06:31

16:06:31
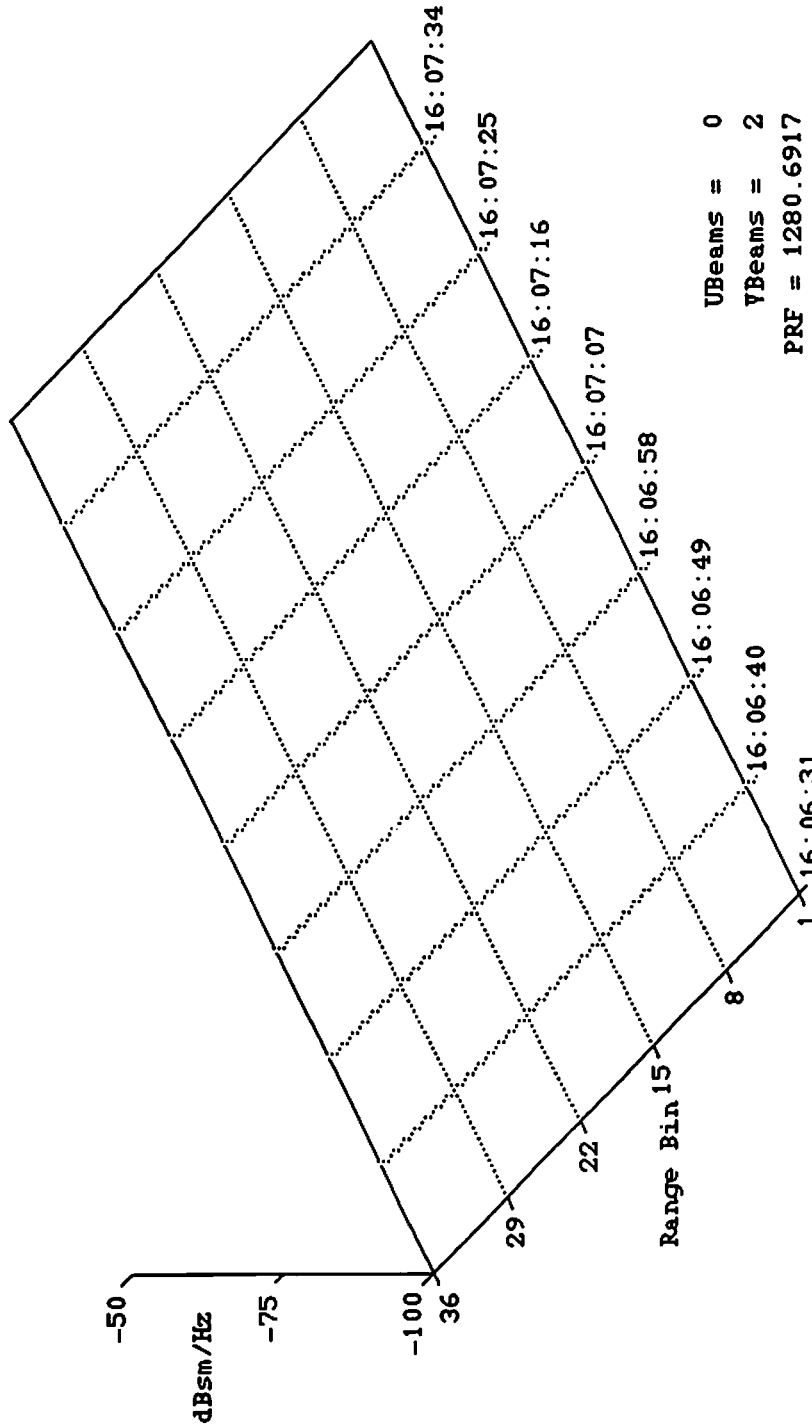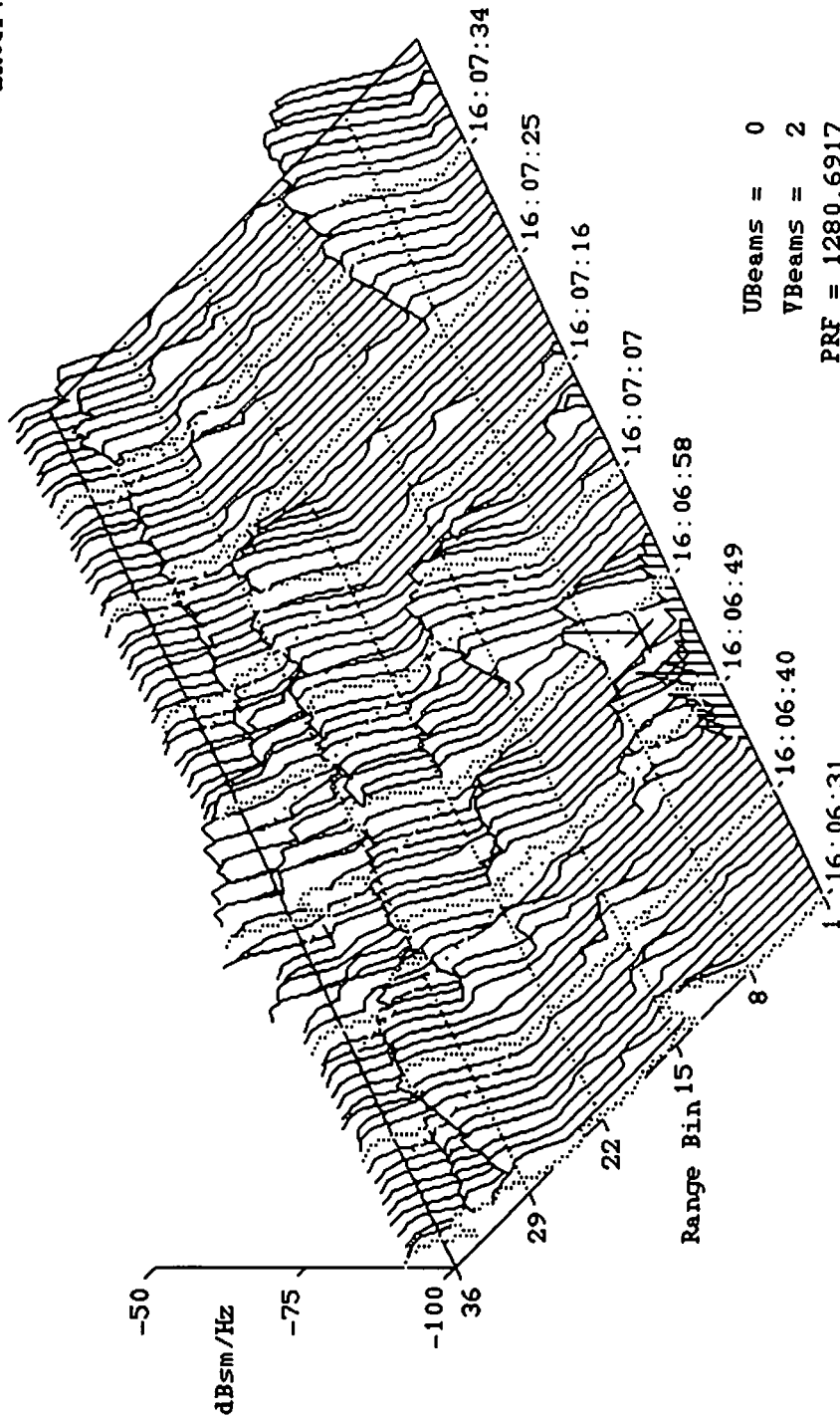
UBeams = 0
VBeams = 2
PRF = 1280.6917
Clutter Suppression:ON
Ambiguous Velocity (yd/s) = 36.896

-50

-75

-100
36

29

22

Range Bin 15

8

1

dBsm/Hz

Mission: 5/ 6/91   16:06
Analysis: 10/18/91   11:57

Figure 13. Doppler amplitude range time (DART) plot.

Figure 14. DART plot for moderately windy day,
6 May 1991 PM scan.

REFERENCES

1. K.R. Hardy, "Studies of the Clear Atmosphere Using High Power Radar," Remote Sensing of the Troposphere Symposium, ed. by V. Derr, University of Colorado, 1972.

2. K.R. Hardy and I. Katz, "Probing the Clear Atmosphere with High Power High Resolution Radars," Proc. IEEE, p. 468, April 1969.

3. V.I. Tatarski, *Wave Propagation in a Turbulent Medium*, McGraw-Hill, Inc., New York, N. Y., 1961.

4. M.I. Skolnik, *Introduction to Radar Systems*, McGraw-Hill, Inc., New York, N. Y., 1980.

5. H. Ottersten, "Atmospheric Structure and Radar Backscattering in Clear Air," Radio Science, Vol. 4, No. 12, Dec. 1969, pp. 1179 -1193.

6. R.B. Chadwick, J. Jordan and T. Detman, "Radar Detection of Wingtip Vortices," 9th Conference of Aerospace and Aeronautical Meteorology, June 1983, pp. 235 - 240.

7. J.D. Friedman, "Airborne Wake Vortex Detection," March 1974, pp. 3-7 through 3-9.

8. R.B. Chadwick and A.J. Bedard, Jr., Private Communications, April 1991.

9. W.H. Gilson, Private Communications, 1991.

THE MEASUREMENT OF WAKE VORTICES WITH A
CLEAR-AIR DOPPLER RADAR

Steven T. Connolly and W.R. Dagle
Applied Technologies, Inc.
Boulder, Colorado

INTRODUCTION

A Doppler radar system is currently under development by Applied Technologies and the U.S. Army to measure wind velocity and turbulence and to detect the atmospheric boundary layer height. For this type of radar high resolution is of prime concern since the top of the atmospheric boundary layer is characterized by small-scale turbulence which can be overlooked by instruments with coarser resolution. Because of the features designed into the radar to accomplish these tasks, a radar of this type may be feasible for operational airport monitoring of aircraft wake vortices to determine if wake vortex separation constraints may be relaxed. The all weather ability of this radar may be used to determine the influence of weather on the persistence and decay of wake turbulence and to assess the hazard presented by weather-reduced strength vortices.

Several different types of radars have been used for wake vortex observation. Easterbrook and Joss (1971) used an X-band pulsed Doppler radar in their study of wake vortices. To enhance the radar return, it was necessary to inject chaff into the wake in order to observe the vortices with the radar. Hydrometeors were also used for reflectivity enhancement in one case. The use of chaff and hydrometeors may be useful in studies of wake vortices, but for operational monitoring of wake vortices the radar must have the sensitivity to detect vortices in clear air.

Frequency Modulated-Continuous Wave (FM-CW) radar technology was successful at obtaining returns off clear air simply by reflecting off irregularities in the refractive index. Other researchers (Campbell et al., 1980, Chadwick et al., 1983) have used FM-CW radars to measure wake vortices from aircraft landing in clear air. This work demonstrated the feasibility of radars for monitoring wake vortices, but the system was never developed into an operational instrument.

Applied Technologies has applied the technologies of pulsed radar wind profiles in order to duplicate the results of the earlier work done with the FM-CW radars. This radar has been designed for continuous, unattended meteorological monitoring by including sophisticated signal processing, built in test equipment, and remote communications. This paper discusses the design features of this radar and how they could be applied to wake vortex detection and monitoring.

THEORY

Clear-air radars depend upon the scattering of electromagnetic radiation off minor irregularities in the index of refraction. A spatial variation in this index encountered by a propagating electromagnetic wave causes a minute amount of the energy to be scattered in all directions. In the atmospheric boundary layer the index of refraction is a function primarily of humidity and temperature fluctuations. Turbulence in the atmosphere creates these fluctuations, or eddies, which occur over a spectrum of sizes ranging from many tens of meters down to centimeters. The maximum radar return from clear-air radars occurs when the Bragg condition is met. This condition requires that the scattering medium must have a length scale of one half of the radar wavelength.

The relationship between radar reflectivity and refractive index fluctuations in the inertial subrange was shown by Ottersten (1969) to be:

$$n = 0.38 \, C_n^2 \lambda^{-1/3} \tag{1}$$

where n is the radar reflectivity, λ is the wavelength and C_n^2 is the radar refractive index structure parameter. The inertial subrange lies between the inner and outer scale of turbulence, in the boundary layer the inner scale is on the order of several millimeters. The outer scale ranges from 5 m up to 2 km. As long as the radar wavelength is twice that of an eddy wavelength in the inertial subrange, the dependence of the radar return on radar wavelength is very weak.

Equation (1) can be used to predict the minimum value of C_n^2 that a radar can observe, provided the system is operating at a wavelength in the inertial subrange. Chadwick et al. (1976) estimated the performance of their FM-CW radar using an equation developed by Strauch (1976):

$$n_{min} = \frac{256 R^2 k \, T_{op} \sigma_v}{\pi^{1/2} P_t A_e \Delta R \, (\lambda \, \Delta v \, T_0)^{1/2}} \tag{2}$$

where:

R   is the range in meters
k   is Boltzmann's constant
T_{op} is the system noise temperature
σ_v is the standard deviation of the Doppler velocity distribution
P_t is the average transmitter power
A_e is the effective aperture of the antenna
ΔR is the range resolution
Δv is the velocity resolution
T_0 is the observation or integration time

Equation (2) was substituted into (1) and solved for C_n^2 to find the minimum C_n^2 needed for detection using the following parameters:

T_{op} = 600° K which is the operating temperature of a system whose noise figure is approximately 5 dB

σ_v = 0.5 m s^{-1}

λ = 0.23 m (1280 MHz)

A_e = 7.9 m^2

ΔR = 10% of the range

Δv = 1 m s^{-1}

T_0 = 120 s

The results of this analysis are shown in Figure 1. In this figure, the average transmitter power is plotted as a function of the refractive index structure parameter, C_n^2, with range and range resolution as independent variables. C_n^2 was allowed to take on values from 10^{-17} to 10^{-13} m$^{-2/3}$ in the program. These values are consistent with the range of C_n^2 values observed in the boundary layer.

The analysis shows that a transmitter with an average power of 2.4 W will be needed to observe the smallest expected values of C_n^2 at 500 m. If a range resolution of 7.5 m is to be obtained then the transmitter must have a pulse width of no greater than 50 nsec. When the range is 500 m, and the pulse repetition frequency is 10 kHz, the resulting peak power must be 32.8 kW. This level of peak power is unacceptably large for a portable system even though it seems to be the best that a simple pulsed radar can do. To reduce the peak power requirement to a more desirable level while maintaining a high range resolution, it is necessary to employ some form of pulse compression in the radar transmitter.

The vortex created by an aircraft wake is on the order of 5-10 m in diameter and therefore in the inertial subrange in most cases. As the vortex decays, the turbulent eddies dissipate down the spectrum toward smaller eddies thus creating a scattering volume for clear-air radars. The reflectivity of this target is further enhanced by the entrainment of heat and moisture produced by the aircraft engines.

Although the ability to detect a wake vortex in clear air with a radar is of primary importance, equally important is the ability of the radar system to resolve a vortex embedded in ground clutter and atmospheric turbulence. The system must have the dynamic range capable of detecting the vortex turbulence above the background turbulence. Chadwick et al. (1983) found that the vortices they observed had an average structure parameter 10-12 dB greater than background.

SYSTEM DESCRIPTION

The Boundary Layer Radar (BLR) is designed as an L-band, 1280 MHz pulsed Doppler radar. This frequency was chosen due to the available band width and the wavelength, 23 cm. Some specifications of the system are given in Table 1.

The following criteria were used as the primary considerations for the boundary layer radar design:

- maximum range resolution
- high level noise rejection
- ability to detect small-scale atmospheric features
- portability
- unattended operation
- economy

The type of radar technology to use, whether FM-CW or pulsed, was analyzed first. FM-CW radars have obtained range resolutions as high as 1.5 m (Gossard et al., 1970) which has been shown to be feasible for wake vortex observation. In an FM-CW radar the timing mark is defined by the existence of a particular frequency, that is, one knows when a particular frequency was transmitted and simply measures the elapsed time to that same frequency in the echo. Of course, if the target has moved, this measurement produces information relative to target velocity as well. The range resolution obtainable depends on the resolution or accuracy of the measurement of the difference frequency between the transmitted and received waveforms. The accuracy, in turn, depends on the bandwidth of the transmitted waveform as given by:

$$\Delta R = \frac{c}{2B}$$

(3)

where ΔR is the range resolution, c is the speed of light, and B is the bandwidth of the transmitted waveform.

From this equation it can be seen that to achieve a ΔR of 10 m, a bandwidth of 15 MHz must be swept by the radar transmitter. FM-CW radars are usually duplex systems, meaning that they transmit and receive simultaneously. In order to reduce crosstalk between the two antennas they must be isolated by 100 dB or more. This level can be obtained only with careful attention to site preparation, shielding between antennas and associated circuits and good design with respect to sidelobe reduction. As the radar power is increased this becomes an increasingly important consideration, one which does not offer a simple solution.

For a low maintenance, operational system, with a range of at least 5 km, a pulsed radar was chosen. Pulsed radars have become increasingly common in clear-air radar studies, and it was decided that the technology had matured to the point where the cost/performance factor exceeded that of the FM-CW radar for boundary layer observation. A method for increasing the range resolution was needed, however, if the pulsed radar was to be used for small-scale feature observation.

Range Resolution

Pulse compression techniques have been used frequently in scanning radars to maintain high resolution despite their relatively long pulse widths. This technique has yet to be used in

boundary layer wind profilers because their normal operation doesn't require resolutions greater than 50 m. In designing a high resolution boundary layer radar, Applied Technology has included a digital pulse compression technique which allows for the phase coding of transmitted pulses. By transmitting two complementing pulses sequentially, the time sidelobes of their autocorrelation functions interfere destructively and the result is a return signal with all the power of the full pulse but with a much higher resolution. In this manner the boundary layer radar can obtain resolutions of up to 7.5 m.

The transmitter is capable of sending out pulses of lengths varying between 50 nsec and 4000 nsec. This allows for versatility in range and resolution selection. In the short pulse mode ranges as low as 100 m can be obtained, while in the long pulse mode, more power will be transmitted yielding a higher range but lower resolution.

Noise Reduction

To effectively measure a return signal in the atmospheric boundary layer, considerable care must be taken to reduce both the ambient and system noise. Significant noise sources are ground clutter, flying aircraft, and background turbulence.

Radar returns from fixed objects, such as the terrain surrounding the radar, are a significant problem when the radar is operated at low elevation angles. Several features have been designed into the radar system to account for and reduce returns from fixed objects. By reducing the main beam angle and attenuating the sidelobes, the signal returned from the target will be enhanced while diminishing the signal returned from fixed objects. The antenna designed for the boundary layer radar is a 256 element, phased array antenna. The antenna pattern is shown in Figure 2. This antenna has a 3 dB beam width of 4.2° and the first sidelobe is attenuated by 18 dB. The perimeter elements are all passive and a clutter fence has been designed to surround the antenna in order to reduce the sidelobes.

A notch filter at zero Doppler shift will eliminate most reflections from stationary objects. Since the atmosphere is always in motion, to some degree, the notch filter shouldn't affect the measurement of the wind, or moving atmospheric features. A clutter map will also be used to characterize the particular ground clutter around the site. The transmitter will be turned off periodically in order that the receiver can take a background measurement of ambient noise at the site.

A type of automatic gain control has been included in the system. A six step attenuator is connected to the receiver and the average transmitted power can be controlled by varying the transmitted pulse width. By adjusting both the average power and the receiver attenuation automatically, the returned signal can be positioned for the largest dynamic range.

Small-Scale Feature Detection

The boundary layer radar obtains three independent parameters from the returned radar signal. These are the three moments of the Doppler spectrum; the zeroth is proportional to the returned

power, the first is the radial wind component, and the second the spectral width. All three parameters can be used to detect features in the atmosphere.

As stated above, the turbulence of wake vortices combined with heat and moisture entrained from the engine exhaust give an enhanced reflectivity. This reflectivity has been seen to be 10-12 dB greater than the reflectivity from the background as observed by Chadwick et al. (1983).

Chadwick et al. found that the second moment of the Doppler spectrum, spectral width, also aided in the detection of wake vortices. Spectral broadening is caused by atmospheric turbulence within the scattering volume. This term is related to the turbulence dissipation rate by:

$$\sigma^2_v = K\epsilon^{\frac{2}{3}}$$

(4)

where K is a function whose form depends on the geometry of the resolution cell. Spectral width is a preferred parameter for measuring wake vortices since the vortices create substantial small-scale turbulence in a volume on the scale of a radar resolution cell. Spectral width is generally calculated with a spectrum normalized to unit area so that radar received power calibration is not important. Chadwick et al. used the non-normalized spectrum so that the parameter is a function of both spectral width and received power. This term is called the weighted spectral width and is given by:

$$wsw = \int^{\infty}_{\infty} v^2 S(v) \, dv$$

(5)

where v is velocity, and S(v) is the spectrum of velocities.

The ability to detect small-scale features in the atmosphere requires more than increasing the simply detecting a signal at a given time. Certain features, such as the top of the atmospheric boundary layer, provide repeatable patterns which can be recognized by the radar system to aid in detection. After a profile of the boundary layer has been completed a number of profiles are made over a meteorological significant amount of time. These profiles are combined to form a pattern which is then matched to a set of standard profile patterns stored in memory. The closest fit to the standard pattern then reveals the location of the boundary layer height.

In a similar manner, the radar return patterns could be matched to a set of standard wake vortex returns. This would then give an indication of the type of vortex that was observed and the behavior that it would most likely exhibit.

CONCLUSIONS

The development of the boundary layer radar has addressed many of the technical shortcomings of earlier clear-air radars in detecting small-scale turbulence. Based on the feasibility of this system, the boundary layer radar may be suited for continuous monitoring of airports for wake vortices.

Figure 3 shows one possible configuration for the operation of a wake vortex detection radar. Because the boundary layer radar has a steerable phased array antenna, the beam can be steered

in five different directions electronically. Two antennas are used in this configuration, one in the wind profiling mode and one is directed approximately 17° above the horizon. This allows one off axis beam to point directly down the glide path at an elevation angle of 2°. Because this is an off-axis beam the sidelobes nearest the ground will be attenuated by more than the 18 dB of the vertical beam sidelobes.

A number of features have been included in the radar system to facilitate operation. The radar has been designed to operate continuously in order to be of use in long term ambient monitoring programs. Signal processing routines are run in real time so that processed data are available on a continuous basis. A minimum of operator attention will be required so as to reduce the costs of operation and communication protocol exists to interface with airport computer systems and control tower personnel.

Table 1. System Specifications

Operating frequency	1280 MHz
Pulse width (compressed)	(50 nsec) 0.5-2.0 μsec
Peak power	2.0 kW
Pulse repetition frequency	10 kHz
Antenna type	phased array
Effective aperture	5.75 m^2
Beamwidth (3 dB)	4.2°
Gain	31.2 dBi
Minimum height	100 m
Resolution	7.5 m
Maximum range	5000 m
Velocity resolution	±0.5 ms^{-1}
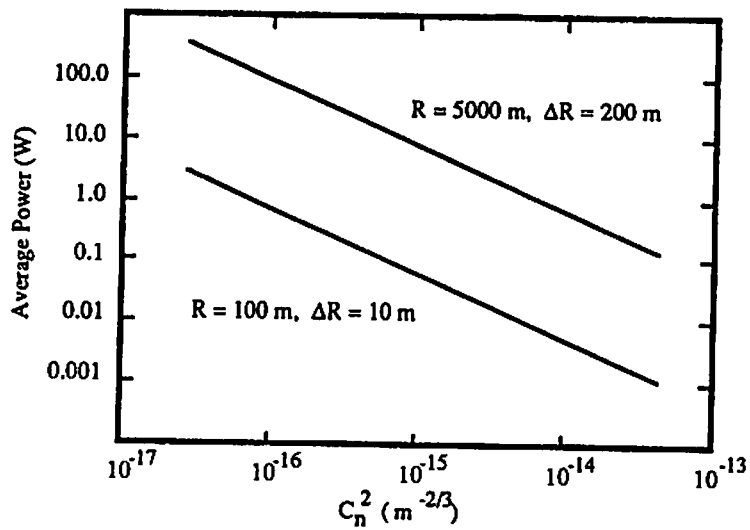
Figure 1. Average transmitter power needed to observe C_n^2 for a given range.

CENTER BEAM
16 Element

-10 Db i

-18 Db i

-20 Db i
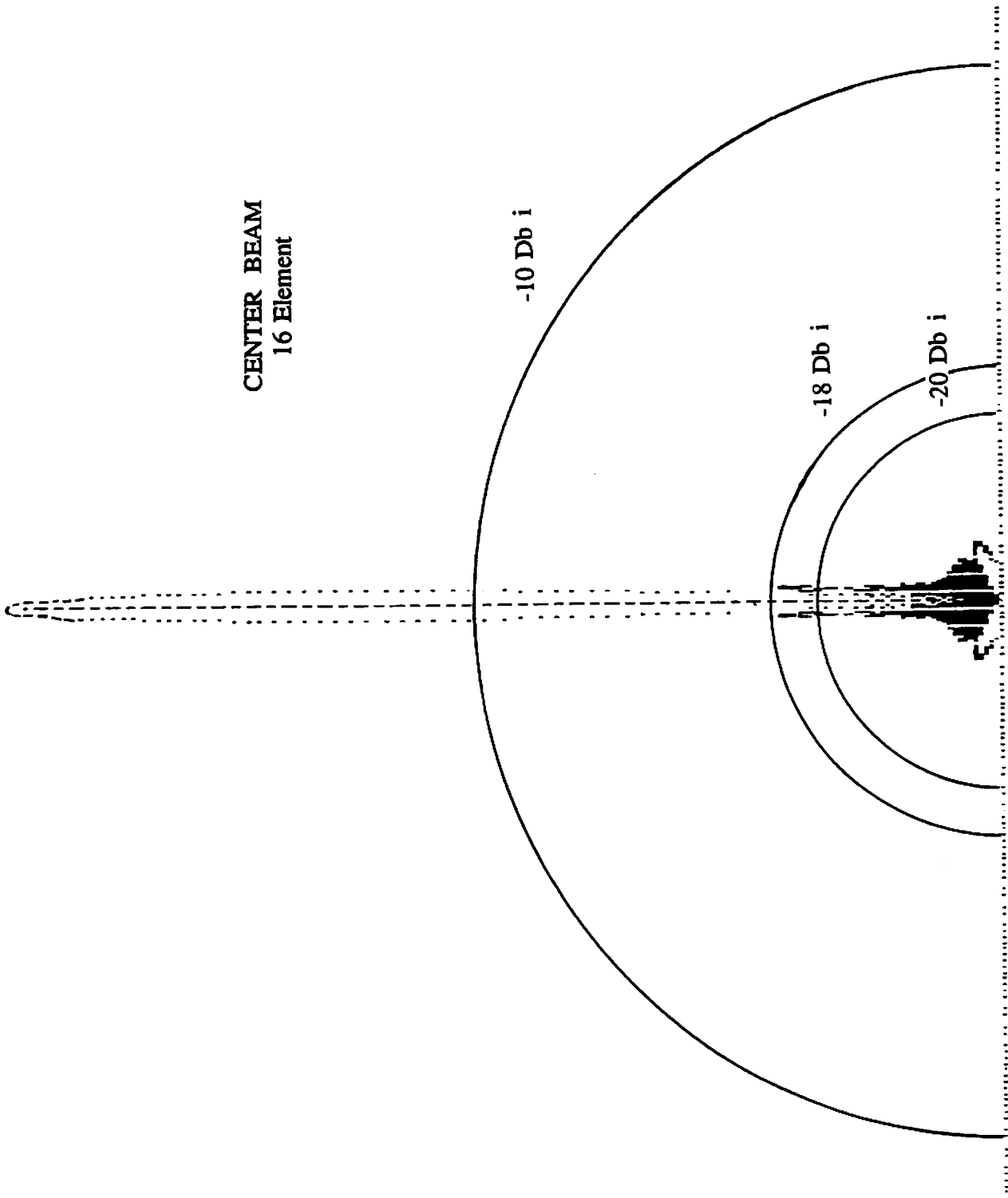
Figure 2. Antenna pattern.
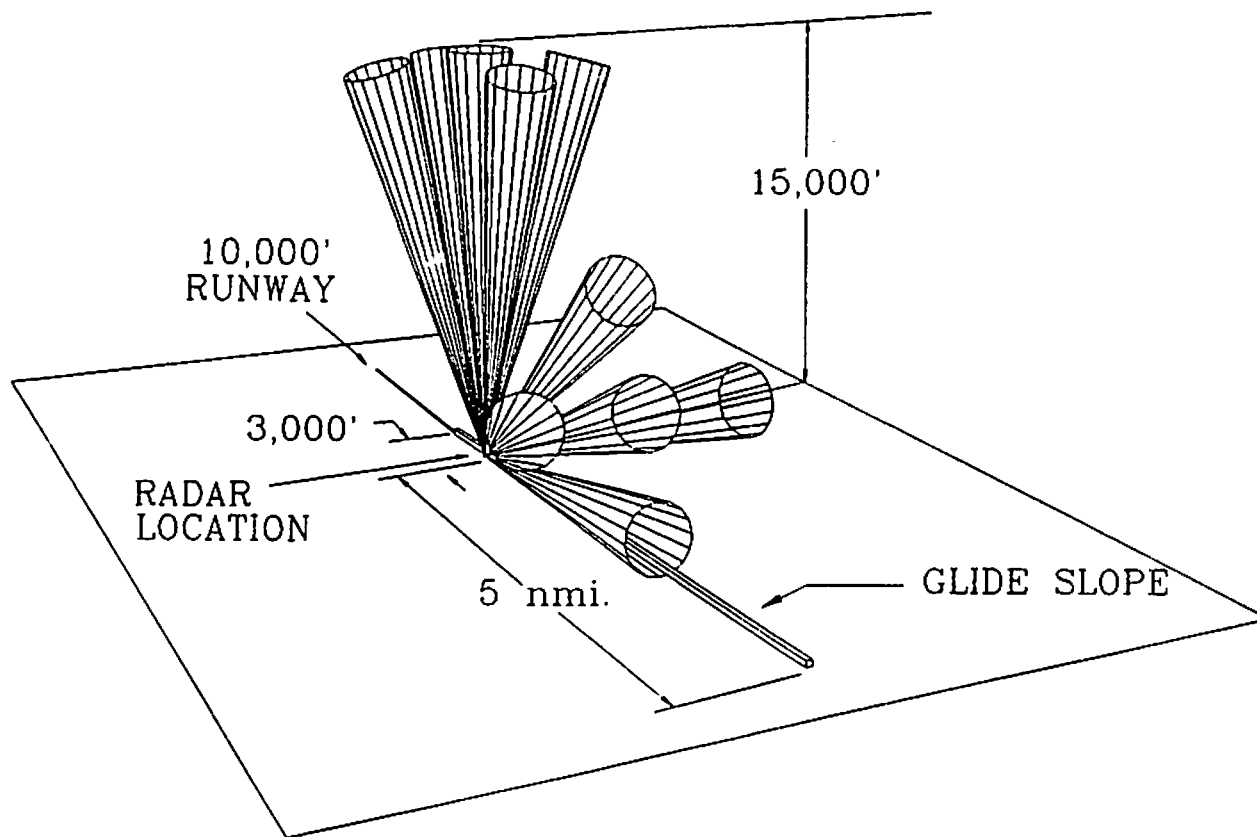
Figure 3. Possible configuration of boundary layer radar at airport.

REFERENCES

Campbell, W.C., R.B. Chadwick, K.B. Earnshaw, and K. P. Moran, 1980: Low elevation angle wind measurements by FM-CW radar. In Preprint Vol., Nineteenth Conf. on Radar Meteor., Miami, Fla., April 1980. AMS, Boston, Mass., 722-726.

Chadwick, R.B., W.C. Campbell, K.P. Moran, and R.G. Strauch, 1976: Boundary layer wind measurements with an FM-CW radar. In Preprint Vol., 17th Conference on Radar Meteorology, Seattle, WA, 26-29 Oct. 1976. AMS, Boston, MA, 326-329.

Chadwick, R.B., J. Jordan, and T. Detman, 1983: Radar detection of wingtip vortices. In Preprint Vol., Ninth Conf on Aerosp. and Aeronaut. Meteor., Omaha, Neb., June 1983. AMS, Boston, Mass., 235-240.

Easterbrook, C.C. and W.W. Joss, 1971: The utility of Doppler radar in the study of aircraft wing-tip vortices. In Proc. of a Symp. on Aircraft Wake Turbulence, eds. J.H. Olsen, A. Goldburg, and M. Rogers, Seattle, Wash., Sept. 1970, Plenum, New York, 97-112.

Gossard, E.E., J.H. Richter, and D. Atlas, 1970: Internal waves in the atmosphere from high-resolution radar measurements. *J. Geophys. Res. 75*, 3523-3536.

Ottersten, H., 1969: Radar backscatter form the turbulent clear atmosphere. *Radio Sci. 4*, 1251-1256.

Strauch, R.G., 1976: Theory and application of the FM-CW Doppler radar. Ph.D. Thesis.

WAKE VORTEX DETECTION USING A PHASED ARRAY SODAR

Alain Donzier
REMTECH
2 et 4, avenue de l'Europe, BP 159
78143 Velizy Cedex, France

PRELIMINARY REPORT

Following the study of windshear at Roissy International Airport, using a REMTECH PA3 phased array system tilted at low elevation angles, the S.T.N.A. decided to grant a study to investigate wake vortex intensity using acoustic techniques.

This contract, 90/1873, covers the following parts that were described in our technical description in OTF 90/066:

- installation and operation of a standard PA3 system at low elevation angles,

- software modifications to allow:

    • emission of more frequencies,

    • storage of instantaneous measurements for further processing.

- data analysis with special attention to echo intensity.

The PA3 system was installed at Roissy/Charles de Gaulle Airport on April 22, 1991 with a revised software version allowing the emission of 5 frequencies in a single acoustic pulse. The sounding range was set from 50 m to 1 km. The averaging time was set to 5 minutes. The system is operating continuously and data are stored on the hard disk. A few other data sets have been collected using different operating modes :

- storage of the instantaneous data,

- modification of the sounding range. A sounding range of 500 m to 1.5 km has been tried successfully as shown in Figure 1 (presently a maximum measurement window cannot exceed 1000 m due to software memory limitations).

Software modifications description

Wake vortex detection makes it necessary to reduce the averaging time as much as possible. To increase the number of measurements during an emission/reception cycle, the number of emitted frequencies is increased. Each emitted frequency can give one measurement (depending on its validation). The previous software version that was used in the summer '90 was using 3 different frequencies and the averaging time had to be set to 10 minutes. In the current version, the number of frequencies is 5, therefore allowing a reduction of the averaging time down to 5 minutes. Further improvements (not part of this contract) can be:

- replacing the DEC computer by a more powerful DELL 386/387 PC compatible computer (thereby reducing the averaging time by at least a factor of 2),

- modifying the transceiver to allow simultaneous measurement on the different antenna beams,

- adding more frequencies to the pulse. However, this has some technical limitations as described in appendix A.

Data analysis

Figure 2 shows the site installation. Data have been gathered and their analysis has begun.

First results can be summarized as follows:

- System range has been improved from what was observed last summer (Figures 3 and 4). Operation up to 1.5 km has shown that higher ranges are possible (Figure 1). Operation from 50 m to 1.5 km has not been selected due to memory limitations on the DEC computer.

- Strong echo regions are observed. These high echo values disappear during night when air traffic is reduced (Figures 3 and 4).

- However, these high echos are observed for landing as well as for take-off (Figure 3 compared to Figure 4), which makes it necessary to try to determine the actual reasons of the increase in backscattered signal. This will be done in:

  ● processing the instantaneous measurements as the ones shown in Figure 5

  ● analyzing the knowledge of wake vortex generation and spatial evolution using the results of the bibliographical study initiated by the S.T.N.A.

Other ideas beyond the scope of this study are:

-   making lateral measurements intersecting the glide path to estimate the lateral width of these high echo regions,

-   flying planes across the antenna beam using different flight configurations (reduced engines, etc.).

APPENDIX A - SIGNAL PROCESSING METHOD

Once the acoustic pulse (composed of several frequencies) has been emitted the Sodar transceiver is switched to the receiving mode. The received signal is sampled and time gated. On each gate an FFT is computed. Each FFT is split into several frequency zones (as many as emitted frequencies) where potential signal peaks are detected and stored in a file that we will call the "beep" file. Before detecting the peaks the spectrum goes through the following processing:

- noise whitening,

- cancellation of 50/60 Hz spurious harmonics,

- cancellation of other steady spurious peaks.

At the end of the averaging period the beep file is read, and detected peaks are screened using a consensus technique. A time series of measured dopplers is then constructed and screened. The cross correlations between the time series for the three beams is computed allowing O~ computation and fluxes estimation. The results are then translated to an orthogonal frame and output to the disk and screen.

Additional information about the December 1990 Sodar software release:

Generally speaking, multiple frequency coding of the emitted pulse may lead to a Doppler determination ambiguity problem when considering the different signals corresponding to the different backscattered frequencies. This comes from the fact that, having a limited antenna frequency bandwidth (of the order of 500 Hz), the distance between the emitted frequencies and therefore the received frequencies may be less than the Doppler shift which corresponds to the considered wind speed component. This cannot happen with the vertical component, but may be the case for the tilted components when wind speed is high.

This problem is solved by using a "learning" process. After the Sodar is started, the two tilted components emit only one frequency at a time, which is alternatively low then high. This allows the Sodar to determine the average Doppler shift without any ambiguity, for each tilted component at the end of the first averaging period. During the learning process the Sodar is a typical mono-frequency system, similar to competitors' systems under normal operation. It therefore shows a much lower range than after the learning process when it uses the multiple frequency technique.

Another problem might occur after the learning process is completed in the case where there is a rapid change on a wind speed component during one averaging period. Therefore, the current average wind speed is monitored for each tilted beam by sending, one by one, the different frequencies of the coded pulse after each multiple frequency pulse, for example: a multiple pulse, first frequency of the pulse, multiple pulse, second frequency of the pulse, etc...

Only the lower layers are sampled in order to save time when operating in this special monofrequency mode. The corresponding data are processed independently of the data gathered from the complete multiple frequency pulses. At the end of the averaging period, both types

of data are compared and, if they do not agree, the Sodar goes through a learning process for whichever tilted component has need of it. Everytime the Sodar is learning, it is recorded at the end of the averaging period on the table output for which DOPP1 (for beam 1) and (or) DOPP2 (for beam 2) are set to -9999 while in normal operation they show the average Doppler shifts in Hz.

```
c:\roissy\files>TYPE ASCII.FI2

 BL#  MONTH   DAY   YEAR   HOUR    MIN    SEC  VAL.1  VAL.2 VAL.3
 845      4    24     91     18     20      6      0      0   173


FREQ1  FREQ2 FRASS  DOPP1  DOPP2  VAL.4  NOIS1  NOIS2 NOIS3
 2045   2045  2143  -9999  -9999    -19    619    210   192


  ALT  CT**2 SPEED    DIR      W

 1450  20000 -9999  -9999    141
 1400  20000 -9999  -9999    184
 1350   1882 -9999  -9999    216
 1300  16077 -9999  -9999    209
 1250  20000 -9999  -9999    192
 1200  20000 -9999  -9999    201
 1150  14669 -9999  -9999    221
 1100   2184 -9999  -9999    227
 1050   3387 -9999  -9999    225
 1000   9346 -9999  -9999    215
  950  12225 -9999  -9999    218
  900  20000 -9999  -9999    217
  850  11700 -9999  -9999    202
  800  12478 -9999  -9999    174
  750   2340 -9999  -9999    153
  700   4440 -9999  -9999    147
  650   1626 -9999  -9999    170
  600    971 -9999  -9999    192
  550   2739 -9999  -9999    200
  500  -9999 -9999  -9999  -9999
 $
```

Figure 1. Sodar data output (5 minute average) showing measurements up to 1450 m.

Figure 2a. Preliminary test of a phased array sodar for wind shear measurement and wake vortex detection at Charles de Gaulle/Roissy International Airport.
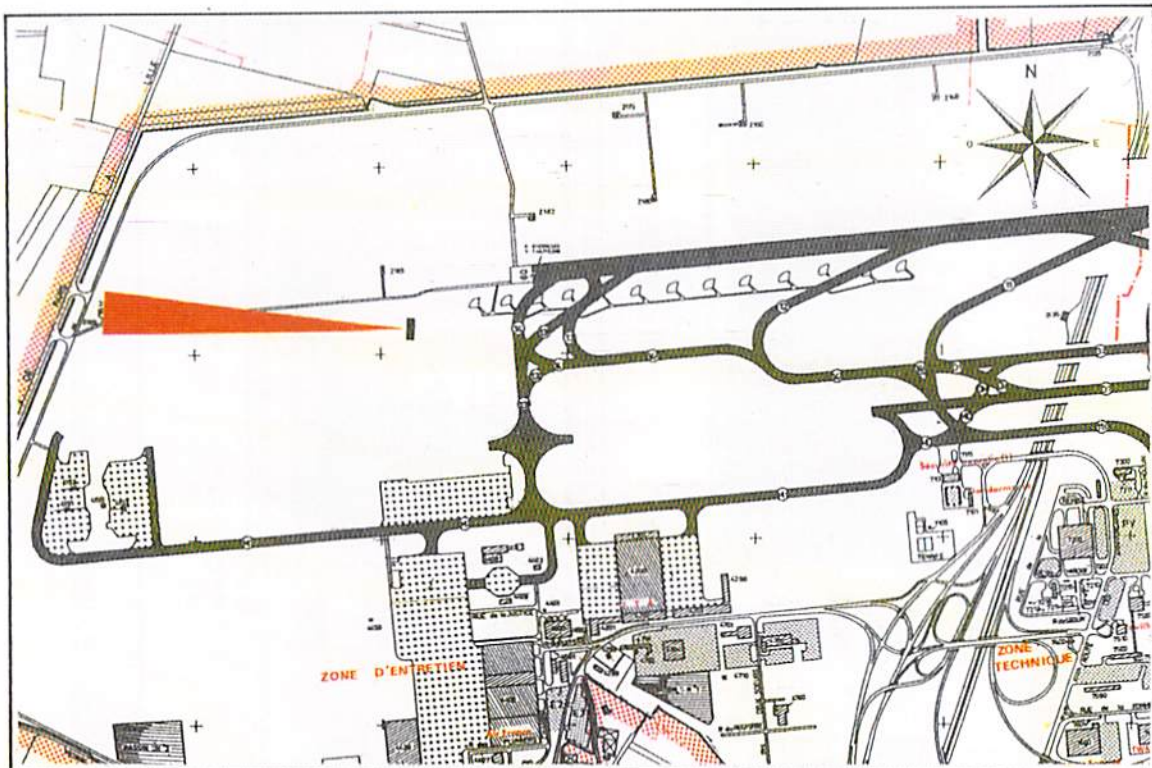
Figure 2b. The phased array antenna location. The antenna beam and range are shown in red.
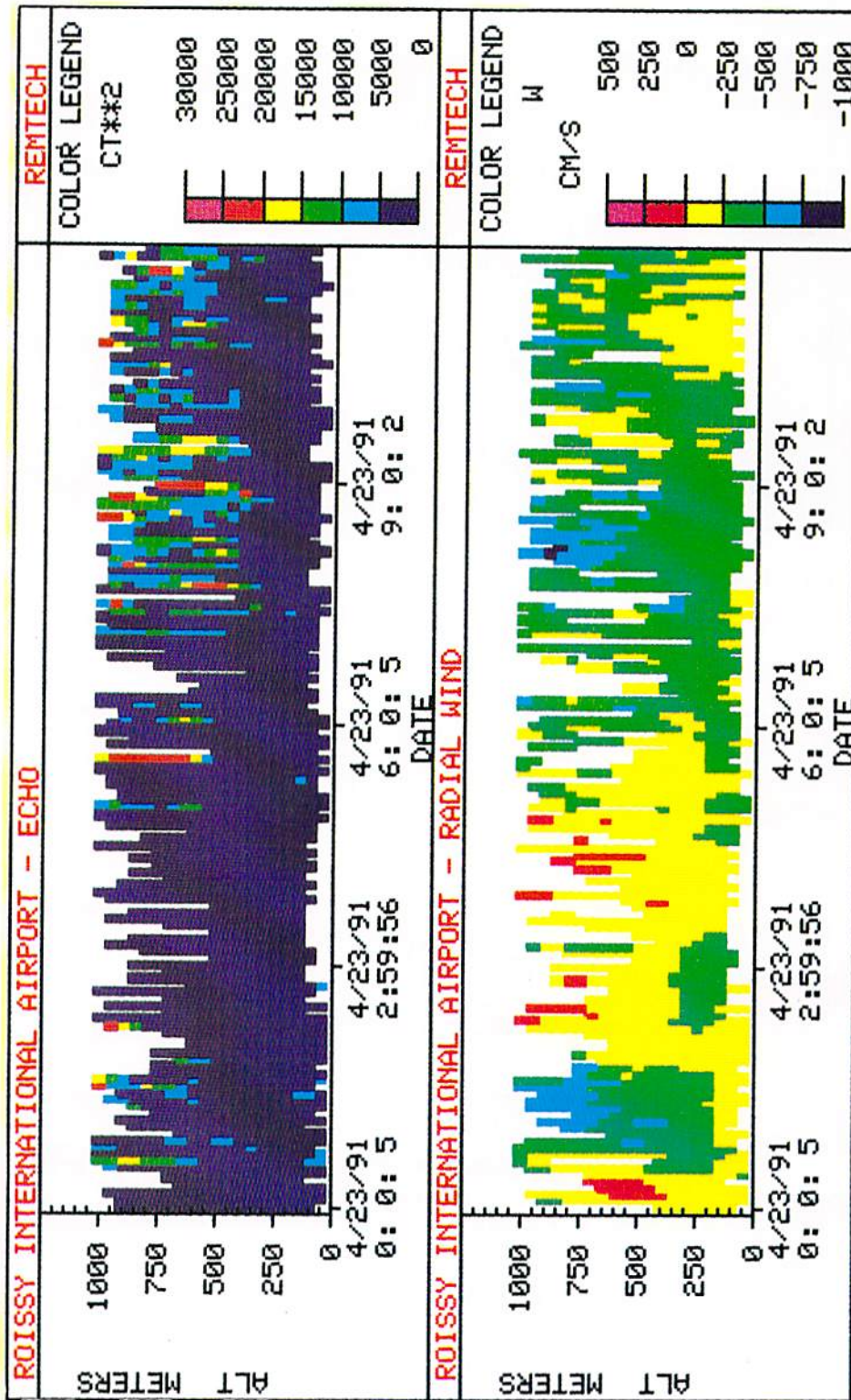
Figure 3. Echo and wind speed facsimile (5 minute averaging periods). Planes at take-off (negative radial wind). Note echo difference between night and day.
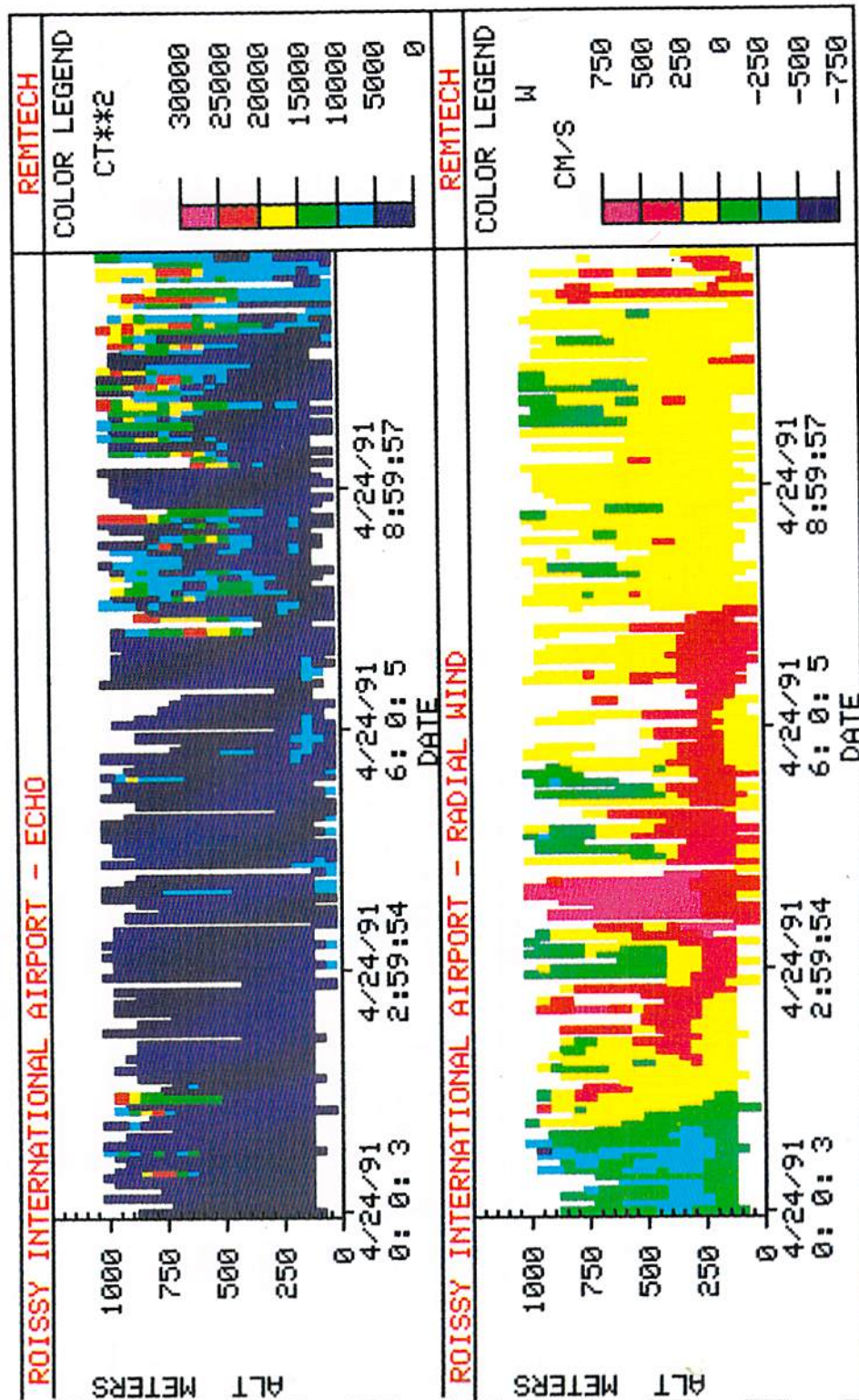
Figure 4. Echo and wind speed facsimile (5 minute averaging periods). Planes on approach (positive radial wind). Note echo difference between night and day.
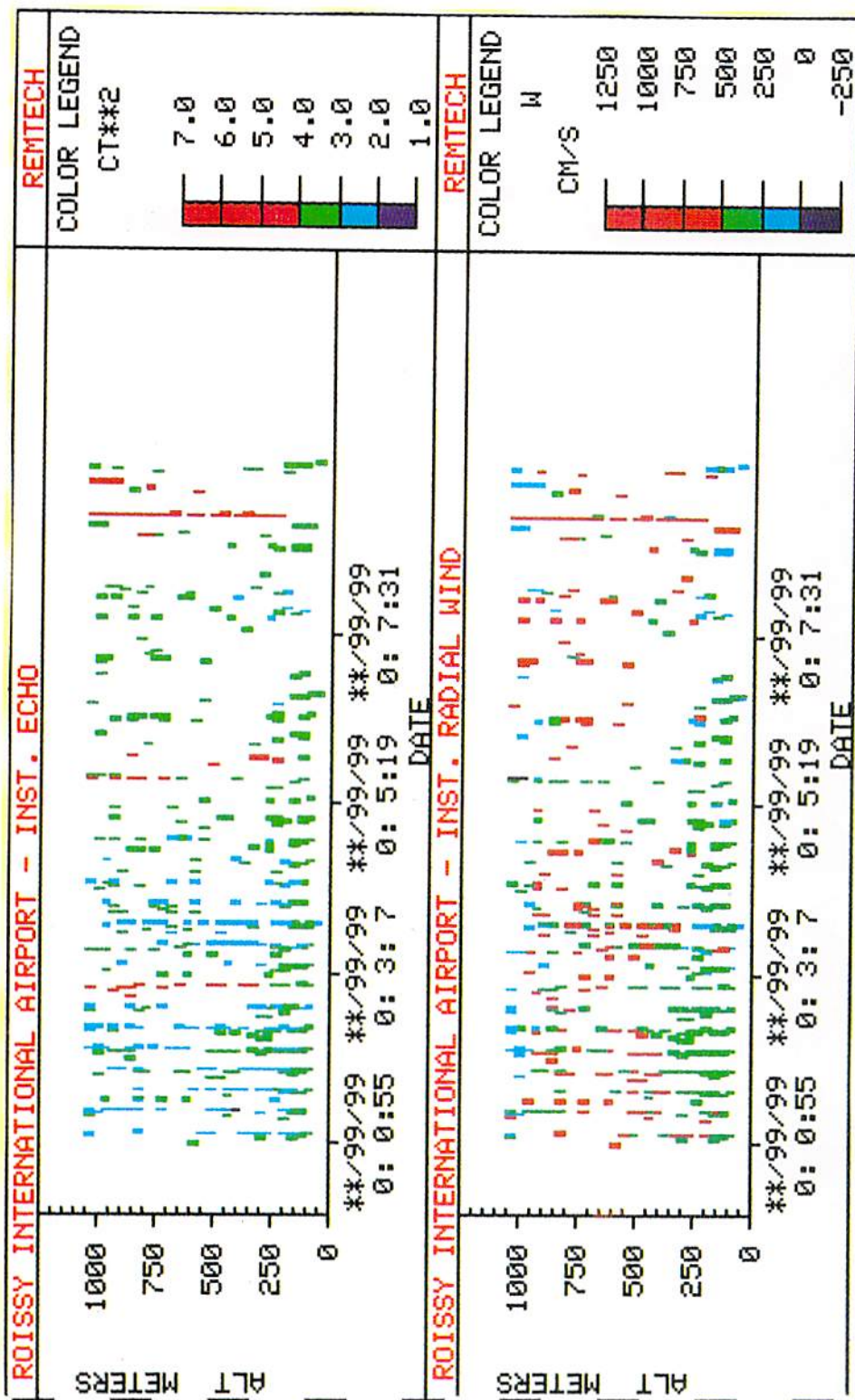
Figure 5. Sodar instantaneous measurements (echo and radial wind). Echo is displayed using a Log scale. Note the 3 distinct red patterns on the echo chart. Measurement date: April 24, 1991 around 5 p.m. The time origin on the graph corresponds to the start of the instantaneous data storage.

LASER SYSTEMS FOR CHARACTERIZATION AND MONITORING OF WAKE VORTICES[1]

Richard M. Heinrichs
James E. Evans
Charles A. Primmerman
M.I.T. Lincoln Laboratory
P.O. Box 73
Lexington, MA 02173

ABSTRACT

Adequate characterization of wake vortices by high-resolution (e.g., 30 cm downrange resolution), noninvasive, measurements in conjunction with measurements of local atmospheric conditions has been a long-standing requirement for operationally oriented studies. We describe a system to provide these high resolution measurements based on a mode-locked, cavity-dumped, CO_2 laser. This system offers the capability of 1' x 1' spatial resolution along with 0.5 m/sec velocity resolution of a vortex. Such a system would also be able to extend the coherent integration time to measure velocities down to 5 -10 cm/sec, thus enabling a measurement of the velocity turbulence in the ambient air towards which a vortex is heading. This measurement capability would provide input regarding the vortex structure and surrounding velocity turbulence for detailed modelling of vortex dynamics.

Wake vortex monitoring as part of an advisory system can be accomplished with a coarser resolution than for characterization. For this application, long-term reliability and overall system cost are key issues. We suggest a system based on a diode-pumped cw solid-state laser at 2.1 μm because of its advantages of smaller optical aperture size, greater reliability, and lower cost over a CO_2 laser based system. A set of these laser radars would be located beneath the glideslope so as to measure the average circulation and location of vortices at operationally relevant spatial scales. A point design based on existing solid-state laser technology is described.

INTRODUCTION

There are two primary needs that wake vortex lidars can fulfill: that of a high-resolution detection system for vortex characterization and that of a monitor for a wake vortex advisory system. A wake vortex characterization lidar would provide measurements of wake vortices with sufficient resolution of the velocity, spatial structure, and temporal behavior to successfully characterize their behavior as a function of aircraft type and local atmospheric conditions. The specifications for a high-resolution vortex characterization lidar must allow for the characterization of the vortex velocity field with the ability to detect azimuthal variations in vortex parameters. The system must also be able to actively track vortices and it would be useful if the system could measure intrinsic velocity turbulence in the vicinity of a vortex. A range resolution of 30 cm x 30 cm with a velocity resolution of 50 cm/sec should be adequate for vortex characterization [1]; whereas a 5 - 10 cm/sec velocity resolution would allow the measurement of low to moderate velocity turbulence [2,3]. The system should also be capable of operating out to ranges of at least 200 m. A wake vortex lidar for monitoring, however, would only be required to track the position and average circulation of a vortex near the end of an airport runway in order to assess the threat towards approaching aircraft [4]. The requirements for a vortex monitor then are different, since the spatial resolution is not as important. A range resolution of 5 m downrange would be adequate in this case along with a 50 cm/sec velocity resolution which must also be achieved out to ranges of 200 m. In addition to satisfying the technical requirements, the vortex monitor must be rugged and reliable as well as cost effective.

This paper describes two lidar configurations which satisfy each of these requirements. The high-resolution vortex characterization lidar is first discussed, then the vortex monitor lidar.

HIGH-RESOLUTION VORTEX CHARACTERIZATION LIDAR

There are three general lidar systems that may be used for high-resolution wake vortex detection. These are a monostatic system based on a cw laser, a bistatic system based on a cw laser, and a monostatic system based on a pulsed laser. The monostatic cw system achieves its downrange resolution from varying the focus; the bistatic cw system obtains both the downrange and crossrange resolution from overlapping fields of view of the transmitter and receiver; and the monostatic pulsed system uses pulse modulation for achieving downrange resolution. The crossrange resolution of both monostatic systems comes from angularly scanning a narrow beam. The velocity resolution of both the cw systems comes from integrating the return for a sufficient period while the velocity resolution for the pulsed system is directly related to the pulse length.

Consider first the monostatic cw system. Previously constructed wake vortex lidars have been of this type [5]. This lidar system scans a cw laser beam across a region while varying the focus. The receiver part of the detector is imaged on the focal region, weighting the return there with a range gate that is proportional to $\lambda R^2/D^2$, where D is the aperture diameter, λ is the wavelength of transmitted radiation, and R is the range [6]. The advantages of this system include the requirement of a relatively low power cw laser, a simple optical configuration, and a fundamental advantage of monostatic systems over bistatic in that they are not sensitive to tilt variations caused by atmospheric turbulence.

The primary disadvantage is related to the R^2 range gate dependence which means that for a 30 cm downrange resolution at R=200 m an 80 cm aperture is required at 2.1 μm and a 170 cm diameter aperture is required at 10.6 μm. These aperture diameters are prohibitively large with the result that this system cannot be realistically considered for this application.

The bistatic cw lidar detector is composed of separate receive and transmit modules, which would be located about 15 m apart, with the range gate determined by the overlap of the transmitted beam and the receiver field of view. The advantages of this configuration include the use of a cw laser and the relative simplicity that accompanies a cw detection system. The disadvantages include the difficulty of maintaining overlap of the transmit beam with the receiver FOV and some ambiguity in the direction of the measured velocity. Since any coherent detection system requires a diffraction limited receiver field of view and since the most efficient use of laser photons occurs when the transmit beam is as small or smaller than the receive FOV at the intersection region, an angular stability of λ/D is required. Initially aligning this system such that overlap is maintained over the full range of motion of the receiver and transmitter may also be difficult. Finally, bistatic systems are sensitive to tilt variations caused by atmospheric turbulence. For these reasons this system was also not considered adequate for a high-resolution lidar.

The monostatic pulsed lidar system, unlike the cw systems, uses a pulsed laser source to achieve the required downrange resolution. High spatial and velocity resolution can be simultaneously achieved by frequency chirping the outgoing pulses in a sawtooth manner. In this case the velocity resolution is determined by the full pulse width, while the spatial resolution is determined by the width of an individually chirped section. The same effect can also be obtained by mode locking the laser, generating a train of coherent short micropulses to make a larger macropulse. The velocity resolution would then be determined by the macropulse width, while the spatial resolution would be determined by the separation of the micropulses. The benefit of these pulse-modulation techniques is that they offer a downrange resolution independent of the range at which the measurement is made, as well as the ability to dynamically vary the range and velocity resolution. Being monostatic, this system also has a decreased sensitivity to atmospheric distortions. The disadvantages include the use of a complicated laser, a signal processing system with a 1 GHz full bandwidth, and the presence of range and velocity ambiguities when the signal exceeds a certain dynamic range. Nevertheless, monostatic systems are fundamentally more flexible than bistatic systems and the ability to dynamically exchange velocity and range resolution makes this system the most attractive.

In considering the proper laser for the wake vortex detector the primary requirement is that the wavelength be greater than 1.4 μm for eye safety. With this in mind the two leading candidates are a 2.1 μm solid-state Tm:Ho-YAG laser and a 10.6μm CO_2 gas laser. The solid-state laser can be diode pumped, which offers the greatest potential for ruggedness and reliability; whereas CO_2 lasers are well developed and readily available. The laser power requirements for these lasers under various atmospheric conditions were calculated from the standard lidar equations, with the results shown in Table 1. The following assumptions were made in the calculations: the receive/transmit aperture diameter was 20 cm, the maximum range was 200 m, the transmit and receive efficiencies of the optical system were 75% and 50%, respectively, the downrange gate was 30 cm, the system bandwidth was 0.5 MHz, the detector quantum efficiency and mixing efficiency were both 50%, the required power signal to noise was 3, and 50 shots would

be averaged. These calculations yield a required average power of 14 watts at 10.6μm and 11 watts at 2.1 μm for one of the most stressing cases of heavy rain. The atmospheric parameters come from the LOWTRAN 6 database, and the estimates of the backscatter are most likely low compared with actual airport environments, which contain a high aerosol concentration from airplane exhaust. The power requirements for the CO_2 laser are generally greater than for the solid-state laser. But, whereas these power levels are easily available from CO_2 lasers, considerable development would be necessary for the solid-state system. Therefore, the CO_2 laser appears to be the most cost-effective choice for this system, but whichever laser is used it will have to be mode locked and cavity dumped.

A block diagram of the high-resolution system configuration is shown in Figure 1. The heart of the system is a mode-locked, cavity-dumped, 15-20 watt CO_2 laser whose output is polarization coupled out of a transmitter with a 20 cm aperture and a focus control for the rough range gate placement. The returning backscattered radiation passes through a polarizing beam splitter, is mixed with cw radiation from a local oscillator, and is directed into a Hg-Cd-Te detector. The local oscillator is a cw CO_2 laser, frequency-locked with the main laser and offset by 250 MHz. The detected signal is amplified, digitized, and then fed into an array processor, which first performs FFT analysis on the data and then signal averaging. The results are transferred to a workstation, where pattern recognition necessary for vortex localization is accomplished. The workstation also controls the scanning mirror, focus control, and cavity dumping of the laser, in order to track and take complete sets of information for each vortex position. The partially reduced data is stored in high band-width memory, such as a hard disk drive, and finally backed up on tape or optical disk.

One of the advantages of using a pulsed-chirped or mode-locked pulse format for laser radar is that the downrange resolution becomes independent of the range. The corresponding disadvantage is that as the range and velocity resolution is improved, the full extent over which the signal remains unambiguous becomes smaller [7]. The product of the full spatial dynamic range, before the signal falls back on itself, and the full Doppler bandwidth is given by $\lambda c/4$, where c is the speed of light. Thus, for example, if one requires a full velocity range of +/- 50 m/sec, one cannot tell which 8 m section of path from the laser in the direction of the target that the signal is actually coming from, since the observed signal will be the sum of the signals from each of the 8m sections. Likewise, when the Doppler signal falls outside of its full bandwidth, it too is folded over in velocity space. One way to resolve these ambiguities is to dynamically change the pulse format from measurement to measurement and trade off unambiguous range for Doppler bandwidth. Initial vortex acquisition and fast tracking can be accomplished using a "low bandwidth" pulse format, with an unambiguous range of 32 m that is larger than the focus range gate in exchange for a reduced velocity bandwidth of +/- 12.5 m/sec. High-resolution measurements can then combine several low and high-bandwidth pulse formats in order to extend the unambiguous range. The dwell time at each unambiguous range region for high resolution measurements would then be ~ 0.5 seconds, which assumes a 50 pulse average with 2 different pulse formats at 200 Hz PRF. Most of this time would be involved with transferring the raw data from the digitizer to the array processor, and the actual length of time over which the measurement would be made would be 2 ms.

As a final point in the consideration of the high-resolution wake vortex detector, we consider the requirements for measuring intrinsic turbulence in the vicinity of vortices. This is turbulence

that has become effectively steady-state and direction independent and shows a power-law spatial frequency dependence. The usefulness of this sort of measurement is that by characterizing the parcel of air toward which a vortex is heading, one can gain insight into the importance of turbulence in vortex decay processes. This kind of turbulence would be measured by fitting velocity versus spatial frequency measurements to a -5/3 power law [2]. The present system would be able to achieve 5-10 cm/sec velocity resolution by going to longer macropulses which would be adequate for measuring low to moderate turbulence. Simultaneously, one would also look for wind shear and "non -Kolmogorov" turbulence over spatial scales comparable to the size of the vortex. This kind of turbulence may be even more important than intrinsic turbulence in affecting vortex decay rates.

The high-resolution system discussed here will use technology similar to that used in the Firepond CO_2 pulsed-Doppler laser radar that Lincoln Laboratory developed for the DoD and located in Westford, Mass. The Firepond laser radar is actually much more complex and uses a more powerful $10.6\mu m$ laser, since it is designed to discriminate low cross-section return targets at very long ranges. The system outlined in this paper would incorporate much of the Firepond technology, but engineered to fit in a smaller, simpler package.

WAKE VORTEX MONITOR LIDAR

The second major need that a vortex-detection lidar can fulfill is that of a wake vortex monitor for an advisory system. For this mode of operation a principal requirement is for a compact, rugged sensor package, with little or no required maintenance. The required resolution is less rigorous than for the characterization system, with a downrange resolution better than 5 m at a range of 200 m, a velocity resolution of 50 cm/sec, and a measurement update rate better than once every 3-5 seconds [8].

We believe that a system based on a miniaturized, diode pumped, 2.1 μm Tm-Ho:YAG laser would fully meet these requirements. With the less rigorous downrange resolution requirement as the monostatic cw concept described earlier, with its inherent electronic and optical simplicity, is the system of choice for this application. The sensor would have a 10-20 cm receive/transmit aperture and a room temperature detector, as compared with the liquid nitrogen cooled detectors used at $10.6\mu m$. This system could be packaged in a rugged, weather-tight, container (see Figure 2). It would provide simultaneous measurements of the location and angular momentum of wake vortices. A 100 - 300 m maximum range would be possible, depending on the aperture size, and the lidar would be able to operate in IFR conditions.

The laser for the vortex monitor would be based on a concept developed at Lincoln Laboratory for "microchip lasers" [9], as shown in Figure 3. A microchip laser is a diode-pumped laser whose total cavity length is short enough to allow lasing on only one longitudinal mode. The laser thus automatically produces a single-frequency, well-polarized beam, with diffraction-limited beam quality. These lasers are small, measuring 1 mm x 1 mm x 0.7 mm, typically. The total laser package, including diode pump, fits into a cubic centimeter. A single microchip laser could produce enough power for the wake vortex lidar monitor (about 300 mW). One of the major advantages of using microchip laser technology is their potential for cheap mass production, since no external cavity optics are required.

A possible monitor configuration is as shown in Figure 4 with one to four sensors situated beneath the glide slope at the end of a runway. The actual number would be determined from the results of the characterization measurements. Each sensor would monitor a region in the vicinity of the glide slope about 400' x 80' wide and would measure the average circulation and clearing time for vortices within this region. A hazardous vortex would be one that remained in the region of interest and had not substantially decayed, i.e., its circulation was still above a level deemed dangerous to the approaching aircraft.

CONCLUSIONS

There are two basic needs that a wake vortex lidar system can fulfill: that of a characterization system for obtaining more information as to the behavior of wake vortices, and that of a monitor system that tracks vortices and measures their strength in the region of approaching aircraft as part of an overall wake vortex advisory service. A system meeting the requirements for a high-resolution wake vortex characterization lidar would be based on a mode-locked CO_2 laser. This sensor could achieve 30 cm x 30 cm spatial resolution at a range of 200 m and would have the capability of measuring ambient velocity turbulence. For vortex monitoring, a lower-spatial-resolution sensor based on a diode-pumped microchip laser is the recommended system both for ruggedness and cost-effectiveness.

Table 1. Results of LOWTRAN 6 Atmospheric Models for Relative Power Returned, P_{REC}/P_L, and Required Laser Power, P_L, for High Resolution Vortex Characterization Lidar at 10.6 and 2.1 μm

10.6 μm

ATMOSPHERIC MODEL	κ (Km^{-1})	β_π ($Km^{-1}Sr^{-1}$) (x10^{-5})	P_{REC}/P_L (x10^{-15})	P_L (Watts)
25 mm/hr RAIN	2.85	4.15	1.17	13.6
HAZE (98% RH)	0.61	4.15	2.87	5.5
MODERATE FOG 500 m VISIBILITY	1.96	62.9	25.4	0.6

2.1 μm

ATMOSPHERIC MODEL	κ (Km^{-1})	β_π ($Km^{-1}Sr^{-1}$) (x10^{-5})	P_{REC}/P_L (x10^{-15})	P_L (Watts)
25 mm/hr RAIN	2.73	122	36.1	11.1
HAZE (98% RH)	0.91	122	74.9	5.4
MODERATE FOG 500 m VISIBILITY	10.38	1300	18.1	22.2
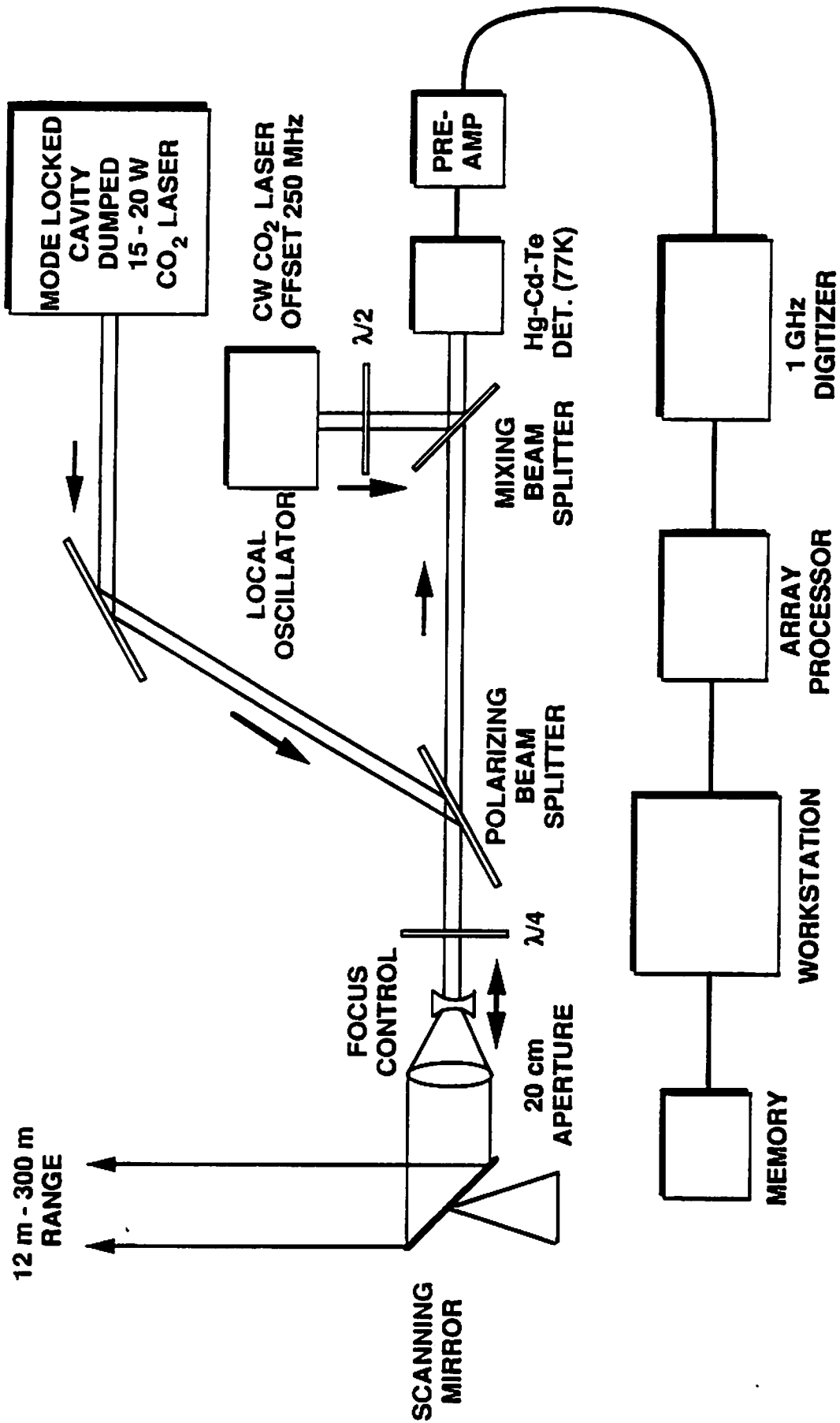
Figure 1. Block diagram of high resolution wake vortex lidar.
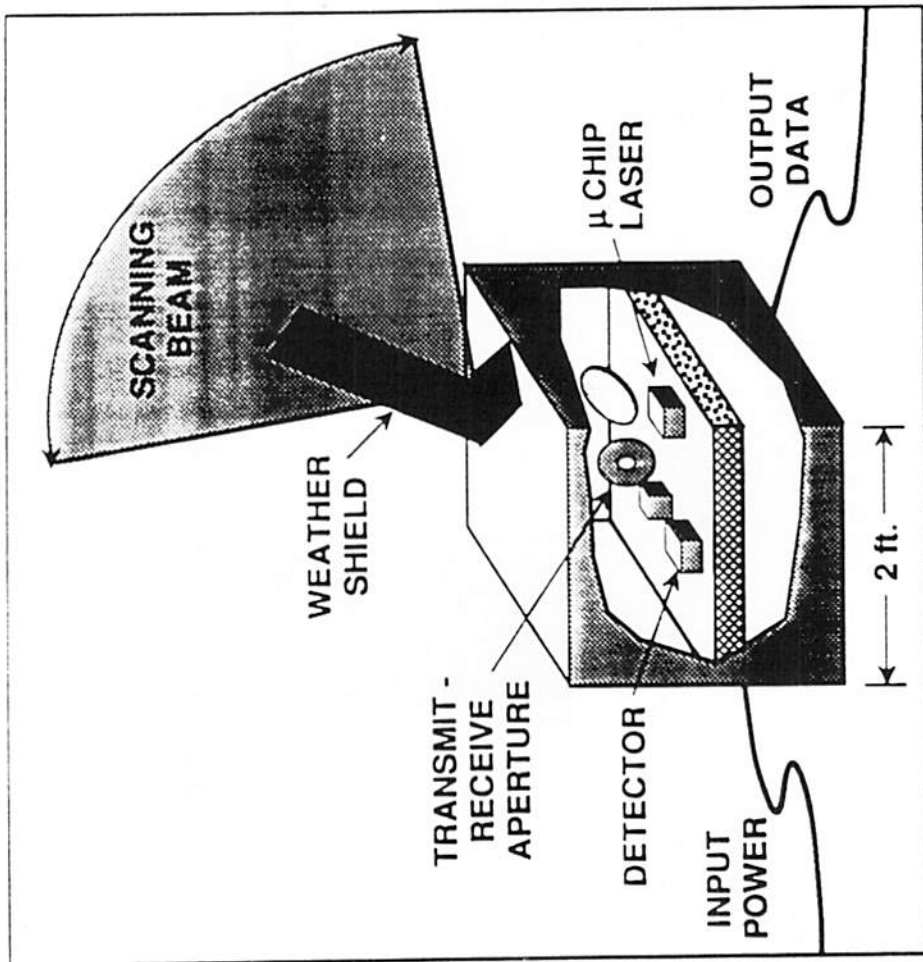
Figure 2. Diagram of wake vortex monitor package.

CAVITY LENGTH
L ~ 0.7 mm

SOLID STATE
LASER MATERIAL

OUTPUT

DIELECTRIC MIRRORS

DIODE LASER
PUMP
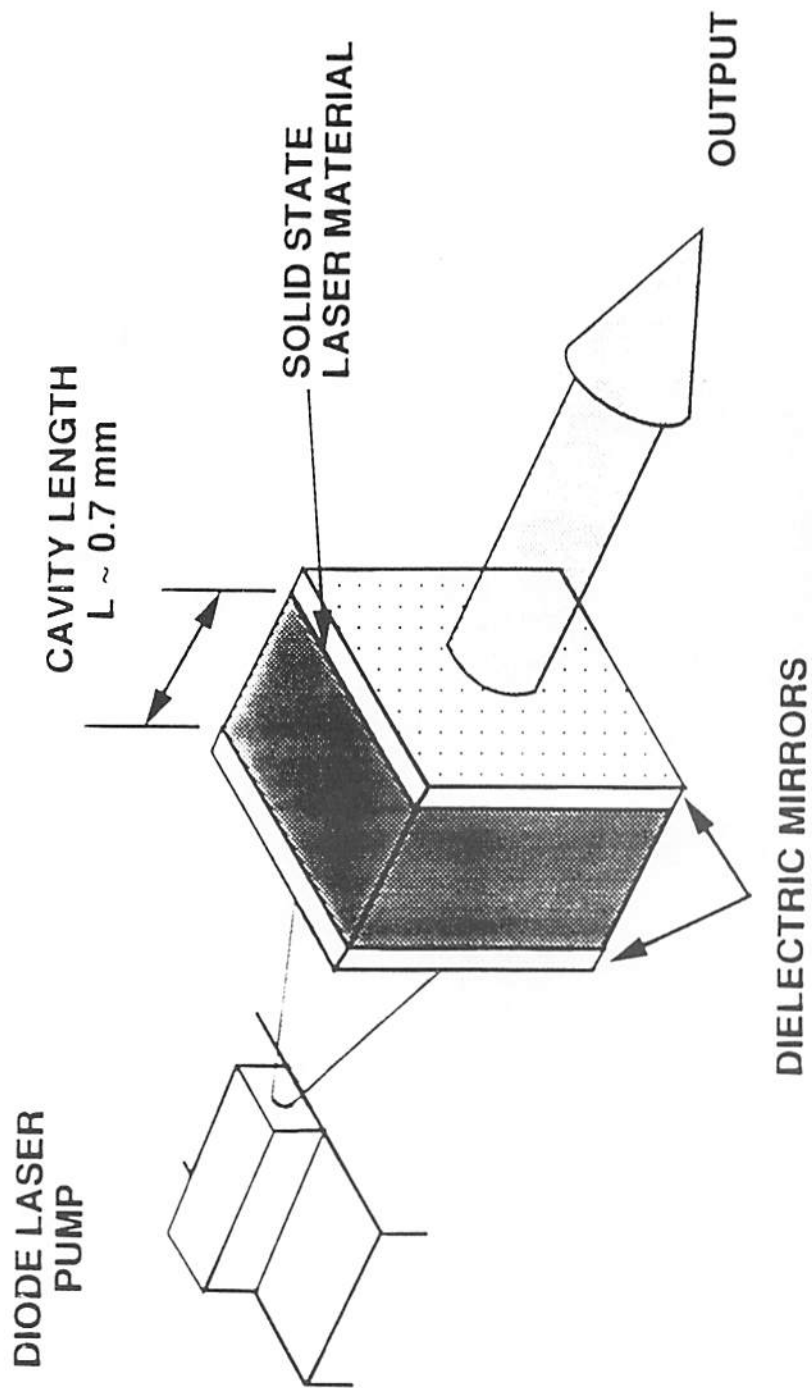
Figure 3. Schematic of miniaturized solid state "microchip" laser.
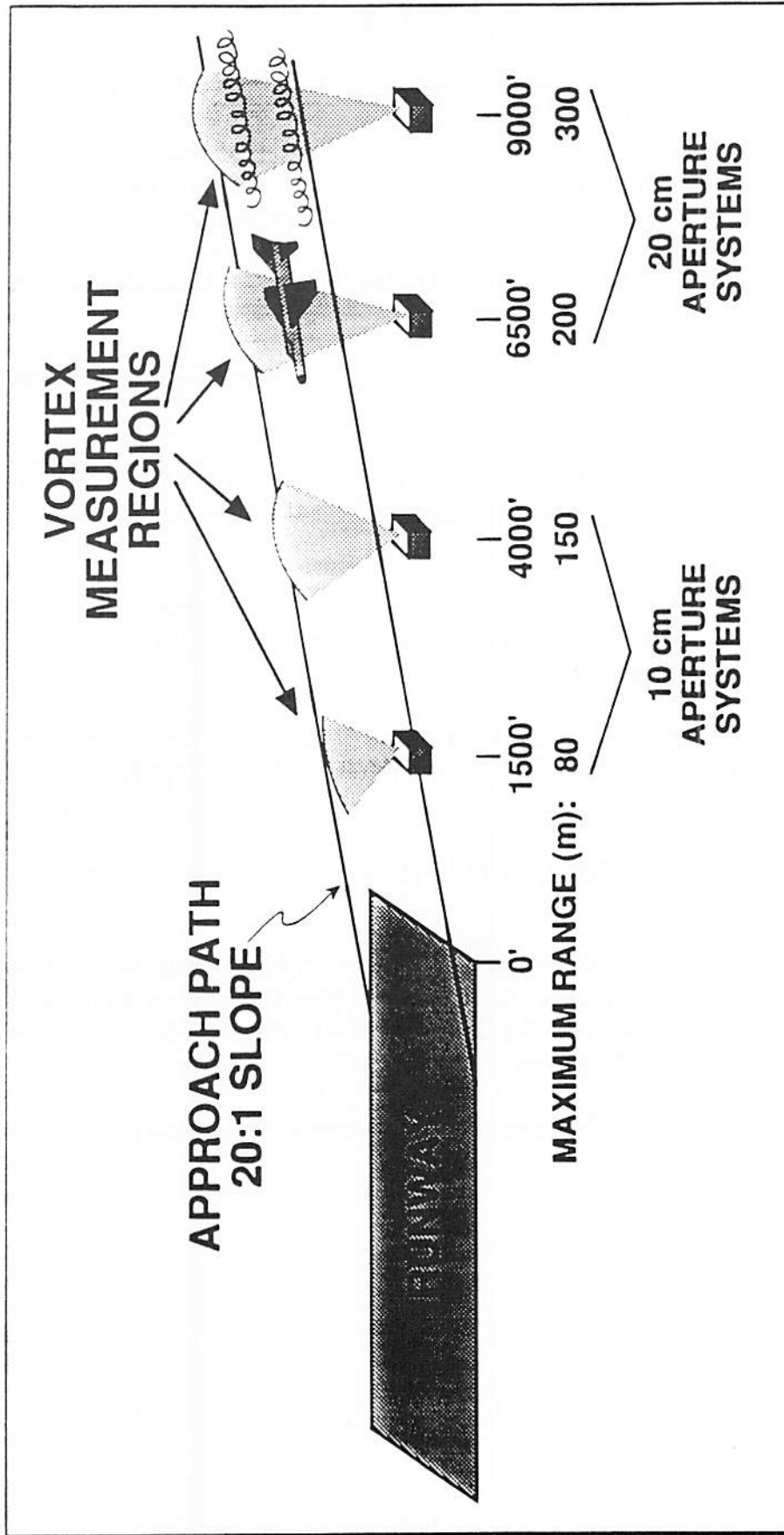
Figure 4. Possible configuration for wake vortex lidar monitors at the end of a runway.

REFERENCES

1. J.W. Bilbro, G.D. Craig, R.W. George, H.B. Jeffreys, P.J. Marrero, E.A. Weaver, M.C. Krause, T.L. Dunn, C.A. DiMarzio, C.E. Harris, G.M. Sonnenschein, and D.W. Toomey, "Laser Doppler Vortex Measurements at John F. Kennedy International Airport," Proceedings of the Aircraft Wake Vortices Conference, March 1977, FAA-RD-77-68, Cambridge, MA.

2. R.J. Doviak and D.S. Zrnic, Doppler Radar Weather Observations, Ch. 10, Academic Press, 1984.

3. C.H.B. Priestley, Turbulent Transfer in the Lower Atmosphere, p. 60, Univ. of Chicago Press, 1959.

4. S.J. Madden Jr. and R.B. Harlan, "A Program to Analyze and Model Trailing Vortices on Airports," M.I.T. Measurement Systems Laboratory Report, RN-69, Oct. 1971.

5. D.C. Burnham, "Review of Vortex Sensor Development Since 1970," Proceedings of the Aircraft Wake Vortex Conference, March 1977, FAA-RD-77-68, Cambridge, MA.

6. C.M. Sonnenschein and F.A. Horrigan, "Signal to Noise Relationships for Coaxial Systems that Heterodyne Backscatter from the Atmosphere," App. Opt., 10, 1600 (1971).

7. A. L. Kachelmyer, "Range-Doppler Imaging: Waveforms and Receiver Design," SPIE 999, 138 (1988).

8. F. Koepp, "The Infrared Doppler Lidar: An important tool for experimental investigation of aircraft wake vortices," in Technical Digest on Coherent Laser Radar: Technology and Applications, 1991 (Optical Soc. of America, Washington, D.C., 1991), Vol. 12, pp. 306-308.

9. J.J. Zayhowski and A. Mooradian, "Single-frequency microchip Nd lasers," Opt. Lett., 14, 24 (1989).

WAKE VORTEX LASER RADAR

A. V. Jelalian
W. H. Keene
T. McDonagh
K. N. Seeber
C. M. Sonnenschein
Raytheon
Sudbury, MA

Coherent laser radar systems have been utilized to remotely detect the motion of the atmosphere, by obtaining Doppler backscattering of the laser energy from aerosols naturally suspended in air. These activities were pioneered by Raytheon under contract to the NASA Marshall Space Flight Facility, when the first remote measurements of a CO_2 laser radar system were utilized to determine the atmospheric wind velocity, with a focused CO_2 laser system[1] in 1967.

These coherent detection systems use the temporal and spatial coherence of a laser radar (LIDAR) to obtain Doppler backscattering from aerosols and particulate matter. These systems operate both in the near field and far field of the system.

Near-Field Operation

In the near field, optical resolution is obtained by operating a coaxial telescope in a focused mode or by using bistatic apertures to illuminate and receive energy from a distinct volume of atmosphere.

Focused systems use the spatial coherence of the transceiver to obtain a resolved volume, which is determined by depth of field of the telescope, while bistatic systems rely on the common intersecting volumes of the transmitting and receiving beams. Sonnenschein and Horrigan[2] showed that the signal-to-noise ratio (SNR) of a focused system could be expressed as:

$$S/N = \frac{\eta \; P_T \beta(\pi) \lambda \eta_{SYS} \eta_{ATM}}{Bhf} \; F[R,\lambda,D] \qquad (1)$$

$$F[R,\lambda,D] = \left[TAN^{-1}\left[\frac{4\lambda R_2}{\pi D^2} - \frac{\pi D^2}{4\lambda R}\right]\left(1 - \frac{R_2}{R}\right) - TAN^{-1}\left[\frac{4\lambda R_1}{\pi D^2} - \frac{\pi D^2}{4\lambda R}\right]\left(1 - \frac{R_1}{R}\right)\right] \tag{2}$$

where the term in the square brackets is the contribution to the SNR of the region between R_1 and R_2 when the system is focused at a range R equal to the focal length of the telescope. When R_1 and R_2 are chosen to correspond to the boundaries of the region within which 50 percent of the total heterodyned backscatter occurs, then:

$$\frac{S}{N} = \frac{\pi \, \eta \, P_T \, \beta \, (\pi) \lambda \, \eta_{SYS} \, \eta_{ATM}}{2Bhf} \tag{3}$$

It should be noted that this expression is independent of the optics diameter and includes the diffuse target loss, as the incoherent integration of random diffuse scatterers was included in the derivation of Equation (1).

The spatial resolution of a system having half of the power obtained from the focused volume may be shown to be:

$$R_2 - R_1 = \Delta R = \frac{8}{\pi} \frac{R^2\lambda}{D^2} \tag{4}$$

It may be observed that this spatial resolution is range-square dependent and as range increases the spatial extent quickly grows.

Assuming a 6-in.-diameter beam (D = 0.15 m), a 100-m spatial resolution (50 percent of return) could be obtained at a range of 910 m and 290 m for system operating wavelengths of 1.06 μm and 10.6 μm, respectively.

Far-Field Operation

Range resolution may also be obtained by utilizing the temporal coherence of the system to provide range resolution by the use of a pulse transmitter where the range resolution is:

$$\Delta R = c\tau/2 \tag{5}$$

Because of the Doppler effect, care must be taken in the choice of the pulse length (τ) as it also determines the velocity resolution of the system.

If the atmosphere is moving uniformly, the Doppler returns from the aerosols being transported by the wind field will provide a mean Doppler signal of:

$$f_D = \frac{2V}{\lambda} \cos\theta \qquad (6)$$

the spectral width of which is given by:

$$\Delta f_D = \frac{2V}{\lambda} \sin\theta \; \Delta\theta \qquad (7)$$

where $\Delta\theta$ = transceiver beamwidth.

As the wind field becomes non-homogeneous, turbulent, shear, etc., a differential velocity will occur over a range cell, which will provide a differential Doppler return, and the Doppler spectrum will now include the effects of the velocity differential:

$$\Delta f_D = \frac{2V}{\lambda} \sin\theta \; \Delta\theta + \frac{2\Delta V}{\lambda} \cos\theta \qquad (8)$$

Matching the Doppler bandwidth Δf_D to the inverse of the pulse length $\Delta f_D = B = 1/\tau$ couples the range resolution, scattering volume, Doppler resolution and scale of turbulence to be measured. This may be illustrated by:

$$\text{Range Resolution } \Delta R = \frac{c\tau}{2} \qquad (9)$$

$$\text{Velocity } \Delta V = \frac{\Delta f_d \lambda}{2} \; (\theta = 180°)$$

$$\text{or} \qquad (10)$$

$$\Delta V = \frac{\lambda c}{4\Delta R}$$

Thus as the range resolution increases (a longer atmospheric sample is measured), the velocity resolution decreases (smaller differential velocity is measured).

Sonnenschein and Horrigan[2] made a comprehensive theoretical evaluation of the remote measurement of atmospheric aerosols and tabularized a variety of equations relating to operation in both the near and far field for systems that were focused or collimated. The analysis used an untruncated Gaussian beam whose diameter was defined by the $1/e^2$ circle of the Gaussian beam. Table 1 illustrates the basic equations, where

$$S/N = \frac{\eta \; P_T \beta(\pi)\lambda\eta_{SYS}\eta_{ATM}}{Bhf} F[R,\lambda,f] \tag{11}$$

and $F(R_A,\lambda,f)$ is the focal volume function.

If the bandwidth of the system is determined by the differential Doppler velocity (ΔV) over the focus volume, then the bandwidth becomes equal to twice the differential velocity divided by the wavelength. Substituting this into Equation (3) along with the fact that the frequency (f) is equal to the speed of light (c) divided by the wavelength (λ) results in the S/N ratio of a focused system, where 50 percent of the return occurs from the focused volume as:

$$\frac{S}{N} = \frac{\pi \; \eta \; P_T \; \beta(\pi) \; \lambda^3 \; \eta_{SYS} \; \eta_{ATM}}{4 \; \Delta V \; hc} \tag{12}$$

The cubic wavelength dependence of the S/N ratio results in long wavelength systems being preferred from a sensitivity point of view for low altitude systems.

In the far field the range resolved volume is determined by the pulse length (τ). Equation (13) illustrates a simplified expression for the far field SNR in terms of the volumetric effective target

cross section $\left[\beta(\pi)\dfrac{c\tau}{2}\right]$

$$S/N = \frac{\pi^2 \; P_T \beta(\pi) \; c\tau \; D^2 \; \eta_{SYS} \; \eta_{ATM}}{32 \; R^2 \; hF \; B} \tag{13}$$

In this expression a diffuse (speckle) target loss of 3 dB (0.5) must be included in the system efficiency (η_{SYS}) to be equivalent to those of Sonnenchein and Horrigan.

Assuming the atmospheric differential motion within a pulse does not result in bandwidth broadening, then the SNR expression may be shown to be dependent upon pulse length squared $(B = 1/\tau)$.

Doppler broadening beyond that of a matched filter will result in an increase in the signal bandwidth and will therefore reduce the atmospheric signal in each filter from that of the unbroadened condition. The signal-to-noise ratio equation for this case will be linearly related to the pulse length. Figure 1 from Wright, et al.,[3] illustrates the atmospheric backscatter coefficient for a variety of wavelength regions that might be considered for system operation.

WAKE VORTEX DETECTION EXPERIMENTS

As early as 1969 the Raytheon system was utilized to remotely measure aircraft wake vortex motion in a field experiment performed in Huntsville, AL,[3] where the laser radar was focused upwind of a tower, emitting smoke to allow visualization of the wake vortex generated by an aircraft flying by. Figure 2 illustrates a time sequence display of the velocity structure of an aircraft trailing vortex[4] obtained with a CO_2 laser and 15-cm optical system focused 100 ft. into the atmosphere. The first picture shows the intensity of the received ground wind signal on a vertical scale, and the Doppler shift or velocity distribution of the ground wind signal on the horizontal scale. The succeeding pictures illustrate the shift in Doppler frequency and broadening of the spectrum as the wake vortex passes through the laser-sensitive volume. The last picture portrays the return to the normal wind spectrum. Figure 3 shows a photograph of a wake vortex entrained in smoke for visualization.

As a result of the success of these experimental systems, the DOT/FAA/NASA agencies cooperated in developing several experimental systems in the 1970-1975 time period, which were field tested at Kennedy International Airport. These systems utilized optical range scanning of the focus telescope to change the range from which the atmospheric returns were being obtained, as well as angularly changing the pointing direction of the beam through the use of a reflecting mirror.

At that time the Raytheon laser utilized a liquid-cooled one-meter-long glass laser, a liquid nitrogen cooled detector, and utilized a surface acoustic wave Doppler signal processor which allowed the measurement of the mean wind speed, turbulence, and velocity strength (peak velocity).

Figure 4 illustrates that a typical wake vortex signal would consist of an atmospheric signal at a ground wind velocity and a vortex return at a higher velocity. In order to help extract these signals the surface acoustic wave spectrum analyzer was thresholded to allow the following four spectrum parameters to be determined - I_{PK}, V_{MAX}, V_{PK}, and N - which may be visualized in Figure 4.

These electronic parameters can then be utilized together with the knowledge of the systems spatial sensitivity to measure the vortex field. As the system sensitivity is peaked at the focus volume, I_{PK} can be utilized to locate the range to the vortex, and N can be utilized to assess the velocity differential over the focus volume, while V_{PK} becomes a measure of the largest tangential velocity.

In References 5 and 6, I_{PK} was utilized in an algorithm to locate each of the vortices in range, along with an assessment of the effective circulation (Γ_{eff}) where

$$\Gamma_{eff} = 2\pi \ dm/db$$

dm/db represents the change in the rolling moment (dm) over the wingspan (b). The experimental measurements of effective circulation of these aircraft were compared with that of a constant circulation vortex model[7] by DiMarzio, Sonnenschein and Jeffreys (Ref. 5).

Two systems were operated perpendicular to the runway, one on either side to measure and track the motion of the aircraft wake vortices as a function of altitude, and position over the runway, as a function of time after aircraft passage utilizing the I_{PK} algorithm. This may be observed in Figure 5. With the field test successes and the FAA growth plan indicating a potential market for several such systems, Raytheon developed an atmospheric laser radar system shown in Figure 6.

This system utilized two 18-inch air-cooled, metal-sealed laser tubes; computer controlled scanners; closed-cycle refrigeration system; surface acoustic wave processor and computer containing algorithms to measure the atmospheric motion. The computer was tied to a modem to allow remote telephone connection to the system test data. Figure 7 illustrates the wind velocity output for such a system.

Since that time (mid 1970's) laser radar systems have been more heavily developed by the military, which have resulted in more rugged, operational components to yield improved cost effective utility. Today the Raytheon CO_2 lasers are made from ceramic and utilize metallized seals for long shelf life (15-year goals) and operating life (thousands of hours). The laser construction utilizes similar technology as that associated with microwave power tubes, and is anticipated to have similar reliability. These lasers are conduction cooled and no longer require six-foot racks of power supplies and cooling equipment.

Cryogenic refrigeration for the 10-μm detectors have also been developed for military applications and are now found in military vehicles and weapons systems throughout the world. Thermoelectric cooling of these detectors has also been achieved.

Electronic developments over the past 15 years have resulted in the Surface Acoustic Wave (SAW) processors designed and built by Raytheon in 1973 (these units are still being utilized by the DOT for field data collection) now capable of being held in one's hand.

Computer capability has similarly gone through a revolution such that the Raytheon 706 Computer which was state-of-the-art commercial processor in 1970, can now be replaced with substantially miniaturized units.

In summary the DOT/FAA/NASA test demonstration of the CO_2 laser radar systems at Kennedy International Airport in the 1970's and the subsequent development of this hardware over time clearly indicates that:

1. CO_2 laser radar systems have successfully been utilized to remotely measure wind, wind shear, and wake vortices.

2. The technology is mature and producible.

3. CO_2 laser radar systems are safe for use at civilian airports.

WAKE VORTEX SENSOR DATA REPORTING

Since the wake vortex is a wind shear phenomenon, it would make sense to integrate it with other existing wind shear systems used by air traffic controllers to warn aircraft of hazardous conditions in the terminal area. The Terminal Doppler Weather Radar (TDWR), scheduled for deployment in 1993, would be a good candidate to display wake vortex warnings. A precedent already exists in that the present Low-Level Wind Shear and Alerting System (LLWAS) and an enhanced version, LLWAS-EN, is already being integrated with TDWR to provide a single display for the air traffic controller.

The TDWR is a pulse Doppler radar used to detect wind shear in the terminal area and provide warning to aircraft via a message read by the air traffic controller. The system had to be designed to impose a minimum, additional workload on the air traffic controller. This was accomplished by a high degree of automation that uses algorithms to generate unambiguous messages that require no interpretation. The LLWAS system, information from which will be superimposed on the TDWR displays, is an array of anemometers around an airport that compares wind speed and direction in the array with a centerfield sensor.

Figure 8 shows the TDWR ribbon (alphanumeric display) that provides a simple, unambiguous message with an audio alarm to get the controller's attention when hazardous wind shear conditions appear on airport approach or departure paths or other AREas Noted for Attention (ARENAs) line of the display (which is designed to be read at 10-ft distance, in full sunlight, up to 60° off axis) reads "Runway 18 Approach, microburst alert, 35-knot loss (in air speed), 1 mile final." This tells the pilot on approach to Runway 18 that there is a microburst at the 1 mile mark that will cause a 35-knot loss in air speed if he flies through it. The air traffic control supervisor in the tower, and the Terminal Area Control (TRACON) Facility have a Geographic Situation Display, Figure 9, which presents a more graphic display of the wind shear situation. The image presented in Figure 9 shows a typical airport layout with ARENAs. The scenario depicted shows three microburst alerts, colored red, with their approximate shape and the predicted air speed loss indicated in the center (e.g., 85 knots). The colored box-shaped areas are the six levels of precipitation using the legend to the right of the displayed image. The

shading behind the 85-knot microburst indicates that the precipitation level associated with that microburst may be attenuating the radar signal sufficiently enough to affect radar performance and indicates that other sources should be used to vector aircraft into that area to avoid hazardous weather.

In the future, these TDWR displays will be replaced when the Advanced Automation System (AAS) comes on-line, and the TDWR information will be integrated onto a common air traffic controller display. Further in the future, the warnings will be uplinked (via Mode S) to the aircraft without air traffic controller intervention. These interfaces are built into the TDWR systems now.

Table 1. S/N Variation

System	$F(R_A, \lambda, f)$
Pulsed-focused	$(\pi R_A^2 \Delta L)/(\lambda L^2{}_{AV})$
Pulsed-unfocused	$(\pi R_A^2 \Delta L)/\{\lambda L^2{}_{AV}[1 + (\pi R_A^2 \lambda L_{AV})^2]\}$
cw-infinite path-focused	$\pi/2 + \tan^{-1}[(\pi R_A^2)/(\lambda f)]$
cw-infinite path-unfocused	$\pi/2$
cw-finite path-focused	$\tan^{-1}\left[\dfrac{\lambda L_2}{\pi R_A^2} - \dfrac{\pi R_A^2}{\lambda f}\left(1 - \dfrac{L_2}{f}\right)\right]$ $- \tan^{-1}\left[\dfrac{\lambda L_2}{\pi R_A^2} - \dfrac{\pi R_A^2}{\lambda f}\left(1 - \dfrac{L_1}{f}\right)\right]$
cw-finite path-unfocused	$\tan^{-1}[(\lambda L_2)/(\pi R_A^2)] - \tan^{-1}[(\lambda L_1)/(\pi R_A^2)]$

R_A = D/2 = Gaussian beam radius

L = range

L_1 and L_2 near and far range of target

Note that the focal length f is equal to R in Equation (1).

Volume: $L_{AV} = \dfrac{L_1 + L_2}{2}$

$\Delta L = L_2 - L_1$

f = focal length

Table 2. Vortex Circulations

Aircraft	Theoretical Circulation Γ	Experimental Effective Circulation Γ_{eff}
B-747	7700 Ft²/sec	9000 Ft²/sec
B-707	4165 Ft²/sec	4100 Ft²/sec
B-727	3309 Ft²/sec	5200 Ft²/sec
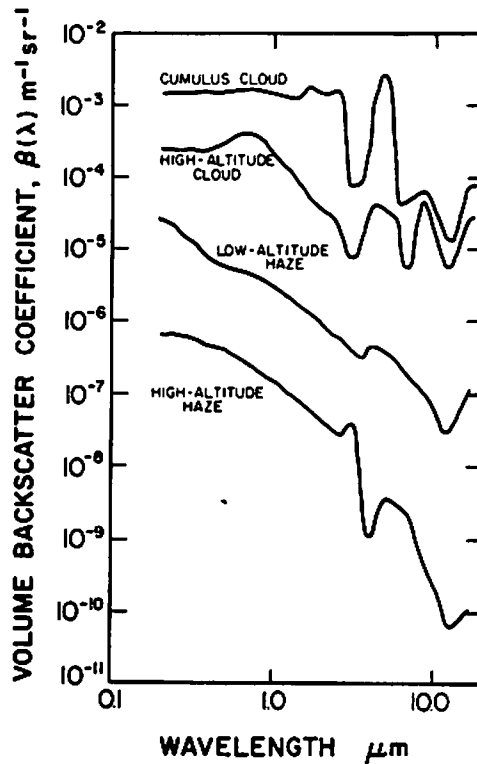
Figure 1. Aerosol volume backscattering coefficient as a function of wavelength (Wright, et al., 1975)[3].

41-10

Figure 2. Time sequence display - aircraft trailing vortex.

EO-3429

41-11

Figure 3. Trailing vortex.
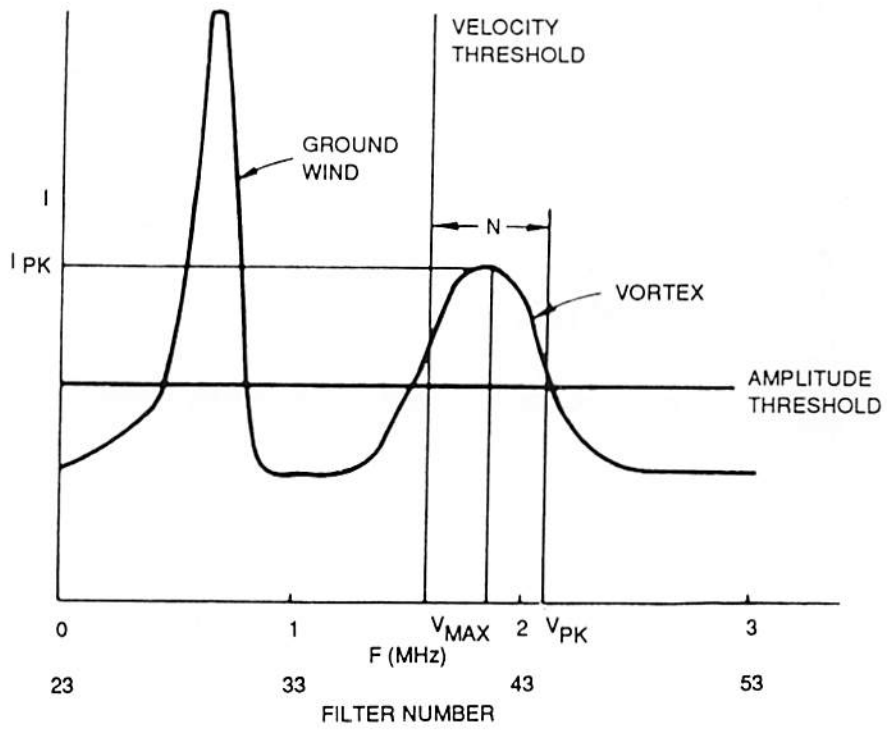
Figure 4. Vortex signal spectrum.

I_{PEAK} ALGORITHM WITH

C = 25   R = 88 FT

RUN 16   DAY 310   (B-747)

KEY:
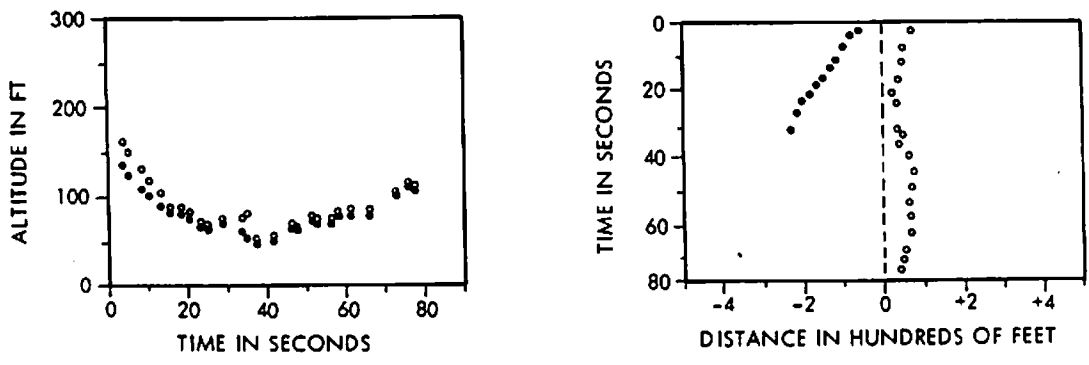
• - LEFT VORTEX

o - RIGHT VORTEX

Figure 5. Wake vortex detection program.
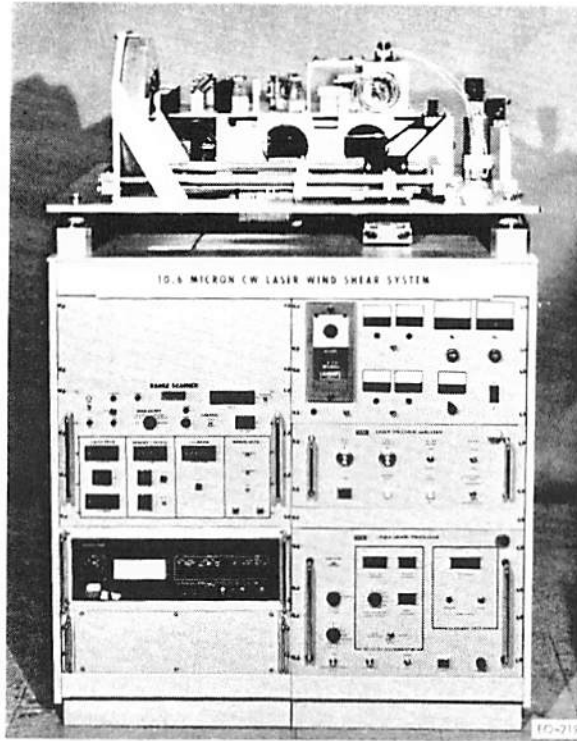
Figure 6. 10.6-micron CW laser wind shear system.

WIND DIRECTION (DEGREES)	WIND SPEED (KNOTS)
325	14.0
342	13.1
350	12.1
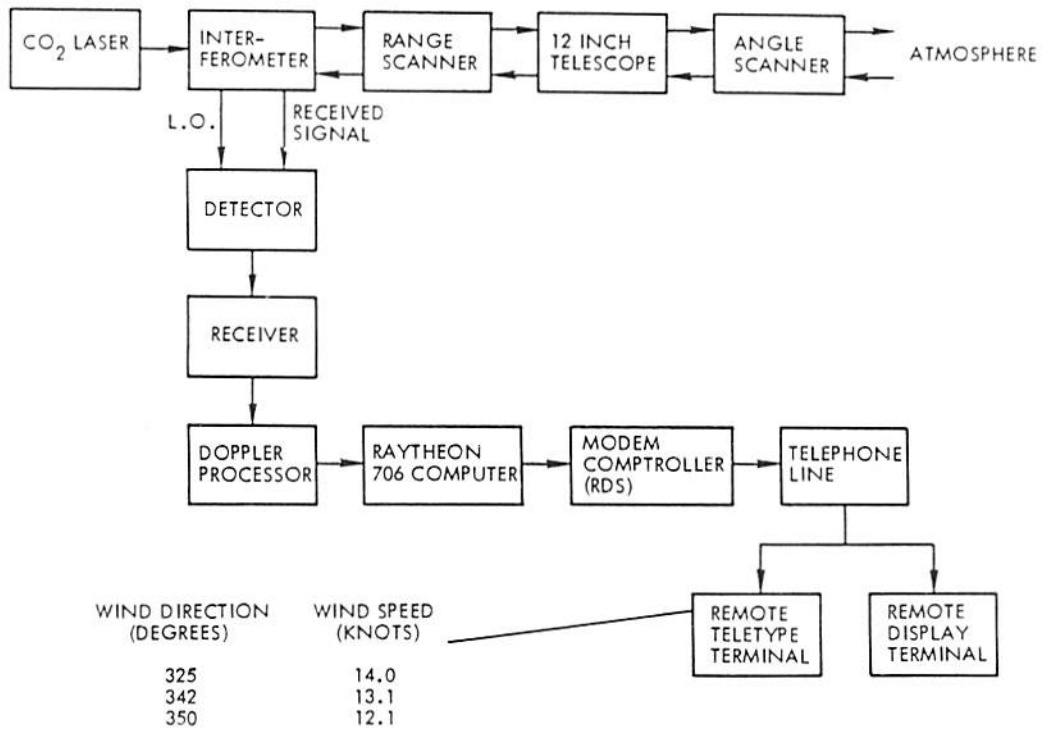
Figure 7. Laser Doppler wind shear system.
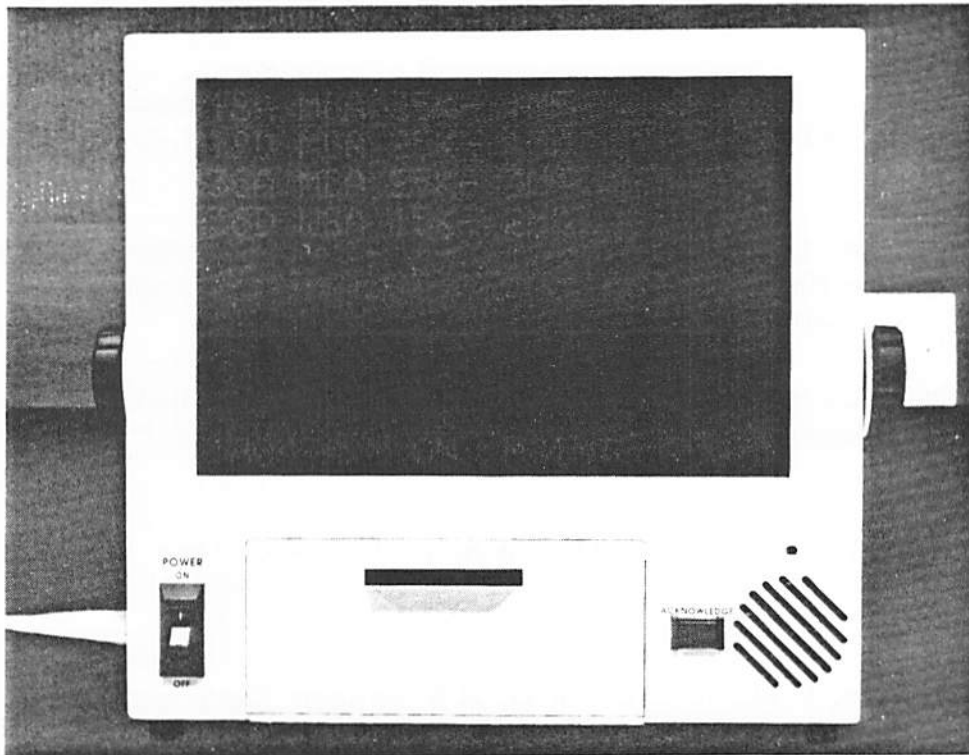
Figure 8. Terminal Doppler weather radar (TDWR) ribbon display.
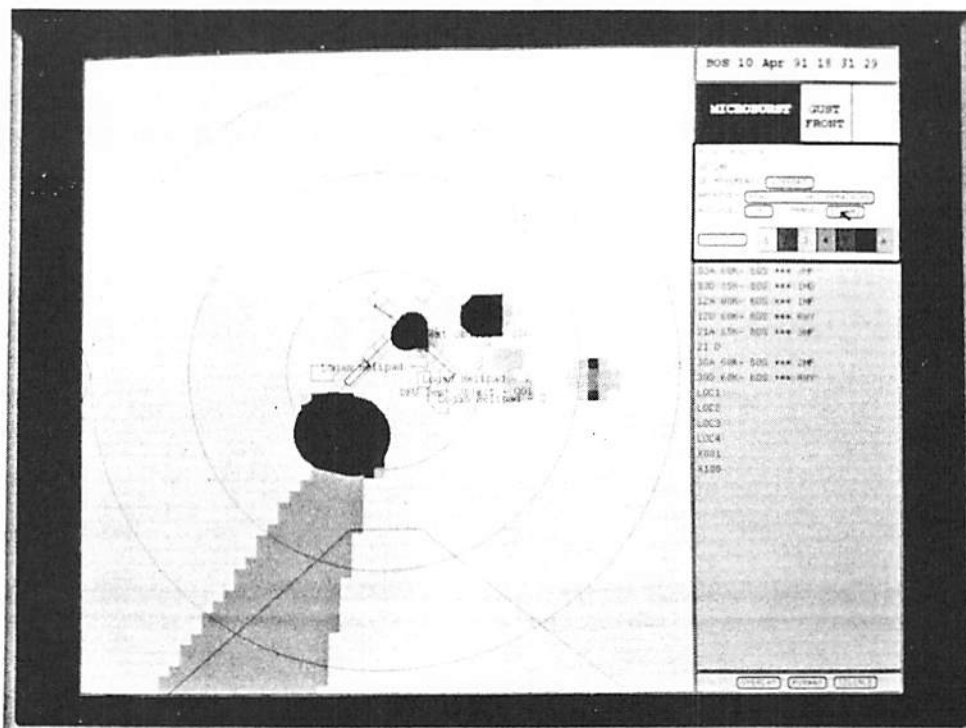
Figure 9. TDWR geographic situation display.

REFERENCES

1. Jelalian, A. V., R. M. Huffaker; "Specialist Conference on Molecular Radiation and Its Application to Diagnostic Techniques," NASA T.M. X-53711, October 5-6, 1967, p. 345.

2. Sonnenschein, C. M., F. A. Horrigan; "Signal to Noise Relationships for Coaxial Systems That Heterodyne Backscatter From the Atmosphere," Applied Optics, Vol. 10, No. 7, July 1971, pp. 1600-1604.

3. Wright, M.L., E.K. Proctor, L.S. Gasiorek, E.M. Liston; "A Preliminary Study of Air Pollution Measurements by Active Remote Sensing Techniques," NASA CR-132724, 1975.

4. Huffaker, R.M., A. V. Jelalian, and A. F. Thomson; "Laser Doppler System for Detection of Aircraft Trailing Vortices," Proceedings of IEEE, Vol. 58, No. 3, March 1970.

5. Sonnenschein, C.M., C.A. DiMarzio, H.B. Jeffreys; "Performance of a CO_2 Laser Vortex Detection System," 1975 IEEE/OSA Conference on Laser Engineering and Applications, Washington, D.C., May 1975.

6. Jeffreys H.B., J.W. Bilbro; "Development of a Laser Doppler System for the Detection and Monitoring of Atmospheric Disturbances," 1975 Electro-Optics/International Laser Engineering and Applications Conference, Anaheim, CA, November 1975.

7. Hallock J., "Wake Vortex Decay Near the Ground," AIAA 8th Fluid and Plasma Dynamic Conference, Hartford, CT, June 1975.

GLOSSARY

where:

S/N   =   Signal-to-noise ratio

η =   Detector quantum efficiency

P_T =   Transmitter power

$\beta(\pi)$ =   Atmospheric backscatter coefficient

λ =   Wavelength

η_{SYS} =   System efficiency

η_{ATM} =   Atmospheric transmission efficiency

B   =   Electronic bandwidth

h   =   Planck's constant

v,f =   Frequency

D   =   Optics diameter

ΔR =   Spatially resolved range resolution

τ =   Pulse length

c   =   Speed of light

θ =   Angle between line-of-sight and velocity vector

$\Delta\theta$ =   System beamwidth

ΔV =   Differential velocity over the range cell

I_{PK} =   Highest amplitude in the spectrum

V_{MAX} =   Velocity associated with this amplitude

V_{PK} =   Highest velocity above the amplitude threshold

N   =   Total number of frequency (velocity) cells above thresholds which may be visualized in Figure 4.

dm/db =   Change in rolling moment (dm) over an aircraft wingspan (b)

Γ =   Vortex circulation

r   =   Radial distance

2 MICRON COHERENT LASER RADAR FOR ON-BOARD AIRCRAFT VORTEX WAKE DETECTION: PATTERN RECOGNITION TECHNIQUES AND TECHNOLOGY ASSESSMENT

J. Alex Thomson
R. Milton Huffaker
Coherent Technologies, Inc.
Boulder, Colorado

Richard D. Richmond
Wright Research and Development Center

INTRODUCTION

A model for estimating the performance of a coherent lidar for detecting and tracking aircraft vortex wakes is described. The goal of the analysis is to assess and predict detection performance of the coherent lidar system as a function of its design and in a variety of operating environments. For this purpose, an existing laser system performance simulator has been modified to apply to aircraft wake detection. The model has three basic elements: a description of the velocity and scattering properties of the wake itself, a specification of the laser optics and scanning procedures, and a simulation and error analysis of the data processing algorithms.

Standard models for atmospheric absorption, scattering and coherence loss together with representations of ambient turbulence are used to describe the operating environment. The numerical simulation provides a detailed emulation of the characteristics of the laser signal returned from the atmosphere. Pulsed, CW, focused and unfocused configurations can be simulated. Various measures of performance can be implemented ranging from simple Doppler exceedances along given lines of sight to relatively complex 2D and 3D pattern recognition concepts. In this paper, we will utilize spatial displays of the detected pattern of line of sight velocity and Doppler spread as well as spatial displays of the probability that a given vortex wake is present as a function of its hypothesized position (matched filter detection).

The wake is modeled as two finite, counterrotating, parallel vortices. Models for the core structure, the wake length and the axial flow are summarized in the second section, Vortex Wake Structure Model. The calculation of the laser signature is outlined in the third section, Lidar Signature, and various design criteria and trade-offs are discussed in the fourth section, Design Trade-offs. Recent developments in solid-state laser technology at 2 microns are reviewed in the fifth section. The sixth section, Performance Simulations, provides examples

of predicted performance for two viewing aspects, one appropriate to a ground-based flyby geometry and one appropriate to an on-board trailing view configuration.

Three basic detection philosophies are considered. The first uses direct detection of the hazardous high velocity, high shear regions as the target. Although such detection provides the simplest and most direct approach to hazard detection, it is also the most costly to implement in terms of laser resources, the target regions being both spatially small and spectrally broad. A less stressing concept relies on detecting the more widely distributed, lower velocity regions of the wake and uses observed spatial and spectral patterns to detect the presence of the known wake structure to infer the locations of the wake vortices. The simulations in the fifth section use this method. The third concept does not rely on detecting the wake directly at all but simply monitors the wind field in the general vicinity of the landing corridor. Potentially hazardous conditions are identified based on coupling reported (or measured) space-time locations of transiting aircraft to a prediction model for wake transport and decay.

In all cases, the lidar must contend with the fact that only the line-of-sight component of velocity is detected directly. Particularly for on-board systems the perpendicular component that will most affect the aircraft is not directly sensed and its presence must be inferred by the data processing system. For this type of detection, pattern recognition concepts that attempt to infer the presence of a familiar target pattern from limited data are needed. Maximum likelihood processing will be used in the examples to provide matched filters that yield the probability that a wake exists at given locations in the scanned volume.

VORTEX WAKE STRUCTURE MODEL

During the 1970s, a number of studies were carried out under government and commercial funding to evaluate the hazard to following aircraft of the intense wind shear that occurs in the wakes of large commercial jet aircraft. Much of our current understanding of the details of aircraft wake velocity structure results from these studies[1-7].

An excellent summary of the morphology of the overall wake development is given by Neilsen and Schwind[2] (Figure 1). For a clean wing configuration, the vortex sheet shed from the wing rolls up rapidly into two typically well-defined longitudinal vortex structures. This rollup occurs sufficiently rapidly (within 5 to 10 wing spans)[2] that this period contributes little to the overall wake detectability. After rollup, mutual interaction between the two vortices causes the wake to drift downwards more or less as a unit until one or more instabilities develop to disrupt the structure. During this period, the overall wake maintains an essentially uniform time invariant flow pattern (Figure 2) which may persist for 100 to 1000 wing spans before breaking up into the more turbulent, late time period. In mildly turbulent atmospheres, the transition between the two stages typically occurs as a result of a self induction instability between the two vortices (the Crow linking instability - Figure 3)[3]. Turbulent diffusion and vortex breakdown may also play a role in modifying the high velocity vortex core regions during this period. Breakup times for a number of different aircraft have been correlated with ambient turbulence levels by Crow, Tombach (Figure 4)[4]. Crow and Bate[5] provide a theoretical prediction of the time of vortex linking in the presence of ambient turbulence that agrees well with observed wake breakup times (Figure 4).

The details of the velocity profiles in the vicinity of the vortex cores have been measured in a number of field studies. Available experimental results have been summarized and compared with theoretical models in a comprehensive review by Donaldson et al.[1] The classic model of the transverse velocity field of a vortex wake given by Spreiter-Sacks[6] describes the velocity field outside the core fairly well. Close to the vortex center, however, a model originally developed by Betz[7] appears to give a better representation of the high-velocity region (see Figure 2). Wake characteristics for a number of aircraft are tabulated in Table 1.

Less well understood are the motions parallel to aircraft flight direction. Although the mean axial momentum of a nonaccelerating aircraft must vanish, motion of ingested smoke inhomogeneities in flow visualization flyby experiments indicate that local axial velocities can have magnitudes comparable to the peak tangential velocities of the separate vortices. No direct anemometer or lidar measurements of these velocities are known to the authors. The CTI wake model includes an induced drag term which produces a forward motion in the vicinity of the vortex cores. As well, a more widely distributed reverse flow is associated with the engine thrust. These axial velocities can provide important signatures for on-board detection systems which must view the wake at small aspect angles.

LIDAR SIGNATURE

VORTEX, the CTI computer simulation model of coherent laser radar vortex measurement performance, integrates various mathematical models of the atmosphere, winds (background, Kolmogorov turbulence, and the vortex wake), and of the instrumentation into a detailed, flexible, unified simulation capable of modeling airborne or ground-based vortex detection and measurement systems.

Input and output parameters include:

Inputs

-lidar system parameters
-lidar platform geometry
-atmospheric parameters
-aircraft (target) parameters
-data processing parameters

Outputs

-range-dependent power signal-to-noise ratio (SNR)   .
-true and measured Doppler spectra
-true and measured radial wind velocities

-true and measured spectral widths
-measurement error analysis

A multidimensional pattern recognition analysis is used to emulate a coherent lidar system which scans a specified volume of space searching for aircraft wakes (Figure 5). The wake is assumed to be horizontal, of finite length, and aligned with the track of the aircraft. Except for the fact that the length of the wake is finite, axial gradients are ignored. The laser radar system scans a succession of two-dimensional planes and, along each line of sight, records the Doppler spectrum of the radial component of the air velocity as a function of range and elevation or azimuth angle for each pulse transmitted. The first three moments of these Doppler spectra are evaluated and presented as two-dimensional patterns on selected scan planes. These moments (area, centroid, and variance or width) describe the main characteristics of the return pulse: 1) the area is proportional to the total scattered energy, 2) the centroid gives the mean velocity, and 3) the width gives the spread of velocities within the pulse.

Detailed detection analysis is carried out in a selected sub volume of the 3D scan space. Three detection modes are considered (Table 2). In the simplest mode, threshold criteria are used to sense local exceedances for the local mean line-of-sight velocity, and/or mean spread of velocity. This mode presumes that the intense velocity gradients near the wake vortex cores provide the critical detection diagnostic. In the second mode, a search for two- or three-dimensional patterns of spatial distributions of velocity or velocity spread is conducted. This latter mode is aimed at detecting the lower magnitude, more widely spread velocity features of the wake, features that may have levels comparable to those of the surrounding atmosphere. Here the unique spatial pattern of the trailing wake is used to discriminate wake returns from the natural ambient velocity structures. Matched filter techniques are used for pattern detection and these require as input multiple hypothesized values for wake structure, orientation and size. It is felt that these two modes should bound the detection estimate. The spatial pattern mode, because it integrates extensive spatial information, is expected to yield substantially higher detectability than a local threshold mode, as well as permitting more widely spaced angular sampling intervals.

DESIGN TRADE-OFFS

A rough measure of system performance is the accuracy with which the Doppler spectrum in a specified volume can be estimated with a given amount of transmitted laser energy. In References 8 to 10, estimation errors for a number of popular processing algorithms have been specified. For the first two Doppler moments: (mean velocity in the resolved detection region and velocity spread) these errors all have the same analytic form:

$$\delta\sigma_V = (\lambda\Delta_V/4T) \, F_V(SNR, \Delta_V T_s/\lambda)$$

$$\delta\sigma_W = (\lambda\Delta_V/4T) \, F_W(SNR, \Delta_V T_s/\lambda)$$

Here SNR is the peak pulse signal to noise and equals the number of photons detected in a signal correlation time, $(=\lambda/4\pi\Delta_V)$, Δ_V is the spectrum width in m/s. T is the net observation time, and T_s the data sampling interval. The spectrum width Δ_V depends on both the pulse length and the velocity spread within the pulse, i.e., on the ambient turbulence and shear levels. For a coherent system viewing a distributed aerosol target, the return signal decorrelates in less than the time required for the pulse to move its own length. The spectral broadening due to this pulse length effect limits the accuracy with which the mean velocity can be estimated with a

single pulse.   Because of the extended nature of the target, this broadening cannot be distinguished from the broadening produced by true sub pulse scale velocity fluctuations.

Pulse Width Trade-offs

In Figure 6, the net spectral width expected for a turbulent atmospheric target is plotted as a function of pulse length. For a given level of expected turbulence an optimum pulse length can be selected to minimize the spectrum width and thus the measurement error.   Shorter wavelengths generally provide a greater Doppler shift for a given aerosol velocity and thus inherently provide a better ability to have simultaneously good space and good velocity resolution.

Pulse Energy Trade-offs

In Figure 7, the measurement accuracy that can be achieved with a fixed amount of laser energy is shown. Here the estimated measurement error, after averaging N pulses, is plotted against the SNR per pulse constrained so that the total energy (NxSNR) is constant.   Optimum performance is achieved by selecting a SNR value roughly in the range 0 to 6 db. When the system bandwidth is limited to be not much larger than the signal bandwidth, the difference between different signal processing algorithms is relatively small and all are relatively close (within a factor of 2) to the Cramer-Rao lower bound. When the system bandwidth is made large compared to the signal bandwidth (in order to capture a wide variety of velocities), the performance of the pulse pair and the spectral algorithm both degrade relative to the Cramer-Rao limit.   Although a more complex processing algorithm may be able to recover this loss, the system design can be expected to be more robust as well as being close to optimum if the system bandwidth can be reduced to be only a few times the signal bandwidth.

Viewing Aspect Trade-offs

At the small viewing aspect angles that will be experienced by an onboard detection system, the dominant tangential and downward velocities in the wake can be nearly perpendicular to the nominal viewing direction and may be difficult to detect by the lidar system. The viewing aspect angle (θ) can be controlled to some extent by increasing the mean depression angle and detecting the wake where it is closer to the laser platform (requiring an inference as to the probable position at longer range).   Although the absolute value of the detected lateral velocity is proportional to $\sin\theta$, the effective path length through the wake increases as $(\sin\theta)^{-1}$. Thus, by choosing the pulse length to match the expected pathlength through the wake, an angle independent ratio of detected velocity to spectrum width due to pulse broadening can be achieved for the lateral vortex velocities.   With such a choice of pulse length any axial velocity component will be rendered relatively more visible as will any atmospheric turbulence component as the aspect angle decreases. Thus, in calm atmospheres, the wake visibility may actually improve as the viewing aspect angle is reduced, up to the point where atmospheric turbulence and the inherent laser coherence limits. Figure 8 shows that for a nominal 40 meter width wake, viewing aspect independence holds for aspect angles $>20°$ in light turbulence.

CW vs. Pulsed Operation

A CW system achieves range resolution by focusing and is thus limited to relatively short range operation. The depths of field at 3 km and at 1 km range are tabulated in Table 3 for three wavelengths for a 0.2 meter aperture system.

With this aperture and at ranges of 1 km or less, focused systems, particularly at 1 and 2 microns, can achieve resolution comparable to the wake dimension. Because of the narrow spectral widths that can be achieved by CW systems, a CW system may be able to operate with poorer spatial resolutions than can a pulsed system. It should be noted that, for the trailing, onboard application, where line-of-sight wake widths at 5° viewing aspect of several hundred meters are typical, a short wavelength 0.2 meter aperture focused CW system can achieve a spatial resolution comparable to that of a well-designed pulsed system. The main disadvantage of a CW system relative to a pulsed system, however, is the high mean power required to achieve adequate SNR. The SNR of a pulsed system is greater than that for the same mean power CW system by the ratio of time between pulses to pulse duration. For the pulsed systems modeled in the next section, the value of this ratio ranges between 2000 and 20000. For such systems, pulsed operation can be expected to provide a much more efficient method for using a given amount of laser energy. The major requirement for pulsed systems is that the spectral broadening due to the finite pulse length not obscure the Doppler shift due to the wake.

Processing Trade-offs

The major characteristics of the three basic processing modes are listed below:

o Single LOS thresholding

-   -Velocity thresholding is used to eliminate atmospheric return
    -Wide bandwidth is needed to capture high velocities
    -Limited by Doppler spectrum fluctuations (shot noise and speckle)
    -Limited to the energetic part of the wake
    -high SNR, dense angular sampling, high bandwidth required
    -shortest forecast time
    -highest requirement for laser resources
    -most reliable sensing of actual hazard

o Pattern Detection (x,y,z)

-   -mean velocity pattern
    -Doppler width pattern
    -processing by a 2D or 3D Matched filter
    -limited by atmospheric turbulence and shear patterns
    + speckle + shot noise
    -senses exterior wake regions
    -low SNR, moderate angular sampling, low bandwidth required
    -intermediate forecast time

-intermediate requirement for laser resources
-senses location of potential hazard, not hazard itself

o Wake Transport Prediction

-lateral wind estimate, turbulence estimate
-prediction of vortex locations vs. time
-prediction of vortex strengths vs. time
-low SNR, minimal angular sampling, low bandwidth required
-senses statistical probability of hazard, not actual hazard; is model dependent
-longest forecast time
-lowest requirement for laser resources

Comparison of these different approaches is most easily accomplished by simulation. Examples of a simulation of 2D pattern detection system will be given in the sixth section, Performance Simulations.

RECENT DEVELOPMENTS IN 2.09 MICRON SOLID-STATE LASER TECHNOLOGY

Coherent Technologies has recently demonstrated the first working coherent lidar using Tm,Ho:YAG lasers operating at the eyesafe wavelength of 2.09 microns. This system, described in more detail in Henderson et al. (1991), utilizes a diode-pumped master oscillator and a flashlamp-pumped slave oscillator. The system operates in the injection-seeded configuration with the master oscillator used to injection seed the slave oscillator driving it into single longitudinal mode operation. The detector used in this system operates at room temperature and has a quantum efficiency of about 70%.

The system has demonstrated accurate velocity and range measuring capability during intensive field tests. Results to date include horizontal atmospheric wind measurements to 30 km, vertical atmospheric returns to 10 km, near-horizontal cloud returns to 10 km, and hard target (mountainside) returns from 145 km. All these returns were obtained with a transmitted pulse energy at 2.09 microns of only 20 mj. The long-range cloud and mountainside returns indicate very high atmospheric transmission at 2.09 microns.

As described in Henderson et al. (1991), the high SNR velocity accuracy of this system is about 11 cm/sec even though the transmitted pulse length is only 200 ns. Figure 9 shows an interesting example of atmospheric wind measured with the 2.09 micron coherent lidar system. The lidar beam was aimed approximately horizontal, and the beam terminated on a mountainside located 16.5 km for the lidar. The gust front seen in the figure was felt at the lidar location 10-15 minutes after the data was taken. Note the estimated radial velocity of 0 meters/second at 16.5 km (the location of the mountainside). Beyond the mountainside, the velocity estimates experience large fluctuations due to the lack of signal.

PERFORMANCE SIMULATIONS

Figures 10-12 depict a simulation of the detection of an aircraft wake by a ground-based system. These particular calculations were carried out to emulate a flyby by a lightly loaded C130 aircraft being used in a test scenario. Two viewing aspects are shown in Figure 10, one a more or less horizontal view at a range of 2.5 km and simulating a candidate airport viewing condition and the other a high elevation angle view at comparable range designed to obtain a more direct look at the downward motion in the wake. In both views, the expected SNR for a 0.7 millijoule pulse at 2.1 microns wavelength is estimated in clear air to be of order 8-10 db. The true value of the line-of-sight velocity is shown in Figure 11a. Expected Doppler spectra seen at a range close to one of the wake vortices are shown in Figure 11b. Because the velocities in this wake do not exceed the 4-meter second bandwidth induced by the finite 40 meter pulse length, the distortion of the spectra by the wake is relatively difficult to see in a single spectrum. The difference is more apparent in the plots of the difference between the ambient spectrum and the wake spectrum (Figure 11c). Figures 11d and 11e show the predicted patterns of pulse averaged mean velocity and spectral width detected using a pulse pair algorithm and after averaging of 90 pulse signals at each range point. Speckle noise, photon shot noise and ambient turbulent (assumed light) contribute to the noise levels. A detectable signature is clearly present in the width image and, with less clarity, in the velocity image. Figure 12 shows similar results for the higher elevation angle view. Here the velocity image is much clearer, presumably due to the broader spatial extent of the unidirectional line-of-sight motion as compared to the horizontal view.

A simulated trailing encounter with the wake of an L1011 aircraft in landing configuration in calm air is shown in Figures 13-15. Here the wake is seen at a 6° aspect angle. The longer (150 meter) pulse yields a relatively narrow spectrum (about 1 m/sec width). For these viewing conditions, a 12 db SNR is predicted for a 0.3 millijoule pulse. The spectral signature seen in Figure 14b is primarily due to the strong forward axial velocity in the vortex cores that obtains for this low-speed, high-drag configuration. Strong easily detectable signatures are obtained (Figure 15) in a dwell time of 3 sec with a mean laser power of 0.6 watts. In this dwell approximately 1 joule of laser energy intercepts the entire wake. Of this, about 0.25 joule intercepts the high axial velocity region (900 pulses in 6 lines-of-sight or 150 pulses per line-of-sight).

SUMMARY

Predicted detection performance depends on several parameters in addition to target wake and viewing platform geometry and mean laser output power including required angular scan area and sampling density, pulse SNR, pulse width, wavelength and ambient turbulence level. In general, four basic criteria should be satisfied to achieve an optimum design: pulse length should roughly match target length, pulse energy should yield a pulse SNR in the range of 0-6 db, the system bandwidth should match as closely as possible the signal bandwidth, and a processing algorithm should be selected to enhance the spatial and spectral pattern of the wake relative to the patterns of background noise or turbulence.

Although the high-velocity core regions represent a relatively small target, relatively dense spatial sampling can in principle be achieved with pulsed systems having high prf and low pulse energy as long as the search area can be suitably restricted. Although such a design provides the most direct sensing of the aerodynamic hazard, it imposes the greatest demand for laser resources and is most limited in search area. At lower prf or for large search areas the distributed lower velocity wake provides a larger, stronger target and is most appropriately detected and distinguished from ambient turbulence as a spatial pattern. A performance analysis of the type discussed in this paper can be used to compare these different design approaches as well as to predict absolute performance levels as a function of the instrument and operating scenario design.

Table 1. Vortex Wake Characteristics at 200 Meter Altitude

Aircraft	Speed (knots)	Core Diam. (m)	Wake Width (m)	Wake Length (km)	Center-line Velocity (m/s)	Core Tang. Velocity (m/s)	Core Axial Velocity (m/s)
B747	510	9.2	76	9.1	3.0	5.7	0.4
	255			4.6	5.9	11.4	3.0
	154			2.7	9.8	18.9	14.0
B737	510	4.4	36	5.5	1.9	3.7	0.2
	255			2.8	3.8	7.4	1.3
	154			1.7	6.4	12.3	5.9
C130	332	6.2	51	4.6	2.5	4.9	0.4
	166			2.3	5.1	9.8	3.5
	100			1.4	8.5	11.3	16.0
Cessna 182	162	2.0	16.5	0.93	1.3	2.4	0.2
	81			0.47	2.5	4.9	1.8
	48			0.28	4.4	8.5	8.9

Table 2. Processing Models

o Spectral thresholding

  - Set velocity threshold to eliminate atmospheric return
  - Choose wide bandwidth to capture high velocities
  - Limited by Doppler spectrum fluctuations (shot noise and speckle)
  - Limited to the energetic part of the wake

o Pattern Recognition (x,y)

  - mean velocity pattern in (x,y)
  - Doppler width pattern in (x,y)
  - processing by 2D or 3D matched filter
  - limited by atmospheric turbulence and shear patterns + speckle + shot
      noise
  - senses exterior wake region

o Wake Transport Prediction

  - lateral wind estimate, turbulence estimate
  - prediction of vortex locations vs time
  - prediction of vortex strengths vs time

Table 3. Depth of Field

λ (microns)	Aperture Diameter (m)	Range (km)	Depth of Field (m)
1	0.2	3	220
2			440
10			2200
1	0.2	1	22
2			44
10			220
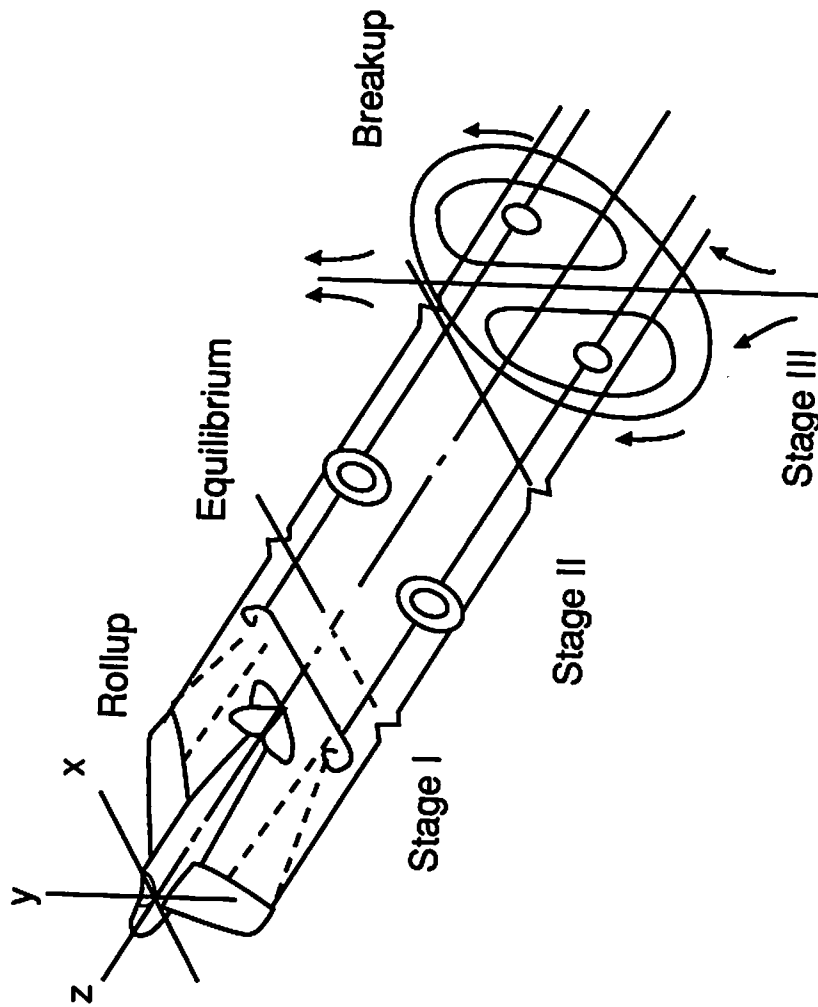
Figure 1. Stages in the development of the trailing vortex wake (Neilsen and Schwind 1944).
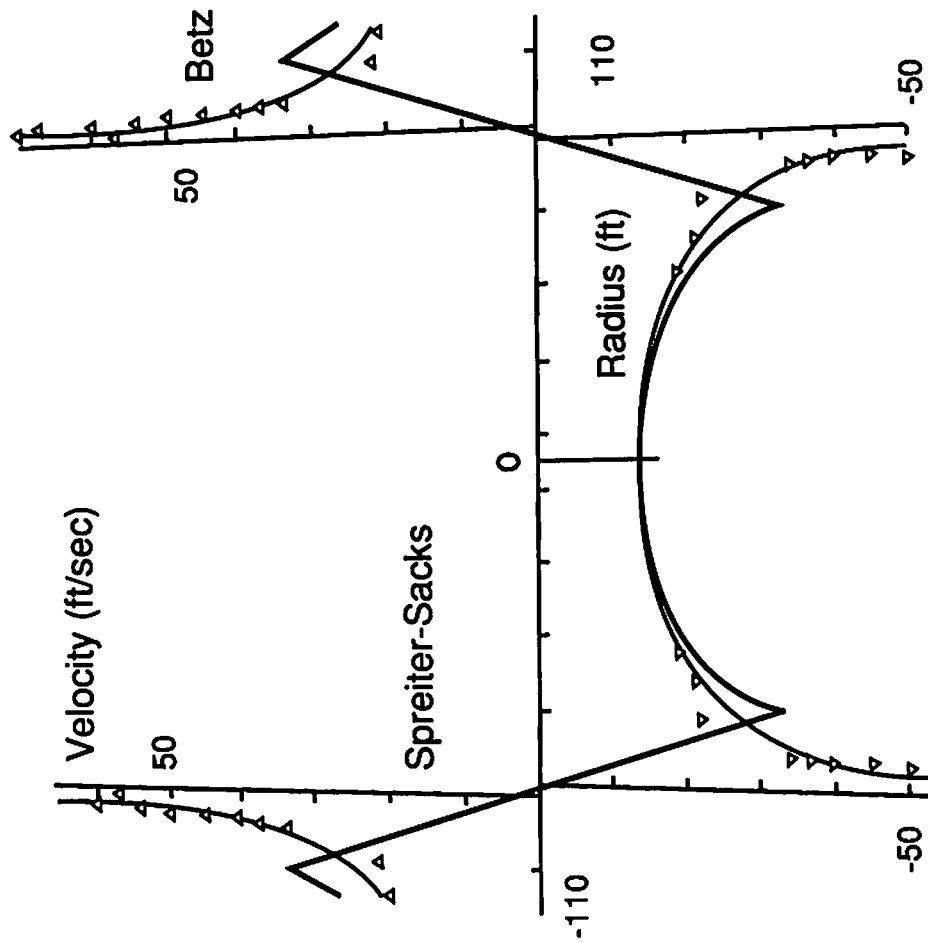
Figure 2. Vertical velocity across the midplane of the wake of a C5A compared to the Spreiter-Sacks model and the Betz model.
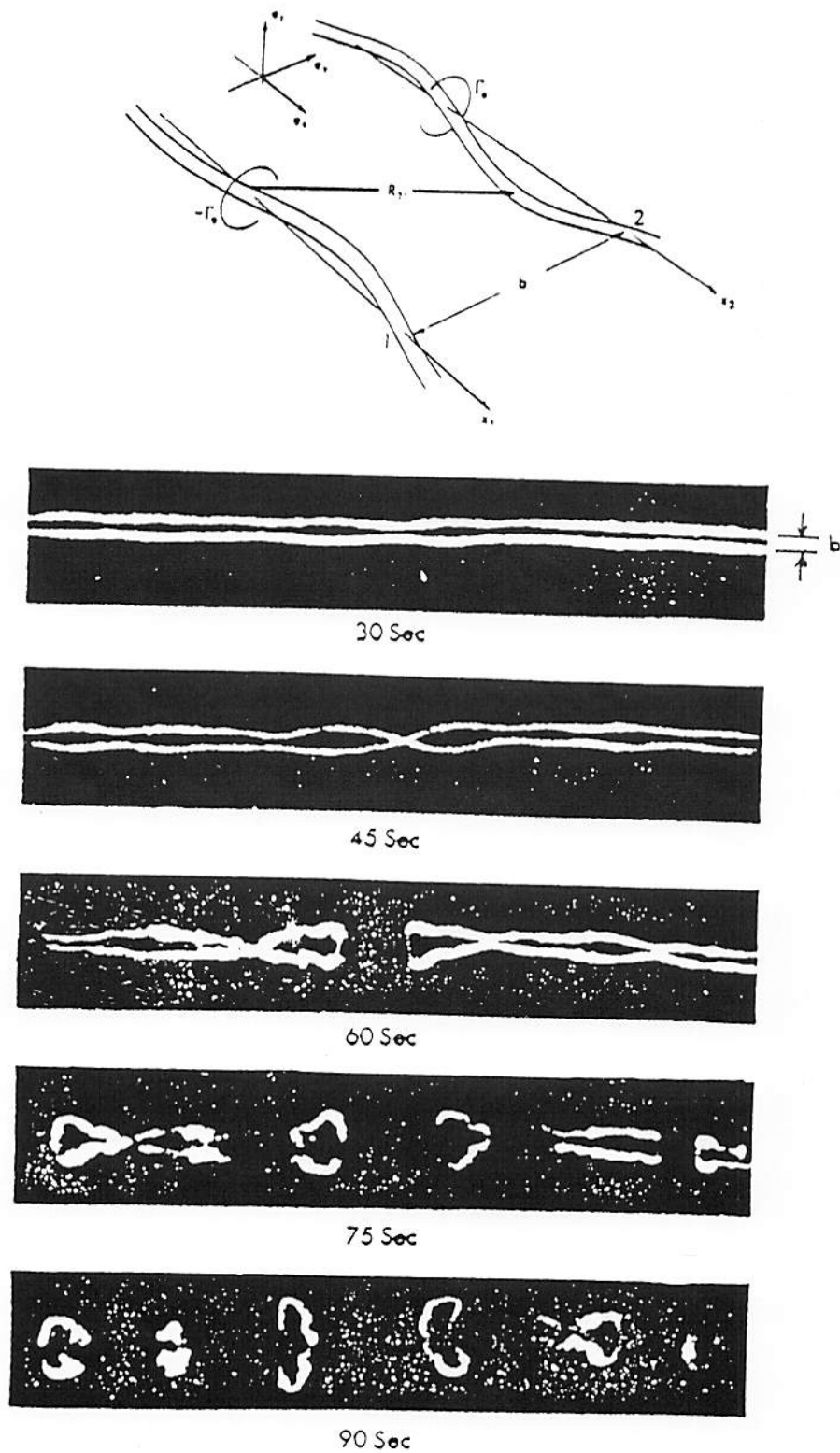
Figure 3. Crow linking instability. The photographs show the wake of a B-47, photographed with a camera aimed straight upwards. The time elapsed since passage of the aircraft appears under each picture (from Crow 1970).
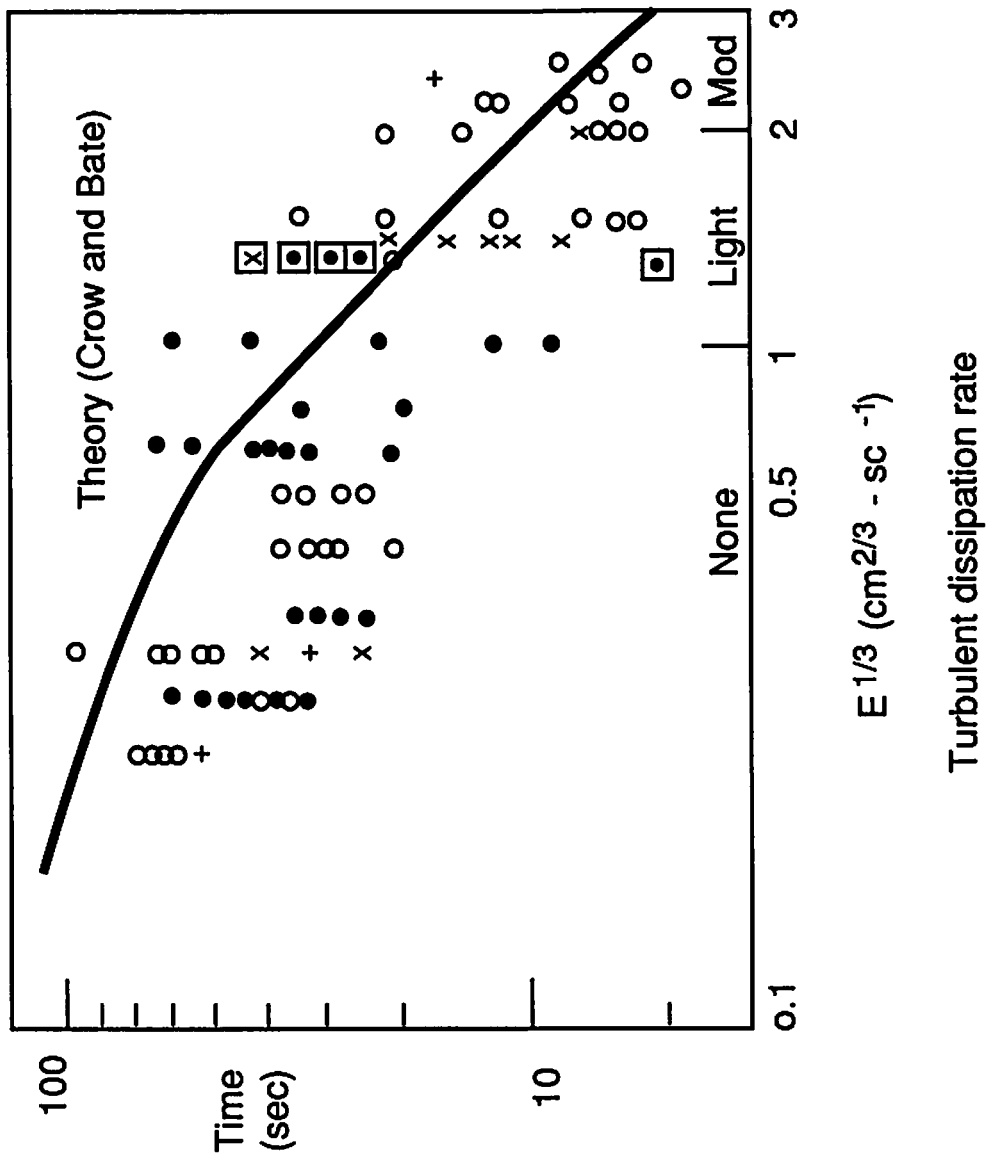
Figure 4. Time of wake breakup as a function of local turbulence level.
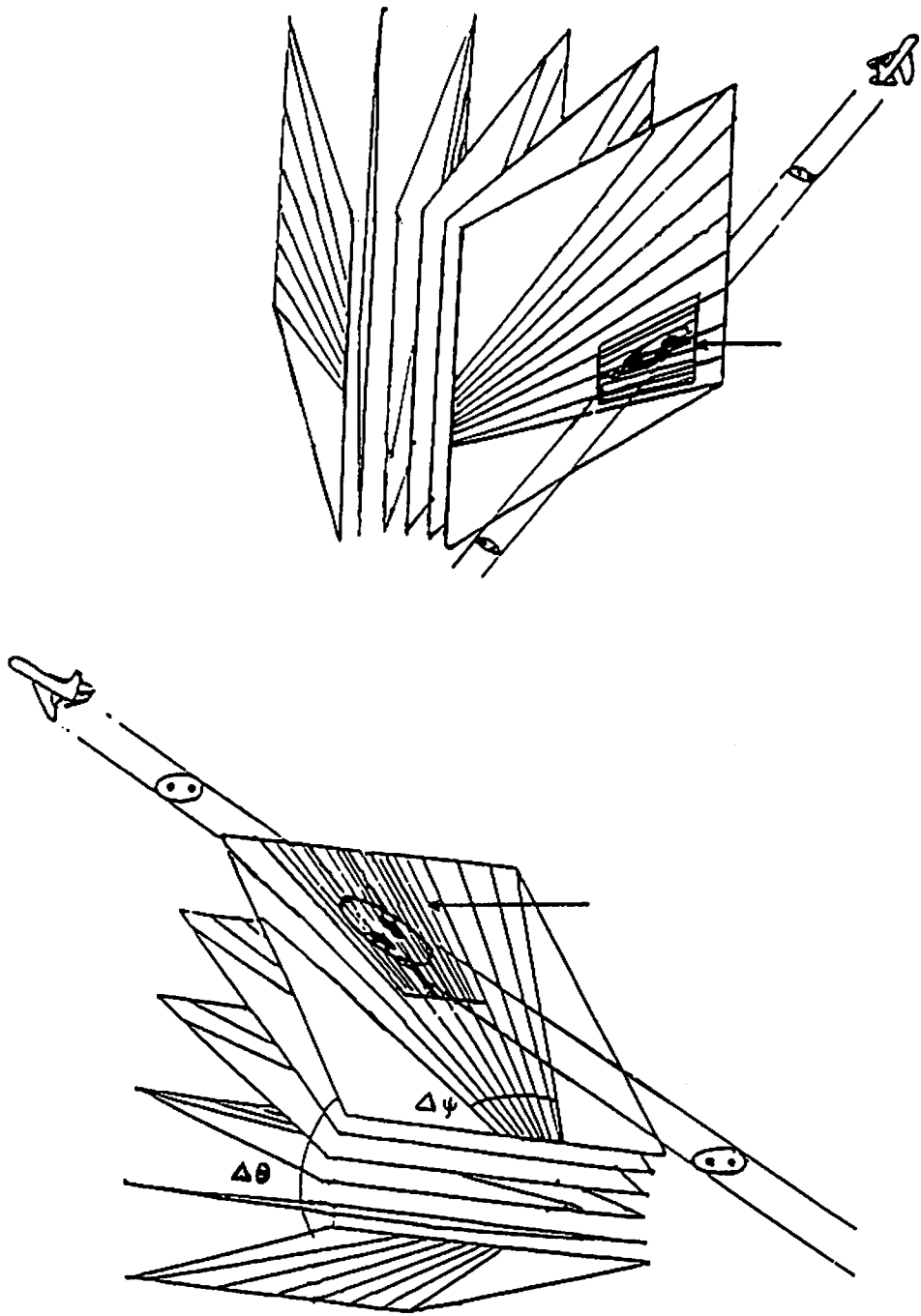
Figure 5. Scan geometries.
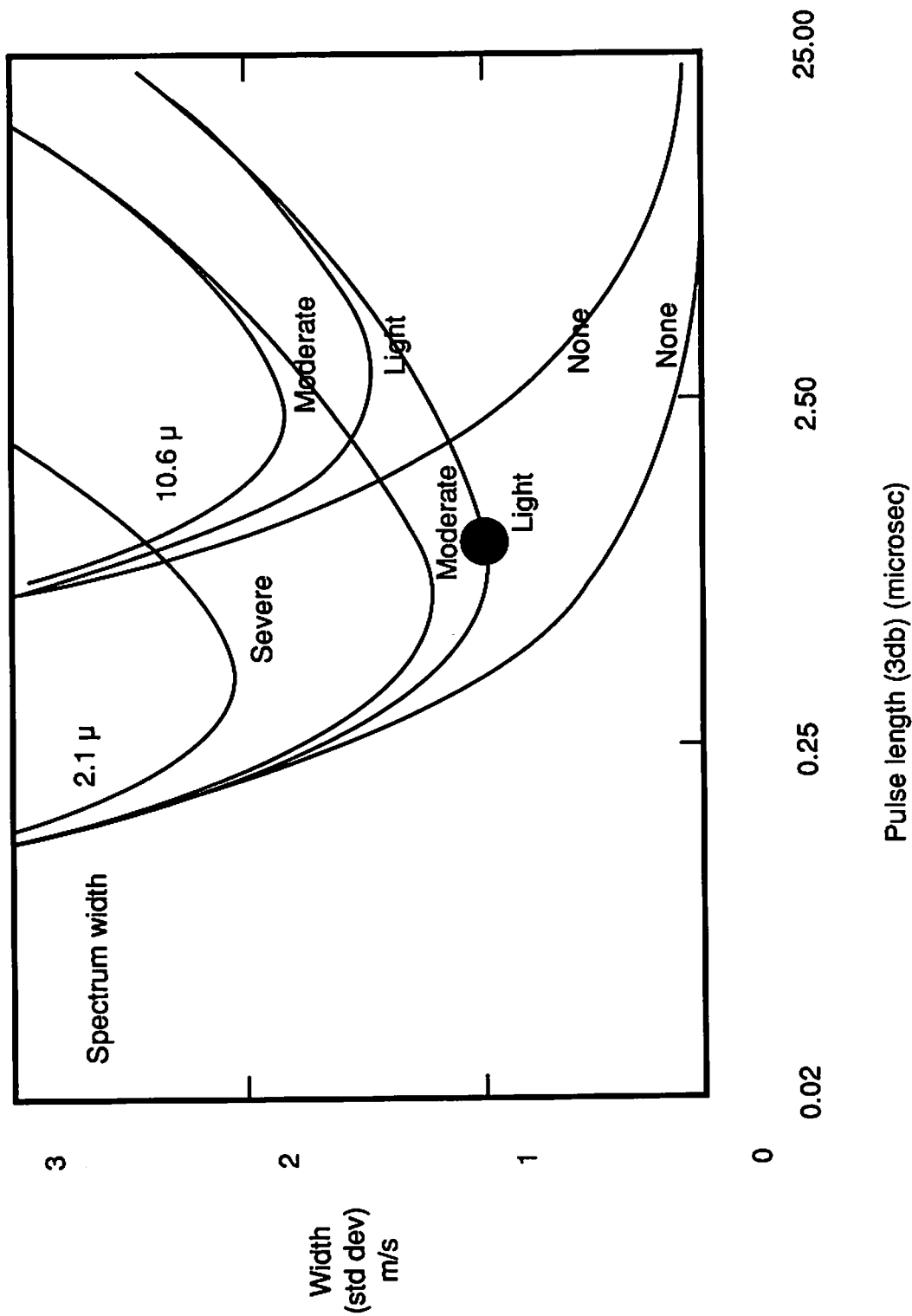
Figure 6. Spectrum width. The Doppler spectrum width can be minimized in the presence of turbulence by appropriate choice of pulse length. Smaller widths can be achieved at shorter wavelengths.
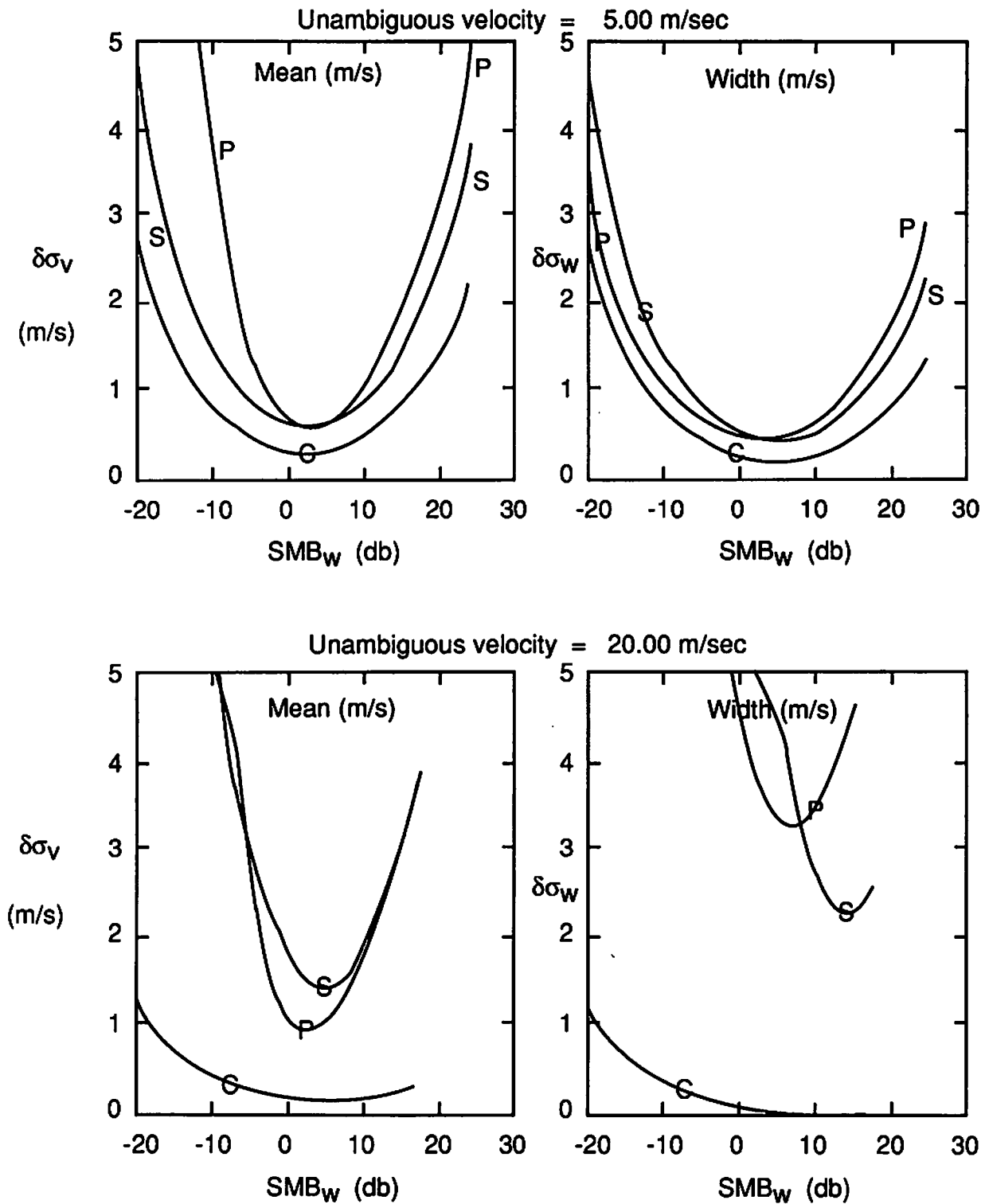
Figure 7. Net error standard deviations as a function of pulse energy for a given total laser energy transmitted. The minima of these curves define the pulse energy and prf that make optimal use of available laser power for a given system bandwidth. The different curves correspond to different pulse processing algorithms: P = pulse pair, S = spectral moment, C = Cramer-Rao lower bound. The upper panels are for a ratio of signal bandwidth to system bandwidth = 0.25 and the lower pair = 0.05.
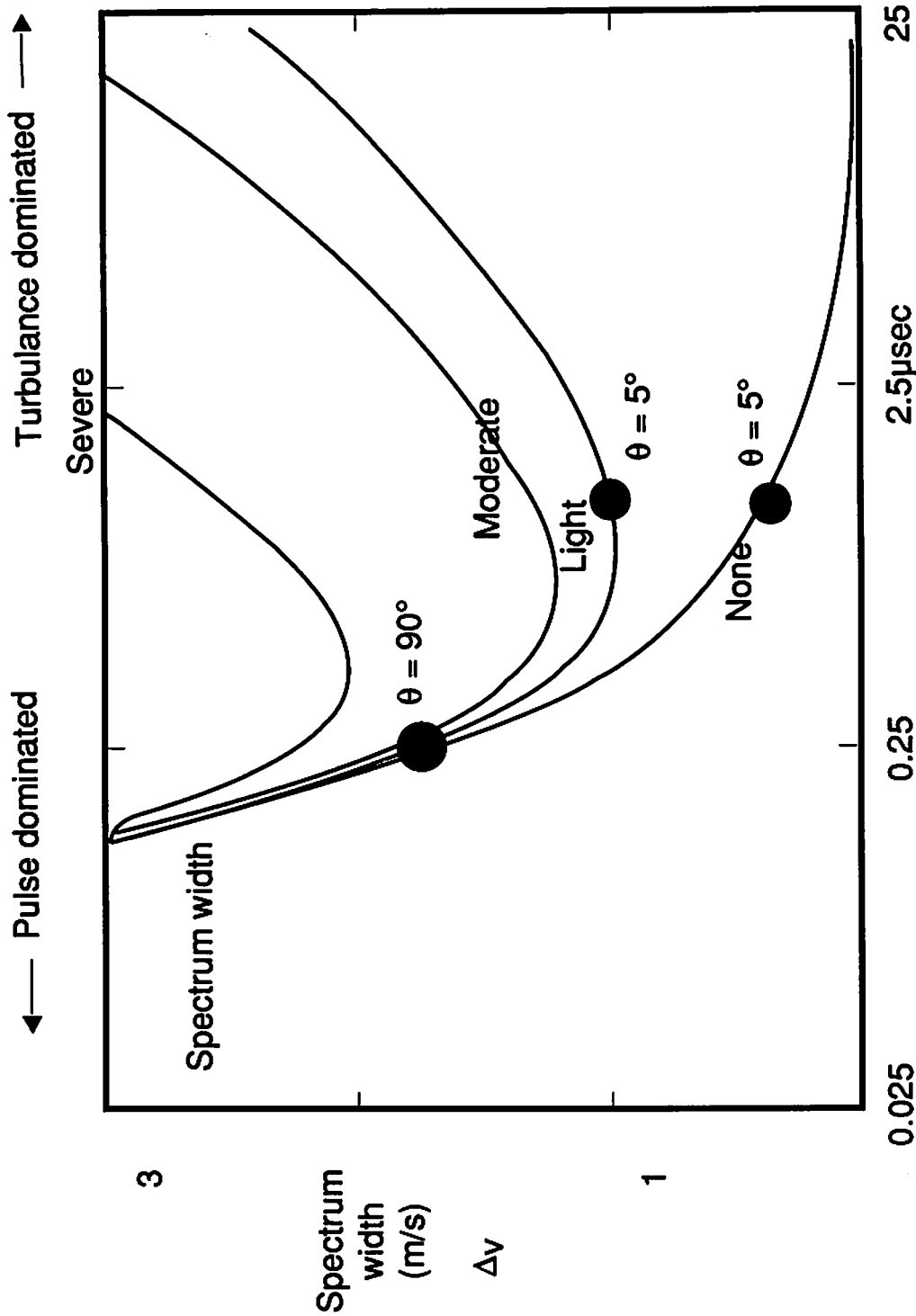
Figure 8. Pulse length should be selected to match the target range dimension. The Doppler spectrum is dominated by the pulse length for a 0.25 microsecond (3 db width) except in moderate to severe turbulence for a perpendicular look. At a 5 degree aspect with a pulse length = 1.25 microseconds, turbulence broadening dominates (light turbulence, dissipation = 0.0033 m²/sec³).
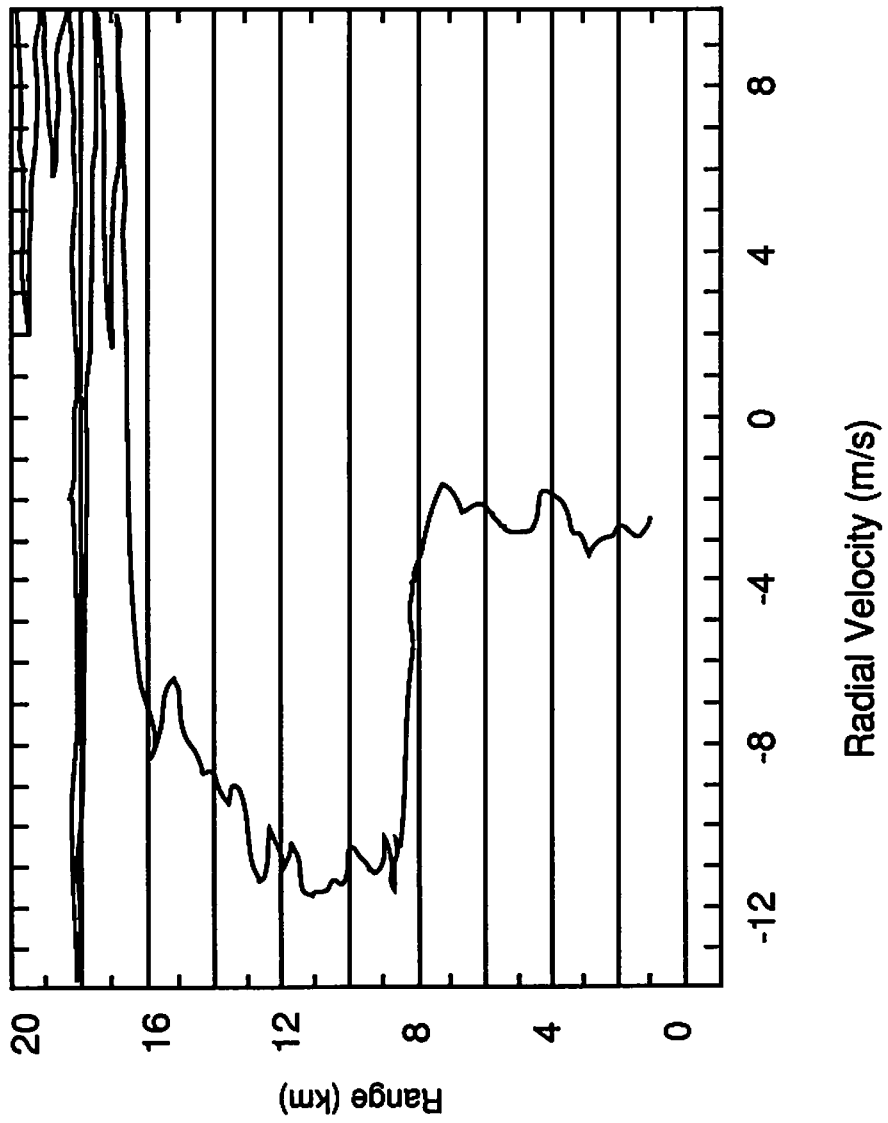
Figure 9. Winds measured with the Tm,Ho:YAG lidar showing a strong gust.

0.7 millijoule pulse, 37 meter width
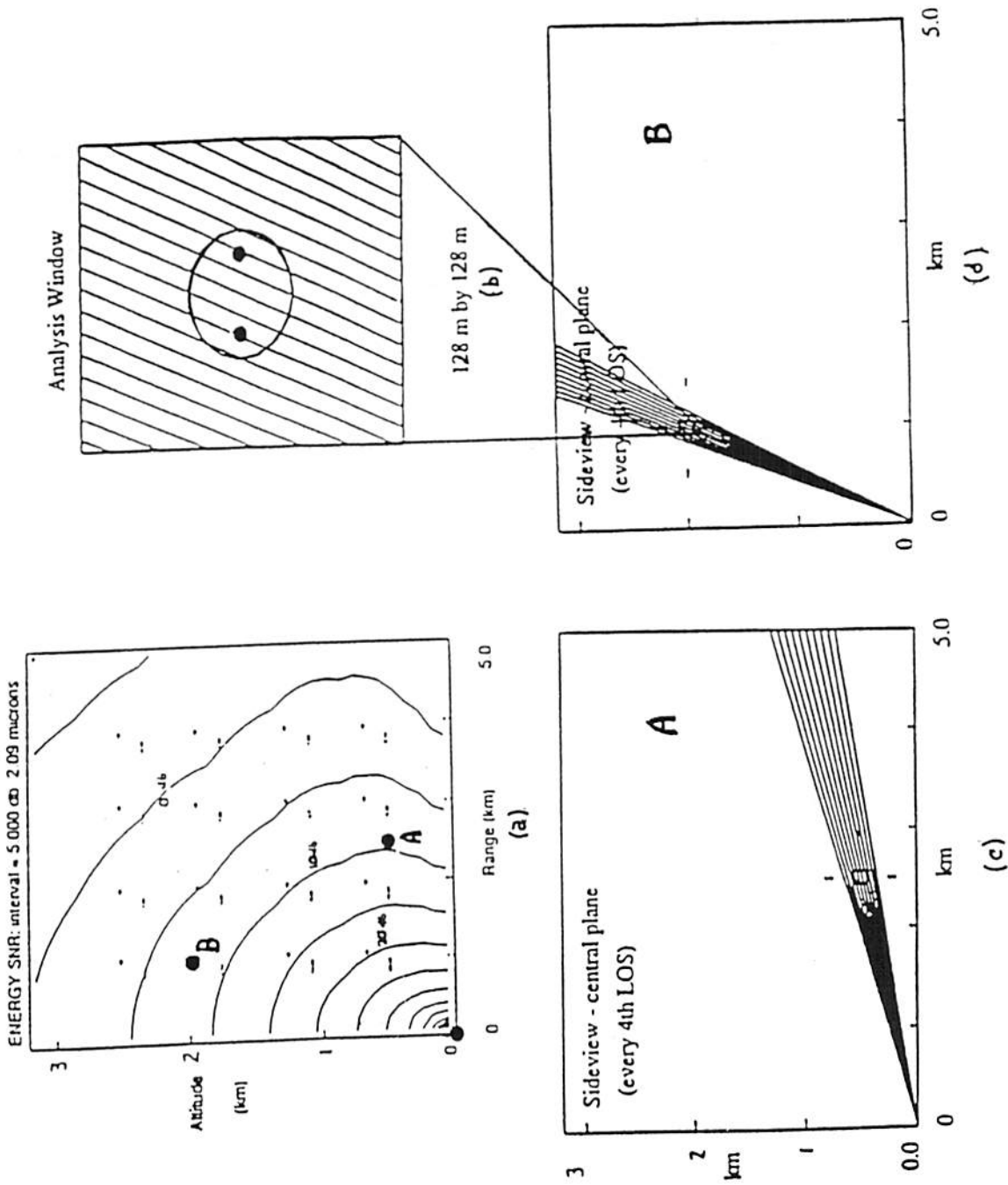
Figure 10. Ground-based measurement geometry. Panel (a) shows the signal to noise expected as a function of wake location (0.7 millijoule pulse, 2.09 microns, midlatitude summer atmosphere). The other panels show the lidar lines of sight and the simulation analysis window for a low and a high elevation angle flyby geometry.
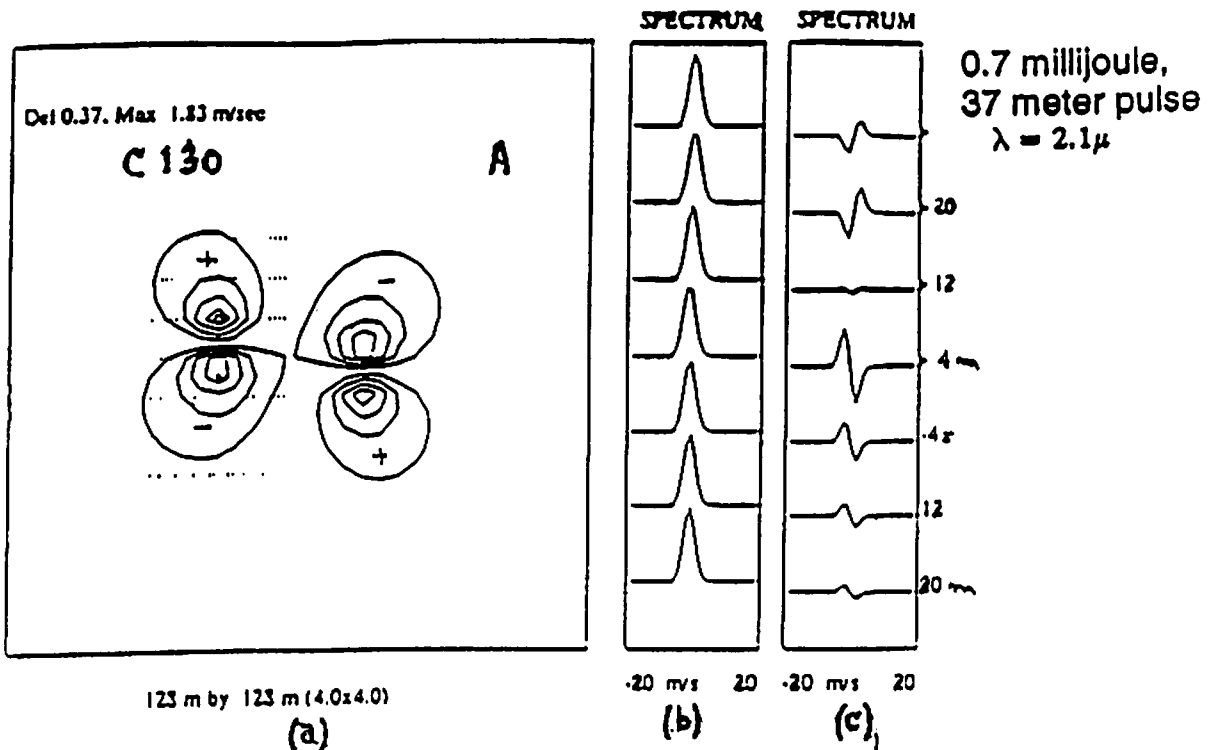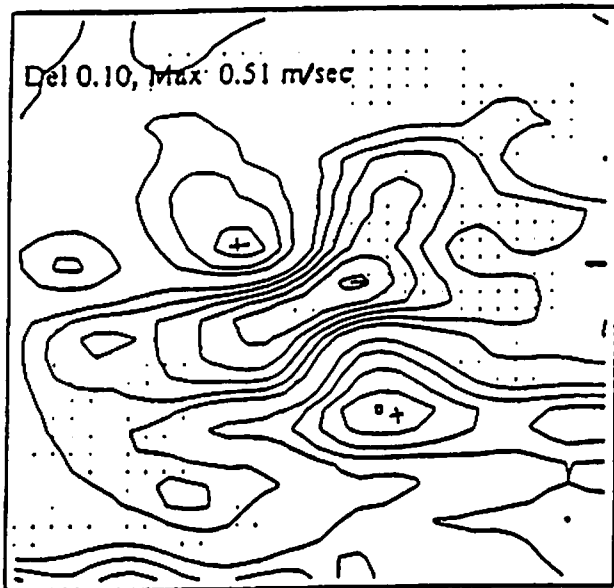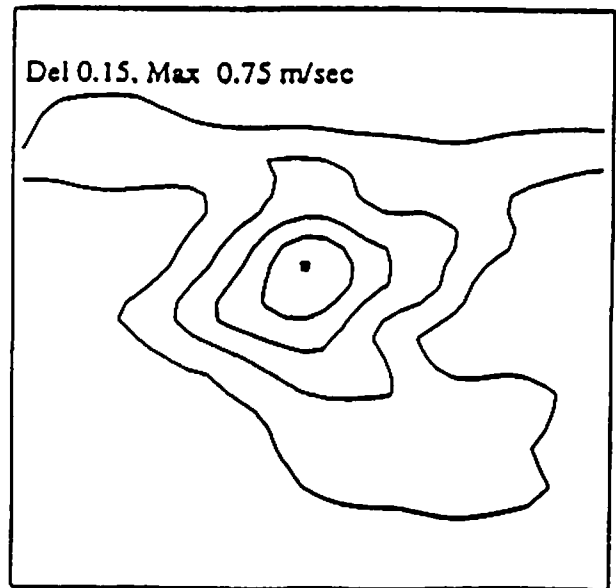
Figure 11. Predicted signatures for a C130 aircraft at 100m/sec flight speed, low elevation view, 90 pulse average.
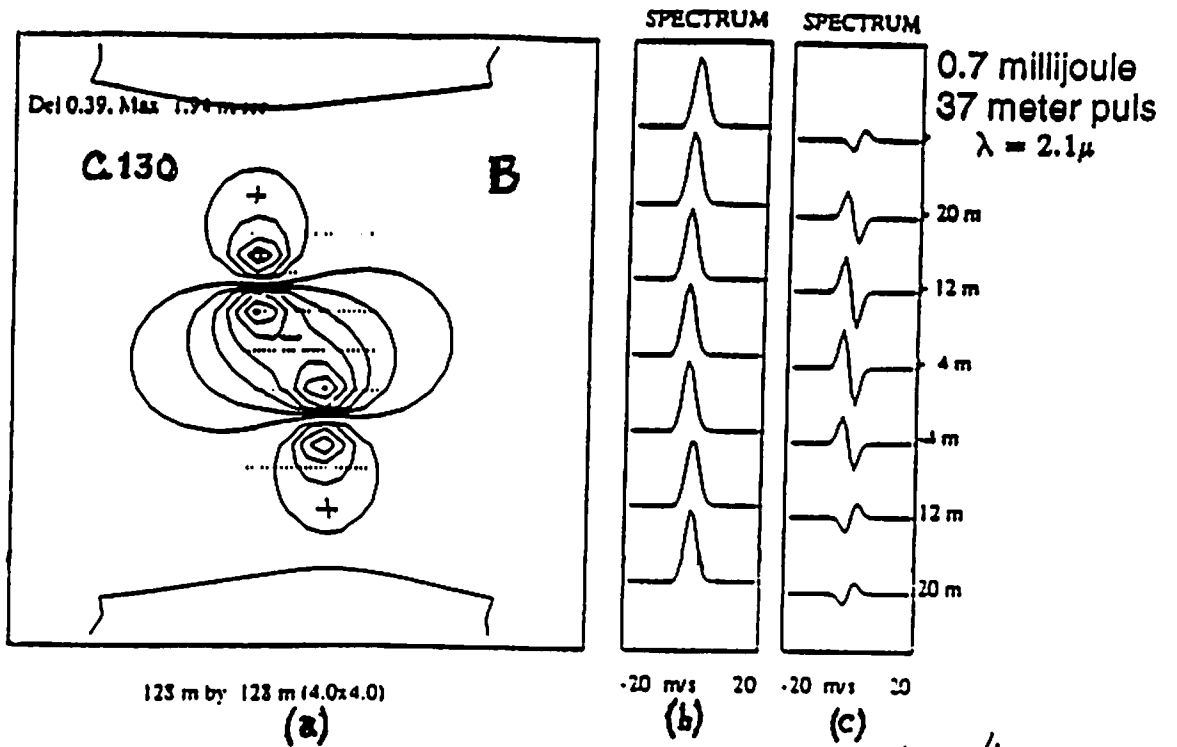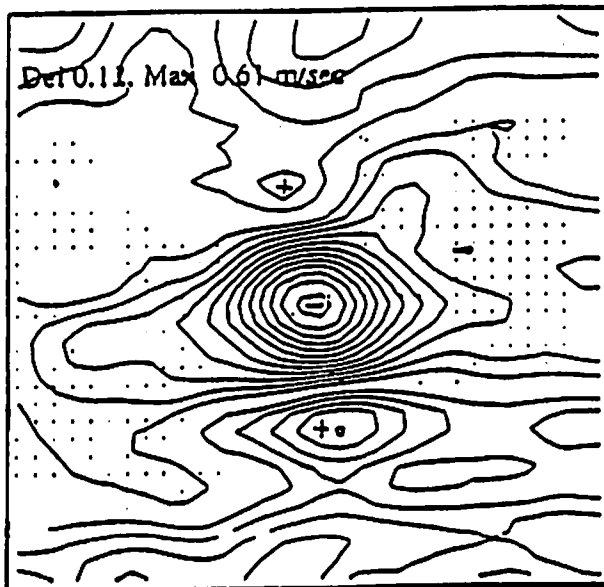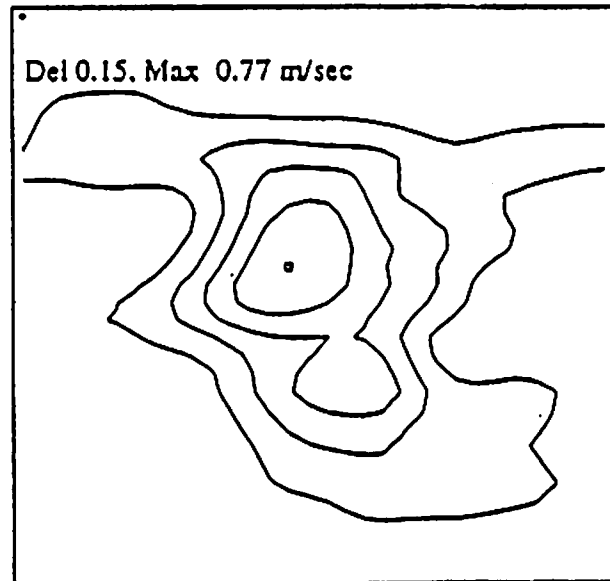
Figure 12. Predicted signatures for a C130 aircraft at 100m/sec flight speed, high elevation view, 90 pulse average.
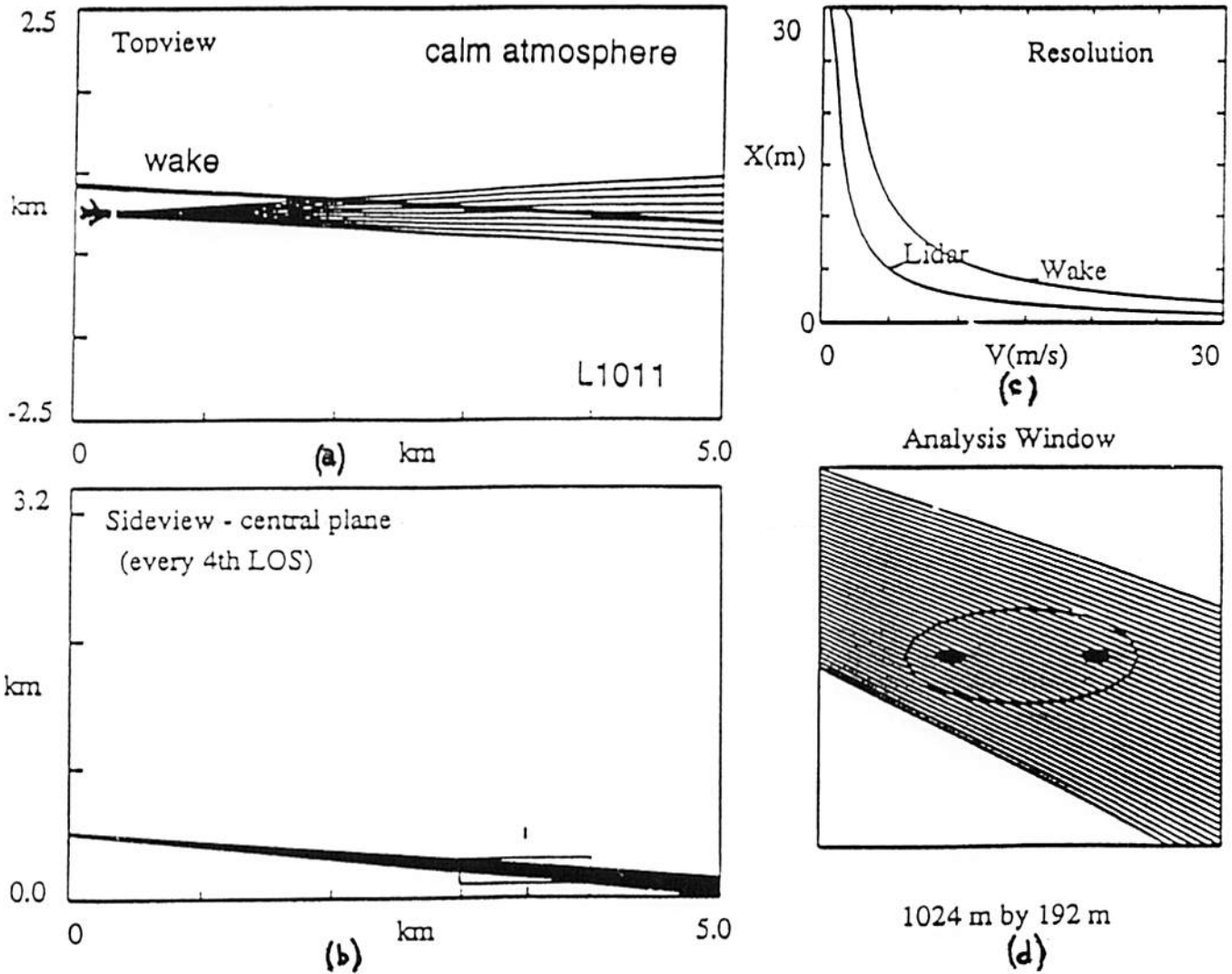
Figure 13. Trailing view geometry. Wake of an L1011 aircraft observed at a mean view aspect of 5.7 degrees.
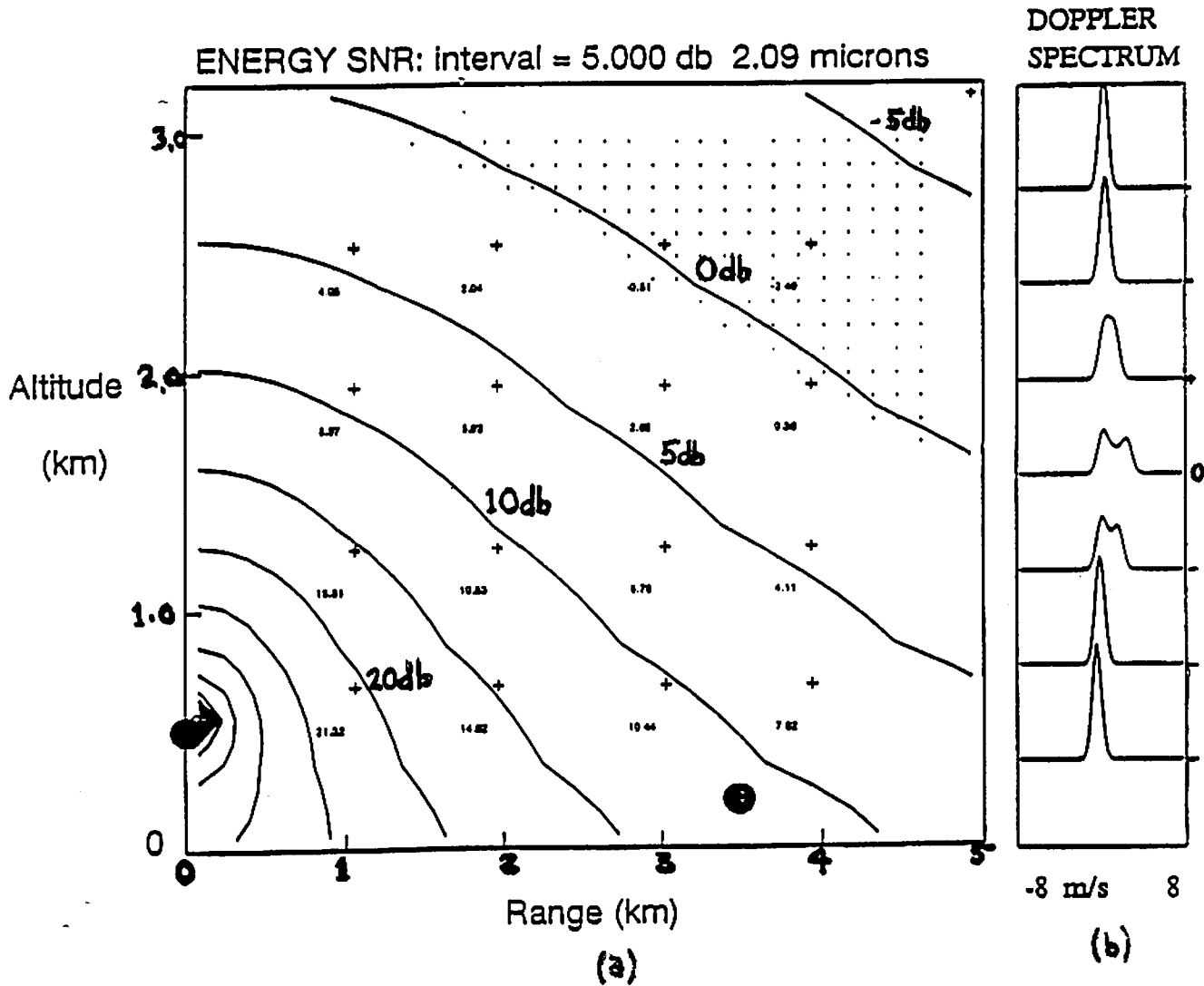
Figure 14. Expected signal to noise for an L1011 aircraft at 200 meter altitude. Lidar at 500 meters altitude, 5.7 degrees viewing aspect, 0.3 millijoule/1 microsecond pulse, calm atmosphere, wavelength = 2.09 microns.

VELOCITY (max 0.83 m/s)   WIDTH (max 0.40 m/s)

Del 0.17, Max 0.83 m/sec   Del 0.08, Max 0.40 m/sec

| 192 m

———————— 2048 m ————————

MATCHED FILTER OUTPUT (2048 m by 192 m)

(a)   (b)

VELOCITY (19.27 db)   DELTA WIDTH (16.77 db)

Del 1.84, Max 9.21 sigma   Del 1.38, Max 6.90 sigma

(c)   (d)
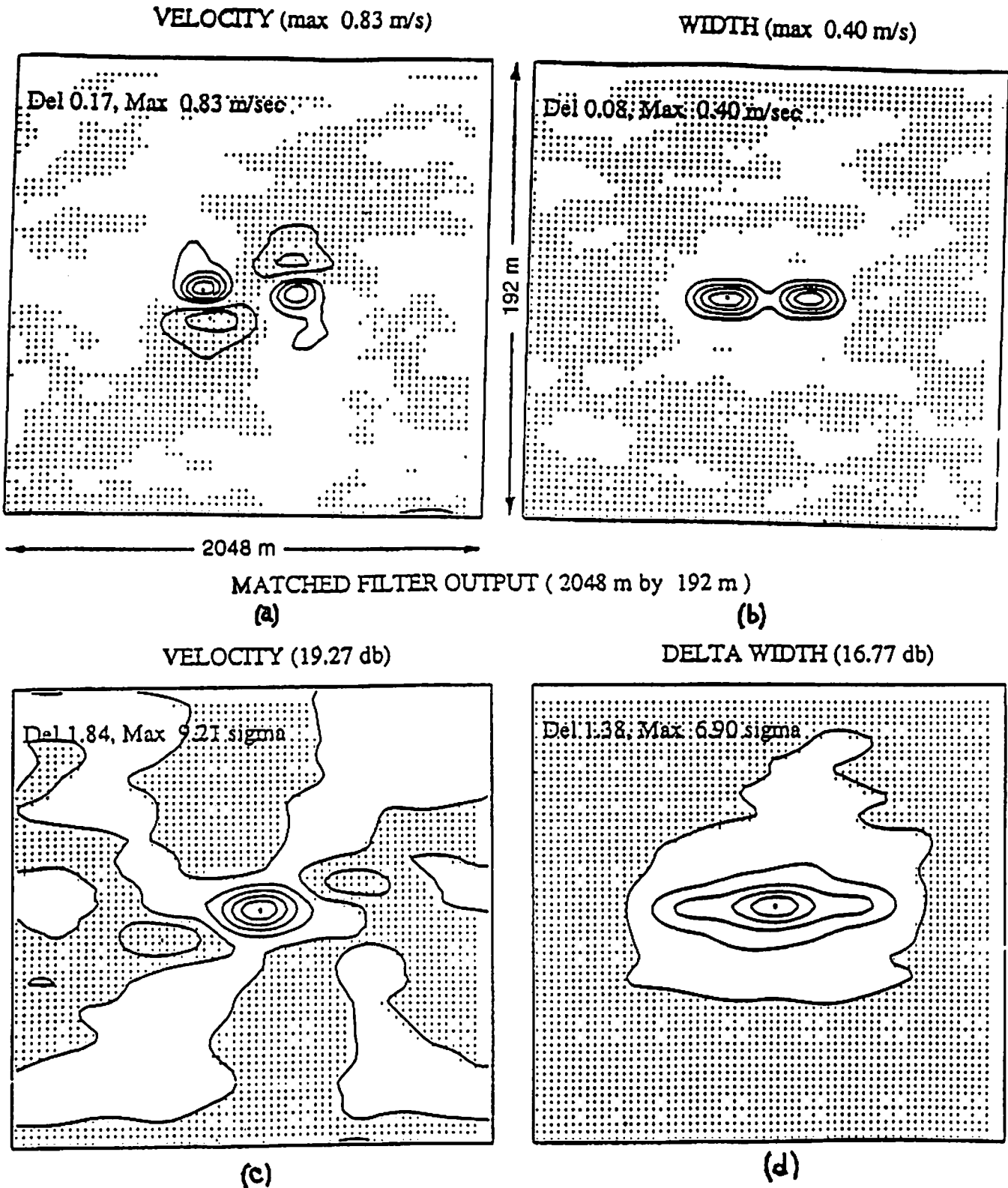
Figure 15. Predicted signatures for an L1011 aircraft, 0,3 millijoule, 1 microsecond pulse, calm atmosphere, 150 pulse average, prf = 2000 per second, total dwell = 3 seconds, 0.5 watts mean power, wavelength = 2.09 microns.

42-26

REFERENCES

1. C. duP. Donaldson and A.J. Bilanin, "Vortex Wakes of Conventional Aircraft," AGARDograph No. 304, (1975).

2. J.N. Neilson and R.G. Schwind, "Decay of a vortex pair behind an aircraft," in "Aircraft Wake Turbulence and its Detection," Olsen and Goldberg, ed., Plenum Press, P. 413, (1971).

3. S.C. Crow, "Stability theory for a pair of trailing vortices," AIAA Journal 8, 2171 (1970).

4. I.H. Tombach, "Observation of atmospheric effects on vortex wake behavior," J.Aircraft 10, 641 (1973).

5. S.C. Crow and E.R. Bate, Jr., "Lifespan of vortices in a turbulent atmosphere," J. Aircraft 13, 476 (1976).

6. J.R. Spreiter and A.H. Sacks, "The rolling up of the trailing vortex sheet and its effect on the downwash behind wings," NACA.

7. A. Betz, "Behavior of vortex systems," NACA TM 713 (trans. from Zeitschrift fur angewandte mathematik und mechanik," 12, Jumw (1932), XII.3, June (1933).

8. T. Berger and H.H. Groginski "Estimation of spectral moments of pulse trains," Int. Conf. Inf. Theory, (1973).

9. R. J. Doviak and D.S. Zrnic "Doppler Radar and Weather Observations," Academic Press, Chapter 6, (1984).

10. S. W. Henderson, C.P. Hale, J. R. Magee. M. J. Kavaya, and A.V. Huffaker, "Eyesafe coherent laser radar system at 2.1 micron using Tm,Ho:YAG lasers," Optics Letters, 16, #10, p773-775 (1991).
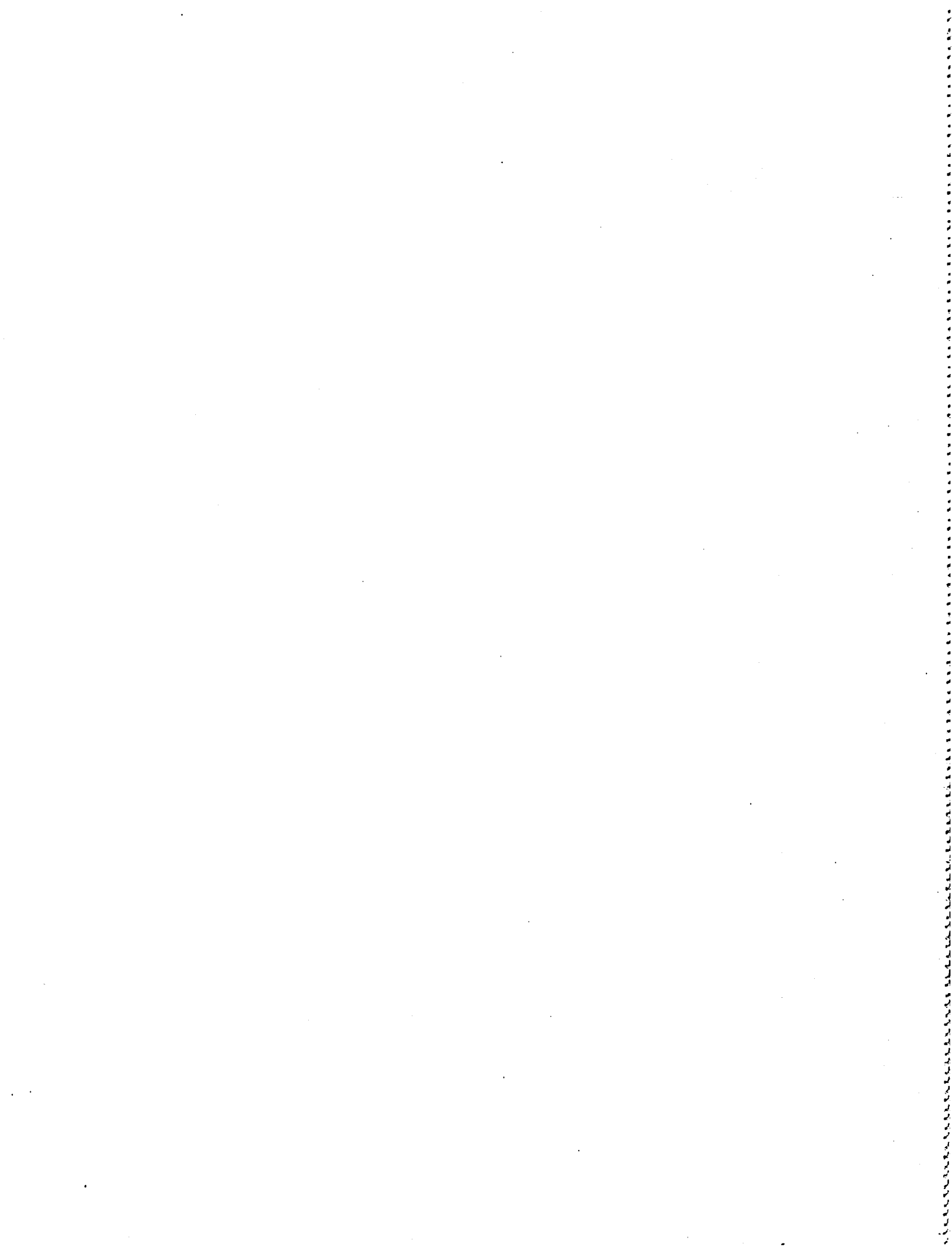
INFRARED AIRBORNE AND GROUND DETECTION OF WAKE VORTICES

H. Patrick Adamson
Charles F. Morrison
TURBULENCE PREDICTION SYSTEMS
3131 Indian Road
Boulder, CO 80301

ABSTRACT

Considerable study of aircraft wake vortices has resulted in a large database on these events. However, little useful data exists for the Infrared (IR) community to study. This paper will assess the feasibility and practicality of Infrared detection of these events. The method will be described. The modelling and field data will be presented. The conclusion is that a dedicated program consisting of additional modelling along with a field data collection program is warranted.

INFRARED METHODOLOGY

Infrared and the detection of wake vortices:

If the wake vortex associated with an aircraft involves air temperature changes, or significant increases of density, carbon dioxide, or water partial pressure, it is possible to sense the presence of the wake vortex with a passive infrared system. Because of our work with precision IR equipment for aircraft safety use, we wished to see if wake vortex phenomena could be detected with our present equipment.

DATA IN THE LITERATURE

Temperatures associated with Aircraft Vortices:

The temperature measurements made by A. J. Bedard, Jr. (Ref.1) of the NOAA/ERL Wave Propagation Laboratory in 1982-83 helped our interest in wake vortices. These measurements included air temperature measurements taken at various heights on a 1000 foot instrumented tower, with a C130 making 170 knot flybys at 700 to 1000 feet AGL, laterally displaced from

tower, with a C130 making 170 knot flybys at 700 to 1000 feet AGL, laterally displaced from the tower. See Figure 1. In order to obtain air motion and temperature measurements at the tower, it proved necessary to have a horizontal cross-wind from the aircraft path to the tower. The measurements indicated interesting air temperature patterns that were blown to the tower. These were of sufficient amplitude that the infrared would be able to sense the wake vortex, and from considerable distance.

The theoretical work by George Greene of NASA (Ref.2) helped us with a number of concepts as to what our measurements might mean when we looked at the wake vortex of a large aircraft. His models provided sizes and shapes for the computer models that we planned. The scanning of the earlier literature showed many considerations, but little agreement on the phenomena that we might expect as we measured the infrared signal from these events.

CONCERNS NOT ANSWERED IN THE LITERATURE

Thermal suggestions in theoretical studies:

The thermal nature of the wake vortex was not well defined in spite of considerable literature. It is not clear if it was warmer or cooler than ambient. Did it contain the exhaust from the engines, such that there was a net heating, or was it only the pattern of air flow from the wings which might be quite cool relative to ambient? Was it a mixture, or was it in layers? The majority of the available measurements did not involve sufficient thermal data to provide certainty as to what one might see with IR. The more we read, the less certain we were of what was truly there.

Data not readily available:

Our attempts to learn from the data generated by the most recent government studies (flybys of Boeing 757 and 767 in Utah) was most unproductive. As a result, we felt that we would need to make our own IR field measurements. Our major interests were relative to takeoffs and landings. There was concern that tower flyby information was not descriptive of these airport operations. There was certainly a need for more information and study.

THE EFFORT AND FUTURE OF THE WORK

The original intent was to create a simplified wake vortex model. Then the AWAS performance would be studied using this simplified wake vortex model and our present computer modelling programs (LOWTRAN/TPS).

We would then go to the field and collect data and compare this data with the computer modelled data. If the results suggested this effort was a reasonable way to detect aircraft induced wake vortices, then the intent was to present this work to the community.

If sufficient interest is generated, we would like to continue this effort with an expanded program.

AIRBORNE:

Our equipment is presently installed on a number of commercial aircraft (3 MD80s and 2 DC9-30s) as a forward looking detection system for low level windshear events (LLWS) and clear air turbulence (CAT). See Figure 2. This shows the use of IR for the prediction of both CAT and LLWS events. It might be possible to provide updated software on the aircraft to also give advance warning of wake vortices remaining from previous aircraft.

GROUND BASED:

It is desirable to establish the usefulness of such a ground based system at airports. It might be possible to add such equipment to the existing suite of sensors at airports to provide assurance that approaches and runways were free of vortices.

MODELLING THE PROBLEM (LOWTRAN/TPS)

Looking up the glide path during the landing:

This was a reasonable view to establish in the computer model. Thus, this was chosen first. Figure 3 shows this arrangement. The lower optical system was aimed at 3 degrees, such that the 2 to 4 degree region was monitored. The upper optical system then was aimed 2 degrees higher, covering the 4 to 6 degree elevation. Between these two optical systems it was thus possible to cover the 2 to 6 degree region in these first measurements from about 2000 meters ($\sim$ 1.2 mile) beyond the end of the runway.

Looking down the runway:

The second choice was that of looking down the runway, for here there could be dangerous effects also. However, here there was even less data upon which to base a computer model. Did the vortex slide down onto the runway? Was it destroyed by contact with the ground? Did it provide a runway hazard for later landings? This choice will be studied later.

Looking across the runway:

The third choice of looking across the runway was complicated, in part because the look distances of the present AWASIII are long. The instrument would sense from distances beyond the runway, and thus not provide a clear picture of the wake vortices. Wavelengths could be chosen that would not look so far and be applicable to only the runway. This choice will be studied later.

Aspects of a Computer Model:

In order to provide a reasonable computer model of the wake vortex by looking up the glide angle, many simplifications and definitions had to be made.

Core Temperature:

From conversations with George Greene, it is assumed that there was a cold center core to the vortex. Computations were done with the cold core. However, they were repeated with a hot center core, as an alternative, but these are not shown in the figures, for they provided nothing different in magnitude.

Delta temperature:

The difference in temperature between the cold core and the ambient air was assumed to be 10 degrees C.. This was rather arbitrary, but was based upon the measurements that were available.

Diameter:

The diameter of the center core of the individual vortices was an item of some discussion. We had recommendations of from 1 to 10 meters (3.3 to 33 feet) for that dimension. Thus, the model was calculated with a 10 meter case, and a 1 meter case.

Length:

The length of the volume of air providing input to the IR system was about 8 miles, the distance traveled by the landing aircraft in 3 minutes, at 140 knots. The volume had a square cross section that was 2 degrees wide.

Lifetime:

The lifetime of the vortex was considered to be 3 minutes, for that seemed about average for the cases reported. It is appreciated that these parameters are only approximate, and that a wide range of values may pertain with different aircraft and weather conditions.

Composition:

The composition of the gas in the volume providing IR light to the AWAS in the computer model was air that was free of exhaust from the engines. This was the gas composition provided by LOWTRAN6, the Air Force atmospheric model.

Outer layer:

The vortex is considered to have an outer layer of rotating air, but this is assumed to have an ambient temperature.

Hot exhaust behavior:

It is not clear among the theoretical models of the wake vortex what happens to the exhaust gas. It is possible that this rises while the wake is driven downward.

Model Simplifications:

These are the further simplifications implied in the computer models.

Wake is stationary horizontally and vertically:

Even though we expect that the wake will move forward, and will probably sink in the ambient air, we do not know these functions in terms of the aircraft type, and the weather. Thus, rather than guess further, we have chosen to leave the wake stationary both horizontally and vertically after its formation in the computer model.

Temperature decay is linear with time over life:

The mechanism of temperature decay does not seem clear cut in the available literature, nor does it's time function. Thus, we have opted to assume a linear decay with time over the life of the event.

INITIAL CONDITIONS

The conditions for the start of the IR study commence with the aircraft passing overhead. Immediately after the aircraft passes over, the model assumes a near wake temperature of -10 degrees C. below the ambient temperature. At this same time, it is assumed that the far wake, which is 8 miles back up the flight path, is at ambient temperature there.

The temperature between the near wake and the far wake are given a linear relationship for the computer model. As time goes by, the ambient temperature moves down the flight path toward the sensor, and the near wake temperature decreases linearly toward ambient. At 180 seconds, the entire path is ambient, as it was prior to the aircraft landing.

The model is run with 14 and 15 micron wavelengths, and these wavelengths are sensitive to both carbon dioxide and water vapor. The AWASIII uses these wavelengths in other functions. In addition, the model has been run in 18 and 20 micron wavelengths. Here, only the water vapor is a contributor to the signals.

The composition of the atmosphere and the distribution with altitude are factors of LOWTRAN6. The lapse rates are a function of the mid-latitude summer profile (2 degree C./1000 feet).

The aircraft landing profile is assumed to be the standard 3 degree glideslope, with a velocity of 140 knots.

The infrared behavior of the AWAS III instrument is also programmed into the model (TPS model).

The IR spectrometer alternates from one wavelength to the other, and the signal is the difference in detector output between the detector responses at the two wavelengths. This system has worked very well in conjunction with interpretive algorithms for use in predicting both low level windshear at takeoff and landing, and for clear air turbulence at altitudes above 15,000 feet.

Sample ambient conditions assume no wake situation, and provide a baseline.

MODELLING RESULTS

Explanation of figures:

Figure 4 shows the results data from the computer model with 10 meter (33 foot) diameter column and the 14 and 15 micron wavelengths. When the entire vortex is visible to AWASIII, the temperature is shown with the two wavelengths. The signal decreases over 180 seconds, back to ambient. This figure indicates that the expected temperature drop sensed by the AWASIII would be three degrees C. (the difference between the sensed temperatures for 14 and 15 microns respectively). Note also that the individual wavelengths record the -10C. vortex as it passes by the site.

Figure 5 shows the 10 meter diameter column with the 18 and 20 micron wavelengths. Here the values are somewhat smaller, and the temperature difference between the two wavelengths is quite small. However, this difference is still at a detectable level.

Figure 6 illustrates the computer model with the 1 meter (3.3 feet) vortex core. The total temperature change is less than with the larger volume for the 14 and 15 micron signals, but the difference between the temperature signals for these wavelengths is larger.

IR can detect wake temperature effects:

In each of these cases, the computer model indicates that a significant difference exists between the power received at these IR wavelengths to provide an AWAS signal for the detection of the wake vortex.

The question that must be answered experimentally is that of the atmospheric noise at these wavelengths. Does the wake vortex create a signal larger than the noise, or a signal with a sufficiently different characteristic than the noise? If one of these requirements is met, then the AWAS may be an effective sensor of wake vortices. A field data collection program can answer these questions.

FIELD DATA COLLECTION

An initial measurement at a commercial airport:

A practical approach was to study the problem from the ground. It is possible to establish a program that would gather ground based data using the AWASIII at an airport. The airport chosen was Stapleton in Denver, Colorado. Here there was an area beyond the end of several of the runways where our equipment could be mounted for initial measurements.

The best view was that looking up the landing corridor. This was the same as our computer model. Figure 7 shows the experimental arrangement. The AWAS has two detectors (each detector has a two degree square field of view) and detector 1 is two degrees lower than detector 2 in the vertical plane. The lower detector would ideally have been aimed at 3 degrees, such that the 2 to 4 degree region was monitored. The upper detector would then be 2 degrees higher, covering the 4 to 6 degree elevation. Between these two detectors it should be possible to observe the 2 to 6 degree region in these first measurements.

However, the first experimental location of AWAS was about one mile beyond the end of the runway, and it proved necessary to use a greater look up angle to cover a portion of the flight path and the region below it.

The setup of this first test was quite crude, and the AWAS was aimed up at an angle of 10 degrees. As can be seen in Figure 8, this provided observation of a rather short region of the flight path and the volume below.

Power for the field system equipment was provided by a small gasoline generator. A laptop computer recorded the data from the AWAS. We included a video camera which recorded each flight and the operators comments on the second day. A time marker was recorded as each aircraft passed directly overhead. We concluded that a very careful setup is needed for future data taking.

Initial Measurements With AWAS:

One set of AWAS measurements was made on 10/22/91 on a 78 degree F (25C.), 18% humidity day, in the absence of clouds, beyond the east/west runway at Stapleton Airport in Denver. The AWAS was located one mile from the end of the runway. The altitude of the landing aircraft was 250 to 300 feet AGL at that location. No large widebody aircraft were observed.

The second set of AWAS measurements was made on 10/24/91 on a 40 degree F (8C.), variable temperature day with 80% humidity, and with heavy clouds moving cross field at relatively high wind velocity. Both sets of data were recorded from the same location. It was very difficult to interpret the data in real time at the site. To study the response, it was necessary to plot the data with some filtering. Data was taken each 2 seconds, and that shown in the following figures has been subjected to an 8 second running average. The long term temperature mean has been subtracted to provide a zero value for the data. Thus zero on the y axis does not mean zero degrees C.. The data plotted represents the change in temperature as the vortex was observed.

There is a decreasing delta temperature with time related to the aircraft passage overhead. The pattern is reasonably consistent from aircraft to aircraft, with changes possibly caused by the altitude, line of flight, pitch and other characteristics of the glide. The separation time between the aircraft seems to have an effect, also.

The shape of the curve is not always the same, but there are sufficient similarities that there is little question of its use for identification of vortex features within the detector volumes. More accurate alignment/setup of the observed volumes is important, as is a better location relative to the runway. It is most probable that these first observations have been made under conditions that could provide only a small fraction of the vortex related signal that is available.

Data from 10/22/91 is shown on Figures 9 and 10. Data from 10/24/91 is shown on Figures 11 and 12. There appears to be much that can be learned in interpretation as we gain understanding of the relationships between these two infrared signals.

The time of the cold air pattern seen by the IR was about 20 seconds, but this could well have been the sinking rather than the decay of the vortex. This rapid sinking is predicted for vortices in hot, dry weather by Greene, but we see little difference between the two field days (10/22/91 and 10/24/91). More and better data is needed before trying to establish serious understanding or interpretation.

The warming secondary part of the curves is also generally present. Even through it is early in the program, we can be quite certain that the consistent regions that are cooler than ambient are a wake vortex property. The warmer regions, however, may be either a part of the vortex, or entrained exhaust.

Figure 13 shows the IR temperature on 10/24/91 in the absence of aircraft. This data has been processed in the same way as the other. This noise is observed to be the order of 2 degrees in total excursion. The aircraft related effects are 5 or more degrees. Thus, we are certain that the data observed is a function of the aircraft vortex. When the AWAS is more appropriately located and oriented, the aircraft related signals will probably be larger, making this ratio of signal to noise even greater.

The time magnitude and frequency aspects of the wake effects are also very different from the noise properties. Thus, it will be possible to separate signal from noise in a future system.

On first try, the AWAS was able to detect the wake vortices with several of its present modes of measurement. The 14, 15 micron wavelength was the most sensitive (mode 3).

This initial data suggests that IR is able to sense the wake vortex, and with adequate development, could be used to determine the time required for the approach of aircraft under various weather conditions. The look over the runway may provide additional information as to how long the wake vortex will be dangerous after each takeoff and landing.

Another possibility is that of IR equipment mounted in the aircraft such that the pilot could be assured that he was not following too close to the preceding aircraft. As airport efficiency is maximized in the future, both of these functions will grow significantly in importance.

CONCLUSIONS

Computer Modelling:

The modeling shows a simplified detection of the vortex, and a linear temperature recovery from the vortex. This model provides encouragement to make field measurements in order to verify the magnitude, and to provide better direction for future work.

FIELD PROGRAM

Two days of field tests (10/22/91 and 10/24/91) provided experience in hot, dry and cold, high humidity weather with moving clouds as a backdrop. Because of the thermal air noise, it was necessary to use some elementary smoothing techniques to achieve clear pictures of the thermal changes caused by the wakes of the landing aircraft. Even though the AWAS was located a mile from the end of the runway for these first tests, the signals provided confirmation of the model temperature change magnitude, and provided significant delta temperature change within a few seconds after the aircraft moved over the AWAS site toward the runway.

This data does provide some measure of the time required regarding the line of sight of the AWAS and the wake vortex. The loss of field vortex effects may result from properties not considered in the computer model. However, the decay of the negative temperature was nearly linear, as in the model.

The field tests provide confirmation that there is strong potential for meaningful use of infrared in the measurement and monitoring of wake vortices of aircraft.

PROPOSED PROGRAM

Additional Modelling:

The computer modeling provides a fast and efficient way to see the effect of changing variables, once the model picture is established. As field data is obtained and analyzed, the computer model can be upgraded. It must continue to fit the earlier data sets. Thus, the computer modeling is a powerful tool in developing an understanding that relates to all of the field measurements on a continuing basis.

ADDITIONAL FIELD DATA COLLECTION

See Figure 14.

Looking up the glide path during the landing:

For study of the vortex laden air through which aircraft are landing, and adding to the vortices, ground based IR measurement looking back along the landing path provides unique information.

This is a direction in which IR needs to be exercised and analyzed in order to establish its value for protection of the landing aircraft. All of these IR measurements need to be studied over a wide range of weather conditions, with many different types of aircraft.

Looking down the runway:

Ground based IR measurement down the runway is also needed, for it is true that vortices on the ground can, in some cases, provide danger to aircraft and especially the lighter aircraft in takeoff, landing, or taxi operations. There are many questions to be answered here before higher efficiency airport operations can be established. Thus, much down runway IR data is needed under all weather conditions with many aircraft types.

Looking across the runway:

Ground based IR measurements across the runway may provide information equivalent to the down runway information, but this can only be established if the data is taken for comparison. This data could potentially indicate if a vortices were blown onto the runway. Thus, this is also an important program.

All of this effort must be developed by both model and field measurement. After the picture is sufficiently consistent, the specific equipment needed to provide a practical warning system can be designed.
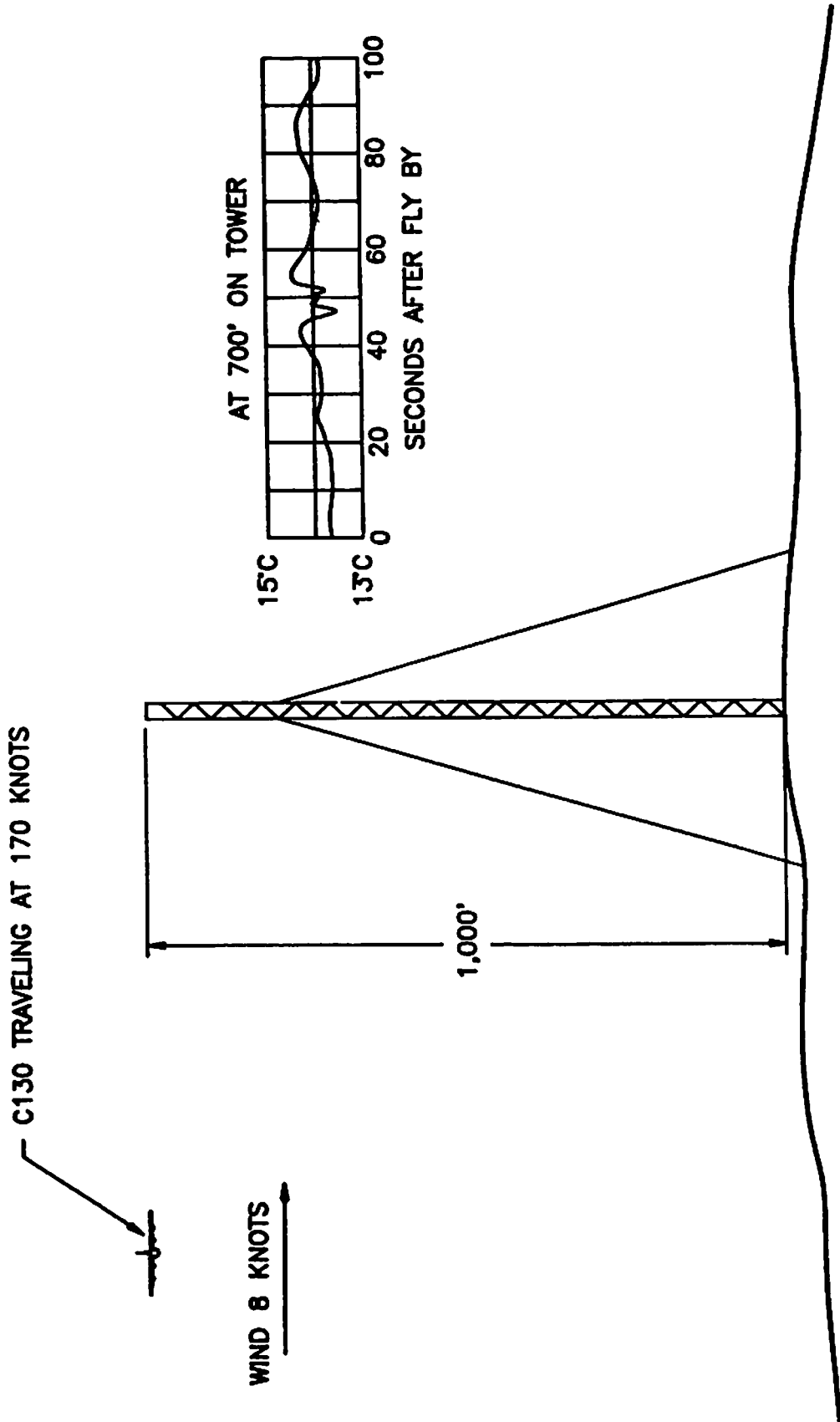
Figure 1. Measurement of an aircraft wake vortex using a meteorological tower. A.J. Bedard, Jr. 9th Conference on Aerospace and Aeronautical Meteorology, June 6-9, 1983, Omaha, Nebraska. Published by American Meteorological Society, Boston, Massachusetts.

CLEAR AIR TURBULENCE ENCOUNTER
FLIGHT LEVEL 310

FIFTY MILES

AWAS III
FIELD OF VIEW

REGION OF
STABLE AIR

CLEAR
AIR
TURBULENCE

LOW LEVEL WIND SHEAR ENCOUNTER

AWAS III
FIELD OF VIEW

NEAR TEMP

FAR TEMP

FLIGHT PATH

WIND SHEAR
EVENT

END OF RUNWAY
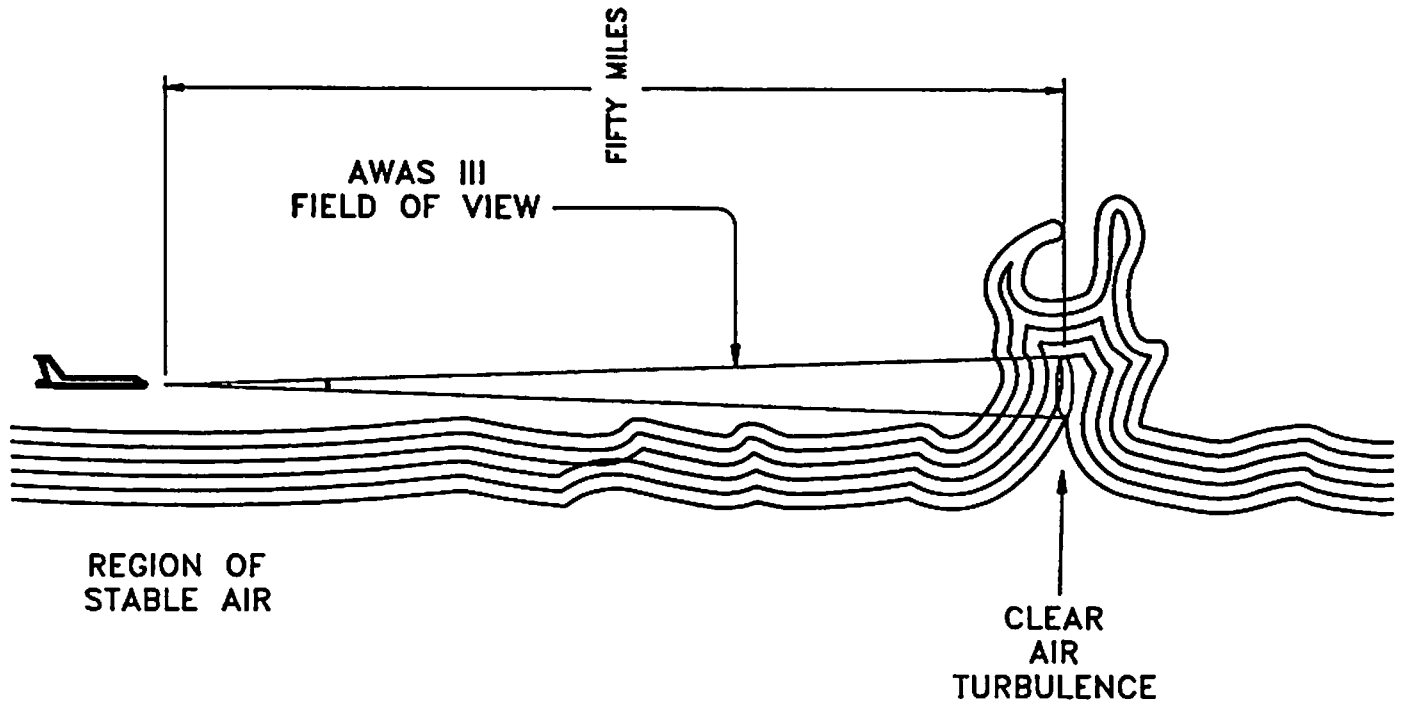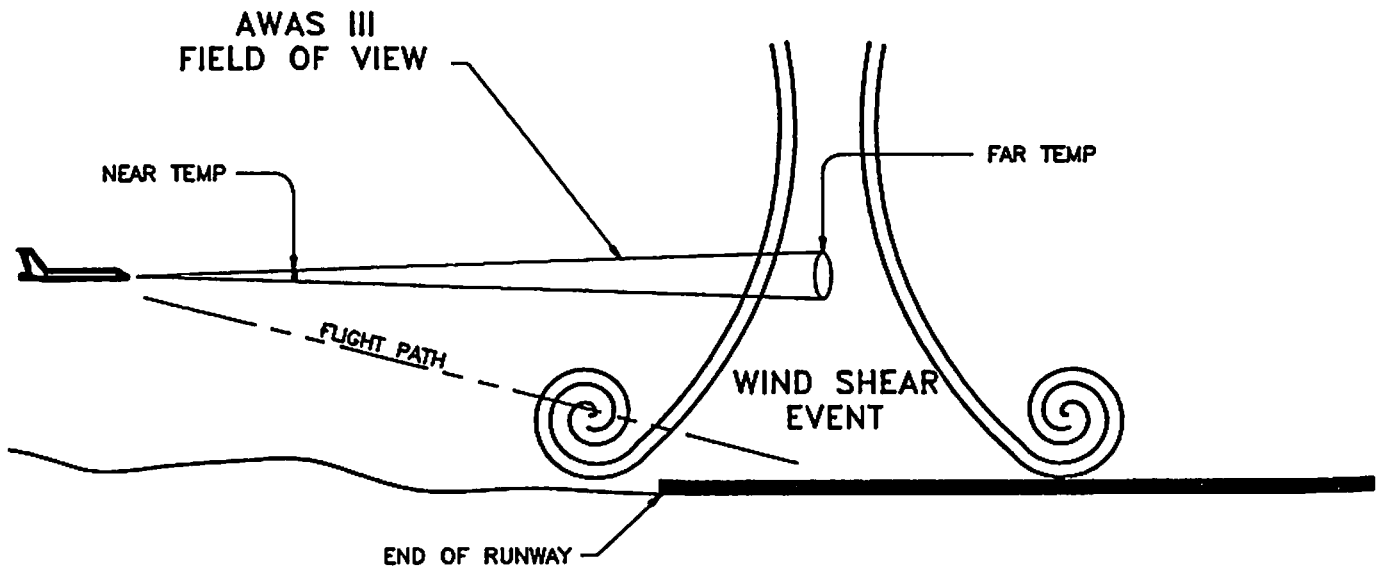
Figure 2. Clear air turbulence encounter/low level wind shear encounter.
Pat Adamson 10/24/91.

33 FEET IN DIAMETER

FLIGHT PATH

AWAS

8 MILES
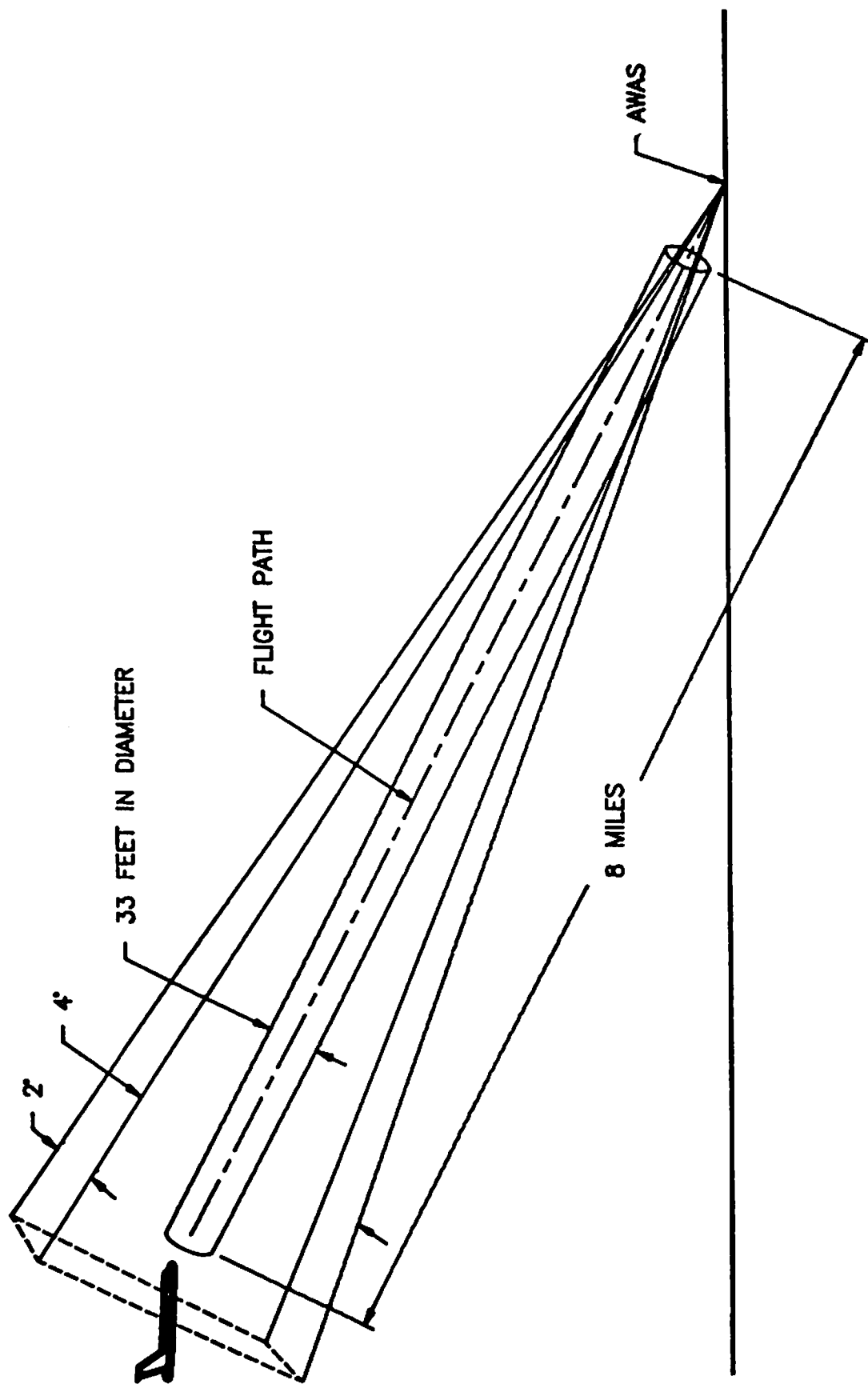
Figure 3. Computer model.
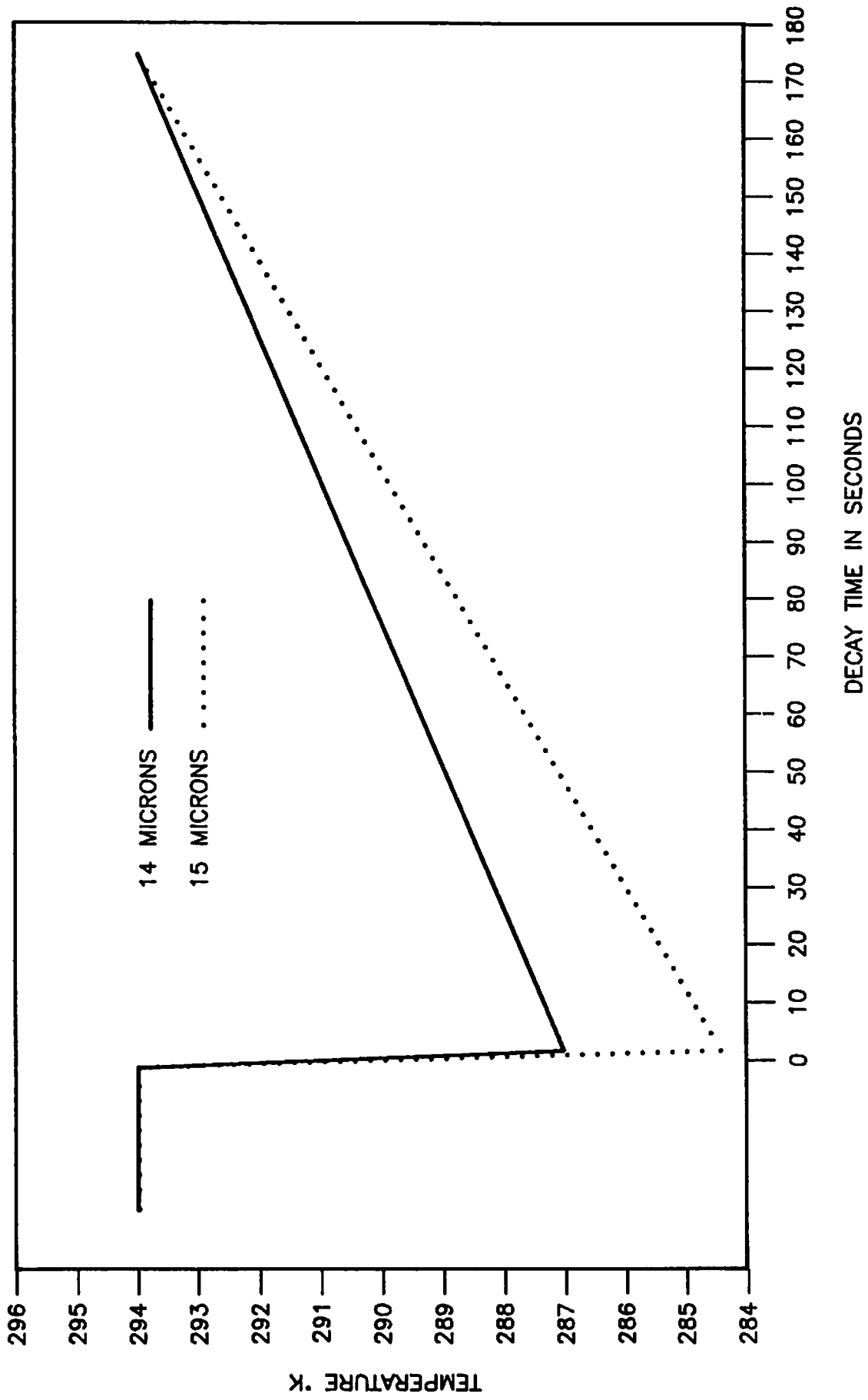
Figure 4. Wake vortex decay temperature profile.
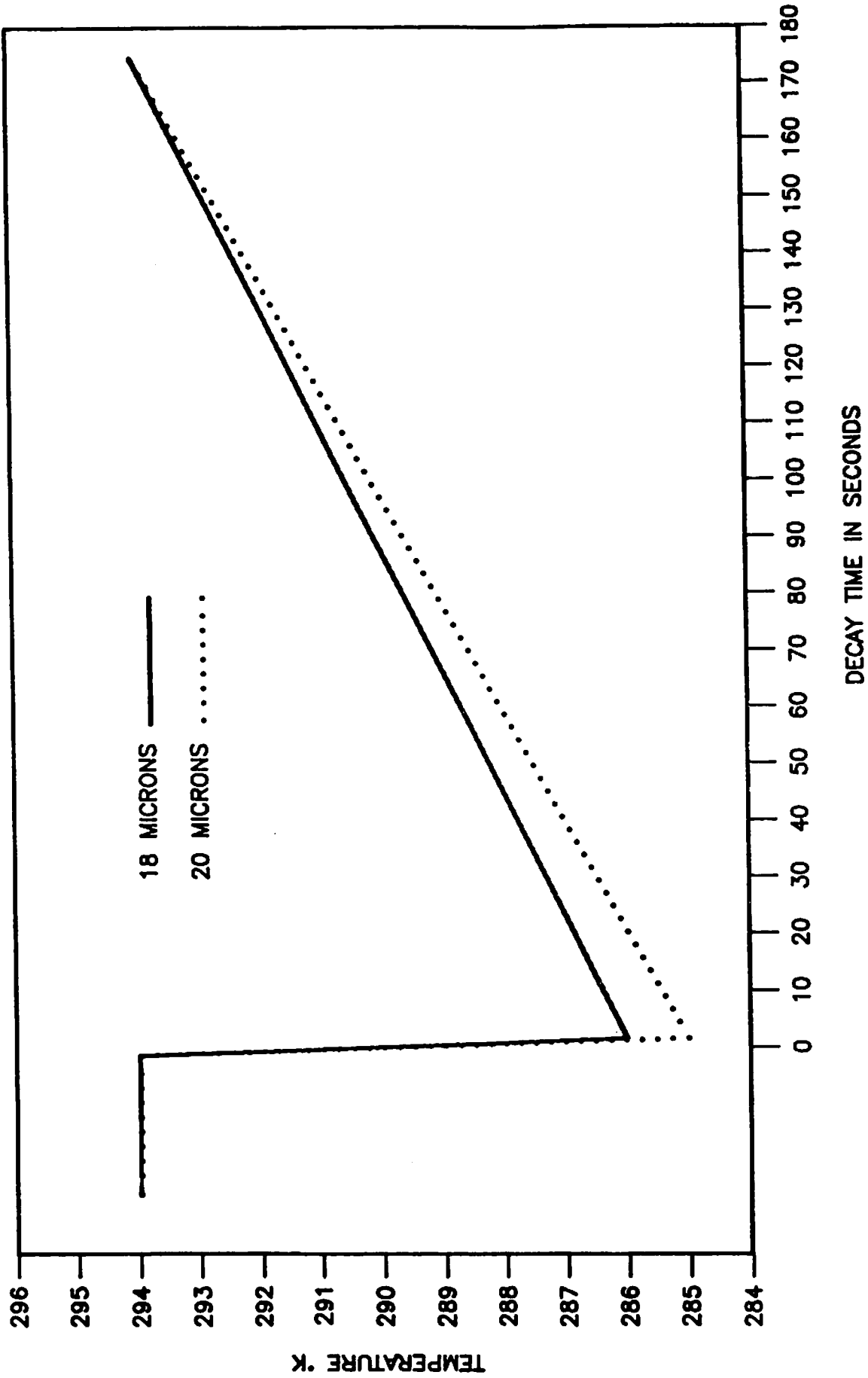
Figure 5. Wake vortex decay temperature profile.
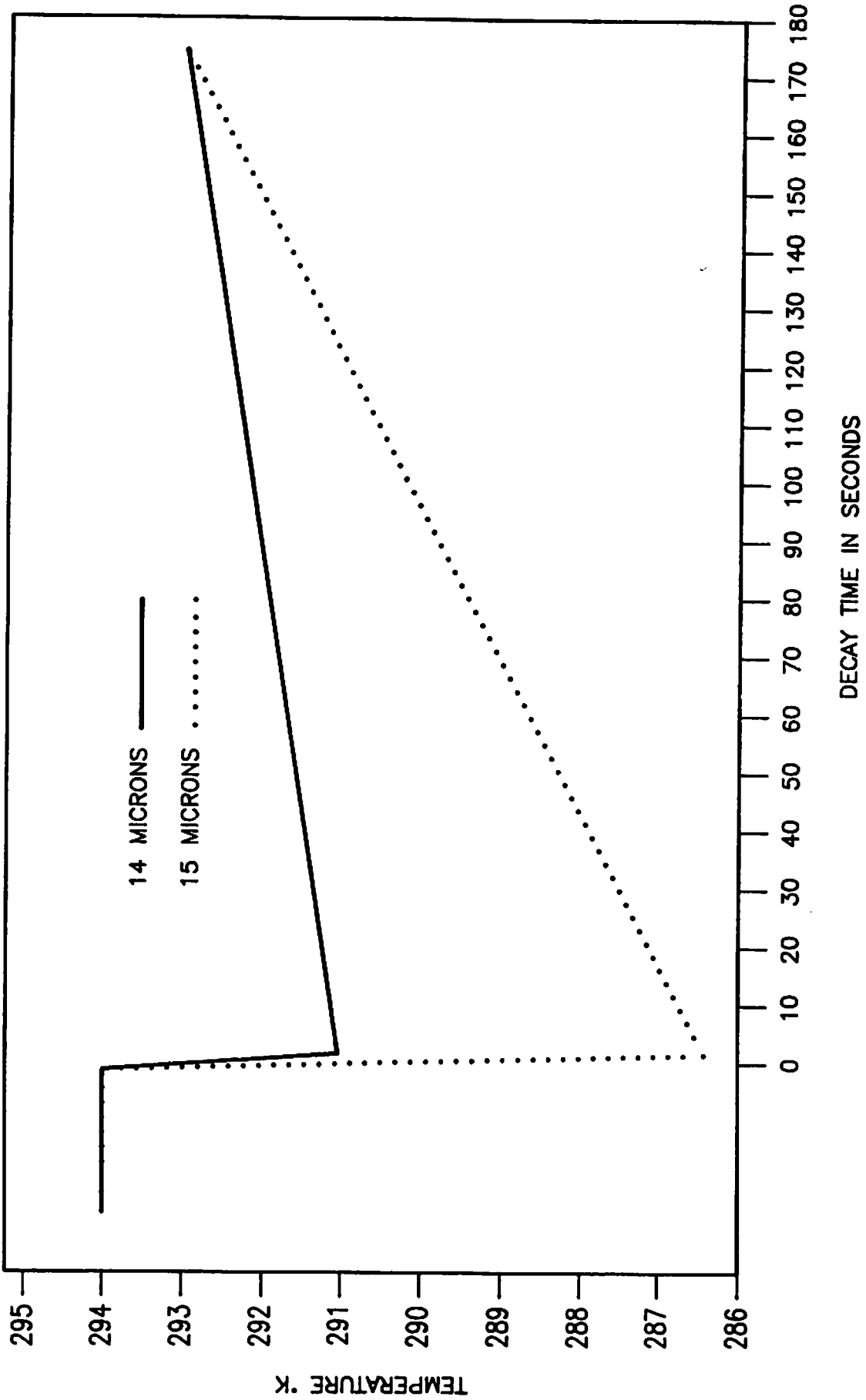
Figure 6. Wake vortex decay temperature profile.
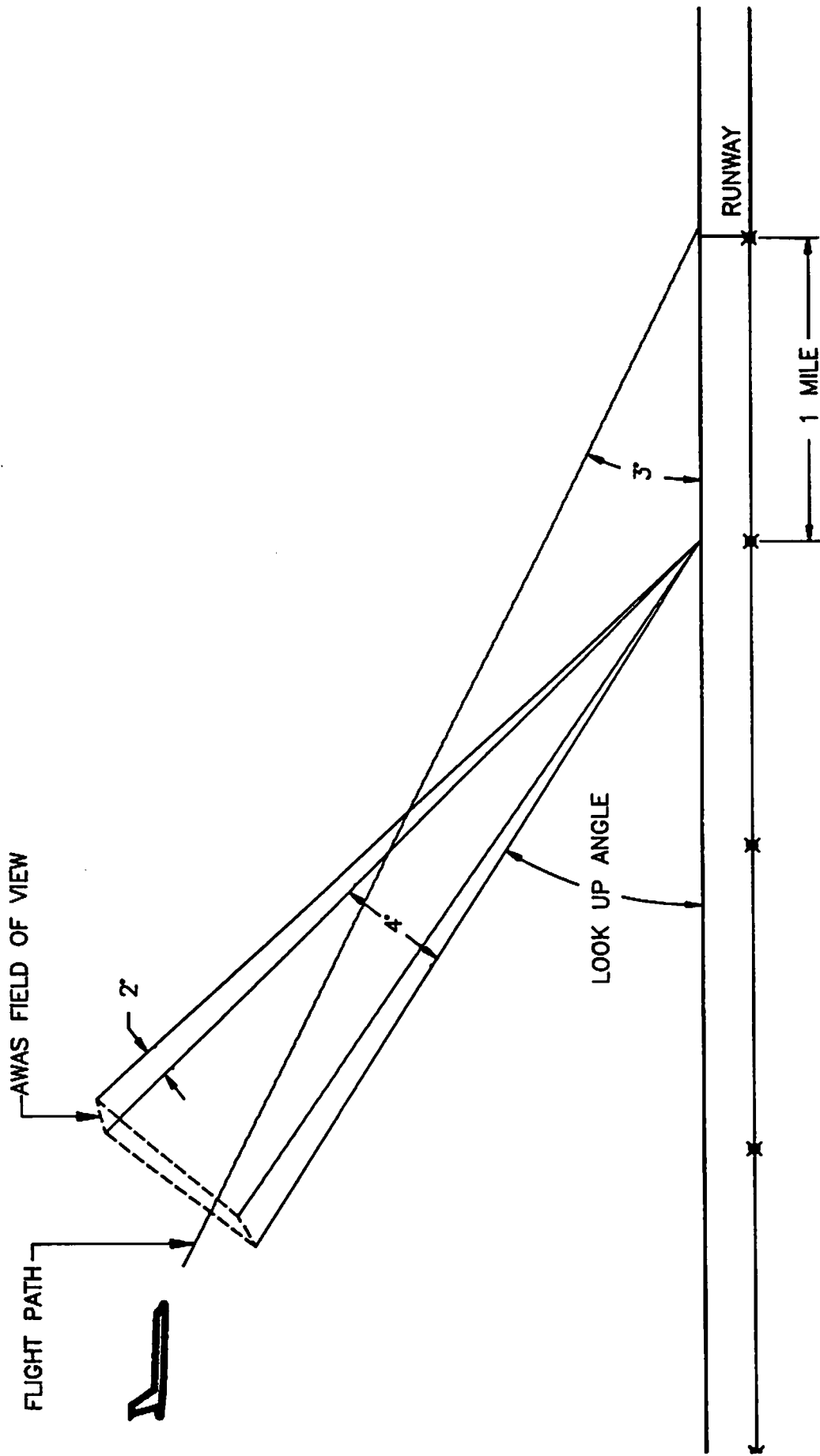
Figure 7. Experimental data.
Pat Adamson 10/24/91.

FLIGHT PATH

AWAS FIELD OF VIEW

2'

4'

3'

LOOK UP ANGLE

1 MILE
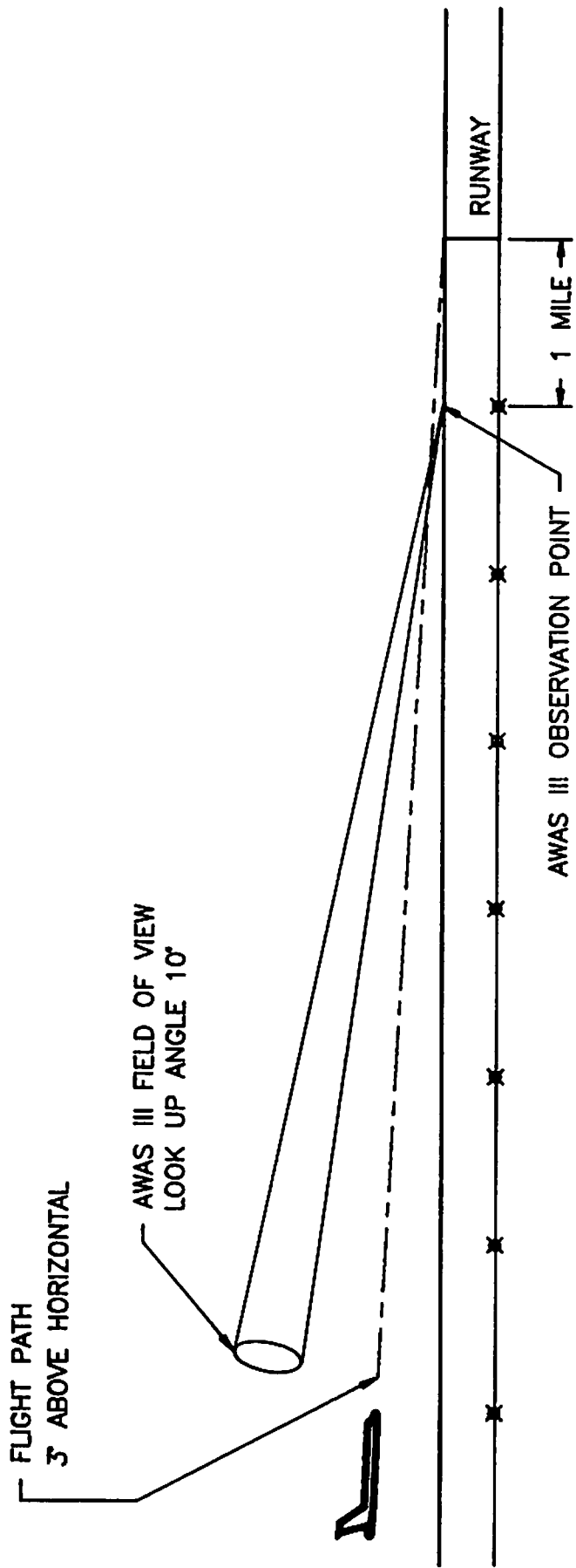
RUNWAY

Figure 8. Experimental data.
Pat Adamson 10/24/91.
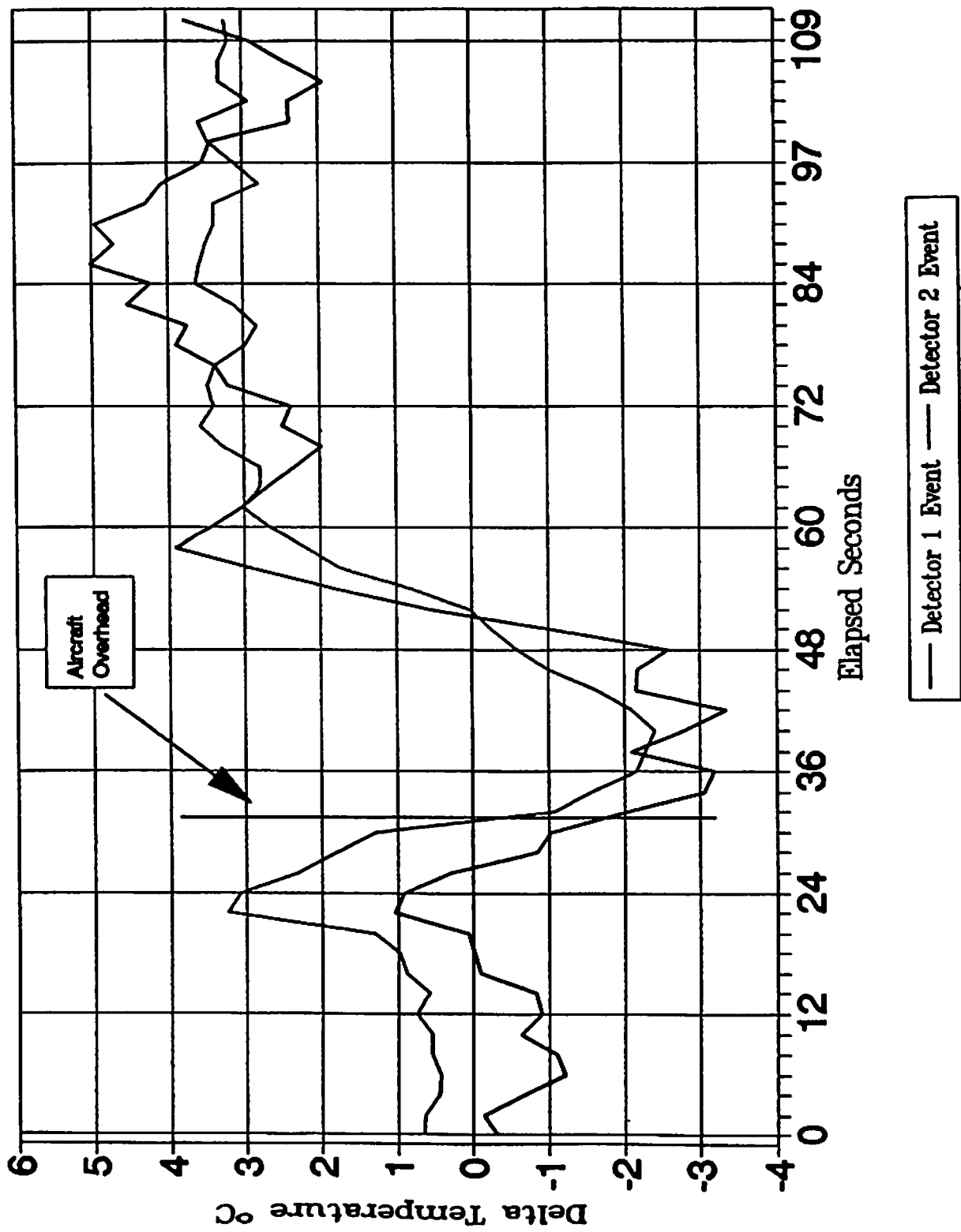
Figure 9. AWAS3 OB#8 MD# scans: aircraft landings, Stapleton east-west runways, 10/22/91.
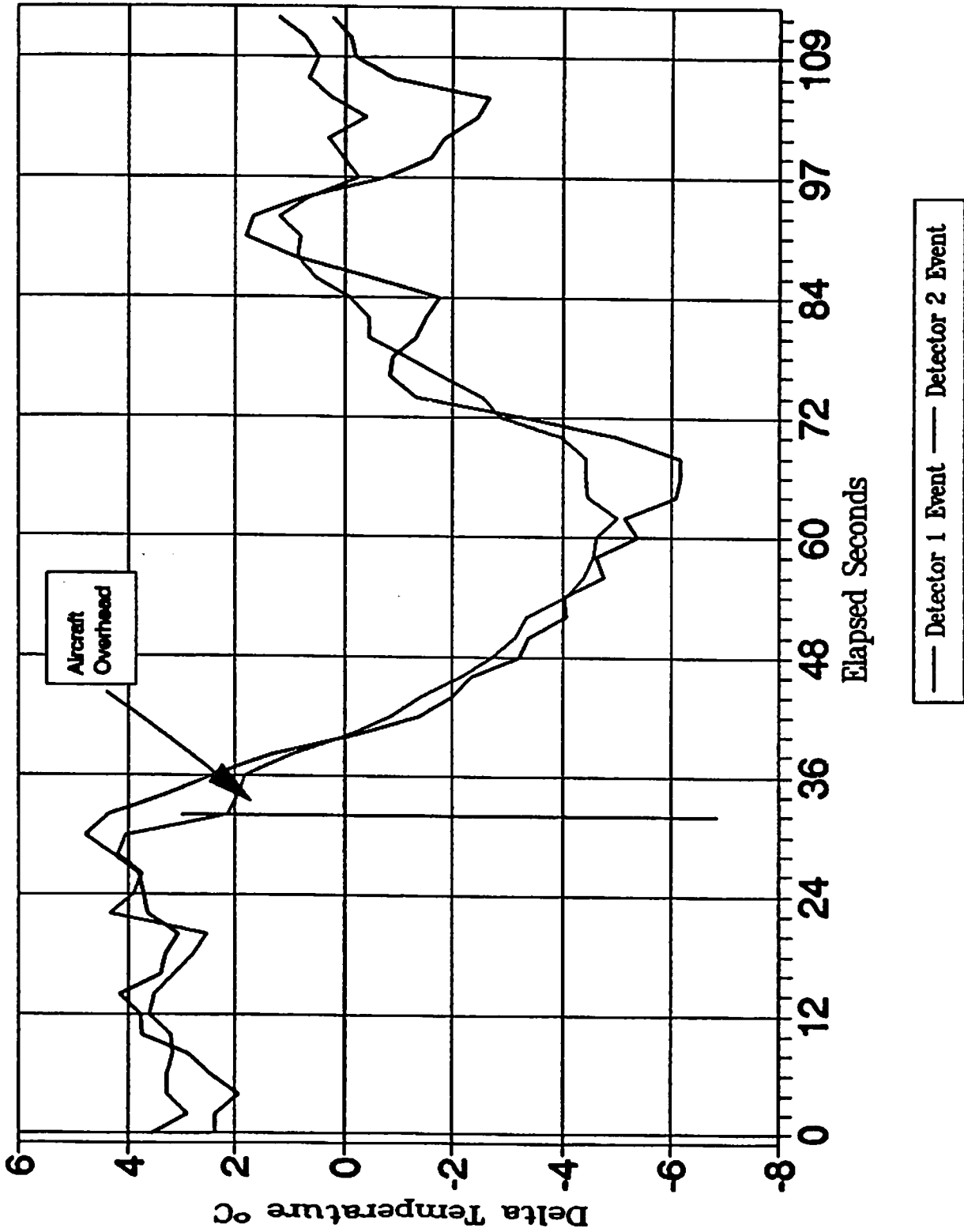
Figure 10. AWAS3 OB#8 MD3s of ncoming MD80, Stapleton east-west runways, 10/22/91.
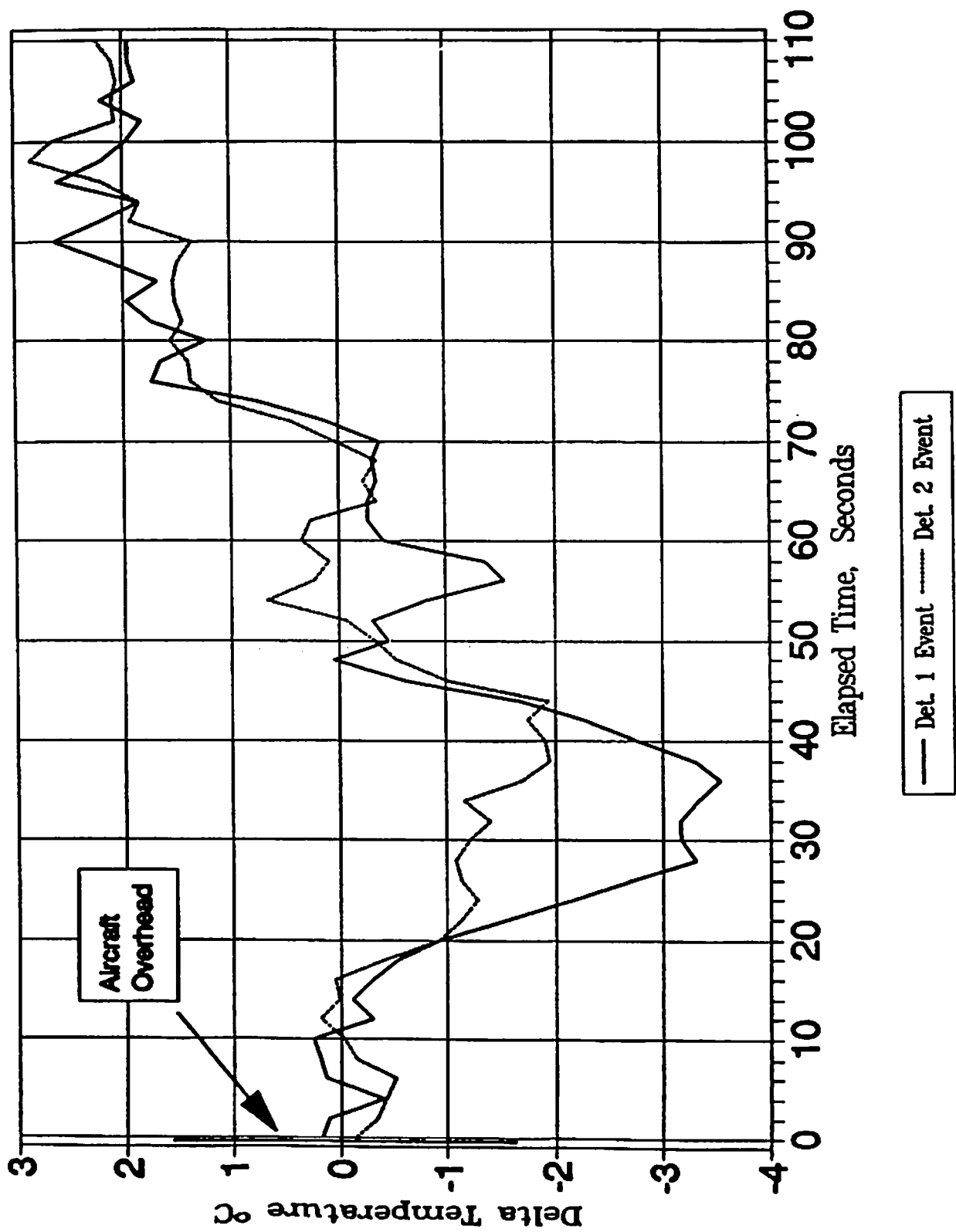
Figure 11. AWAS3 MD3s of incoming 737, Stapleton, air temp. 8°C, RH%=81, 10/24/91 KSN, CM.

Det 1 Event —— Det 2 Event
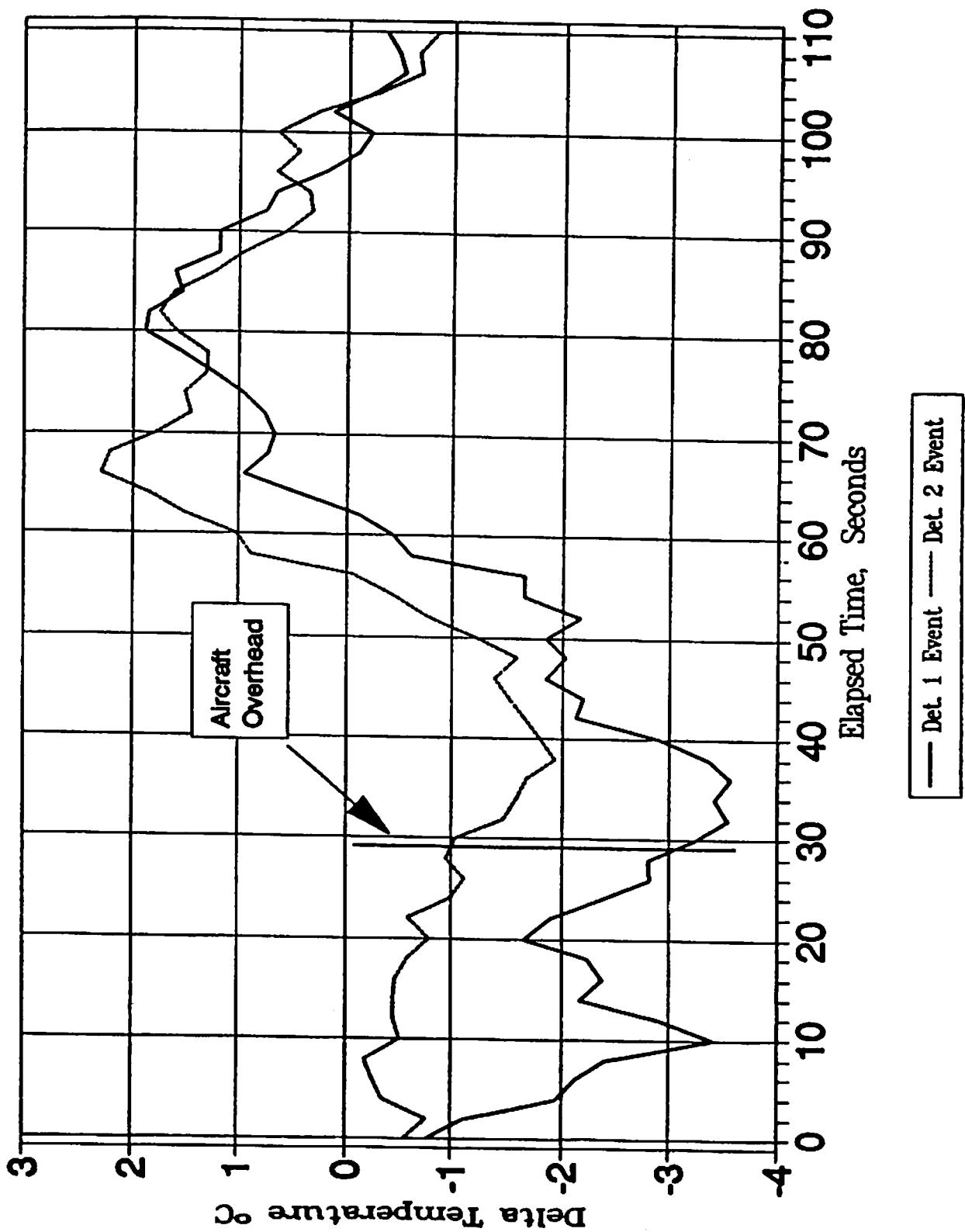
Figure 12. AWAS3 MD3s of incoming 737, Stapleton, air temp. 8°C, RH%=81, 10/24/91 KSN, CM.
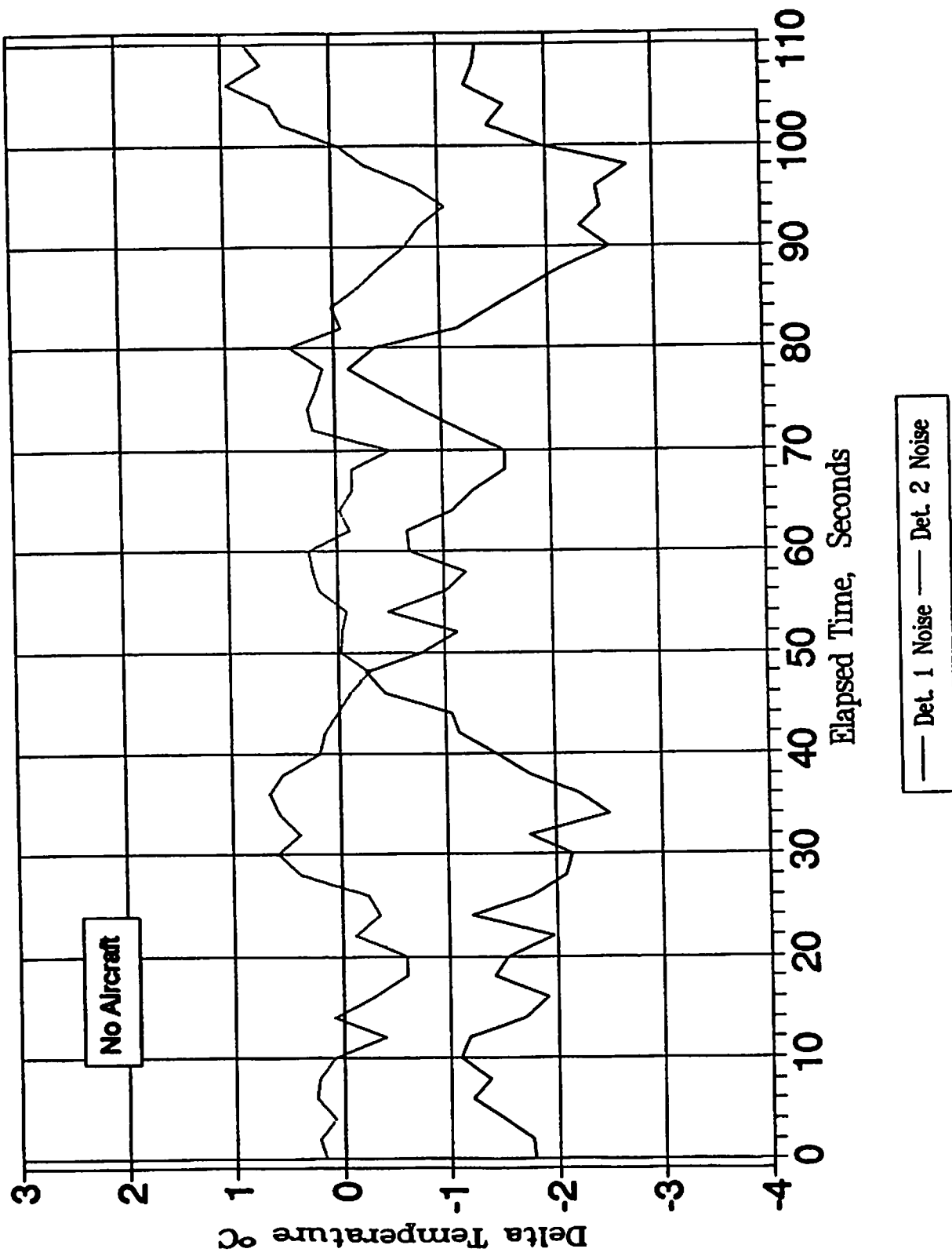
Figure 13. AWAS3 MD3s noise sample, Stapleton, air temp. 8°C, RH%=81, 10/24/91 KSN, CM.

AWAS III LOOKING ACROSS RUNWAY

8 MILES

AWAS III AT END OF RUNWAY
LOOKING ● AC FLT PATH

AWAS LOOKING
DOWN RUNWAY

8 MILES
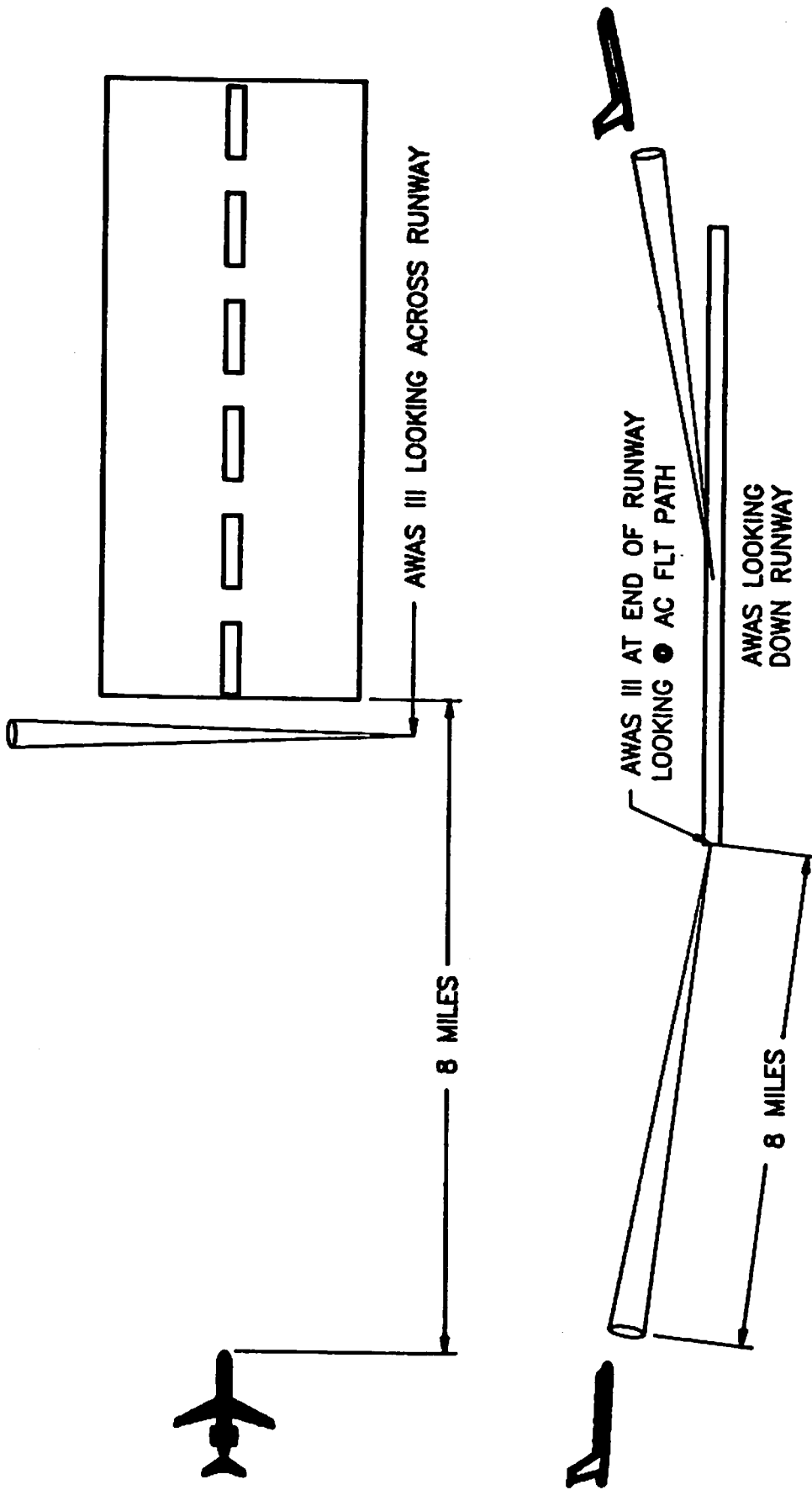
Figure 14. Proposed field data collection locations, 2 AWAS III.

REFERENCES

1. Bedard, A.J., Jr., Measurements of an Aircraft Wake Vortex System Using a Meteorological Tower, , AMS 9th Conference on Aerospace and Aeronautical Meteorology, 6/6/83.

2. Greene, G.C., An Approximate Model of Vortex Decay in the Atmosphere, AIAA 12th Atmospheric Flight Mechanics Conference, AIAA-85-1835-CP, 8/19/85.

3. Kneizys, F.X., E.P. Shettle, et al., Atmospheric Transmittance/Radiance: Computer Code LOWTRAN 6, Air Force Geophysics Laboratory, Hanscom AFB, MA, AFGL-TR-83-0187, 8/1/83.
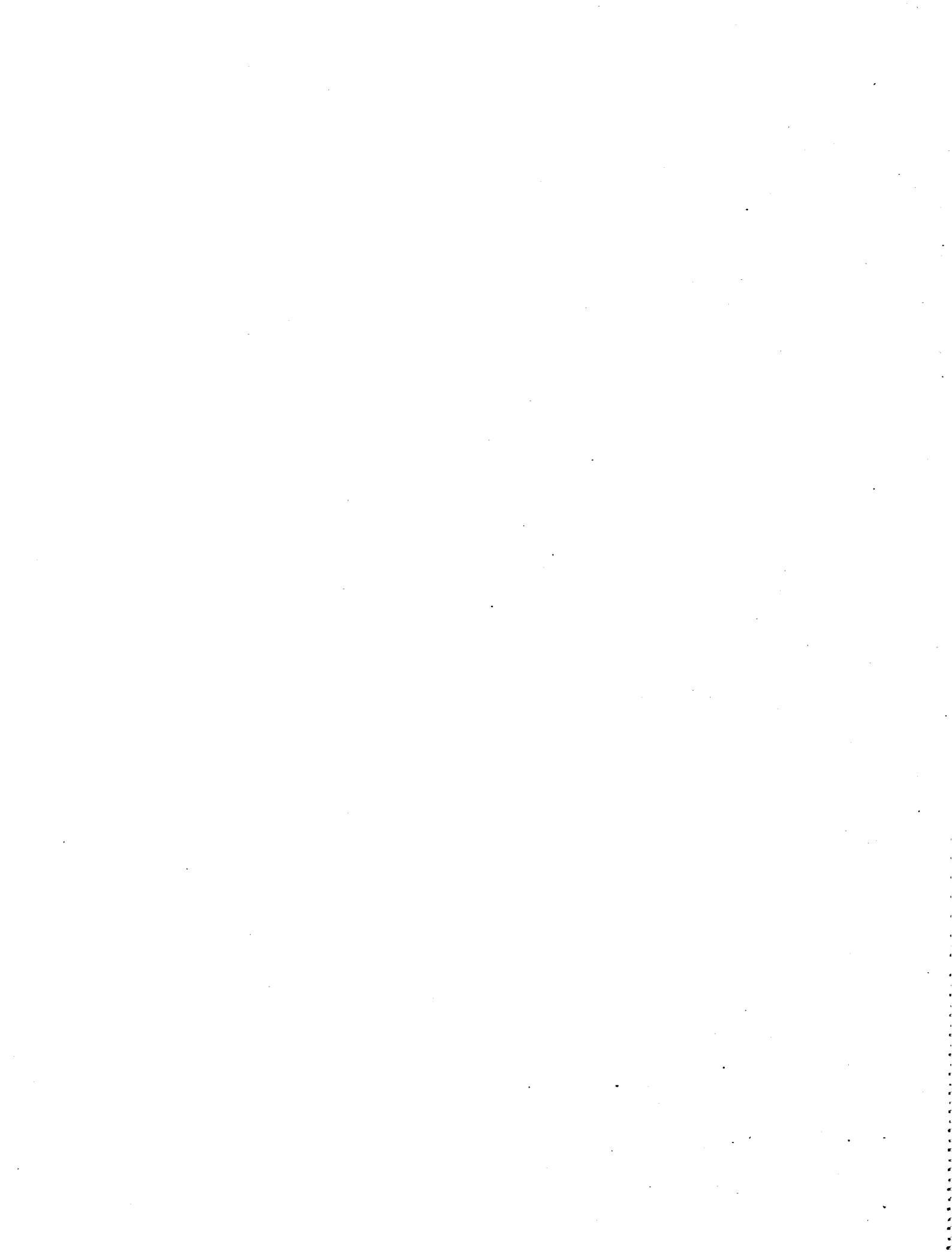
FLIGHT-TEST EVALUATION OF A DIRECT-MEASUREMENT
AIRBORNE WAKE-VORTEX DETECTION CONCEPT

Eric C. Stewart
NASA Langley Research Center
Hampton, Virginia

ABSTRACT

Flight measurements of the flow field in an airplane wake vortex have been analyzed to determine the feasibility of developing the sensor technology for an airborne wake-vortex detection and avoidance system. The measurements were made with relatively low-cost instrumentation on a light airplane flying at small angles to the path of a 90,000 lb turboprop airplane. Algorithms were developed to isolate the effects of the wake vortex on the measurements and produce candidate wake vortex detection parameters. Video recordings of the light airplane relative to a smoke trail in the wake vortex were used to determine the separation distance of the light airplane to the wake vortex. The measured wake vortex detection parameters are compared to values predicted using potential theory. The results indicate that the presence of the wake vortex can be detected with relatively simple instrumentation at a distance of about one wing span of the generating airplane for the flaps retracted configuration and about one-half to three-fourths wing span for the flaps extended configuration. The location and strength of the wake vortex, however, cannot be determined uniquely without more sophisticated instrumentation. A short discussion of the effects on an operational system of guidance constraints, turbulence, wake vortex irregularities, and ground effect is also presented.

INTRODUCTION

The current standards for separation of aircraft near airports were established in part because of the hazard associated with the wake vortex left behind airplanes. Reducing these separation standards can significantly increase the capacity of major airports to accept large numbers of aircraft in a given period of time. One concept which might make such a reduction possible while maintaining current safety levels has recently been explored at the NASA Langley Research Center. This concept involves supplying the pilot with wake-vortex warning and avoidance information similar to that presently employed for ground proximity, air traffic conflicts, and windshear hazards. This wake-vortex warning information could be derived from on-board sensors capable of detecting the presence of a

vortex using advanced remote sensing technology. However, such technology may not be available for some years or it may be prohibitively expensive. Therefore, it has been suggested that conventional motion and/or air data sensors already on many airplanes might be able to detect the direct effects of a wake vortex in sufficient time to allow avoidance, ref. 1.

To explore airborne vortex detection, a flight test was conducted in which an instrumented, light airplane was flown in the vicinity of another, larger airplane's wake vortex. The vortex was made visible by injecting smoke into the airstream near the wing tip of the generator airplane. The small probe airplane was equipped with flow angle sensors as well as attitude and attitude rate sensors. These measurements were processed after the flights to produce parameters which were due to the flow field around the vortices. These detection parameters were then correlated with the lateral distance from the probe airplane to the vortices. The distance was determined from video recordings taken from a third airplane flying above the probe airplane and smoke trail.

The present paper presents some of the results from these flight tests. The results illustrate some of the practical considerations and limitations of the concept. The results indicate the need for accurate measurement of the probe airplane's inertial velocities in order to locate and determine the strength of the vortices instead of merely detecting their presence. Finally, a short discussion is given of some additional considerations in developing an operational system which were not addressed in the present flight tests.

SYMBOLS

A_x, A_y, A_N	longitudinal, lateral, and normal acceleration of probe airplane, g's
b_s	separation of vortices in wake vortex, ft
d	horizontal distance from nearest vortex of the vortex pair to c.g. of probe airplane (always positive), feet
h	pressure altitude, ft
$\dot{h}_v$	measured altitude rate due to wake vortex, ft/sec
p, q, r	roll, pitch, and yaw angular velocities of probe airplane, rad/sec
p_v	effective roll rate due to wake vortex, deg/sec
v	lateral velocity due to wake vortex in X,Y,Z earth-fixed axis system, ft/sec
w	vertical velocity due to wake vortex in X, Y, Z earth-fixed axis system, ft/sec

X,Y,Z	earth-fixed axis system (Figure 2)
y,z	coordinates of probe airplane in earth-fixed axis system (Figure 2), feet
$\dfrac{dv}{dy}$	gradient of lateral vortex velocity in y direction, 1/sec
$\dfrac{dw}{dy}$	gradient of vertical vortex velocity in y direction, 1/sec
α	angle of attack, rad
α_v	incremental angle of attack due to wake vortex, rad
$\Delta\alpha$	difference between vortex-induced angle of attack at right wing tip and vortex-induced angle of attack at left wing tip, rad or deg
β	angle of sideslip, rad
$\Delta\beta$	difference between vortex-induced angle of sideslip at right wing tip and vortex-induced angle of sideslip at left wing tip, rad or deg
Γ	circulation strength of wake vortex, ft^2/sec
ψ,θ,ϕ	Euler attitude angles of probe airplane, rad or deg
ϕ_p	rotation angle of the plane containing the center of a pair of vortices in a wake vortex system (Figure 16), deg
δ_a	aileron position (positive trailing edge down on right wing), deg
δ_{stab}	stabilizer position (positive trailing edge down), deg
δ_r	rudder position (positive trailing edge to left), deg

Subscripts

R	Right wing tip of probe airplane
L	Left wing tip of probe airplane
M	Measured value before processing
v	due to vortex
est.	estimated
cal.	calculated
meas.	measured

DESCRIPTION OF CONCEPT

Flight hazard warning systems are a part of the modern cockpit. Airliners now have ground proximity and air traffic warning systems as well as windshear alerting systems. These systems indicate a recognized need for supplying the pilot with real-time hazard information based on measurements made on board the airplane. If separation distances are reduced, it seems reasonable that a real-time warning/alert system for possible wake vortex hazards would be required, or at least welcomed by the piloting community. Although many human factor and operational issues must be resolved before another warning system is added to the cockpit, the basic wake vortex sensor technology has not been developed. Developing that technology using instrumentation already on many airliners is the subject of this paper.

Although the hazardous region of a wake vortex occupies a relatively small region, the flow velocities theoretically extend to very large (infinite) distances in all directions, Figure 1. One conceptually simple and direct way to sense these far-field velocities (and their gradients) is to use conventional flow direction and speed sensors on board the trailing (probe or encounter) airplane. Assuming the measurements can be made, a special algorithm could then be used to determine the location and strength of a wake vortex using the measured velocity components and their gradients, ref. 2. This information could then be used to drive the appropriate cockpit displays, warning devices, or even the control system. Such a system would be intended only for near parallel encounters where the probe airplane is slowly approaching the wake vortex. For perpendicular approaches, the probe airplane would penetrate the wake in about 1 second after the earliest possible detection. Such a short period of time would not be sufficient for any conceivable avoidance maneuver. However, this restriction is not too severe because the near-parallel encounters are the most hazardous due to the large roll angles which are induced by the vortex. Near-parallel encounters are also the most likely encounters for long straight-in IFR approaches.

There are at least three basic practical problems with this concept. First, the theoretical invisid velocities in the far field are extremely small and provide a very weak signal. It is well known that the tangential velocity of a single vortex diminishes as an inverse function of distance from the vortex. However, at large distances from a pair of vortices in a wake vortex the velocity diminishes as a function of the inverse squared distance due to the fact the vortices are rotating in opposite directions and cancel each other's effect. The attenuation of the signal is even more rapid for the gradients of velocities, because they vary as the inverse cube of the distance. These last two relationships are valid only for distances greater than approximately two or three the times the separation distance between the two vortices (200 or 300 feet in the present tests). At closer ranges the signal will be much stronger as the inverse relationship to the nearest vortex will dominate.

The second major problem is that the probe airplane on which the measurements are being made is an accelerating, rotating, non-inertial measurement platform. Thus, in addition to the conventional flow directions and speed measurements, measurements of the probe airplane's inertial velocities must be made. The vortex flow velocities are then determined by subtracting the inertial velocities from the velocities of the flow relative to the airplane.

Such a subtraction of one large number from another large number can lead to large errors in the final result.

The third major problem with the concept is that any practical system must be able to rapidly and accurately discriminate between vortex velocities (and gradients) and atmospheric turbulence velocities. An algorithm must be developed which can reliably recognize the unique rotational flow signature surrounding a wake vortex. If such discrimination is not possible, the system would produce a large number of false alarms and thus be unacceptable.

FLIGHT TEST DESCRIPTION

The flight tests were conducted at the NASA Wallops Flight Facility in Virginia during the fall of 1989. The general formation of the three airplanes used in the flight tests is shown in Figure 2. The large wake-vortex generating airplane, Figure 3, was flown along a straight and level flight path while injecting smoke into one of the wing tip vortices at a time. An altitude of about 5000 feet was used, and tests were conducted only on days when the atmosphere was relatively stable. The smaller probe airplane, Figure 4, was flown about 1 to 1.5 n.m. behind the larger wake-vortex generating airplane. Approaches to the wake vortex were nominally limited to the horizontal plane containing the vortex smoke trail in order to simplify the analysis. The pilot of the probe airplane attempted to track the (slowly descending) altitude of the smoke trail as he gradually approached and then retreated from the smoke trail from the side (laterally).

Data System

The probe airplane was equipped with an experimental data system which recorded the flow angles and speed at the end of booms in front of each wing tip, several airplane motion state variables, and the control surface positions, see Table 1. A noteworthy limitation of the present data system was that the inertial velocity components of the airplane were not measured. One of the purposes of these tests was to determine if the simple (non-inertial) instrumentation used in the present tests would suffice for detecting the vortices.

A third airplane, Figure 5, equipped with a downward-looking video camera was flown about 500 feet above the probe airplane and smoke trail. Video recordings, Figure 6, of the probe airplane and the smoke trail were made in order to determine the lateral separation distance.

Data Processing

Although all the data (except the video recordings) could have been processed in real-time using modest computer resources, all the data were processed after the test flights. The two

wing-tip flow angle measurements were corrected for upwash around the wings, as well as the flow velocities induced by rotational motions of the probe airplane. Special corrections to the angle of attack and roll rate were also made to remove the effects of the pilot's elevator and aileron inputs respectively. The final result of the calculations was five candidate vortex detection parameters (α_v, $\dot{h}_v$, $\Delta\alpha$, p_v, $\Delta\beta$). The vortex angle of attack at the center of gravity α_v and the vortex altitude rate $\dot{h}_v$ are derived from different sensor measurements, but are both conceptually related to the vertical component w of the vortex velocity. The vortex angle of attack α_v is the incremental angle of attack due to the vertical vortex velocity and will be shown to be effectively masked by the probe airplane's static longitudinal stability. The vortex altitude rate $\dot{h}_v$ is simply the negative of the vertical vortex velocity, but it will be shown that it could not be accurately measured without a precision altitude rate measurement. The differential angle of attack across the wing span $\Delta\alpha$ and the effective roll rate due to the vortex p_v are independent measures of the gradient of the vertical component of the vortex velocity along the wing dw/dy. The differential angle of sideslip Db is a measure of the gradient of lateral component of the vortex velocity along the wing dv/dy.

The video recordings were used to calculate the lateral, but not vertical, distance of the center of the probe airplane to the center of the vortex smoke trail. The span of the wing of the probe airplane as seen in recordings like Figure 6 was used to provide the scaling of each frame analyzed. The separation distance data were merged with the data taken on board the probe airplane. Details of the data reduction process are given in Ref. 2.

FLIGHT TEST RESULTS

The uncorrected sensor measurements of the vortex flow effects were contaminated by both the effects of airplane motion response to the vortex and the effects of pilot inputs. For example, the angle of attack at the wing tips included components due to the roll rate of the airplane as well as the wake vortex. Thus, the uncorrected or unprocessed sensor measurements did not correlate well (have the same wave shape) with the lateral separation distance and could not be used to detect a wake vortex. This is illustrated in Figure 7 which presents data for a run in which the vortex flow was strong and well-defined because the flaps were retracted on the vortex-generating airplane. Most of the angle of attack variations can be traced to the rolling response of the airplane which in turn is due not only to the pilot's inputs but also to the airplane's response to the vortex.

The five corrected or processed vortex detection parameters for the same data run are presented in Figure 8. Much of the noise or contamination has been removed from the processed parameters, especially α_v, $\Delta\alpha$, and p_v . These three parameters correlate fairly well with the separation distance to the vortex d. That is, they are (generally) large when the distance is small and small when the distance is large. The differential angle of sideslip $\Delta\beta$ does not correlate well with the lateral separation distance which is to be expected for the basically lateral maneuver used in most of the runs in these tests, see Ref. 2. The last parameter $\dot{h}_v$ is very noisy despite the processing and does not correlate well with the separation distance. The reason for this is that $\dot{h}_v$ is primarily based on differentiation of the

pressure altitude. An accurate measurement of the inertial vertical velocity is needed to replace this differentiated pressure altitude.

A cross plot of the $\Delta\alpha$ against the separation distance d is compared to potential theory predictions in Figure 9. The measured $\Delta\alpha$ is slightly less than the theoretical values, but indicates that for the condition of the test, the vortex could be detected at a distance of about 100 feet depending on the assumed threshold value. A similar result was obtained for the effective roll rate p_v due to the vortex, Figure 10. The vortex roll rate p_v, like $\Delta\alpha$, is a measure of the lateral gradient of the vertical velocity component dw/dy. At 100 feet or less the canceling effect of the far vortex on the near vortex begins to drop off rapidly and a usable signal is generated. Since the span of the generating airplane was 100 feet it appears detection of the vortex velocity gradient is possible at a distance of about one span of the generator airplane.

The detection distance was generally about 50 to 75 feet when the flaps were extended on the vortex-generating airplane, Figure 11. Note that the wake vortex induces a negative $\Delta\alpha$ in Figure 11 rather than a positive $\Delta\alpha$ as in Figure 9 because the probe airplane was approaching the wake vortex from the opposite side. The maximum differential angle of attack was smaller and appeared to contain more small structure than that for the flaps retracted case. Evidently, the flow field was not as well defined, possibly because the vortices shed from the flaps had not completely merged with the wing tip vortices. Although the detection distance was smaller (approximately one-half to three-fourths generator spans) when the flaps were extended, the hazard may have also been proportionally less than the flaps retracted case. The hazard was not determined in these tests because the probe airplane never made a full encounter.

Although the angle of attack at the center of gravity αv appears to be correlated with the separation distance in Figure 8, a crossplot of these data indicate that this may be fortuitous, see Figure 12. That is, unlike the gradient parameters, αv is only a fraction of the theoretical value. This is really to be expected considering the fact that the probe airplane was statically (angle of attack) stable and attempted to maintain its original (trim) angle of attack whenever it encountered an atmosphere disturbance of any kind. The airplane will maintain its trim angle of attack as long as the atmospheric disturbance changes at a rate slower that the airplane's short period response. If the probe airplane had approached the vortex at a very slow closure rate, αv would probably have been much smaller. This was indeed the case on other data runs not shown here.

Since α_v and $\dot{h}_v$ were not viable detection parameters, the vertical component of the vortex velocity could not be determined in these tests with the simple instrumentation. With only $\Delta\alpha$ (and $\Delta\beta$) measurements, only the presence of the vortex, and not its location or strength, can be determined as shown in ref. 2. For example, three possible trajectories are shown in Figure 13 for a run in which the pilot accidentally flew over the top of the vortex system. Either one of these three trajectories has the same combination of $\Delta\alpha$ and $\Delta\beta$. Thus, with the simple instrumentation system used in these tests, only the presence of the vortex could be detected. Without the location of the vortex, the pilot would not in general know which direction he would need to maneuver in order to avoid it. Also, knowing only

44-7

the presence of the vortex, he could not tell if he was a long distance from a strong vortex or a short distance from a weak vortex.

Being able to detect the presence of the vortex without knowing its strength or location could still prove useful in some circumstances. For example, if the pilot had already been advised that a heavy airplane was on final approach immediately ahead of and below him, detection of a nearby vortex would probably be sufficient cause to initiate a go-around to avoid the vortex. In addition, if the rate of change of the strength of the detection signal could be quickly determined, it could be determined whether the encounter airplane was approaching or retreating from the vortex. Finally, it may be advisable to execute a go-around regardless of where the vortex is relative to the following airplane. That is, when close to the ground on final approach it may be safer to try to "punch" up through a vortex above the airplane than to dive to avoid the vortex. The best maneuver strategies can only be determined in a well-validated simulation.

The only way the location and strength of the vortex system can be determined is by measuring both the differential flow angles and the inertial velocities (and deriving the vortex velocity components). Measuring the inertial velocities requires a much more sophisticated (and expensive) data system than that used in these tests. Although an enhanced Global Positioning System (GPS) might possibly be used to measure the velocities, an inertial navigation system (INS) would most likely be required to achieve the short term (within 1 sec.) accuracy needed in this application.

Even after the velocity components and their gradients (w, v, dw/dy, dv/dy) are measured, it is not always trivial to determine the vortex location and strength (y, z, Γ, b_S). There are four simultaneous equations involving trigonometric functions which must be solved. A closed-form solution for (y, z, Γ, and b_S) in terms of (w, v, dw/dy, dv/dy) could not be found easily. A flow chart of a possible algorithm to solve the equations from airplane measurements is shown in Figure 14. To test the "iterative loop" part of the algorithm, simulated airplane sensor measurements ($\Delta\alpha$, $\Delta\beta$, w, v)$_{meas}$ were generated by assuming a vortex position and strength (y, z, Γ, b_S), an airplane geometry, and a probe airplane attitude (θ, ϕ, ψ). The simulated sensor measurements ($\Delta\alpha$, $\Delta\beta$, w, v)$_{meas}$ were rounded off to three significant figures and entered into the iterative loop shown in Figure 14. Using an initial "guess" for (y, z, Γ, b_S) which was "near" the previously-assumed set, the algorithm rapidly converged on the correct values. In other cases, when the initial "guess" was some "distance" from correct values, the algorithm failed to converge. During this limited testing, the algorithm never converged on a wrong set of values which seems to indicate the solution is unique. In fact, convergence of an algorithm like that in Figure 14, might be a very effective "filter" to remove noise due to random atmospheric turbulence. The unique signature of a wake vortex may be the only flow field which will allow convergence on a solution (y, z, Γ, b_S). These results are only of an exploratory nature, and much more research is needed in this area.

OTHER CONSIDERATIONS

The tests in this study were conducted under ideal weather conditions out of ground effect. Thus, in addition to the practical instrumentation and numerical issues already raised, there are additional concerns. For example, in many situations, the two vortices are not nearly as linear as they were in these tests. The vortex filaments shown in Figure 15, for example, have numerous irregularities which would distort the flow field and complicate the relatively simple math model used in this study. Although such irregularities are usually an indication of reduced hazard to the probe airplane, the limits of the present approach in this regard need to be established.

Another irregularity in practical flow fields is illustrated in Figure 16. Due to the shear generated by the crosswind, the plane of the vortex pair has been rotated through an angle ϕ_p. Since the rotation angle is in general not known, the location of the vortex cannot be ascertained.

A final distortion of the ideal vortex flow field is illustrated in Figure 17. In this case, one of the vortices in the pair has essentially decayed to zero leaving a single vortex which may last for a significant period of time. A single vortex has a completely different flow field pattern from that shown in Figure 1 for a pair of vortices. A different flow field pattern would require a different vortex model in the detection algorithm shown in Figure 14. This would essentially require twice as many calculations as an algorithm which only searches for vortex pairs.

A second major area of concern which was not addressed in this study, is the effect of the natural motion of the atmosphere. Both steady winds and random fluctuations will contaminate the vortex flow field measurements. Steady winds will contaminate the measurements of the flow field velocities but not the measurements of the flow field velocity gradients. Random wind fluctuations, on the other hand, will contaminate both the velocities and their gradients. Since the present tests were conducted in smooth air conditions and only gradients were successfully measured, the effect of natural atmospheric motions were not, in general, evaluated. Special filters, in addition to the filtering action of the detection algorithm mentioned earlier, may be necessary.

Many operational and human factor issues will have to be considered. As mentioned earlier, if a vortex is detected above the present flight path, does the pilot maneuver downward (toward the ground) to avoid the vortex or does he maneuver upward to increase altitude? Lateral maneuvering control strategies may have to be included. Any maneuvering commands would most logically be incorporated into the airplane's flight director as is done with some wind shear detection systems, ref. 3. But just how the wake vortex information is blended with other flight director commands is one of many human factor issues which must be resolved. The commands, of course, must not induce other hazards such as a stall, impact with the ground, or maneuvers which would conflict with other aircraft in the terminal area.

CONCLUDING REMARKS

A flight test of an airborne direct-measurement wake vortex detection concept has been conducted. The tests were conducted without the benefit of instrumentation of the quality used in inertial navigation systems. Even with the simple instrumentation, the presence of the wake vortex for a flaps-retracted configuration was detected at a distance of approximately one wing span of the generating airplane depending on the assumed threshold signal level. With the flaps extended on the vortex generating airplane, the wake vortex was detected at about one-half to three-fourths of a wing span. In both cases the presence of the wake vortex was detected using differential wing tip flow-angle sensors which are sensitive to the spatial gradients of the vortex flow velocities. The vortex flow velocities themselves could not be measured without inertial-grade instrumentation. Without flow velocity measurements, only the presence and not the location and strength of the vortex could be determined. However, for near-parallel vortex encounters, detection alone may provide useful information for a pilot in some situations. The ultimate usefulness of the concept, whether it uses inertial-grade instrumentation or not, depends on a number of operational, human factor, and other issues not addressed in this study.

Table 1. Detecting Airplane Instrumentation System

Measurement	Type Sensor	Resolution
Stabilizer position, δ_{stab}	Control Position Transducer	0.1 deg
Aileron position, δ_a	Control Position Transducer	0.2 deg
Rudder position, δ_r	Control Position Transducer	0.2 deg
Longitudinal Acceleration, A_x	Accelerometer	0.004 g
Lateral Acceleration, A_v	Accelerometer	0.008 g
Normal Acceleration, A_N	Accelerometer	0.015 g
Right Wingtip Angle of Attack, $\alpha_{R.M}$	Flow Direction Vane	0.12 deg
Left Wingtip Angle of Attack, $\alpha_{L.M}$	Flow Direction Vane	0.12 deg
Right Wingtip Angle of Sideslip, $\beta_{R.M}$	Flow Direction Vane	0.12 deg
Left Wingtip Angle of Sideslip, $\beta_{L.M}$	Flow Direction Vane	0.12 deg
Pitch Attitude, θ	Gyro	0.24 deg
Roll Attitude, ϕ	Gyro	0.5 deg
Pitch rate, q	Rate Gyro	0.5 deg/sec
Roll rate, p	Rate Gyro	0.5 deg/sec
Yaw rate, r	Rate Gyro	0.5 deg/sec
Right Wingtip Airspeed, $V_{R.M}$	Tachometer	0.6 knots
Left Wingtip Airspeed, $V_{L.M}$	Tachometer	0.6 knots
Pressure altitude, h	Altimeter	39 feet
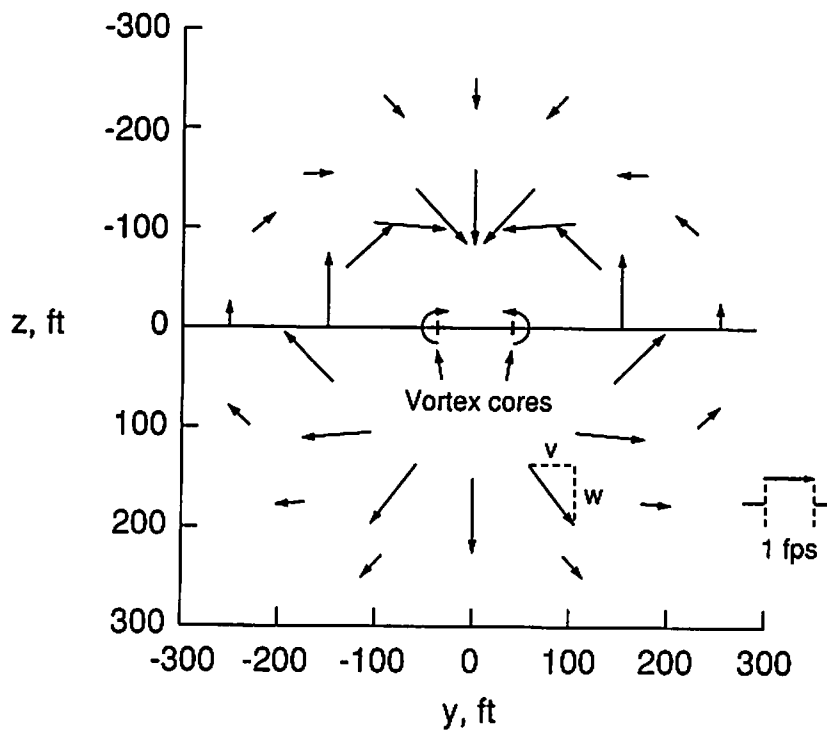
Figure 1. Wake vortex flow field velocity vectors. P-3 airplane at approach speed.
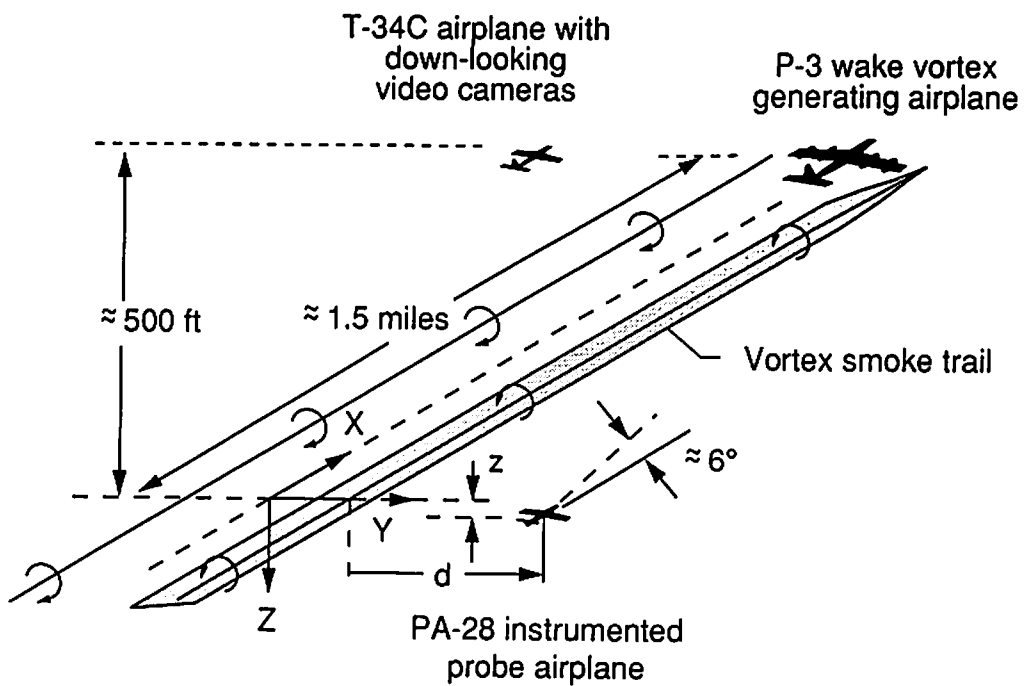
Figure 2. Wake vortex airborne detection experiment arrangement.

Figure 3a. P-3 airplane used to generate wake vortices (on the ground).
(in flight with wingtip vortices made visible with smoke).
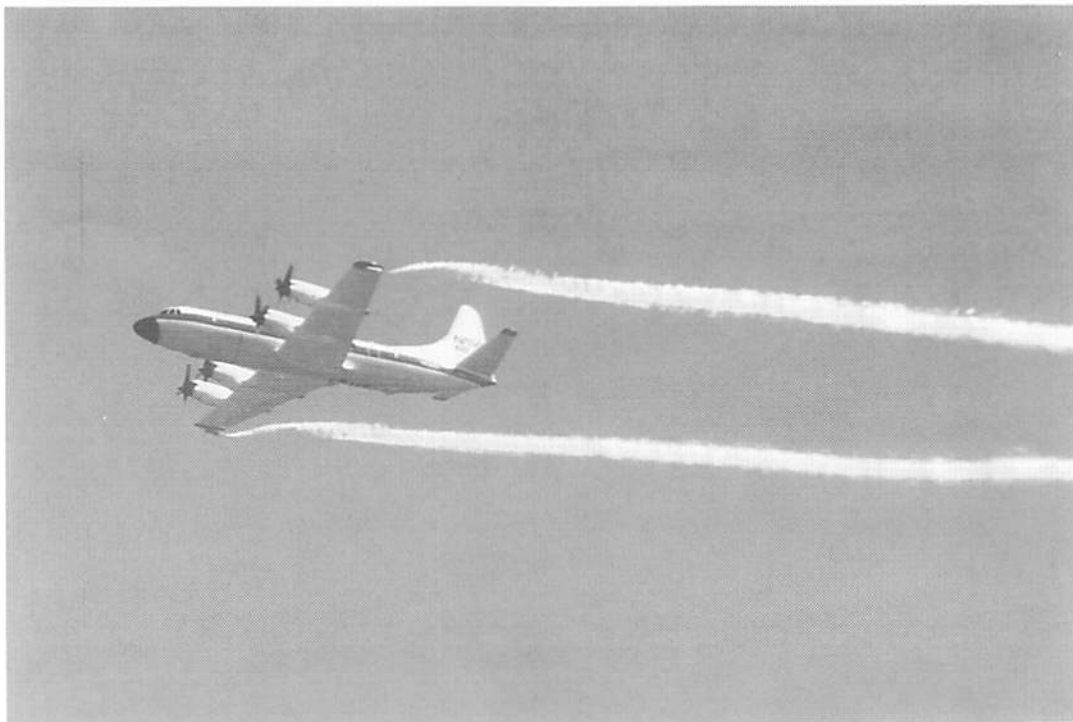
Figure 3b. P-3 airplane used to generate wake vortices.
(in flight with wingtip vortices made visible with smoke).

Figure 4. PA-28 airplane used to detect wake vortices.
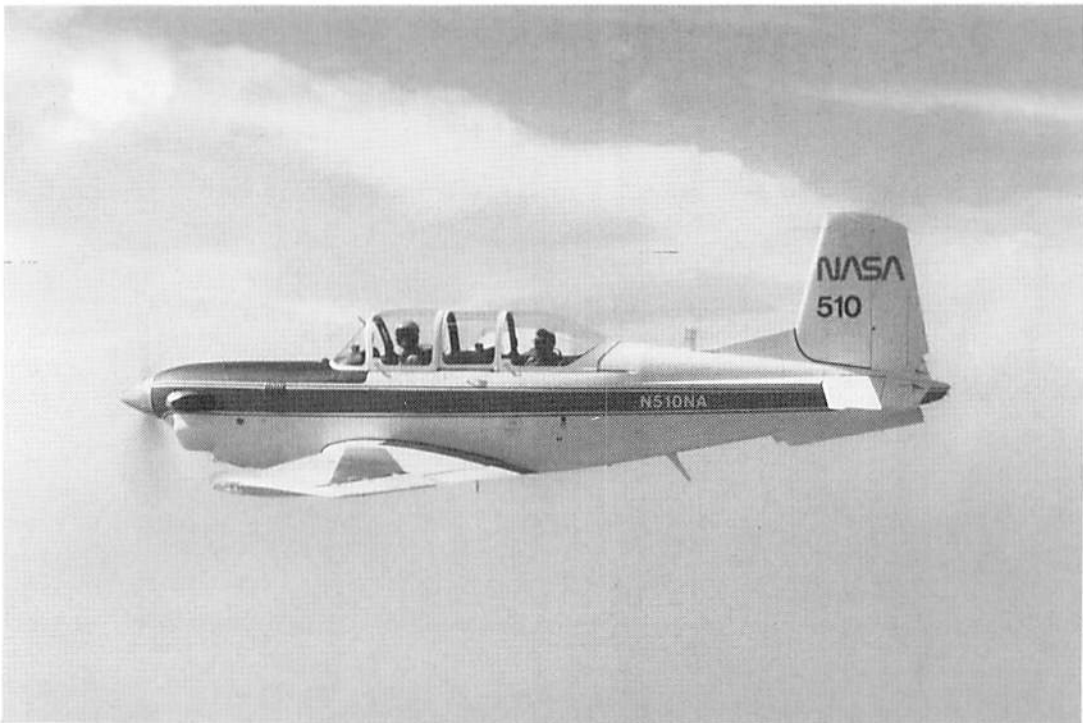
Figure 5. T-34C airplane used to photograph PA-28 airplane approaching
smoke trails in wake vortices of the P-3 airplane.
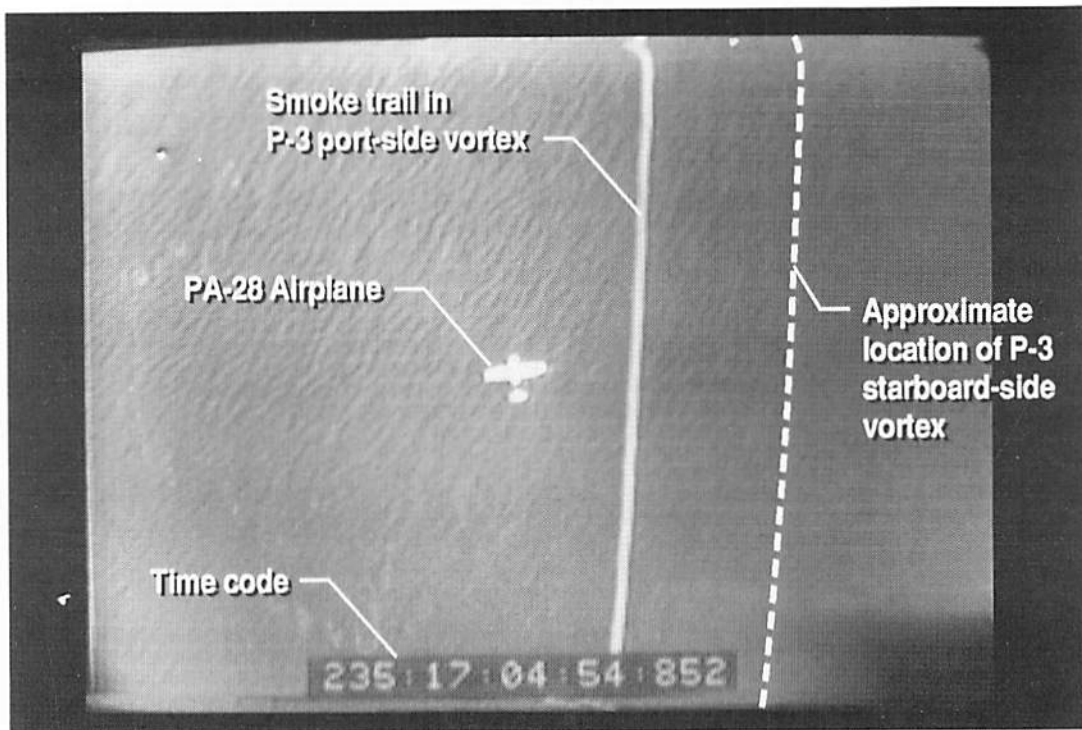
Figure 6. Single frame of video recording taken from T-34C airplane showing PA-28 airplane flying in vicinity of smoke trail in P-3 wake vortex.
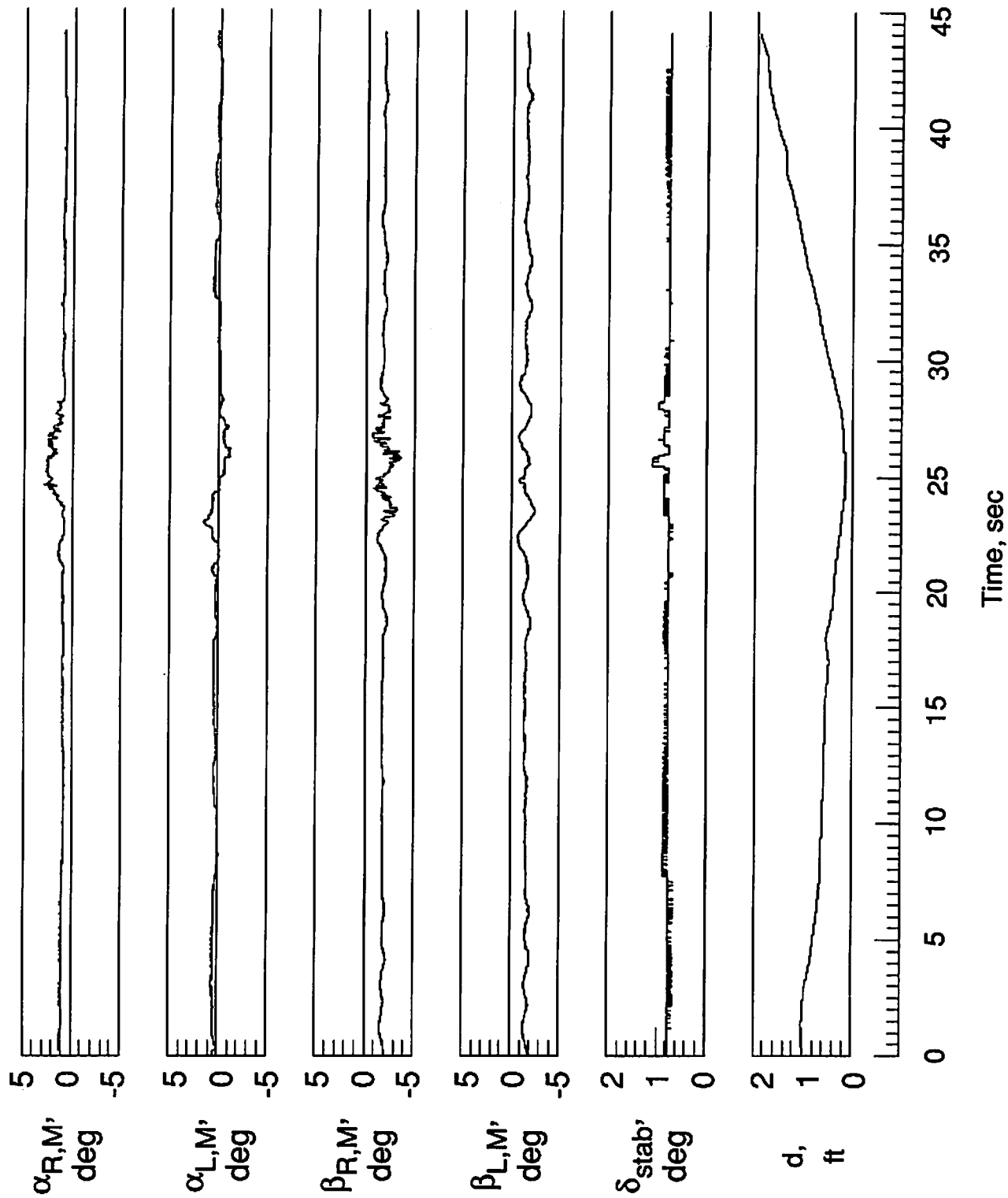
Figure 7. Unprocessed data with flaps retracted on vortex-generating airplane.
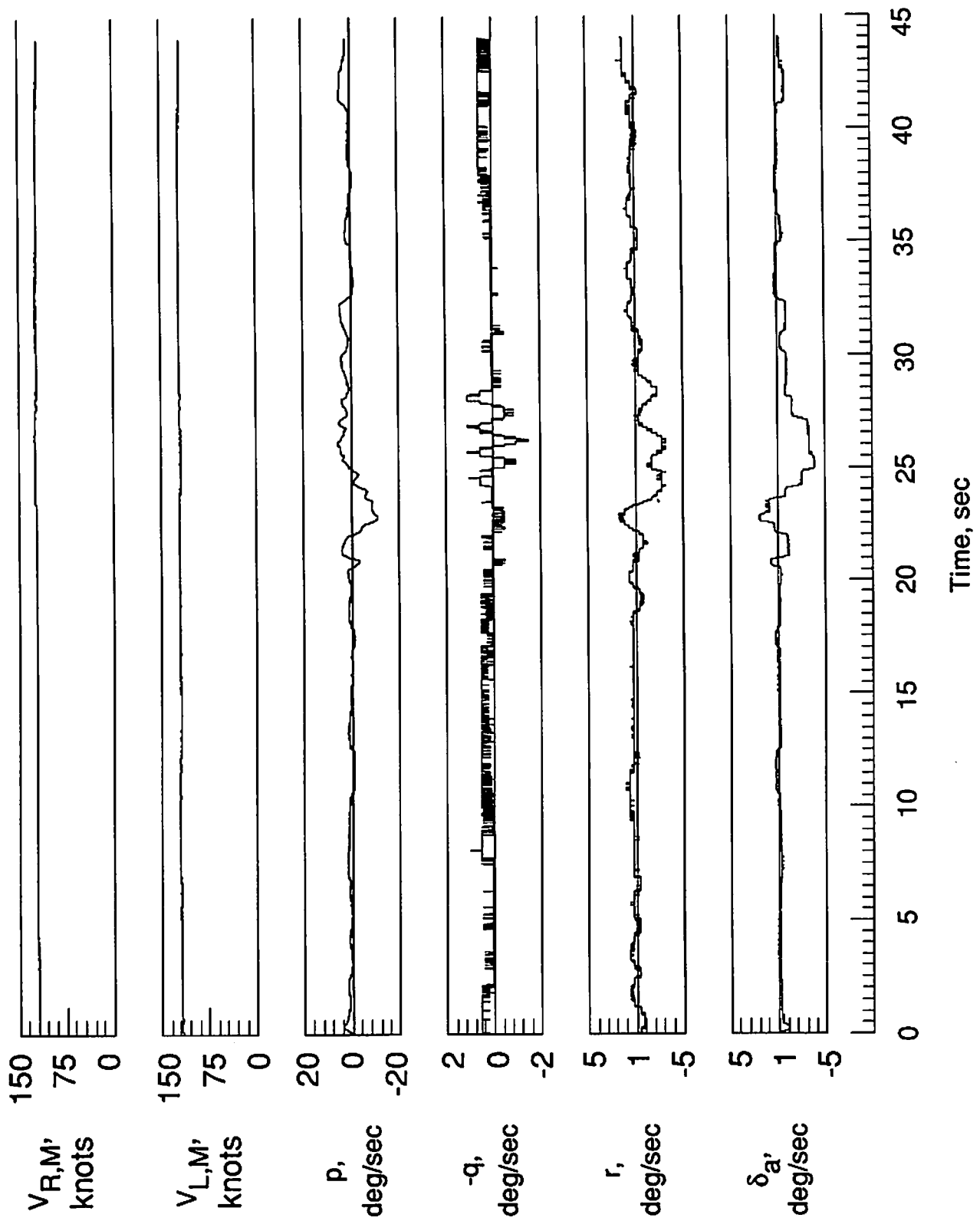
Figure 7. Unprocessed data with flaps retracted on vortex-generating airplane (continued).
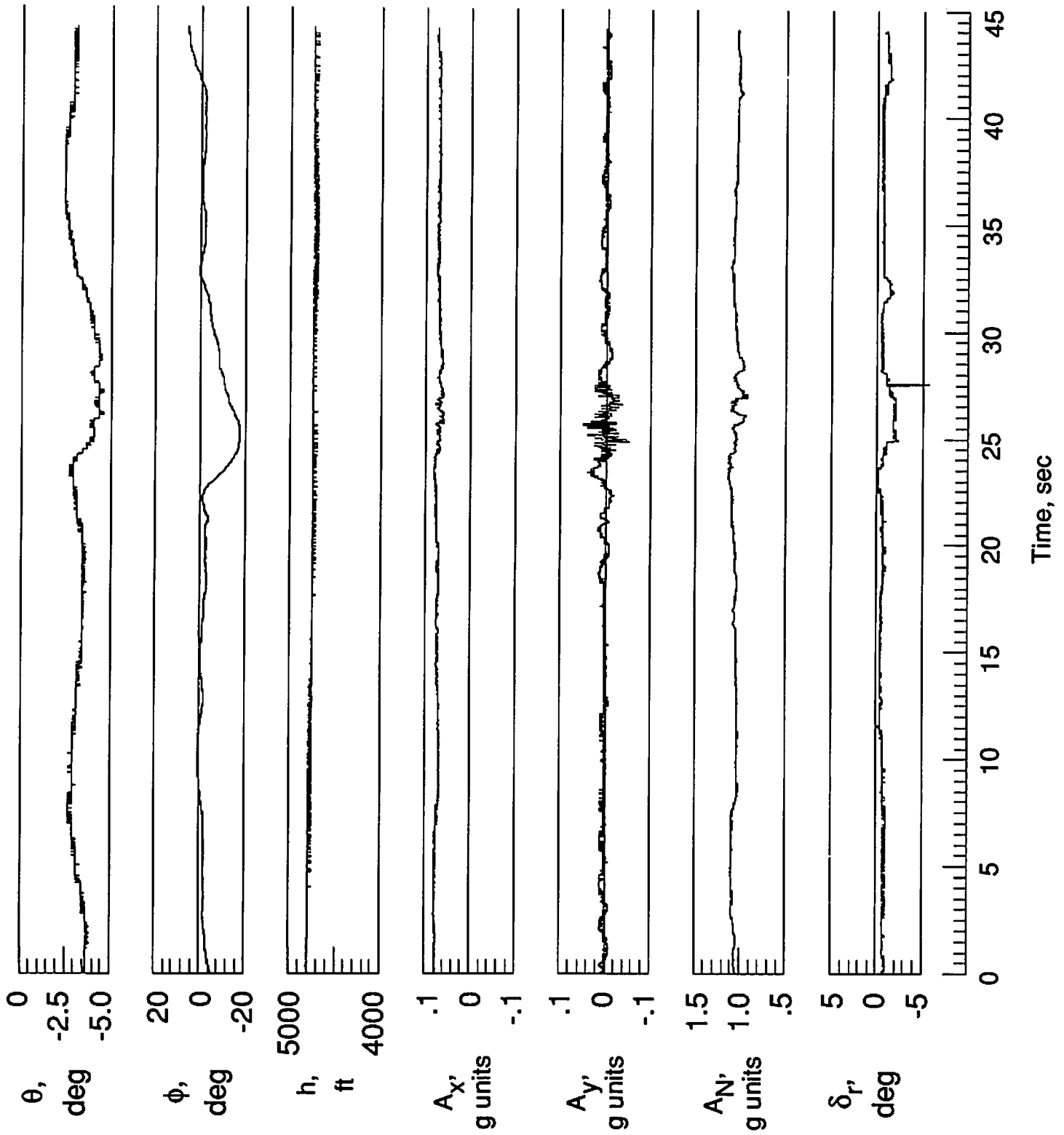
Figure 7. Unprocessed data with flaps retracted on vortex-generating airplane (concluded).
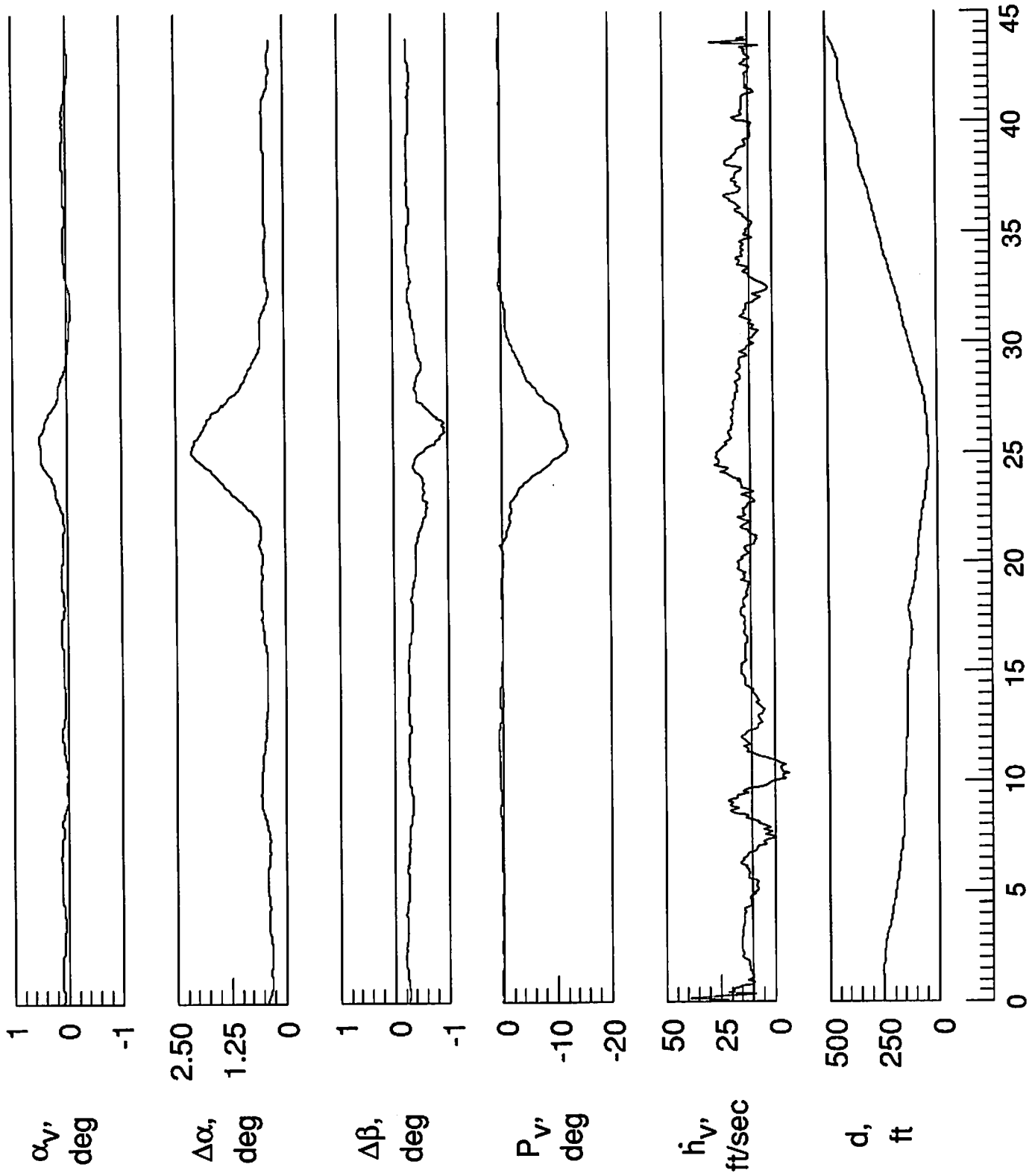
Figure 8. Processed data with flaps retracted on vortex-generating airplane.
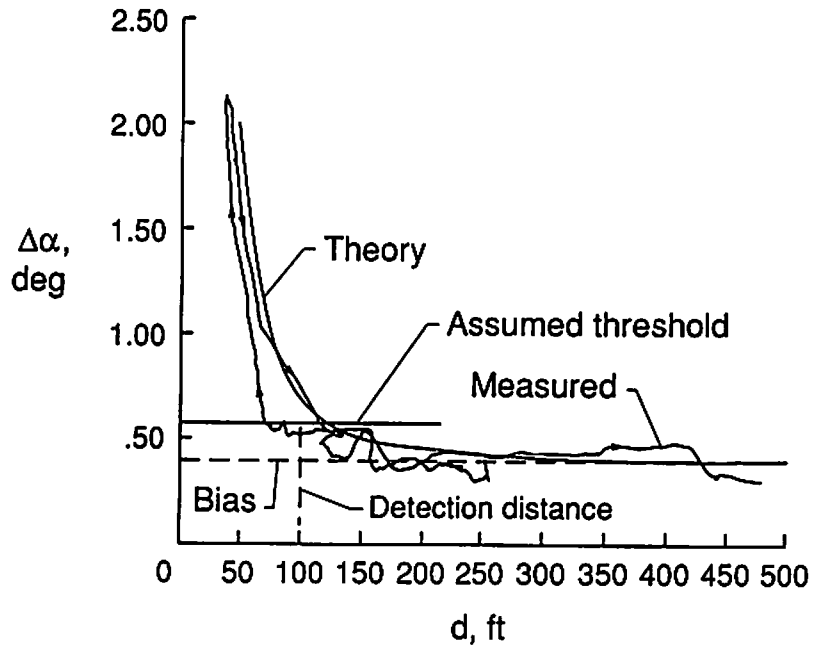
Figure 9. Effect of vortex flow field on differential angle of attack. Flaps retracted on vortex-generating airplane.
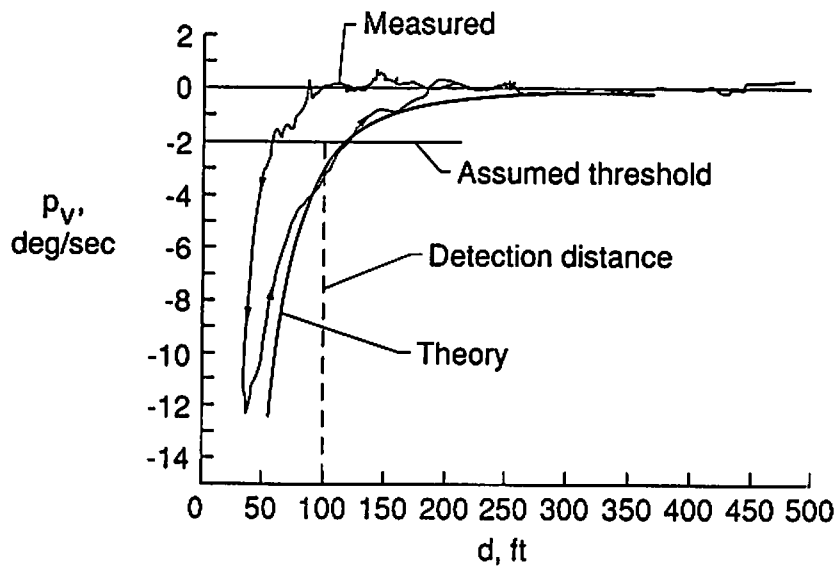
Figure 10. Effect of vortex flow field on vortex roll rate parameter. Flaps retracted on vortex-generating airplane.

44-20
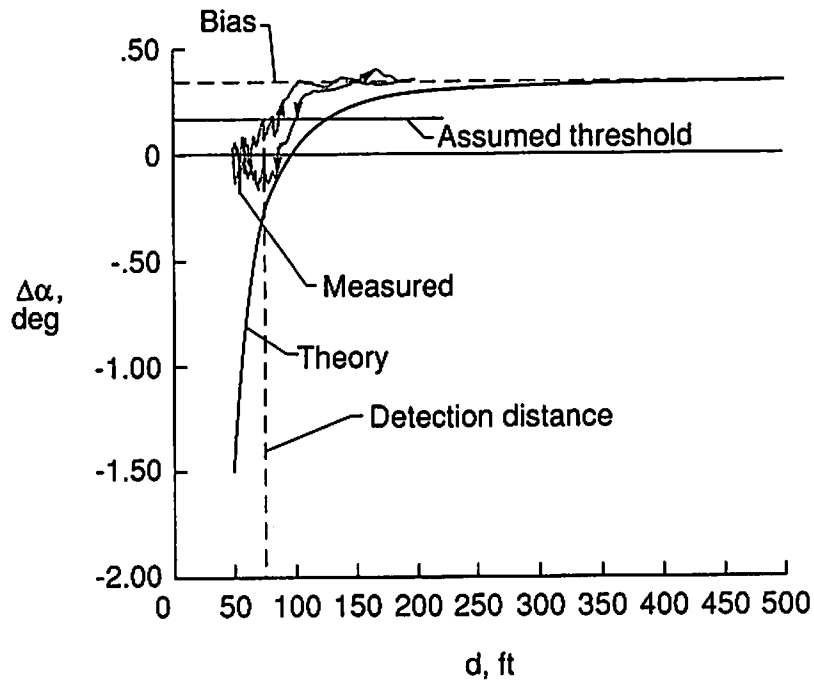
Figure 11. Effect of vortex flow field on differential angle of attack. Flaps retracted on vortex-generating airplane.
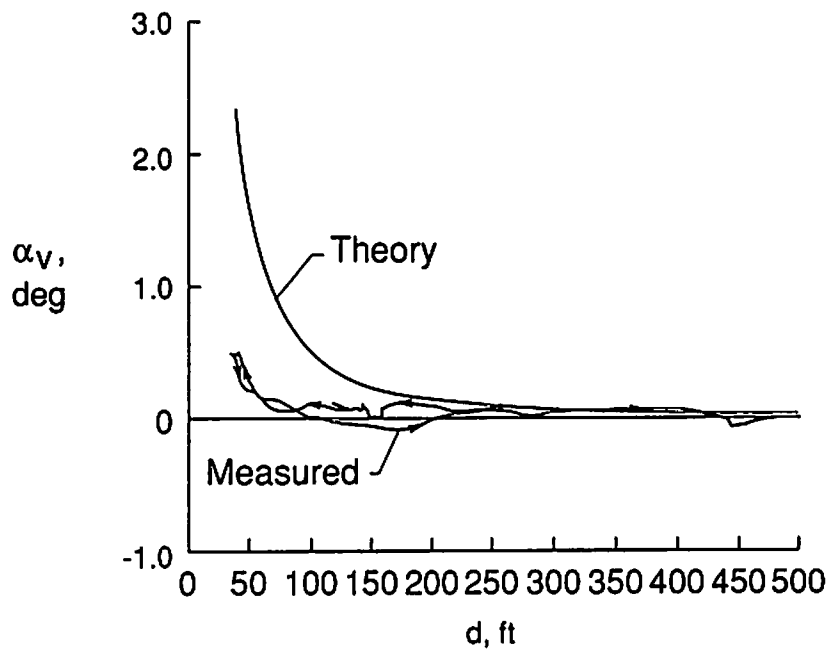
Figure 12. Effect of vortex flow field on angle of attack. Flaps retracted on vortex-generating airplane.

44-21
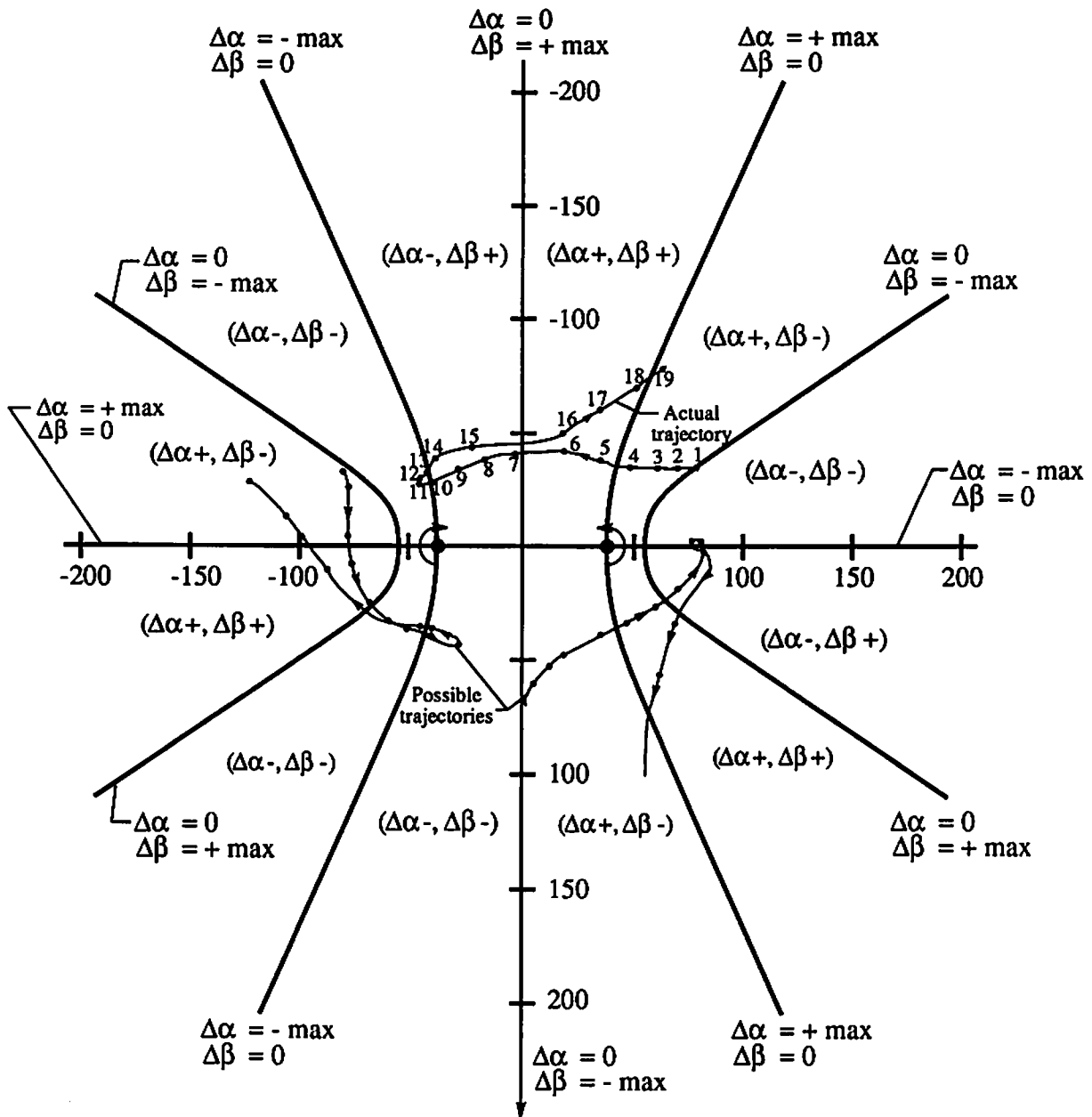
Figure 13. Trajectories reconstructed from differential flow-angle measurements and video data.
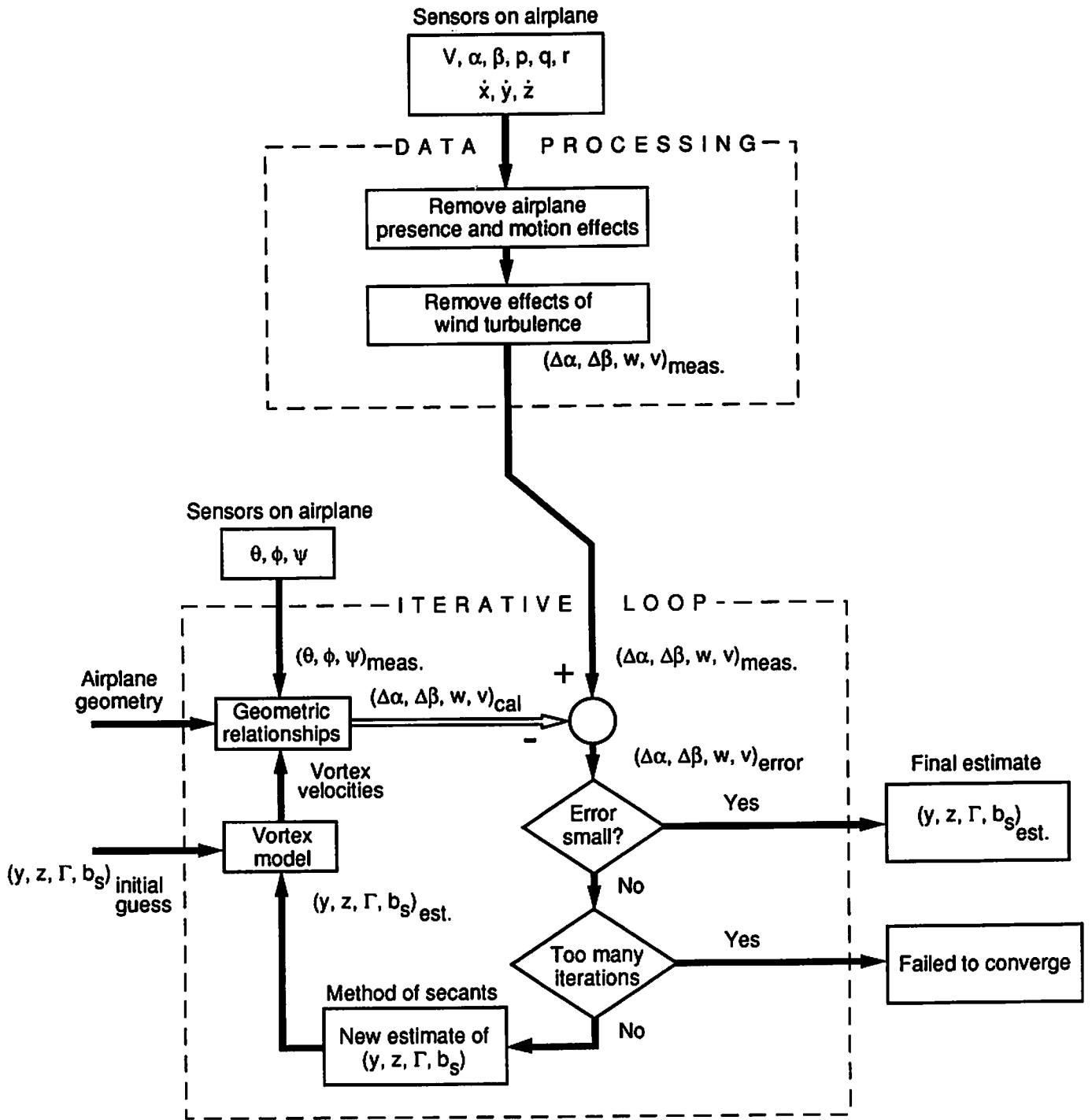
Figure 14. Candidate algorithm for estimating vortex strength and location from measurements on probe airplane.
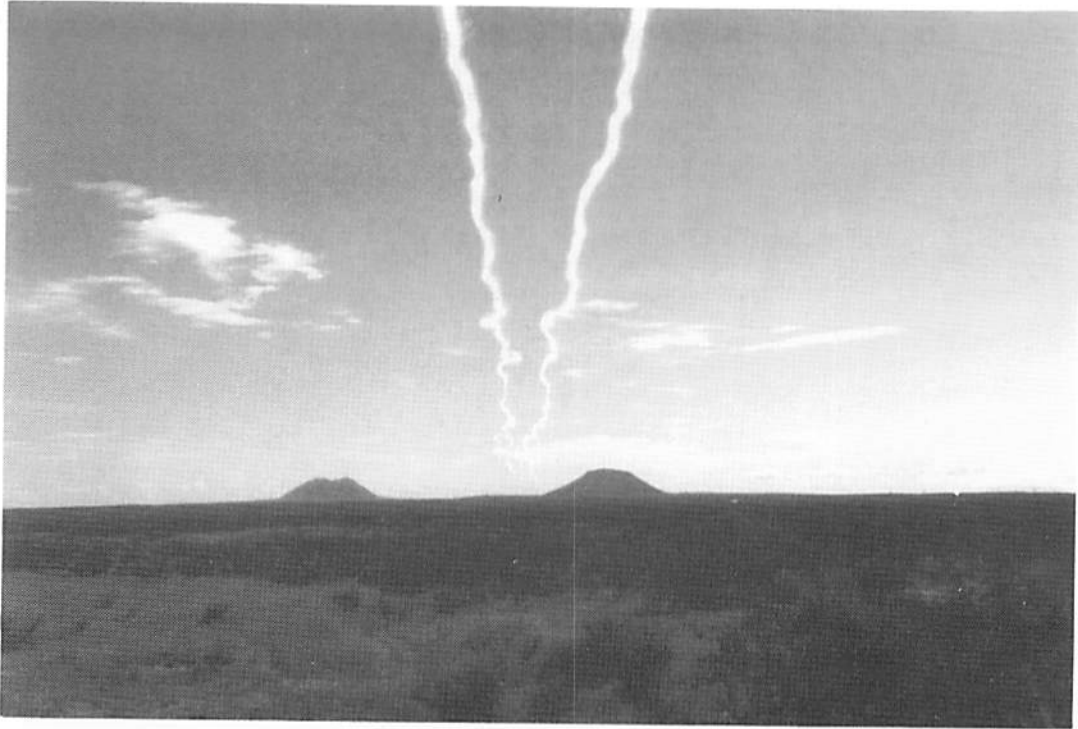
Figure 15. Wake vortex smoke trails illustrating distortion
of ideal linear vortex models.
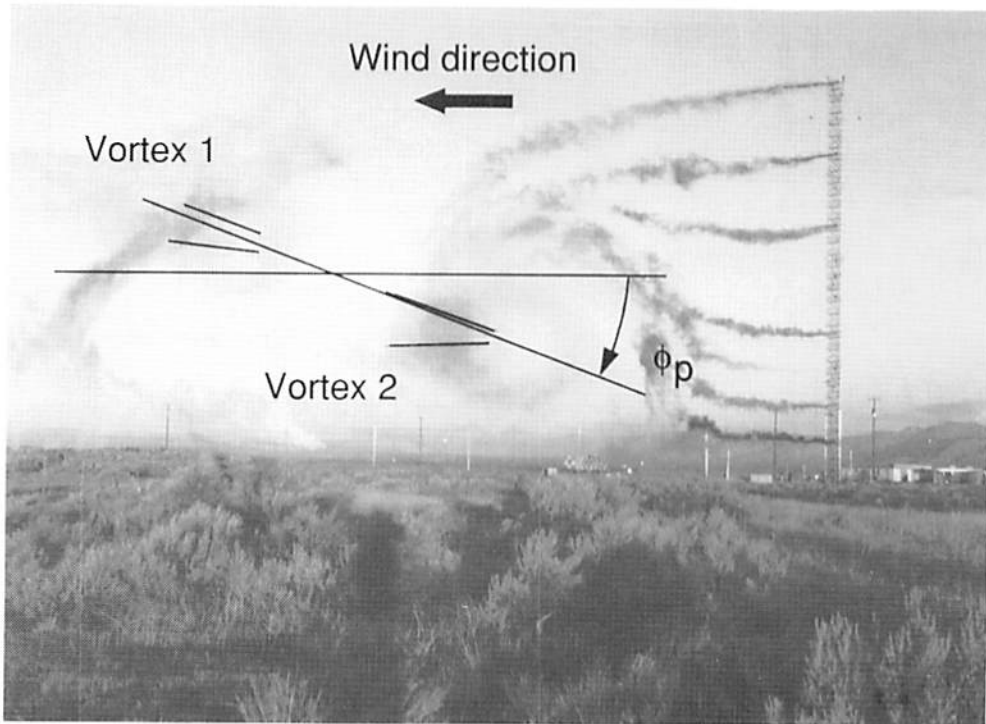
Figure 16. Wake vortex pattern illustrating rotation of the plane
of the vortex pair due to shear in crosswind near the ground.
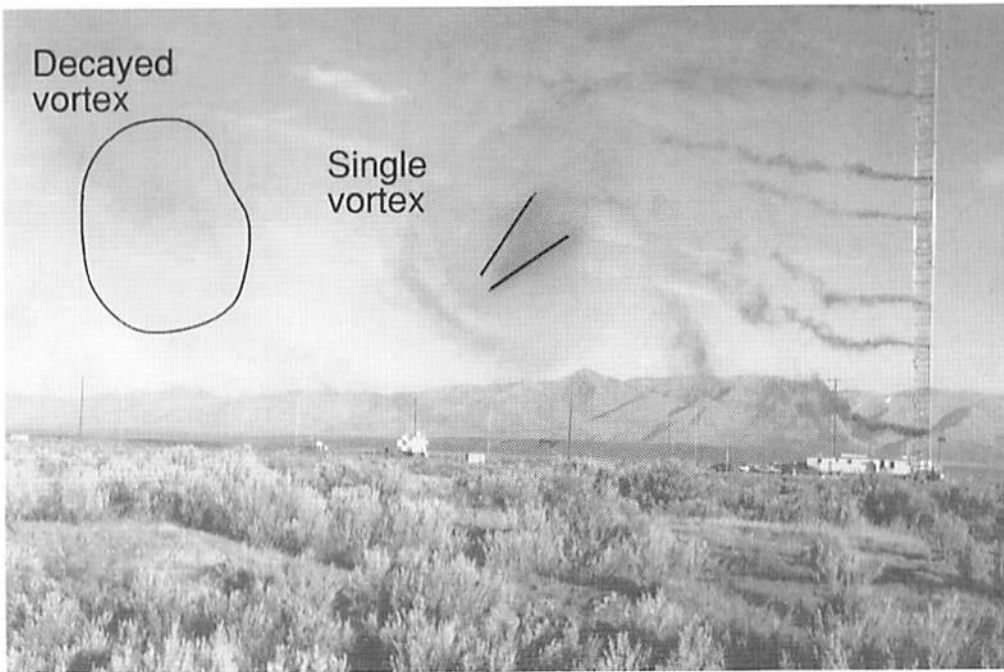
Figure 17. Wake vortex pattern illustrating the decay of
one vortex in the vortex pair.

REFERENCES

1. Bilanin, Alan J.; Teske, Milton E.; and Curtiss, Howard C., Jr.: *Feasibility of an Onboard Wake Vortex Avoidance System.* NASA CR-187521, 1987.

2. Stewart, Eric C.: *A Comparison of Airborne Wake Vortex Detection Measurements With Values Predicted From Potential Theory.* NASA TP 3125, 1991.

3. Glover, Howard: *Windshear Detection and Recovery Guidance: An Equipment Manufacturer's Perspective.* Windshear Conference Proceedings, Royal Aeronautical Society; November, 1990.

REAL RESEARCH OF DIFFERENT CLASS
AIRPLANE VORTEX WAKES AT LOW ALTITUDES

A.N. Zamyatin
Flight Research Institute
Moscow, USSR

The paper is intended to investigate airplane wake vortex in real flight at low altitudes. The paper is aimed at obtaining real flight data for wake vortex generation, development and decay processes of an airplane flying at modes approaching the takeoff and landing ones. The acquired data are anticipated to be used in designing means of affecting the wake vortex structures to decrease their unfavorable effects on other flying airplanes, as well as in developing mathematical models of the airplane wake processes.

To perform studies special techniques were worked out which allow synchronous measurements of spatial kinematic and geometrical wake characteristics, airplane flight and environmental parameters to be made. The techniques use the hot-wire method for measuring the instant velocity, a method of wake visualization and a stereophotogrammetric survey method. These techniques are presented in detail in the report [1] at this symposium. Using these methods, wake vortices of two classes of airplanes were studied: a medium-haul Tu-124 weighing about 35,000 Kgs and a light highly maneuverable L-39 with a weight of 3,500 Kgs. Flights were performed at altitudes below 400 m.

As the investigations have shown, the measurement results are in good agreement with the airplane wake development scheme devised earlier and presented at the 14th ICAS [2]. According to the scheme, an airplane vortex wake has five phases in its development. The first one is the wing trailing-edge vortex sheet rolling-up and the vortex system generation. As a rule, among these vortices there are dominating ones which involve the rest vortices in the common vortex motion, with an intensive vortex pair having a high concentration of the core vorticity being formed. Figure 1 shows corresponding photos of vortices in the Tu-124 and L-39 wakes.

There are no changes in the kinematic and geometrical characteristics of the vortex pair throughout the second phase and the entire vortex system descends at a low speed that fits the estimated one. Special attention was paid to the flow in the vortex core. Spatial quantitative and qualitative characteristics were obtained in the flight experiment, which permitted an insight into the vortex core flow. Figure 2 gives the vortex core flow pattern obtained using smoke visualization (Figure 2a), averaged distributions of the tangential and axial vortex flow velocities from the measurement results (Figure 2b), and a pattern of the airplane wake flow in Phases II

and III of its development, constructed using the experimental data (Figure 2c). The intensive axial flow is observed on the vortex axis; its velocity is opposite to the airplane flight direction. Around the core periphery the axial flow velocity decreases and even the flow direction changes.

Two opposite wake vortices which affect each other contribute to periodic disturbances in their motion. The presence of the perceptible spatial disturbances in the vortex geometry indicates the completion of the development Phase II. Figure 3a shows a representative geometric change of the vortex core axes in the vertical and horizontal planes for the Tu-124 and L-39 airplanes at speeds of 360 km/h and 270 km/h, respectively, which was obtained using the stereophotogrammetric method.

Phase III of the wake development is characterized by a growth in the geometric disturbance amplitude of the vortex axis and a dominating disturbance having a certain wavelength. From the experimental results, at V=350 km/h this length for the Tu-124 is about 160 m and 70 m for the L-39. In Phase III the flow pattern typical of the previous phase remains. As an example, Figure 3b gives distributions of the flow lateral and vertical velocities for the Tu-124 airplane flying at V=360 km/h and H=350 m, which were observed in the wake at distances corresponding to Phases II and III. The completion criterion for Phase III is the presence of substantial changes in the wake kinematic characteristics.

Phase IV is characterized by two kinds of the wake kinematics change: the vortex core growth with the maximum circular velocity decrease and a sudden localized circulation reduction accompanied by generation of diverging toroidal vortices (vortex core "burst"). This vortex core growth fits well the Squire theory (Figure 4a). As a rule, "bursts" occur in the areas of considerable vortex axis curvatures. Figure 4b is an illustration of the vortex core "bursts" occurred in the Tu-124 and L-39 wakes. Phase IV transits to Phase V — completing the wake development — with the vortices approaching each other or the ground surface when the vortex breaking or joining occurs.

Phase V is characterized by generation of the distorted vortex rings (Figure 5b) or arched vortices resting on the ground (Figure 5). In this case the burst-type vortex core destructions continue developing on the arches and rings.

When conducting flight research of the airplane wake vortex structures at low altitudes, about 80 flights were performed on the Tu-124 and 45 flights on the L-39 at different time of the day and the year. Each flight included from 8 to 15 operating modes. The results obtained for similar flight conditions were averaged. These data are given in Table 1.

Based on the results of Table 1, the wake phase lengths are seen to reduce with decreasing flight speed and altitude and flaps extension. Atmospheric conditions also influence the vortex wake phase lengths. Longer phases were observed under more stable atmospheric conditions with a low level of the wind speed fluctuations. In all the cases of the studies the final phase (Phase V) was characterized by the creation of the closed vortices which shall not have any hazardous effect on a crossing airplane. These vortex structures are due to the development of the wave instability, a vortex pair occurring with the flight altitude under the effect of the ground proximity in the form of the vortex arches and with no ground effect in the form of the vortex rings. Since, as the flight experiment has shown, the wake vortex pair wave instability in flying

at low altitudes is the dominating wake development process resulting in its destruction, the most effective influence to speed up the wake decay is the influence upon this particular wake development process. It is well-known that, the duration of the vortex pair decay (t_b) due to the wave instability depends on the vortex circulation (Γ), core radius (r_b) and the distance (l_b) between the vortex axes and equals

$$t_b = \frac{4\pi l^2}{\Gamma} \, bl_n \, \frac{l_b}{r_b}$$

If the values

$$R_b = \frac{\Gamma_o}{\Gamma} \quad \text{and} \quad L_b = \frac{\Gamma_o}{\Gamma} \, l_b \quad \text{are introduced,}$$

where Γ_o is a certain representative circulation value, the vortex pair condition can be characterized by a point on a plane ($R_b L_b$). Figure 6a shows lines of the equal decay durations because of the wave instability of different vortex pairs. For the Tu-124 and L-39 airplanes different points are obtained experimentally, and for the Yak-42, Il-62, Il-86 and Tu-154 airplanes the points are derived from calculations.

Obviously, to accelerate the decay caused by the development of the vortex wave instability it is necessary either to reduce L_b or to increase R_b. One of the wake affecting means, namely winglets, was tested in flight. The winglet installation scheme is given in Figure 6b. They were installed on the L-39 and resulted in velocity redistribution in the vortex core. Figure 6c indicates the tangential and axial velocity variations caused by the winglets effect. This clearly increases R_b accompanied by the wake length reduction by an average of 20%.

Thus, based on the flight test results we obtained experimental data widening the idea of the airplane wake vortex structure. In this case:

-    the spatial structure of the vortex core flow was determined in the flight experiment;

-    it was noted that in flying at low altitudes wake development and decay due to the vortex pair wave instability are dominating ones;

-    it was demonstrated that in flights at altitudes close to the wing span the arched vortices resting on the ground surface develop because of the ground proximity effect.

The flight results for various daytime and season of the year showed the influence of the airplane flight parameters and atmospheric conditions on the vortex wake length.

With the winglets installed on the light maneuverable airplane in the flight experiment, as an example, a possibility of reducing the wake length using the effect on the wake vortex flow structure was demonstrated.

Table 1.

AIRCRAFT	VELOCITY V_∞, km/h	ALTITUDE H, m	POSITION T/E FLAPS	POSITION U.F. FLAP	DISPERSION D_v, m²/s²	ATMOSPHERIC CONDITION	L_1, m	t_1, s	L_2, m	t_2, s	L_3, m	t_3, s
Tu-124	500	350	0	DOWN	0.55	LOW INSTABILITY	800	5.8	2000	14.4	3500	25.2
Tu-124	500	350	0	DOWN	0.80	MODERATE INSTABILITY	900	6.5	1500	10.8	2200	15.8
Tu-124	350	350	0	DOWN	0.30	INDIFFERENT	800	8.2	2000	20.6	3600	37.0
Tu-124	350	350	35°	DOWN	0.30	INDIFFERENT	700	7.2	1200	12.3	2600	26.5
Tu-124	350	350	0	UP	0.30	INDIFFERENT	400	4.1	1000	10.3	2000	20.5
Tu-124	300	12	0	DOWN	.	.	150	1.8	400	4.8	600	7.2
L-39	270	320	0	DOWN	0.35	INDIFFERENT	320	4.3	750	10	1250	16.7
L-39	250	320	44°	DOWN	0.35	INDIFFERENT	300	4.2	680	9.5	1000	14.4
L-39	340	320	0	DOWN	1.2	MODERATE INSTABILITY	250	2.6	610	6.5	790	8.4
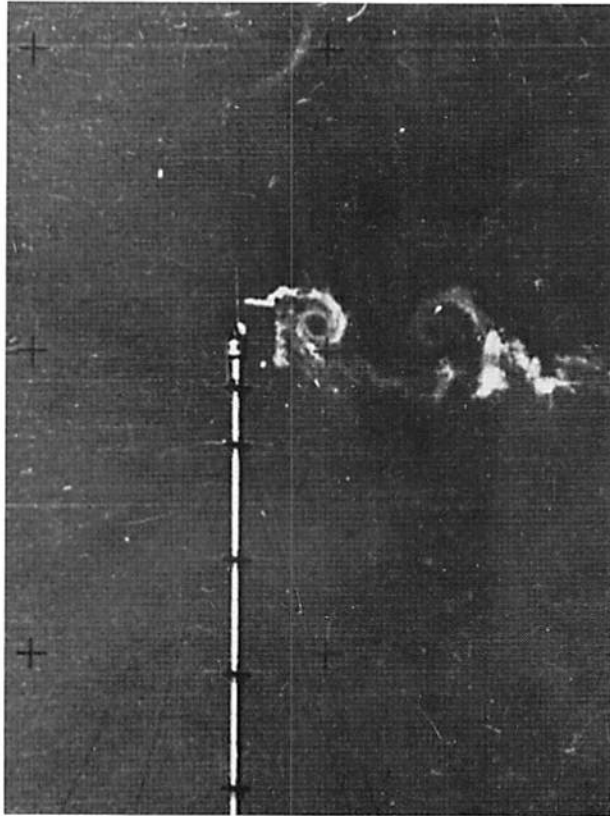
Tu-124
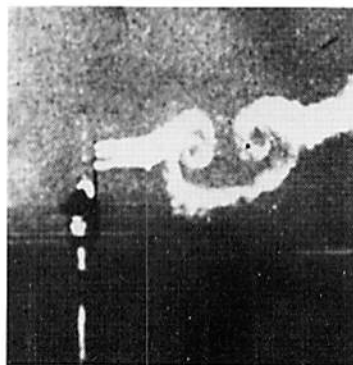
L-39

Figure 1. Two whirling vortices in the wake of aircraft.
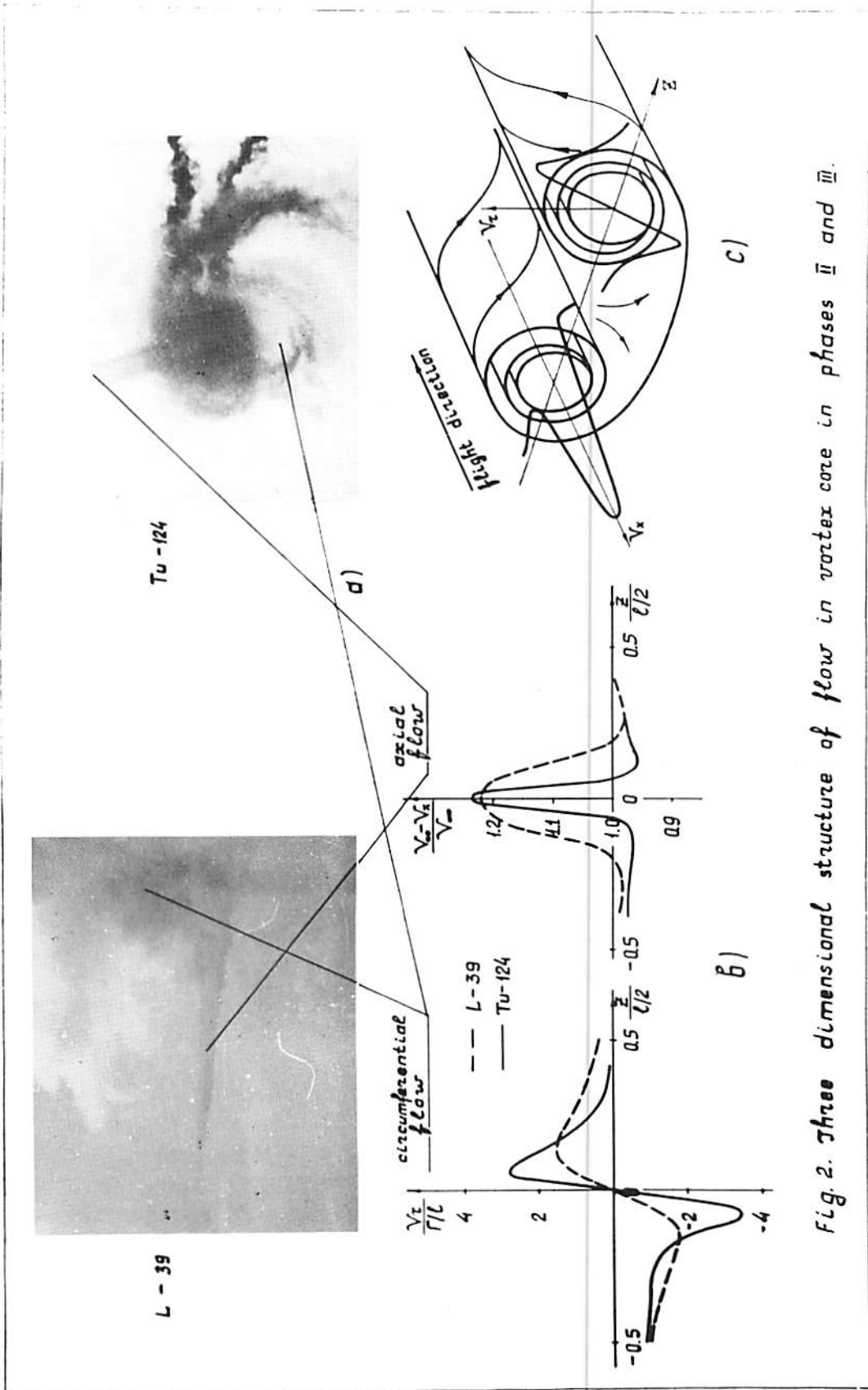
Fig. 2. Three dimensional structure of flow in vortex core in phases II and III.

Figure 2. Three-dimensional structure of flow in vortex core in phases II and III.
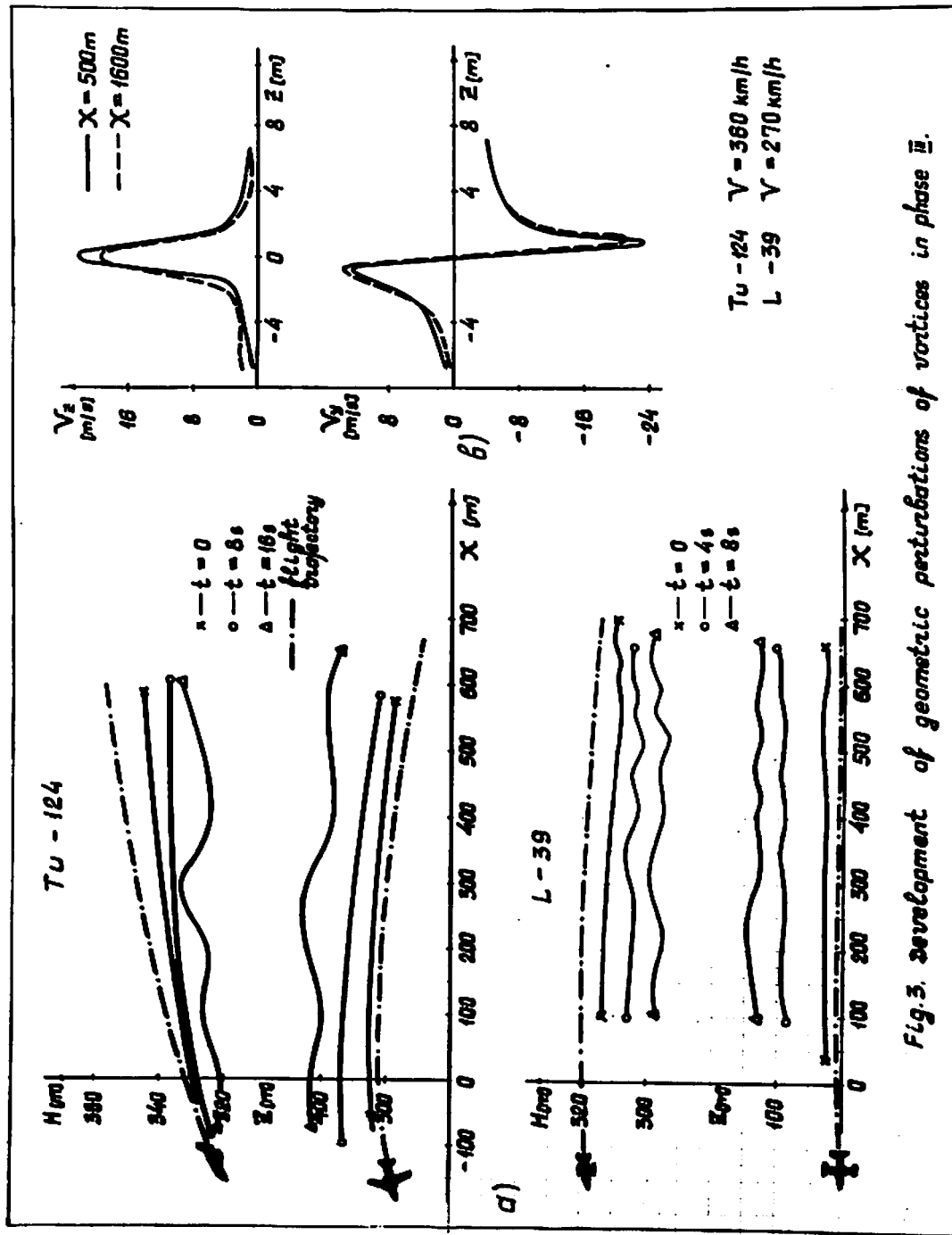
Fig. 3. Development of geometric perturbations of vortices in phase III.

Figure 3. Development of geometric perturbations of vortices in phase III.
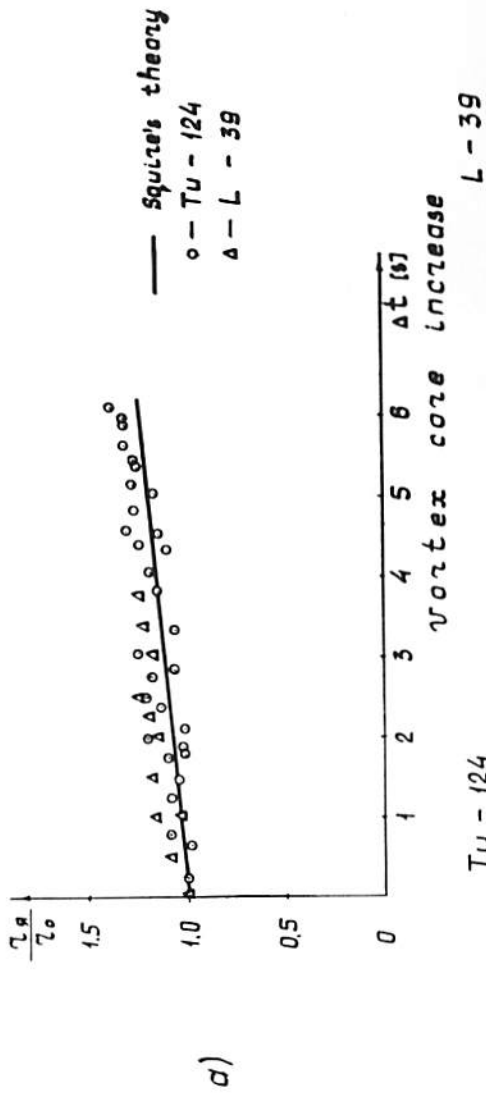
Fig.4. Variations in the vortex flow in phase IV.

Figure 4. Variations in the vortex flow in phase IV.
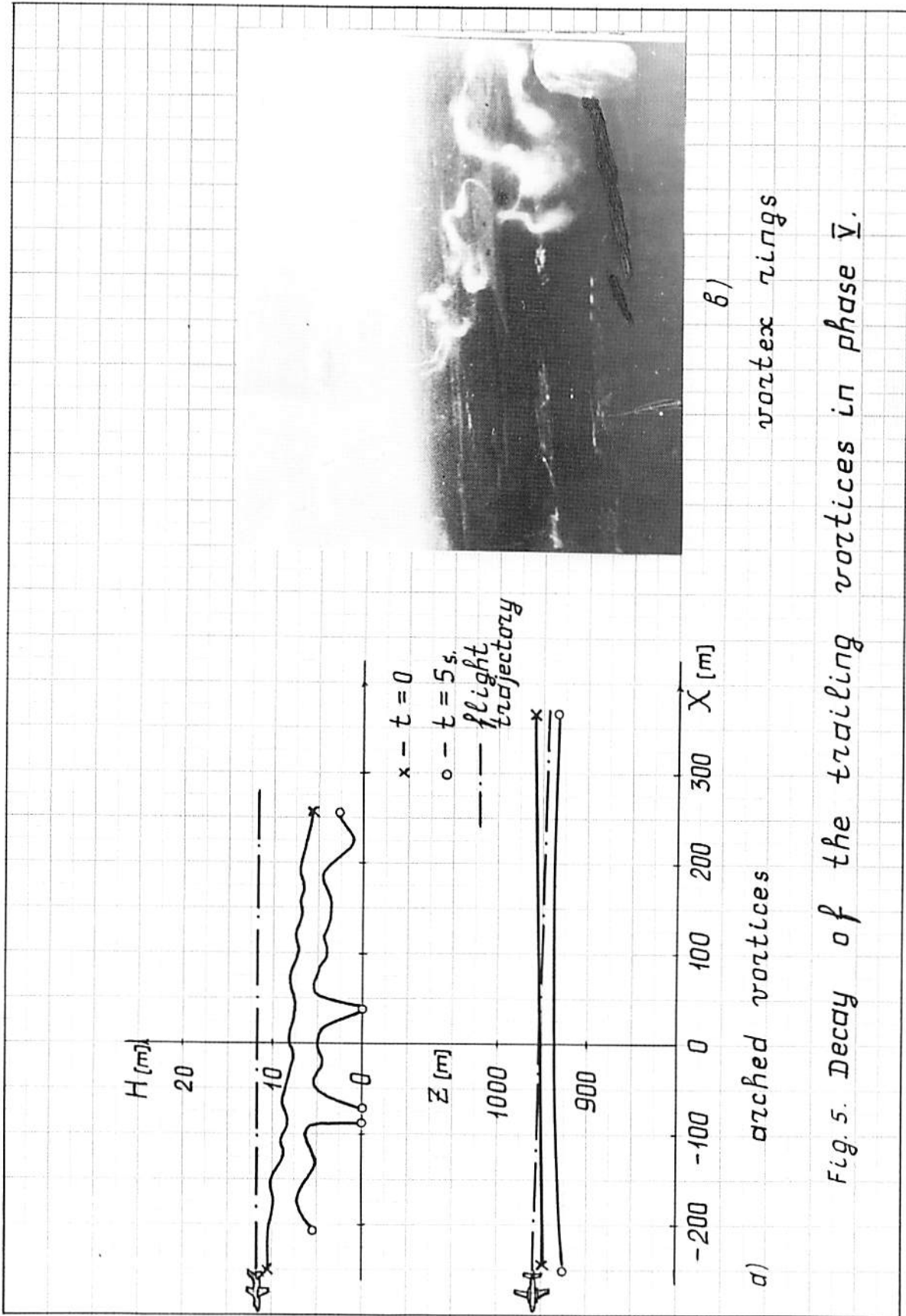
Figure 5. Decay of the trailing vortices in phase V.
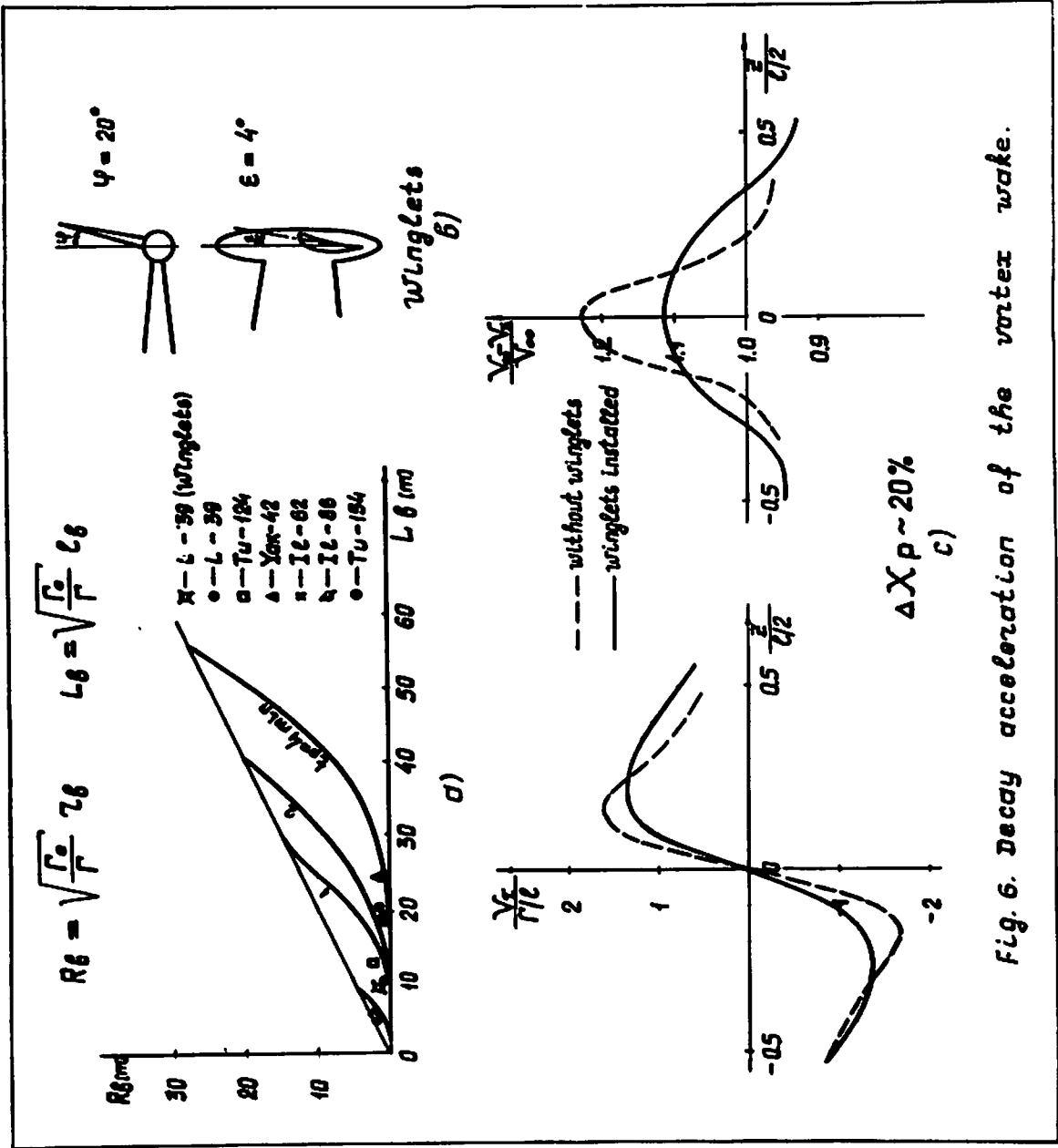
Figure 6. Decay acceleration of the vortex wake.

REFERENCES

1. Zavershnev, Y.A., Kushnerev, V.K., Zamyatin, A.N., "Methods of Studying a Wake Vortex Structure in Flights at Low Altitudes." International Wake Vortex Symposium, 1991, Washington, DC.

2. Zamyatin, A.N., Gratchov, V.S., "Full-Scale Studies of Structure and Development of a Vortex Wake of a Medium Trunk-Route Aircraft in the Atmospheric Boundary Layer." 14th ICAs Proceedings, 1984. Toulouse.

EXPERIMENTAL INVESTIGATION OF WAKE VORTEX STRUCTURE AND PROPAGATION USING THE DLR LASER DOPPLER ANEMOMETER

Friedrich Koepp
DLR-Institute of Optoelectronics
D-8031 Oberpfaffenhofen, FRGermany

OBJECTIVES

Extensive experiences in the USA and Germany have proved that the infrared Doppler Lidar is the most effective and flexible remote sensing method for wake-vortex detection, measurement, and tracking. Therefore, the DLR Laser Doppler Anemometer has been incorporated into the German Wake Vortex Program. This program is concentrated on the highly frequented Frankfurt Airport where additional capacity limitations are caused by the separation of 1700 ft between the two parallel runways. This separation is often too small for operating both runways independently with respect to wake vortices. Therfore, the main objectives are the determination of the strength and propagation of the vortices of "new generation" aircraft, such as B757, B767, and A320, and the identification of atmospheric conditions where vortex-independent operation of the parallel runways is possible.

FIELD EXPERIMENT

The DLR Laser Doppler Anemometer (LDA) has been developed for Boundary Layer wind and turbulence investigations. It is a continuous wave system based on a 4 watt CO_2 laser and a transceiver telescope of 30 cm diameter. The range can be varied between 40 and 1000 m. The flexible scanning device enables one to point the measuring beam in all directions. Control of scan procedures, data acquisition and on-line evaluation is performed by a Compaq 386. Up to 160 frequency or velocity spectra per second can be stored. These features are the basis for precise vortex measurement with an elevation-angle resolution better than 0.2°, a localization accuracy of a few meters, and a repetition rate of a few seconds.

During several extended field experiments in the years 83-85 and 89-90, the LDA has been operated at Frankfurt Airport measuring the vortices of more than 1400 landing aircraft of both a heavy and large variety.

For vortex investigations with ground effect, the LDA container was positioned between the landing corridors of runways 25R and 25L, about 850 m in front of the thresholds. As sketched in Figure 1, a section of the vertical measurement plane across one of the approach corridors

is covered by a fast elevation scan at fixed range setting. The right side of the figure shows the measured velocity profile of a B747 port vortex. This profile is the superposition of the vortex rotational field and the lateral vortex transport including the cross-wind component. Even though the LDA is operated in homodyne mode, it is possible to distinguish positive and negative velocity components by using the known cross-wind direction for reference. After the vortex has passed that sensing region, the next one is chosen by changing the range setting. As soon as the vortex has reached the LDA position, the measurement plane is turned in azimuth by 180° and the vortex tracking is continued toward the parallel runway.

EXPERIMENTAL RESULTS

Vortex Structure, Strength, and Aging

The potential of the Doppler Lidar method for wake vortex investigations can be illustrated by means of some selected examples starting with the structure of single vortices.

The velocity profiles of a B757 vortex pair are drawn in Figure 2 using the prevailing cross wind of 4.4m/sec for centerline. The grey curve represents the compact downwind vortex measured 28 sec after aircraft passage. Its core axis lies 46 m above ground level and the core diameter is less than 4 m. In contrast to that, the 33-sec-old upwind vortex centers at 24 m altitude. Due to its ground proximity, the core diameter is increased to 6 m and the velocity maxima are already reduced.

This B757 measurement is a nice example of vortex-pair tilting induced by cross-wind shear. Both profiles were measured at a fixed range setting of 97 m from the LDA system. The 22-m height difference and the 5-sec time delay can be converted in a slant distance of 30 m between the vortex cores. Considering the vortex pair embedded in the so-called wake oval, this oval is drifting above the ground with a tilt angle near 45°.

Another phenomenon of interest is the aging of vortices. It can be observed, for example, by means of a single vortex generated by a landing C5A Galaxy. Figure 3 shows the passage of the downwind vortex at 63 m range setting, before the azimuth rotation (55 sec) and afterwards (87 sec). In this time period the vortex center rose from 31 to 33 m and the core diameter grew from 4 to 8 m. This vortex growth is the beginning of the decay process.

In principle, the vortex circulation can be evaluated by integration over the velocity profiles. But, it is more convenient to describe the vortex strength by the maximum tangential velocity measured. A velocity of 4 m/sec has been identified as a hazard limit for encountering aircraft. For example, Figure 4 comprises the temporal behavior of the tangential velocities of different aircraft. After a roll-up period of a few seconds, the velocity remains almost constant for about 40 sec. Then, the decrease phase begins and the velocities approach the grey 4 m/sec area after 80 sec. The spread of the data points is rather large. For worst-case considerations the envelope of this distribution has to be taken into account.

Vortex Transport and Bouncing

The horizontal vortex propagation in ground effect is of special interest for the operation of parallel runways with separations of less than 2500 ft.

In Figure 5 the results of one complete measurement sequence are compiled which is the landing of a B747 on runway 25L. In the upper part, the maximum tangential velocities are shown; the vortex ages in seconds are labelled by the numbers. The lower part shows the positions of the downwind vortex during the transport extending over the LDA container towards the parallel runway.

Driven by the cross wind, the vortex descends on a slant slope to ground proximity. There, the lateral motion is intensified by the self-induced velocity. In this example, the horizontal shift velocity is at a maximum value of 8 m/sec directly after descent and approaches the cross-wind value of close to 4 m/sec after 61 sec. Under cross-wind conditions of that amount, the vortices actually reach the safety area of the parallel runway with high probability, in this case after 87 sec still exhibiting critical strength.

Besides the horizontal propagation, the transport curve of Figure 5 shows the tendency of increasing height after the vortex has reached ground proximity. Figure 6 illustrates that this so-called bouncing effect is not an isolated case but is more or less common behaviour. The bouncing vortices of a number of B747 landing on 25L and 25R respectively partly show a steep ascent towards the parallel runways. This bouncing effect may enhance the hazard, since the vortices have a tendency to cross the parallel runway near the altitude of the approaching aircraft.

CONCLUSION

During several extended field experiments at Frankfurt Airport, the DLR Laser Doppler Anemometer has acquired excellent data sets from the vortices of more than 1400 landing aircraft. They are the basis for investigations of vortex structure, strength, and decay and for the description of vortex transport in the area of ground influence. The bouncing effect seems to be unusually pronounced at this airport.

A Joint Experiment together with the US Laser Doppler Velocimeter is recommended for the investigation of special questions, like long distance propagation, total decay, axial flow, and all types of three-dimensional problems.

For airborne measurements of wake vortices, wind shear, and clear air turbulence, a 2-μm wavelength Doppler Lidar looks promising, as soon as it has reached the technological maturity of the 10-μm systems.
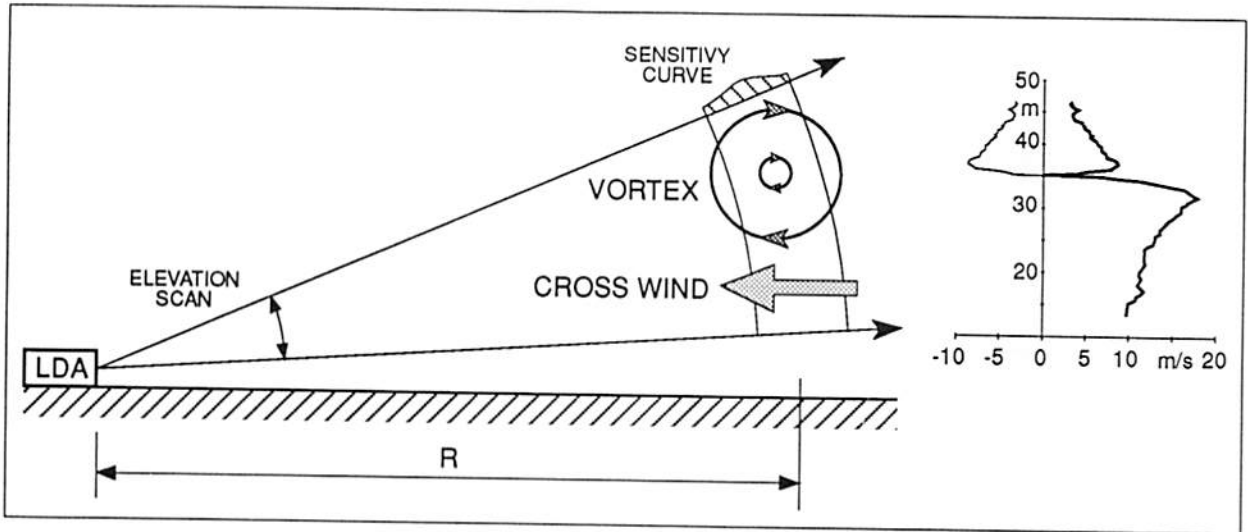
Figure 1. Strategy of wake vortex measurement using the LDA system.
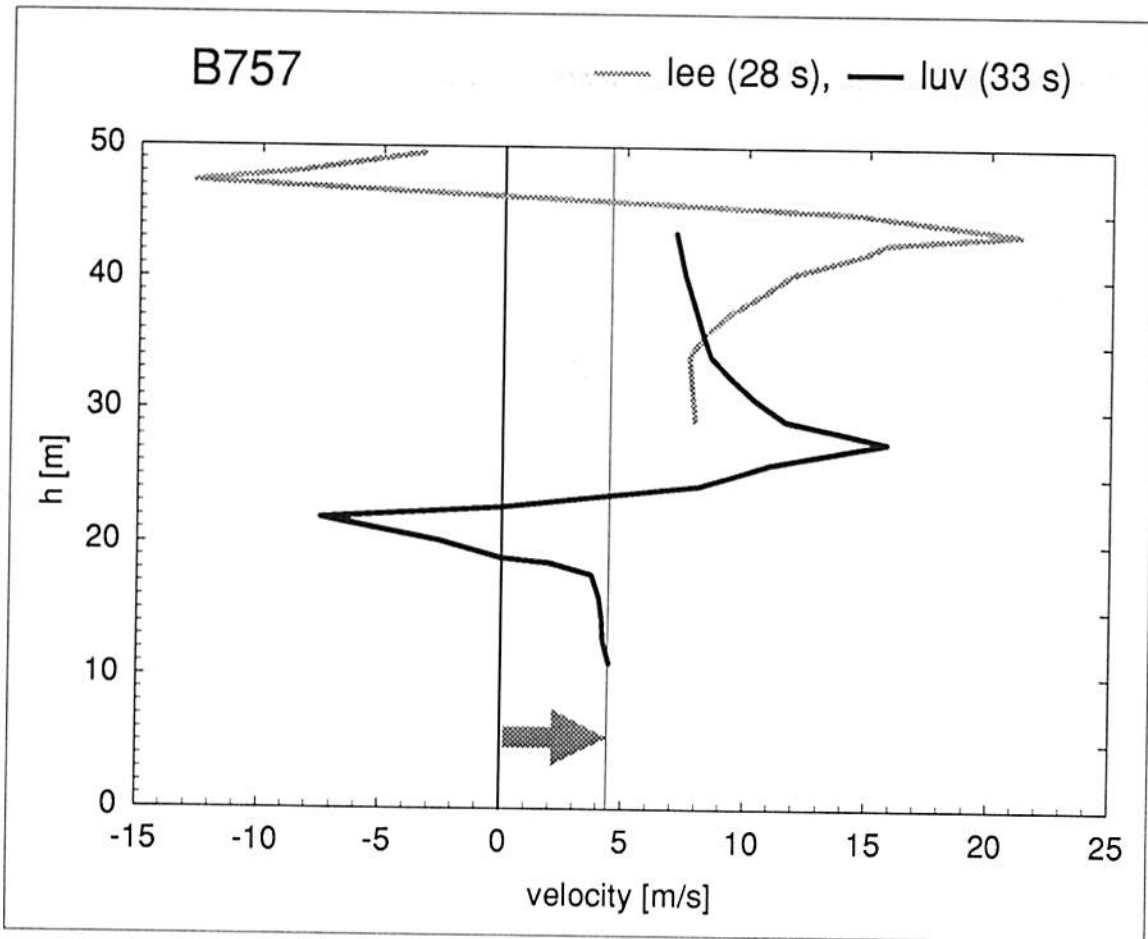
Figure 2. Velocity profiles of both vortices of a landing B757 aircraft.
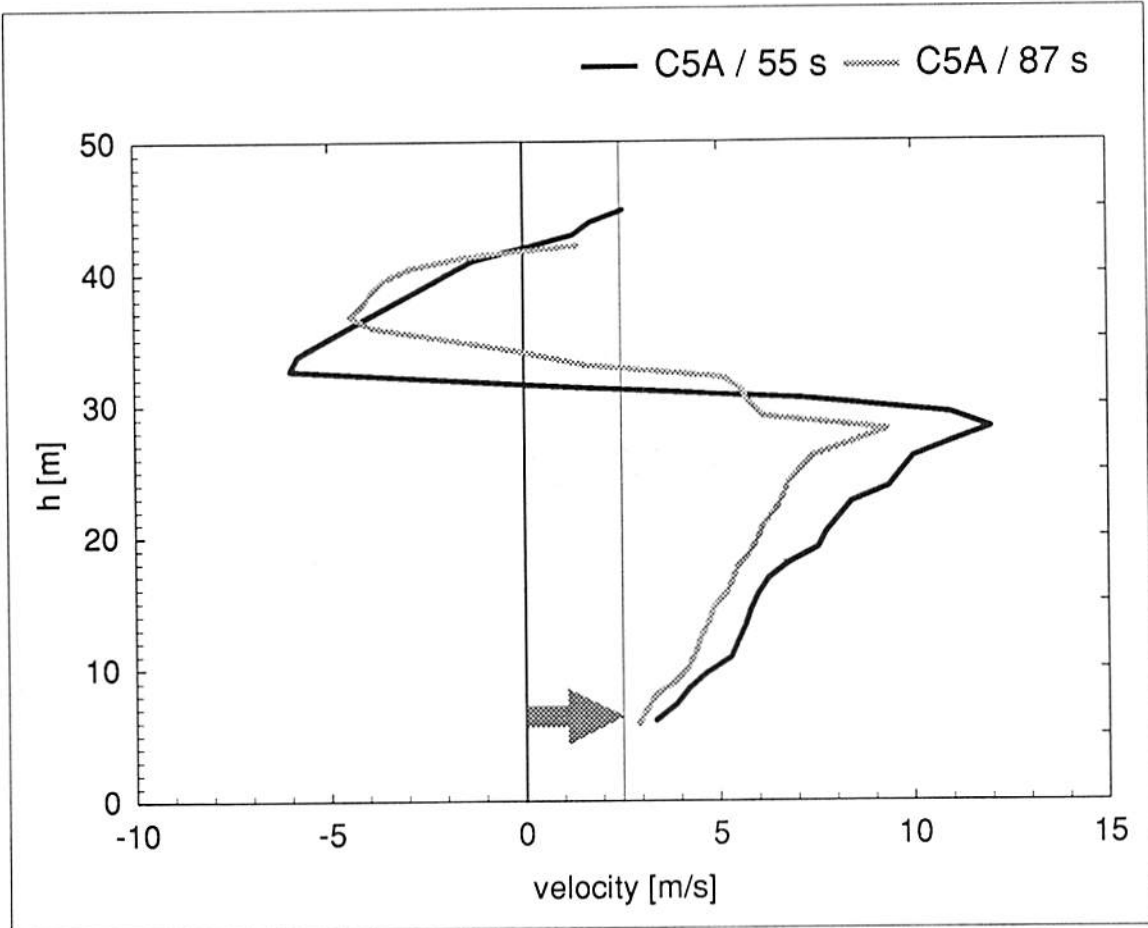
Figure 3. Comparison of C5A velocity profiles measured
55 sec and 87 sec after vortex generation.
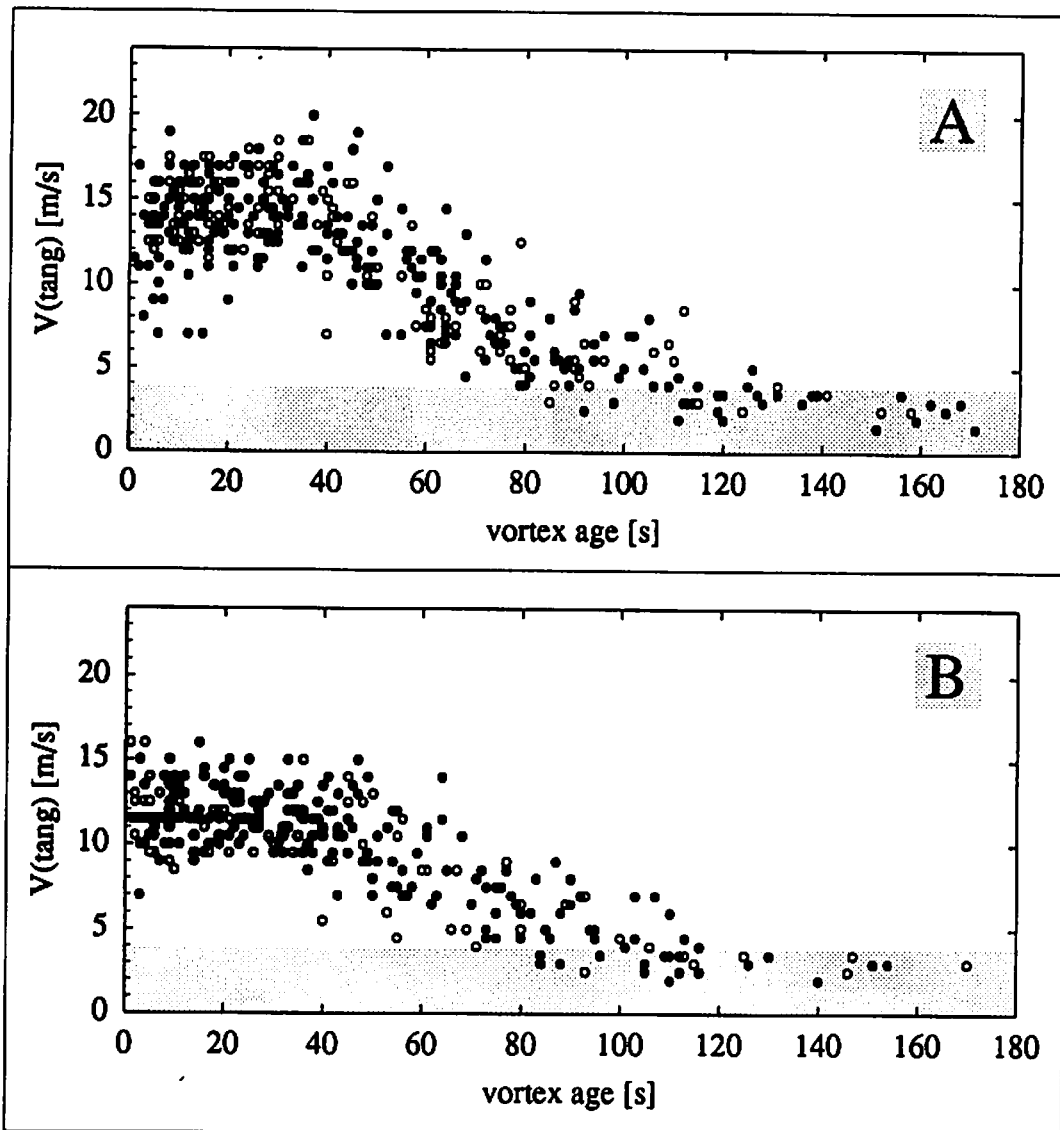
Figure 4. Temporal behaviour of the maximum tangential velocities measured in the vortices of B747 (upper part) and other heavy aircraft (lower part).
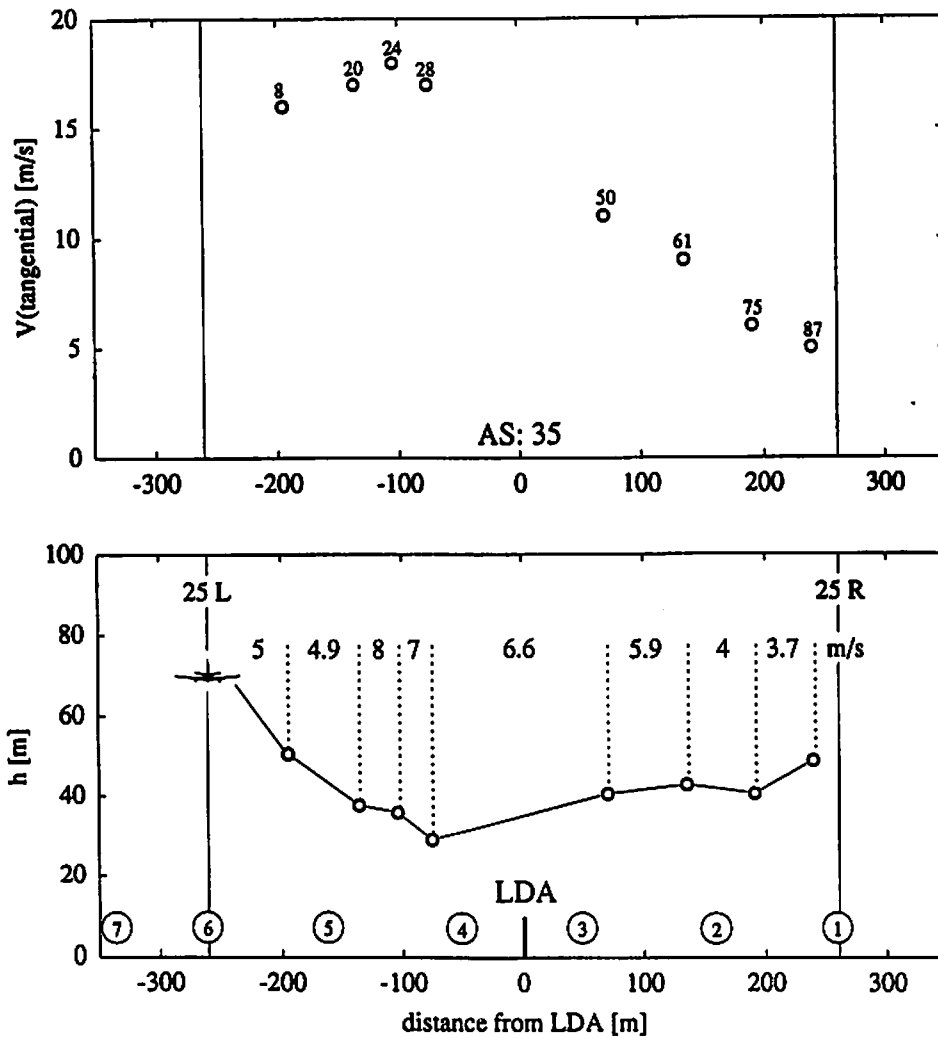
Figure 5. Results of one complete measurement sequence, showing vortex strength (upper part) and vortex location (lower part).
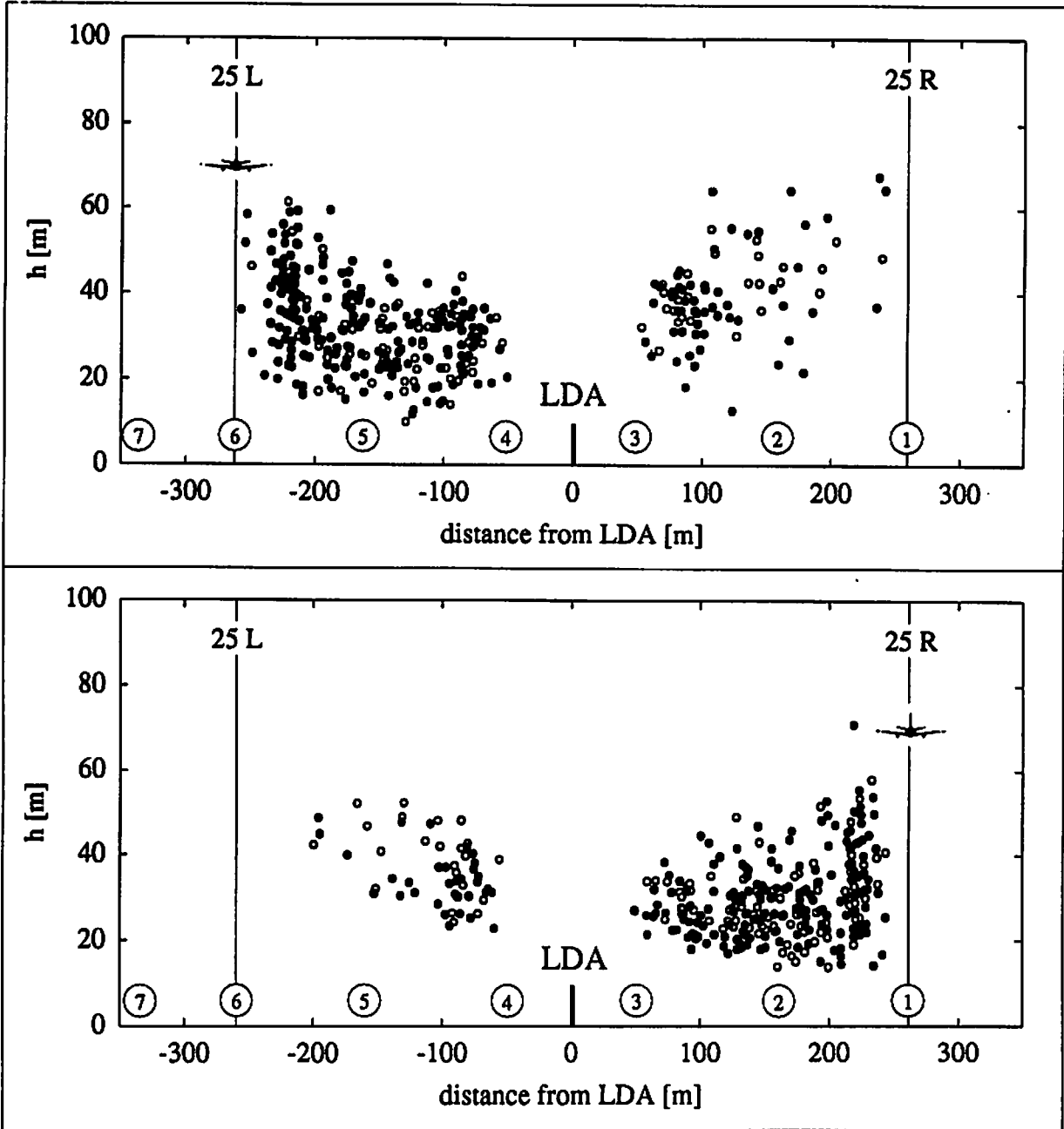
Figure 6. Propagation of B747 vortices generated on runway 25L (upper part) and 25R (lower part) towards the parallel runways.

WAKE VORTEX PROPAGATION IN THE ATMOSPHERIC BOUNDARY LAYER

G. Tetzlaff, J. Franke, and V. Schilling
Institut fur Meteorologie und Klimatologie
Universitat Hannover
F.R. Germany

INTRODUCTION

In many years past wake vortices found the appropriate attention. They were responsible for the formulation of many flight regulations such as the spacing of aircraft on the landing glide path. Furthermore, the distance between parallel runways was scaled with an estimated maximum value of the propagation distance of such vortices at the surface. For independent operation a minimum spacing of 775 m (about 2500 ft.) was put in the regulations.

There is one major airport in Germany where the problem of the parallel runways has some bearance. The situation of the eastern ends of the parallel runways on the "Rhein-Main-Flughafen" is shown in Figure 1. The airport is situated in the wide river valleys of the rivers Rhein and Main with a chain of hills, the Taunus, to the northwest. The two runways are oriented 250° with a distance of 518 m. According to regulations this distance is not sufficient to independently operate them. However, in particular recent air traffic developments made it desirable to investigate conditions allowing part time independent usage of the parallel runways. However, this can only be seriously considered when all safety standards are met.

In order to achieve such a part time independent operation for Frankfurt a three-phase program was designed. In a first phase wind sensors were deployed to simply answer the question whether or not wake vortices are capable to travel across to the other runway in critical strength. The second phase tries to define the weather situations and their operational handling during which an independent operation would be within regulations. The methods employed in this phase do not solely rely on the experimental findings but also include the results of numerical simulations of the vortex propagation at the surface. The third phase will incorporate the findings of the first two phases in the actual running of the airport. This will happen stepwise and carefully scaled in close contact with all involved parties.

THE DESIGN OF THE FIELD MEASUREMENTS

The measurements were primarily designed for the space between the runways, because the most critical site for an aircraft to hit a vortex is located close to the landing threshold. The actual siting of the sensors is shown in Figure 1. The two landing thresholds are marked. The masts each had a height of 12 m (10 m in the first phase). On the top of each mast a 3-component-vector-wind-sensor was mounted. The three axes of the sensor were oriented vertically, perpendicularly and parallel to the runways. The propeller sensors were calibrated in a wind tunnel with an accuracy of 0.1 m/s over the major part of the relevant wind speed range. The sensors do need rather careful calibration, because their response deviates from the ideal cosine-response and in addition is spoiled by a rather extended stall zone with virtually no response at all. However, the main interest was inclined towards vortices with a noticeable vertical wind component avoiding pure horizontal flow in conditions of interest. Figure 2 gives the detailed geometrical setting of the 12 m masts used during phase two.

The experimental setup comprises the data acquisition system as well. The required sampling rate was determined to be about 2 to 3 times per second. A vortex with an extension of about 20 m moves across a sensor with typically 2 to 5 m/ s. This means the coverage of the whole vortex with a total number of usually more than 10 measurements. This is a sufficient number of data to usually detect a vortex. To achieve this sampling rate and to allow an automatic data sampling procedure the data flow was automated using two interlinked data networks. The data flow scheme is shown in Figure 3. The data of each individual wind sensor are taken into a data logger which is mounted at the foot of each mast. There scanning, digitization and transfer to the bus are conducted in the sensor side network. All data loggers are connected with a two wire bus cable transporting the digitized data. The control unit for all data loggers is in a PC which is located in a building at a distance of about 40 m from the middle masts. The PC taking in the data stores them for one hour (a total of about 320 kByte per 1 full hour). After 1 hour these raw data are transferred to a second PC via a network and there processed into data in physical units. Some basic statistical summaries are produced as well. The processed and compressed data are then stored on a streamer cassette. This cassette is regularly transferred from Frankfurt to the main office in Hannover. There the data are dumped to a more openly accessible mass storage unit and then further processed after some automatic quality and plausibility tests are performed.

Altogether the data set comprises an amount of about 1100 aircraft passages with wake vortices identified at most of the masts. Including a certain number of cases with not very well defined structures this means a total amount of more than 1 GBytes. The evaluation of these data and the subsequently produced results are the contents of the following sections.

MEASUREMENTS OF INDIVIDUAL WAKE VORTICES

The anemometers in their presented configuration were actively taking data for a period of about one year. Within this one year's period several campaigns were conducted during which all data were recorded in particular allowing to match the wind observations and the cases with almost complete flight data, i.e. type of aircraft, landing weight, landing speed, possible deviations from the glide path, and the precise timing of the touch down. To achieve the complete data

required the continuous presence of observation personnel, i.e. operating a video camera allowing to get at eventually missing flight data.

A typical case of vortex propagation is presented in Figure 4. The figure shows the mast positions and the height above the ground. The numbers at the two symbols (squares stand for the lee-vortex, rhombes for the luff one) designate the age of the respective vortex after its shedding from the wings of the aircraft. The distances are given in meters from the centrally (with respect to the runways) positioned Laser-anemometer. The lee-vortex starts at M6 at a height of 66 m above the ground. At this position it is not yet in touch with the ground and thus still in the sinking phase in strong interaction with the luff-vortex. Following the path of the vortices with time shows quite clearly the sinking of the vortex core, reaching its minimum height in the vicinity of mast position 4, there only 23 m above the surface. With increasing age and hence more exchange of momentum with its environment the vortices reduce their strength (in terms of the maximum tangential velocity) but gain in diameter and height of the vortex center. After 84 seconds the lee-vortex leaves the range of the mast chain. The luff vortex takes more time to cover the whole chain of masts and can be traced up to 110 seconds when it crosses mast position 2 at a height of about 40 m.

The method to fix the vortex positions needs three-component wind measurements. This means to base the finding of the vortex core height on the finding of the tangential winds as measured by the anemometers, comprising the filtering of the wind data to avoid purely nature imposed turbulence. Experience proves that this method would not give very satisfactory results using the data of only one individual mast position. However, the sequence of masts allowed to rule out disturbances in particular in the cases of weaker or weakening vortices. To make sure the deformation of the vortices near the ground was under sufficient control the data for a series of vortices was intercompared between the chain of anemometers and the Laser anemometer. This required a fair amount of effort and time and therefore, had to be limited to a number of cases. The total intercomparison data set comprised about 100 vortices. Figure 5 shows typical results, when all went well. There are a few cases with some major degree of disagreement between the results of the two systems (about 15 cases of the total). In most of these cases the vortex strength is so low (small aircraft, adverse wind direction, high level of turbulence) that the vortex identification became obsolete for the anemometer chain, the vortices identifiable only at intermittent mast positions.

Figure 6 gives a 40 seconds time series of the passage of a luff-vortex shed by a DC-9 as observed directly underneath the glide path. The cross wind component of 0.8 m/s apparently almost balances the propagation of the vortex itself. Therefore, the vortex core passes the anemometer after about 60 seconds, the tangential velocity then reaching a peak strength of about 15 m/s.

DERIVED QUANTITIES AND MODEL CALCULATIONS

The measurements well documented the fact that wake vortices of landing aircraft are capable of reaching the parallel runway under certain circumstances. It is these conditions that are to be investigated in more detail to systematize the propagation conditions for the vortices and a potential endangerment of landing aircraft.

The vortex propagation against still air depends on several parameters, mainly on the environmental wind speed and the propagation speed of the vortex against still air. Figure 7 gives a summary of all recorded individual vortices. The net propagation speed of the vortex is presented as a function of the vortex age. The starting time was taken when the aircraft intersected the extended line of anemometers on the glide path. The scatter of the data is rather large; the average values well organized. The propagation speed systematically decreases with vortex age. After about 20 seconds most of the detected vortices have reached the ground moving with about 2 m/s, about 20 seconds later the speed has decreased to about 1.5 m/s. For vortex ages over 60 seconds the propagation speed slowly decreases, remaining close to 1 m/s to slightly more than 0.5 m/s for a wide age range.

To find the relevant transporting wind speed wind data of the vertical wind profile and propagation speeds were coupled both for experimental data as well as for numerically simulated ones. The average transport velocity usually occurs at a level of 30 m above the ground. The vertical wind shear in this level typically reaches values of 0.1 m/s per 7 meters in the vertical. This means a relatively small sensitivity towards height differences of the vortex cores in most wind situations. Thus the application of just the one 30 m wind value seems to be justified. As Figure 4 showed the main propagation of the vortex occurs in heights close enough to the 30 m level.

The influence of the stability of the atmosphere and the horizontal wind speed were also investigated. The stability proved to be a complicated factor. Though a physical relationship is plausibly established, the analysis of the data gave ambiguous results.

The horizontal wind speed exerted no influence on the propagation speed of the vortices (Figure 8). The figure shows all measured data. The total propagation speed consists of two components, the transporting speed of the wind represented in very good approximation by the average wind speed at 30 meters above the ground and the proper speed of the vortex as a whole relative to the air. Furthermore, the relative wind speed relative to the vortex's center of rotation has to be considered, this component being the critical one as far as landing aircraft are concerned. The horizontal wind components moving the vortex as a whole control the frequency of occurrence of vortices from the other runway. The average maximum vortex age slightly varies with the strength of the cross wind component (Figure 9).

The effects of differences in the average flow and the turbulence also do influence the height of the core above the ground. Figure 10 gives an impression of the different increase of the height as a function of age and cross wind component.

The theory of the vortex propagation uses the equation of motion in a formulation particularly adjusted to vortices, the vorticity form. The formulation of the equations required a space discretisation of 0.5 meter which increases the computer time very excessively. The initial plans to conduct a series of sensitivity studies varying several parameters had to be dropped because of this side effect. The simulation started from a pair of vortices as shown in Figure 11. The maximum wind speed exceeds a value of 15 m/s. In the core the speed drops to 0. In some cases the pair of vortices develops a small secondary vortex on the lee side of the lee vortex slowing down its propagation speed. This has some consequences for the interpretation of some extreme values of propagation speeds. The secondary vortex is formed at the surface and then afterwards

moved around the initial lee vortex. Enough life time available, the secondary vortex finally reaches the backside of the lee vortex (Figures 12a - c). The simulation results of tangential velocity (Figure 13) and the position of the vortex axis above the ground (Figure 14) are in agreement with observed values.

The agreement between simulated propagation properties and measured ones was rather satisfactory. The decisive parameter for propagation is the cross wind component, the maximum vortex age is influenced by several parameters, i.e. stability. There are no vortices that can cover the whole distance between runways in critical strength (that is 4 m/s maximum tangential speed) when the average cross wind component directed towards the other runway is smaller than 2.4 m/s at 30 m height above the ground. On the other side almost all vortices will arrive at the other runway when the cross wind component exceeds 5.4 m/s at 30 m height. In the range between the two speeds several influencing parameters are active; in the beginning of the measuring campaigns this effect was primarily ascribed to the effects of stability, closer inspection gave a somewhat more unfocussed impression. This is due to the short life time of the wake vortices their maximum age being rather short compared to the time scale of the standard turbulent fluctuations evoked both by mechanical and thermal excitation.

Altogether the measuring program coupled with the numerical simulations and a 30 year climatic data set gave a solid background of data allowing to quantify the wake vortex propagation between the two runways under the local climatic and site conditions.

Figure 1: Airport area

Figure 1. Positions of the masts with 3-component-propeller-anemometers (#1 to #7) and the position of the Laser-Doppler-anemometer at the Rhein-Main-Flughafen Frankfurt.
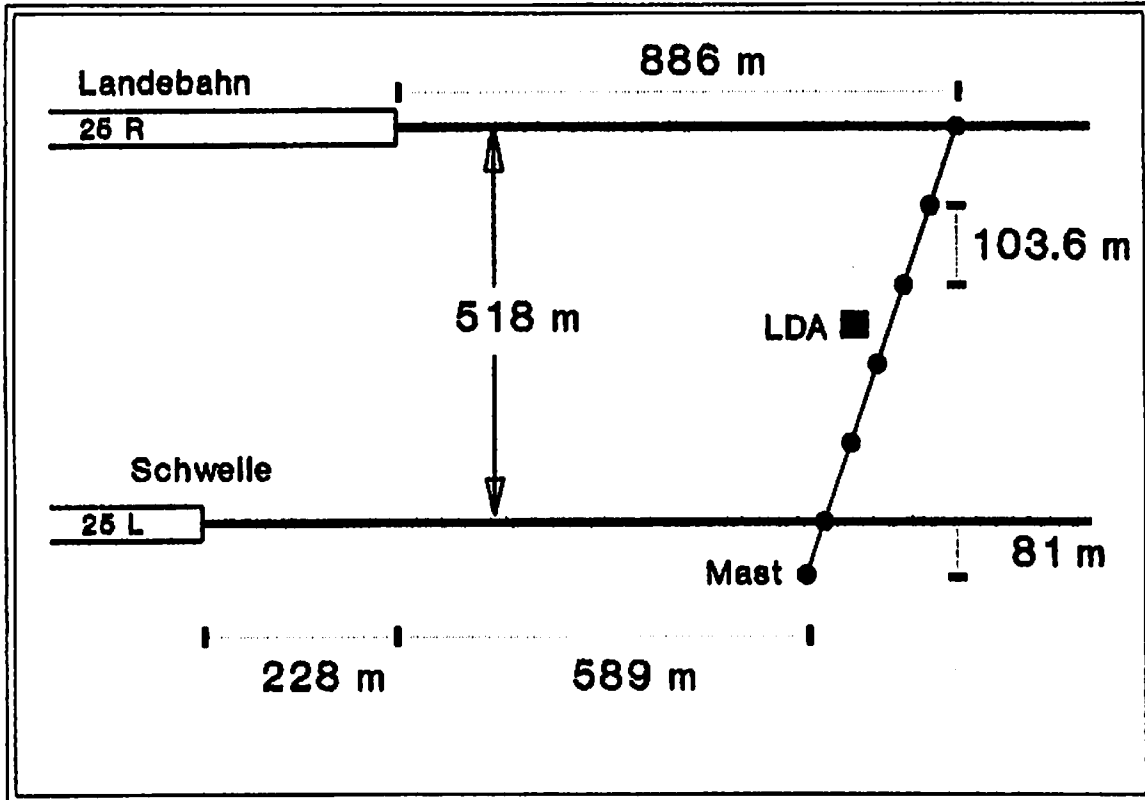
Figure 2. Schematic representation of the locations of anemometers, runways and Laser Doppler anemometer.
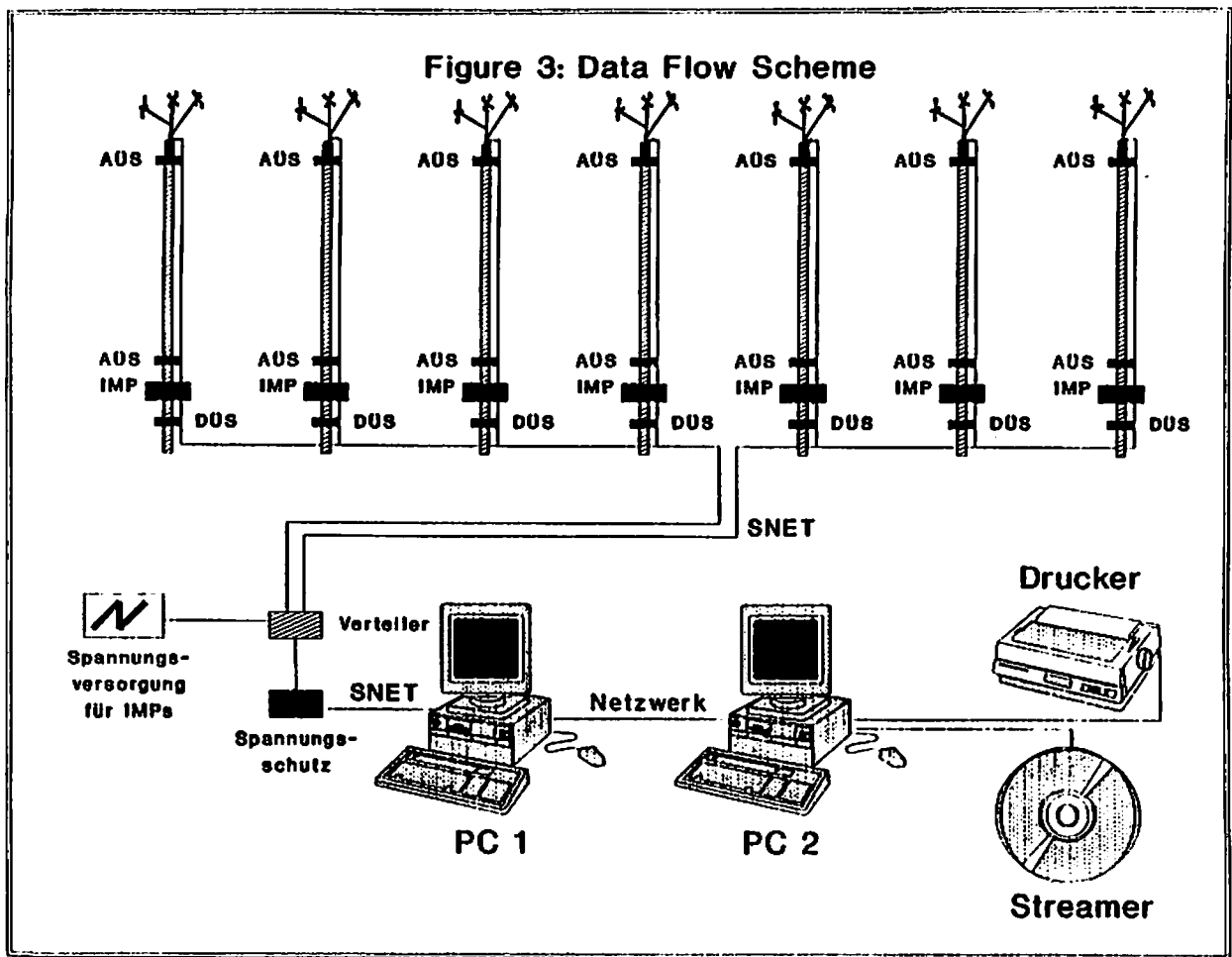
Figure 3. Schematic representation of the data flow for the seven 3-component anemometers.
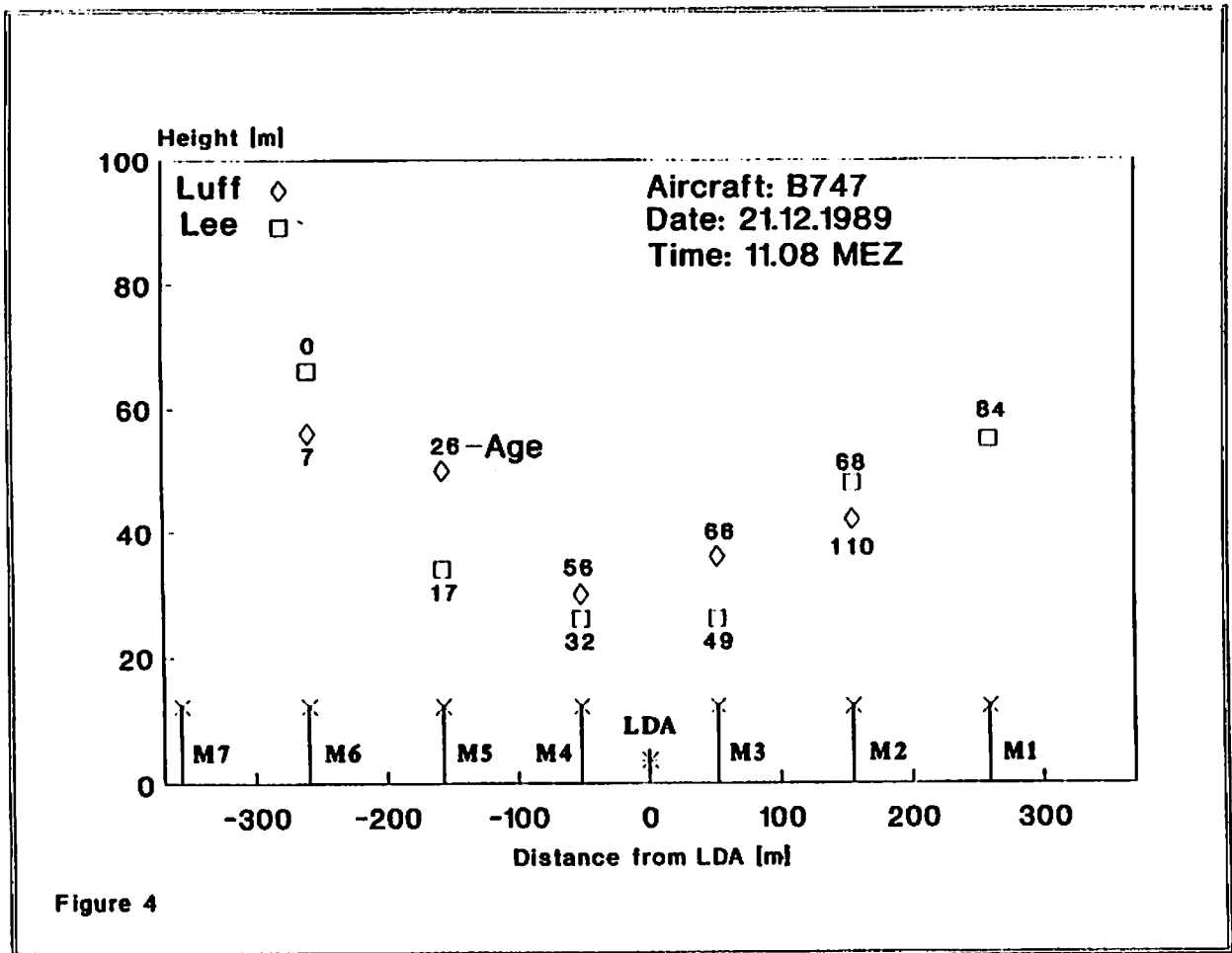
Figure 4. Schematic representation of age and height of the pair of wake vortices for a B-747 21.12.1991 11h08 a.m. MEZ.

Figure 5. Intercomparison of observed vortex heights between the anemometer chain (squares) and the Laser Doppler (asterixes) system.
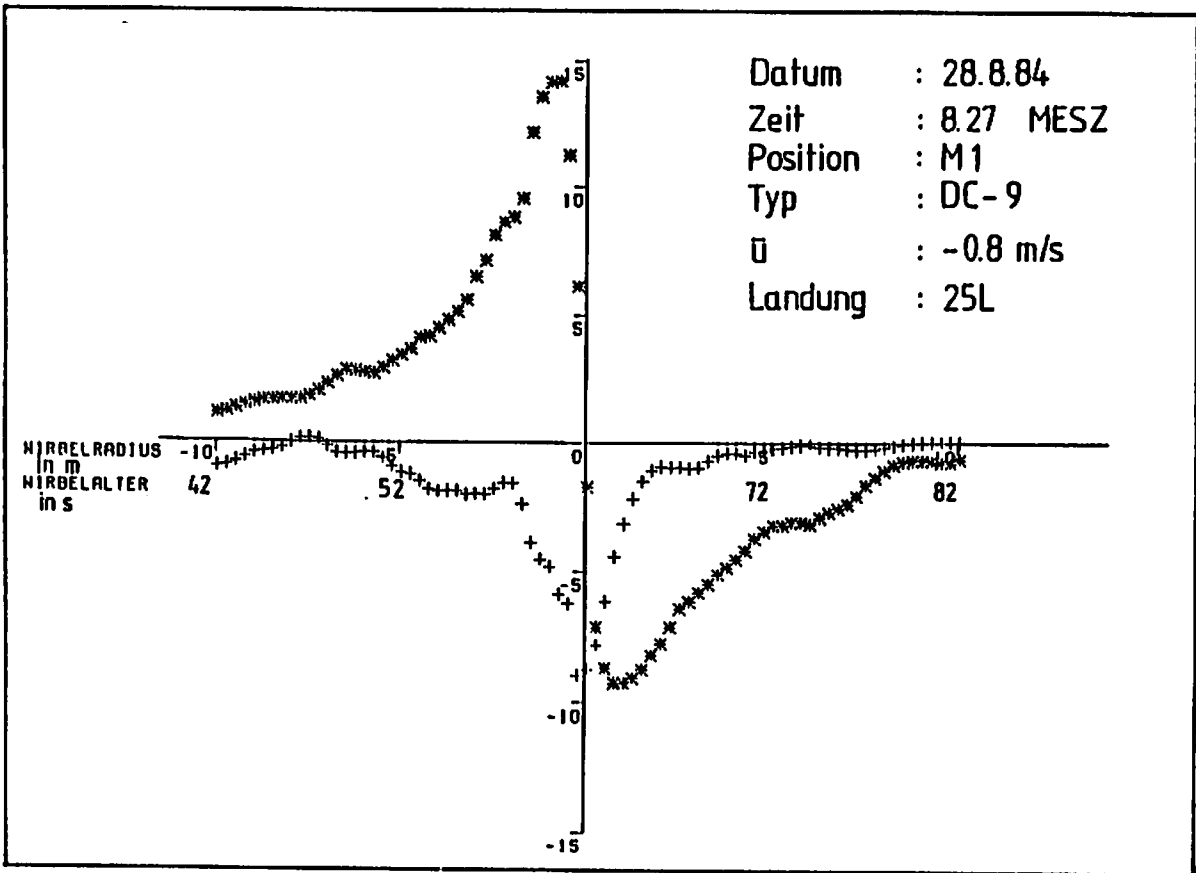
Figure 6. Observation of a lee vortex with its core close to the anemometer height propagating across an anemometer. The * represent the tangential wind component, + the vertical component.
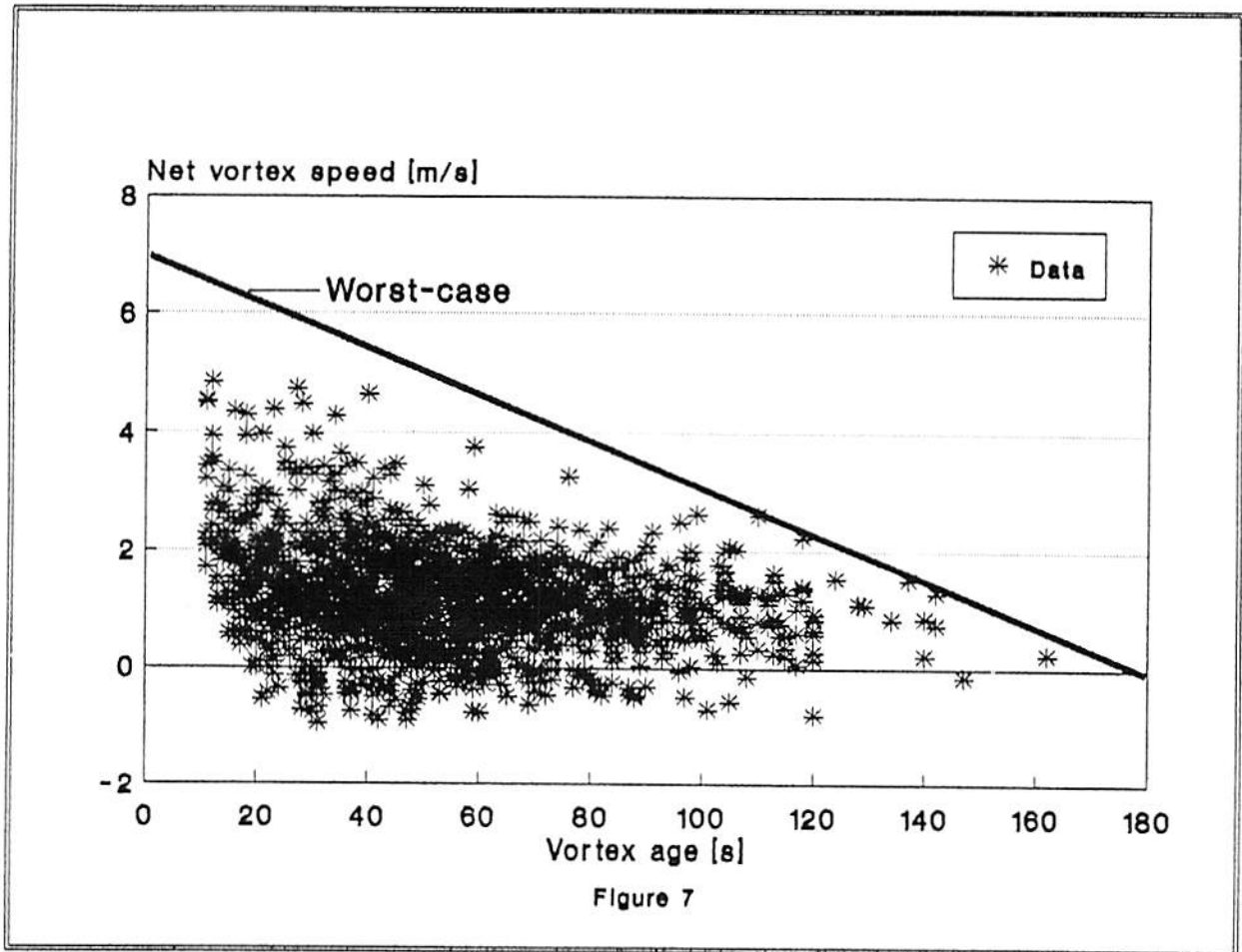
Figure 7. Summary of all propagation speeds relative to the surrounding
air of vortices as a function of their age. The line denotes an
estimate of the "worst case."
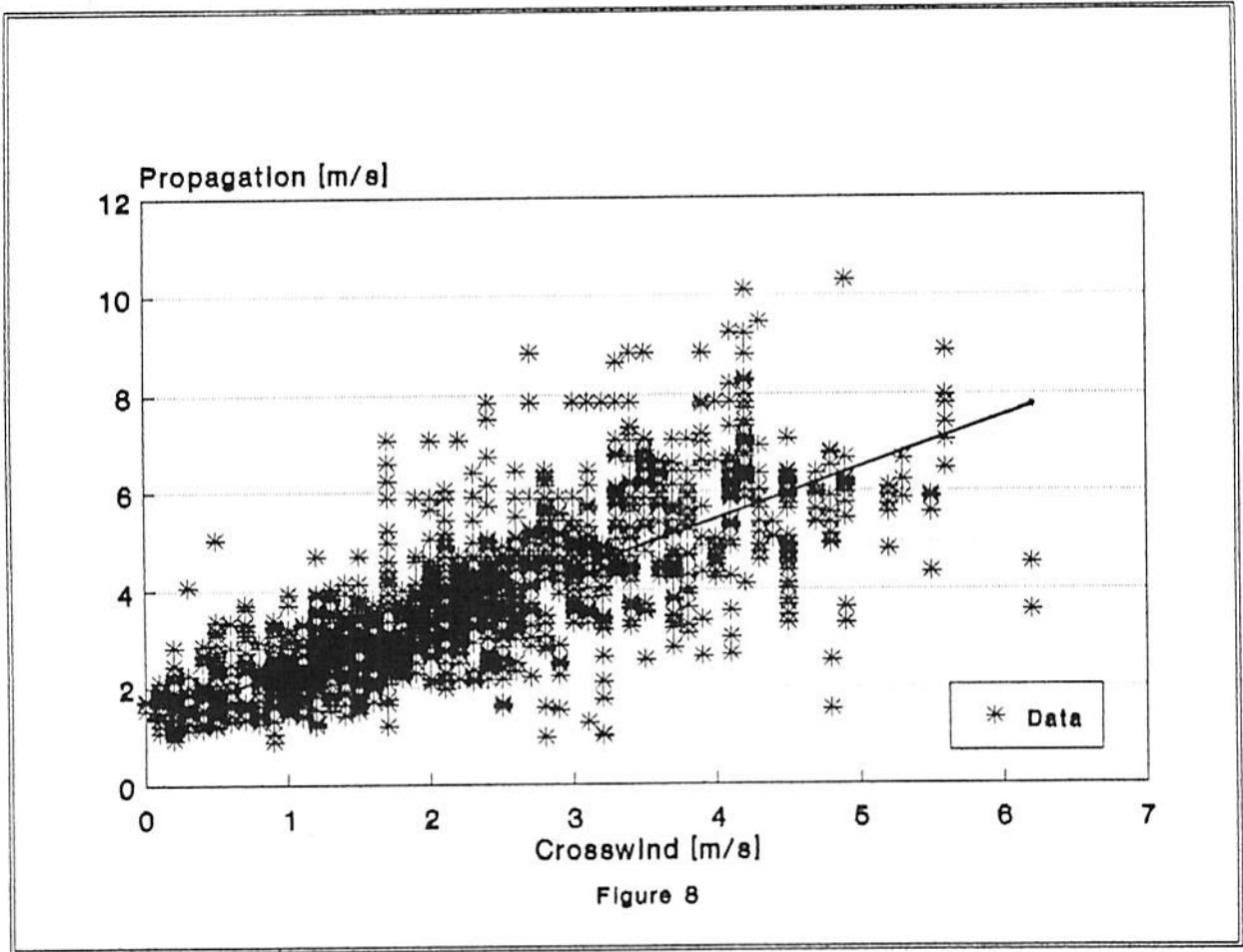
Figure 8. Total propagation speed of vortices as function of propagation speed relative to the surrounding air. Each asterix denotes a measured value.
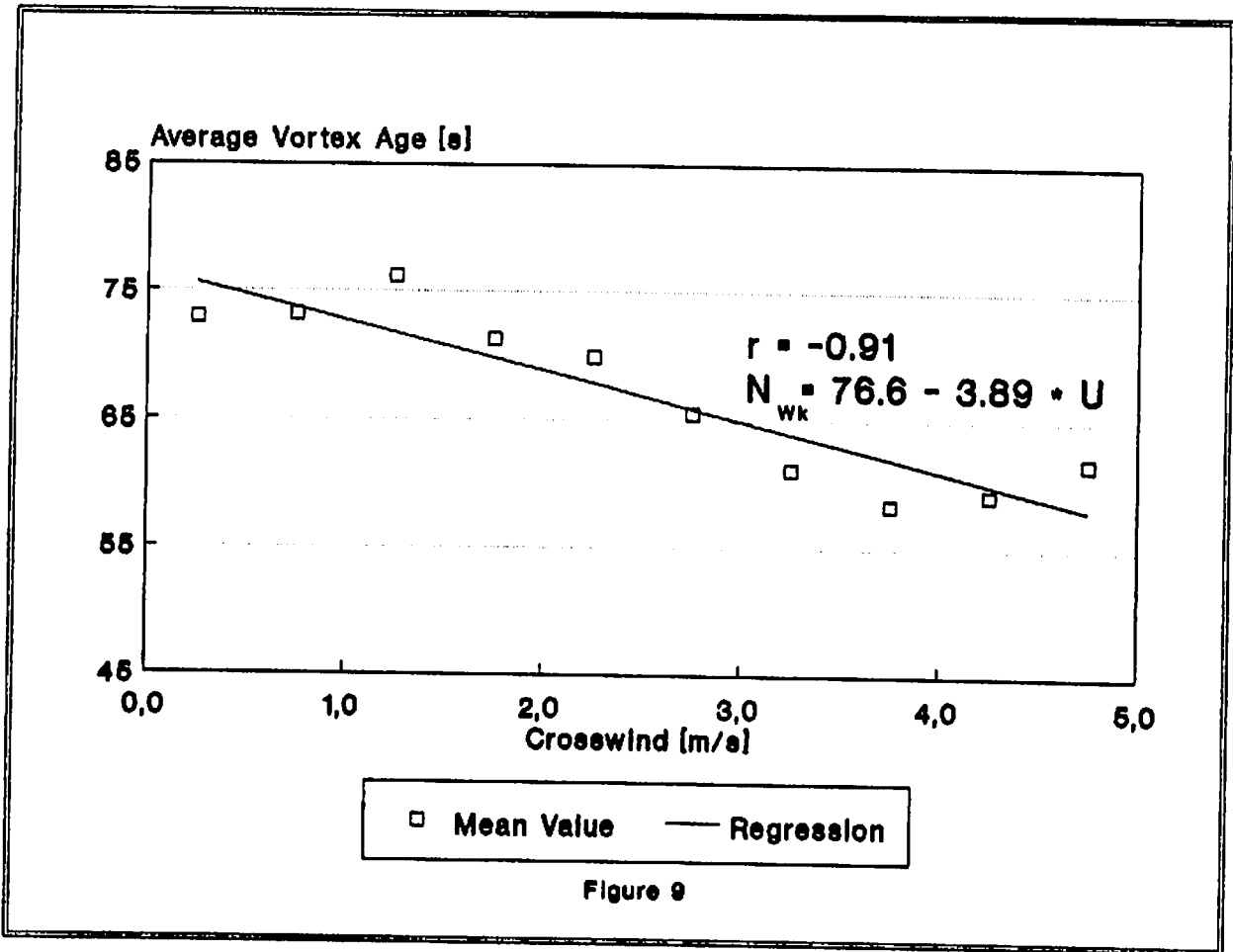
Figure 9. The average observed maximum age of a vortex as a function of the cross wind component.
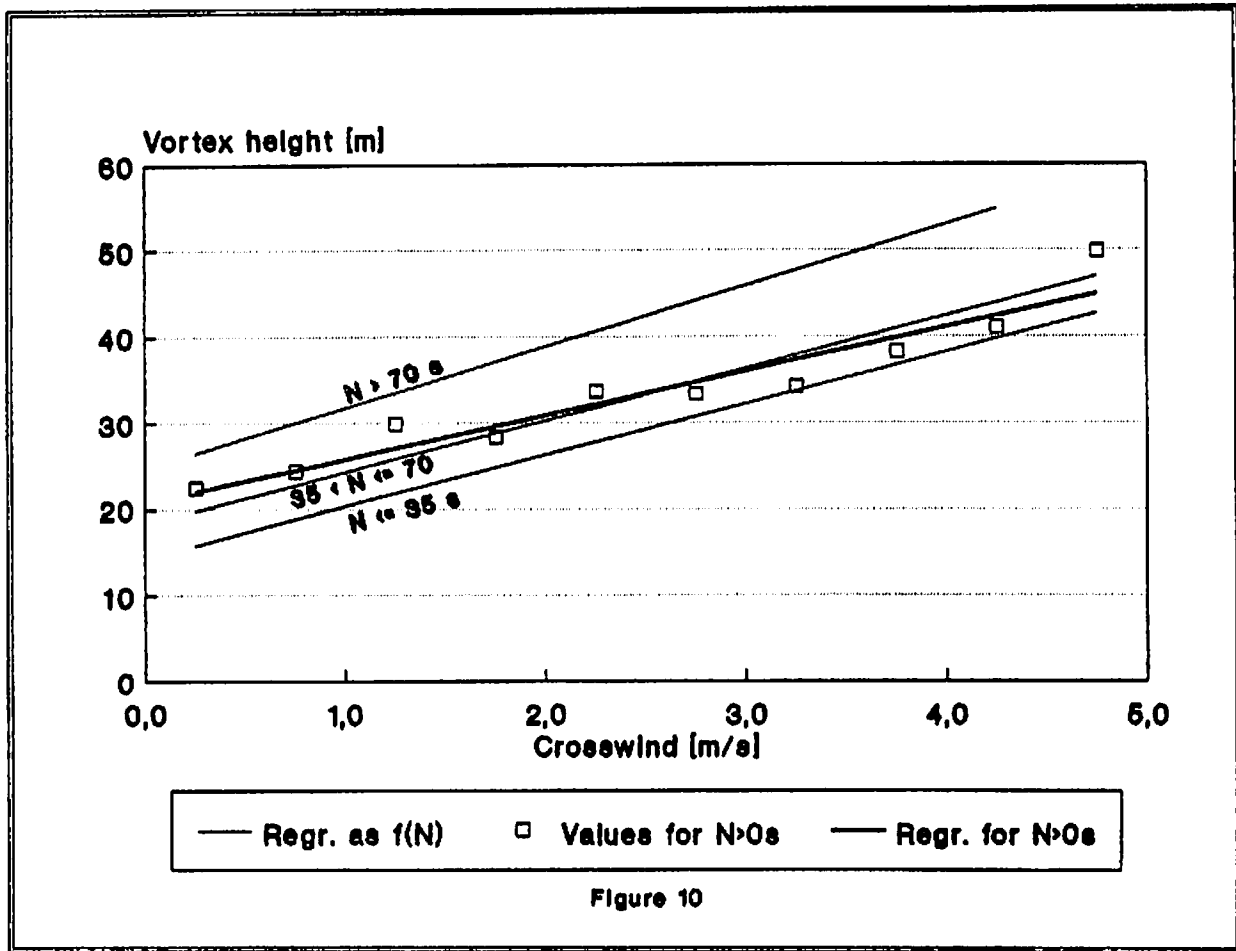
Figure 10. Height of the vortex core as a function of the cross wind component and as a function of the vortex age.
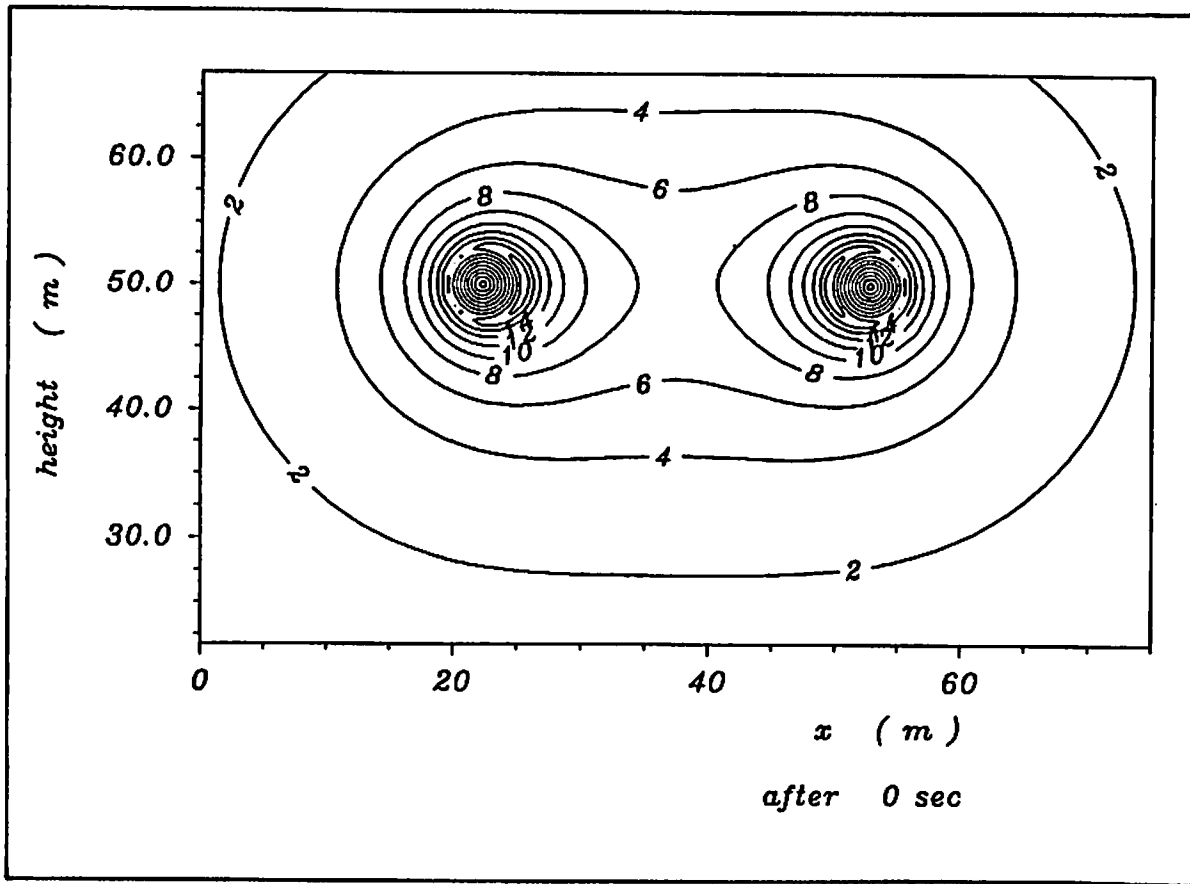
Figure 11. Wind speed at the moment of initiation of the vortex as used in
the numerical simulation of the vortex propagation.
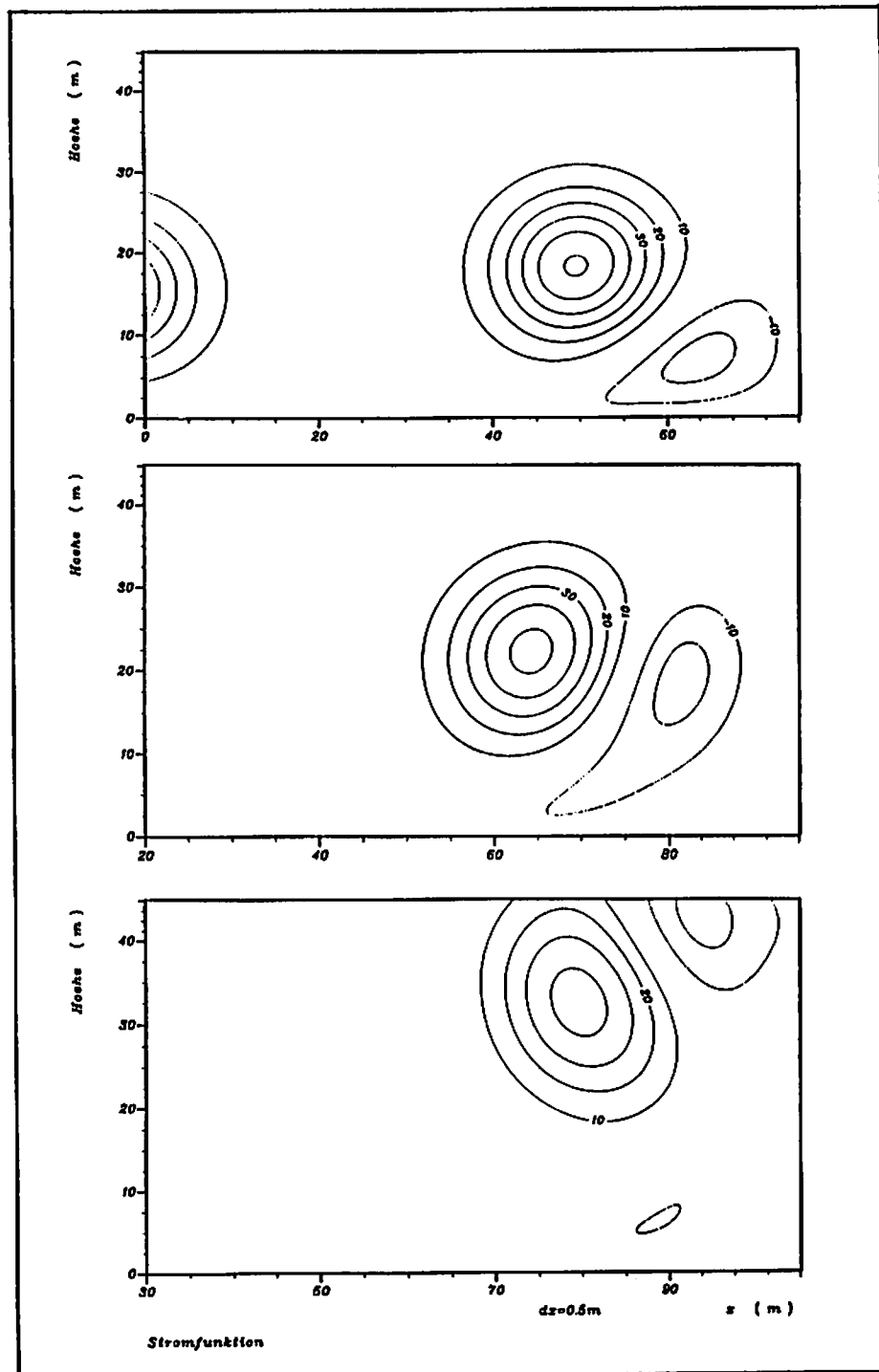
Figure 12a. Results (streamfunction) of the numerical simulation of the vortex propagation. The lee vortex develops a secondary vortex reducing strength and propagation speed of the initial vortex itself.

Figure 12b. as Figure 12a, 10 seconds later. The luff vortex has disappeared, the secondary vortex starts to move upwards.

Figure 12c. as Figure 12b, 18 seconds later. The secondary vortex has reached a height above the original lee vortex.
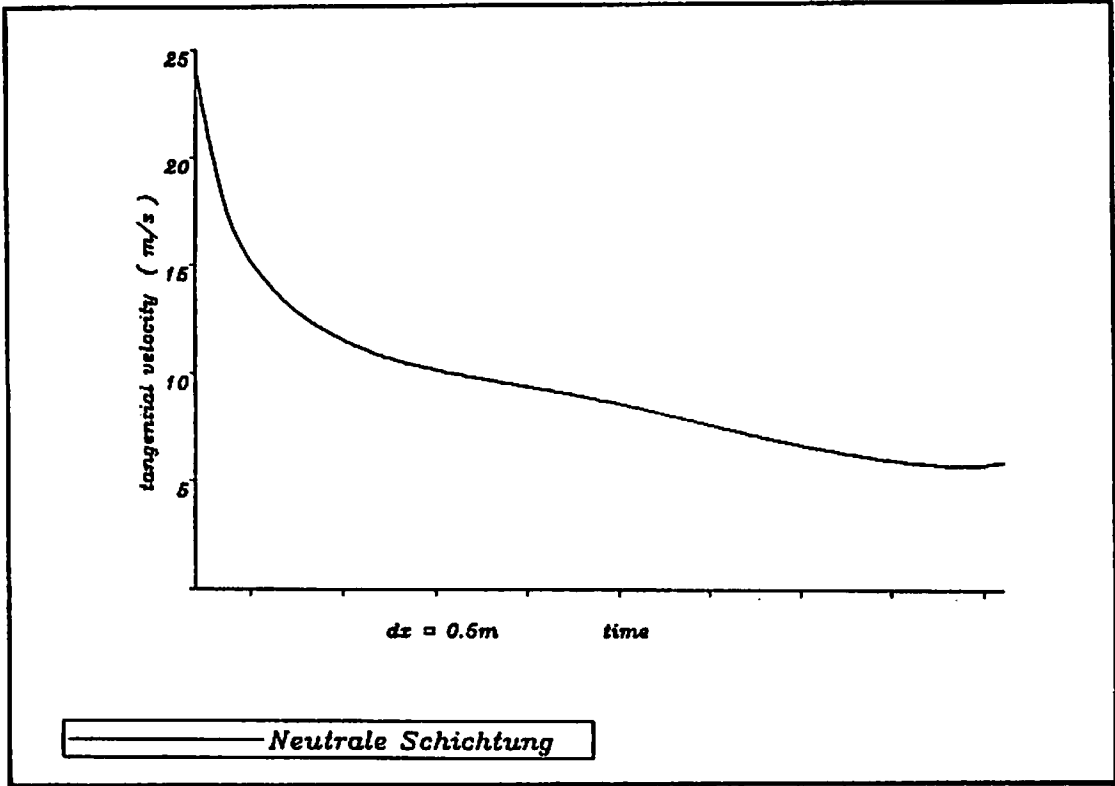
Figure 13. Simulated maximum tangential speed of the lee vortex as a function of time.
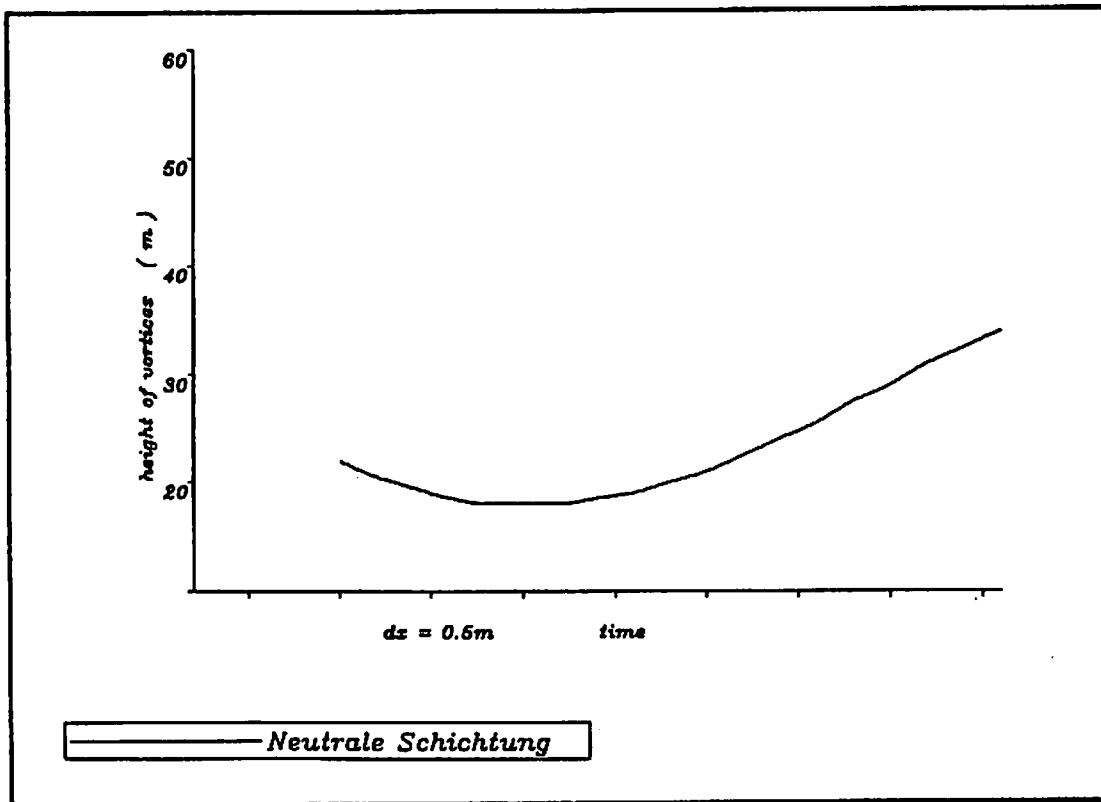
Figure 14. Simulated height of the core of the lee vortex as a function of time. The minimum height is reached after about 30 seconds agreeing with the observed time.
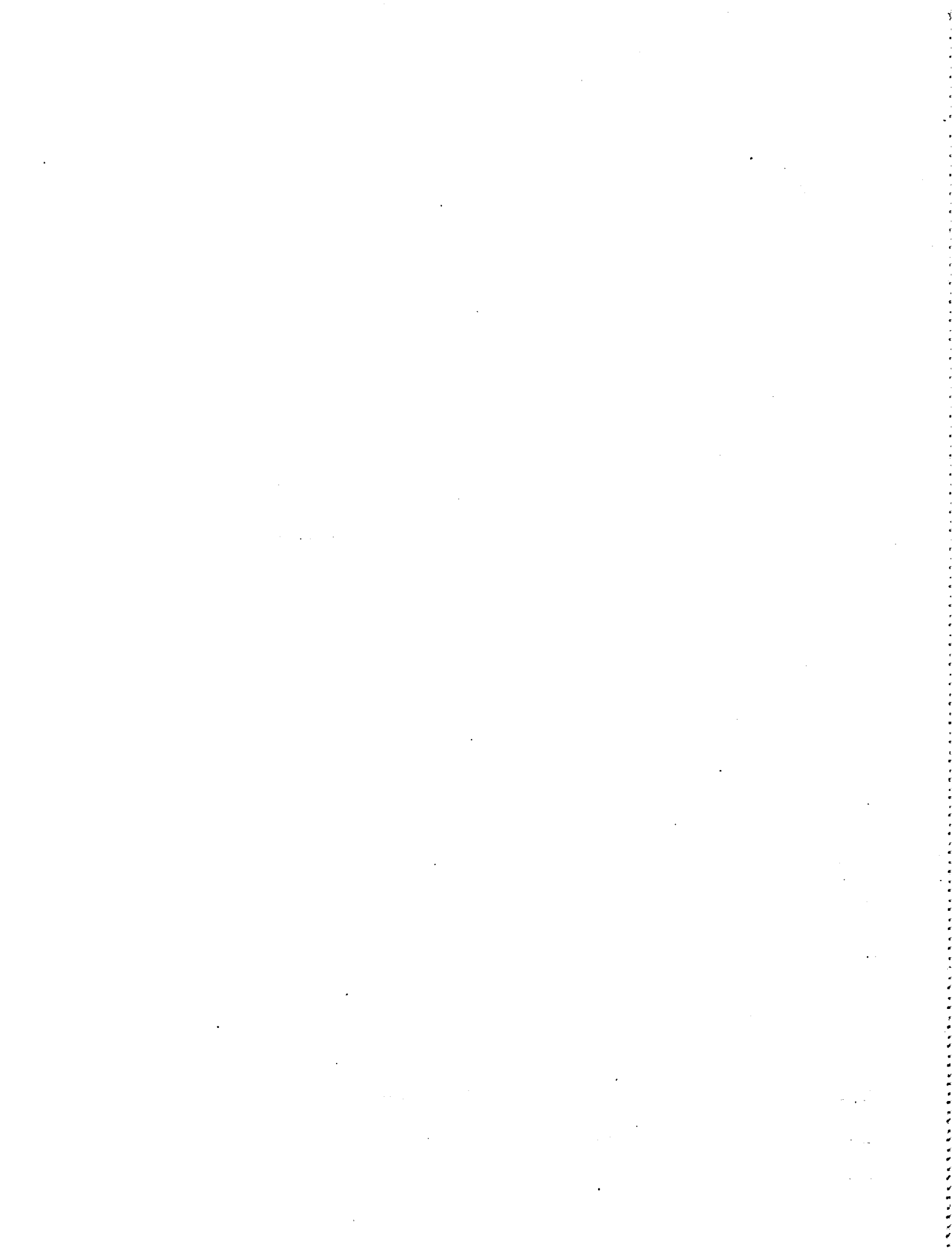
WAKE TURBULENCE LITIGATION

William Gallo
Federal Aviation Administration
Washington, D.C.

All of the published wake turbulence encounter legal decisions have been analyzed and summarized to present a picture of the bottom line effect of the wake turbulence dangers. Eighteen such cases, which at least have alleged wake turbulence as the cause of an airplane crash, are listed in appendix one and a brief set of circumstances or particulars are included to show a brief history of such litigation. Obviously, the mere allegation, as found in a lawsuit, brought by some lawyer, does not always translate into an actual wake turbulence encounter. Some courts have decided, that despite allegations and testimony by a so-called expert in the field, the subject accident although alleged to be a wake turbulence accident was not attributable to wake turbulence at all.

Of the 18 cases reviewed (Table 2), 2 were found not to have been related to wake turbulence. A further review would convince most technical people that several more of the 18 were also not wake turbulence related.

Surprisingly, of all the cases found, only two were decided which placed the blame, or at least part of the blame on other than the pilot. That is, most of all cases, have alleged that the air traffic controllers failed to warn the pilot of the possibility of wake turbulence resulting in an accident although they found the pilot at fault. In one of the cases, and one of the first tried, Furimizo, the controller, was blamed for not following up on an initial wake turbulence warning with some further action to stop the pilot of a Piper Cub from takeoff after a warning was issued. A careful reading of the case, however, causes some doubt on the impartiality of the court and the actual encounter of wake turbulence which occurred supposedly at the intersection of two runways.

In only three cases was it asserted that the generating aircraft was somehow negligent in causing wake turbulence to affect a smaller aircraft. In only one case however, in re 500L, did the court's finding attribute blame to a generating aircraft. In that case the court found an Eastern L 1011 pilot 20% responsible for the crash of a twin Beech, the air traffic controller 20% negligent and the Beech pilot 60%. On appeal of this case, the First Circuit Court of Appeals affirmed the trial courts apportionment of fault, but seemed to strongly imply that it believed the total, or 100% of the fault should lie with the twin Beech pilot who suffered the encounter.

It is interesting to ascribe, from reading a majority of these cases which were mainly 1960 and 1970 cases, a definite trend on the part of the judges in their written decisions to make the pilots responsible for their own actions and not to delegate duty to someone else like the air traffic controllers, as the cause of the pilot's grief. This appears to contrast sharply with modern-day case law which contains more of a tendency to absolve wrongdoing on the part of an actor (pilot). The language is quite clear in most of these earlier cases that pilots are responsible for following the directions and warning given to them in the AIM (Airmens Information Manual), advisory circulars, films, posters and the like. In the Sanbutch case, the judge in strong language stated:

> The function of avoiding wake turbulence in VFR conditions must rest with the pilot as he is the person who can best do something about it and is in complete control of his aircraft; he is in the best position to observe the aircraft landing before him as he has a better overall view of the runway and can better correlate the totality of events with his instruction.

In reviewing the yearly trends, and the decreasing number of cases, it just may be, that with the amount of information presented to pilots, their awareness of wake turbulence has significantly reduced the number of encounters previously evident in the '60s and '70s. Seven cases occurred in the '60s, five in the '70s and so far only three have occurred in the '80s.

With the body of wake turbulence litigation and the expertise now possessed by those in the field, courts are also probably less likely to mistakenly ascribe wake turbulence encounters. One of the earlier cases, Lightenburger, may be looked at today with some hindsight amusement at the court's finding. In that case a Cessna 310 crashed while attempting to land at Los Angeles International where the conditions were "indefinite ceiling zero, sky obscured, visibility zero with fog, RVR less than 1000 ft. Plaintiffs alleged that the crash of the 310 was caused by the wake turbulence of a Boeing 707 which had made a missed approach to the runway some 12 minutes prior to the crash.

The court in forming its conclusion followed (swallowed) the supposedly expert opinion of one Vance Breese who opined that this was a once-in-a-million encounter with wake turbulence but nevertheless was the cause of the crash and that wake turbulence could last up to 12 minutes. The appellate court while not completely rejecting this theory nevertheless held that such an encounter "was not reasonably foreseeable" and therefore the controller could not be faulted for failing to give a warning. The idea of a 12-minute time period for wake turbulence today would probably all but close down many airports.

Every wake vortex encounter does not result in an accident and, of course, every accident does not result in a lawsuit. Nor does every lawsuit result in a published opinion. Therefore, the 18 cases here reviewed are not the sum total of either the encounters or accidents resulting from wake turbulence. Table 1 shows a summary from 1982 to 1989 of the accidents listed by NTSB as wake turbulence encounters. Of the 59 accidents or incidents, however, only 10 are thought to be real encounters.

One recent example in a case I was involved in, just to take an example of air crash litigation, involved a crash in Jacksonville, Florida during an ILS approach by a Piper Cheyenne. The graphic shows the ground paths of an Eastern DC-9 and the Cheyenne. As was shown in the NTSB report, these paths show a lack of the required separation between aircraft with a spacing of about 1 minute and 2.5 miles with a resulting crash just short of the runway. The NTSB proclaimed that this was a wake turbulence accident and issued a probable cause to this effect. Since no plots were done by the NTSB of the altitude path, the altitude paths of the two aircraft were plotted to more fully explore the possibility of such an encounter.

The plot shown clearly demonstrates that at all times, up until the final dive of the aircraft, originating well above the DC-9 the Cheyenne was well above the DC-9 flight path, at all times, and therefore never could have been subject to the possibility of a wake turbulence encounter. When brought to the NTSB's attention, to their credit they issued a subsequent amendment which ruled out wake turbulence as a causative factor. This obviously changed the thrust of the lawsuit and as an aside brought into question the history of prior Cheyenne crashes.

Thankfully, the body of knowledge regarding wake turbulence has been greatly refined, due in large part to experimental data collected by NASA and FAA. With this knowledge and the expertise of men like Dr. Jim Hallock from Cambridge, the preparation and trial of lawsuits, wherein wake turbulence is alleged, is on a sounder and firmer basis. Dealing with wake turbulence is less of a mystery now, with most if not all pilots aware of the proper actions needed to avoid its dangers.

Table 1. NTSB Reports of Wake Turbulence

No.	Date	Type A/C	W.T.?	Encounter Reported by Pilot
1	4/82	Sprayer 5-2R	No	Own A/C
2	6/82	KR-2	No	From A/C Below
3	7/82	Aeronca	No	Own A/C
4	7/82	Bell 47	No	Own A/C
5	8/82	Hiller	No	Own A/C
6	10/82	PA-23	?	747 Climbing
7	2/83	H-35	Yes	727 Landing
8	2/83	C-150	No	Prop Wash C-130
9	7/83	C-188	No	Spraying Other A/C
10	7/83	PA-28	No	Truck W. T.
11	7/83	C-188	No	Other Sprayer
12	3/84	C-172	No	Some Other A/C
13	3/84	PA-12	?	Convair 580 On Landing
14	4/84	Ultra Light	?	Some other A/C
15	4/84	Hughes Hel	Yes	DC-10 T.O.
16	5/84	CL-600 T'Fan	?	767 @35,000'
17	6/84	C-150	?	Shorts on Appch.
18	6/84	C-172	?	Behind a OH-1
19	7/84	Sprayer G-164	No	Own Prop Wash
20	10/84	C-172	?	Behind a 727

21	10/84	J-3	?	Behind a Helicopter
22	2/85	A-75 Sprayer	No	Behind Other A/C
23	2/85	PA-32	Yes	Behind a Heavy
24	6/85	C-152	No	Mid air w/helicopt.
25	7/85	AT-6	No	Behind Another AT-6
26	7/85	C-152	?	Behind Departing DC-9
27	7/85	AGRS	?	Behind Another Sprayer
28	12/85	C-150	Yes	Behind C-130
29	1/86	C-182	?	Behind 737
30	3/86	C-210	?	Parallel Rwys
31	5/86	Aerosp.	Yes	Behind C-130
32	6/86	AT-6	No	Formation T.O.
33	10/86	PA-18	No	Behind a Cherokee
34	10/86	C-182	No	Behind 4 Jet Fighters
35	10/86	PA-28	?	Behind CG Heli.
36	11/86	C-421	Yes	Behind L-1011
37	2/87	C-170	No	Own W.T.
38	3/87	PA-34	No	Behind 737 Adeq. Spacing
39	5/87	Agric.	No	Other A/C
40	7/87	C-172	Yes	Behind 727
41	8/87	7 AC	No	Own A/C
42	9/87	Bell 47	No	Own A/C
43	9/87	BE-95	?	Behind BAE-146

44	12/87	C-402	?	Parallel Rnwy
45	1/88	Helicopt	Yes	Taxi Behind C-141
46	1/88	C-152	?	Behind C-130
47	3/88	C-199	No	Behind other A/C
48	6/88	Agric	No	Own W.T.
49	7/88	Agric	No	Own W.T.
50	11/88	C-210	Yes	Behind 727
51	11/88	C-152	?	Behind P3 on Low Approach
52	11/88	C-152	No	Own A/C
53	11/88	PA-28	?	Seconds Behind a King Air
54	12/88	C-152	?	Student Pilot
55	2/89	WACO YAF	No	Steep turn at 100'
56	5/89	PA-32	Yes	Behind a 737
57	6/89	PA-5	?	Behind a 737
58	6/89	C-150	No	Student Behind a JU-52
59	9/89	C-152	No	Student Pilot Behind Small A/C

Table 2.

Case	Date	Accid.	Def.	a/c	Encounter	Wake Turb Net	Result	Significance
1. Johnson v. US	April	1957	ATC	B47/C195	Landing	Yes	Pilot negligence improper approach	duty on ATC to warn
2. Wenninger v. US	Sept.	1958	AF	C124/Tri Pacer	rt. angle over	Yes/No	AF negligence overflight wing separation	Pilot Duty
3. Furimizo	June	1959	ATC	DC-8/cub	Take off	Yes/?	Pilot negligence	2 warnings req. 1 when 1st one not followed.
4. Wasilko v. US	Oct.	1961	ATC	Constellation/Bonanza	Take off	Yes/?	Pilot negl.	Pilot Duty
5. Hartz v. US	Nov.	1961	ATC	DC7/Bonanza	Take off	Yes/?	Pilot duty re take off	Pilot duty to avoid
6. Lightenburger v. US	Dec.	1962	ATC	707/C310	Landing	Yes/No	no cont. negl. not reason foreseeable	1st jet case 12 min. theory 1st time decus.
7. Thingulstad	Sept.	1966	ATC	Conste/Cherokee	appoach	Yes/?	Pilot negligence	Pilot Duty
8. Richardson v. US	March	1967	ATC	707/	appoach	Yes/?	Pilot negligence	w.t. warning given
9. Technicolor v. US	Sept.	1969	ATC	727/Jet	Landing	No	Pilot negligence low approach	Pilot duty re approach, no duty when no reason to warn
10. Sanbutch	Nov.	1969	ATC	PSA?/C310	Landing	Yes	Pilot negligence	No duty to warn if no reason
11. Dickens	April	1970	ATC	BAC111/Twin	Landing runways	Yes/No	Cont. Negligence 1,250,000 vs US	Susp. about
12. Miller	April	1971	ATC	L100 Her/Piper	Takeoff	Yes	Pilot neg	2 minutes w.t. warnings given
13. Jenrette	Aug.	1972	ATC	737/Cherokee	Landing	no made	Pilot negligence decision	Pilot best poss
14. Kaca	Dec.	1973	ATC	707/Cherokee	Landing	Yes	Pilot Negligence	warning given & adequate
15. Soul	Sept.	1978	ATC	L1011/Beech Twin	Landing	Yes/?	Pilot Neg.	20% L1011 20% ATC
16. Dyer	March	1981	Coast Guard Helicopter	HH3/piper arrow	Approach	Yes/?	No negligence of Helicopter	Pilot
17. New Hampshire	July	1981	ATC	L1011/Twin	Takeoff	No	Pilot Neg. a/c stall on take off	
18. 1st Am. Bank	Sept.	1981	ATC	727/arrow	approach	Yes	gross pilot neg. low approach no radio contact	allegation vs. airliner tatc fails
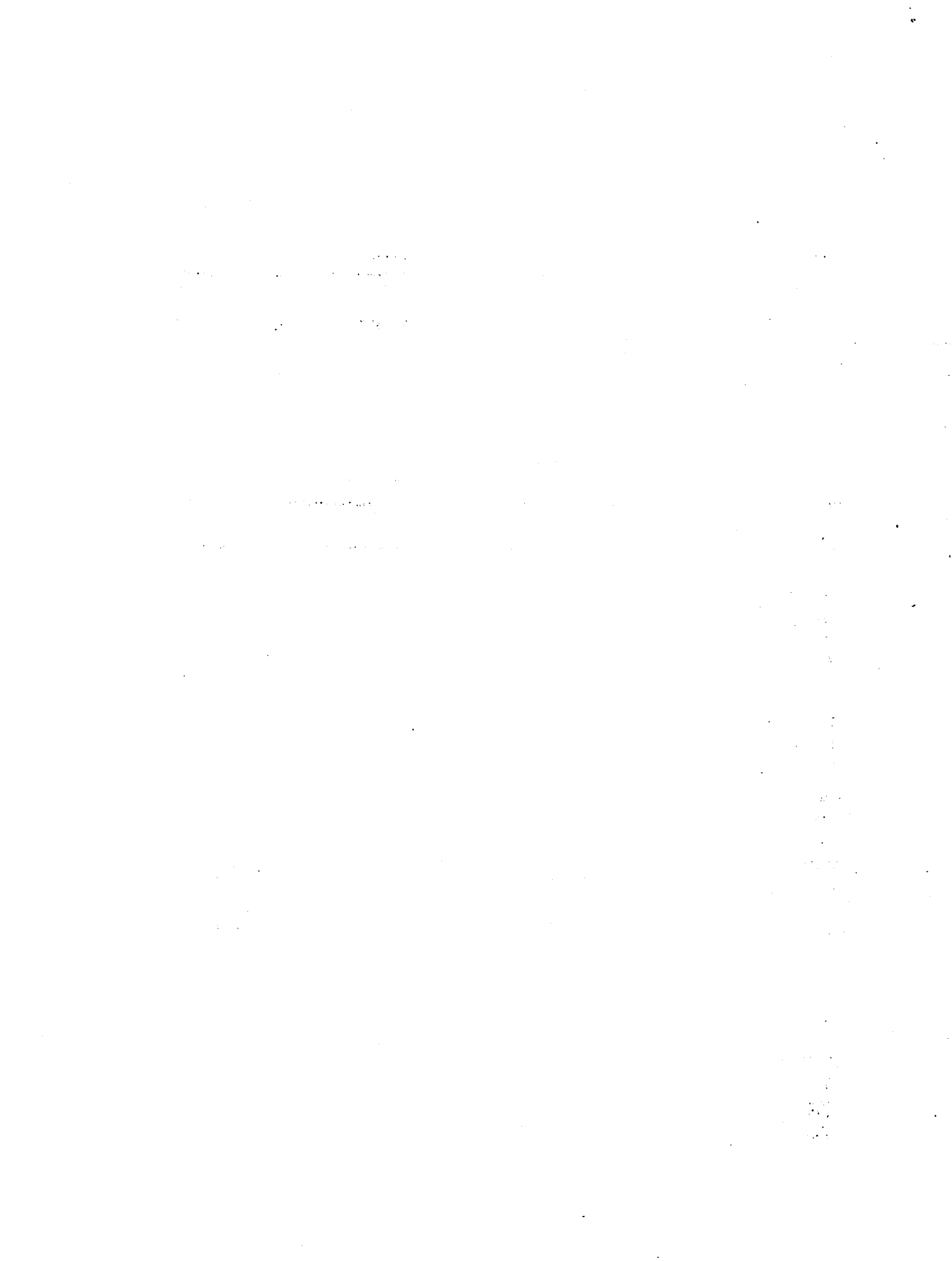
PANEL DISCUSSION ON TOWER FLY-BY TESTING - 1990 FALL SERIES

Richard D. Page
Federal Aviation Administration
Technical Center
Atlantic City, NJ

Kirk L. Clawson
National Oceanic and Atmospheric Administration
Environmental Research Laboratory
Idaho Falls, ID

Leo J. Garodz
Galaxy Scientific Corp.
Turnersville, NJ

Robert P. Rudis
John A. Volpe National Transportation Systems Center
Cambridge, MA

ABSTRACT

In September 1990 the FAA conducted tests at the National Oceanic and Atmospheric Administration (NOAA) Wake Vortex test facility in Idaho to study the wakes of new generation aircraft (B-757, B-767). Also studied were the wakes of a Boeing 727 equipped with smoke generators to enhance flow visualization. The tests were conducted to determine the characteristics of the vortices produced by these new generation aircraft and to see how they might fit into existing or new separation standards.

A number of measurement techniques and systems were employed to gather the necessary data. Included were: a 200 foot high tower instrumented with hot film anemometers and meteorological sensors; a laser doppler system; a monostatic acoustic doppler system; a high resolution anemometer system; and long line sensors.

An overview is presented of the techniques and equipment used and preliminary results of the data analyses. Comparisons of B-727 versus B-757 and B-767 wakes are presented. Similar tests were conducted in 1987 using only the tower fly-by technique to study the vortices of the Lockheed C5A/B Galaxy, the C-141B Starlifter and the C-130E Hercules. Pertinent findings from this activity are also presented.

INTRODUCTION

The growth of commercial aviation has demanded that the nation's airports safely and efficiently accommodate increasing levels of air traffic. At the same time, environmental, economic, and other constraints have not allowed airports to increase capacity to meet demand. Coupled with growing traffic, these constraints have contributed to flight delays and to delay-related fuel consumption.

Because aviation demand is not being met with new airports or runways, the Federal Aviation Administration (FAA) is increasing capacity by modernizing the air traffic control (ATC) system. Although technology exists to improve capacity, restrictions imposed because of wake vortices tend to cancel out some of the benefits of ATC system improvements. Wake vortex imposed separation standards present an obstacle to increased capacity, and may substantially limit the future growth of air transportation.

The primary objective of the Wake Vortex Program has been and will continue to be to reduce or minimize the effects of the aircraft trailing vortex hazard on the flow of air traffic, both arrivals and departures in terminal area-type flight operations, and thereby safely increase airport capacity. One of the secondary objectives of the program is to reexamine and update our knowledge of aircraft vortex wake characteristics as a function of aircraft make and model, configuration (takeoff and landing), flight performance, and ambient atmospheric conditions, and to determine their effects on following aircraft. The tower fly-by technique and aircraft vortex probing technique, respectively, have been previously used successfully to investigate the above two subject areas. The research effort performed in Idaho during the spring and fall of 1990 was intended to meet those objectives for new generation aircraft.

BACKGROUND

With the planned introduction in early 1970 of the so-called "jumbo" or "wide-bodied" jet transport aircraft, namely the Lockheed C5A Galaxy and the Boeing 747-100 airplanes, into the National Airspace System (NAS), considerable concern was expressed by aviation oriented organizations, both within the United States and abroad, regarding the vortex wake hazard of these, as well as other, large jet-transport airplanes, e.g., Boeing 707-300 and Douglas DC-8-63 series aircraft which had maximum permissible take-off gross weights of greater than 300,000 pounds. Accordingly, it became imperative, based on this anxiety on the part of the aviation community, to investigate the vortex wake characteristics of these relatively large, and heavy, aircraft and their potential or real effects on other aircraft encountering these trailing vortices. Then, using a combination of the two sets of derived or acquired information, i.e., "cause" and "effect," establish a safe longitudinal separation criteria for ATC use in terminal area-type flight operations, both departures and arrivals. The FAA took the lead in this program and the program primarily involved full-scale flight testing inasmuch as this approach, although costly, would provide useable and "sellable" results in a timely fashion for operational application. Such flight tests and analyses were performed by various government agencies and private industry, the results of which helped to determine and establish our present ATC separation standards which were initially discussed with the aviation community at an FAA symposium on turbulence in 1971 (Reference 1). It is pertinent to point out (again) that these separation

standards were based on, and still are, categorizing aircraft according to their maximum permissible gross take-off weight which was not necessarily agreeable to all participating parties some of which recommended using the aircraft wing span ratio b_f/b_g (following/lead aircraft). These full-scale flight tests and associated investigations are well documented and are covered in numerous reports published during this period and will only be mentioned at times in this paper.

Previous flight test investigations have included the majority of "Large" and "Heavy" three-engine and four-engine jet transports currently in operation in the U.S. Until the tower fly-by tests in 1990, such flight test investigations had not been conducted with the more recent generation of "Large" and "Heavy" twin-engine jet transports, namely the Boeing B-757, B-767, and the French Airbus A-300, A-320. Accordingly, a need exists to scientifically determine the vortex wake characteristics of this relatively "newer" breed of jet transport aircraft and to determine the vortex wake effects on following aircraft so as to ensure that they have been placed appropriately in the various aircraft categories, i.e., "Large" or "Heavy," established by the FAA for aircraft separation standards based on the vortex hazard. Thus, some limited (B-757 and B-767), but critical flight tests to gather good quantitative data on the nature of the vortex wakes of these aircraft were conducted in 1990 to assess their potential hazard on following aircraft. Based on previous investigations in this subject area, it has been most emphatically brought out that the aviation operational community, particularly ATC controllers and pilots, will find those separation standards which are based upon actual full-scale flight testing most acceptable as compared to analytical, theoretical, or small-aircraft model (wind-tunnel, water-tank) studies.

During the past ten years much progress has been made in modeling the effects of meteorological conditions on wake vortex motion and persistence. The meteorological parameters found to be important are wind shear, temperature lapse rate and turbulence level. Two types of models have been developed. The first provides approximate analytical solutions to the fluid mechanical equations governing wake vortex evolution. These models have been used to study the effects of turbulence level, lapse rate, wind shear and ground proximity. A second class of models developed empirical relationships, partially based on analytical results, between the meteorological parameters and vortex behavior.

Much of the validation of the vortex meteorological models for full-sized aircraft is based on very limited meteorological measurements made concurrently with vortex measurements during the 1970s. In many cases the same quality and quantity of meteorological data left much to be desired. The recent tests performed in Idaho provided the opportunity to greatly increase the amount of validation data for these models. "High quality" meteorological data (supplied by NOAA) was collected along with the vortex data.

The meteorological data collected for each run was the vertical profile of wind, temperature and turbulence throughout the volume of space where the vortices were generated and moved.

OBJECTIVES

The tower fly-by testing activities during the spring and fall of 1990 have the following objectives:

Primary:

1) To characterize vortex wakes of B-757 and B-767 aircraft in terminal area type flight operations,
2) to compare new generation aircraft wakes with baseline B-727 vortex wakes,
3) and to recommend categorization changes, if any, for ATC applications.

Secondary:

1) To compare vortex characteristics of aircraft on 0° and 3° flight paths,
2) to compare vortex characteristics as a function of various indices of ambient atmosphere in which vortices are generated and transported,
3) to compare measurement techniques (Tower-LDV-MAVSS),
4) and to refine the probe technique.

APPROACH

The FAA Wake Vortex Program planned to collect wake vortex data using three different data collection procedures and techniques. All three parts involved dedicated vortex-generating aircraft and were carried out at the National Oceanic and Atmospheric Administration's (NOAA) Idaho Falls, Idaho, facility. Due to budget constraints, the number of aircraft types and total number of wake vortices investigated were limited. Phase one investigated wake vortex characteristics using the tower fly-by technique and tower instrumentation. Phase two investigated wake vortex effects using the aircraft vortex probing technique. Phase three investigated wake vortex characteristics using ground-based remote sensors, i.e., primarily a Laser Doppler Velocimeter (LDV) and a Monostatic Acoustic Vortex Sensing System (MAVSS).

The Idaho Falls tests investigated vortex behavior at three different flight altitudes:

1) Completely away from the ground, i.e., out of "ground-effect."
2) Away from the ground, but close enough that the vortices may descend into ground-effect before they completely decay (termed "600-foot tests").
3) Near the ground (termed "tower fly-by tests").

Three test plans were written to perform the necessary testing activities. The first test plan was "Investigation of the Wake Vortex Characteristics of Large Twin-Engine Jet Transports Using the Tower Fly-By Technique," prepared by Galaxy Scientific Corporation. The second test plan was "Investigation of the Wake Vortex Effects of Large Twin-Engine Jet Transports Using the Vortex Probing Technique," prepared by Galaxy Scientific Corporation. The third test plan was the "Investigation of the Wake Vortex Characteristics of Large Jet Transport Aircraft at Idaho

Falls, ID Using Ground-Based Remote Sensors," prepared by Volpe National Transportation Systems Center.

LOCATION OF TESTING

The tower fly-by tests took place at the National Oceanic and Atmospheric Administration test facility on the Idaho National Engineering Laboratory (INEL) complex which is operated by the U.S. Department of Energy (DOE), Figure 1. The site is located approximately 45 miles west of Idaho Falls, Idaho, at the western edge of the Eastern Snake River Plain. The "floor" of the Snake River Plain is a broad rolling ridge with an average elevation of 5000 feet above mean sea level (AMSL) and the base of the vortex test tower is at 4900 feet AMSL. Two predominant buttes, located in the southeast corner of the INEL complex, rise approximately 1400 and 1600 feet above the average elevation of the site. A few miles south of the INEL complex is Big Southern Butte, a major landmark, at an elevation of 7576 feet AMSL. The Bitteroot and Centennial Mountain Ranges, which border the INEL complex on the west, rise to approximately 11,000 feet AMSL. Aircraft were requested to avoid the airspace immediately above the widely spaced research buildings located around the INEL complex.

At the test site proper, the terrain is fairly level with no significant vegetation (height-wise). In addition, there are no other protuberances or man-made structures which would cause generation of undesirable atmospheric turbulence in the vicinity of the flight test area. The test site is a high security area and is free of transient aircraft. It is also fairly unpopulated, particularly with regard to the projected surface area of the aircraft's flight path over the ground. This helps to minimize any unwanted outside test interference regarding low flying aircraft and aircraft noise.

For pilot guidance, because of the precision track and glide-slope required to be flown, ground-based pilot aids were installed. For flight track and lateral offset guidance, high intensity course alignment lights were installed. For glide-slope guidance, a Precision Approach Path Indicator (PAPI) system, was installed and used to provide 3-degree glide-slope guidance for the pilot when such was required to be flown on certain data runs. This was a portable system which could be accurately repositioned longitudinally to pre-surveyed ground locations so as to change the desired aircraft height when abeam of the tower when different vortex time-histories and associated trajectories were desired.

For obstruction clearance recognition and pilot alert, a high visibility strobe light was mounted on the top of the 200 foot tower.

TEST PERIODS

Two test periods were conducted in 1990 during which data were collected for the purposes of characterization of vortex wakes of aircraft. The first test period was used for training of personnel and initial equipment checkout. The second period was the full flight test effort. The following provides a synopsis of the data runs:

1)   SPRING TEST PERIOD - JUNE 1990 FOR 2 DAYS

   •   June 20 -- 18 Fly-Bys (B-727-100)
   •   June 21 -- 16 Fly-Bys (B-727-100)
          Total   34

2)   FALL TEST PERIOD - SEPTEMBER 1990 FOR 7 DAYS

   •   September 21 -- 18 Fly-Bys (B-727-100)
   •   September 23 -- 36 Fly-Bys (B-727-222)
   •   September 24 -- 24 Fly-Bys (B-727-222)
   •   September 25 -- 41 Fly-Bys (B-757-200)
   •   September 26 -- 29 Fly-Bys (B-757-200)
   •   September 29 -- 21 Fly-Bys (B-767-200)
   •   September 30 -- 38 Fly-Bys (B-767-200)
            Total   207

Note: Additional Tower Fly-Bys were made in support of LDV and MAVSS data requirements.

A total of 207 flight test data acquisition runs were made past the vortex measurement tower during the second test period of this test program. Of these, 156 were for the sole purpose of acquiring vortex data via tower instrumentation. Other data runs (51 total) were specially flown at the tower, or in its immediate vicinity, for the benefit of other agencies at the test site who were gathering data with their own unique data acquisition systems such as the Laser Doppler Velocimeter (LDV) and a Monostatic Acoustic Vortex Sensing System (MAVSS). For the latter effort, the aircraft altitude and/or lateral offset from the tower were such as to preclude concurrent vortex passage through the tower. However, meteorological data from both tower mounted sensors and a tethersonde were gathered concurrently during these special flyovers for data correlation purposes with the vortex data. The recorded data from these other systems, data analysis, and results thereof will be the subject of separate reports generated by these other agencies who were in command of their own data acquisition systems.

PARTICIPATING AGENCIES/ORGANIZATIONS

The major participants in this flight test program were:

1)   The FAA Technical Center, Atlantic City, NJ, which had overall Wake Vortex Program Management responsibility and provided two of the test aircraft involved in these flight tests. This included a vortex generator and a vortex probe aircraft.

2)   The National Oceanic and Atmospheric Administrator (NOAA) Environmental Research Laboratory (ERL), Idaho Falls, Idaho, provided the highly instrumented tower for vortex characterization and meteorological measurements.

3)   The Volpe Center, Cambridge, MA, provided two ground-based vortex measurement systems: 1) a Laser Doppler Velocimeter (LDV) and 2) a Monostatic Acoustic Vortex Sensing System (MAVSS).

4) United Airlines provided, via lease through NOAA, other vortex generating aircraft.

Other organizations participated in the testing, but they are too numerous to mention here. Their assistance, however, was greatly appreciated.

DATA ACQUISITION SYSTEMS

Test Aircraft

The primary vortex generating aircraft tested was the B-757-200, B-767-200 and a B-727-222 with flow visualization. The test aircraft were leased from United Airlines. No special instrumentation or equipment was required on the generating aircraft except for the aircraft with flow visualization. The FAA also provided a B-727-100 for comparative tests.

Tower

The NOAA Grid III, 200 foot tall fly-by tower, Figure 2, was the focal point for the vortex measurement flight tests. The tower and adjacent area had vertical and horizontal data acquisition/instrumentation systems installed to provide as complete a coverage as was reasonably possible on the nature of the trailing vortex systems, in and out of ground-effect, of the aircraft being used in these tests. These systems included sensors, data acquisition and recording systems, vortex flow visualization systems (ground-based), video coverage and still photography, and, for controlling flight operations, ground-to-ground and ground-to-air communications.

The tower was instrumented with hot-film type anemometers spaced at two-foot intervals along the vertical span of the tower, and on opposite sides, 180° apart. This instrumentation measures vortex intensities, i.e., radial distribution of vortex tangential velocities. The anemometers also determine vortex/tower intercept heights above the ground for ground-effect analysis, and determine vortex persistence as a function of ambient atmospheric characteristics.

Colored smoke generators provided vortex flow visualization as the vortex passed through and downwind of the tower. They were installed at eleven levels spaced at 18 foot intervals along the vertical span of the 200 foot test tower. The smoke generators had a smoke duration time of approximately 90 seconds. Therefore, ignition time of the smoke generating system was judiciously determined and applied by the on-site Flight Test Controller for each particular data run. It was based on the age of the vortex desired for that particular data run. For obstruction clearance recognition and pilot alert, a high intensity, high visibility strobe light was mounted on top of the Grid III tower, and on obstructions at the widely dispersed research facilities.

A specially designated person, referred to as "Smoke Control," was assigned to operate the ground-based ignition panel which could selectively ignite the smoke generators on the tower as specified by the on-site Flight Test Director. Ground-to-Ground communications was mandatory between the latter and "Smoke Control" and was achieved using radios provided by NOAA.

Laster Doppler Velocimeter (LDV)

The LDV, Figure 3, transmits a coherent continuous-wave beam of 10.6-micron radiation through a telescope and scanning system that can focus the beam anywhere in space. The light backscattered from aerosols in the beam is collected by the telescope and mixed at a far-infrared detector with a portion of the transmitted signal. A spectrum analysis is done on the received signal to determine the magnitude (but not the sign) of the line-of-sight wind velocity.

The LDV, which has very good angle resolution and relatively poor range resolution, samples the line-of-sight velocity along its beam over a relatively large distance. For wake vortex studies the LDV normally scans a plane perpendicular to the aircraft path. Thus, the basic LDV data are the backscatter signal doppler spectra as a function of range and elevation angle.

The spectrum analyzer and scanner are interfaced to a PDP-11/34 data acquisition computer. The data acquisition software displays enough vortex velocity data in real time to permit the operator to change the scanner range and angle parameters to track the vortex locations. The scanner and spectral information are recorded to disk or magnetic tape for subsequent analysis. Most previous LDV data collection saved only those spectral data points above a fixed hardware threshold. A new, more efficient data format was developed for the Idaho Falls tests to save the complete spectrum for a more sophisticated off-line analysis.

The LDV was located about 300 feet to the southwest of the 200 foot tower.

Monostatic Acoustic Vortex Sensing System (MAVSS)

A MAVSS antenna transmits a short (20-30 msec) acoustic pulse (2960 or 3600 Hz) into a narrow vertical beam. A separate but similar receiver antenna (to avoid transmitter ringing) receives the acoustic energy backscattered from temperature fluctuations in the atmosphere. Wake vortices were found to have enough fluctuations to give good signal-to-noise ratios under all conditions. The received signal is broken up into range gates and spectral analyzed to obtain the vertical component of the wind in each range gate. Since the ambient wind is horizontal near the ground, the ambient wind is not measured by the MAVSS; the vertical wind signature produced by wake vortices can therefore be readily identified. The MAVSS antennas, Figure 4, were installed on a baseline 30° from the perpendicular to the aircraft flight path and provided a measurement of the vortex strength whenever a vortex drifted past an antenna. To further reduce interference from adjacent antennas, alternate antennas used different frequencies.

Prior to the 1990 test series, the MAVSS was last used in 1980 during takeoff vortex measurement tests. Some of the equipment remaining from that era was used to put together ten MAVSS antennas. For the 1990 tests, the original MAVSS signal processing electronics was used (with one narrow-band filter disabled to permit a better estimate of aircraft noise). The processed MAVSS signals were digitized by a data acquisition computer which also generated the transmitted signals. Only eight signals could be recorded simultaneously. Because of data rate limitations, alternate data runs were recorded on two different computers. The digitized data from all eight channels was first stored on disk and then copied to digital tape during the next run. Data reduction and analysis took place at VNTSC at a later date.

Long-Line Sensors

For vortex ground-effect studies, particularly vortex persistence and lateral movement, two horizontal ground arrays of towers, with hot-film sensors installed at the top, were placed and oriented so as to extend radially from opposite sides of the tower base in the SW and NE directions, to about 2500 feet away. (See Figure 5.) These towers were approximately 30 feet in height and horizontally spaced at 100 foot intervals. These arrays were similar to those used in support of other flight test programs at this site to gather data on jet transport vortex wake characteristics.

Tethersonde

This system acquired atmospheric soundings using a tethersonde attached to a $3m^3$ tethered kitoon which operated approximately 2000 feet northeast of the 200 foot tower. Wind speed, wind direction, atmospheric pressure, air temperature and wet bulb temperature were measured. Collection began 15 minutes before the first scheduled fly-by and continued until 15 minutes after the last fly-by on a given day. The measurements were taken up to heights of 1000 feet AGL. The accuracy of the differential temperature measurements was great enough to characterize the lapse rate (stable, neutrally buoyant or unstable) in 100 feet of vertical displacement and was used to compute the Richardson number.

High Speed Data Acquisition System

High resolution anemometer data were collected in parallel with the NOAA data collection system, which operated at 100 Hz data rate. Eight tower anemometers were selected for recording (heights of 100, 110, 120, 130, 140, 150, 160, and 170 feet). The high resolution data collection equipment consisted of a spare MAVSS data collection computer with modified software to permit continuous data recording of eight channels at 4000 Hz per channel. The data resolution was 12 bits and the data range 0 to 10 Volts. Data collection started when the aircraft was abeam of the tower and terminated about 60 seconds later. These data were taken back to VNTSC and analyzed; however, the results are not provided in this paper.

Video and Still Camera Equipment

Both video and still camera equipment were used to document the testing activities. Two sets of cameras were located 90° apart from the tower at sufficient distance to provide adequate coverage. Both were started approximately 30 seconds before tower passage by the test aircraft and continued until approximately 15 seconds after tower passage. Still cameras were operated every 4 seconds while the video cameras operated continuously during the run sequence.

It is pertinent to point out that the video and photographic coverage are mandatory when characterizing the vortex dissipation mode, i.e., bursting, Crow instability, viscous dissipation, or vortex atmospheric interaction, and for data correlation with the other recorded data such as vortex/tower intercept height and time.

Aircraft Performance - Knee-Pad Data

Knee-pad data were collected aboard the aircraft for every run by project personnel. It included the following pertinent data:

1) time the aircraft was abeam of the tower,
2) aircraft configuration,
3) gross weight,
4) indicated airspeed,
5) radar altitude above the ground,
6) pressure altitude,
7) magnetic track,
8) estimated lateral distance from the tower (actual distance determined by ground personnel),
9) engine performance,
10) and, flight test altitude atmospheric turbulence according to subjective pilot opinion (none, light, moderate, or severe).

DISCUSSION, CONCLUSIONS AND RECOMMENDATIONS
TOWER FLY-BY TESTS

The following sections describe the technique, data analyses and partial results of the fly-by tower, and meteorological data acquisition systems.

Fly-By Tower Discussion

Approximately 85% of the vortices of the possible 312 vortex "hits" (two vortex hits per data run) were found to have gone through the tower and recorded at the test site data acquisition system. This high data acquisition percentage was considered very gratifying considering all of the variables involved which affect vortex transport and decay. The most pronounced or noticeable undesirable environmental factors were, in order of degree of adversely affecting these flight test operations: 1) wrong wind direction, 2) low or zero ambient wind velocity, 3) 90 to 180 degree wind shear along the vertical span of the tower, and 4) vortex sinusoidal-type instability and vortex bursting. This is clearly noticeable on the B-727-222 because of its vortex flow visualization shown in (Figure 6). These conditions are also assumed to have existed for the B-757/B-767 vortices when similar atmospheric, thermal, or mechanical activity existed at the test site. This explains why some of the vortices never arrived at or went through the test tower even though wind conditions were favorable for such transport.

For data analysis purposes, individual sensor vortex time-history plots were generated in the general area, height-wise, where the vortex core passed through the hot-film sensor array. These can, to some extent, be used to determine vortex core size and proximity of the core axis to a particular sensor and for resolving the 180-degree ambiguity level in vortex flow direction on the tower. To provide the reader with an idea of the type of data available for this individual run, the following detailed data analysis is offered: Figures 7 and 8 are typical hot-film sensor

velocity time-history plots showing the B-757-200, run number 10, "Landing" configuration on a 3-degree glide slope, recorded vortex tangential velocities at the peak sensor level, 168 foot (for downwind vortex) and 132 feet (for the upwind vortex), respectively. Also included on Figures 7 and 8 are the two adjacent sensor levels, both above and below the peak level, for comparative purposes. Additional plots can be generated for succeeding sensor levels both above and below the cited peak sensor level for further vortex characterization, particularly its "field of influence," however, this can be quite time consuming, unless it is absolutely necessary for data validation. Therefore, the following type plots are resorted to. Figures 9 and 10, from the same data run, are pseudo 3-dimensional plots of the entire vortex flowfield and can encompass either one or both vortices depending on whether one or both went through the tower and their separation time during tower passage. As is obvious in the figure, one can learn very quickly about the nature of a particular trailing vortex that has passed through the tower, by looking at this type of presentation.

Graphs of peak recorded vortex tangential velocity (V_θ) versus age are presented in Figures 11-19, for the B-757-200, B-767-200, and B-727-222. For each aircraft model the graphs show three sets of plots: "All" configurations, "Take-off" and "Landing" configurations, and "Holding" and "Cruise" configurations, respectively. This depiction was made to give the reader a quick glance capability to compare the relative vortex intensities of one aircraft against another and, within a particular aircraft model, to compare the effect of aircraft configuration changes on vortex characteristics. Two of these three configuration groupings are pursued, except as noted otherwise, throughout the plots and graphs presented in this section, i.e., "Take-off" and "Landing" as one set and "Holding" and "Cruise" as the other. The separation was obvious because of landing flaps and leading edge slats deployed in one grouping and not required in the other. Further categorizations could have been made and examined, e.g., the effect of landing gear position, i.e., being "Up" or "Down" on the vortex wake characteristics, but this was beyond the scope of this particular effort. In this vein, the FAA/NASA did find, during vortex wake flight tests conducted in the mid-seventies with the Boeing 747-100, that landing gear position did affect the trailing vortex system by interaction of landing gear generated turbulence with the landing flap vortex.

The graphs include both upwind and downwind vortices obtained from all configurations of the aircraft. It was attempted to follow standard consistent symbology depicting the various configurations and glideslope flown as well as downwind versus upwind vortices in the various plots and graphs, as appropriate for the analysis of the data.

Inasmuch as the B-727 series aircraft was designated by the FAA as the "baseline" aircraft against which to compare vortex wake characteristics of other aircraft for potential aircraft classification purposes for ATC application based on the vortex hazard, additional vortex data were required on this model. Accordingly, vortex wake data previously acquired by the FAA Technical Center, formerly called the National Aviation Facilities Experimental Center (NAFEC), on its own B-727-100 using the tower fly-by technique, (Reference 3), were retrieved and incorporated in this report as Figure 20, to increase our statistical database. Although a -100 series aircraft, the wing geometry and operational configurations are identical with that of the -200 series flown by UAL for this program, the main difference between the two aircraft being the fuselage length. Although not considered to be significant for the purposes of the objectives of this paper, it is conceded that the tower fly-by flight tests performed at NAFEC

were conducted at approximately sea level altitude levels (67 ft MSL) whereas those at the NOAA Vortex Flight Test Facility were conducted at about 5000 MSL. In addition the vertical sensor spacing of the hot-film anemometers on the NAFEC tower was at one foot intervals as compared to two feet for the NOAA tower thus increasing the probability of a vortex core passage across a sensor at the former site.

The correlation of V_Θ with ambient wind speed, as measured at the top of the 200 foot vortex test tower, was examined as has been previously performed by the FAA Technical Center and NOAA as well as others. Plots of V_Θ versus ambient wind speed for the three aircraft are presented in a series of figures. The graphs include both upwind and downwind vortices for all configurations of the aircraft tested. The graphs are subdivided into aircraft model and vortex age groups, i.e., 30-60, and greater than 60 seconds. (See Figures 21 - 25.)

Conceivable correlations were also investigated between V_Θ and Richardson Number (Ri) to characterize the turbulence level, or, more appropriately, the stability level of the surrounding atmosphere at the test site. Graphs with identical categories as those in Figures 21 - 25 were developed for V_Θ versus Ri as illustrated in Figures 26 - 30. Richardson Number was expressed as the following equation:

$$ Ri = \frac{g \left(\frac{d\theta}{dz} \right)}{\bar{\theta} \left(\frac{du}{dz} \right)^2} $$

Ri is an expression of the ratio of buoyancy to inertia forces, where Θ is potential temperature. However, for the first few meters AGL, Ri may be calculated with the atmospheric dry bulb temperature (T). This substitution was effected for the calculated data presented herein. The sign of Ri is determined by the temperature lapse rate. Normally, an Ri at or near zero $(0.001 > Ri > -0,001)$, (Reference 4), is indicative of neutral stability conditions in the atmospheric boundary layer. Outside of this region, stable conditions are indicated for positive values while instability is indicated for negative values.

The plots of vortex tangential velocity, V_Θ, versus Ri are based on wind speed and air temperature from 6 feet (1.8 meters) to 200 feet (60.6 meters) AGL. These heights were selected to facilitate data processing. The levels could very well have been from 100 feet (30.5 meters) to 200 feet, or from 6 to 50 feet (15.2 meters) AGL, or some combination thereof. The larger height difference was selected to span the vertical areas in which the "largest" vortices, i.e., "field of influence" of the B-757 and B-767 were observed, most notably in the "Landing Configuration." Even if Ri should be found, based on these somewhat limited flight tests, to be a potential reliable and useful indicator of vortex persistence, an airport installation would most likely preclude the erection of tall meteorological towers. Shorter towers would be required in close proximity to the runway Middle Marker (MM) or threshold area because of concern regarding aircraft obstruction clearance limits.

Accordingly, Ri would need to be calculated from sensors placed at lower levels (AGL). The question then arises as to how high AGL can one extend or extrapolate these data recorded at these lower altitudes and still have a high degree of confidence that this Ri computation is indeed applicable to altitudes AGL commensurate with those being flown by an arrival aircraft positioned at the Outer Marker (OM), normally about 1000 to 1200 feet AGL, down to altitudes associated with the MM. The ATC final approach controller normally establishes appropriate aircraft longitudinal separations based on the vortex hazard at this OM position and has the aircraft maintain this separation down to touchdown.

Correlations were also investigated for V_θ with the atmospheric temperature gradient γ . Plots of V_θ versus ambient atmospheric temperature gradient ($\delta T/\delta Z$) from 6.25 to 200 feet AGL are shown in Figures 31-35. Identical time categories were employed as those used in Figures 26-30. It was believed that this meteorological parameter might provide a simple, yet more reliable, correlation with vortex strength versus time, i.e., persistence, than Ri.

As stated earlier, of particular interest in and an objective of this particular flight test program was to look at the effects of engine thrust variations on the vortex wake characteristics of the particular aircraft model involved. This interest was based on reports from several investigators, e.g., NASA, that during full-scale flight tests engine thrust variance did indeed affect vortex wake strength and persistence. These engine thrust variation effects were most noticeable when the vortex probing technique was used to investigate the effects of vortex wakes on following aircraft in climbing and descending flight, (Reference 5). The generating aircraft was a B-727-222, in fact the same UAL aircraft as used in these tower fly-by tests, and the probe aircraft a Learjet LR-23. According to the pilots of the probe aircraft, the vortex wakes appeared to be more intense when the generating aircraft was in descending flight than in climbing flight for like gross weights, aircraft configurations, and airspeeds. Accordingly, for consideration for the final approach and landing operation at airports, several tower fly-bys were performed with the test aircraft on a three degree glideslope, which is the most flown glideslope path for instrument approaches in line operations, sequentially with the same test aircraft in level flight on other data runs.

These potential effects of engine thrust settings were first investigated by the FAA on its Convair 880 airplane back in 1972 (Reference 6). Two engines were put at idle thrust on one side of the aircraft while conducting tower fly-bys and compensating engine thrust increase was applied to the engines on the opposite wing. There was no noticeable difference in far downstream vortex intensity in the vortex generated by the wing with the engines at idle thrust as compared to the vortex from the opposite wing. However, cross-control of the aircraft by the pilot to compensate for this asymmetric thrust condition may well have so distorted the far downstream vortex flowfield as to make intelligent analysis of the recorded vortex data impossible.

The effects of engine thrust settings, i.e., aircraft on three degree glideslope and in level flight, on vortex wake strength and persistence are shown in Figures 36 - 38 for all data points.

Investigation of engine thrust effects with the aircraft in take-off configuration with take-off/initial climb power settings applied was considered but found to be too complex and variable for the tower fly-by technique, i.e., aircraft on a data run at an initial very low base altitude AGL, then accelerating and climbing, and attempting to be abeam of the tower at the proper altitude to ensure vortex tower intercept.

A summary chart of vortex persistence as a function of both ambient wind velocity and aircraft height above ground level and above mean sea level, as appropriate, is shown in Figure 39, and covers data points obtained by full-scale flight testing conducted by several different organizations over the past several years.

Continuing, we then have a graph of vortex persistence as a function of atmospheric turbulence dissipation factor $\epsilon^{1/3}$, along with a corresponding adjectival turbulence level description normally used by pilots in flight Figure 40. This derivation is from Figure 4 of Reference 2, and is repeated herein as Figure 41. The highlights of this flight test program, analyses, and results are summarized in the conclusions listed herein.

Fly-By Tower Conclusions

1. In general, the maximum *recorded* duration of the vortex systems for all three airplanes as tested was approximately 135 seconds for the B-767, 85 seconds for the B-757, and 60 seconds for the B-727 series.

2. The above conclusion does not necessarily mean that the vortices do not persist for longer time periods than recorded and, in fact, many times do as they are seen to pass downwind of the tower as visualized by tower smoke. However, their intensity (tangential velocity) is not known after tower passage. Previous flight tests conducted with the B-727 by the FAA (NAFEC) and NASA revealed that its vortices persisted on the order of 90 to 100 seconds as revealed by vortex probing and flow visualization tests.

3. The B-757-200 exhibited the highest vortex tangential velocities recorded during this flight test series being on the order of 50 percent higher than the B-767-200 and B-727-100/222 series aircraft for similar vortex time-history bands.

4. The highest peak tangential velocity ever recorded on any aircraft trailing vortex system using the tower fly-by technique occurred during these flight tests and was for the B-757 in the "Landing" configuration on a 3-degree G/S. This was 326 feet per second, downwind vortex. The second highest tangential velocity was also recorded on this data run and was 281 feet per second, upwind vortex.

5. The vortex intensity, in the form of tangential velocity, of the B-757 increases with increased landing flap deflection, which, with the exception of the B-727 model, is directly opposite of our previous findings when testing other large jet transport type aircraft and landing flap configuration, i.e., percent deflection, effects on the trailing vortex system.

6. This relatively high tangential velocity of the B-757 in the landing configuration is attributed to the clean trailing edge of the wing flap when deflected thereby decreasing the possibility of multiple vortices, and associated interaction, in the vicinity of the engine exhaust area.

7. The B-757 vortex time-history Summary Plot reveals that insufficient tower recorded data were gathered at the upper age span to make any valid judgement as to the persistence and associated intensity of the vortex system of this particular aircraft model. The lack of this longer time-history data was beyond the control of the test crew, being based on uncooperative winds and short availability of the aircraft for testing.

8. The ambient surface wind velocity appeared to provide fairly good correlation with vortex persistence for vortex ages over 60 seconds in duration. In particular, the spectra were 4 to 6, and 3 to 8 knots for the B-757-200 and B-767-200, respectively. Insufficient data were collected on the B-727 for this correlation.

9. The Richardson Number, Ri, as calculated from the data from the tower-mounted instrumentation, proved to have too much scatter in the respective atmospheric stability bands, as defined, to be of any valid use regarding correlation with vortex persistence.

10. The test site setup, i.e., sensor deployment, and flight test procedures, i.e., short turn-around times between data runs, might have compromised the ability to obtain adequate data for more representative Ri calculations.

11. Temperature gradient profiles provide a fairly good "first cut" as to predictability of vortex persistence at the test site during the course of conducting the flight tests as well as fairly good correlation with vortex persistence in plotted results.

12. During these tests it was found that, generally, for the aircraft in the Approach/Landing Configuration, the tangential velocities of the vortices generated when the aircraft were on a 3-degree G/S were on the order of 28 feet per second average greater than those generated by the aircraft on a 0-degree glideslope for similar time-spans and atmospheric conditions.

13. It is hypothesized that added jet engine thrust has an attenuating effect on the trailing vortex system by direct interaction with the wing vortex sheet during roll-up on the B-757 and B-767 and, with some reservation, also on the B-727.

14. The vortices shed by the B-757-200 were heard to "whistle" very loudly with the aircraft in "Landing" configuration with the level of the whistling increasing with an *increase* of flap deflection.

15. Likewise the B-767-200 vortices were heard to whistle very loudly when the aircraft had landing flaps down. However, unlike the B-757, the noise level increased with a *decrease* in landing flap deflection.

16. In neither case cited above is the reason for the whistling known. It is conjectured that shearing action between the tightly wound vortices rotational flowfields and the surrounding air mass is the primary causal factor.

17. Lack of an aircraft mounted vortex flow visualization system precluded determination of the transport trajectory and dissipation mode of the B-757 vortices when they never passed through the tower.

18. A logarithmic variation of vortex tangential velocities with radius appeared to fit the data fairly well in most cases.

19. The tower fly-by technique continues to be a proven and reliable method to obtain good, useful full-scale vortex intensity data and correlation thereof with ambient atmospheric test conditions.

Fly-By Tower Recommendations

1. Additional full-scale flight tests be conducted using the tower fly-by technique with the B-757-200 to gather additional data on vortex characteristics of longer age vortices, on the order of 60 to 120, or greater if they persist, seconds to fill out the vortex persistence envelopes, primarily in the "Landing" and "Take-off" aircraft configurations, and to form the basis for inputs to reconsideration of aircraft reclassification and associated separation standards based on the vortex hazard.

2. The B-767-200 should remain in the "Heavy" category as presently defined in the FAA ATC Handbook.

3. For the additional B-757 vortex flight tests, both level and 3-degree glideslope approaches should be flown using the PAPI for glide slope guidance.

4. The above flight tests should be conducted under the three general categories of atmospheric stability conditions, namely, stable, neutral, and unstable, as defined herein for the boundary layer temperature gradient inasmuch as this parameter, for the present, was the most favorable for data correlation purposes.

5. Should proper instrumentation be available at the time of the future tests then atmospheric turbulence data should also be collected for separate vortex/atmospheric data correlation purposes.

6. A vortex flow visualization system similar to that used in these flight tests, i.e., Frank Sander Smoke Generators, should be installed on the test aircraft to determine vortex characteristics, particularly transport and dissipation mode.

7. A ground-based sound recording system be installed at the NOAA vortex test site, underneath the general flight path course of the test aircraft, to gather data on the characteristics of the vortex generated noise ("whistling") for potential use in future

design considerations of vortex advisory or warning systems, as well as noise-abatement programs.

8. Vortex probing be conducted behind the B-757-200 with a suitably instrumented, high g-load capable aircraft to determine vortex effects on following aircraft. If at all possible, it would be most productive to have a B-767-200 concurrently fly at a suitable distance abreast of the B-757 aircraft, with the probe aircraft sliding from one vortex system to the other, to determine the relative order of intensity of the two trailing vortex systems. This was previously done jointly by the FAA and Boeing with a B-707 and B-747 aircraft and the results proved to be every useful in establishing our present separation criteria.

9. Pending the results of additional flight testing as cited above, the FAA should recommend, via appropriate dissemination means, that pilots maintain the same separation distances behind the B-757 during VFR operations as they do during IFR operations on final approach to landing. This may require ATC controller advisories in terminal area-type flight operations.

DISCUSSION AND CONCLUSIONS -- LDV AND MAVSS

The following sections are the discussion and conclusions of the effort for the testing process using the LDV and MAVSS.

LDV Discussion

The installation layout of the LDV and MAVSS at Idaho Falls is shown in Figure 42. The LDV was 300 feet from the tower along the MAVSS line. The position of the LDV was such that vortex scanning was done after the tower in order to ensure a perpendicular scan. In general, LDV scanning would begin when the aircraft was abeam of the tower. Scanning would continue until the vortices were beyond the range of the LDV or dissipated within the scanning volume.

From the doppler shift of the laser frequency, a velocity profile of the vortex was generated. The average circulation was calculated at different radii, 30-ft and 45-ft, until the vortex dissipated or left the scanning volume.

The vortex circulation is often referred to as the vortex "strength." The circulation $\Gamma(r)$ is defined by the equation:

$$\Gamma(r) = 2\pi r v(r),$$

where r is the vortex radius and v(r) is the tangential velocity. Theoretical values exist for the limiting value of $\Gamma(r)$ for large r, but that value is hard to measure because small errors in v(r) can produce large errors in $\Gamma(r)$.

The average circulation for radius r is defined by the equation:

$$\Gamma'(r) = (1/r)\int_0^r \Gamma(r')\,dr'.$$

The average circulation will be used in this report to quantify the strength of a wake vortex. It is a useful parameter because it represents a robust average over the data and is therefore relatively insensitive to velocity measurement errors.

The previous equation is modified for calculating the average circulation from measurements that actually include values for v(r) on both sides of the vortex and is defined by the equation:

$$\Gamma'(r) = (1/2r)\int_{-r}^r \Gamma(r')\,dr'.$$

Averaging over both sides of the vortex approximately cancels out the effects of vortex motion, which can cause higher velocities on one side of the vortex than the other. The vortex motion can be caused by the flowfield of the other vortex or the ambient wind. Because this approximation breaks down when the measurement gets near to the other vortex, the average circulation radius is limited going no more than 60 percent of the way (time for MAVSS, elevation angle for LDV) toward the other vortex. Subject to these restrictions, the average circulation is calculated for 20 values of averaging radius, 5 through 100 feet.

The LDV data is presented as Average-Circulation vs. Vortex Age plots for each of the aircraft (Boeing B-727, B-757, B-767) for the following aircraft configurations:

1)   3-degree glide slope, landing;
2)   0-degree glide slope, landing; and
3)   clean and level flight.

The plots for the configuration A for each type of aircraft, at a vortex radius of 45-feet, are shown as examples in Figures 43, 44, and 45.

LDV Conclusions

Some general conclusions drawn from comparison of data from different aircraft and from the same aircraft under different configurations are:

1.   Vortex strengths under configurations A and B above, are higher than under configuration C for young (<60 seconds old) vortices.

2. Vortices generated by the B-767 persisted longer within the measurement rage of the LDV. This may have been impacted by the prevailing wind conditions.

No definitive conclusions could be drawn on the basis of different glide slopes or different aircraft.

MAVSS Discussion

The MAVSS consists of an array of vertically pointing narrow-beam acoustic antennas. A short pulse of acoustic energy is transmitted and the signal back scattered from temperature fluctuations in the atmosphere is received. Doppler processing of the return signals gives a vertical profile of the vertical wind. Since the ambient winds are horizontal near the ground, the vertical vortex winds are measured without being affected by the ambient wind. Separate transmitter and receiver antennas were used to eliminate the effects of transmitter ringing on the low altitude return signals. The two antennas were tilted to overlap completely at 75-foot altitude.

The locations of the eight MAVSS antennas are listed in Table 1 and are shown on a site layout map in Figure 42. The antennas were located to accommodate northeast winds that would blow the vortices through the tower and then along the MAVSS array. The MAVSS data were sometimes affected by the road traffic noise from the road passing between antennas 4 and 5.

The MAVSS transmit pulses were generated by the data collection computer. The pulse shape was a truncated gaussian (20 msec between half voltage points) for optimum range and velocity resolution. The total pulse length was 42 msec. Two different transmit frequencies, 2950 and 3600 Hz, were used for alternate antennas to minimum acoustic interference between adjacent antennas. The peak transmitted power (electrical input) was about 200 Watts.

After the computer completed the pulse generation, it converted to a data collection mode, sampling the eight antenna signals at 16,000 Hz. The received signals were processed by a tuned preamplifier at the antenna site. At the central data collection
trailer a linear gain ramp was used to compensate for the normal inverse square range power response for distributed targets. The repetition period was 458 msec, which gave a maximum range of about 235 feet.

Since the MAVSS antenna locations are fixed, they cannot scan the vortex as the LDV does. Instead, each MAVSS antenna scans the vortex velocity profile as it passes over the antenna. Thus, the MAVSS is ideal for measuring vortices travelling in a crosswind (as required for the tower flyby measurements), but cannot easily measure stalled vortices.

The MAVSS data were used to determine vortex lifetimes in order to make comparisons based on configurations A and B discussed in the LDV section. The data statistics are shown in Table 2.

It should be noted that vortices that were detected at MAVSS unit 8 were assigned lifetimes values that corresponded to their arrival time at unit 8.

49-19

MAVSS Conclusions

Some general conclusions drawn from comparison of data from different aircraft and from the same aircraft under different configurations are:

1)   The starboard vortex had a longer lifetime than the port vortex.
2)   Vortices generated by the 767 had the longest lifetimes.

Table 1. MAVSS Antenna Locations Relative to the NOAA Tower.

Antenna	Location (feet)	
	SL	PAP
1		0
2	200	185
3	450	416
4	700	657
5	950	878
6	1200	1109
7	1450	1240
8	1700	1571

SL = Along Sensor Line
PAP = Perpendicular to Aircraft Path

Table 2. Vortex Lifetimes

3-degree Slope

Aircraft	B-727-222		B-757-200		B-767-200	
Vortex	1	2	1	2	1	2
Count	4	4	12	10	10	10
Mean	128	169	111.5	135	112.2	173
Std. Dev.	21.80596	44.38468	28.72716	25.65541	49.59193	34.60925

0-Degree Slope

Aircraft	B-727-222		B-757-200		B-767-200	
Vortex	1	2	1	2	1	2
Count	25	24	21	18	16	19
Mean	89.52	122.875	93.52381	157.9444	92.52	175.5263
Std. Dev.	50.80718	51.59806	32.20414	32.94182	32.99053	46.11127

NOTES:

1. Count refers to the number of vortices tracked
2. Vortex 1 is the port vortex
3. Vortex 2 is the starboard vortex
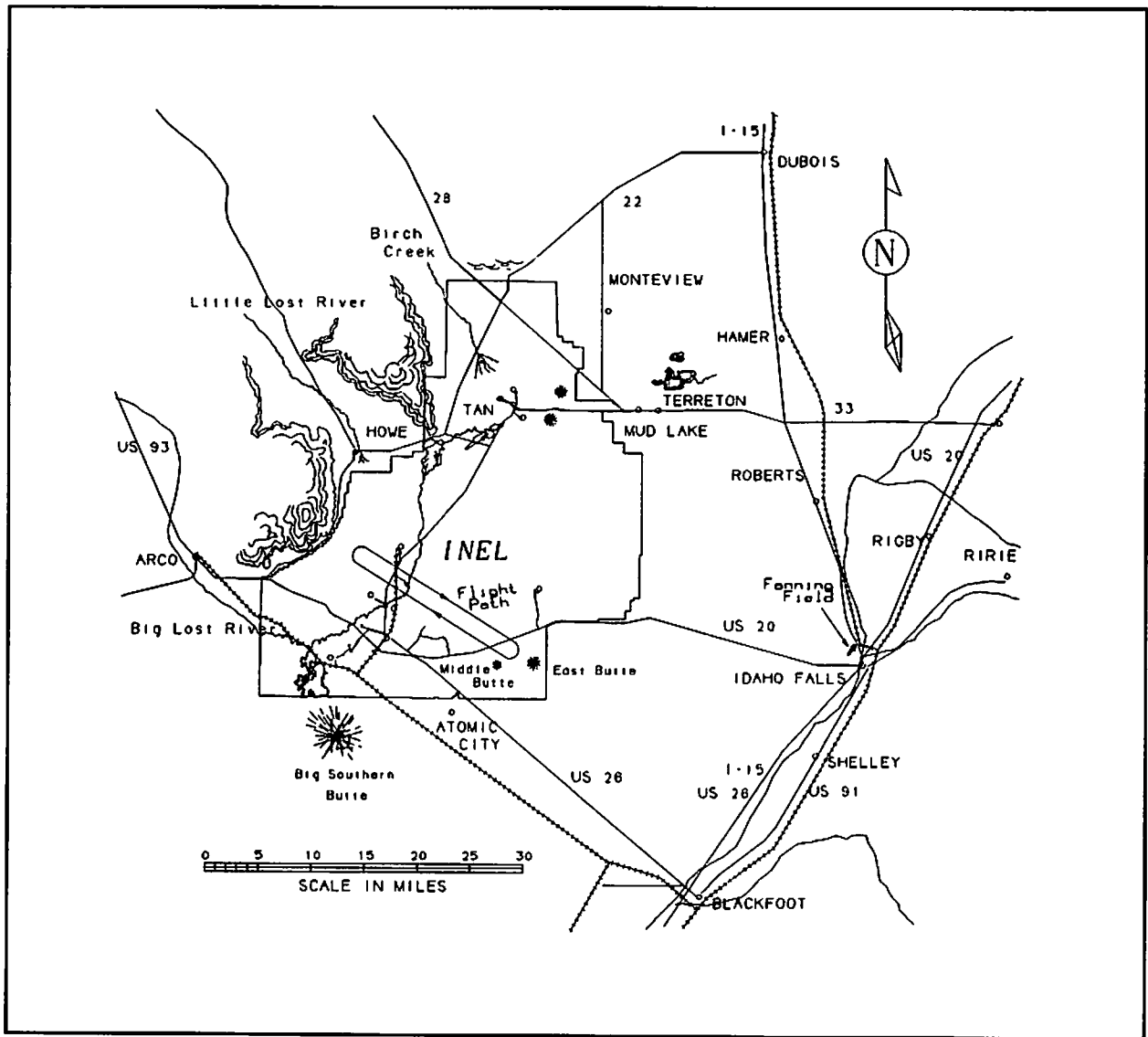4. Mean lifetime is in seconds

Figure 1.   Idaho National Engineering Laboratory (INEL) and vicinity.

Figure 2.   NOAA Grid III 200 ft. tall fly-by tower.
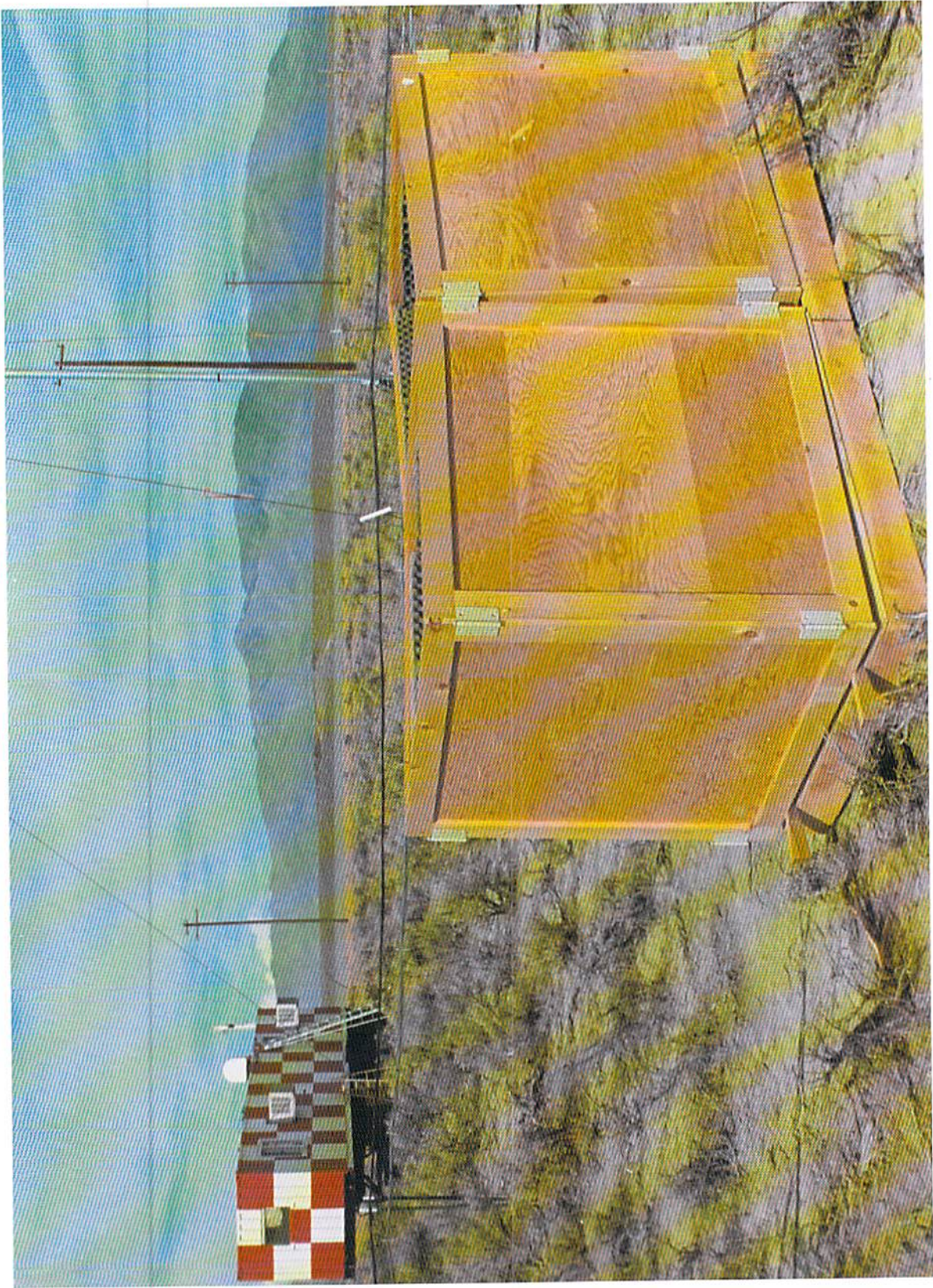
Figure 3. Laser doppler velocimeter (LDV).

Figure 4. Single set of MAVSS antennas (LDV in background).

Figure 5. Ground array of hot-film sensors.

Figure 6.   B-727-222 airplane visualized trailing vortex system showing extreme sinusoidal instability.
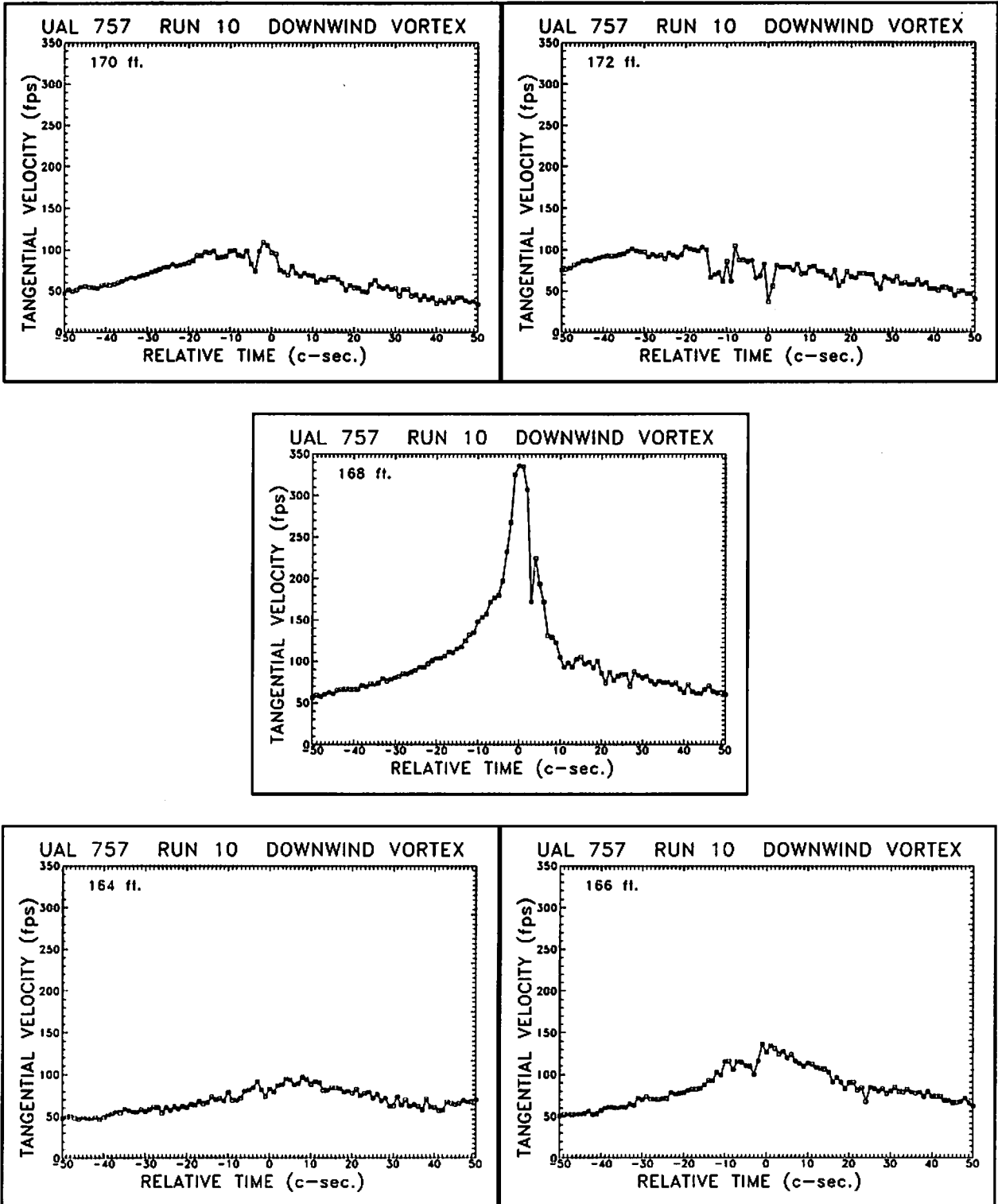
Figure 7. Sample plots of tangential velocity time histories for the downwind vortex of run 10 of the B757-200. The center graph (168 ft) illustrates the highest velocity recorded for this vortex, together with data from adjacent sensors (top and bottom graphs).
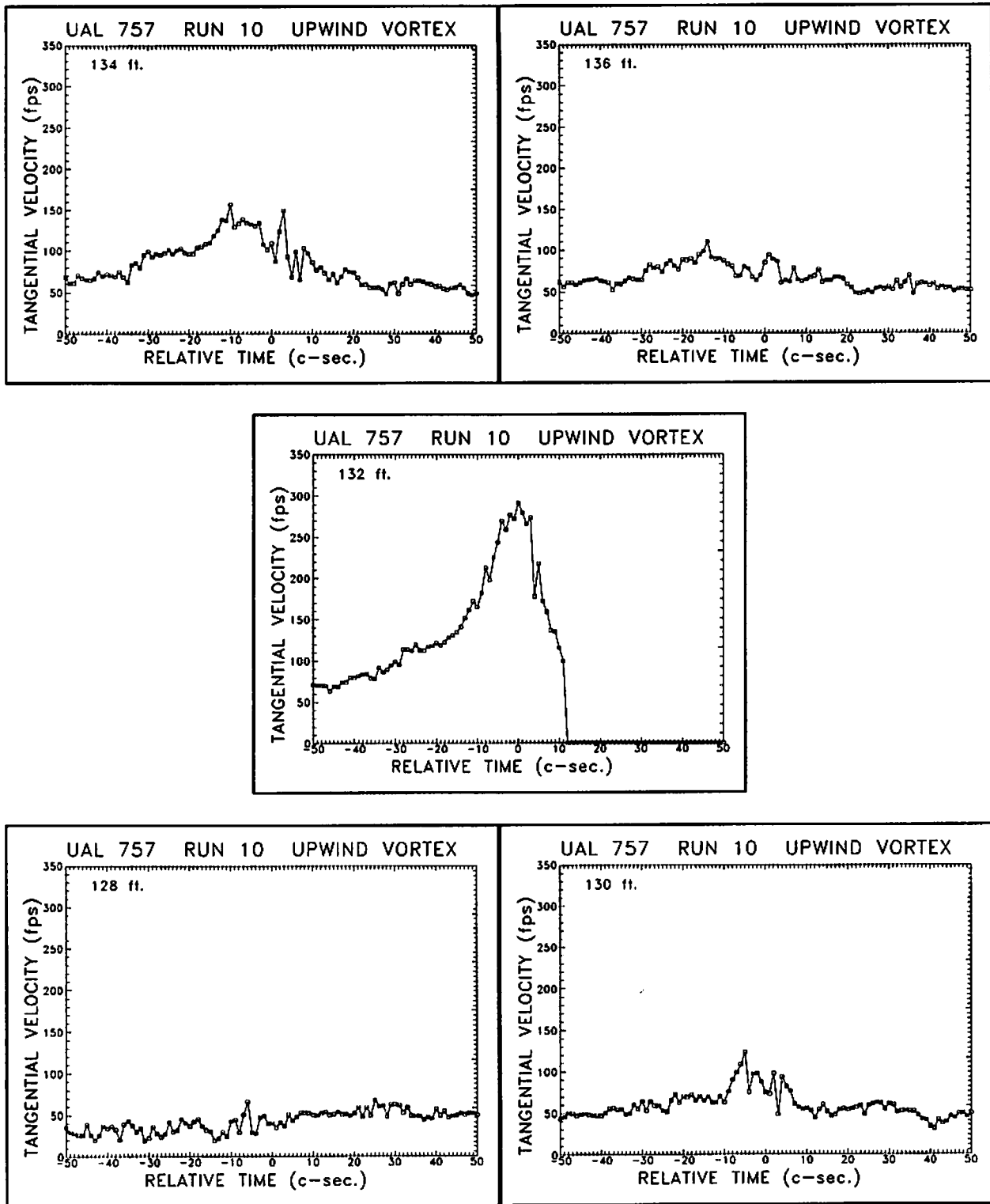
Figure 8. Sample plots of tangential velocity time histories for the upwind vortex of run 10 of the B757-200. The center (132 ft) illustrates the highest velocity recorded for this vortex, together with data from adjacent sensors (top and bottom graphs).
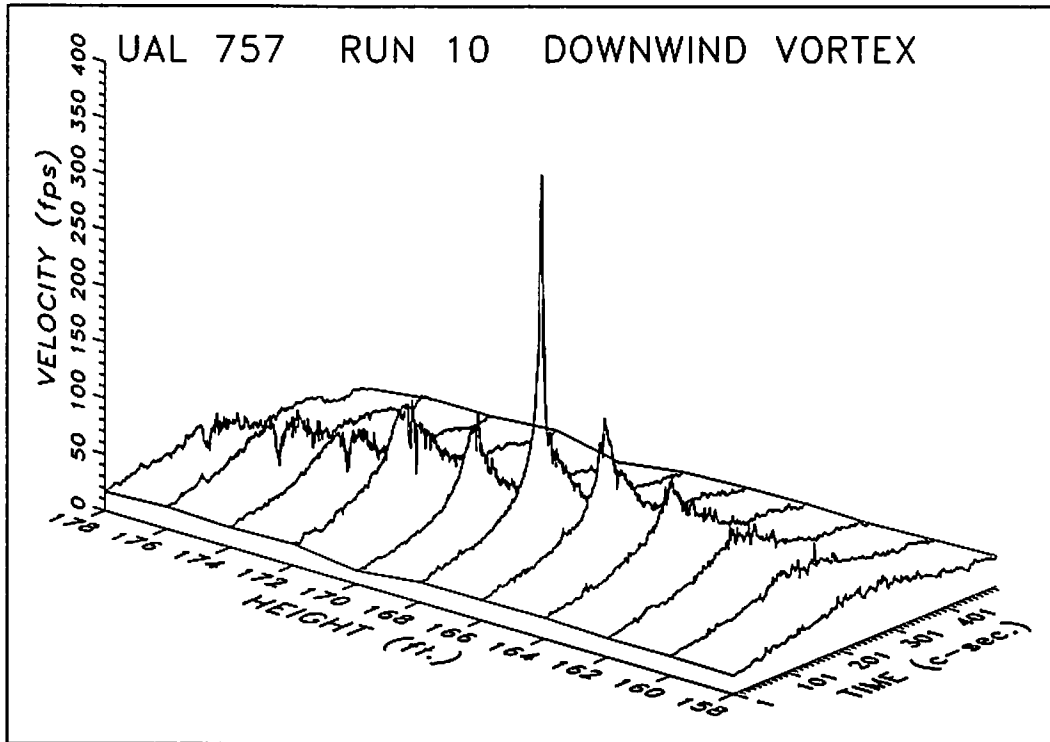
Figure 9. Sample pseudo 3D plot of the downwind vortex flowfield for run 10 of the B757-200. The vortex core passed through or near the sensor at 168 ft AGL.
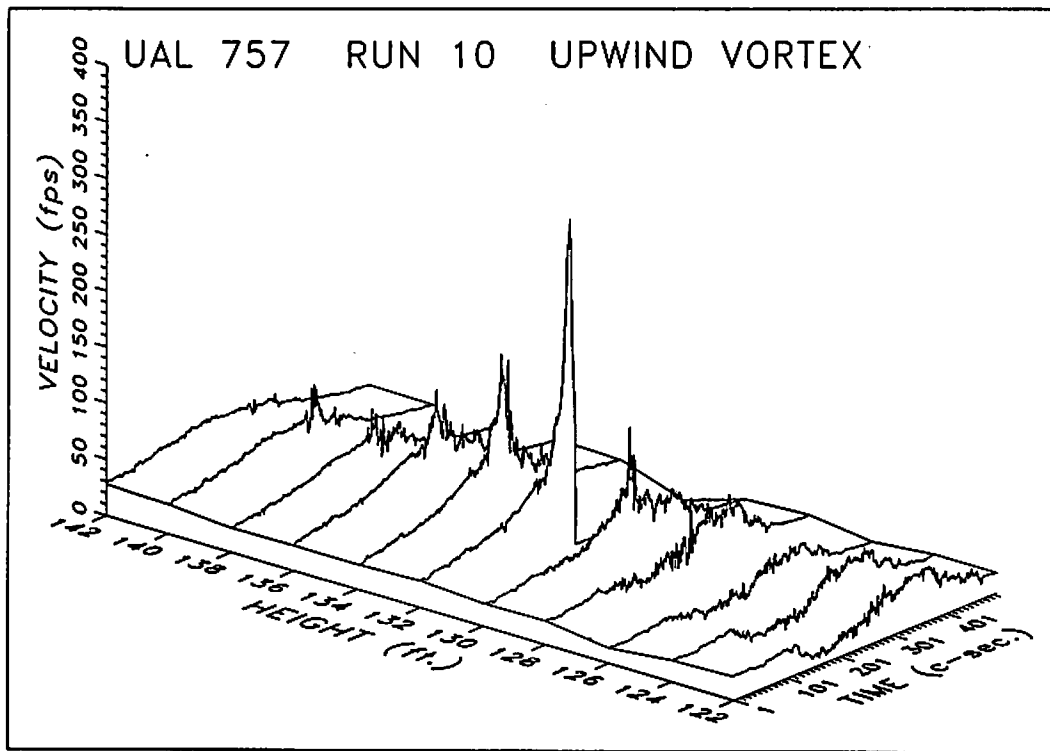

Figure 10. Sample pseudo 3D plot of the upwind vortex flowfield for run 10 of the B757-200. The vortex core passed through or near the sensor at 132 ft AGL.
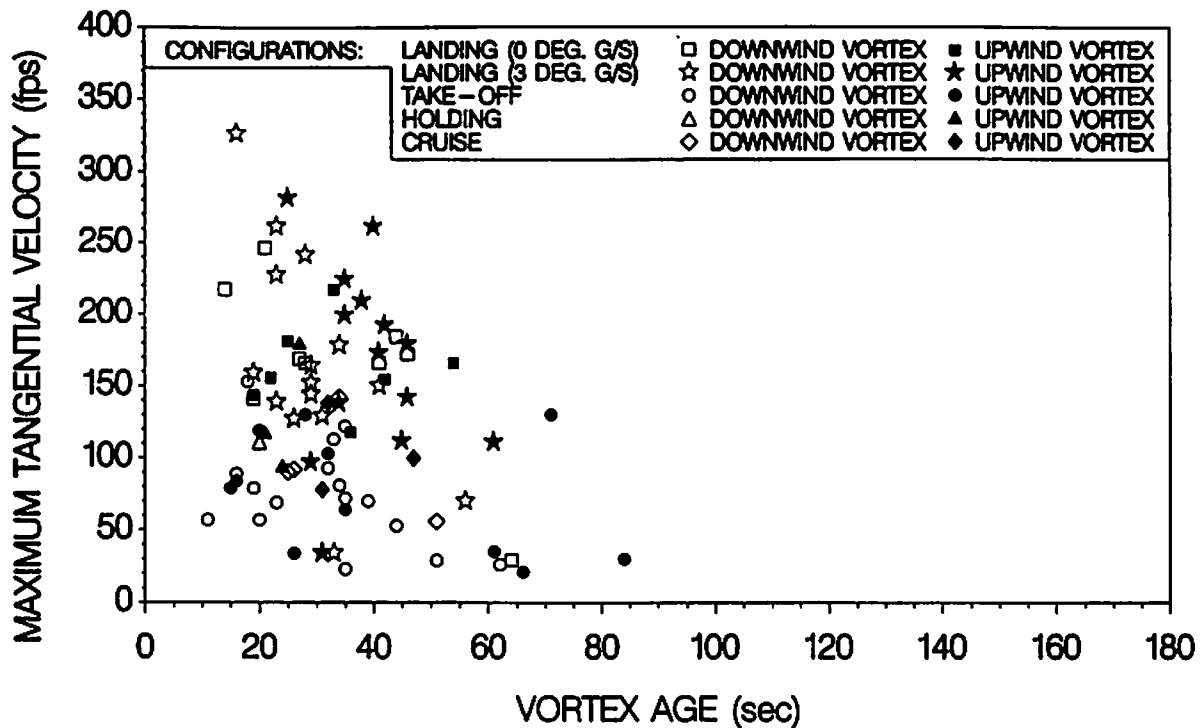
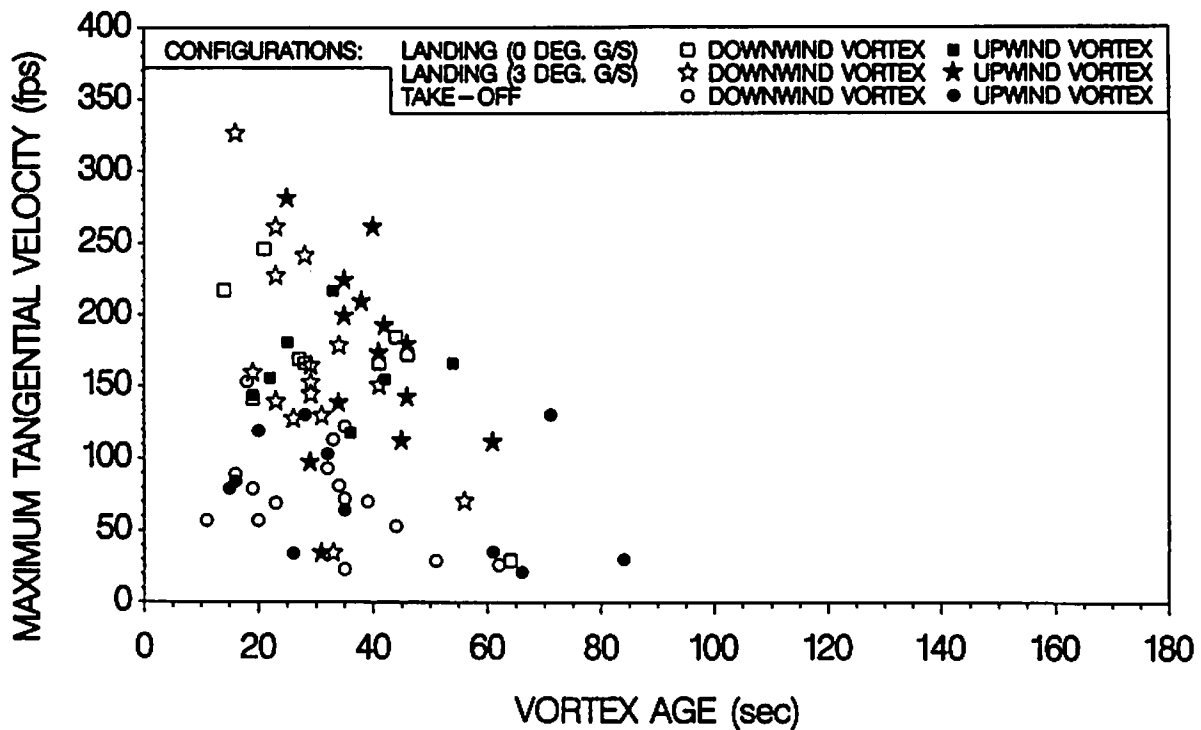**Figure 11. B-757-200 peak vortex tangential velocity (V_θ) vs. age, all configurations.**

Figure 12. B-757-200 peak vortex tangential velocity (V_θ) vs. age, "take-off" and "landing" configurations.

Figure 13. B-757-200 peak vortex tangential velocity (V_θ) vs. age, "holding" and "cruise" configurations.

Figure 14. B-767-200 peak vortex tangential velocity (V_θ) vs. age, all configurations.

Figure 15. B-767-200 peak vortex tangential velocity (V_θ) vs. age, "take-off" and "landing" configurations.

Figure 16. B-767-200 peak vortex tangential velocity (V_θ) vs. age, "holding" and "cruise" configurations.
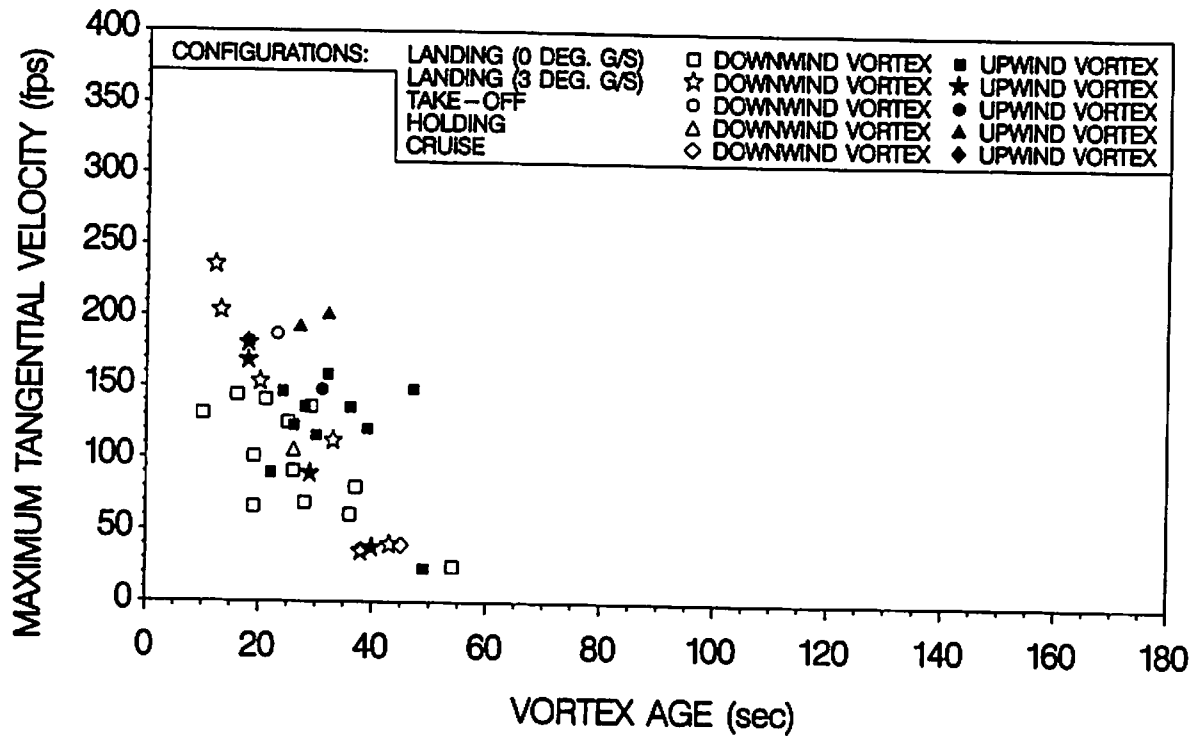
Figure 17. B-727-222 peak vortex tangential velocity (V$_\theta$) vs. age, all configurations.
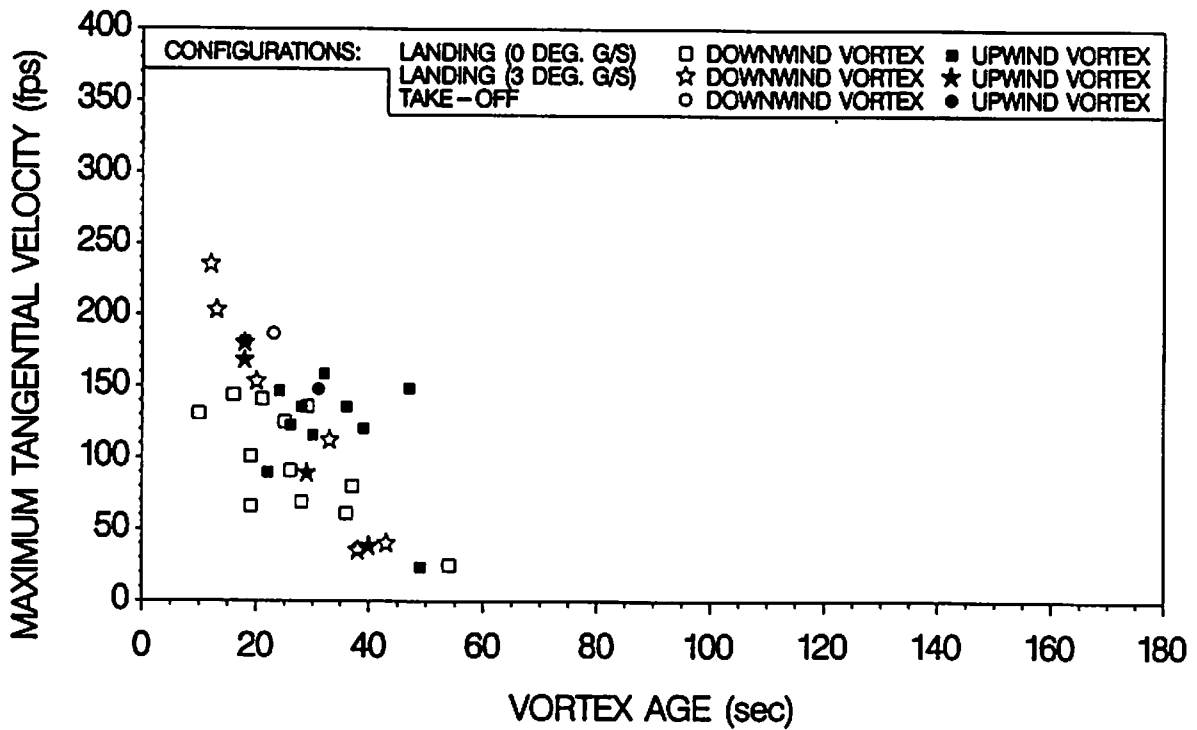
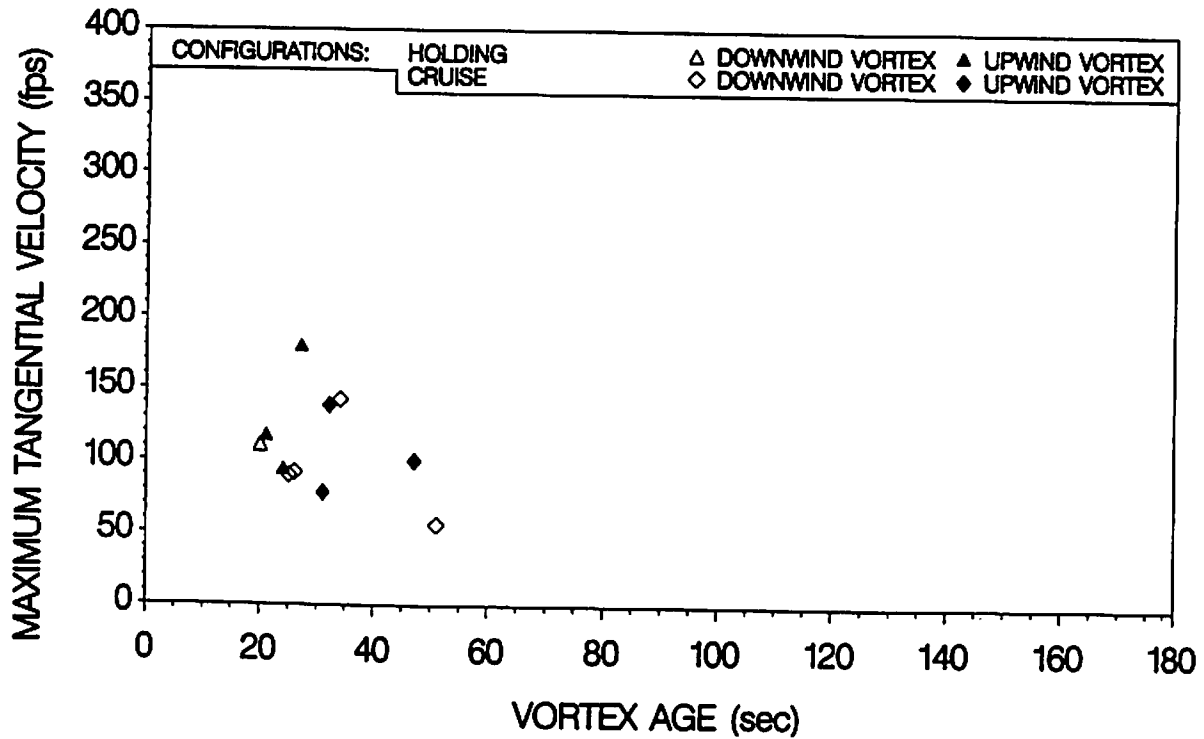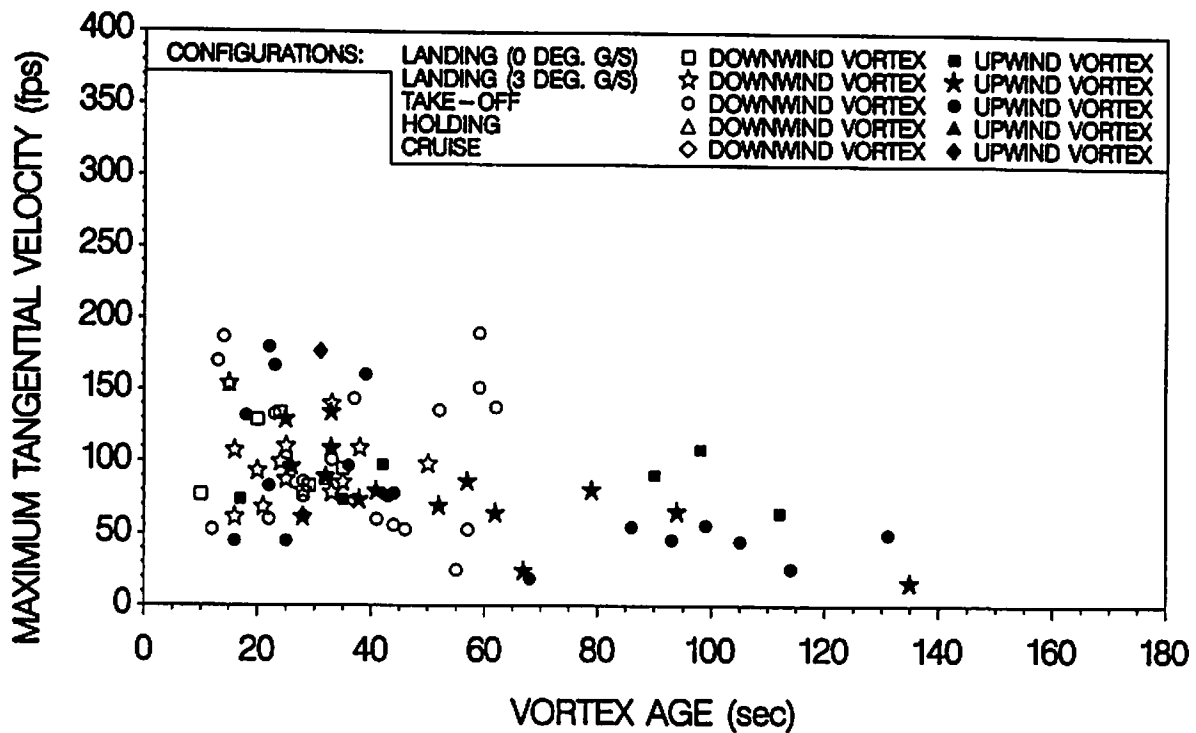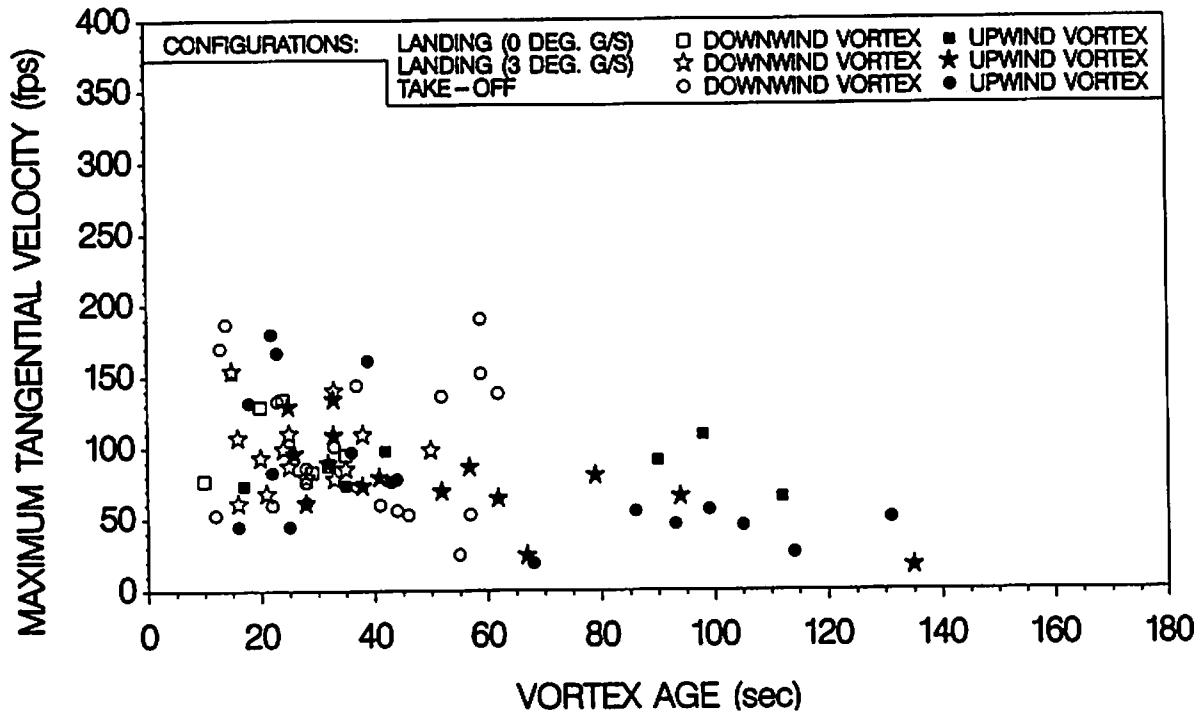Figure 18. B-727-222 peak vortex tangential velocity (V$_\theta$) vs. age, "take-off" and "landing" configurations.
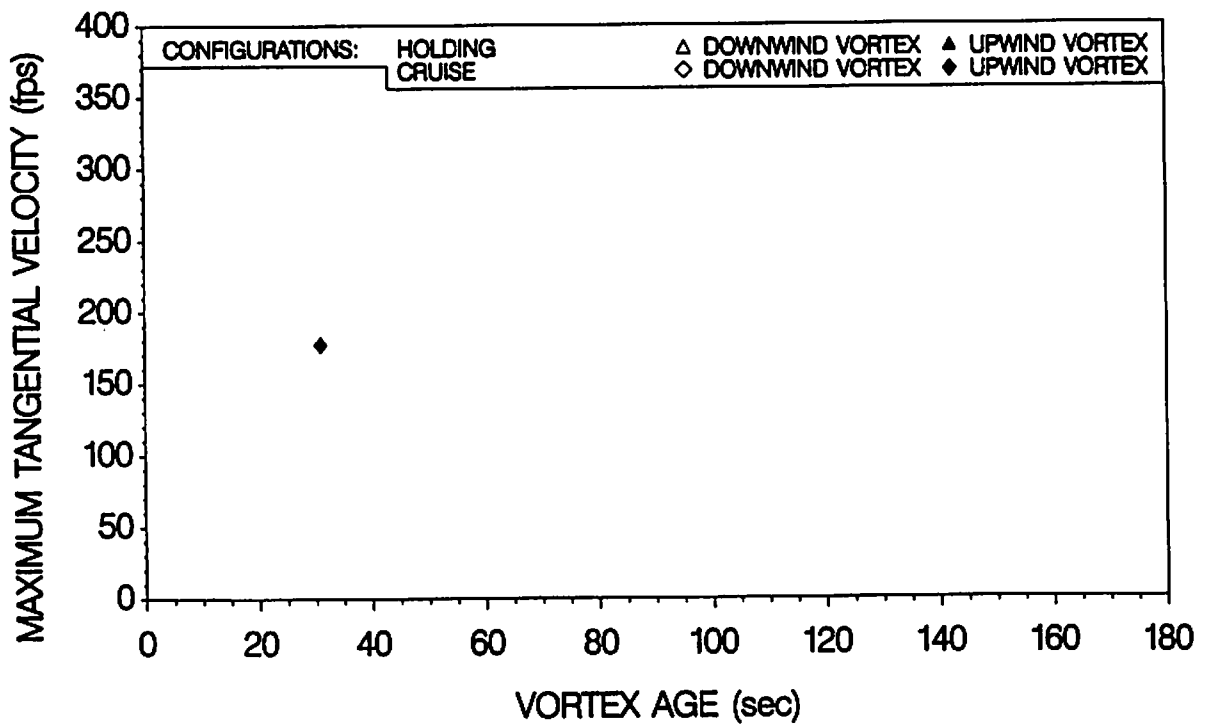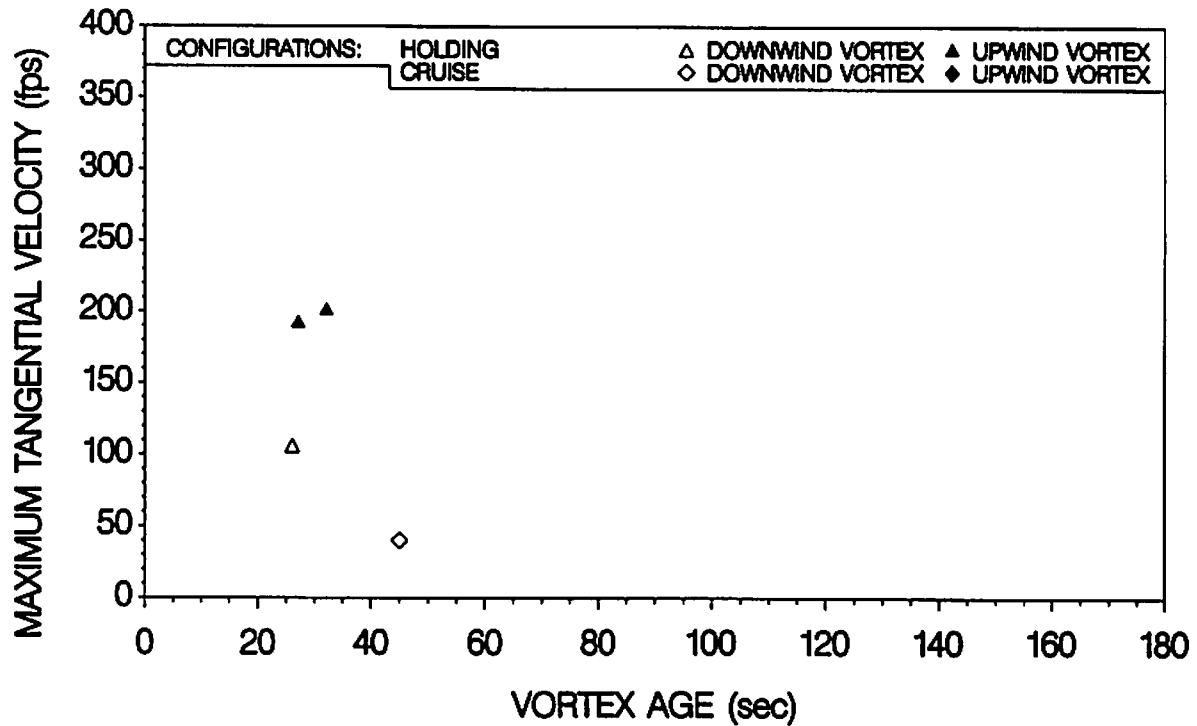
Figure 19. B-727-222 peak vortex tangential velocity (V_θ) vs. age, "holding" and "cruise" configurations.
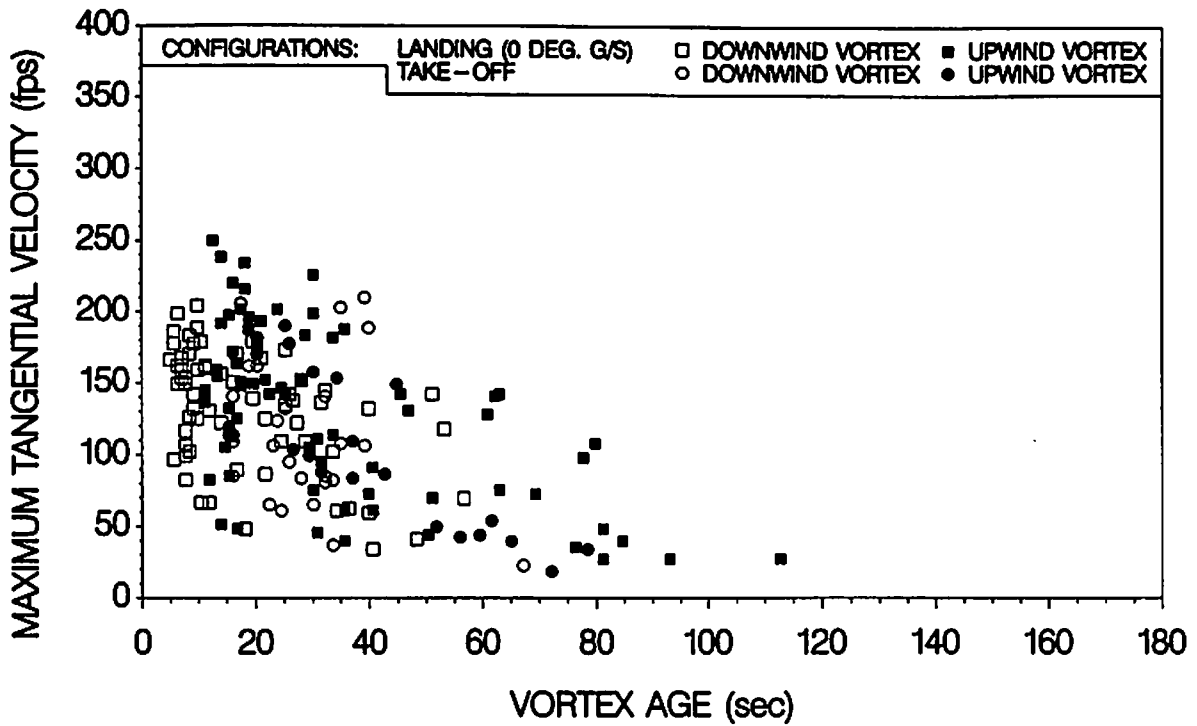
Figure 20. B-727-100 peak vortex tangential velocity (V_θ) vs. age, "take-off" and "landing" configurations (1973 NAFEC flight tests).
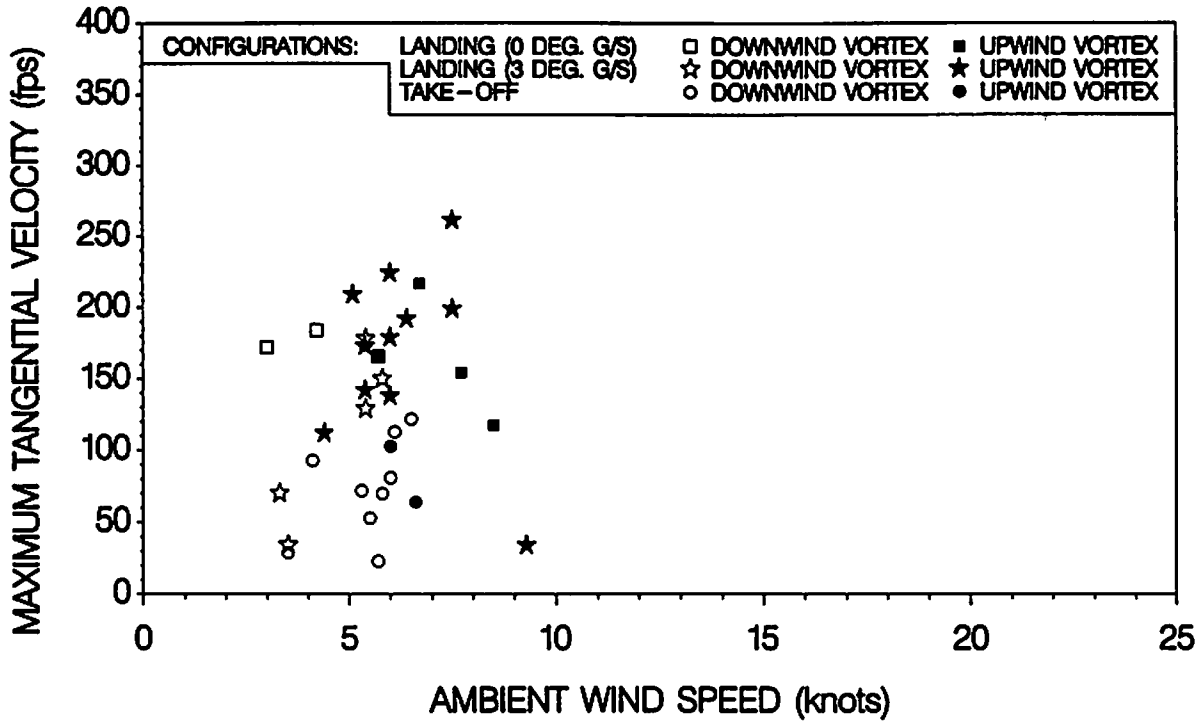
Figure 21. B-757-200 peak vortex tangential velocity (V_θ) vs. ambient wind speed, "take-off" and "landing" configurations -- 30 to 60 seconds age.
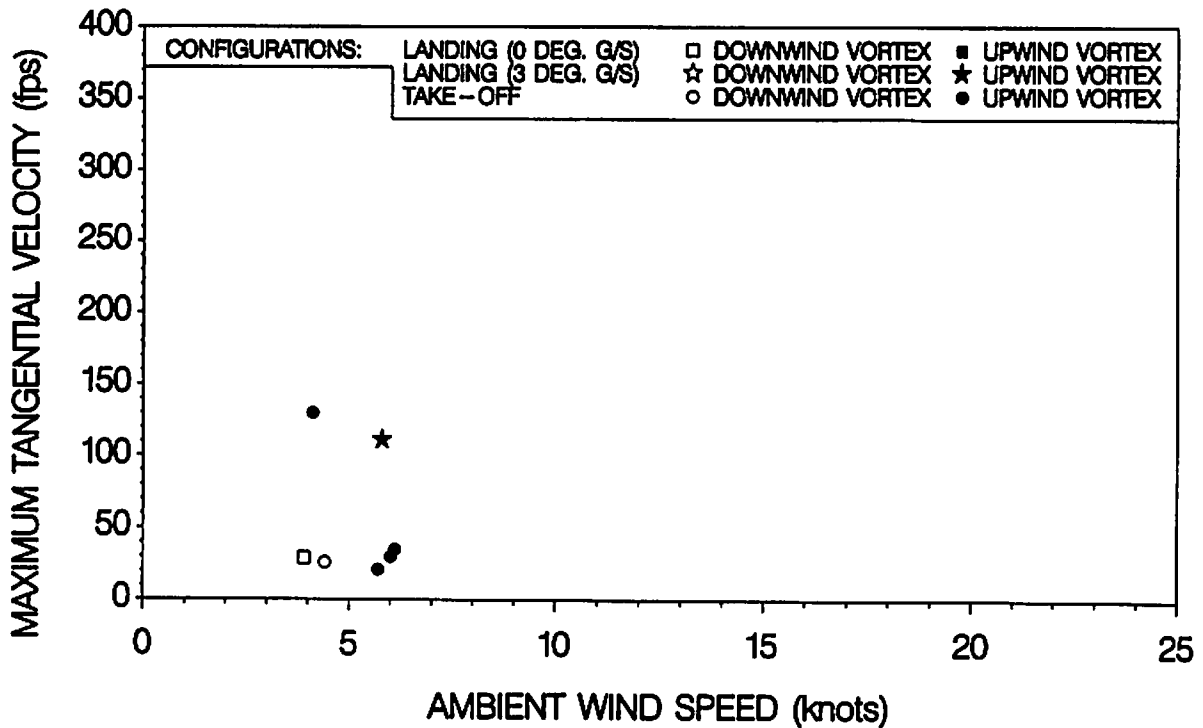
Figure 22. B-757-200 peak vortex tangential velocity (V_θ) vs. ambient wind speed, "take-off" and "landing" configurations -- >60 seconds age.
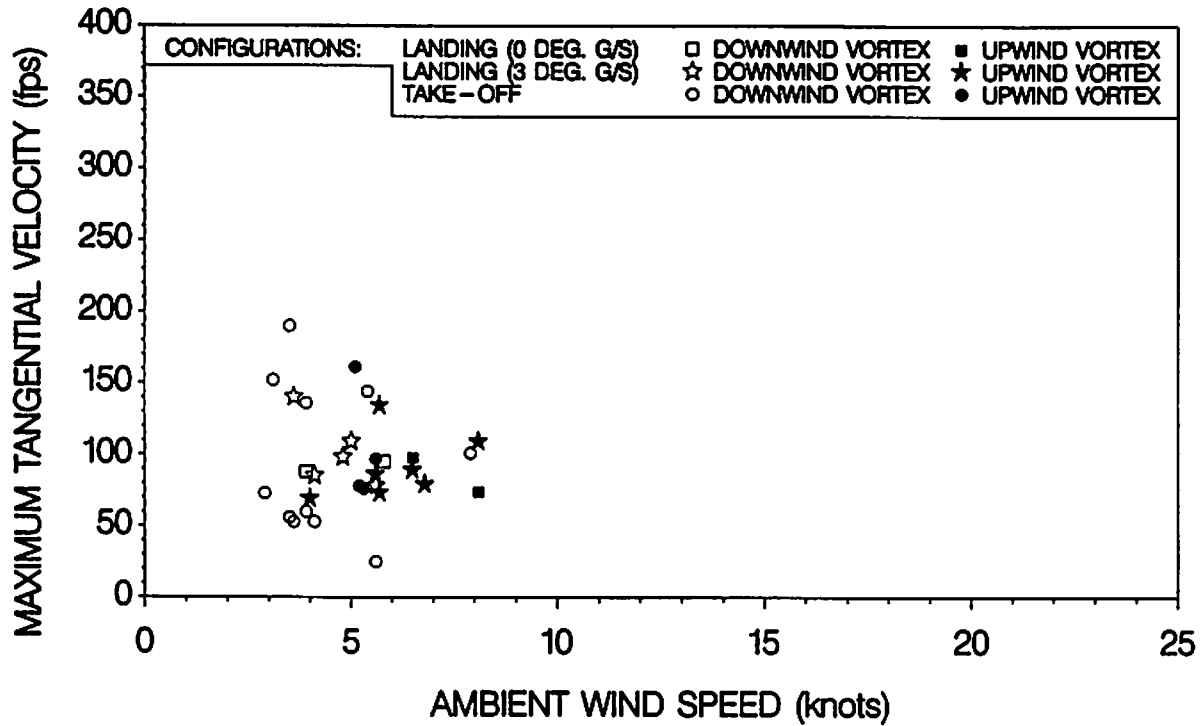
Figure 23. B-767-200 peak vortex tangential velocity (V_θ) vs. ambient wind speed, "take-off" and "landing" configurations -- 30 to 60 seconds age.
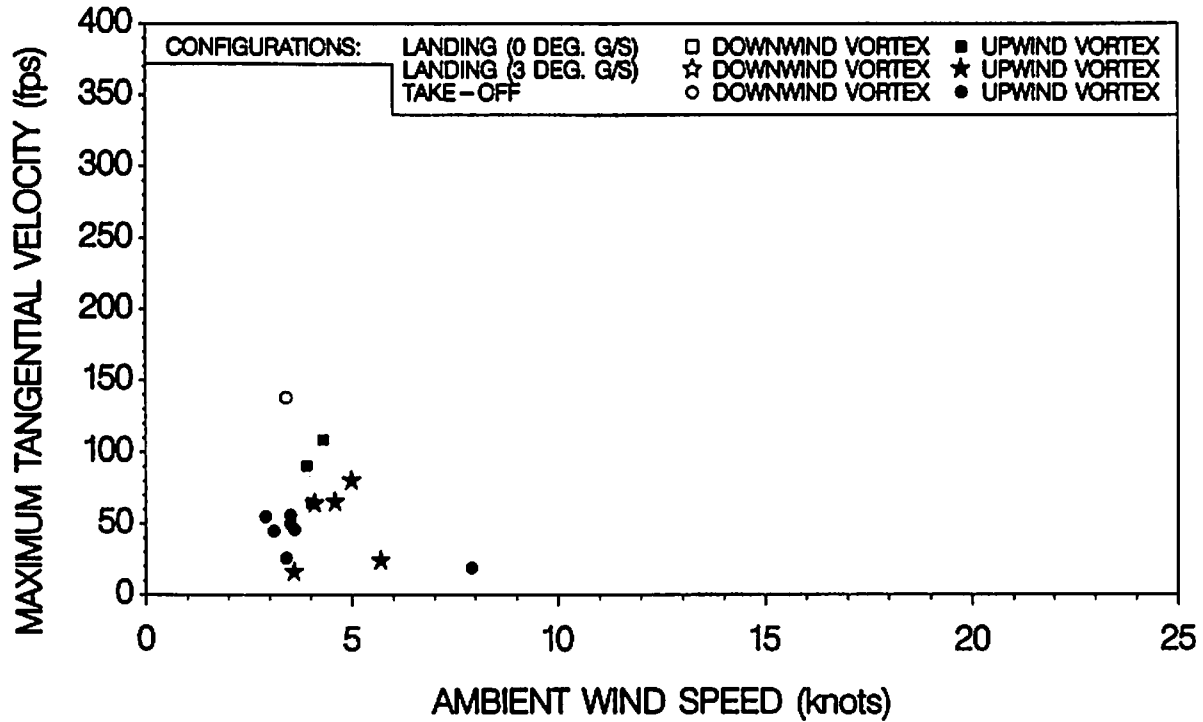
Figure 24. B-767-200 peak vortex tangential velocity (V_θ) vs. ambient wind speed, "take-off" and "landing" configurations -- >60 seconds age.
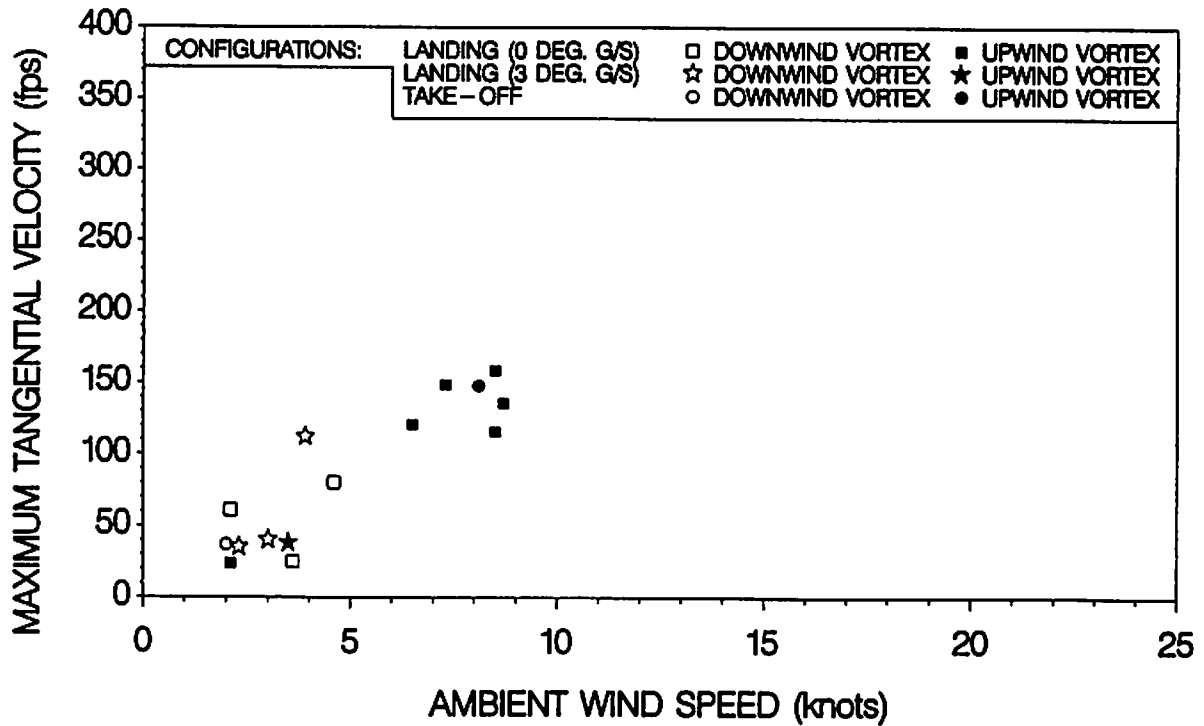
Figure 25. B-727-222 peak vortex tangential velocity (V_θ) vs. ambient wind speed, "take-off" and "landing" configurations -- 30 to 60 seconds age.
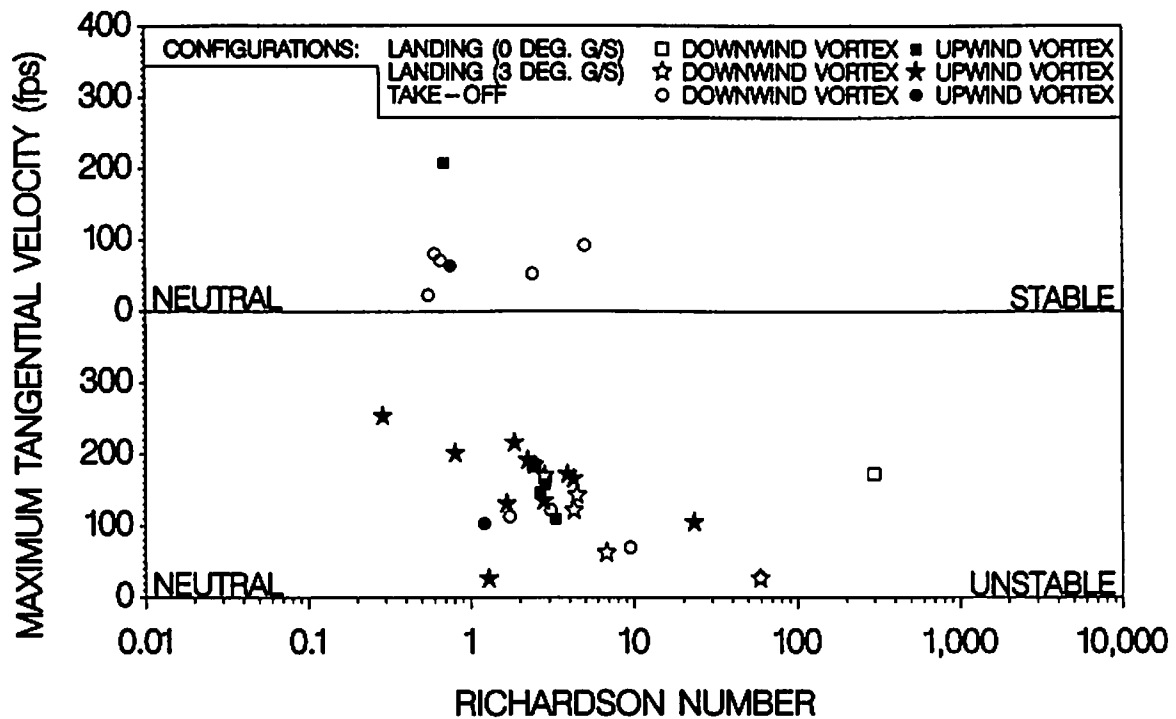
Figure 26. B-757-200 peak vortex tangential velocity (V_θ) vs. Richardson number (Ri), "take-off" and "landing" configurations -- 30 to 60 seconds age.
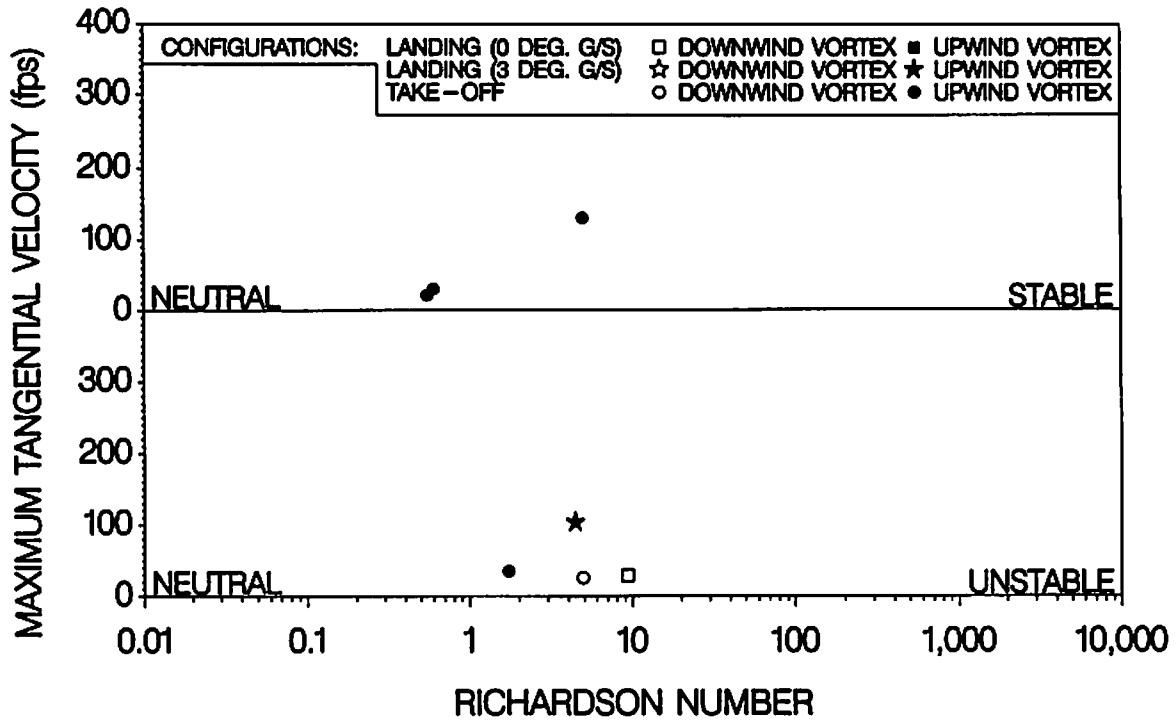
Figure 27. B-757-200 peak vortex tangential velocity (V_θ) vs. Richardson number (Ri), "take-off" and "landing" configurations, -- >60 seconds age.
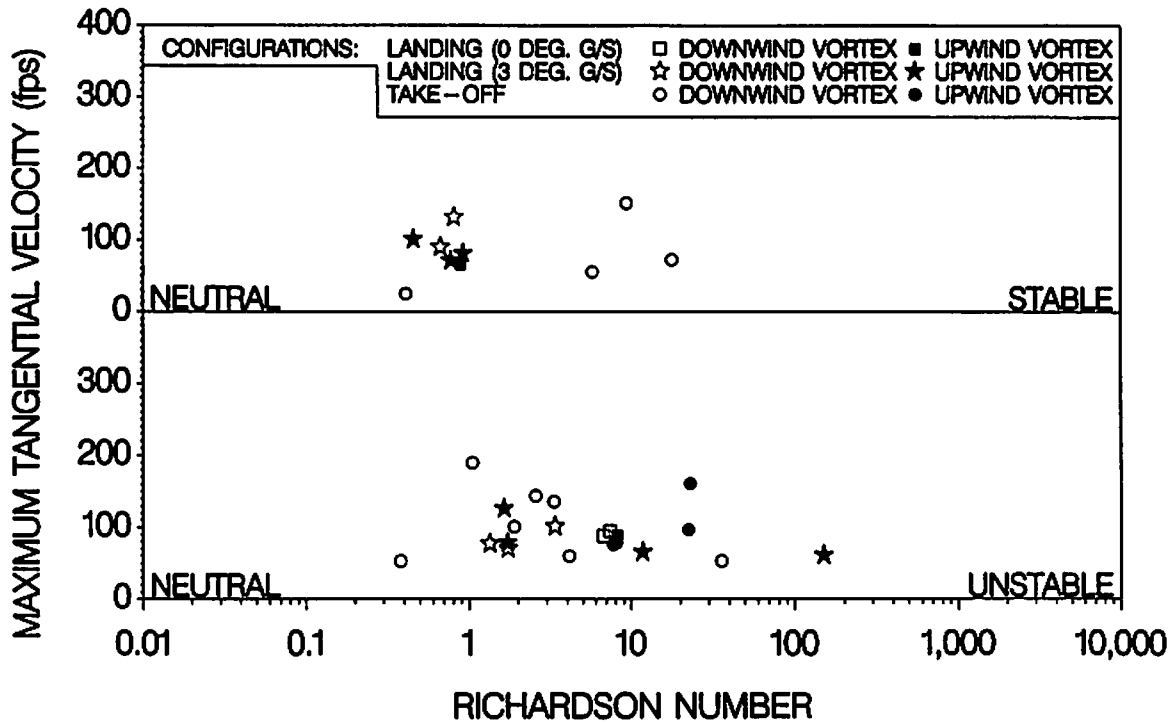
Figure 28. B-767-200 peak vortex tangential velocity (V_θ) vs. Richardson number (Ri), "take-off" and "landing" configurations, -- 30 to 60 seconds age.
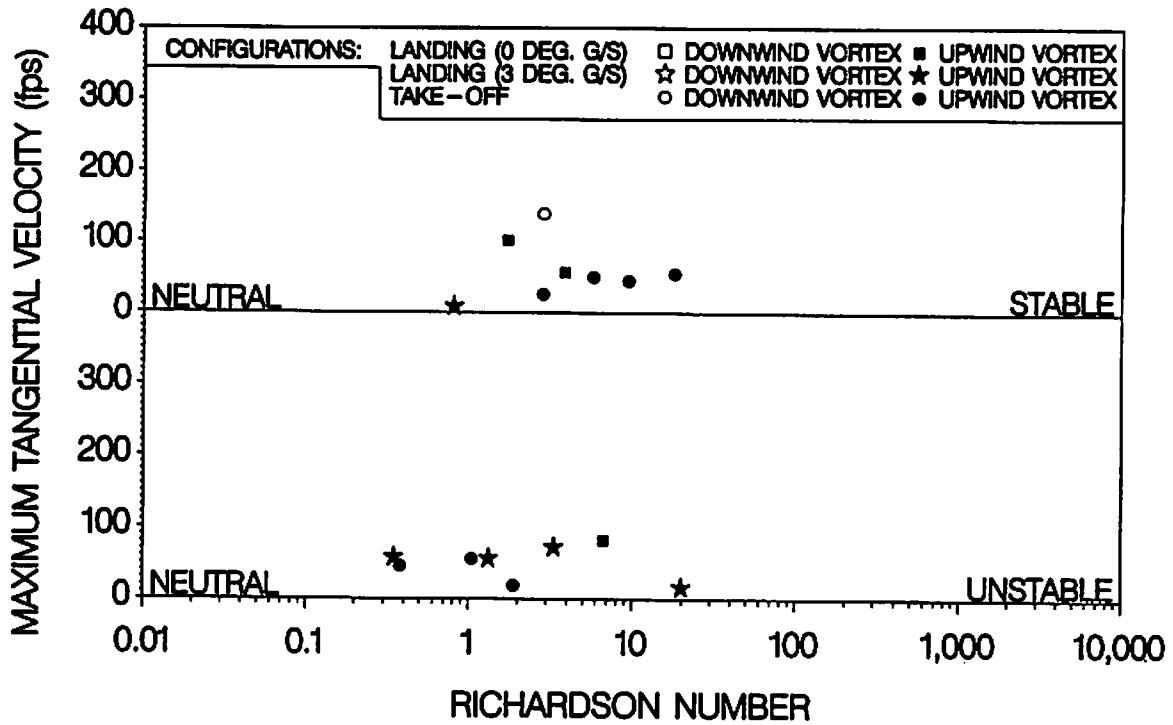
Figure 29. B-767-200 peak vortex tangential velocity (V_θ) vs. Richardson number (Ri), "take-off" and "landing" configurations, -- >60 seconds age.
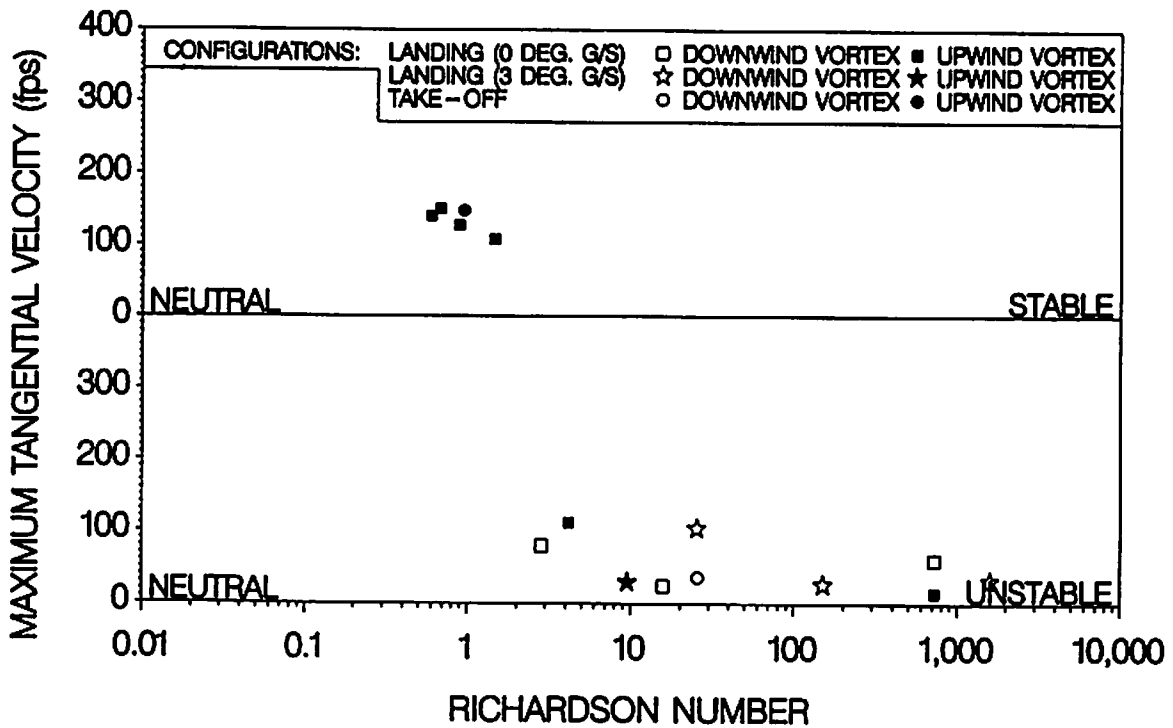
Figure 30. B-727-222 peak tangential velocity (V_θ) vs. vertical air Richardson number (Ri), "take-off" and "landing" configurations, -- 30 to 60 seconds age.
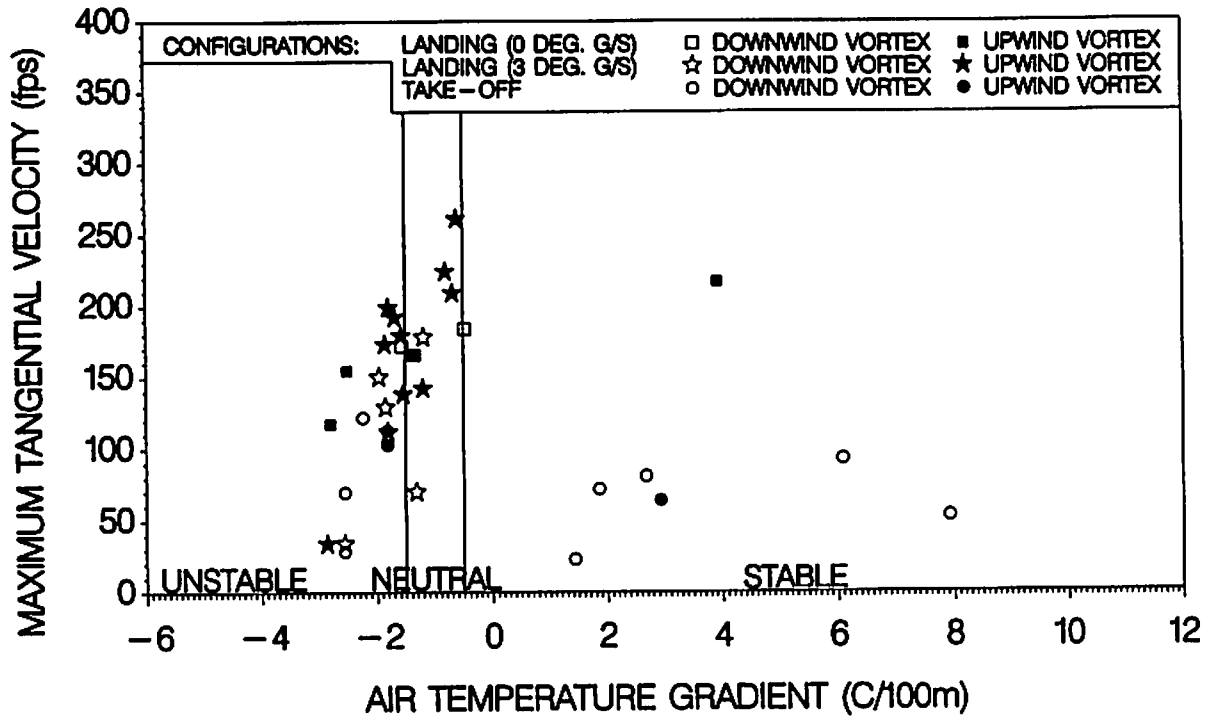
Figure 31. B-757-200 peak tangential velocity (V_θ) vs. vertical air temperature difference, "take-off" and "landing" configurations, -- 30 to 60 seconds age.
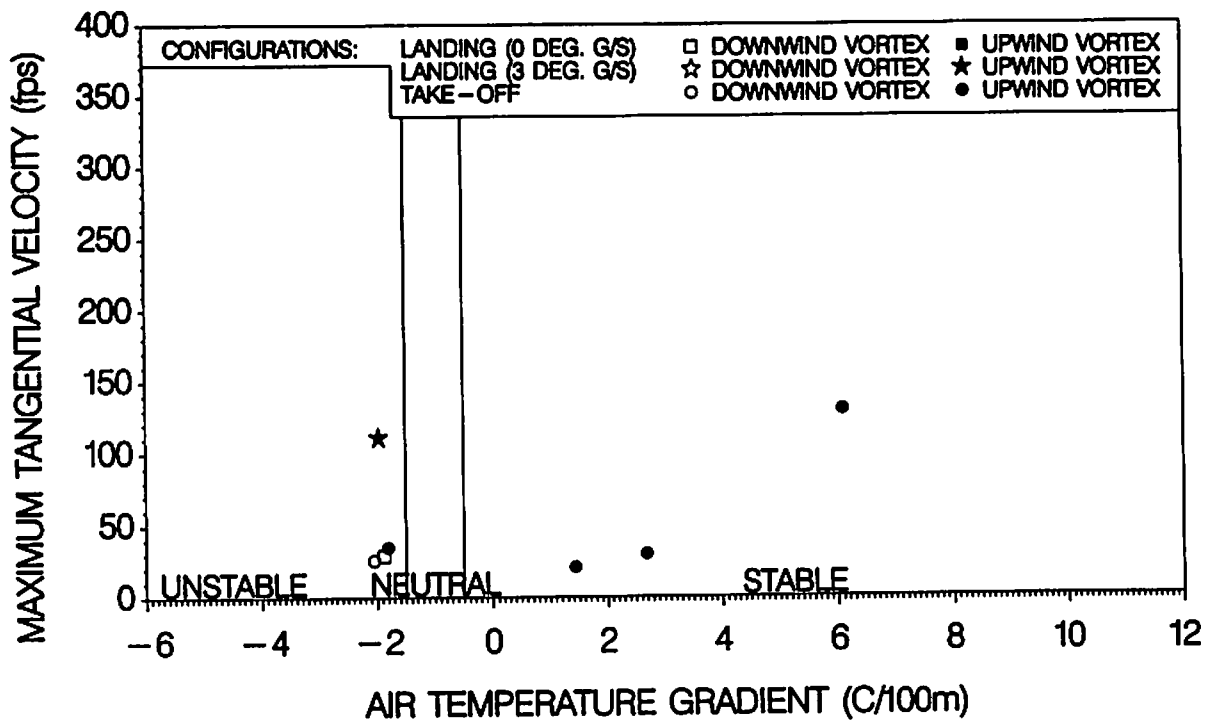
Figure 32. B-757-200 peak tangential velocity (V_θ) vs. vertical air temperature difference, "take-off" and "landing" configurations, -- >60 seconds age.
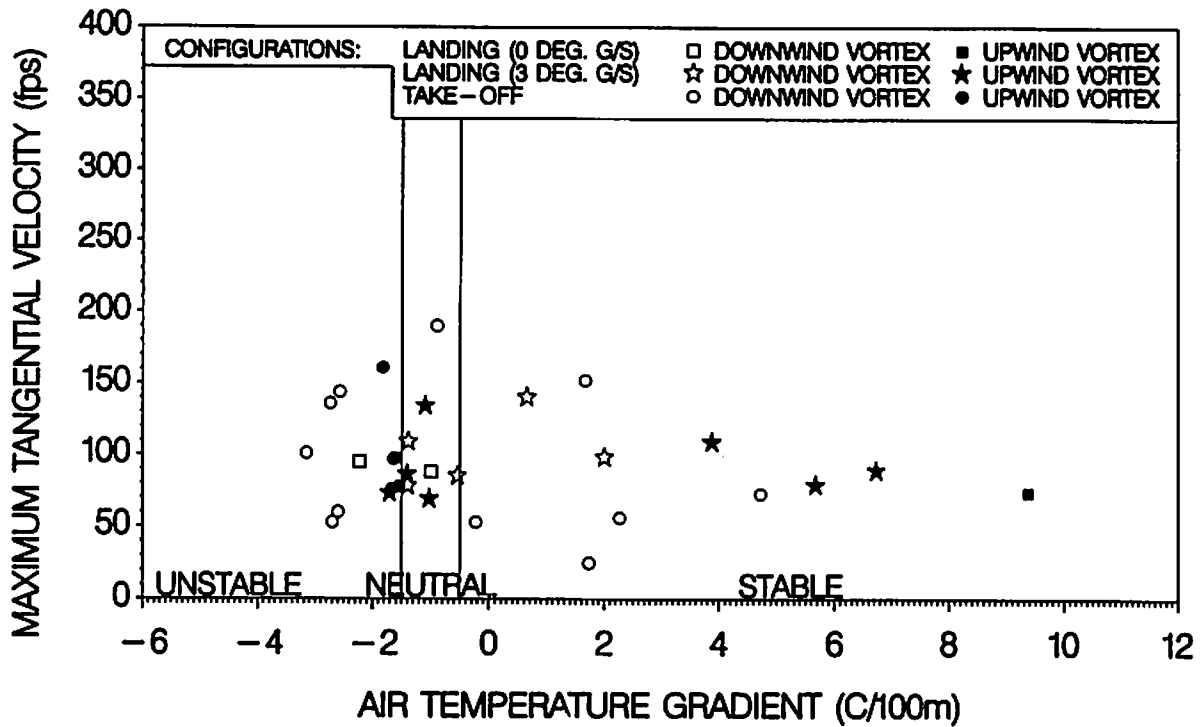
Figure 33. B-767-200 peak tangential velocity (V_θ) vs. vertical air temperature difference, "take-off" and "landing" configurations, -- 30 to 60 seconds age.
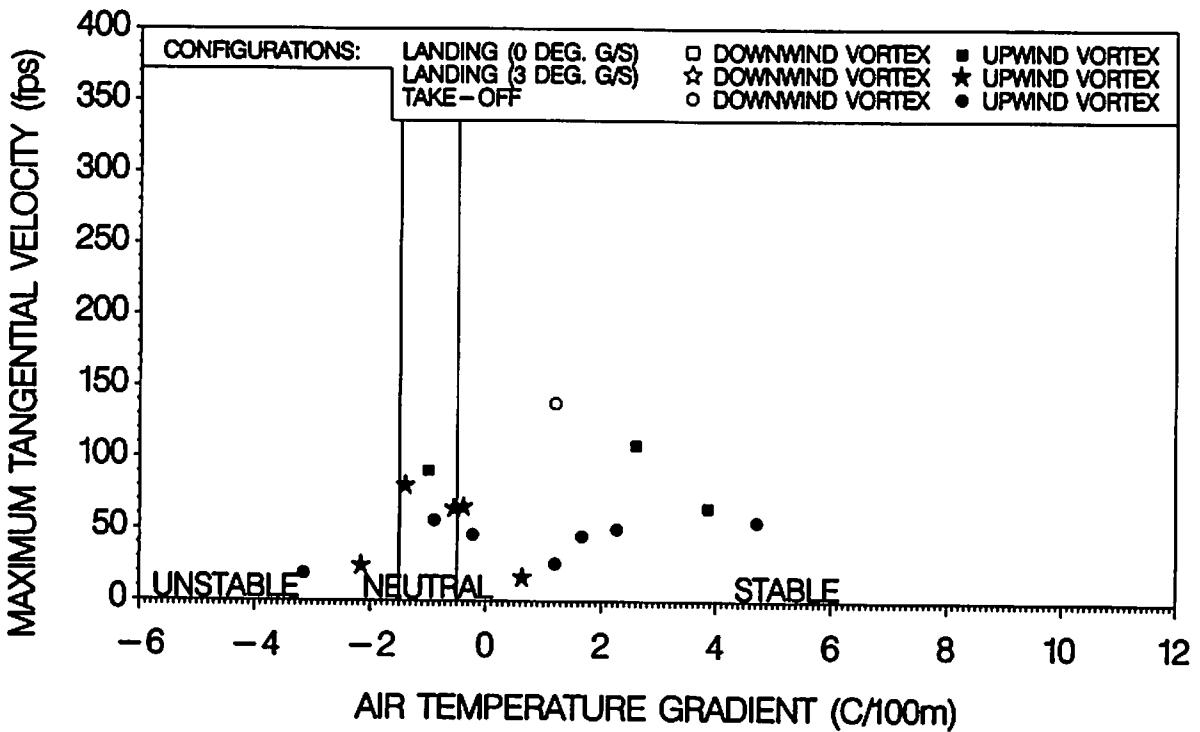
Figure 34. B-767-200 peak tangential velocity (V_θ) vs. vertical air temperature difference, "take-off" and "landing" configurations, -- >60 seconds age.
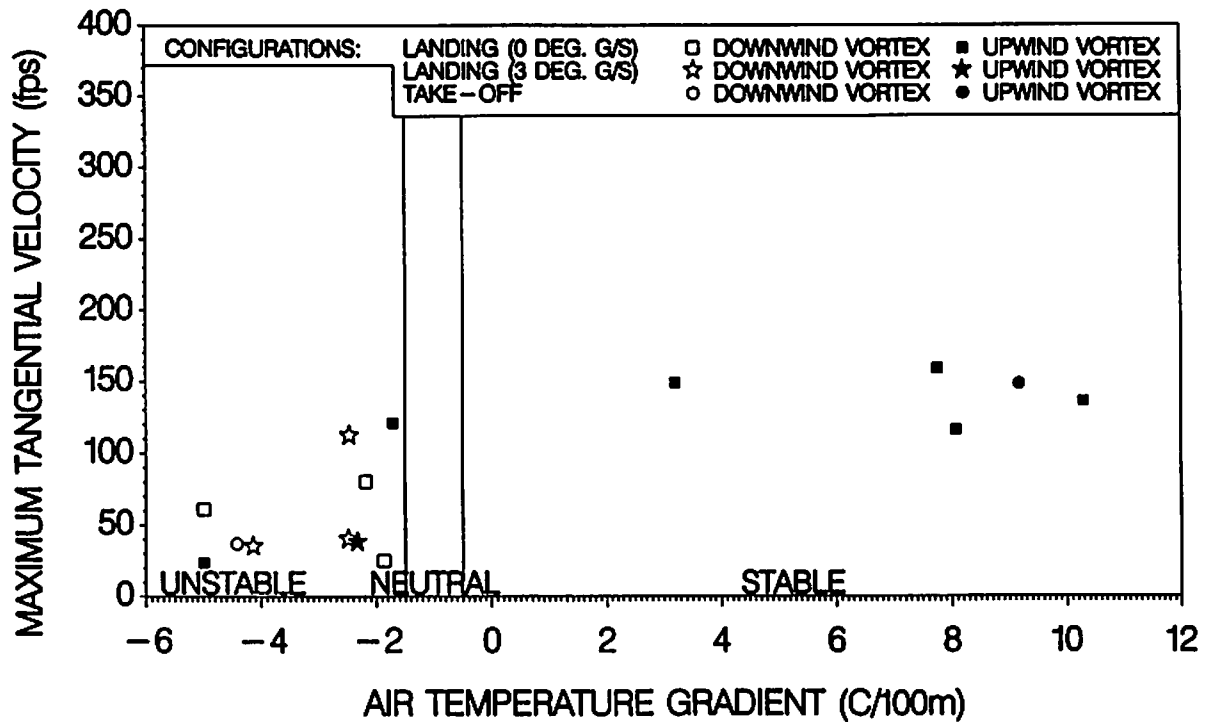
Figure 35. B-727-222 peak tangential velocity (V_θ) vs. vertical air temperature difference, "take-off" and "landing" configurations, -- 30-60 seconds age.
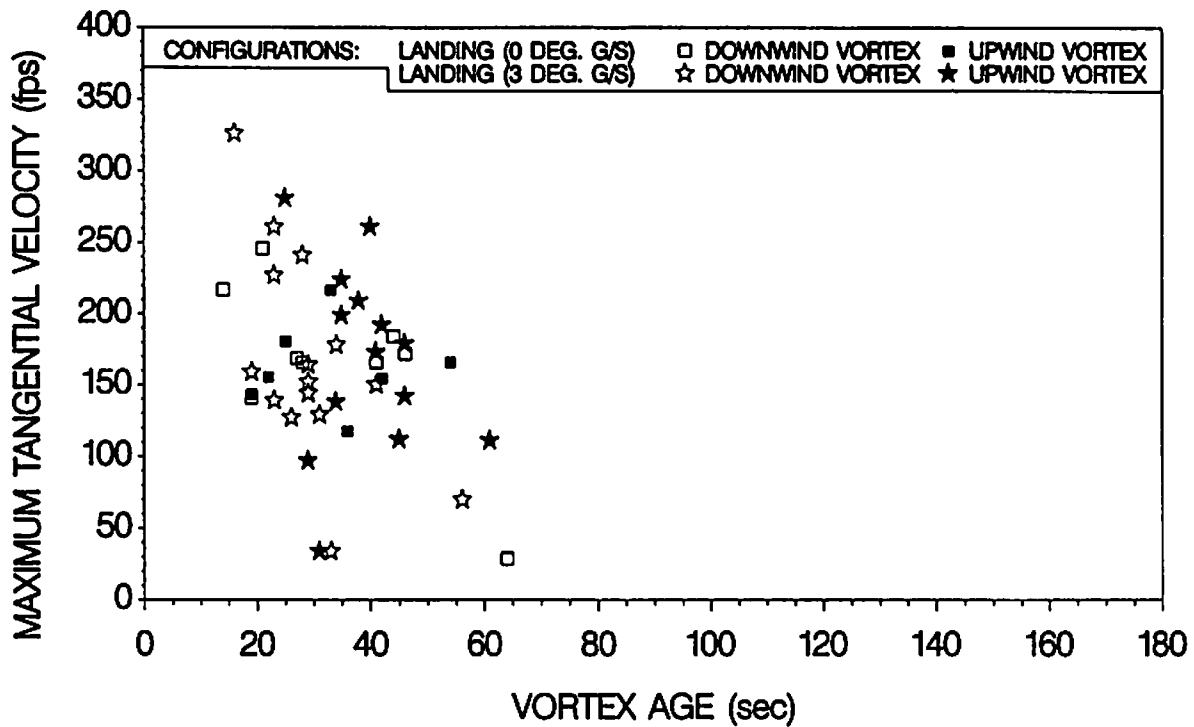
Figure 36. B-757-200 peak vortex tangential velocity (V_θ) vs. age, for 0 and 3 degree G/S, "landing" configuration.
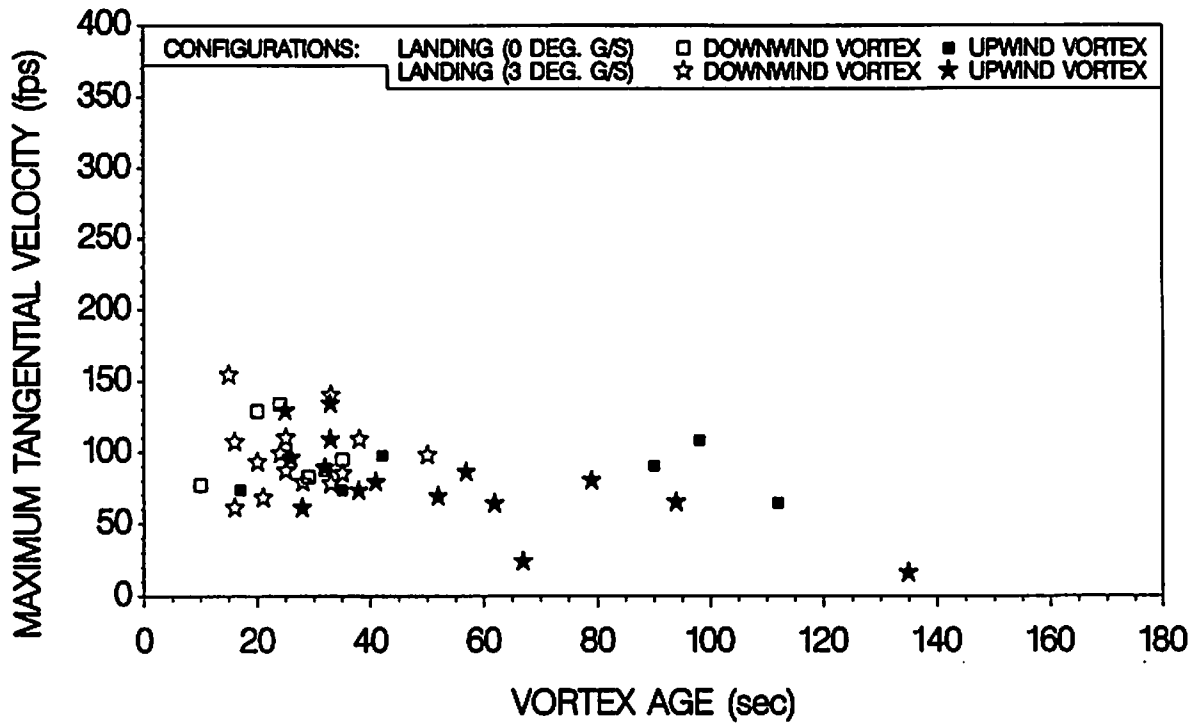
Figure 37. B-767-200 peak vortex tangential velocity (V_θ) vs. age, for 0 and 3 degree G/S, "landing" configuration.
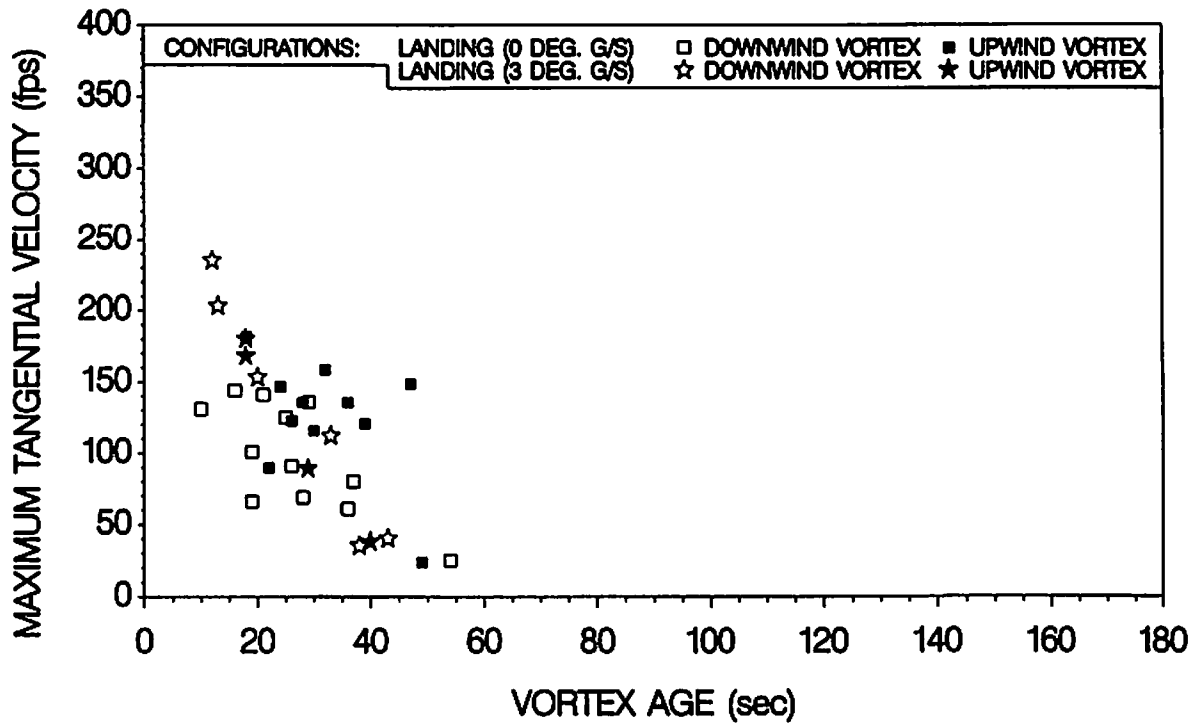
Figure 38. B-727-222 peak vortex tangential velocity (V_θ) vs. age, for 0 and 3 degree G/S, "landing" configuration.
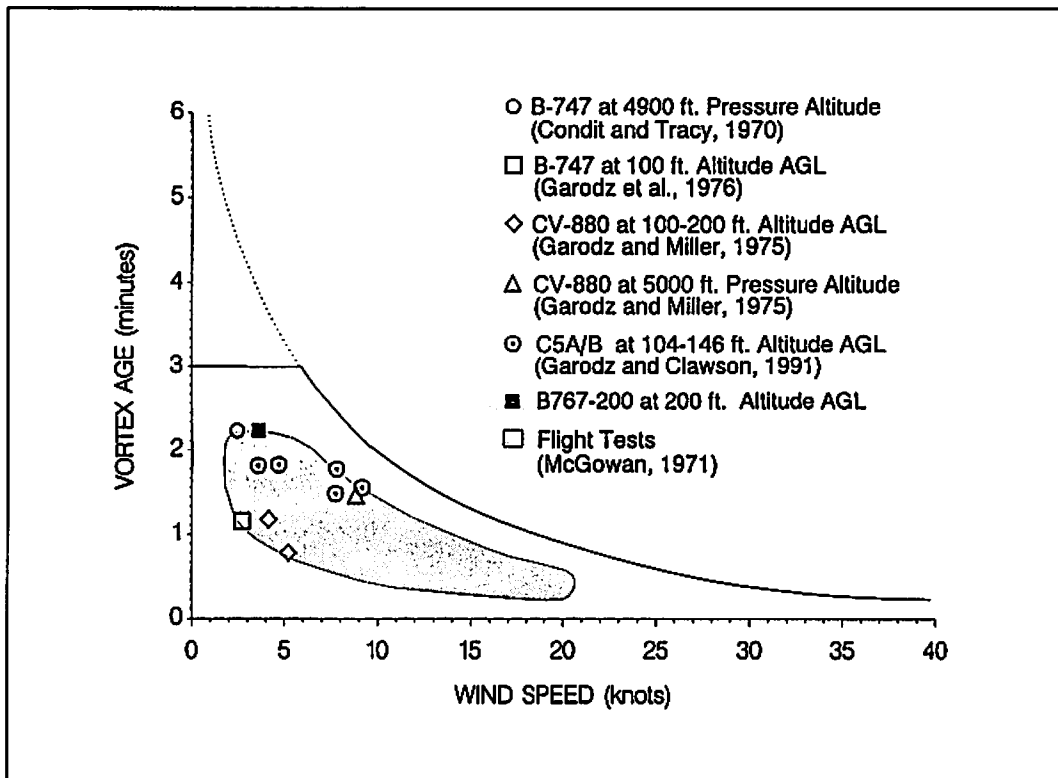
Figure 39. Summary plot of vortex persistence as a function of ambient wind speed and height above the ground.
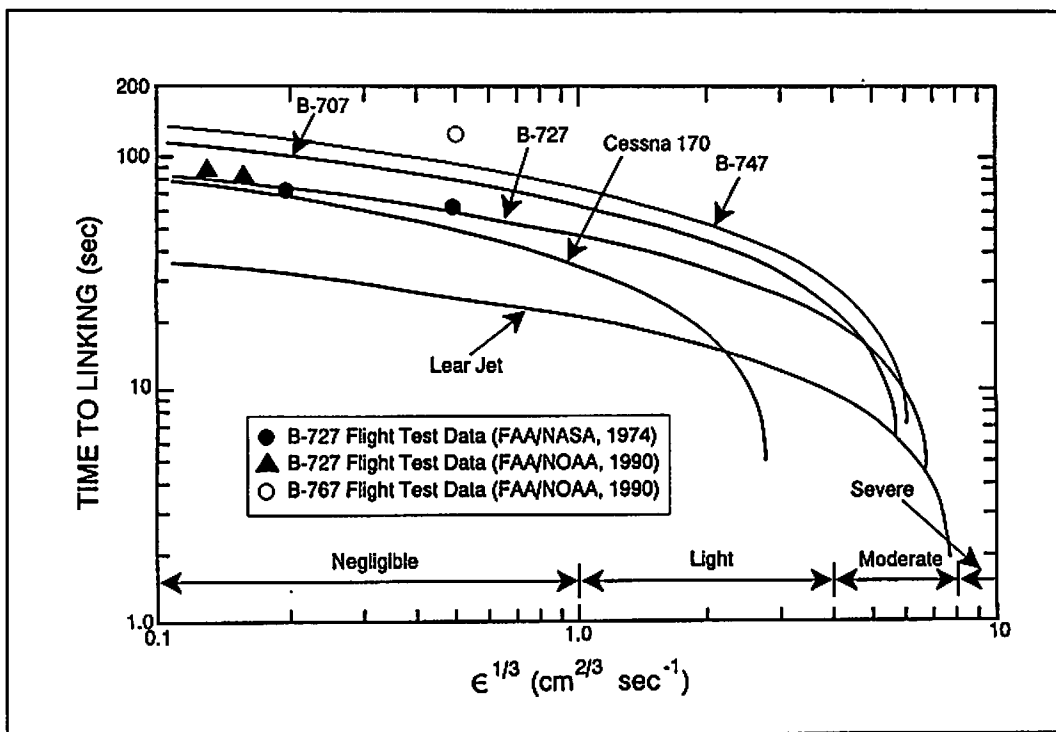
Figure 40. Vortex persistence as a function of atmospheric turbulence dissipation factor $\epsilon^{1/3}$.

	ε	A R G CESSNA 180	M R I SAILPLANE	B-66 THUNDERSTORM	STEINER & RHYNE

PILOT REPORTS
COMPARISON FLIGHT REPORTS FROM FOUR PROJECTS

$\epsilon^{1/3}$ scale: 15, 10, 8, 7, 6, 5, 4, 3, 2, 1, .8, .7, .6, .5, .4, .3

ϵ scale: 5000, 1000, 100, 10, 1., 0.1

ARG CESSNA 180: HEAVY, MODERATE, LIGHT, ZERO (UNDETECTABLE)

MRI SAILPLANE: TURBULENT STRONG WAVE, MODERATE CONVECTION & SLOPE CURRENT, SMOOTH WAVE

B-66 THUNDERSTORM: MOST SEVERE, STRONG

STEINER & RHYNE: MOST SEVERE THUNDERSTORM, AVERAGE LARGE THUNDERSTORM, CUMULUS, CLEAR AIR

Figure 41. Qualitative pilot reports of in-flight atmospheric turbulence levels versus turbulence dissipation factor $\epsilon^{1/3}$ (Reference 2).
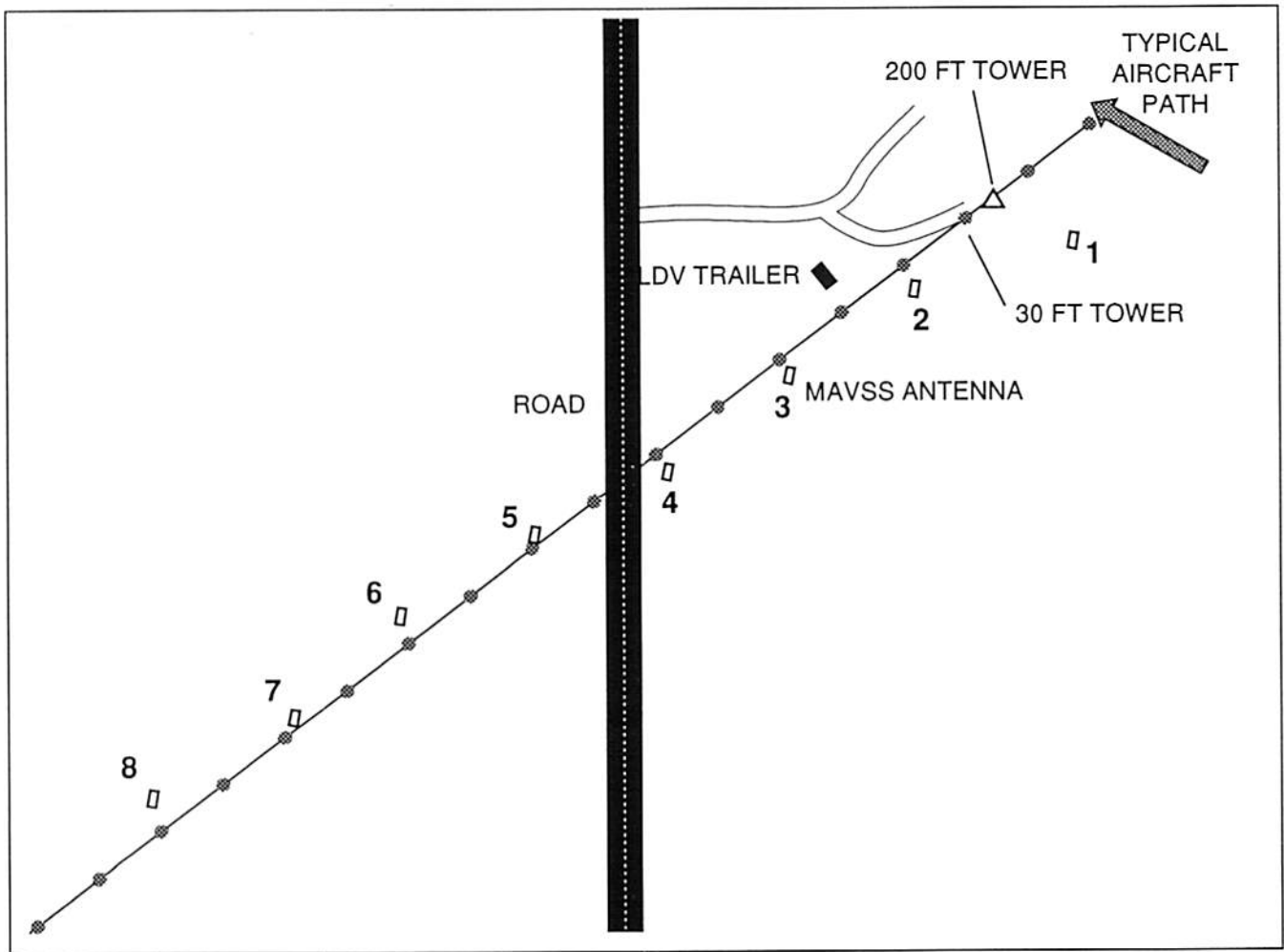
Figure 42. LDV and MAVSS test site locations.
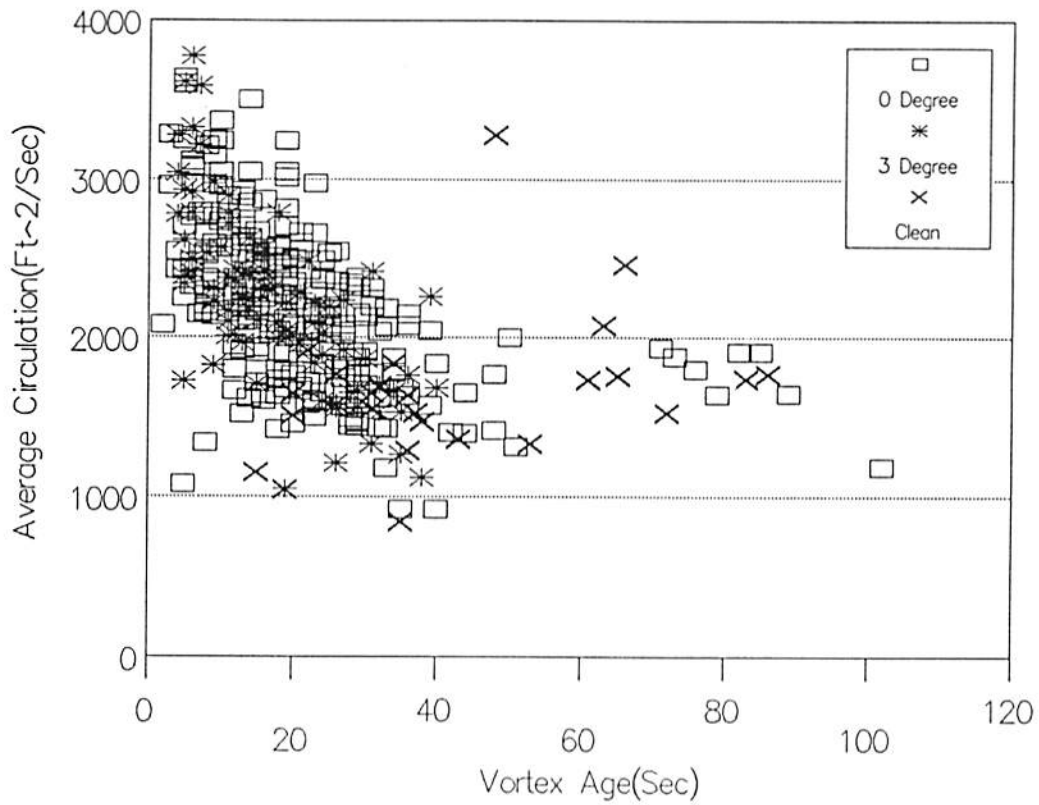
Figure 43. B-727-222 30-foot average circulation, all configurations.
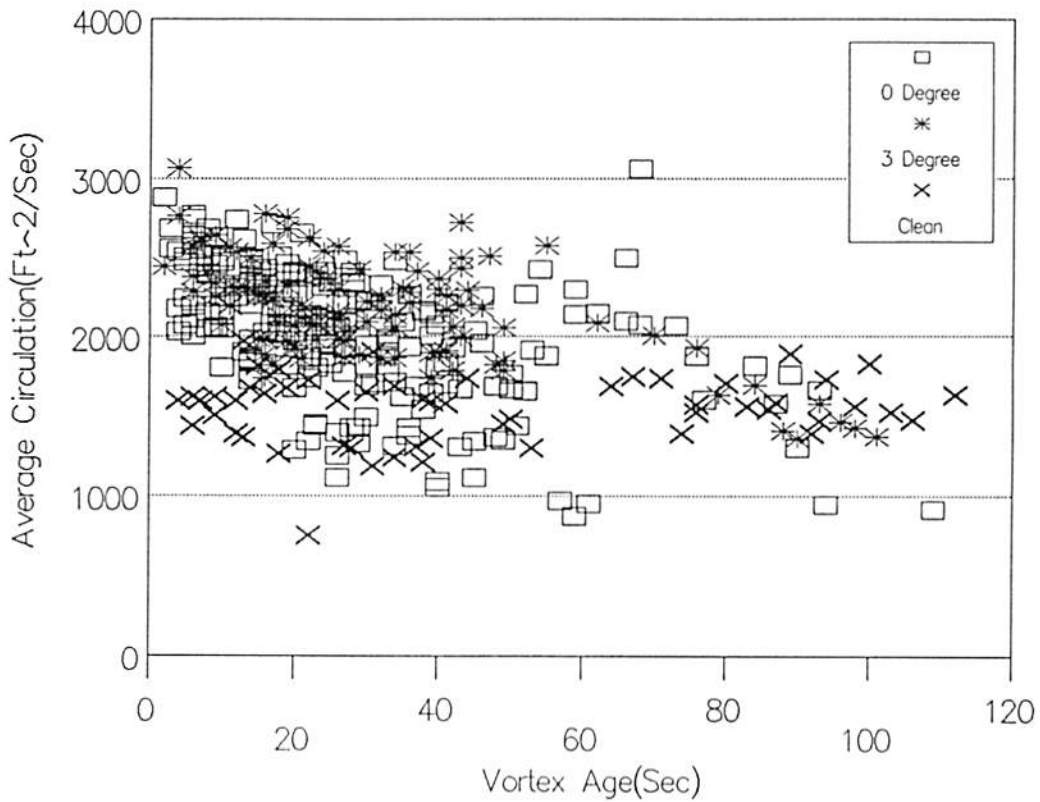
Figure 44. B-757-200 30-foot average circulation, all configurations.

49-48
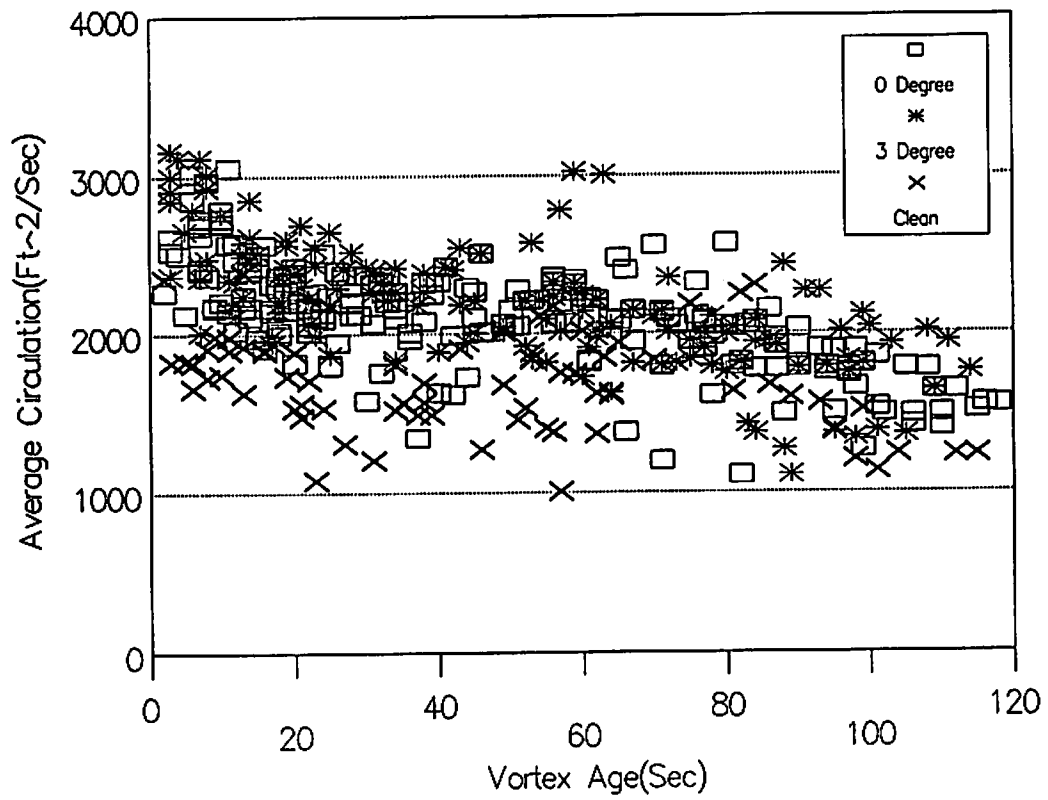
Figure 45. B-767-200 30-foot average circulation, all configurations.

REFERENCES

1. Anon, FAA SYMPOSIUM ON TURBULENCE, Final Report, 22-24 March 1971, Department Of Transportation, Federal Aviation Administration, Washington, D.C.

2. MacCready, Paul B., "Standardization of Gust Values from Aircraft," Journal of Applied Meteorology, Vol. 3, No. 4, August 1964, pp. 439-449.

3. Garodz, Leo J., Lawrence, David, and Miller, Nelson J., "The Measurement of the Boeing 727 Trailing Vortex System Using the Tower Fly-by Technique," Report No. FAA-RD-74-90, Federal Aviation Administration, Systems Research and Development Service, Washington D.C., 20590.

4. Garodz, Leo J. and Clawson, Kirk L., "Vortex Characteristtics of C5A/B, C141B and C130E Aircraft Applicable to ATC Terminal Flight Operations," NOAA, ERL, Air Resources Laboratory Field Research Division, Idaho Falls, Idaho, April 1991

5. Kurkowski, Richard L., Barber, M. Russ, and Garodz, Leo J., 1976. "Characteristics of Vortex Wake Generated by a Boeing 727 Jet Transport During Two-segment and Normal ILS Approach Flight Paths". NASA Technical Note NASA TN D-8222. Ames Research Center, Moffett Field, California

6. Garodz, Leo J., "Investigation of the Relatively Long Time-History Vortex Wake Characteristics of the CV-880 Airplane in Terminal Area-Type Flight Operation," FAA Data Report, Project No. 504-303-03X, (Special Task No. 3), November 1970.

APPENDIX A

RESULTS OF INVESTIGATION OF THE VORTEX WAKE CHARACTERISTICS OF THE AIR FORCE C5A/B, C141B, AND C130E AIRCRAFT USING THE TOWER FLY-BY TECHNIQUE

The following Abstract was taken from NOAA Technical Memorandum ERL ARL-190, Garodz, L. J and K. L. Clawson. Only the conclusions and recommendations were presented at the 1991 Wake Vortex Symposium.

ABSTRACT

During the spring of 1987, the National Oceanic and Atmospheric Administration (NOAA) conducted a full-scale flight test program to investigate the vortex wake characteristics of the 3 primary U.S. Air Force (USAF) Military Airlift Command (MAC) jet transport aircraft, namely the Lockheed C5A/B Galaxy, the C141B Starlifter, and the C130E Hercules. The test program required vortex data at low airspeeds and low altitudes to meet certain operational considerations. The tower fly-by technique was employed for vortex data acquisition purposes. The study was successful in that the objectives of the study were completely fulfilled.

The Federal Aviation Administration (FAA) subsequently commissioned NOAA to reexamine the data with the objective of extending the existing knowledge of vortex behavior in terminal area flight operations. The FAA was particularly interested in the application of the data to Air Traffic Control (ATC) separation standards. The data had not previously been analyzed with this goal in mind. This report describes the results of that effort.

Of significance in the reexamination of the USAF data was the length of vortex persistence even under somewhat turbulent or unstable atmospheric conditions. Although no vortex ages older than 2 minutes were observed in the anemometer data, visual observations of vortex-entrained smoke indicated that C5A/B vortices persisted for as long as 3 minutes. Correlation of the Richardson Number (Ri) with vortex persistence indicated the difficulty of using this atmospheric turbulence index as an indicator of vortex decay. The effect of the high wing configuration of all three aircraft and the T-tail configuration of two of the aircraft on trailing vortex system characteristics is also discussed.

MILITARY TOWER FLY-BY CONCLUSIONS

1. The C5A/B data revealed vortex persistence for ages > 120 seconds.

2. Many of the vortices persisted at high tangential velocities for ages > 60 seconds even under relatively high unstable ambient air mass conditions.

3. Richardson Number, Ri, may be oversold as being the magic parameter with which to correlate vortex persistence in the earth's boundary layer.

4. Good correlation was found between vortex persistence and ambient wind speed for vortex ages over 60 seconds in duration. The wind speed spectra were 2.5-5.5, 4.0-7.5, and 4-10 knots for the C130E, C141B, AND C5A/B aircraft, respectively. These results correspond fairly closely with those acquired during previous full-scale flight test investigations of aircraft vortex wake characteristics which simulated terminal area type flight operations and which were conducted at various locations over the past 20 years.

5. Crow-instability was most pronounced on the C130E aircraft as visualized by the vortex flow visualization system mounted on the wings. Although exact causal factor is not known, vortex/propeller slipstream interaction is suspected.

6. In general, there appeared to be good correlation between peak recorded vortex tangential velocities and the percent of landing flap deflection. V_θ decreased with increased δ_F on the C5A/B and C141B. This was to be expected, based upon previous flight tests of this nature with other aircraft. For example, for identical vortex ages for the C5A/B, V_θ went from 191 to 259 feet/second for 15% flaps, to approximately 77 to 79 feet/second for 100% flaps.

7. The C130E did not exhibit a correlation between peak recorded vortex tangential velocity and the percent of landing flap deflection. This is attributed to the higher engine thrust required because of the increased airplane drag. This in turn added momentum to the slipstream and circulation to the wing - a pseudo jet-flap condition.

MILITARY TOWER FLY-BY RECOMMENDATIONS

1. In view of the findings on the C5A/B vortex wake characteristics, particularly the persistence of the wake with still relatively high residual vortex tangential velocities, the FAA should consider some additional limited, but very precisely controlled, C5A/B vortex wake tower fly-by and vortex probe flight tests. These should be conducted at high gross weights to ensure that this airplane, when operated from commercial airports, properly fits in the "Heavy" category regarding separation standards in terminal area-type flight operations. It may well be that a "Super-Heavy," or similar new category, should be designated for this high weight aircraft (greater than 700,000 pounds), and appropriate separation standards established.

2. It is strongly recommended that flight tests be undertaken as soon as possible with the Boeing 747-400 using the tower fly-by technique for the same reason. The B-747-400 should be operated at the maximum take-off gross weight of 800,000 pounds, or as close to it as reasonable. If the flight test results are similar to those of the C5A/B, then it too may belong in a "Super-Heavy" category.

3. Either NASA or large aircraft manufacturers, e.g., Boeing and McDonald Douglas, should undertake studies to examine and compare the vortex wake characteristics of high-wing versus low-wing, and T-tail versus conventional tail large jet transport type aircraft. This could be for either proposed or currently operational aircraft, with the objective of determining if one particular aircraft geometry produces trailing vortex systems which are more intense or persistent than another.
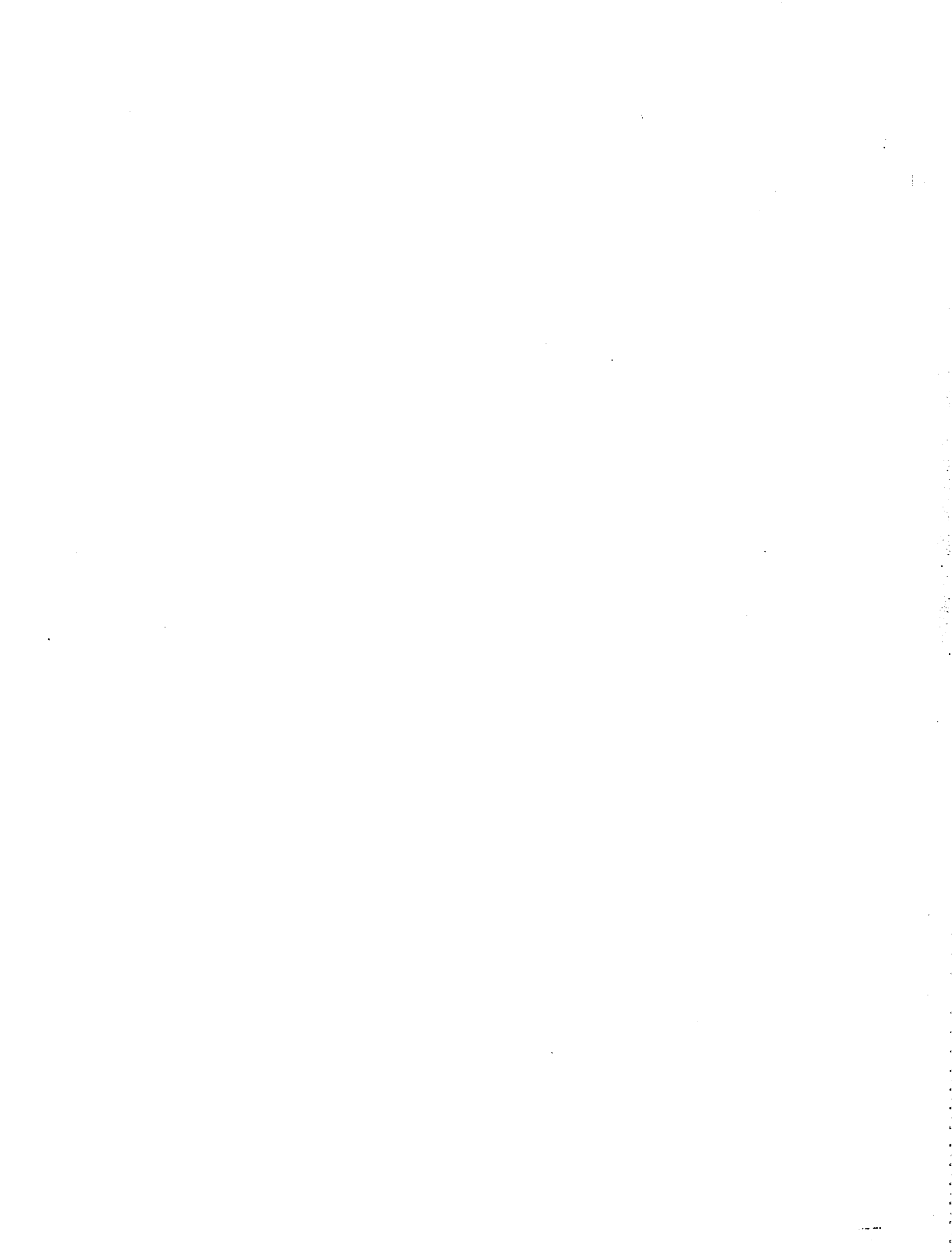
THE USE OF REMOTE SENSORS AND LABORATORY SCALE MODELS IN WAKE VORTEX ADVISORY SYSTEMS

A.J. Bedard Jr.
NOAA/ERL/WPL
325 Broadway
Boulder, Colorado,80303

INTRODUCTION

Wake vortex advisory systems require improved definition of wind, temperature and turbulence profiles at airports. For example, in light wind situations a vortex can remain in the vicinity of a runway, not moving under ground effect to a safe location. The numerical simulations shown in Figure 1 for several horizontal wind speeds show the variety of motions that can result. Also, the wake vortex vertical position and decay is influenced by vertical profiles of temperature and turbulence, as well as the presence of organized atmospheric structures (such as thermal plumes and gravity/shear waves). More knowledge is required about the three-dimensional structure of the atmosphere for operational use.

As closer aircraft spacings become practical, interactions between wakes of different aircraft will become more likely with the result that a variety of unusual propagation paths could result. Some of these "pathological" propagation paths are illustrated in Figures 2 through 7. Such potential interactions, as well as the important effects of vertical atmospheric structure changes on individual wakes, make real-time monitoring of the airport lower atmospheric boundary layer a critical need. This paper addresses two main topics. Initial sections describe newly available remote profiling technologies capable of fulfilling these measurement needs with potential for contributing to other airport requirements, such as microburst and icing forecasting, low-level wind measurement, and enhancing wind shear monitoring capabilities. The second topic reviews ways that laboratory scale model experiments can help improve our knowledge of wake vortex instabilities, transport, and decay. Finally, potential applications of integrated remote sensing systems are reviewed in the context of verifying laboratory experiments for test bed experiments as well as operational environments.

BOUNDARY LAYER PROFILING

Contrails assume complex forms. The series of Crow instabilities has been documented by past observations of contrails (e.g., Scorer, 1978). Observations of contrails under a variety of conditions show a wide range of responses to the atmosphere. These responses can be expected

to be magnified near the ground because of strong changes of stability, wind, waves, and turbulence, as well as other organized structures. There is a great need to improve our understanding of wake vortex interactions with the lower atmospheric boundary layer.

Remote sensing developments permit continuous profiling of atmospheric boundary layer winds and temperature in all-weather conditions. The following sections review profiling capabilities in the context of defining the state of the boundary layer for wake vortex applications as well as other operational uses (e.g., terminal low-level winds, icing conditions, and enhancement of wind shear detection systems). Because of ground clutter problems, terminal Doppler radars should not be expected to fulfill wind profiling needs at glide slope altitudes. Lower boundary layer profilers can provide low-level winds with high resolution, also using Radio Acoustic Sounding Systems (RASS) to give temperature profiles.

Wind Profiling

Strauch et al. (1989) review potential uses for wind profilers in support of flight operations, concentrating primarily on applications where upper level winds are required. A wind profiler demonstration network at 403.5 MHz now being evaluated should show valuable uses (e.g., providing in route winds with the potential for obtaining significant savings by optimizing flight plans). Neff et al. (1991) describe a 915 MHz wind profiling system that should be ideal for wake vortex applications. This system jointly developed by the Wave Propagation Laboratory (WPL) and Aeronomy (AL) of the National Oceanic and Atmospheric Administration should be available commercially at reasonable cost. The system characteristics are summarized in Table 1.

The wind field in the lower boundary layer can be quite variable and not represented adequately for terminal operations by the twice-per-day rawindsonde launches. Significant changes in wind profiles occur over short time scales. Furthermore, stable air at lower levels is one reason why surface wind measurements at lower levels using anemometers may not be representative of the winds above the surface. Bedard (1984) provides more information on this point. Significant vertical gradients in wind direction and speed can occur in the lowest kilometer. Thus, this type of lower boundary layer profiler can provide valuable wind information for wake vortex and other applications. In addition, combinations of profiling capabilities can give other needed meteorological information.

Temperature Profiling

Atmospheric stability has been demonstrated to have important effects upon wake vortex transport, decay, and breakdown. For example, the works of Tombach (1973), and MacCready and Lissaman (1977) indicate the strong effects of turbulence on time-to-vortex-breakdown. Recent developments (e.g., Strauch et al. (1989)) have established the capabilities of RASS to routinely measure temperature profiles within and above the atmospheric boundary layer. Since the principle of RASS involves the use of a wind profiling Doppler radar to detect the Bragg returns from refractive index changes produced by vertically propagating sound waves, such combined systems can provide both wind and temperature profiles. In addition, the Richardson

number (an index of turbulence) can be computed, since both the wind and temperature profiles are known. The capabilities of a wind profiler/RASS combined system serve key requirements for defining physical processes important for wake vortex transport, decay, and breakdown. Table 2, based on the work of Strauch et al. (1989) and Moran et al. (1991), summarizes the capabilities of RASS operating at 915 MHz.

Such combined wind profiler/RASS technology can also address the aircraft icing problem as described by Stankov and Bedard (1990). The continuous profiles of temperature can identify height ranges where supercooled liquid water can occur.

LABORATORY SCALE MODEL MEASUREMENTS

The same set of questions concerning wake vortex/atmospheric boundary layer interactions studied using full scale field experiments can also be addressed by laboratory investigations. There is a need to perform parallel analytical, numerical, field, and scale model studies. This section provides examples showing how wake vortex dynamics can be explored using laboratory simulations of specific situations, exploring parameter spaces under controlled conditions extremely difficult to measure in the atmosphere. Figure 8 shows an example of the organized structures that can occur in the atmospheric boundary layer (in this case large amplitude gravity waves are evident). Laboratory scale models have investigated such processes as microburst circulations (Bedard and Caplan, 1987), colliding density currents (Intrieri et al., 1990), downdraft interactions with inversions (Young et al., 1989), generation of gravity waves by downdrafts and density currents (Johnson et al., 1991), and penetration of a shear layer by a downdraft (Bedard and Cunningham, 1991). These examples have given insight into atmospheric processes that are difficult to model and understand. Bedard (1990) has reviewed these and other scale modeling approaches.

Laboratory wake vortex simulations have been performed (e.g., Barker and Crow, 1977, and Bedard, 1990) and these can be extended to more complex situations. The method we have developed consists in abruptly moving an initially stationary airfoil through a quiescent medium. The starting vortex generated will have a circulation that depends upon the airfoil characteristics and speed, producing flows that can be calculated from first principles. Thus, the circulation

$$G = 4W/(\pi * U * s * \rho),$$

where W is the aircraft weight or lift generated by the airfoil, U is the airfoil speed, s is the airfoil span, and ρ is the density of the medium.

If standard airfoils are used the lift will be known from the angle-of-attack and the resulting circulation computed. Figures 9a and 9b show how the wake vortex generating apparatus was implemented using two airfoils at different angles-of-attack spanning a water tank. Moving the airfoils rapidly upward using the yoke assembly generated a vortex pair with known properties. The vortex pair will be expected to move downward with a speed

$$w = G/(2 * \pi * s).$$

Thus, if the downward speed is measured the circulation can be computed. The airfoils were painted with condensed milk and the surface shear removed the milk from the surface, making the vortex formation and transport processes clearly visible. Figures 10a, 10b, and 10c show the evolution of the model wake vortex system at three successive times. Figure 11 presents successive locations of the leading edge of the circulation oval, indicating good comparison between theory and experiment. However, these results are only an indication of the range of possibilities that can be explored using laboratory scale models. Table 3 summarizes the possible areas of investigation, indicating experimental approaches that could be used.

CONCLUDING REMARKS

A number of developments in remote sensing technologies should permit the characterization of the airport environment in sufficient detail to initialize wake vortex transport and decay models. It is in the areas of definition of the atmospheric boundary layer and its influence on wake vortex transport decay and breakdown that both boundary layer profiling and scale model investigations can improve our understanding. Hopefully, such interactive approaches where numerical, analytical, scale model and field approaches applied in tandem will help reduce the impact of energetic aircraft wakes on flight operations.

Table 1. 915MHz Lower Boundary Layer Wind Profiler Characteristics

PC-based

Three fixed microstrip antennas
    vertical (1x2 m)

    two oblique (1x3 m) at 15 degrees

Short pulse
    height 1 to 2 km

 resolution 60 to 100 m

Long pulse
    height 2 to 4 km

    resolution 200 to 400 m

Table 2. Characteristics of 915 MHz RASS

Radar Frequency	915 MHz
Radar Wavelength	0.3 m
Acoustic Frequency	2000 Hz
Acoustic Wavelength	0.15 m
Rass Coverage (Typical AGL)	0.6 to 1 Km
Temperature Accuracy (Typical)	< 0.6 degrees C

Table 3. Suggested Experimental Approaches for Studying a Variety of Problems Using Laboratory Wake Vortex Generating Systems

Vortex Property	Experimental Approach
a. Vortex core formation	-adjust airfoil type,angle-of-attack,speed,and rate-of change of speed
b. Vortex core characteristics, distribution of vorticity, instabilities,and turbulence	-same as above
c. Vortex self-induction instabilities	-move surface having shape and amplitude of the desired instability near the vortex
d. Axial flow effects	-Adjust the spanwise circulation possibly by twisting the airfoil to produce a continuous change in angle-of-attack
e. Interactions between multiple vortices of arbitrary strengths and separations	-use multiple airfoils of various types and angles of attack
f. Mutual induction instabilities	-have vortices pass a surface or surfaces with a shape approximating the mode to be excited
g. Boundary layer effects	-adjust roughness of system surfaces
h. Interactions with density discontinuities	-prepare layers of known density differences and study vortex pair impact
i. Strong nonlinear effects (e.g., core bursting)	-modify a small section of an airfoil to induce strong axial gradients
j. Interaction between vortex systems and complex objects	-observe flow/obstacle interactions
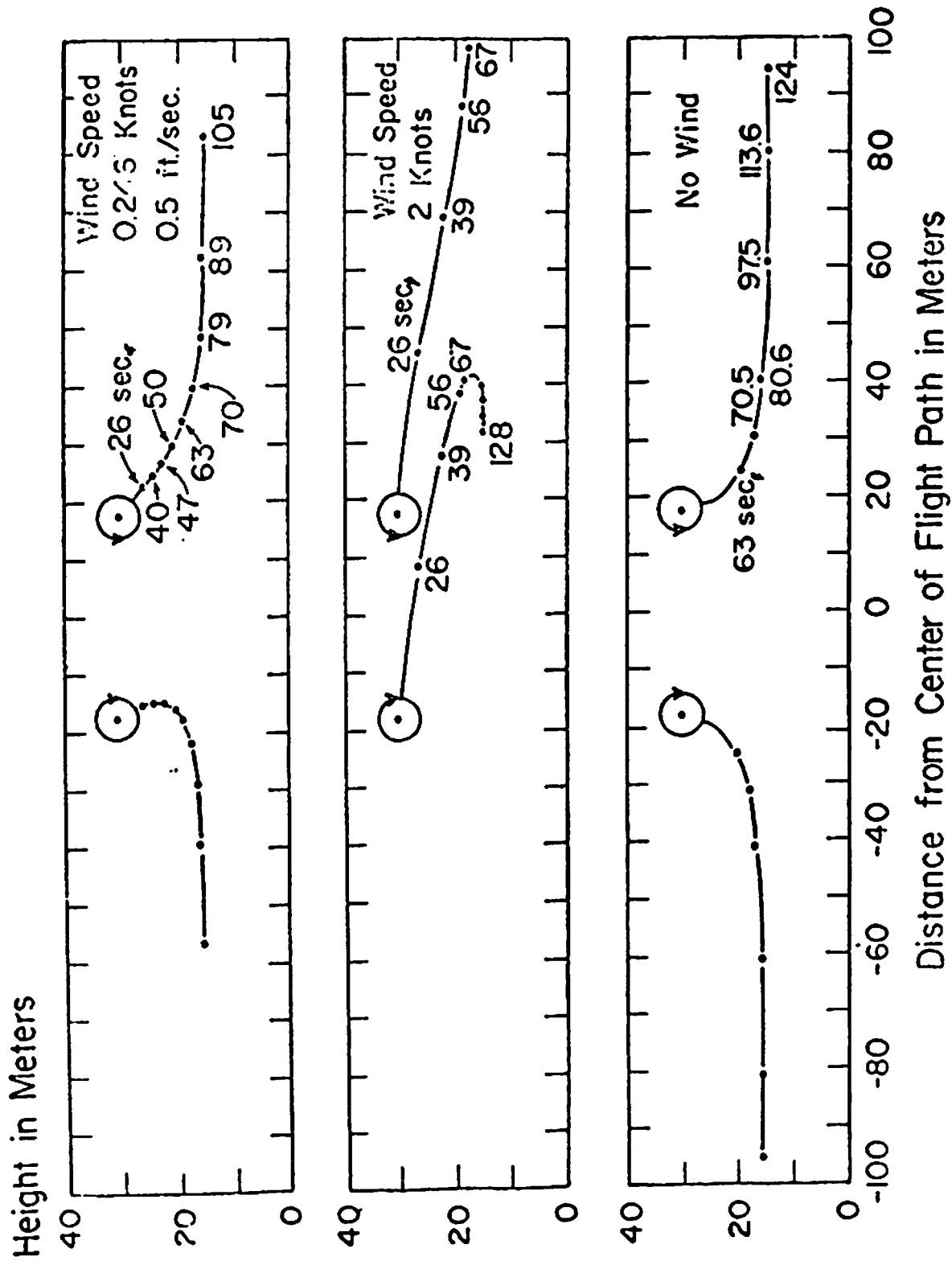
Figure 1. Motion of a wake vortex system in ground effect showing the importance of cross-winds.
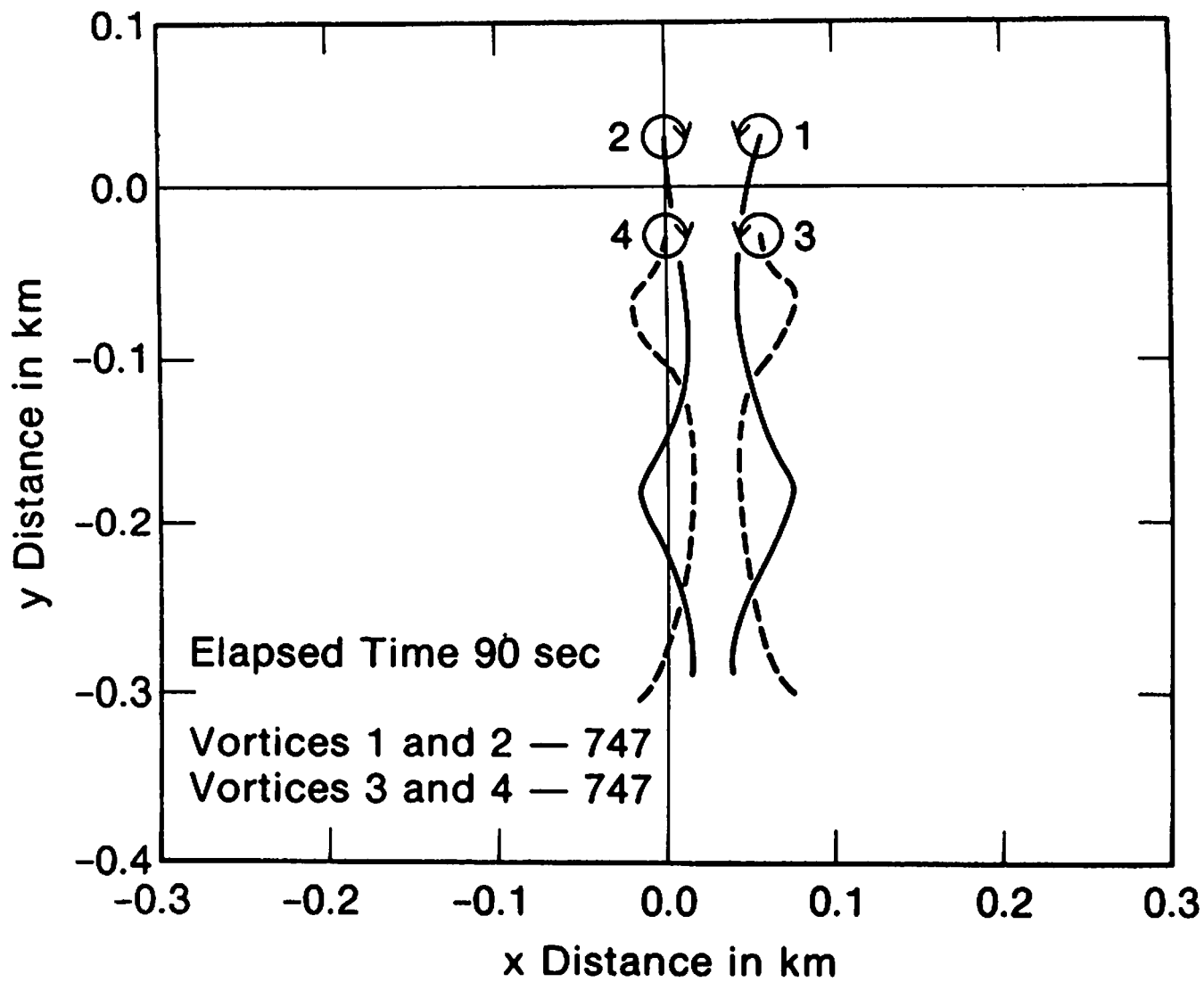
Figure 2. Interactions between wake vortex systems from two aircraft.
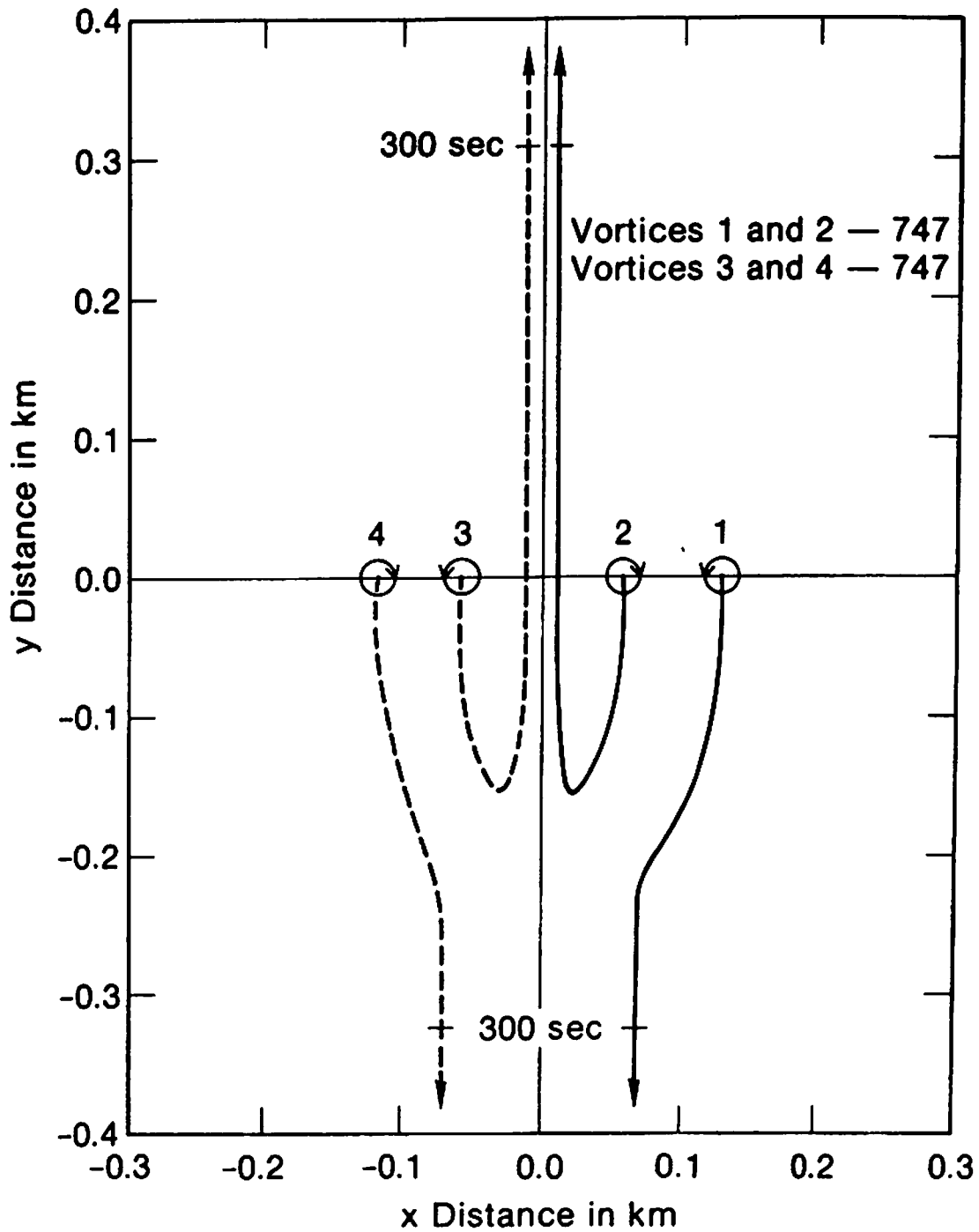
Figure 3. Interactions between wake vortex systems from two aircraft.
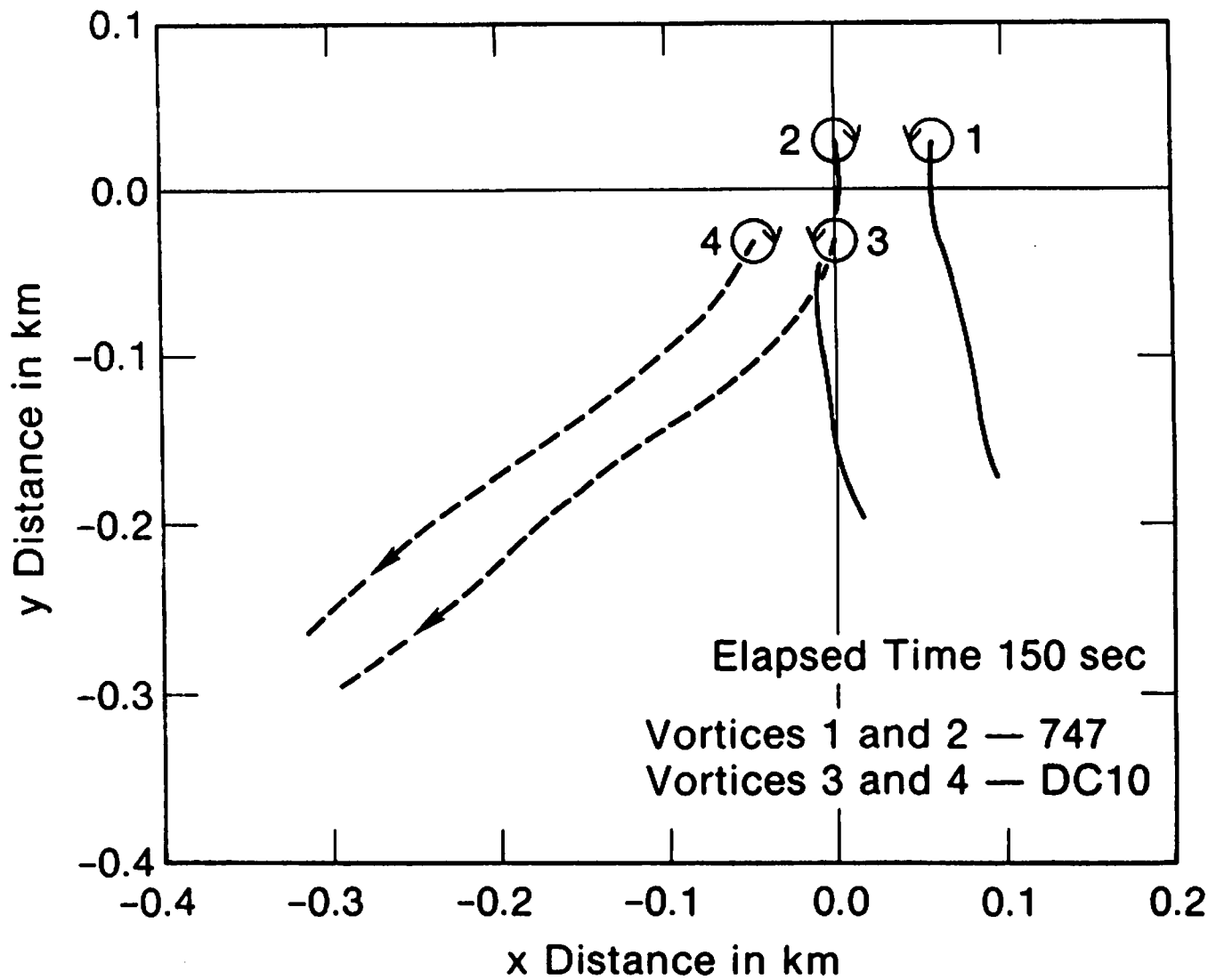
Figure 4. Interactions between wake vortex systems from two aircraft.
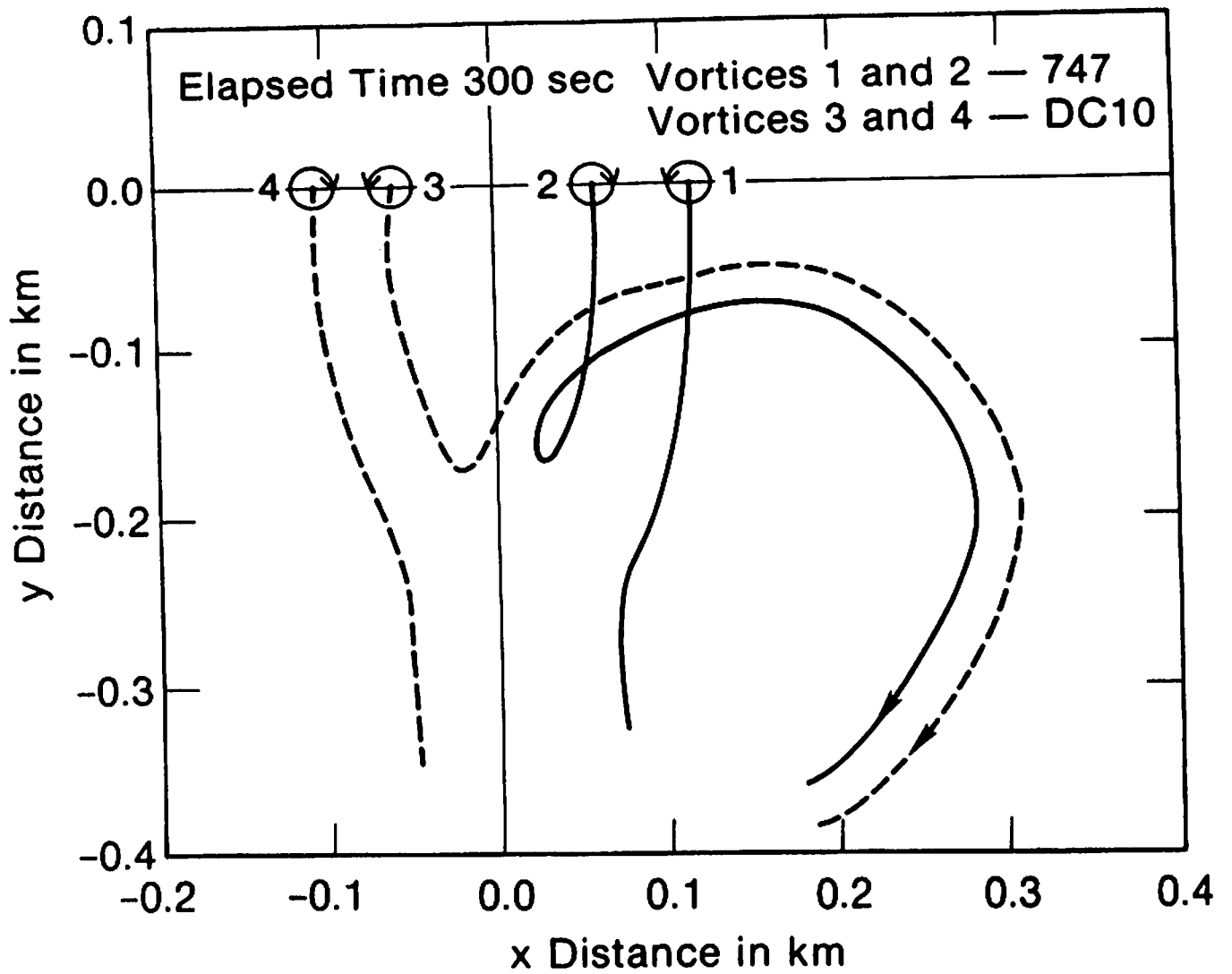
Figure 5. Interactions between wake vortex systems from two aircraft.
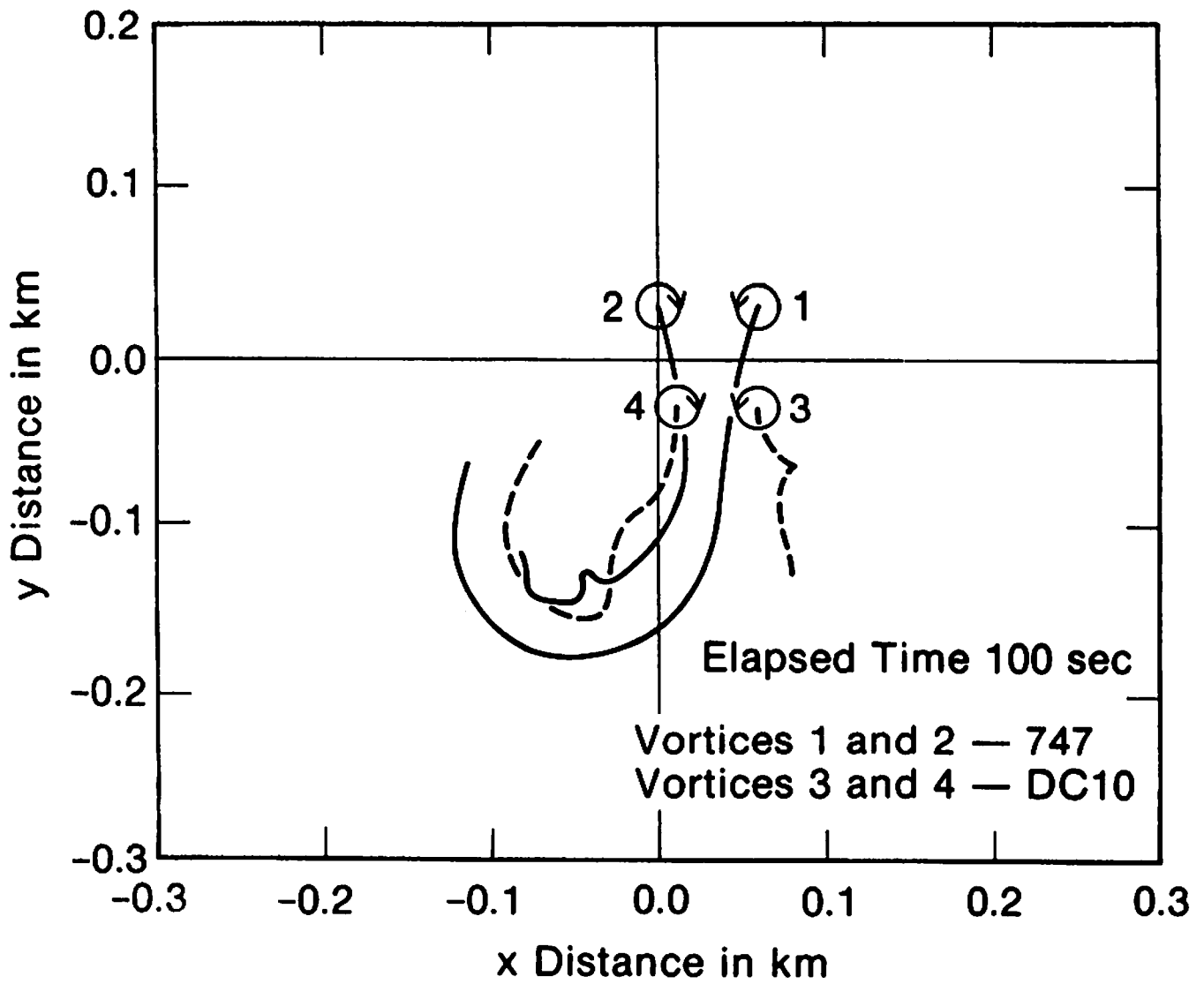
Figure 6. Interactions between wake vortex systems from two aircraft.
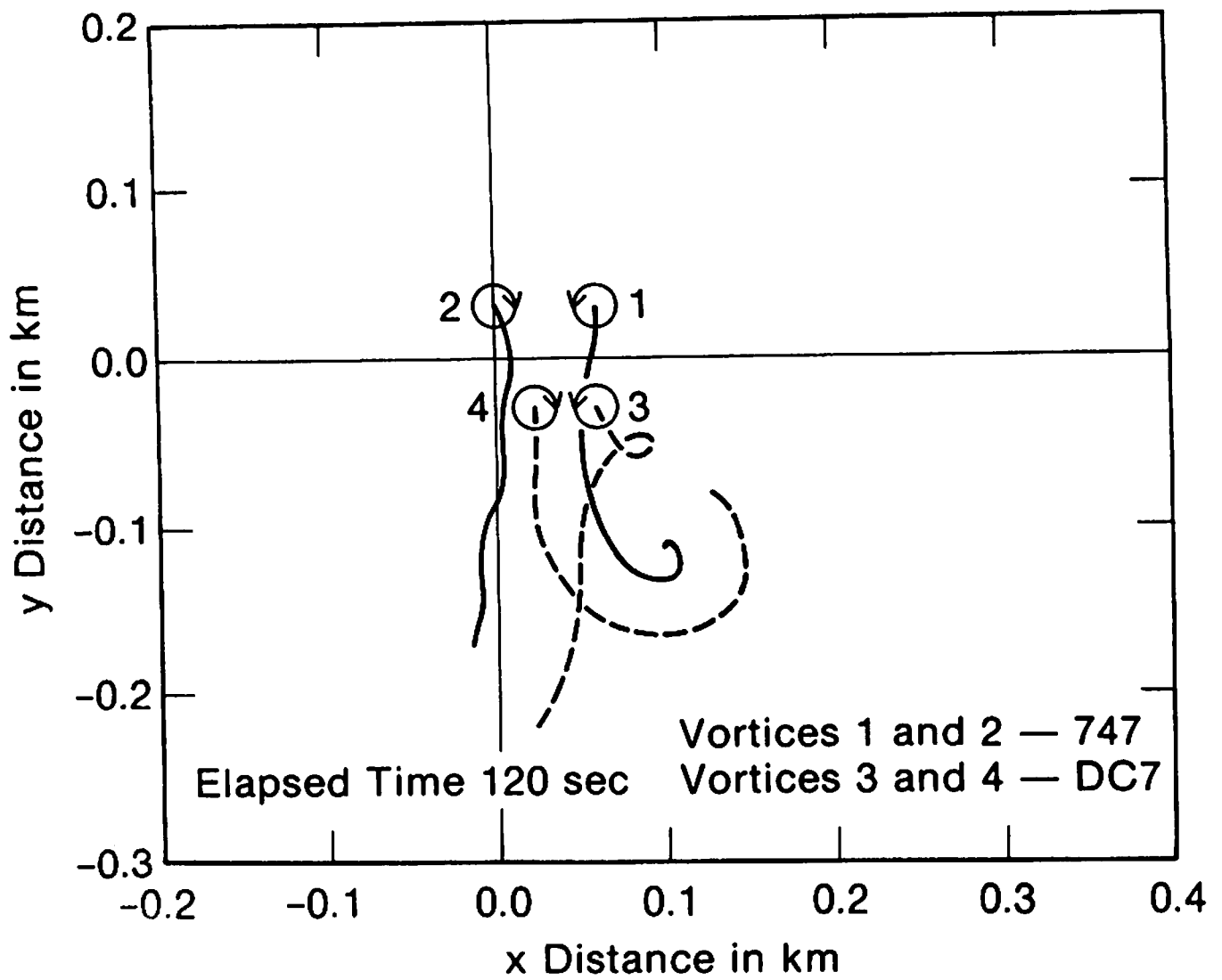
Figure 7. Interactions between wake vortex systems from two aircraft.
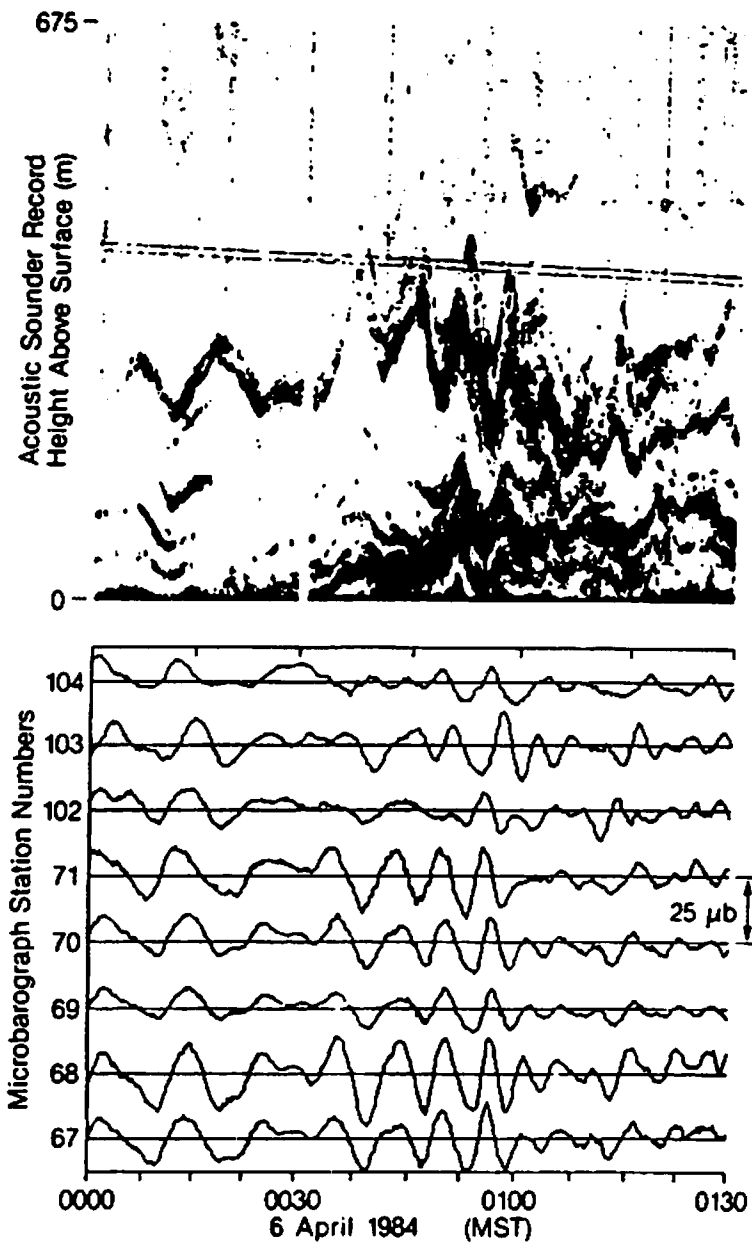
Figure 8. Acoustic sounder record showing an example of the large amplitude gravity waves that can occur in the atmosphere.
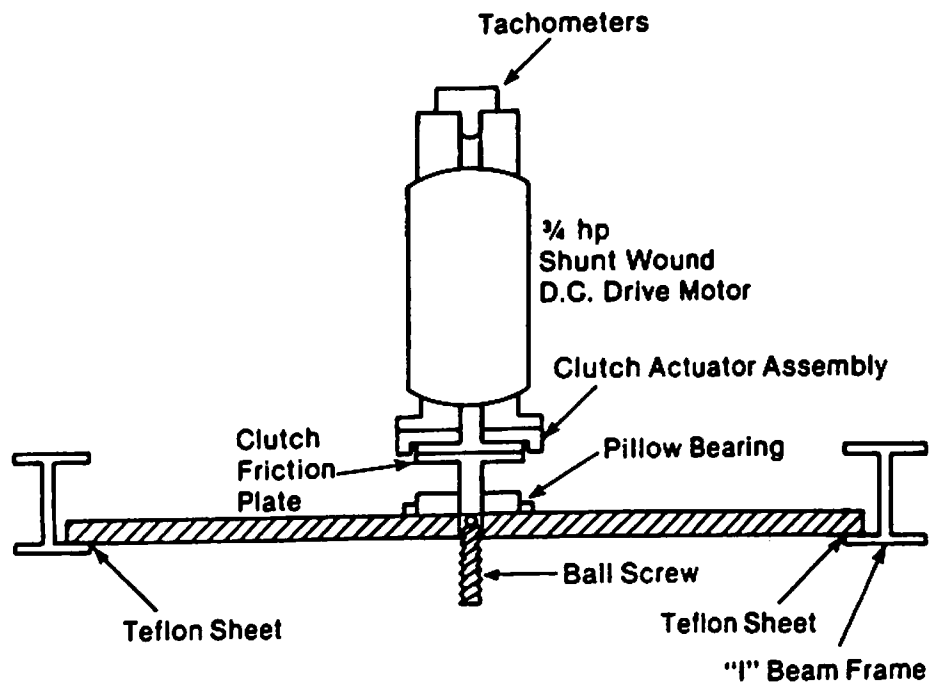
Figure 9A. Drive assembly for wake vortex scale model.
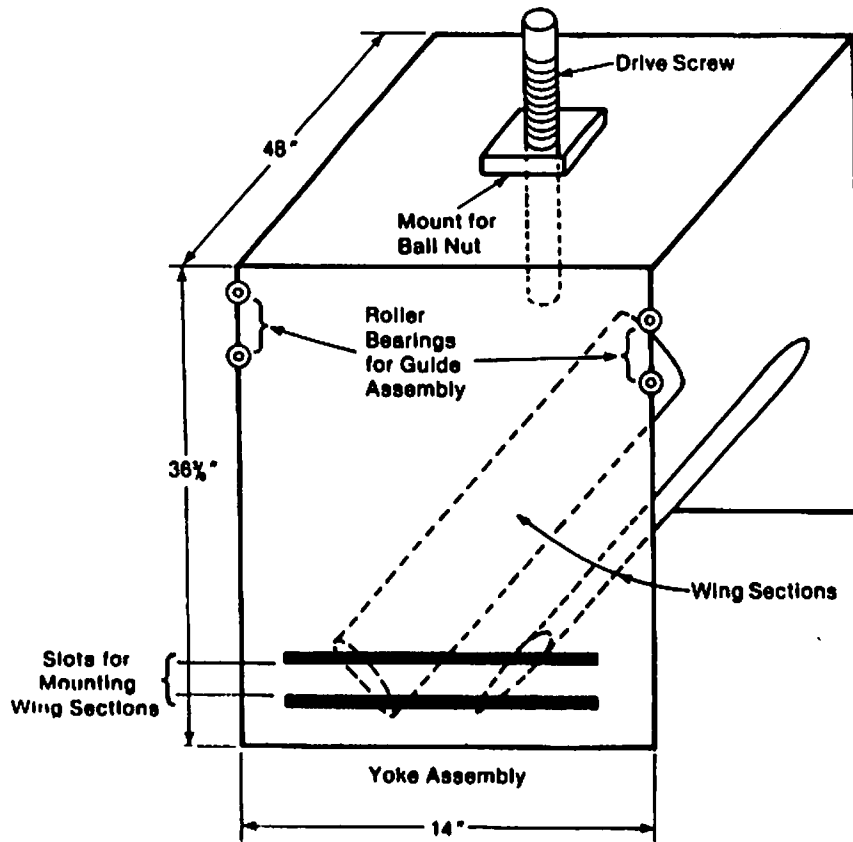
Figure 9B. Yoke assembly for wake vortex scale model.

6 Sec.
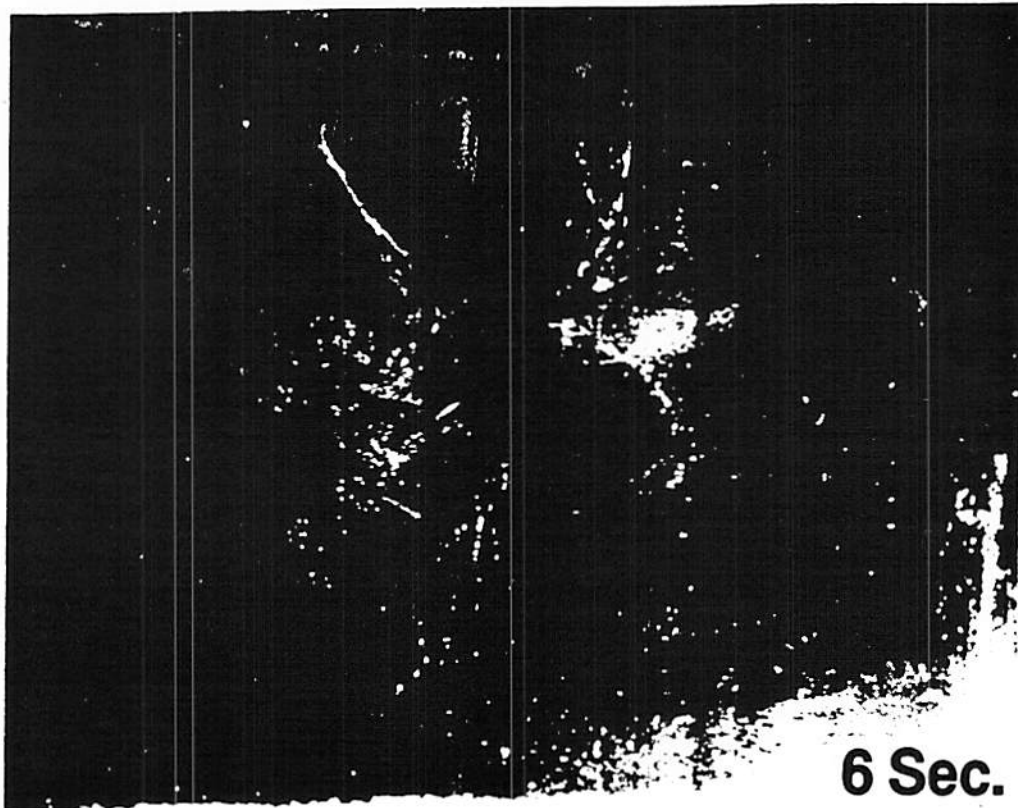
Figure 10A. Wake vortex system at three successive times.

8 Sec.
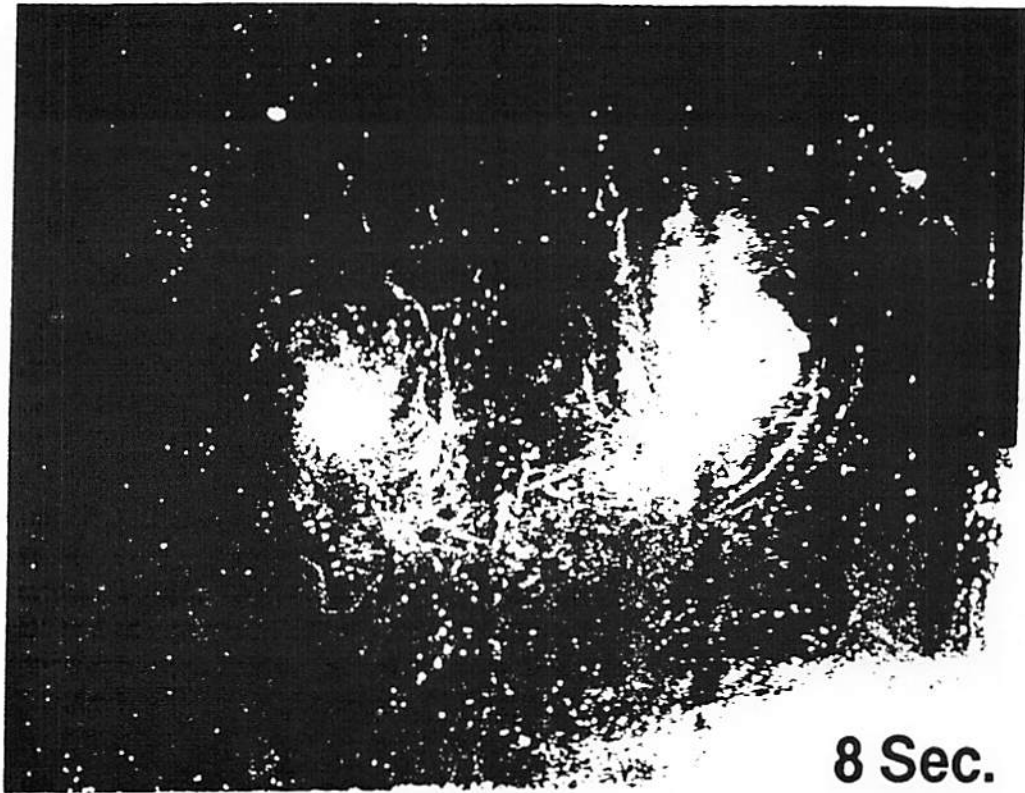
Figure 10B. Wake vortex system at three successive times (continued).

10 Sec.
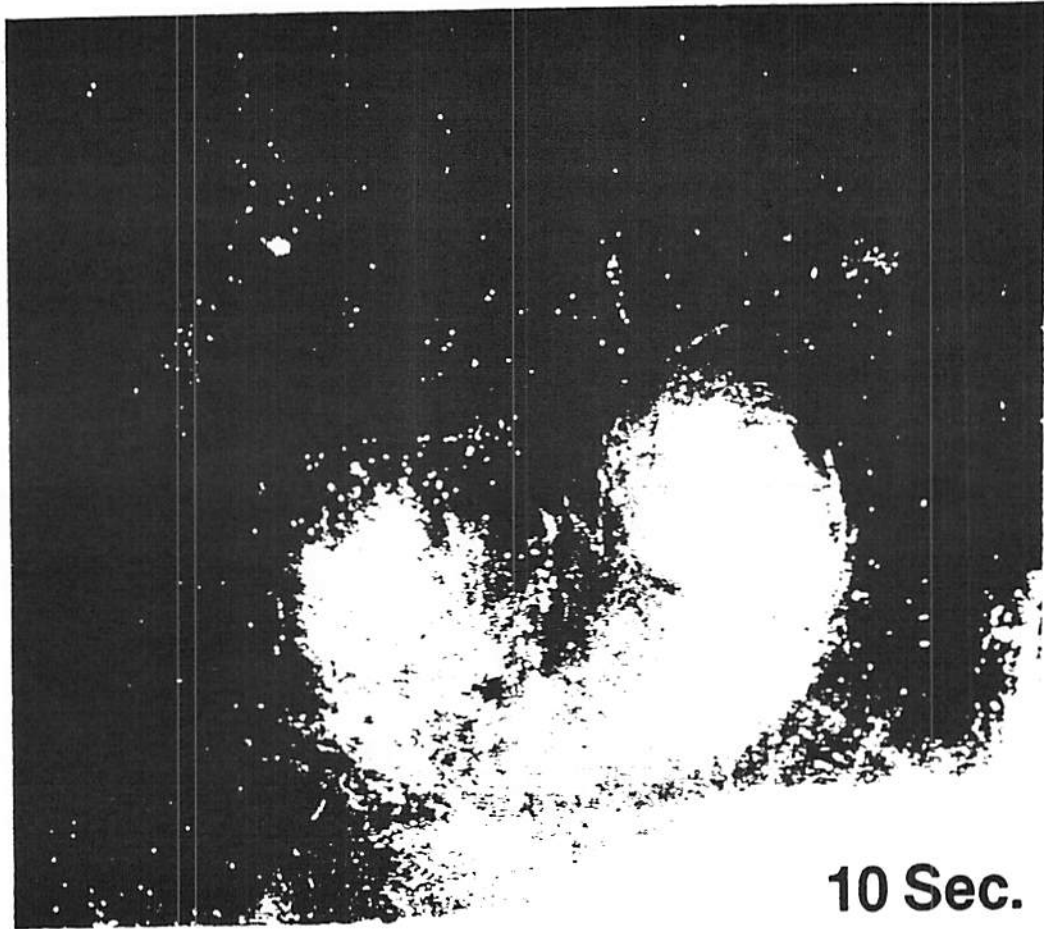
Figure 10C. Wake vortex system at three successive times (continued).
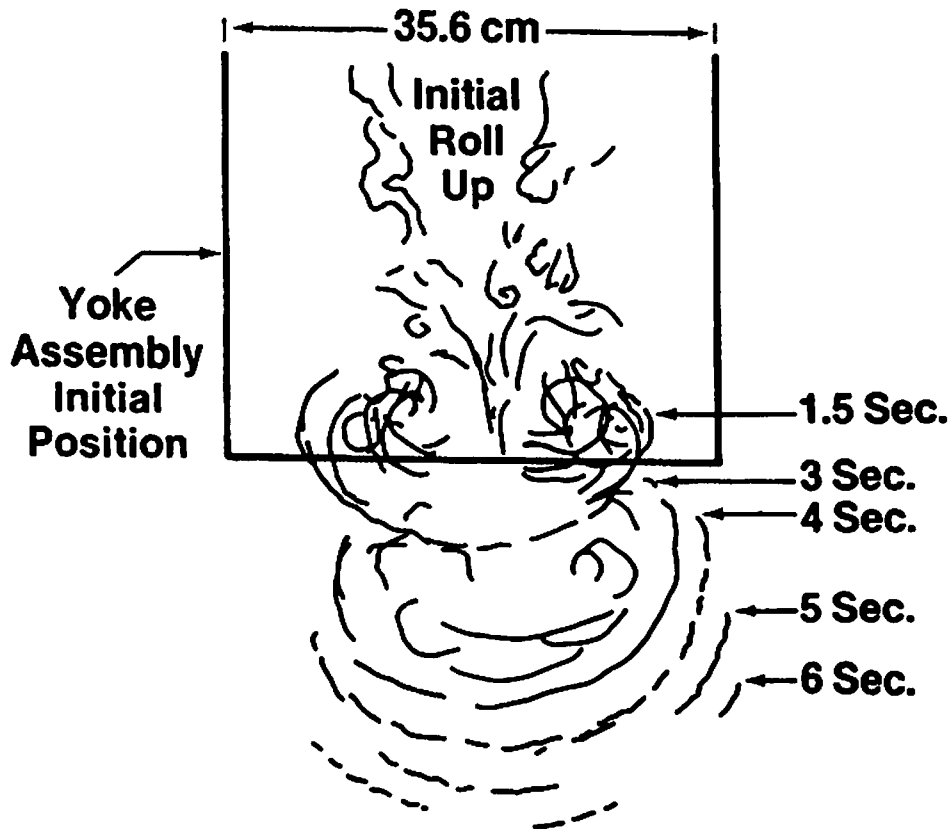
Figure 11. Descent of the circulation oval as a function of time. Comparison between theory and experiment.

REFERENCES

Barker, S.J. and S.C. Crow (1977): The motion of two-dimensional vortex pairs in ground effect. J. Fluid Mech. 82, 659-671.

Bedard, A.J. Jr (1984): Optimizing the use of surface sensors for wind shear detection. J. Aircraft, 21, 971-977.

Bedard, A.J. Jr. (1990): Using sensors for physical scale modeling of atmospheric fields. Proc. Sensors Expo90, March 1990, Long Beach, Ca., 39-038-1 to 10.

Bedard, A.J. Jr. and S.J. Caplan (1987): Microburst Vorticity. American Institute of Aeronautics and Astronautics, Wash. D.C., 25th Aerospace Sciences Meeting, Jan. 12-15, 1987. Published Manuscript AIAA-87-0440.

Bedard, A.J. and W. Cunningham (1991): Potential aircraft hazards in the vicinity of convective clouds: A review from the perspective of a scale model study. Proc. 4th International Conf. on Aviation Weather Systems, May 24-28, 1991, Paris, France, pp66-70.

Johnson, K., K. Prette, B. Robbins, and A.J. Bedard Jr.(1991): Gravity wave generation by atmospheric downdrafts and the possible role of gravity waves in the initiation of microbursts: A comparison between laboratory and atmospheric measurements. Proc. 8th Conf. Atmos. and Oceanic Waves and Stability, Oct. 14-18 (1991), Denver, Co.

Intrieri, J.M., A.J. Bedard Jr., and R.M. Hardesty (1990): Details of colliding thunderstorm outflows as observed by Doppler lidar. J. Atmos. Sci., 47, 1081-1098.

MacCready, P.B. Jr., and P.B.S. Lissaman (1977): Assessment of atmospheric effects on the behavior of aircraft wake vortices conference. Mar 15-17, FAA Rept. No. FAA-RD-77-68, 310-315.

Moran, K.P., R.G. Strauch, and P.T. May (1991): Lower tropospheric temperature profiling. Proc. 25th International Conf. Radar Meterol. 24-28 June 1991, 237-240.

Neff, W., J. Jordan, J. Gaynor, and D. Wolfe (1991): The use of 915 MHz wind profilers in complex terrain and regional air quality studies. Proc. 7th Symposium on Meteorological Observations and Instrumentations, Jan. 14-18, 1991, New Orleans, La., Amer. Meterol. Soc., Boston, Mass., j230-j234.

Scorer, R.S. (1978): Environmental Aerodynamics. J. Wiley, N.Y., N.Y., 488pp.

Stankov, B. and A.J. Bedard Jr. (1990): Atmospheric conditions producing aircraft icing on 24-25 January 1989: A case study utilizing combinations of surface and remote sensors. 28th Aerospace Sciences meeting, Jan 8-11, 1990, Reno, Nev., AIAA-90-0197.

Strauch, R.G., D.A. Merritt, K.P. Moran, B.L. Weber, D.B. Wurtz, and P.T. May (1989): Wind profilers for support of flight operations. J. Aircraft, 26, 1009-1015.

Strauch, R.G., K.P. Moran, P.T. May, A.J. Bedard Jr., and W.L. Ecklund (1989): Rass temperature sounding techniques. NOAA Tech. Memo. ERL-158, NOAA Environmental Research Laboratories, Boulder, Co., 12pp.

Tombach, I. (1973): Observations of Atmospheric Effects on Wake Vortex Behavior. J. Aircraft, 10, 641-647.

Young, J.W., F.D. Lane, and A.J. Bedard Jr. (1989): The effect of a ground based inversion layer on an impacting microburst. AIAA Aerospace Sciences Meeting, Jan 9-12, 1989, Reno, Nevada. Published Manuscript.

A UK ASSESSMENT OF APPROPRIATE TECHNOLOGIES FOR DETECTING AND TRACKING WAKE VORTICES IN THE APPROACH AREA

Trevor J. Gilpin
Chief Scientist's Division
Civil Aviation Authority UK

INTRODUCTION

In response to the signing of a Memorandum of Cooperation between the US FAA and the UK CAA on wake vortex research the UK was asked specifically to investigate technologies which might lead to a ground based real-time wake vortex detection and tracking unit. If the precise position and track of vortices in the approach area are accurately known then under some meteorological conditions it might be possible to safely decrease the separation and hence reduce delays in favourable conditions at runways. See Figure 1. Initially three technologies were considered, laser, radar and sodar. A Memorandum of Cooperation was signed with the French DGAC who were supporting work on the detection of vortices by sodar leaving the UK to concentrate on laser and radar technology. This paper describes two recent field trials carried out in the UK using these technologies to attempt to detect wake vortices.

LASER TECHNOLOGY

The Laser Equipment

The equipment used in this trial belongs to the UK's Royal Signals and Radar Establishment. Figure 2 shows a schematic diagram of the optics of the equipment. A frequency stable CO_2 waveguide laser operating on the P20 transition gives a nominal output of 4 watts at 10.6 microns. A few milliwatts of power are fed from a beamsplitter, through a P20 filter, and brought to a focus on the detector to form the local oscillator beam. The laser output is linearly polarised; the main beam is fed through a Germanium beam splitter, and is then converted into circularly polarised radiation by a quarter wavelength plate before being expanded and brought to a focus by the output telescope. A small linear movement of the diverging lens of the telescope enables the focal distance of the telescope to be changed via a DC motor. Scattered radiation received through the telescope is converted by the quarter wavelength plate to a linear polarisation which is orthogonal to that of the originally transmitted beam. This signal is totally reflected by the Germanium beamsplitter and is directed onto the detector where it is mixed with the local oscillator beam. The detector can be considered to be a non-linear element at optical frequencies and thus develops an output signal at the difference frequency between the signal and

local oscillator beams; it thus generates a signal at the Doppler frequency and is therefore a direct measure of the radial velocity of the aerosols in the focal volume. The detector requires to be cooled to 77°K for efficient operation and this is achieved using a Joule Thomson cooler operating from compressed air which is generated by a Hymatic mini-compressor.

The detector output is a time-varying signal and one requires a frequency spectrum. This is produced by using a surface-acoustic-wave (SAW) analyser. This produces a time varying output signal which is effectively the Fourier Transform of the input signal; it generates a frequency spectrum every 50 microseconds. The SAW bandwidth is from 0 to 6 MHz, thus giving a maximum velocity capability of 31.7 m/sec (approximately 65 knots). In general, the signal to noise (S/N) ratio of a single spectrum is insufficiently high and needs to be increased by integration. The output from the SAW is digitised by a fast A-to-D converter and is divided into 375 bins, each corresponding to an element of the frequency spectrum 16 kHz wide. The ultimate frequency resolution of the system, and thus its velocity resolution, is limited by the integrator and corresponds to 0.085 metre/second. However, a single frequency presented to the SAW produces an output which spreads over about 3 channels, giving a velocity resolution of about 0.25 metre/second. Successive spectra are added into the integrator until an adequate S/N ratio has been achieved. Typically, between 256 and 1024 integrations are used, corresponding to 12.8 mS and 51.2 mS per complete spectrum; thus up to 80 complete spectra could be generated per second if required.

The output from the integrator can be converted into a time-varying analogue signal which enables the frequency spectrum to be displayed on an oscilloscope for visual inspection or it can be stored digitally for subsequent evaluation. Operation of the equipment is controlled by an Acorn Archimedes A440 RISC-based microcomputer; this can be programmed to control the focus of the output optics, and the timing and duration of the measurements. It monitors the local windspeed using a conventional weather-vane and anemometer which can be mounted on a 10 metre hydraulic mast and also the equipment orientation using an electronic compass. To obtain adequately rapid data acquisition, each complete spectrum is stored in the computer's random access memory until the end of the run. The memory is approximately 4 megabytes and thus contains room for just over 5000 spectra; they are then stored on the computer's internal hard disc and subsequently transferred to floppy disk for back-up. Sampling at 5 spectra per second would thus be possible for about 16 minutes before permanent storage would be required.

The complete equipment is housed in a Landrover which is a Jeep sized vehicle and is powered by a 2.5 KVA generator mounted on the front of the vehicle so that operation is completely self-contained when on site. Supporting rails can be deployed from the rear of the Landrover and the LDV equipment is withdrawn from within the vehicle on these rails so that it can be pointed in the desired direction. Services to the LDV head, such as liquid cooling to the laser, electrical power and interfaces to the computer, are provided through a long flexible umbilical supply.

The principal function of the equipment has been to measure horizontal wind in the height range from 10 to 300 metres; this is a difficult region to access by other means. In order to measure the wind speed the laser beam is swept in a conical scan about a vertical axis using a Germanium prism; this produces a deviation with a half angle of 30°. The prism is rotated once per second and about 78 data points are sampled; the frequency corresponding to the strongest signal in the spectrum gives the component of the horizontal wind along the instantaneous

direction of the laser beam. The frequency component should vary sinusoidally and by performing a least squares fit upon the data the horizontal wind speed and direction can be derived. Because positive and negative Doppler shifts are not distinguished in the current system, there is an ambiguity of 180° in the wind direction which has to be resolved by other means; this is usually done by reference to the conventional weather vane.

The Laser Trial

For the detection of wake vortices the equipment was modified slightly by the addition of a large, adjustable plane mirror placed immediately above the deflecting prism. This enabled the beam to be pointed at any angle from below horizontal up to about 50° from the horizontal. The equipment was to be situated to the side of the flight path with the unscanned laser beam cutting the vertical plane containing the flight path at some convenient height so that the vortices would pass through the beam some seconds after the generating aircraft had overflown the equipment.

The equipment was transported to Heathrow and set up on the grass verge on a public road encircling the airport and situated about 300 feet from the runway. It was estimated that at this point aircraft were passing by at a height of about 150 feet.

The beam deflecting mirror was set so as to deflect the laser beam at angles between 15 and 25 degrees to the horizontal so that the beam was between 70 and 10 feet below the aircraft's track.

Signals from a large number of aircraft of differing size and type were studied during the course of the two day trial.

Results of the Laser Trial

Signals which had the characteristics to be expected from wake vortices were often observable by eye on the oscilloscope, particularly from some of the medium size aircraft. Although a considerable amount of turbulence was observable after the passage of B747s, which manifested itself in a spreading out of the normal wind signal lasting over a minute after the passage of the aircraft, no vortex signals were observed. It was subsequently realised that with the beam focussed at the runway centre at a distance of 300 feet, where the depth of focus would be about ±32 feet, the vortices from an aircraft with a wing-span of 200 feet would be well out of focus. Also at that height the ground effect would produce a considerable horizontal component to the descending vortices so that they would be even further out of focus.

Nevertheless, signals which were believed to be from wake vortices were observed and recorded. Figure 3 shows a time-varying sequence from an unidentified twin-engined aircraft, taken at 5 spectra per second; each spectrum corresponds to the full 6MHz bandwidth (32 metre/sec). The elevation angle was 20° so that the beam was about 40 feet below the flight path. The wind speed was between 8 and 10 knots and coming approximately from the east (ie along the runway and therefore almost perpendicular to the LDV). A low wind component signal can be seen at the left hand edge of each spectrum. The plot was produced by a screen dump from a computer monitor and does not therefore have as much vertical resolution as is

contained in the actual data giving rise to additional noise. Even so, a signal can be traced which breaks away from the wind signal and rises up to about 16 metre/second over a 3 second period, the signal is lost in the noise for almost two seconds and can then be seen descending into the wind signal over a further 3 seconds. This is just the sort of pattern which would be anticipated to arise from the traversal of a single vortex. A similar pattern is shown in Figure 4 which shows a vortex produced by a TU 154 aircraft. Although on occasions two vortices could be observed by eye on the oscilloscope no recorded data of this effect was obtained during this initial trial.

Conclusions from the Laser Trial

Although clear evidence of wake vortices were found during this trial, it must be said that the signal to noise ratio of the vortex signals observed was disappointing. That the equipment was working satisfactorily was demonstrated by the presence of a wind signal of about average strength. The wind speed was typically 8 to 10 knots during the trial, sometimes being more than 10 knots but hardly ever less than 8 knots. It would be desirable to repeat some measurements in less windy conditions. However, the presence of such wind conditions should not have dissipated the vortices too quickly for observation. The relative extent of the vortex and the focal region need to be considered carefully; whereas aerosols carried by a uniform wind contribute to the wind signal over the whole of the focal volume, a localised phenomenon, such as a vortex, needs to be located precisely at the peak of the sensitivity curve to produce an optimum signal. It will inevitably be less than the wind signal when the vortex occupies only a small fraction of the focal volume. The answer probably lies therefore in the need to take great care over focussing. At a range of 300 feet, with the equipment also focussed at this range, the focal distance would extend to about 325 feet, but the far wingtip of even a B-707 with a wing-span of only 145 feet would be at 375 feet and the vortex centre could be even further away after descending 50 feet or so. It may be necessary to attempt to follow the vortex by manual adjustment, both in range and elevation, in order to optimise the signal strength.

There are several steps which could be undertaken to further increase sensitivity. Firstly, the system could be thoroughly checked to ensure that system alignment is optimum to give maximum heterodyne sensitivity; this is a relatively straight forward procedure and would not be too time consuming. Secondly, a higher power laser could be used; the equivalent FAA system uses a 20 watt laser. This would not be a trivial modification to the existing system. Thirdly, a larger output lens could be employed; this would not lead to greater sensitivity by itself, but would enable a tighter focus to be achieved at a given range. Coupled with more precise control over the focus, this could lead to enhanced vortex signals by increasing the ratio of vortex size to focal depth. Coupled with the last two modifications would be the need to have better control over the positioning of the focal volume; a motorised scanning output mirror would therefore be required.

RADAR TECHNOLOGY

The Radar Equipment

The equipment used for the radar trial was the GEC-Marconi DX 04 Radar. This is a coherent pulse doppler radar that operates at F-Band (10 cms wavelengths at 3 GHz nominal centre frequency). It is an experimental radar situated at the GEC-Marconi Research Centre, Chelmsford UK and its main function is to explore new techniques and in particular to investigate the application of digital modulation and pulse compression techniques to surveillance and tracking radars. Typical operational ranges are a few tens of kilometres.

A block diagram of the radar is shown in Figure 5. The baseband signal is synthesised digitally in the waveform generator. The nature of the digitally generated waveform is such that a wide variety of waveforms and modulation methods can be selected directly under software control. This gives the system great flexibility of operation enabling pulses of up to 30 microseconds duration and bandwidths of up to 90 MHz to be generated.

At the output of the waveform generator the baseband signal is modulated on to a carrier frequency to form the intermediate frequency signal. Up-conversion then occurs and the radio frequency signal is formed. The waveform generator, modulator and up-converter are located in the main equipment rack in the radar control room.

Various solid state driver amplifiers are employed at the transmitter input. The main transmitter element is a helix travelling wave tube amplifier. It has a peak output power of ten kilowatts and a duty cycle of up to 2.5%. After amplification the signal is directed through the duplexer. This divides the transmitted signal from that received and forms part of the receiver protection system.

The signal is then radiated by the antenna. This is of the offset parabolic type and has dimensions of 2 metres by 1.5 metres. It has a gain of 33 dB and vertical polarisation is employed. A majority of the antenna sidelobe levels are below 40 dB. Two vertically stacked beams are available that can be used for height finding of aircraft targets.

On reception the signal is directed from the antenna via the duplexer into the receiver. An active receiver protection switch is employed that exhibits high attenuation during the transmitted pulse and low attenuation on receive. The current receiver design has a basic recovery time of 10 to 12 microseconds after transmission, so that for pulses of length 4 microseconds a minimum range of 2.4 kilometres is obtained.

The front end low noise amplifier (L.N.A.) is a microwave field effect transistor that has a noise figure of less than 2 dB. The signal then undergoes further amplification and down-conversion to baseband. In-phase and Quadrature channels are generated prior to digitisation. These enable both the amplitude and phase of the signal to be measured, so allowing coherent pulse-Doppler processing to follow, if required.

After digitisation the signal data can be processed in the computer, displayed or stored for further processing off-line.

All of the operations are controlled by the computer, which is accessed via the radar control terminal. The antenna's position and motion are determined by a slave computer which operates from basic instructions provided by the system's master computer.

The pulse repetition frequency of the radar is up to 10 kHz. Pulse compression ratios of up to 400:1 are employed and typical compressed pulse lengths used are in the range 4 microseconds to 13 nanoseconds, corresponding to range resolutions from 600 metres to 2 metres. Typical target velocity measurement resolution is in the range one to ten knots and is dependent on the time on target of the radar mode selected. In addition to the coherent modes, incoherent and frequency agile modes are also available.

Modifications to the Radar

In order to maximise the probability of detecting vortices in the trial, the radar's performance and trial conditions were optimised for vortex detection, within the constraints set by the main radar parameters, the characteristics of the vortices, and the allowable flight tracks, speeds, altitudes and accuracy of the HS 748 trials aircraft.

As there was only a short time available before the planned trial for preparing the radar, only relatively minor modifications could be made. In order to match the maximum expected diameter of the vortex to the radial resolution of the radar, a value of 50 metres range resolution was selected. This correponded to a transmitted bandwidth of 3 MHz. As the radar was unable to accommodate an unmodulated pulse of 1/3 microsecond duration, pulse compression techniques were required.

Hardware and software modifications to the radar were needed to provide a suitable waveform. Initially, the waveform had to be designed. A 4 microsecond linear frequency modulated chirp was selected, with a pulse compression ratio of 12:1. Over the 4 microsecond pulse the modulation frequency was linearly varied from 0 Hz to 3 MHz at 750 kHz per microsecond. This waveform was selected as its time sidelobe performance was good, it was Doppler tolerant and had low associated processing losses.

Software had to be written to generate a waveform of this type, modify the main radar control software to include a new waveform and associated mode of operation, and to provide the signal processing for this waveform.

In order for the dual channel analogue to digital converter to efficiently digitise the received baseband waveform, the Nyquist sampling criteria had to be met. For sampling a 3 MHz bandwidth signal in in-phase and Quadrature format, simultaneous digitisation at a 4 MHz rate was selected. This necessitated a re-design of the system's clocks, as there had been no previous requirement for 4 MHz sampling. Additional circuits were developed for generating a 4 MHz signal from the system's master oscillator. Also, electronic switches were integrated and associated control software written for selecting this frequency when required.

At the time of the trial, the design of the radar utilised a maximum of 200 pulses on target and a buffer memory size of 50 kilosamples. Working within these constraints, pulse repetition

frequencies of 2 kHz and 5.5 kHz were selected for the trials and corresponded to radar integration periods of 100 milliseconds and 36 milliseconds respectively. The radar had to be programmed to specify these parameter values, which had not previously been used.

After designing and integrating the various hardware and software modifications discussed above, initial trials on ground targets and aircraft targets of opportunity were performed to prove that the new modes had been satisfactorily implemented.

As vortices have a very small radar cross-section in comparison to "conventional" radar targets, measurements had to be made to check that any trials site selected would be relatively free from effects due to ground clutter and moving vehicles. Various "clutter" maps of the local area were generated using the DX 04 radar. The trials site selected, over which the aircraft would fly, was confirmed to be free from large clutter returns. An elevation angle of 9.8° was selected for the antenna, so that any ground clutter returns were confined to areas where the antenna sidelobes' performance was good. The main elements of clutter appeared near the "0 Hz" filter and are close to stationary as would be expected. The maximum levels correspond to radar cross sections of -66 dBsm. The mean noise level is equivalent to a radar cross-section of -86 dBsm at the selected trials site. The results indicated that the radar was well set up and that the required sensitivity was being achieved.

A trials area at a distance of 2.4 kilometres from the radar was chosen. This range represented the minimum time delay of the receiver to recover from leakage due to the transmitted pulse (plus the length of the pulse). At 9.8° antenna elevation, this range corresponded to an altitude of 1,500 feet for the trials aircraft.

The Radar Trial

To avoid the costs associated with transporting the radar to a major airport in the UK it was decided to leave the radar in place at the GEC-Marconi site and carry out the flight trials at that location. The aircraft chosen for the trials was the CAA Flight Calibration Unit's HS 748 aircraft. This is a twin turboprop of MTOW of about 44,500 lb and is in the ICAO "medium" and the UK "small" category for wake vortex.

The basic plan adopted for the trial was for the aircraft to overfly the same point on the ground from a variety of directions. This would allow the radar to effectively view any vortices generated by the aircraft from a number of diferent aspect angles. The radar would then be locked onto that point throughout the trials. The trials site was located approximately 2,400 metres due east of the radar installation.

The data collected by the radar would be stored for analysis after the flying programme. The radar data would take the form of complex amplitudes representing received signals from the vicinity of the trials site, before, during and after the aircraft's overflight. For each signal received by the radar the following parameters would be stored automatically by the computer:

Frequency Band
Modulation Type

Bandwidth
Pulse Length
Digitiser Rate
Clock Mode
Number of Pulses on Target
Range Acquisition Window
Antenna Elevation Angle
Radial Velocity (if track generated)
Digitiser Sensitivity Level
Date/Time
Data Reference Number

On the aircraft, flight data would also be collected on each run and the parameters are listed below:

Heading (Magnetic)
Ground Speed
Drift (Degrees)
Indicated Air Speed
True Air Speed
Height (Pressure)
Height (Radar Altimeter)
Estimated Visibility
Wind Velocity
Outside Air Temperature
Estimated Cloud Level
Engine R P M
Configuration
Aircraft all up Weight
Pitch Angle/Attitude
Bank Angle

A total of 12 runs were planned of which runs 7 to 12 would duplicate runs 1 to 6, but with the opportunity to change the radar parameters. During the trials radio communications were maintained between the radar site and the trials aircraft.

The first trial took place on the morning of Monday September 23rd 1991. The trial lasted approximately one and a half hours and all the planned 12 runs were completed, including two runs on which the undercarriage and flaps were deployed.

The cloud base was typically two to three thousand feet and the outside air temperature at the trials altitude of fifteen hundred feet was 12°C. The weather during the trial was cloudy and some moderate showers were experienced at the radar site. During the trial a large rain cloud was in the vicinity of the trials site and was moving in an easterly direction. The amplitude of the rain cloud is up to 20 dB above the system's sensitivity limit, so that the received signal from a vortex would have to compete against this background to be detected.

51-8

On runs 1 to 6 a pulse repetition frequency of 2 kHz was employed, with a bandwidth of 3 MHz, providing a 50 metre range resolution. For runs 7 to 12, a 90 MHz bandwith signal was transmitted, corresponding to a 2 metre range resolution.

The second trial took place on Thursday September 26th around midday and was of one hour's duration. The cloud base was at three thousand feet and the outside air temperature at fifteen hundred feet was 13°C. The weather was sunny, but there was some cloud cover co-range with the trials area which could have contributed to obscuring some of the vortex radar returns.

On run 1 a light aircraft went into the locality of the trials site immediately after the HS 748 had passed the area. As its radar signature would have swamped that of any vortex generated, the run was repeated as run 13.

Results of the Radar Trial

It is known that the radar cross-sections of vortices are very small, so that any processing techniques employed to detect them have to overcome the effects of clutter and any effects associated with the aircraft. Various coherent and incoherent processing techniques were used to investigate the presence of vortices in the trials data. Typically forty to fifty data sets of results were obtained for each trials run. In total several hundred sets of data were taken during the two trials.

In the trials, pulse repetition frequencies (P.R.F.'s) of 2 kHz and 5.5 kHz were employed with a main transmitted bandwidth of 3 MHz, corresponding to 50 metres range resolution and 200 pulses were processed in all cases. The coherent pulse-Doppler processing provided 200 frequency (Doppler velocity) channels, with bandwidths of 10 Hz and 27.5 Hz at the 2 kHz and 5.5 kHz P.R.F.'s respectively. The 10 Hz filter was equivalent to a Doppler velocity resolution of 0.8 knots and the 27.5 Hz filter equivalent to 2.2 knots.

Difficulties were experienced in establishing the presence of a vortex under the rainy weather conditions that prevailed during the first trial. Although the system noise floor represents a sensitivity equivalent to 86 dB below a one square metre target in the trials area, the rain cloud amplitude is up to 66 dB below a square metre, 20 dB above the system's sensitivity limit. The velocity and range of the rain could be coincident with any vortices measured. It would be anticipated that the basic velocity of the vortex would be similar to any clouds or rain in the vicinity, as they would be subject to similar wind conditions. Hence, to measure the presence of a vortex under these weather conditions would be a challenge.

For the second trial the weather was sunny, with some "wispy" strato-nimbus clouds in the vicinity of the trials area, which were quite distinct on the radar return having a peak radar cross-section of the order of 66 dB below one square metre which is 20 dB above the sensitivity limit of the radar.

Using the coherent processing technique resulted in no clear indications of vortices. Some measurements were also performed with a bandwidth of 90 MHz corresponding to a range resolution of two metres. This radar mode although high in resolution, was less sensitive than the 3 MHz mode and no new features were observed.

Incoherent processing techniques were then utilised to investigate the detection of vortices. The contributions from a number of coherently processed range-frequency cells were incoherently integrated. The objective of using this technique was that if a vortex were distributed in range and velocity beyond the limits of the standard resolution cell, the probability of detection could be improved using the extended range and velocity cells.

Figure 6 shows a good indication of a detected vortex. The power scale is in dB relative to the mean noise level and the timescale is in seconds, with zero time referenced to the aircraft passing through the trials site. Before the aircraft passes, the outputs from the eight frequency filters are similar. On passing, the aircraft presents a very large radar return and all the filter outputs are large. After the aircraft has passed the trials area, the radar response of that volume of atmosphere is shown. (At approximately ten seconds are short "blips" due to an effect associated with the aircraft appearing in the antenna sidelobes). However, it can be clearly seen that the 0 to 10.7 m/s channel filter response has suddenly increased in comparison to the others and has stayed high for a few tens of seconds. There is an indication at eighty to one hundred seconds that the response is beginning to decay. This filter response consists of Doppler frequencies in the range zero to twenty knots approaching the radar. At the time of this run 3 on the second trial the wind was north easterly, at ten knots, and the aircraft was flying on a north-south route, to the east of the radar.

It is concluded that the aircraft generated a disturbance of the air with a radial velocity range from zero to twenty knots, at a level equivalent to 80 dB below a one square metre target at 2.4 to 3 km range from the radar.

As a result of the difficult signal to noise conditions prevailing during the trial at the ranges concerned, the effects of the radar returns from the clouds and possible slight inaccuracies in the aircraft's position, only a few additional examples of indications of detected vortices have been found.

It is interesting to note that this incoherent processing technique is more effective than the coherent pulse-Doppler processing technique. It is considered that the method used here integrates a wider frequency spread and range spread of received energy of the vortex and hence makes detection more efficient.

Conclusions from the Radar Trial

The trials, although organised in a relatively short timescale, went according to plan and there were indications that the vortices generated by the HS 748 aircraft had been detected by the GEC-Marconi DX 04 radar. The observations showed that detections were made at ranges of 2.4 km to 3 km and a typical radial velocity measured was 10 knots. The associated radar cross-section was of the order of 80 dB below a one square metre target.

On the two trials days useful radar data was also obtained that was associated with the weather conditions. Rain and clouds were consistently detected with larger radar cross-sections than the vortices, so that any radar and processing techniques employed to detect vortices, particularly under UK weather conditions, would have to discriminate between this type of clutter and the vortex.

Hence, in addition to requiring a very sensitive radar with a high dynamic range for vortex detection, an important conclusion reached was that sophisticated processing techniques would be required for an all weather detection system, using radar.

FURTHER WORK

These early experiments are not conclusive enough to determine whether laser or radar technology would be the most suitable to implement a real-time wake vortex detection and tracking device. Therefore the UK hopes to pursue both technologies in the coming year.

With regard to the laser work the frequency spectra seen during the Heathrow trial were not exactly as anticipated and were also somewhat different from those seen with the US equipment. This may reflect the differing spatial and frequency resolutions of the two equipments. It appears that there is no generally accepted theoretical treatment of what should be seen when a LDV beam intercepts a vortex.

The UK is therefore considering a programme involving a brief literature search to look at any previous theoretical work and if no adequate treatment is found, to go on and produce a simple model. This should be backed up by an experimental study to determine the precise range and sensitivity of the equipment and to optimise it for wake vortex detection. The actual sensitivity of the focal region to Doppler signals could then be explored in detail.

Ideally the system should then be used to study a vortex under controlled conditions, perhaps in a wind tunnel.

After the system has been fully characterised further trials at Heathrow could be undertaken. Initially these could be with an unscanned system to study the characteristics of real vortices with particular emphasis on the high frequency Doppler components observable with a high resolution spectrum analyser.

It may also be useful to pursue a system having a conical scan with the LDV set up underneath the flight path which has a number of novel and advantageous features.

Considering the radar work the trials have shown that there were good indications of vortices being detected, but only limited characterisation could be achieved at the ranges concerned. In order to satisfactorily detect vortices under a variety of conditions, the characteristics of their radar signatures first have to be quantified in a dedicated measurement programme. For precise measurements a good signal to noise ratio is required, which would probably be 10 - 20 dB above that employed in these trials. The DX 04 radar is currently undergoing a major modification programme that will provide it with two orders of magnitude more real time data

storage capability. This means that in any future trial far more energy can be integrated from the target with a significant improvement in signal to noise ratio. In addition, future modifications to the radar to improve its receiver recovery time would mean that vortices would be detected closer to the radar and the associated signal to noise ratio would again improve.

With the improvement in effective sensitivity it would be anticipated that higher resolution techniques could be employed using a few metres range resolution. This could provide range, velocity, height, tracking and decay time informaton on the vortex.

The employment of a larger aircraft to generate the vortices should also be addressed, as it would be more representative of civil aircraft that cause the basic vortex hazard to other aircraft.

Coverage region

- Monitor the approach phase to an airport
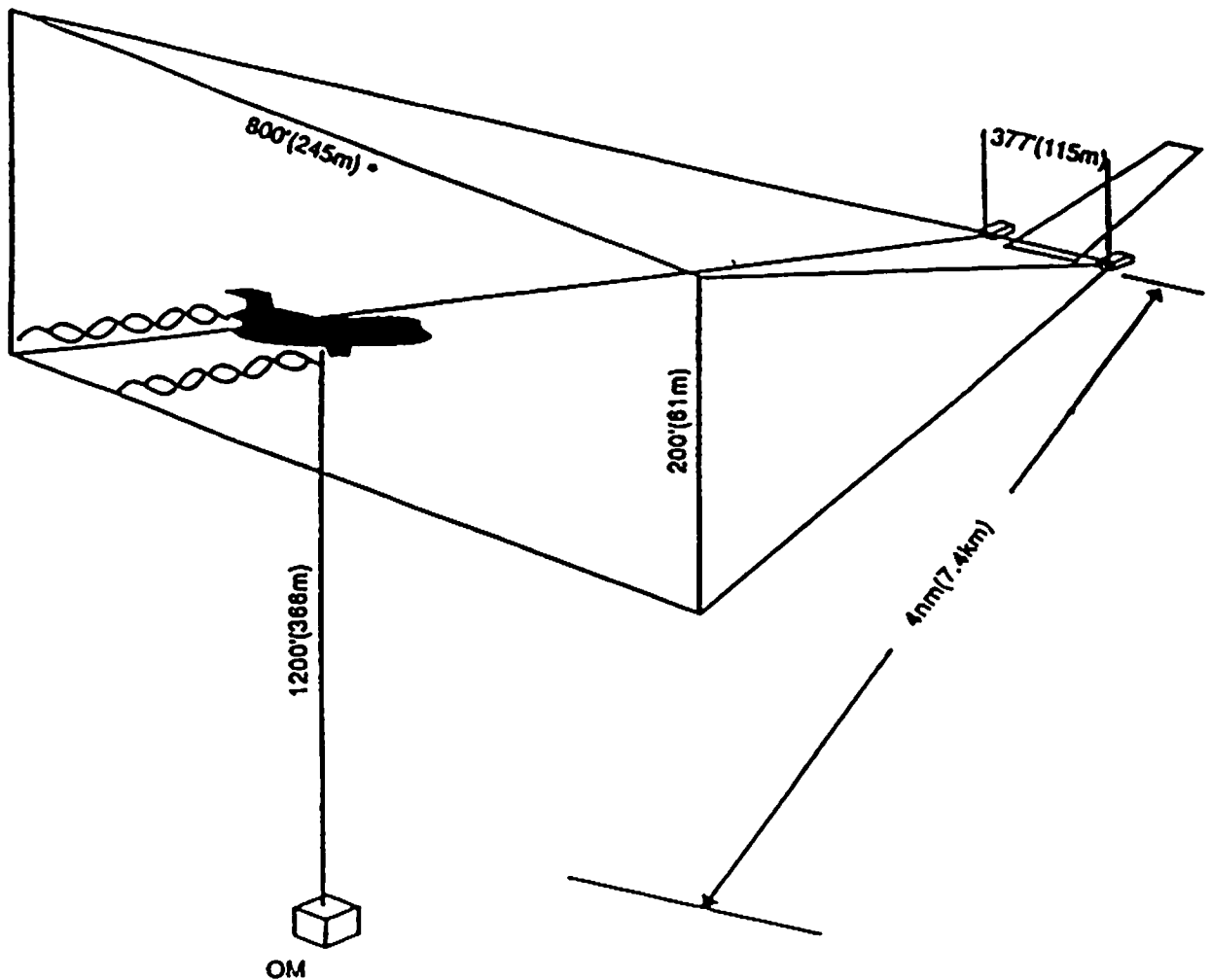
Figure 1.
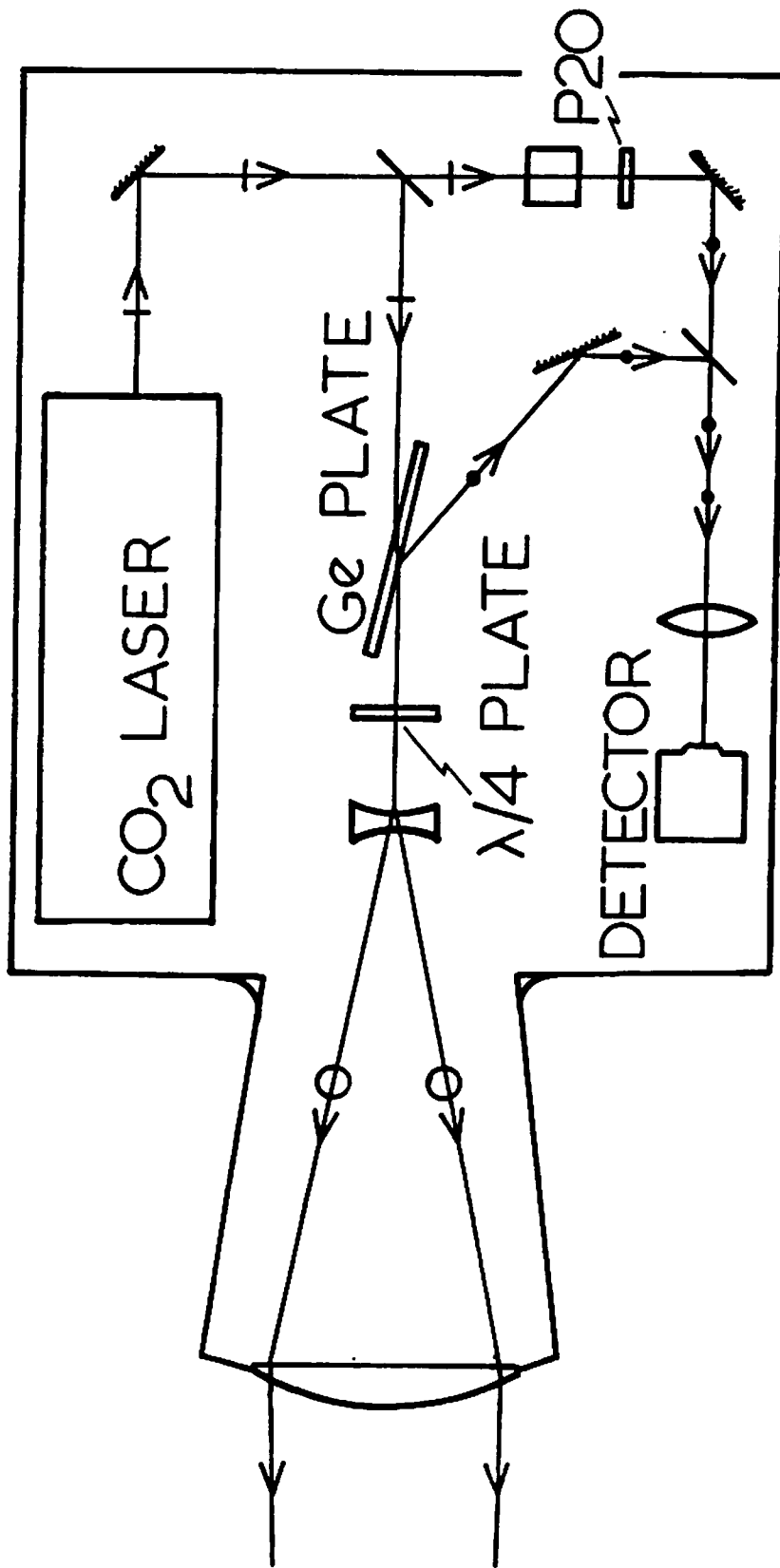
Figure 2. Schematic layout of the 10 micron heterodyne system.
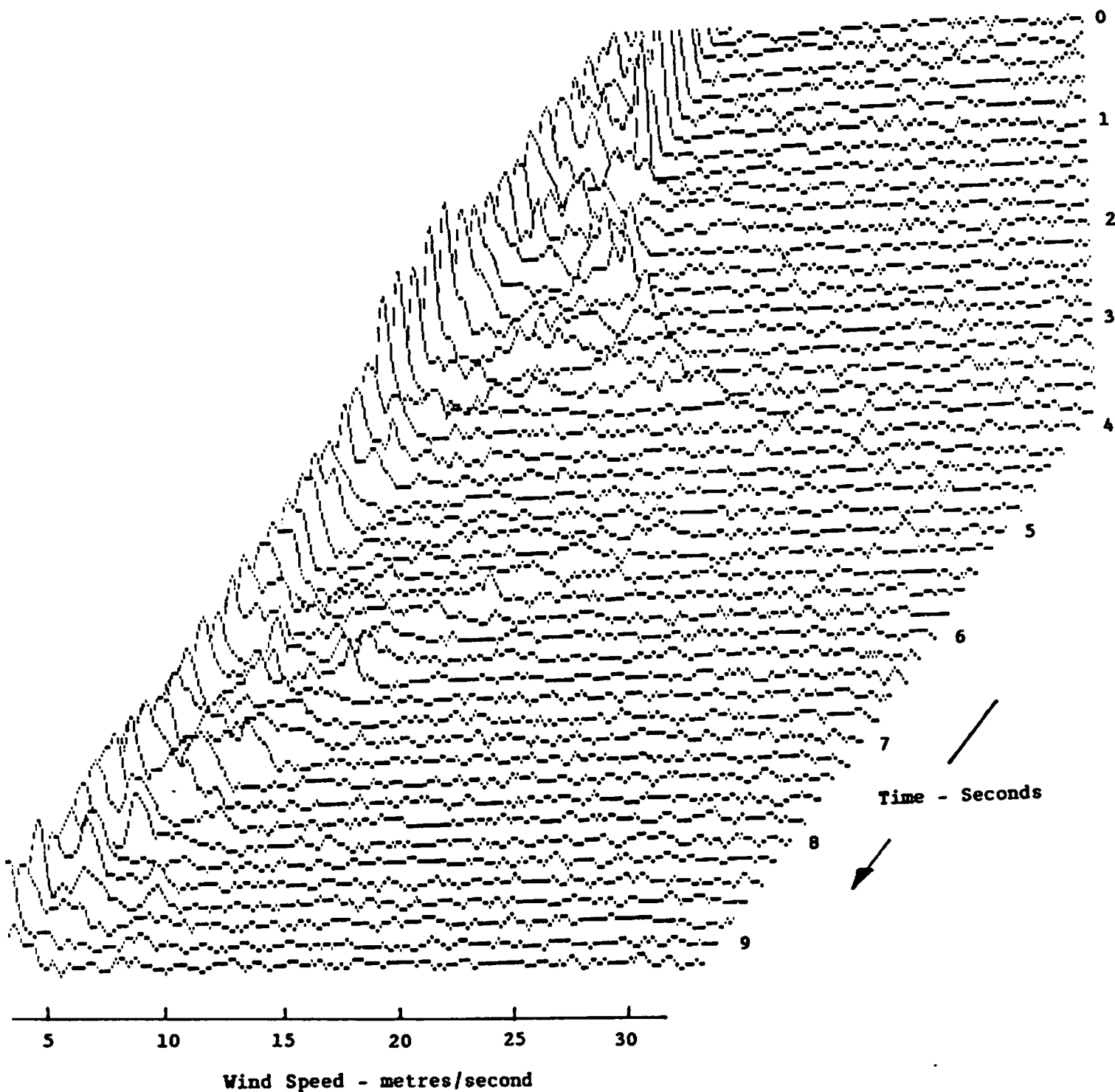
Figure 3. A wake vortex spectrum from an unidentified twin aircraft.
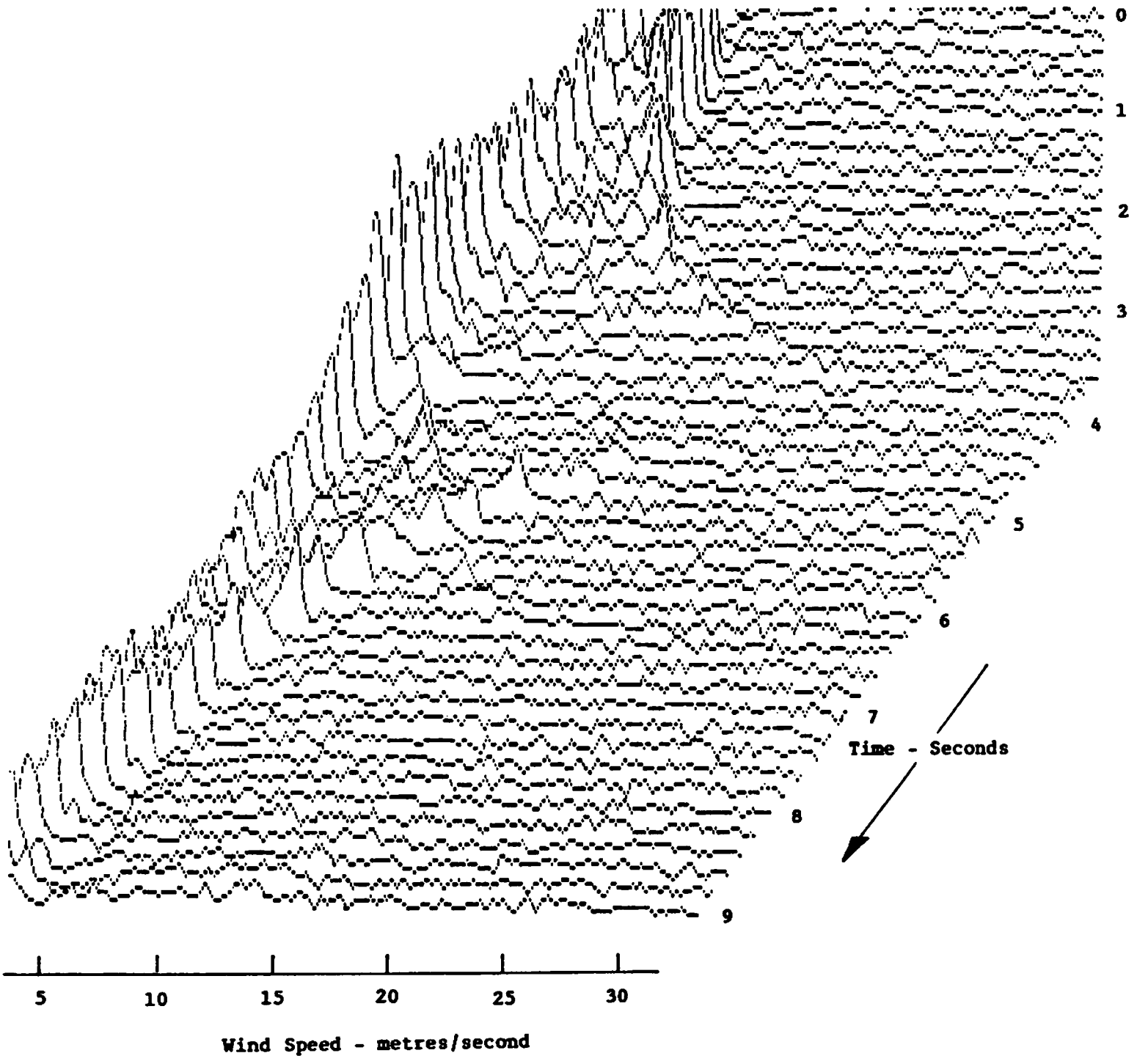
Figure 4. A wake vortex spectrum from a TU154 aircraft.
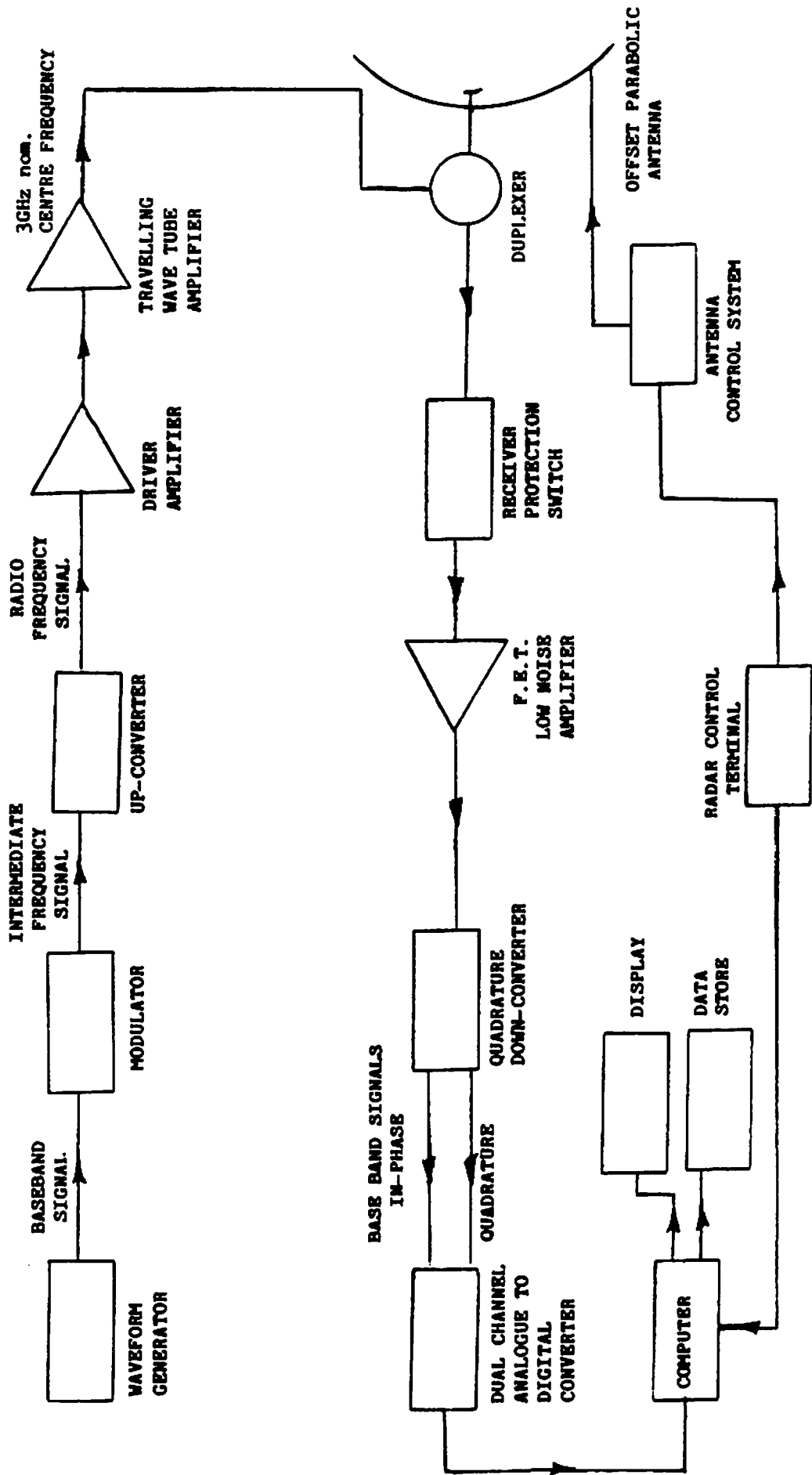
Figure 5. The GEC-MCR DX 04 radar: block diagram.
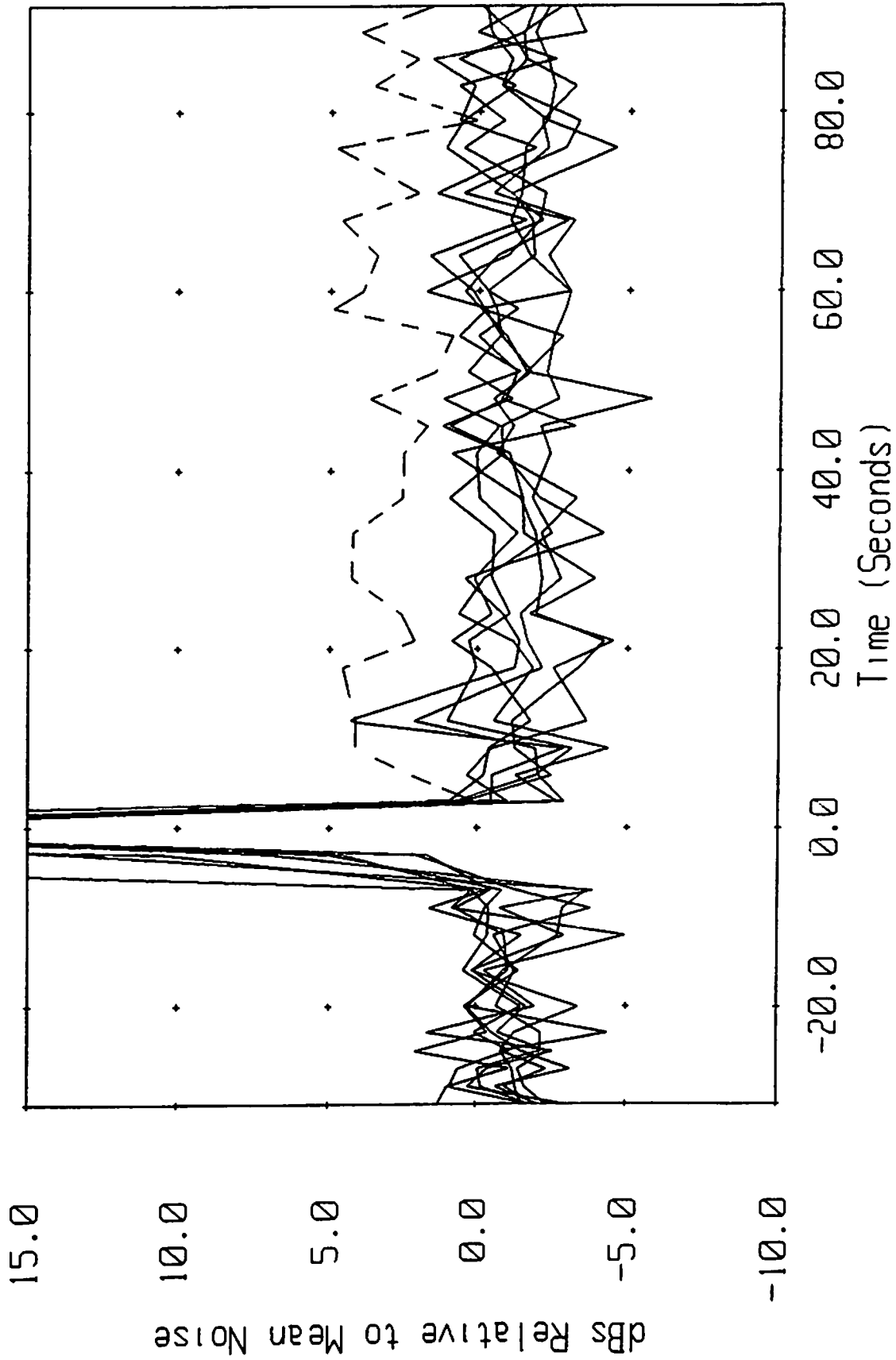
Figure 6. An indication of vortex detection

REFERENCES

1. Huffaker, R.M., A.V. Jelalian, and J.A.L. Thomson, 'Laser-Doppler system for detection of aircraft trailing vortices,' Proc IEEE, 58, pp. 322-326, 1970.

2. Francis, D.G., 'Development of a vortex laser Doppler velocimeter', Proceedings of the National Aerospace Electronics Conference 1971, IEEE, 1971.

3. Wilson D.J., A.D. Zalay, M.R. Brashears, C.E. Craven K.R. Shrider and A.J. JORDAN, 'Full-scale wake flow measurements with a mobile laser Doppler velocimeter', J Aircraft, 16, pp. 155-161, 1979.

4. Wake Vortex Research Data Package No.: VNTSC/IDF-1 Laser Doppler System, Acoustic Doppler System, High Resolution Anemometer. FAA, December 1990.

5. Wake Vortex Research Data Package No.: VNTSC/IDF-2A Volume I - Boeing 727 Laser Doppler System, Acoustic Doppler System, High Resolution Anemometer. FAA, May 1991.

6. Wake Vortex Research Data Package No.: VNTSC/IDF-2B Volume II - Boeing 757 Laser Doppler System, Acoustic Doppler System, High Resolution Anemometer. FAA, May 1991.

7. Wake Vortex Research Data Package No.: VNTSC/IDF-2CVolume III - Boeing 767 Laser Doppler System, Acoustic Doppler System, High Resolution Anemometer. FAA, May 1991.

8. Hallock, J.N., Aircraft Wake Vortices - An Annotated Bibliography, DOT-FAA-RD-90-30, DOT-VNTSC-FAA-90-7, January 1991.

9. Hallock, J.N., Aircraft Wake Vortices - An Assessment of the Current Situation, DOT-FAA-RD-90-29, DOT-VNTSC-FAA-90-6, January 1991.

10. Chadwick, R.B., J. Jordan, and T. Detman, 'Radar detection of wingtip vortices', Conference on Aerospace and Aeronautical Meteorology, pp. 235-240, American Meteorology Society, 1983.

11. Offi, D.C., W. Lewis, and T. Lee, 'Detection of hazardous meteorological and clear air phenomena with an air traffic control radar', International Conference Radar 82, pp. 316-320, IEE, 1982.

12. Easterbrook, C.C., and W.W. Joss, 'The utility of Doppler radar in the study of aircraft wing-tip vortices', Aircraft Wake Turbulence and its Detection, pp. 97-112, Plenum, New York, 1971.

13. Ottersten, 'Radar backscattering from the turbulent clear atmosphere', Radio Science, 4, pp. 1251-1255, 1969.

14. Chadwick, R.B., K.P. Moran, and W.C. Campbell, 'Design of a wind shear detection radar for airports', IEEE Transactions on Geoscience Electronics, GE-17, pp. 137-142, 1979.

WINGTIP TURBINES FOR VORTEX ALLEVIATION

Patrick Curran
Sundstrand Aerospace
Rockford, Illinois

INTRODUCTION

Finite wings generate high-energy vortices at their wing tips while producing lift. These vortices create spacing problems at airports because of the tremendous rotational energy contained within the vortices, and because these vortices persist for extended periods of time before dissipating. Departures and arrivals at busy airports are governed largely by the presence of the vortices generated by the incoming or outgoing aircraft. Eliminating, or significantly reducing the strength of the vortices, would greatly reduce the danger to trailing aircraft, and permit closer spacing of aircraft at busy airports.

It has been shown that the strength of a vortex can be alleviated by installing a vortex turbine at the trailing edge of a wingtip. The initial interest in the vortex turbine, however, was not in the area of vortex alleviation. The vortex turbine concept was first investigated as a potential means of producing power and reducing aircraft drag. Power can be generated by taking advantage of the high-speed rotational flow that is present near the core of the vortex. By properly placing a vortex turbine within the high intensity vortex core (Figure 1), rotational energy can be extracted for use in secondary power applications onboard the aircraft. The rotational energy can be converted to electrical, hydraulic, pneumatic, or a combination of these modes of power. The unique feature of the vortex turbine in generating power is that it extracts power from the rotational flow rather than from the free-stream velocity component; the free stream flow is not utilized and the drag penalties associated with extracting power from the free stream are avoided.

It has been demonstrated in both wind tunnel tests and small-scale flight tests that the vortex turbine is capable of reducing the induced drag of an aircraft by disrupting the formation of the vortex. During flight the vortex exerts an upward flow component outboard of the wing tips, and a downward component directly behind the wing (Figure 2). This downward component, or downwash, contributes to the induced drag of an aircraft, and can be reduced by locating the vortex turbine in the center of the vortex flow field where the rotational velocities are greatest. The vortex turbine hinders the formation of the vortex, and is capable of reducing the induced drag of the wing by as much as 20 percent.

Although the primary interest in the vortex turbine has focused on the aspects of power generation and drag reduction, the additional benefit of vortex alleviation is equally important, especially as it relates to inbound and outbound aircraft at airports. The degree of vortex alleviation correlates closely with the amount of induced drag reduction obtained with the vortex turbine. The correlation is to be expected because of the phenomenon that occurs when the vortex turbine reduces induced drag; the vortex turbine reduces the downwash effect of the vortex by hindering the initial formation of the vortex. The turbine blades essentially interfere with the high-speed rotational flow near the core of the vortex, which results in a turbulent flow trailing the wingtip, rather than the fully-formed rotational flow that is found in the typical vortex.

The text that follows summarizes the work that has been done to determine the effectiveness of the vortex turbine in producing power and reducing induced drag. The extent to which the vortex turbine is able to achieve these two goals reflects its ability to reduce the strength of vortices. The results of wind tunnel tests and the small-scale flight tests with a vortex turbine are discussed. A smoke test to visually determine the extent of the vortex disruption was also performed, and the results of this test are presented.

Wind Tunnel Tests

Exploratory investigations were conducted at NASA Langley Research Center to determine the feasibility of using a vortex turbine to recover a portion of the energy loss associated with the lift-induced vortex system (ref. 1). The wind tunnel tests were conducted on an unswept NACA 64_1A012 airfoil section semispan wing with an aspect ratio of 6.39 in the NASA 8-Foot Transonic Pressure Tunnel. The semispan wing was tested with and without a vortex turbine installed at the wingtip.

Tests were conducted at a Mach number of 0.7, at angles of attack that varied from 0° to 4°. Three types of blades were tested to determine the effect of the blade shape and planform. Measurements of forces and moments were obtained from a five-component electrical strain gauge balance. The power generated by the turbine was obtained by measuring the torque and speed of the turbine.

The basic semispan wing was tested first to establish a baseline for comparison against the wing with the vortex turbine installed. Three types of turbine blades were then tested. The first blade type was untapered and had a symmetrical airfoil section. The second set of blades was also untapered, but had a cambered airfoil section. The third set was symmetrical and tapered. All sets of blades were set at zero incidence angle relative to the turbine nacelle centerline. Tests were run with the turbine blades locked, or nonrotating; then at their free spin, or no-load speed; and finally at a speed approximately one-half of the no-load speed. A drawing of the turbine blade planforms is shown in Figure 3.

The results of the wind tunnel tests clearly demonstrated the benefits of installing the vortex turbine on the semispan wing. The various types of blades, however, yielded different results in terms of power recovery or drag reduction. The untapered cambered blades recovered approximately three times the power of the symmetrical blades. This could be expected because

the cambered blade produces more lift than a symmetrical blade at a given angle of attack, and thus produces more power. There was little difference between the tapered and untapered symmetrical blades in producing power; this would indicate that the outer area of the untapered blades is of little benefit in producing torque, and could therefore be removed to reduce the blade drag. This effect would also indicate that blade tapering would be advantageous for a cambered blade.

The wind tunnel tests were not specifically aimed at determining the extent of vortex alleviation that could be achieved; there is, however, a relationship that exists between the amount of energy recovered from a vortex and the strength of the vortex that remains after the energy is extracted. Removing energy from a vortex during its formation results in a weaker vortex system that dissipates much more quickly than an undisturbed vortex. The ability of a vortex turbine to alleviate trailing vortices can therefore be measured in terms of the power extracted from the vortex or by the amount of reduction in drag due to lift. The greater the power extraction or induced drag reduction, the weaker the resulting vortex. An overview of the test results is given in Figures 4 and 5.

Figure 4 is a plot of the power recovered versus angle of attack for the wing with the vortex turbine installed. While all the blade configurations produced power, the cambered blade configuration was clearly better than the symmetrical blades. Figure 5 shows the variation of drag coefficient (C_D) versus lift coefficient (C_L) for the basic wing, and with the vortex turbine in place. As shown in the figure, the drag is lower for the basic wing at the lower C_L values. This would be expected at the low angles of attack where the wing is producing a small amount of lift and the vortex strength is low; the turbine blades actually add drag at this condition because of the form drag of the blades. However, at the higher C_L values where a wing normally operates during flight, an improvement in drag was demonstrated by all turbine blade configurations.

Small-Scale Flight Tests

The results from the initial wind tunnel tests were promising and warranted additional investigation. Sundstrand and NASA joined together to conduct additional testing of the concept on a small-scale aircraft. The aircraft chosen for the flight test was the NASA PA28RT aircraft that had been previously used in NASA's spin recovery tests at the Langley Research Center. The aircraft is shown in Figure 6, and further described in reference 2.

Two sets of turbine blades were tested, one with a 15° twist (washin) and one with no twist. The results of the previous wind tunnel tests indicated that cambered blades generated more lift, and hence more power; while the tapered blades had less drag. The turbine blades for the small scale flight test were therefore designed with both camber and taper. The blades with the 15° twist were designed to compensate for the lower velocities that occur near the turbine tips, since the vortex flow velocities vary inversely with the spanwise distance from the center of the vortex. The angle of the blades relative to the turbine centerline was variable and adjustable to approximately 0.5°.

The power output from each turbine was obtained by measuring the flow and pressure produced by a calibrated hydraulic pump driven by the turbine. A diagram of the turbine assembly is

given in Figure 7. Speed-power tests were conducted to determine the total airplane drag with the vortex turbines installed, and this data was compared to the baseline airplane configuration without the vortex turbines. Tests were conducted for each blade configuration and blade angle setting at turbine speeds from zero to free-wheeling. The flight tests consisted of a series of level-flight, constant speed runs at an altitude of approximately 5,000 feet. Drag was determined by analyzing 30 to 60 seconds of data after the aircraft had stabilized at a steady altitude and airspeed. The power required for level flight at each test condition was determined using the engine manufacturer's and propeller manufacturer's performance charts. Tests were conducted in smooth, stable air; and data was adjusted to account for variations in density altitudes between test flights.

The results of the flight tests are summarized in Figures 8 and 9. As with the earlier wind tunnel tests, the flight test focused on determining the horsepower extraction and drag reduction that could be achieved with the vortex turbine. The degree of vortex attenuation, as mentioned earlier, is related to the amount of energy removed from the vortex by the vortex turbine. A high level of power extraction or drag reduction would result in a significant decrease in the vortex strength.

The results of the flight tests are presented for both stationary and rotating turbine blades at an aircraft cruise speed of 140 mph ($C_L = 0.325$). The data is presented as a comparison against the baseline aircraft without the vortex turbines. Figure 8 corresponds to a stationary turbine; no power was generated since the turbine was not allowed to rotate. A maximum drag reduction of 21 drag counts was obtained at a blade pitch angle of -4°. This corresponds to about a 6 percent drag reduction for the aircraft. As the blade pitch angle increased, the drag reduction benefit was reduced because the blades approached their stall regime where the blade form drag increases significantly. At a pitch angle of approximately +2.5°, the drag reduction obtained from the turbine blades is equal to the form drag of the blades; at this condition the turbine configuration is equivalent to the baseline configuration without the vortex turbine. At even higher blade pitch angles the drag of the turbine configuration exceeds that of the baseline configuration, again because of the blade form drag. Figure 8 shows that a significant drag reduction can be obtained by a stationary turbine, and the degree of drag reduction is a function of the blade pitch angle.

Figure 9 summarizes the results of the flight test with the turbines rotating at approximately the midpoint between zero and free-wheel speed. The figure shows that at -4° blade pitch angle, the turbines generate two horsepower from the rotational vortex flow, and reduce the aircraft drag by 16 counts. The configurations tested showed that there is a correlation between drag and horsepower, with each horsepower generated corresponding to approximately 3 drag counts (.0003). The drag reduction obtained by a rotating turbine may therefore be traded for rotational energy by increasing the blade pitch angle. As an example, increasing the blade setting to +2.5° increases the power output to approximately 6 horsepower, but the change in drag relative to the baseline aircraft is zero. Even greater amounts of power could be generated, but only at the expense of increasing the drag due to the turbine blades.

Reducing the strength of the vortex can be achieved with either a stationary turbine or a rotating turbine. With a stationary turbine, the result is manifested in drag reduction alone. With a rotating turbine, the result is power generation and drag reduction, although the drag reduction

is somewhat less when power is extracted from the vortex. In either case the energy is removed from the vortex and the strength of the vortex is decreased.

Smoke Visualization Tests

The recovery of a portion of the energy from the high speed rotational flow that is present in and near the core of a vortex was discussed in the above paragraphs. The shape and strength of the vortex that remains after the energy is extracted was also of interest because it provides insight into the effectiveness of the vortex turbine at disrupting the formation of a high energy vortex.

Smoke tests were therefore conducted to obtain a qualitative visualization of the vortex downstream from the vortex turbine. Sundstrand funded Vigyan Inc. to conduct a small-scale wind tunnel test using smoke generators located at the wingtip of a semispan model to obtain a visualization of the vortex flow field. A 13-inch semispan wing with a chord length of 5 inches was tested at an angle of attack of 8°. The free stream flow velocity was approximately 7.5 mph. A light sheet located approximately 5 chord lengths downstream of the semispan test wing was used to obtain a clear view of the flow field at that station.

The semispan wing was first tested without the vortex turbines installed. A photograph of the fully developed vortex is shown in Figure 10. The photograph clearly shows the high intensity core surrounded by the circulation flow associated with a vortex.

The semispan wing was then tested with the vortex turbine installed, but in the stationary or nonrotating mode. A photograph of the light sheet with the stationary vortex turbine in place is shown in Figure 11. The pronounced high energy vortex core is no longer present in the flow field, and the flow is obviously turbulent. The photograph of figure 11 would indicate that the vortex turbine was effective in disrupting the formation of the vortex.

A similar result was observed when the vortex turbine was allowed to rotate. A photograph of the light sheet taken while the turbine was rotating is shown in Figure 12. Again, the high energy core is missing from the flow field, thus indicating that the turbine was effective in disrupting the formation of the vortex. The flow field observed at the light sheet with the rotating turbine appeared to move about in a random fashion, noticeably more than when the turbine blades were stationary. This effect could be attributed to the fact that the blades were rotating. Further tests indicated that small vortices appeared to be present at the tips of the turbine blades. This could be expected because the blades are essentially small airfoils that develop lift from the rotational flow of the vortex generated at the wingtip.

Concluding Remarks

The results of the initial wind tunnel test and the small-scale flight tests indicate that the strength of a vortex can be weakened through the use of a vortex turbine. Power can be extracted from the vortex, and the induced drag can be reduced by eliminating or reducing the downwash caused by the vortex.

The smoke visualization tests clearly show that the vortex turbine hinders or alters the flow field of the typical high energy vortex that forms at aircraft wingtips. Because the typical high speed core of the vortex is absent from the turbulent flow that occurs downstream from the vortex turbine, it can be surmised that the strength and persistence of the vortex is significantly reduced.

Although the results of the testing thus far have been encouraging, additional testing and analysis remains to be done. Flow field modeling, blade design optimization, and optimizing the mode of turbine operation are technical issues that Sundstrand plans to address as part of our vortex turbine development program. A flight test program using a full-scale aircraft is also envisioned, which would eliminate the conservative Reynolds number effects associated with the small-scale testing conducted to date, and would provide baseline data from which an aircraft impact and benefits study could be performed. The vortex turbine has demonstrated its potential as a device for producing secondary power, reducing induced drag, and alleviating following vortices. If this potential is exploited, the vortex turbine may prove to be a beneficial concept for aircraft in the future.
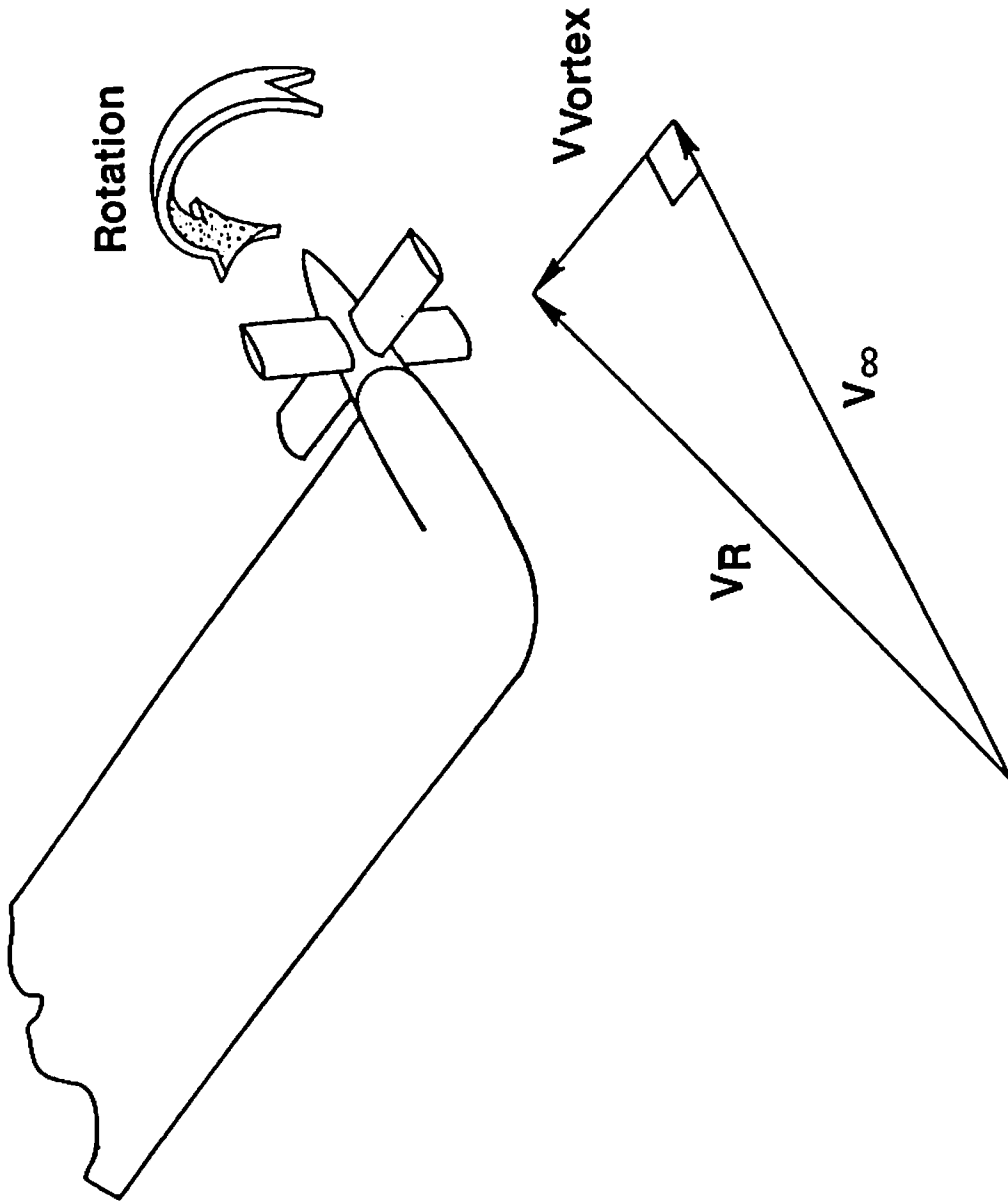
Figure 1. Wingtip vortex turbine.
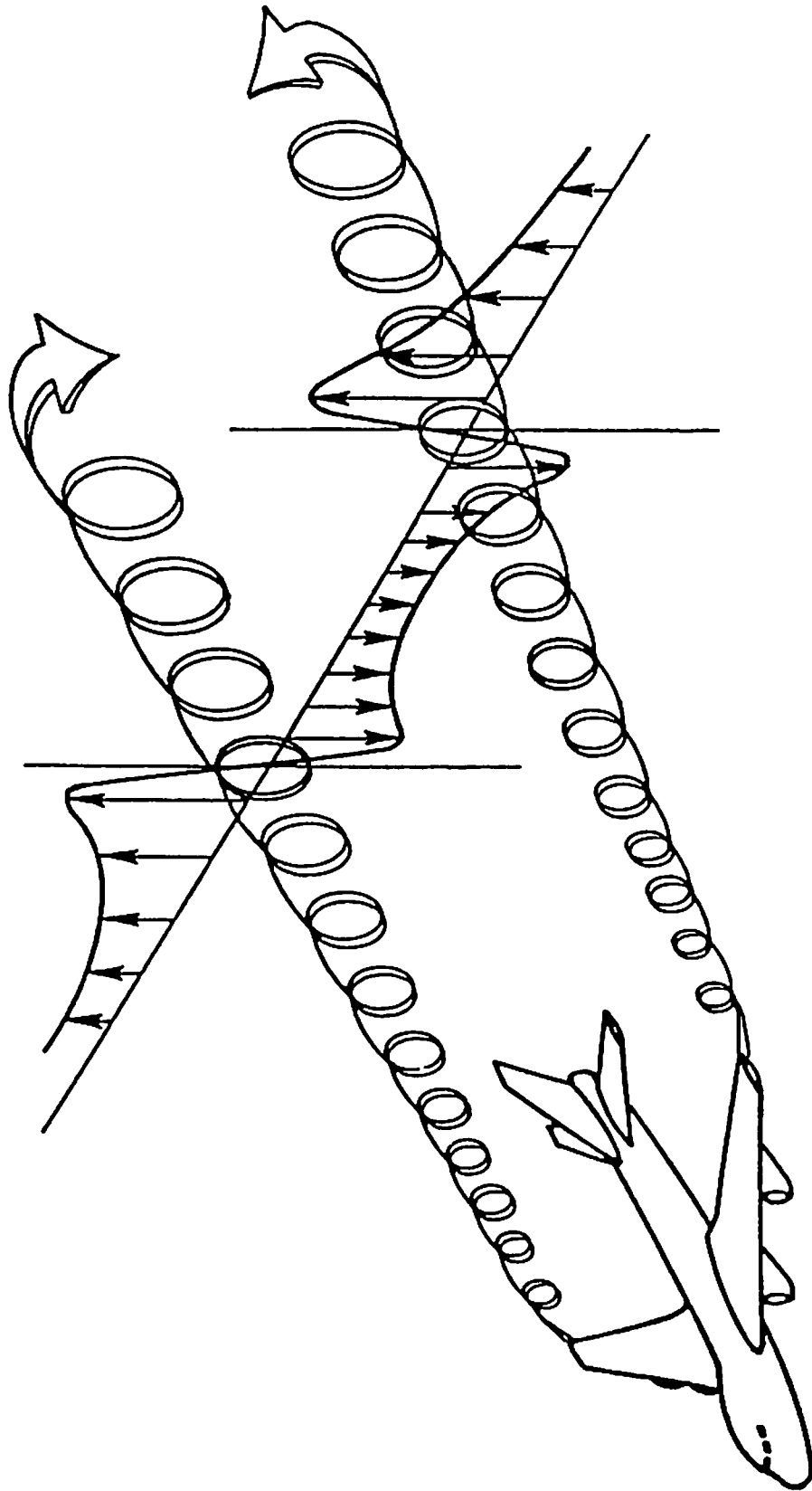
Figure 2. The lift-induced vortex.

1.25

2.5

Tapered Blades

2.5

Cambered Blades

2.5

Symmetrical Blades
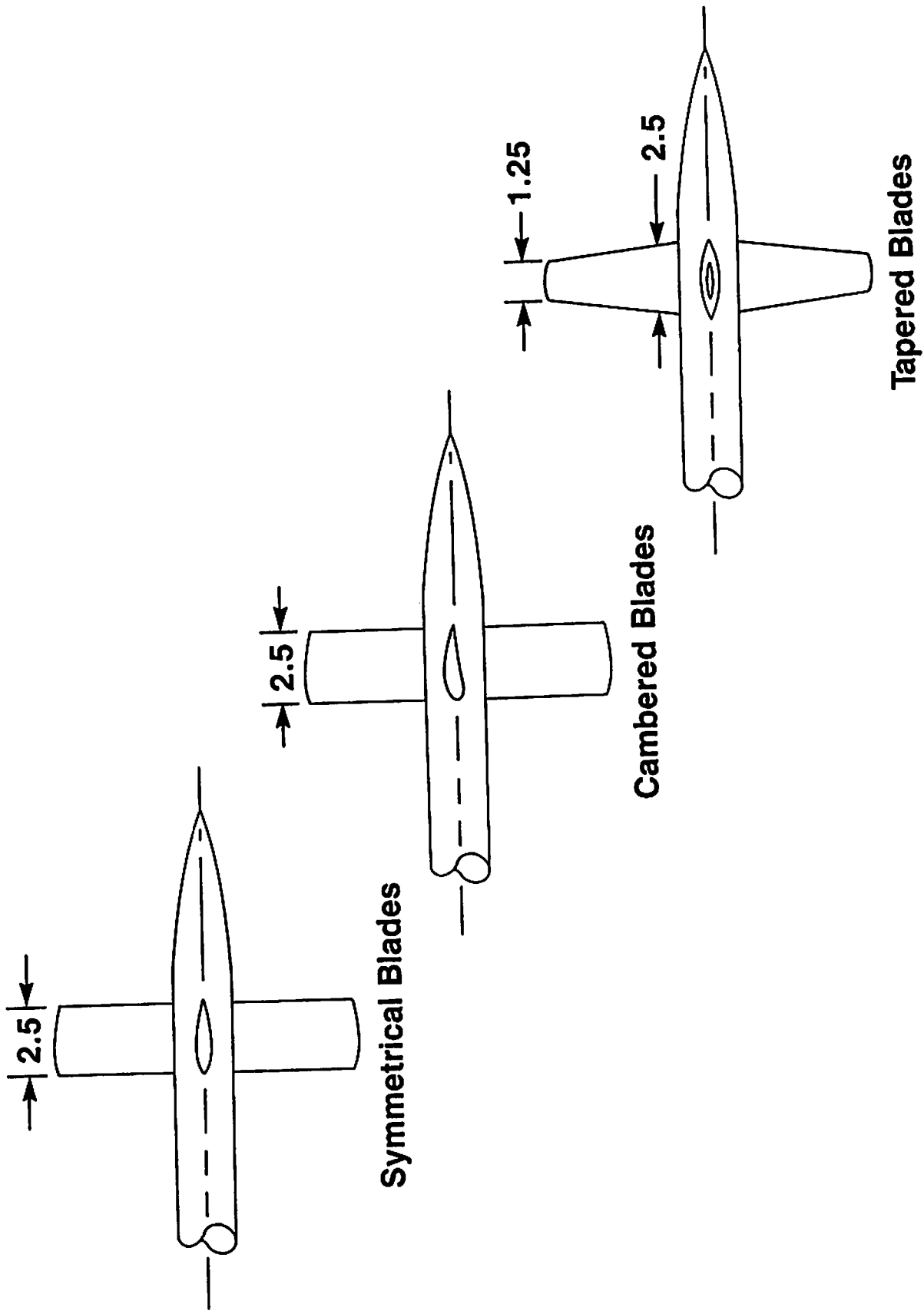
Figure 3. Turbine blade planeforms.
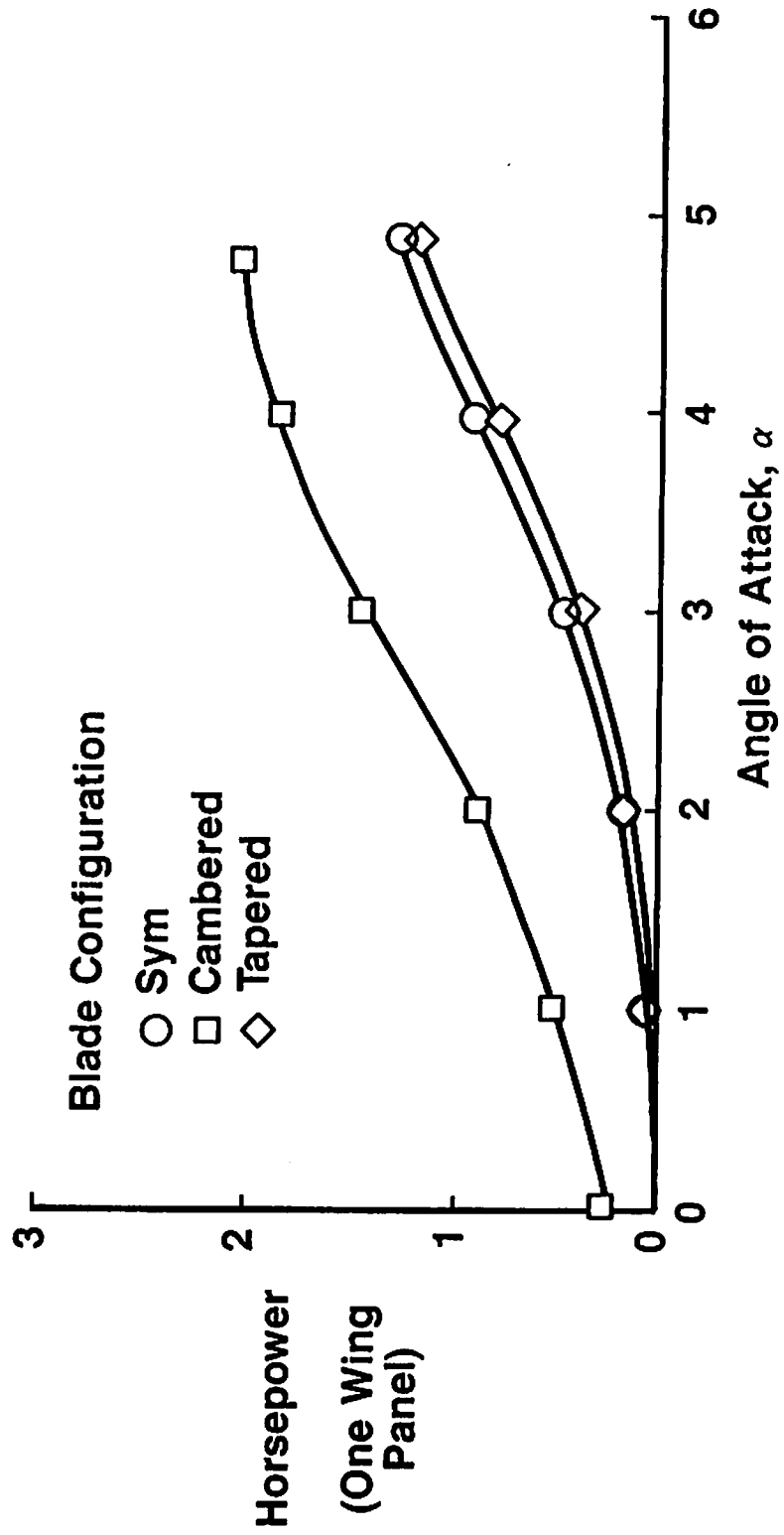
Figure 4. Small-scale wind tunnel results.

Figure 5. Small-scale wind tunnel results.
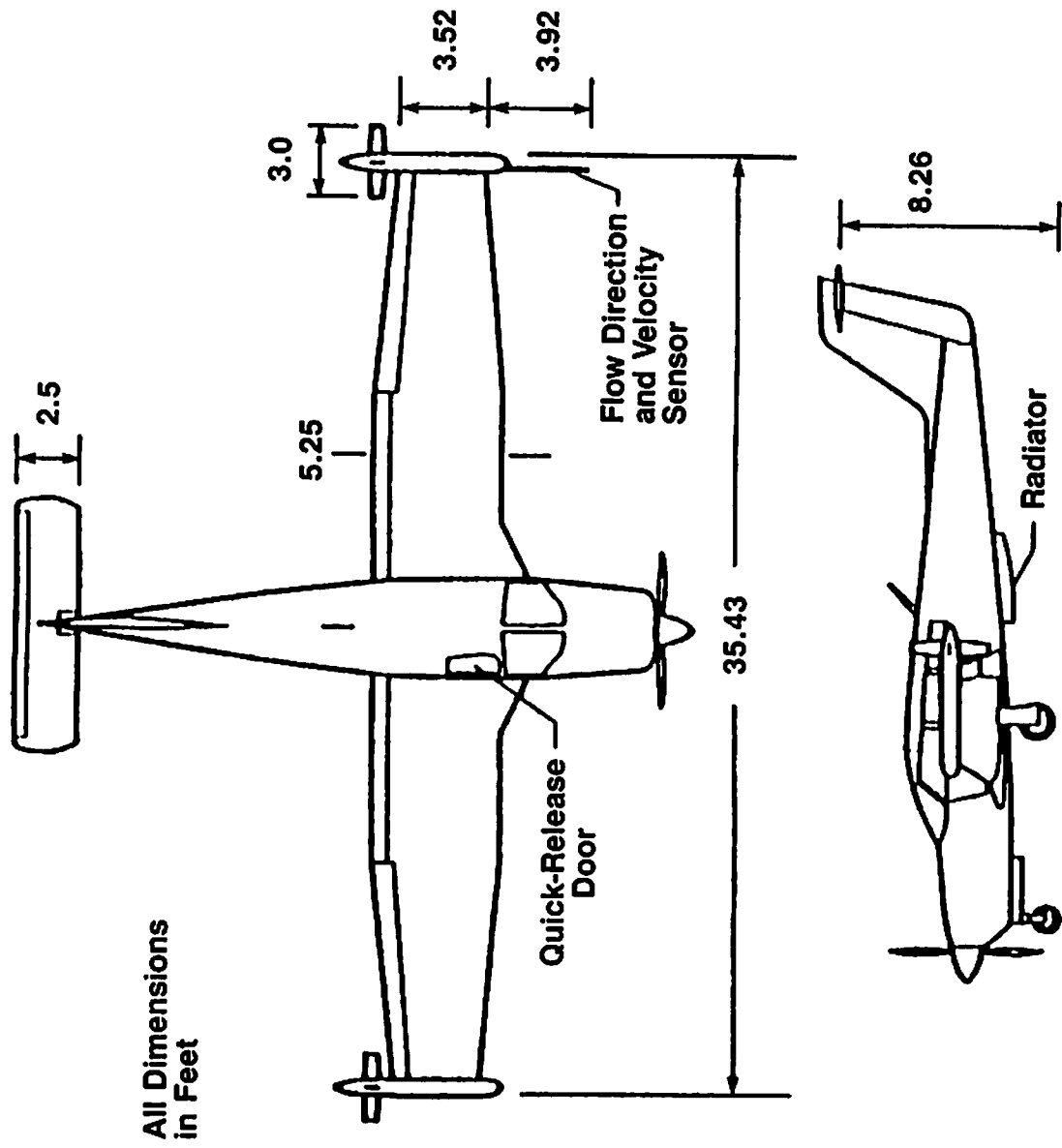
Figure 6. Flight test aircraft.

All Dimensions in Feet

2.5

3.52

3.92

3.0

5.25

35.43

Flow Direction and Velocity Sensor

Quick-Release Door

8.26

Radiator
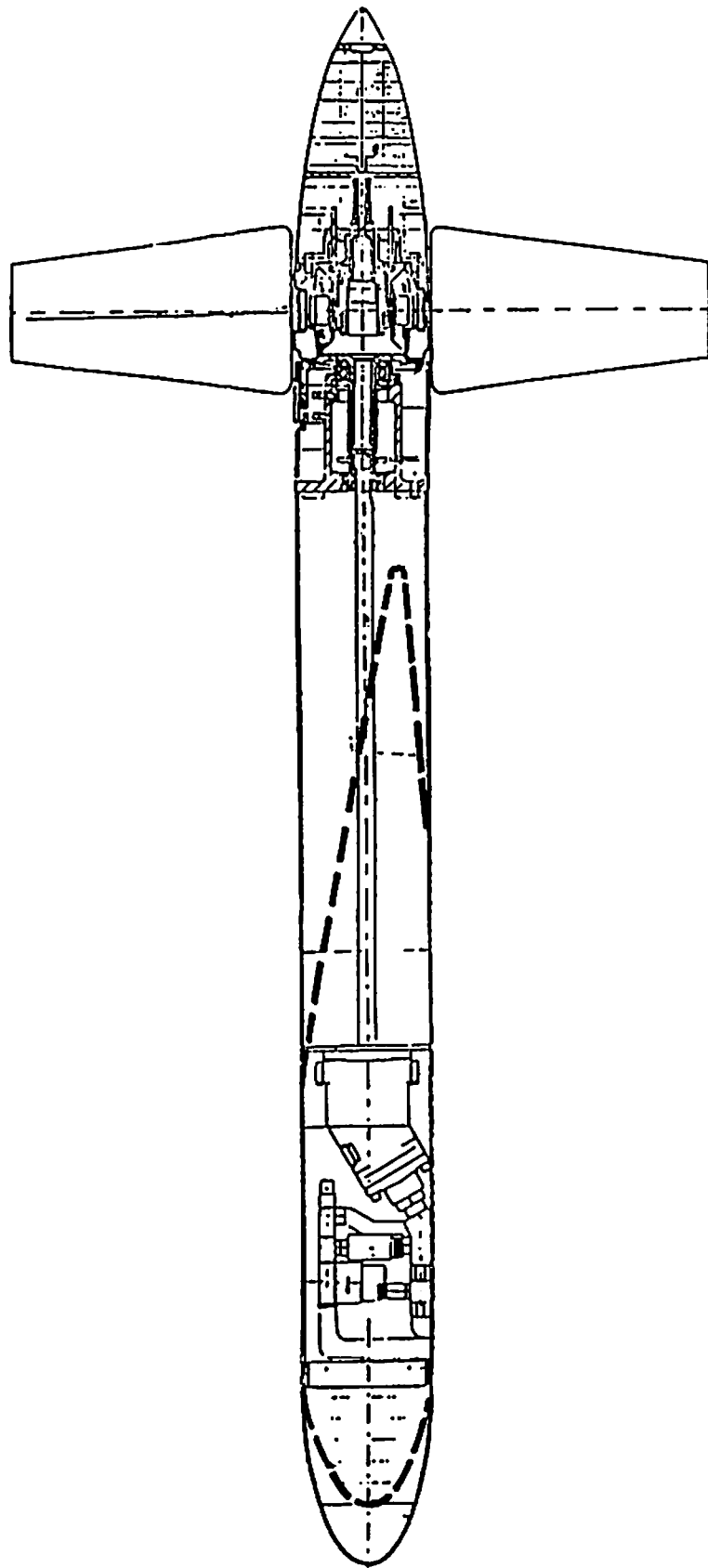
Figure 7. Wingtip vortex turbine assembly.
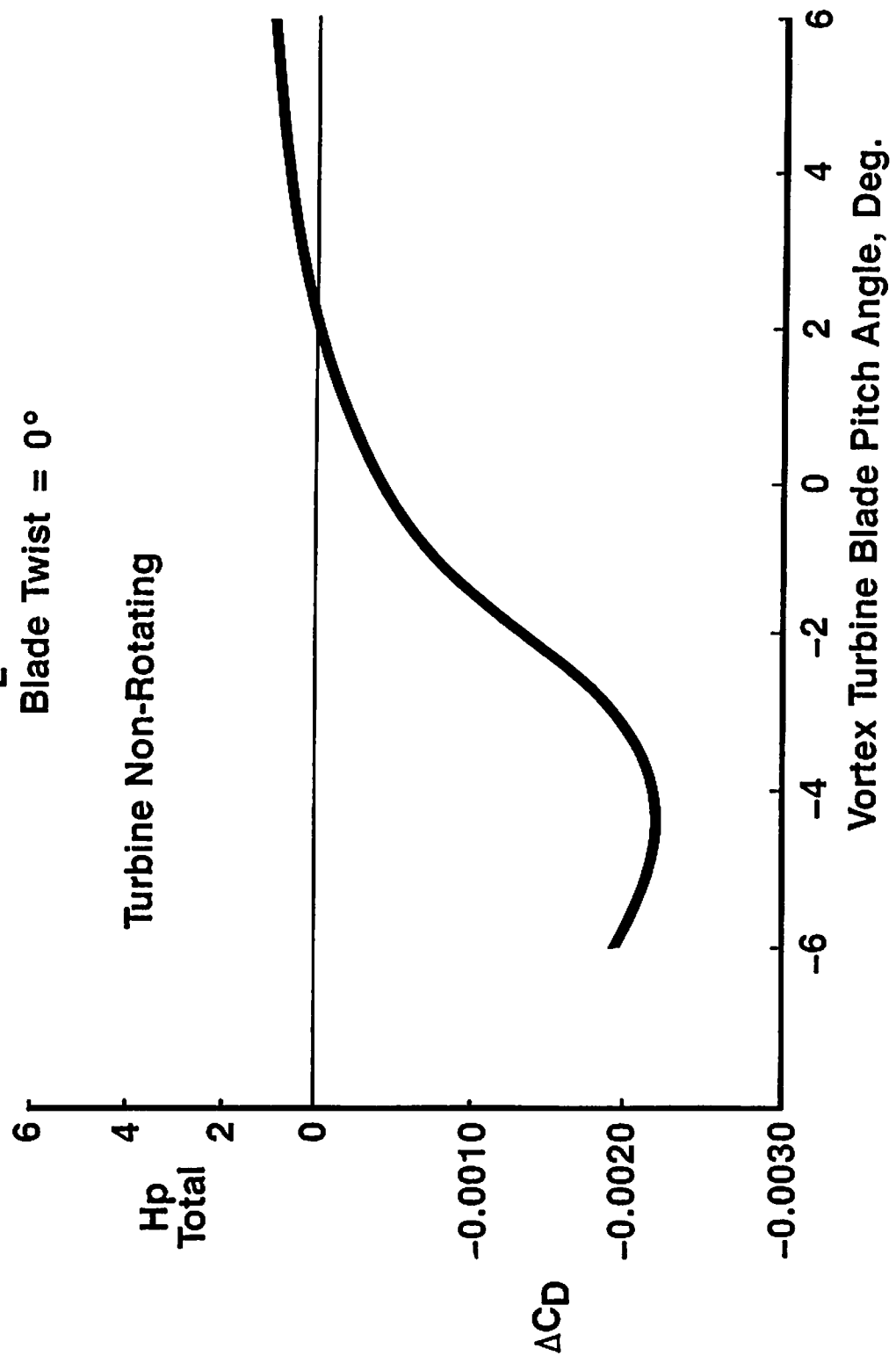
Figure 8. Flight test results - static turbine.
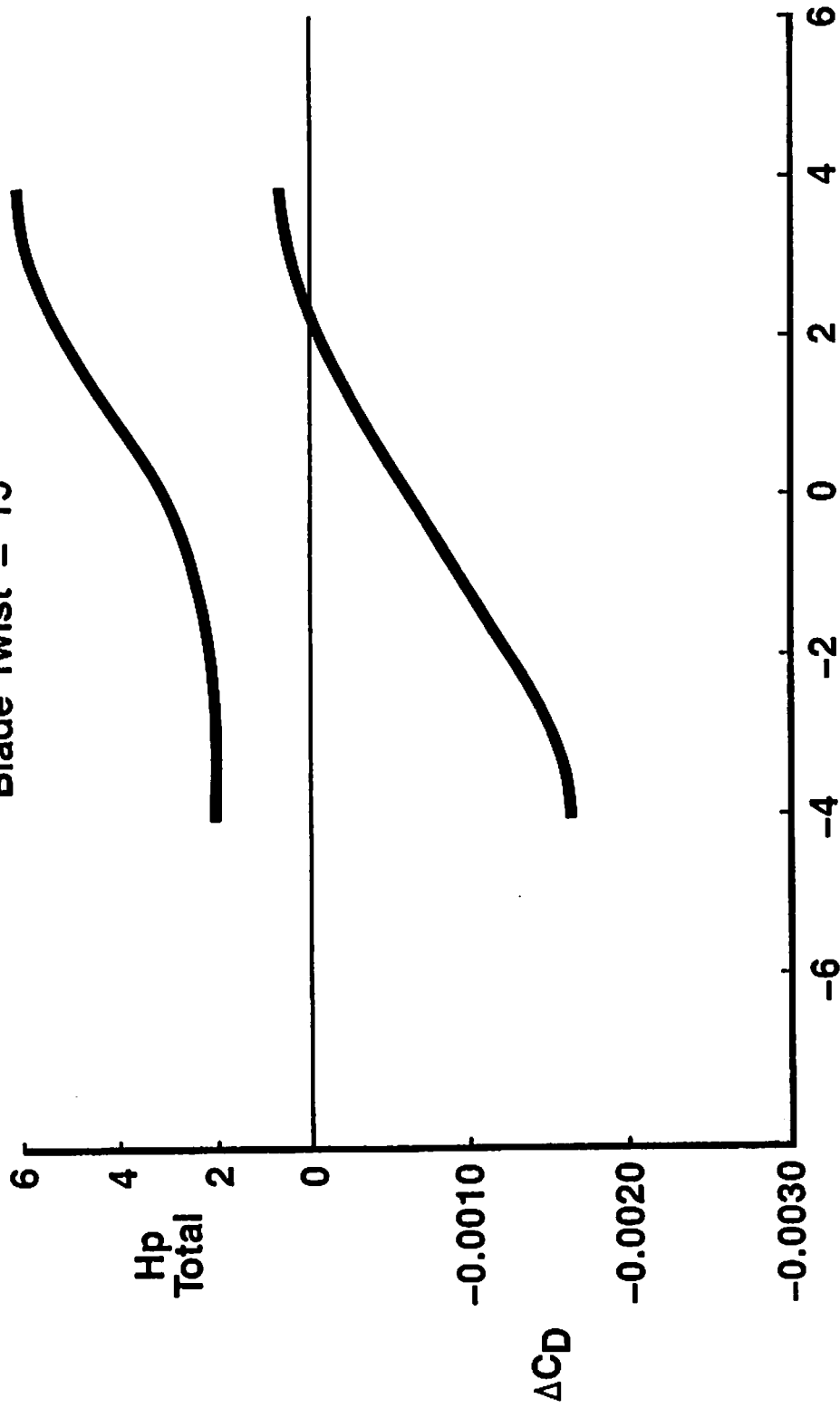
Figure 9. Flight test results - rotating turbine.

Figure 10. Basic wing flow field.

Figure 11. Static turbine flow field.

Figure 12. Rotating turbine flow field.

REFERENCES

1. Patterson, J.C., Jr. and Flechner, S.G., "Exploratory Wind-Tunnel Investigation of a Wingtip-Mounted Vortex Turbine for Vortex Energy Recovery." NASA TP 2468, 1985.

2. Stough, H.P., III; DiCarlo, D.J., Patton, J.M., Jr. "Flight Investigation of Stall Spin, and Recovery Characteristics of a Low-Wing, Single-Engine, T-Tail Light Airplane." NASA TP 2427, 1985.

3. Abeyounis, W.K.; Patterson, J.C., Jr.; Sough, H.P., III; Wunschel, Lt. Col. A.J.; Curran, P.D., "Wingtip Vortex Turbine Investigation for Vortex Energy Recovery." SAE Tech Paper 901936, Aerotech '90, October, 1990.

HOW TO USE WAKE VORTEX MEASUREMENTS
TO SET SEPARATION STANDARDS

Dr. David C. Burnham
Scientific & Engineering Solutions, Inc.
P.O. Box 64
Orleans, MA 02653

"WORST CASE" METHODOLOGY

The current U.S. wake vortex separation standards were based on vortex encounter flight tests carried out under "worst case" conditions (low turbulence at high altitude). Because the resulting worst case separation standards would have severely reduced airport capacity, the separations adopted were reduced from those indicated by the flight tests. Operational experience for the last 20 years indicate that the current separations standards are safe; no accidents have occurred when the required separations have been observed. Many wake vortex incidents, however, have been reported.

Since the most critical region for wake vortex encounters is near the ground, the apparent contradiction between "worst case" flight tests and operational experience has generally been explained as the consequence of faster vortex decay near the ground. This hypothesis is more difficult to support, however, in light of measurements taken at airports in the late 1970s and in recent vortex studies. According to the hazard model used for analyzing such data, the vortex hazard appears to persist significantly longer than the current separation standards under "worst case" conditions, just as observed in tests at altitude. If the hazard model can be validated, this observation leads to three conclusions: 1) Worst case conditions cannot be used to set realistic separation standards. 2) Worst case conditions must be rare in operational scenarios. 3) Safety would be enhanced if the rare worst case meteorological conditions can be identified and increased separations employed.

"NORMALIZED SAFETY" METHODOLOGY

An alternative procedure[1] for setting separations from wake vortex measurements is based on the assumption that the current separation standards are "safe." A vortex hazard model is used to assess the hazard threshold for vortex strength. Vortex decay measurements are processed to give an empirical model for vortex decay, which specifies the probability of the vortex strength remaining above a given value as a function of vortex age. These two models can be combined to determine the vortex hazard probability at a given separation time. If the hazard

probability under current standards for a frequently occurring aircraft pair is defined as safe, then the safe separation for other aircraft pairs can be determined. The sensitivity of the results to the assumed hazard model is then assessed. Two sample applications of this methodology will be presented: 1) 2.5-mile separation of Small and Large aircraft smaller than the B-757 and 2) reduction of Heavy-Heavy separation from 4 to 3 miles. These cases have become operational goals in the years since the original study was carried out.

The two models to be presented here are not perfect, but will serve to illustrate the methodology. Improvements in the models or alternative models could be used to give more reliable safety predictions. A discussion of model limitations is outside the scope of this paper but was included in the original reports.

VORTEX HAZARD MODEL

The hazard model estimates the hazard caused by vortex-induced roll on a following aircraft. The basic parameter of the model is f, the ratio of the largest acceptable induced rolling moment to the roll control authority of the encountering aircraft. If f is set at one, the pilot can safely control the aircraft unless the induced roll exceeds the roll control authority. If one considers pilot reaction times and other factors, the effective value for f may be as low as 0.5. The value of f can be varied to determine the sensitivity of the analysis to the choice of this basic parameter. The result of the hazard analysis is that a vortex is hazardous if its average circulation (evaluated for a radius equal to half the wingspan of the following aircraft) is above a threshold value which is proportional to f. The simplified version of the hazard model, developed in References 1 and 2, was verified by vortex lattice calculations.

VORTEX DECAY MODEL

The vortex decay model in reference 1 is based on measurements taken on landing aircraft at O'Hare airport in the late 1970s using the Monostatic Acoustic Vortex Sensing System (MAVSS). The MAVSS measures the velocity profile of a vortex as it passes over a fixed, vertically pointing acoustic radar. A series of antennas are installed on a baseline perpendicular to the flight path and vortex measurements at successively greater vortex ages are obtained as the vortex passes over each antenna in the series. Because of limited spatial resolution and other problems, the MAVSS cannot resolve the core velocities of most wake vortices.

The MAVSS data are processed to yield the average vortex circulation out to radii of 5, 10, 15 and 20 meters for each vortex detection. If a vortex is not detected at an antenna at the time expected from the arrival times at antennas closer to the runway centerline, then the vortex strength is assumed to be zero at that expected arrival time unless the vortex detection would be obscured by the arrival of the next aircraft. The MAVSS data thus yield a history of vortex average circulation for the two vortices: Vortex 1 which is the first to arrive and Vortex 2 which is the second to arrive. Vortex 2 is observed to last longer than Vortex 1 and is also the vortex that will linger near the runway centerline to pose a possible hazard to the next aircraft. Therefore, data on Vortex 2 is used to analyze the safety of longitudinal vortex separation standards.

The vortex hazard model defines a hazard threshold for the average circulation for a radius equal to half the wingspan of the encountering aircraft. The MAVSS average circulation histories are processed at 10-second intervals to determine what fraction of the vortices remain above the hazard threshold as a function of vortex age. This fraction is defined as the "hazard probability." For old vortices this probability decays as the square of the vortex age. A variety of mathematical models were investigated to fit the probability decay curves. A two-parameter model was selected to represent the decay of hazard probability with vortex age. The first parameter is the mean average circulation at vortex age 10 to 15 seconds. The second is a decay time parameter.

The methodology of Reference 1 was modified somewhat to produce the following tables. The average circulation values for 15 and 25 meters were obtained by fitting the 10 and 20 meter values to an analytical vortex model. The 20-meter time parameter was used for 25 meters. Some round-off errors were eliminated.

SEPARATION ANALYSIS

Since the current separations are assumed to be safe, a "safe" hazard probability can be determined by looking at the hazard probabilities for the current separation standards. Table 1 shows the three wake vortex aircraft classes, Small, Large, and Heavy, depend upon the maximum certificated cross takeoff weight (MCGTOW). Table 2 shows the U.S. landing radar separation standards in distance (nautical miles) for the nine pairs of aircraft classes. The corresponding separation times are also listed, assuming a nominal landing airspeed of 135 knots.

Tables 3 and 4 show the vortex hazard probabilities at minimum separation for two values of the hazard parameter f. Values less than 10^{-6} are left blank. Note that the B-707 and DC-8 vortex generators were divided into the Heavy and Large classes according to their radio calls. Note also that the following aircraft are specified by both weight class and wingspan b.

These two tables show how much the hazard probability can vary for different pairs of aircraft. The highest probabilities occur for 20-meter wingspan Large (e.g., Gulfstream II) behind the Large DC-8 and B-707 aircraft. However, this combination has occurred too infrequently in normal operations to constitute a reliable choice for a safe vortex hazard probability. The next highest probability in the tables occurs for a 30-meter wingspan aircraft following a Large DC-8. Since this size follower represents the DC-9 and B-737, this combination has occurred often enough in normal operations to represent a safe level of hazard probability. The separation safety analysis will therefore consider a separation safe if it leads to an equal or smaller hazard probability, i.e., 0.0020 for f=1.0 or 0.13 for f=0.5.

Since the current separation standards may be overly conservative, it is not possible to assess whether hazard probabilities higher than the value for a DC-9 behind a DC-8L are actually dangerous. Nevertheless, the safety level can be graded according to the hazard probability. Probabilities equal to or lower than the DC-9/DC-8L values would be considered safety level "A." Probabilities comparable to the 20-meter Large aircraft behind a DC-8L would be considered safety level "C." Probabilities in betweeen these values would be graded safety level

"B." Probabilities significantly higher than the C level would be graded safety level "D" or perhaps "F." These levels will be used in interpreting the results of the following examples.

2.5-MILE SEPARATION FOR SELECTED LARGE AND SMALL AIRCRAFT

In the mid 1980s the FAA developed a special 2.5-mile separation standard to be used at airports where the runway occupancy times are short enough to permit such separations. This separation was intended for Small aircraft and Large aircraft other than the B-757. Since the Large B-707 and DC-8 aircraft were no longer in service, the B-727 remains the largest vortex generating aircraft subject to this separation. Table 5 shows the hazard probabilities calculated for the DC-8, B-707, B-727, B-737 and DC-9 for 2.5 nm separation. The 30-meter wingspan aircraft following the last three aircraft easily meet the "A" level safe separation criterion developed above. Thus, B-737 and DC-9 aircraft would be expected to safely follow the B-727 and other B-737s and DC-9s at 2.5-mile separation. The hazard probabilities for 20-meter wingspan aircraft behind these three aircraft are at the B or C level of safety. Finally, the 10-meter wingspan aircraft following the B-727 or B-737 has a D level of safety. Note that all three aircraft sizes have safety levels of C or below behind the B-707 and DC-8 at 2.5 miles; such pairs are therefore unlikely candidates for reduced separation.

THREE-MILE SEPARATION FOR HEAVY AIRCRAFT

The safe Heavy-Heavy separation is determined by the smallest Heavy aircraft following the largest Heavy (B-747). The aircraft at the bottom end of the Heavy class (B-767, DC-8H) have wingspans in the range of 40 to 50 meters. The hazard probabilities for these aircraft behind a B-747 at three nautical miles are shown in Table 6 and are all above the "A" level probability. The 50-meter wingspan followers have a "B" level of safety and the 40-meter wingspan followers have a "C" level of safety.

DISCUSSION

This paper has illustrated a methodology for using wake vortex measurements to assess the safety of proposed new separation standards. The results were found not to depend upon the hazard parameter f. The results obtained for the two cases examined are interesting but cannot be considered definitive until the hazard and vortex decay models are more thoroughly analyzed and validated. The simplified sensitivity analysis presented in Reference 1 is a starting point for this process, but may be incorrect on some points and has not considered all the relevant issues.

Table 1. Wake Vortex Aircraft Classes: Limits on MCGTOW

Wake Vortex Class	Lower Weight Limit (lbs)	Upper Weight Limit (lbs)
Small	0	12,500
Large	12,500	300,000
Heavy	300,000	none

Table 2. Wake Vortex IFR Separation Standards at Runway Threshold

Leading Aircraft Class	Following Aircraft Class		
	Heavy	Large	Small
Heavy	4 nm, 107 sec	5 nm, 133 sec	6 nm, 160 sec
Large	3 nm, 80 sec	3 nm, 80 sec	4 nm, 107 sec
Small	3 nm, 80 sec	3 nm, 80 sec	3 nm, 80 sec

Table 3. Hazard Probability at Minimum Separation for f=1.0

Leading Aircraft	Following Aircraft						
	Heavy		Large			Small	
	b = 50m	b = 40m	b = 40m	b = 30m	b = 20m	b = 20m	b = 10m
Heavy							
B-747	3.1×10^{-6}	2.4×10^{-5}					
L-1011		1.1×10^{-5}			1.8×10^{-5}		
DC-10							
B-707H							
DC-8H							
Large							
DC-8	1.8×10^{-5}	2.5×10^{-4}	2.5×10^{-4}	2.0×10^{-3}	1.0×10^{-2}	2.2×10^{-5}	2.2×10^{-4}
B-707		2.5×10^{-5}	2.5×10^{-5}	3.0×10^{-4}	5.2×10^{-3}	5.0×10^{-6}	8.4×10^{-6}
B-727				1.2×10^{-5}	4.8×10^{-4}		
B-737				4.5×10^{-6}	3.0×10^{-4}		
DC-9					8.9×10^{-5}		

Table 4. Hazard Probability at Minimum Separation for f=0.5

Leading Aircraft	Following Aircraft						
	Heavy		Large			Small	
	b=50m	b=40m	b=40m	b=30m	b=20m	b=20m	b=10m
Heavy							
B-747	1.1×10^{-2}	2.3×10^{-2}	1.0×10^{-4}	4.3×10^{-4}	1.8×10^{-3}	1.8×10^{-4}	6.6×10^{-4}
L-1011	7.7×10^{-3}	1.9×10^{-2}	6.5×10^{-5}	3.8×10^{-4}	3.3×10^{-3}	4.1×10^{-4}	3.1×10^{-4}
DC-10	1.9×10^{-3}	5.7×10^{-3}	4.4×10^{-6}	4.4×10^{-5}	9.6×10^{-4}	7.8×10^{-5}	8.7×10^{-4}
B-707H	3.9×10^{-4}	2.3×10^{-3}		4.0×10^{-5}	5.9×10^{-4}	4.1×10^{-5}	1.3×10^{-3}
DC-8H	3.9×10^{-5}	3.1×10^{-4}			3.3×10^{-6}		
Large							
DC-8	3.1×10^{-2}	6.7×10^{-2}	6.7×10^{-2}	1.3×10^{-1}	2.3×10^{-1}	2.2×10^{-2}	5.4×10^{-2}
B-707	1.3×10^{-2}	3.4×10^{-2}	3.4×10^{-2}	6.9×10^{-2}	1.8×10^{-1}	1.3×10^{-2}	3.8×10^{-2}
B-727	2.0×10^{-3}	7.1×10^{-3}	7.1×10^{-3}	2.3×10^{-2}	8.1×10^{-2}	2.0×10^{-3}	5.1×10^{-3}
B-737	2.0×10^{-3}	7.4×10^{-3}	7.4×10^{-3}	2.7×10^{-2}	8.7×10^{-2}	2.4×10^{-3}	8.5×10^{-3}
DC-9	2.0×10^{-4}	1.1×10^{-3}	1.1×10^{-3}	1.4×10^{-2}	5.6×10^{-2}	8.7×10^{-4}	2.9×10^{-3}

Table 5. Vortex Hazard Probabilities and Safety Levels for 2.5-Nautical-Mile Separations

Leading Aircraft	Following Aircraft		
	b = 30 m	b = 20 m	b = 10 m
f = 1.0	Hazard Prob. A = 0.0020, C = 0.010		
DC-8	0.026 D	0.073 F	0.14 F
B-707	0.0074 C	0.047 D	0.11 F
B-727	0.00087 A	0.010 C	0.021 D
B-737	0.00028 A	0.0058 B	0.015 D
DC-9	0.000080 A	0.0027 B	0.0096 C
f = 0.5	Hazard Prob. A = 0.13, C = 0.23		
DC-8	0.33 D	0.45 F	0.55 F
B-707	0.23 C	0.39 D	0.50 F
B-727	0.12 A	0.25 C	0.31 D
B-737	0.13 A	0.26 C	0.35 D
DC-9	0.085 A	0.20 C	·0.27 C

Table 6. Three-Nautical-Mile Hazard Probability and Safety Level Behind the B-747

	b = 40 m	b = 50 m
f = 1.0	0.011 C	.0041 B
f = 0.5	0.23 C	0.17 B

Burnham, D.C. and Hallock, J.N., "Chicago Monostatic Acoustic Vortex Sensing System Volume IV: Wake Vortex Decay," Report No. DOT/FAA/RD-79-103, IV, DOT Transportation Systems Center, Cambridge MA 02142, July 1982, Chapter 6. (Please note interchange of Figures 21 and 22 in this report and reversed vortex labels on Figure 40.)

Burnham, D.C. and Hallock, J.N., "Chicago Monostatic Acoustic Vortex Sensing System Volume IV: Decay of B-707 and DC-8 Vortices," Report No. DOT/FAA/RD-79-103, II, DOT Transportation Systems Center, Cambridge MA 02142, September 1981, Chapter 4. See also Chapter 4 of Reference 1.

Burnham, D.C. and Hallock, J.N., "Chicago Monostatic Acoustic Vortex Sensing System Volume IV: Decay of B-707 and DC-8 Vortices," Report No. DOT/FAA/RD-79-103, II, DOT Transportation Systems Center, Cambridge MA 02142, September 1981, Chapter 4. See also Chapter 4 of Reference 1.

Burnham, D.C., "B-747 Vortex Alleviation Flight Tests: Ground-Based Sensor Measurements," Report No. DOT-FAA-RD-81-99, DOT Transportation Systems Center, Cambridge MA 0-2142, February 1982, Appendix B.

WAKE VORTEX PROGRAM FOR CROSS-VORTEX ENCOUNTERS AT LAGUARDIA AIRPORT[1]

William R. Eberle
Lockheed Missiles & Space Co.
P. O. Box 070017
Huntsville, AL 35807

Archie E. Dillard
Mike Monroney Aeronautical Center
P. O. Box 25082
Oklahoma City, OK 73125

INTRODUCTION

One of the primary runway configurations for LaGuardia Airport is departure on Runway 31 and landing on Runway 22. This runway configuration is shown in Figure 1. Because of wake vortex considerations, the FAA enforces the standard 3/4/5/6 n.mi. vortex separations between a heavy[2] aircraft departing on Runway 31 and a landing aircraft on Runway 22. Thus, when aircraft separations are established by IFR control, when a heavy take-off aircraft on Runway 31 crosses the intersection, any large aircraft landing on Runway 22 must be five miles from the intersection. As discussed in Reference 1, the capacity of LaGuardia Airport is significantly degraded by this spacing requirement.

A study was initiated to determine if a rationale for eliminating the additional spacing imposed by wake vortex considerations of Runway 31 aircraft could be developed. If such a rationale were developed, aircraft performing IFR landings on Runway 22 would maintain normal separations for landing aircraft without consideration of the type of aircraft departing on Runway 31. The initial approach to developing such a rationale was to analyze vortex transport and

---

[1] The work described in this paper was sponsored by the Port Authority of New York and New Jersey under contract to Lockheed Missiles & Space Co. Simulation of cross-vortex encounters in the Boeing 727 simulator was conducted by the Federal Aviation Administration.

[2] Heavy aircraft are aircraft having a maximum gross take-off weight exceeding 300,000 pounds. Large aircraft are aircraft having a maximum gross take-off weight of greater than 12,500 pounds, but less than 300,000 pounds.

demise to determine if vortex encounters could be avoided. The initial study showed that vortex encounters would be very rare, but could not be completely avoided. The second approach was to demonstrate that aircraft response to a cross-vortex encounter is significantly different from aircraft response to an in-trail encounter and to demonstrate that a cross-vortex encounter is innocuous for transport category aircraft. Therefore, in the rare conditions for which a cross-vortex encounter would be experienced by a landing aircraft, it would not be hazardous to that aircraft. The innocous behavior of a cross-vortex encounter was verified by a scientific simulation of cross-vortex encounters by Boeing 727 and deHavilland DHC-7 aircraft. These aircraft were selected for simulation because they represent large jet transport aicraft and commuter aircraft, respectively, and have significant use at LaGuardia. Verification of the innocuous nature of cross-vortex encounters by use of moving base simulators for Boeing 727 and deHavilland DHC-7 aircraft is planned for the next few months.

VORTEX TRANSPORT AND DEMISE

The first approach to addressing the vortex problem at LGA was an attempt to demonstrate that vortex encounters would not occur for the runway configuration of interest. This was done with a Monte Carlo simulation of vortex generation, vortex transport, and vortex demise. A mix of fourteen aircraft types, ranging from the BAC 111 to the Lockheed L-1011 and apportioned as they are used at LGA, was used for the simulation. Aircraft take-off weight for each Monte-Carlo take-off was randomly selected for the aircraft type between a minimum (empty weight plus 25% of the difference between empty and maximum gross weights) and maximum gross take-off weight for LGA[3]. Take-off aircraft altitude at the intersection was calculated from the randomly-selected take-off weight, and this was used as the initial conditions for vortex transport and demise calculations. Cross-wind was randomly selected from a normal distribution given by a selected mean and standard deviation. Vortex demise times were selected from the distribution given in Reference 2, based on data measured at Heathrow.

From the Monte-Carlo simulations, a distribution of vortex strengths and positions was generated. Figure 2 shows the distribution of vortex positions 60 seconds after take-off aircraft passage. Figure 3 shows the distribution of vortex strengths of vortices remaining after 60 sec. The distribution in vortex strength is due to a distribution in aircraft take-off weight in the Monte Carlo simulation. Figure 4 shows the vortex positions of vortices remaining after 60 seconds. The 3 degree glideslope is shown for reference. Vertical and horizontal scales are different. Figure 5 shows vortex position 90 seconds after take-off, and Figure 6 shows vortex position 120 seconds after take-off. Because heavy generator aircraft were the aircraft of primary interest, Figures 7, 8, and 9 show vortex position for heavy aircraft only.

One of the interesting aspects of these figures is that for a given mean wind speed, the maximum vortex transport does not increase as time increases. For a given distribution of crosswind, the greater values of crosswind are the values which give the greater transport distance at 60 sec.

---

[3] For wide body aircraft, take-off weight at LaGuardia is limited by capacity of the runway decks. The maximum weights used were those appropriate for LaGuardia.

However, the greater value of crosswind also is more likely to cause early vortex death. Hence, for a given mean value of crosswind, the maximum transport distance does not increase significantly with time.

These results show that vortex encounters cannot be avoided, and therefore there is no rationale for reduced separations based upon vortex avoidance. However, such encounters will be very rare. The next aspect of the study was directed toward demonstration that when the rare vortex encounters occur, they present no hazard to aircraft landing on Runway 22.

VORTEX ENCOUNTER SIMULATIONS BY SCIENTIFIC SIMULATION

Because vortex encounters could not be completely avoided, the second aspect of the program was based upon the observation that a cross-vortex encounter, such as that encountered for the Runway 31 takeoff-Runway 22 landing configuration at LGA, is completely different than the in-trail encounter for which the separation standards were developed. The premise of the second part of the study was that the difference was of such a significance that a cross-vortex enounter would be innocuous. This premise was based on two observations: (1) the angular response would be in pitch rather than in roll and the moment of intertia of the aircraft is much greater in pitch than in roll and (2) exposure time would be much less for a cross-vortex encounter than for an in-trail encounter. Therefore, a scientific simulation of the encounter was generated to demonstrate that the vortex encounter was innocuous. Figure 10 shows the cross-vortex encounter geometry with an indication of the distance that the aircraft travels in 0.5 seconds.

The simulation was a three degree-of-freedom (longitudinal direction, vertical direction, and pitch angle) dynamic simulation which calculated the velocity and position in both the longitudinal and vertical axes and angular acceleration, angular velocity, and angular position in pitch. In addition, angle of attack and relative velocity at the wing are also calculated. The plots show only the most significant parameters: aircraft flight path, vertical component of aircraft velocity, vertical acceleration, and pitch angle. The simulation starts 300 feet before vortex encounter and continues to 300 feet after vortex encounter, although the first 100 feet of flight are not shown in the figures.

Figure 11 shows the Boeing 727 flight path angle, vertical velocity, vertical acceleration, and pitch angle for an encounter with a vortex strength of 4900 ft²/sec, which is based on the theoretical vortex strength of a DC-10 at take-off speed and maximum gross weight for LaGuardia. This is somewhat conservative since measurements have shown the actual vortex strength to be somewhat smaller. For Figure 11, the initial altitude of the aircraft has been fixed so that the aircraft center of gravity would pass ten feet over the vortex axis if the vortex strength were very small. The effect of the vortex causes the aircraft to pass 12.6 feet over the vortex. The nominal flight path of the aircraft is a straight line 3-deg glideslope. The nominal flight path is not shown. However, at the right side of the plot, the aircraft altitude is 51.5 feet and the altitude of an aircraft with no vortex is 54.5 ft. Therefore, the presence of the vortex causes a loss of 3 feet of altitude in 600 feet of flight. Figure 12 shows similar results with the aircraft passing 10 feet below the vortex, and Figure 13 shows results with the aircraft passing 25 feet below the vortex

The most significant effect of the vortex encounter is the significant vertical acceleration and the significant change in vertical acceleration. The maximum vertical acceleration experienced during the encounter is shown as a function of vertical spacing from the vortex core in Figure 14. When the aircraft passes above the vortex, as the aircraft approaches the vortex, it experiences an updraft and a loss of airspeed. These two effects combine to produce a small vertical acceleration on the aircraft. However, after the aircraft passes the vortex, it experiences a downdraft and loss of airspeed. Each of these effects causes a loss of lift, and the net effect is a significant downward acceleration. This effect causes the acceleration profile shown in Figure 10. However, the duration of the large negative acceleration is very short, lasting approximately 0.15 sec.

There are three simplifying assumptions in the simulation, all of which are "conservative" in the sense that they predict a greater aircraft acceleration than that for the actual aircraft. First, the simulation has used a rigid wing. For a flexible wing in a short duration gust, the initial acceleration would cause an upward deflection of the wind, rather than an acceleration of the entire aircraft. Therefore, the fuselage acceleration would be less than that shown. Second, the vortex core is smaller than the wing chord, but the simulation assumes that the entire wing is immersed in a flow field described by that at the wing center of lift. This means that if at a given time the center of lift is located at the edge of the vortex core, lift is calculated as if the entire wing is immersed in air with that velocity. Therefore, the magnitude of the gust which the aircraft experiences is overestimated, and the lift generated by the wing near the vortex core is overpredicted. Third, it is assumed that the aircraft has no effect on the vortex. In fact, the aircraft wing would actually tend to suppress the vortex.

The simulation was repeated for a smaller aircraft, the deHavilland DHC-7. The results are shown in Figures 15, 16, and 17. Vertical displacements are significantly larger than for the B-727 because of the slower landing speed (and greater exposure time to significant accelerations) for the DHC-7. For example, a Boeing 727 landing at 135 knots would require 0.18 seconds to traverse a 40 ft diameter vortex, whereas a DHC-7 landing at 75 knots would be exposed to the same vortex for 0.32 seconds. Pitch excursions are greater for the DHC-7 because of the greater exposure time and because of the much smaller moment of intertia in pitch for the DHC-7.

The conclusion of these simultions is that a cross-vortex encounter does not present any situation which could be considered as hazardous to the aircraft. The large magnitude of vertical acceleration may produce some discomfort, but this effect would be somewhat mitigated when the effects of a flexible airframe were considered. The acceleration-time curve of the most severe cross-vortex encounter approximates that of a normal hard landing. This analysis does not imply that all aircraft will experience these accelerations. The altitude versus range plots show that vortex encounters will be rare. For the normal encounter, the aircraft will pass under the vortex at a distance of 25 feet to 40 feet. The normal vortex encounter will be during flare or after touchdown. This section shows that when the rare close vortex encounters occur, they do not produce a hazardous condition for the landing aircraft.

VORTEX ENCOUNTER SIMULATIONS BY MOVING-BASE FLIGHT SIMULATOR

The scientific simulation produces accelerations and pitch excursions which the author (a licensed pilot) believes are manageable. However, a simulation on a moving base simulator was deemed to be required for two reasons: (1) independent verification of the scientific simulation results and (2) assessment by operational airline pilots of the effects of a cross-vortex encounter. For this reason, the cross-vortex encounter was programmed into the Boeing 727 simulator at the FAA Academy in Oklahoma City. The simulator to be used is a B-727-200-JT8D-15 simulator owned by the FAA and manufactured by CAE Electronics, LTD. of Montreal, Canada. It is a six axis digital flight simulator and is equipped with a Rediffusion SP-1 visual system. The visual display for the simulator has the capability for displaying the approaches for many commercial airports in the United States, including the Runway 22 approach for LGA. Ceiling and visibility are selectable by the test operator. Figure 18 shows a photograph of the FAA 727 simulator.

The cross-vortex encounter geometry to be flown in the simulator is shown in Figure 19. The vortex positions to be used in the simulation are shown in Figure 20. Each pilot will fly at least two approaches with the vortex at each of the six positions shown in Figure 20. The vortex altitude of 60 feet is the theoretical descent altitude for vortices generated by DC-10 and L-1011 aircraft. The 52 foot aircraft altitude at the threshold is the nominal altitude of the glideslope at the threshold. Vortex positions have been selected for the glideslope to pass through the vortex axis, 15 feet above and below the vortex axis, and 30 feet above and below the vortex axis. These conditions allow for a distribution of vortex positions along Runway 22.

Except for the description of the vortex, the development of the moving base simulation (equations of motion and definition of aircraft dynamics) has been independent of the scientific simulation. The FAA 727 simulator uses an aerodynamics package provided by Boeing, and actual aircraft parameters are used.

The programming of the 727 simulator has been completed, and the vortex encounter simulation has been flown by several people, including a former Eastern Airlines captain, a Trump Shuttle captain, and a private pilot (author of this paper). All have landed successfully with no problems after the cross-vortex encounter. An initial assessment of vertical accelerations and pitch excursions experienced in the simulator has shown them to be very close to those predicted in the scientific simulation. The official assessment program with approximately 18 airline pilots will be completed in the fourth quarter of 1991. Table 1 shows the evaluation form which will be used for pilot evaluation. The primary purpose of the assessment program is to determine if the accelerations and pitch excursions are acceptable to airline pilots and passengers.

Plans have been initiated for a similar simulator test program using the Flight Safety DHC-7 simulator in Toronto. Programming of the DHC-7 simulator has not yet been initiated.

FUTURE PLANS

Immediate future plans include completion of an official pilot assessment of the cross-vortex encounter on the FAA Boeing 727 simulator and a similar program of pilot assessment on the Flight Safety DHC-7 simulator.

Ostensibly, a flight test program would be desirable, but it will be very difficult to accomplish, especially at high altitude. A flight test program with an A-4 penetrator aircraft was attempted in September of 1990, but the vortex could not be located. However, there are several difficulties with such a program if the vortex could be located. Since the A-4 is a small aircraft with a small moment of inertia in pitch, its pitch characteristics are much different from those of transport category aircraft. The aerodymamic characteristics of an encounter at low altitude are difficult to emulate from a flight test at high altitude. Near the surface, the vortices separate as a result of transport in ground effect, and the encounter aircraft will encounter only one vortex, while a flight test program at altitude has no method of separating the vortices, and a test aircraft would encounter both vortices of the pair.

It is likely that there will be some vortex measurements at LaGuardia, either by a laser Doppler velocimeter or by an anemometer array. The exact nature of these measurements has not yet been defined.

At the conclusion of the Boeing 727 and DHC-7 simulator programs, the program results will be reviewed and a path toward reduced separations, based on all data accumulated to that point, will be defined.

CONCLUSIONS

LaGuardia is an airport which is operating very near its capacity with the expectation that air traffic to the airport will increase significantly over the next few years, and the use of heavy aircraft will increase. The vortex spacing required at the intersection for the Runway 31 departure-Runway 22 landing configuration at LaGuardia causes a significant decrease in airport capacity with the concommitant increase in aircraft delay. The spacing standards currently in use for the intersecting runway condition have been developed for in-trail encounters, whereas the condition at LaGuardia is a cross-vortex condition.

The vortex geometry at LaGuardia has been examined, and it has been determined that vortex encounters by aircraft landing on Runway 22 can occur, although they will be very rare. A scientific simulation of a cross-vortex encounter has shown that such encounters produce effects which are easily manageable for Boeing 727 landing aircraft. Preliminary results obtained from the FAA 727 moving base simulator confirm this conclusion, although a more comprehensive assessment program is planned. For the DHC-7 aircraft, pitch excursions are significantly greater than they are for the Boeing 727. Assessment by airline pilots in a moving base simulation will be required to determine if such pitch excursions are acceptable.

Table 1.

Date_____   Time_____

Pilot Number_____   Total B-727 Flight Time _____hours

Total Flight Time_____hours   Total Instrument _____hours (est.)

Airline _____   Captain _____ F/O _____

---

1. What was your first reaction to the wind disturbance (please circle the appropriate number)

| 1 | 2 | 3 | 4 | 5 | 6 | 7 | 8 | 9 | 10 |

Dismissed as minor turbulence   No significant cause for concern   Had some cause for concern   Significant concern over safe completion of landing

---

2. For your first approach, what was your perception of the probability of a safe landing?

| 1 | 2 | 3 | 4 | 5 | 6 | 7 | 8 | 9 | 10 |

Safe landing never in doubt   Some doubt about safe landing from encounter to touchdown   Doubt about safe landing, but safe go-around possible   Reasonably certain neither safe landing nor safe go-around was possible

---

3. Were you able to make any assessment of the cause of the disturbance?
   a. Wind shear
   b. Thermal activity
   c. Wake turbulence
   d. Other (please specify)
   e. No idea

---

4. What was your perception of the probability of a safe landing after several approaches?

| 1 | 2 | 3 | 4 | 5 | 6 | 7 | 8 | 9 | 10 |

Safe landing never in doubt   Some doubt about safe landing from encounter to touchdown   Doubt about safe landing, but safe go-around possible   Reasonably certain neither safe landing nor safe go-around was possible

---

Table 1. (continued)

5. What do you think would be the perception and/of concern of the passengers?

| 1 | 2 | 3 | 4 | 5 | 6 | 7 | 8 | 9 | 10 |

Little or no notice by passengers

Some concern by inexperienced passengers

Some concern by experienced passengers

Serious concern by experienced passengers

---

6. How do you think that experienced passengers would compare a vortex encounter with other experiences of flight such as turbulence, hard landings, short field landings, approaches to IFR minimums, etc.

| 1 | 2 | 3 | 4 | 5 | 6 | 7 | 8 | 9 | 10 |

Much less significant than other experiences

Somewhat less significant than other experiences

Somewhat more significant than other experiences

Greatly more significant than other experiences

---

7. Did any of the approaches stand out as being particularly severe? If so, please identify the approach and tell why you thought that it was particularly severe.

8. Given that these enounters will be rare at LGA, what can be done to properly prepare pilots for it?
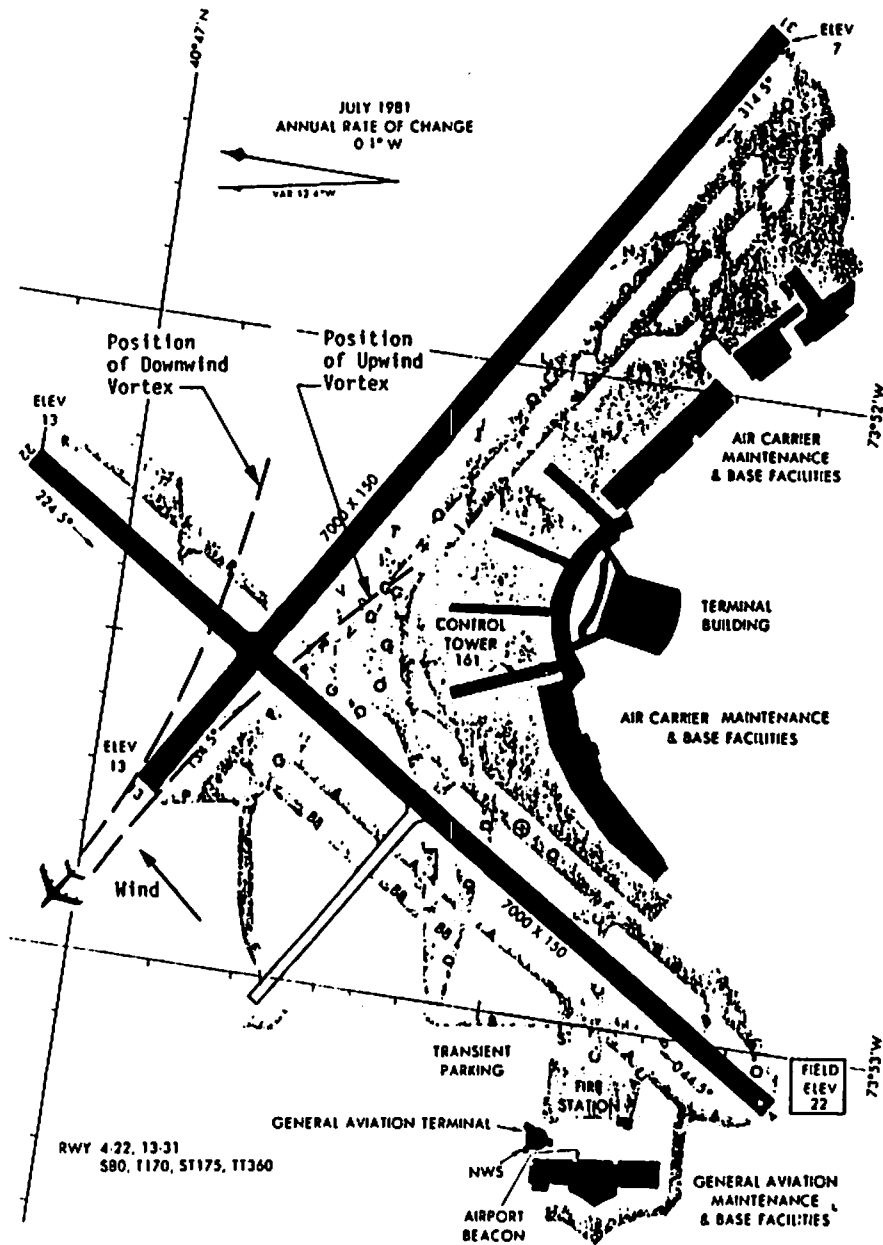
9. Any additional comments

Figure 1. LaGuardia Airport diagram showing position of vortex pair from heavy aircraft departing on Runway 31.
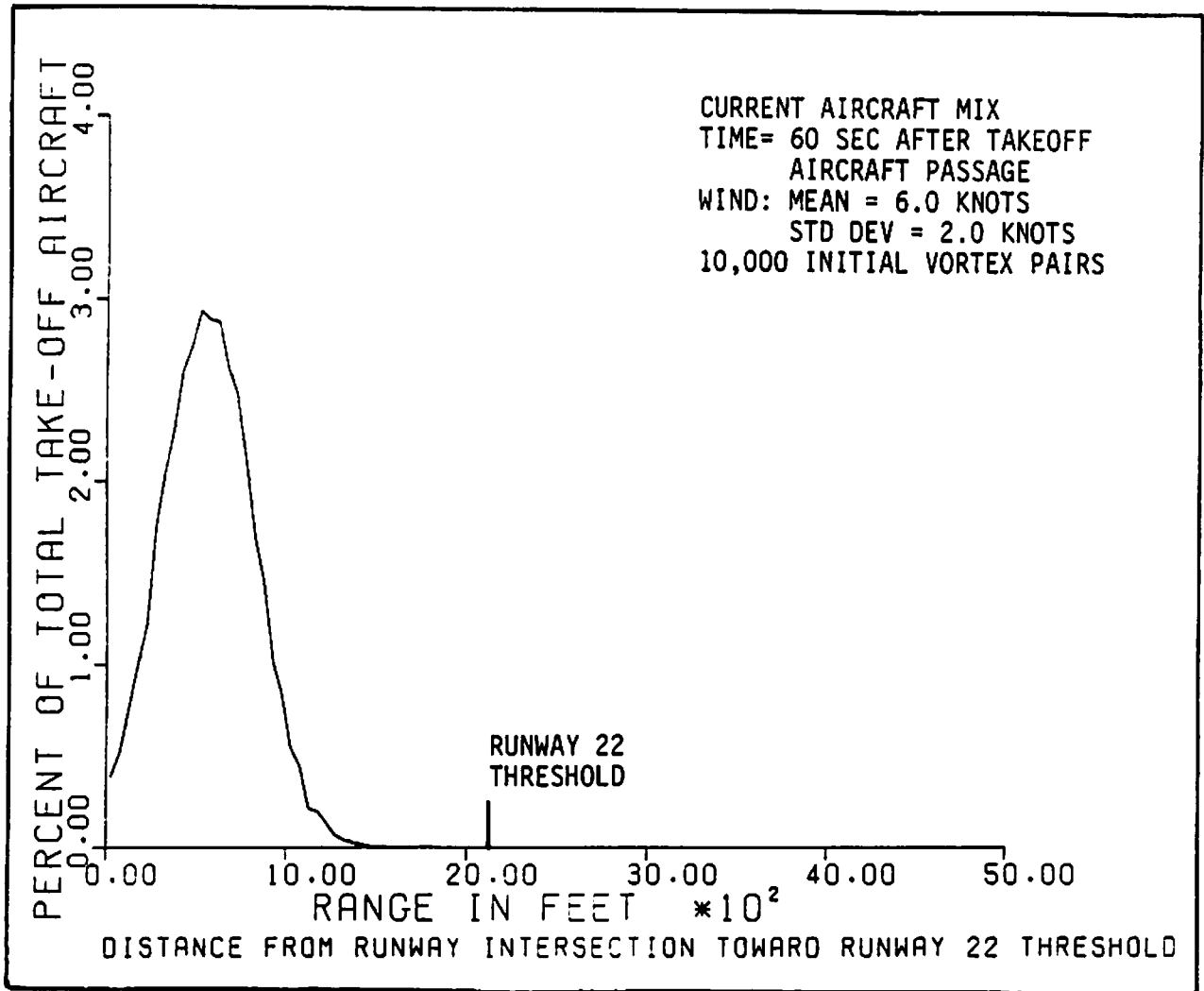
Figure 2. Probability density function of vortex location on Runway 22 at 60 sec after takeoff aircraft passage.
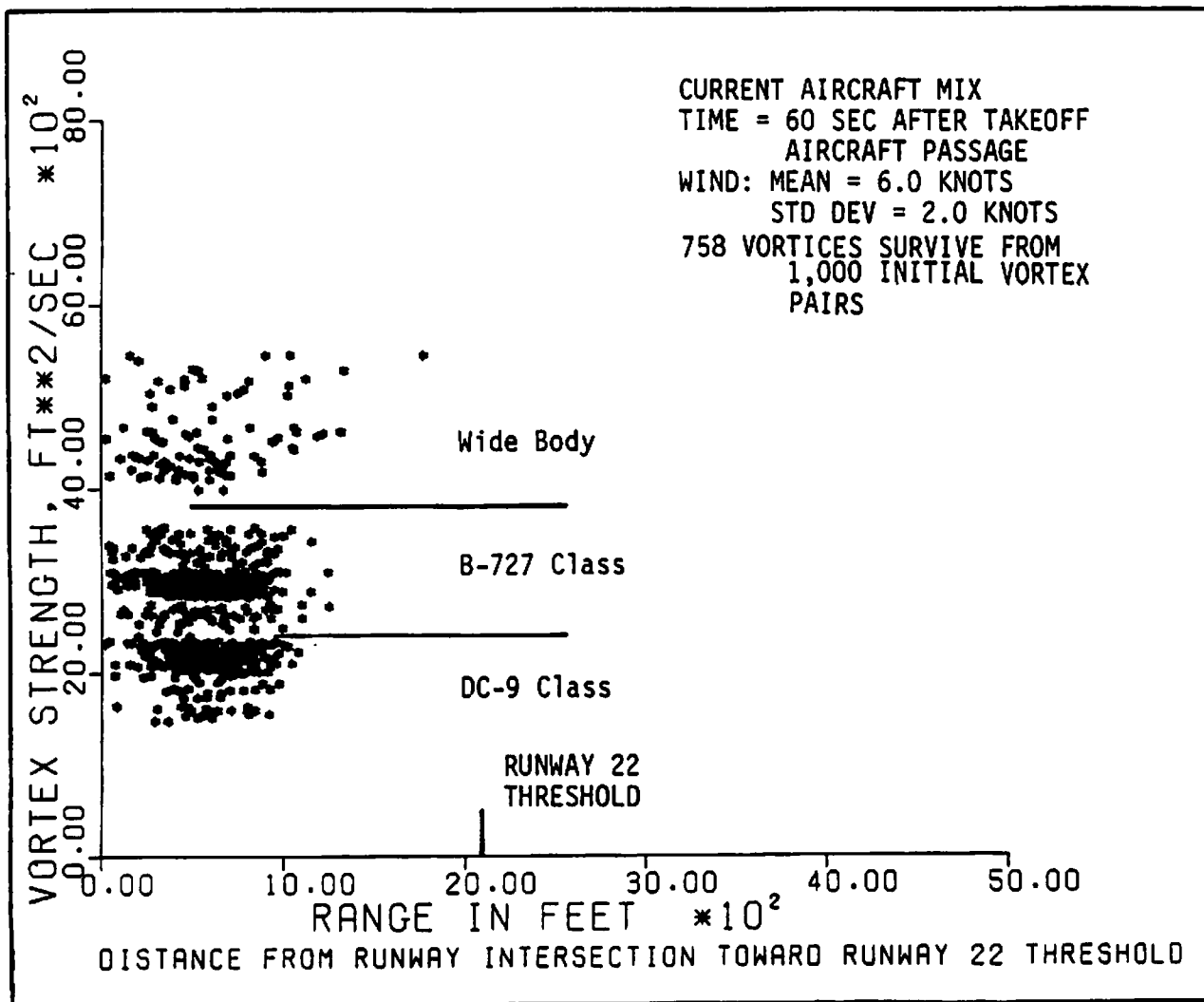
Figure 3. Scatter diagram of vortex strength on Runway 22 at 60 seconds
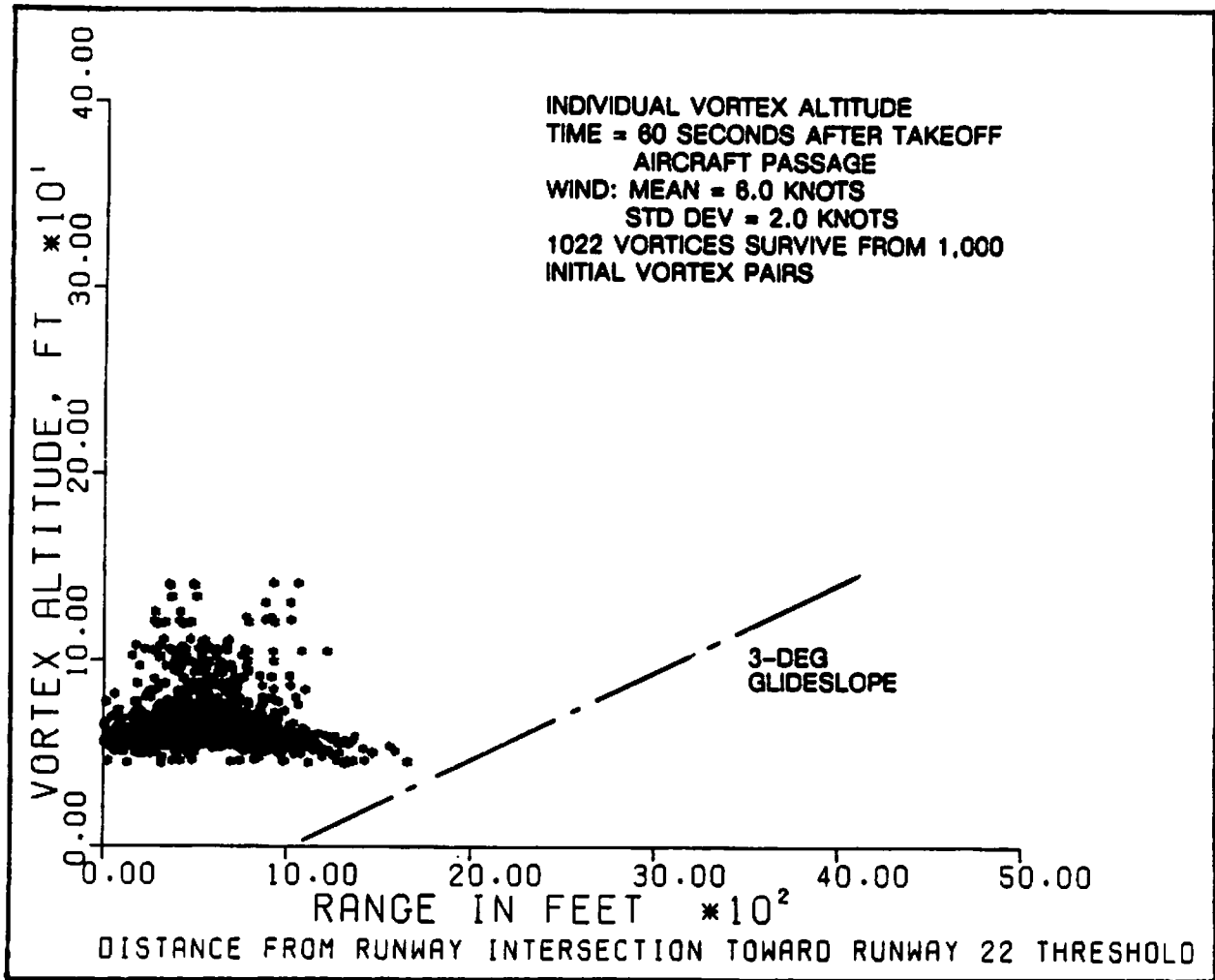after takeoff aircraft passage.

Figure 4. Scatter diagram of vortex position along Runway 22 at 60 seconds after take-off aircraft passage.
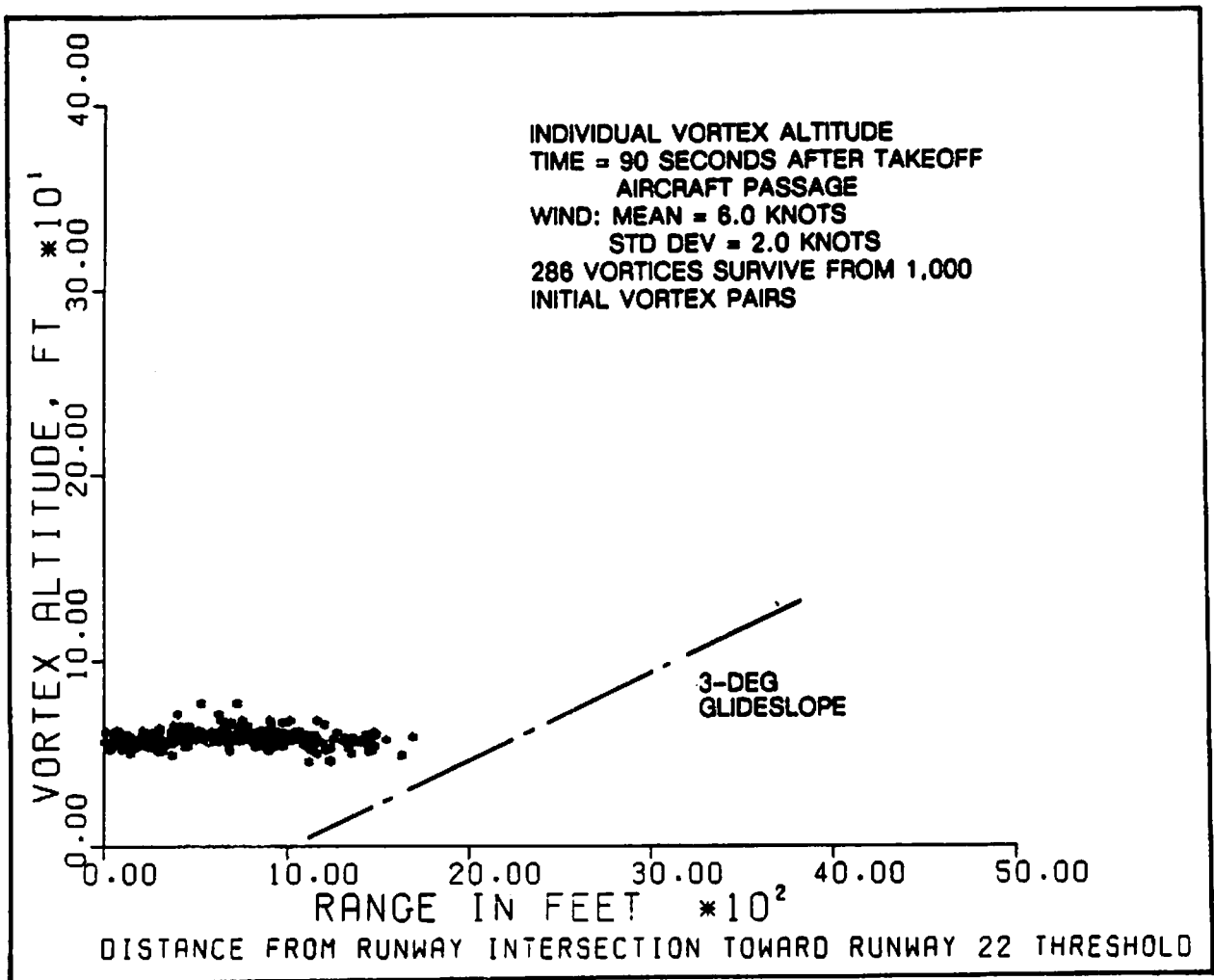
Figure 5. Scatter diagram of vortex position along Runway 22 at 90 seconds after take-off aircraft passage.
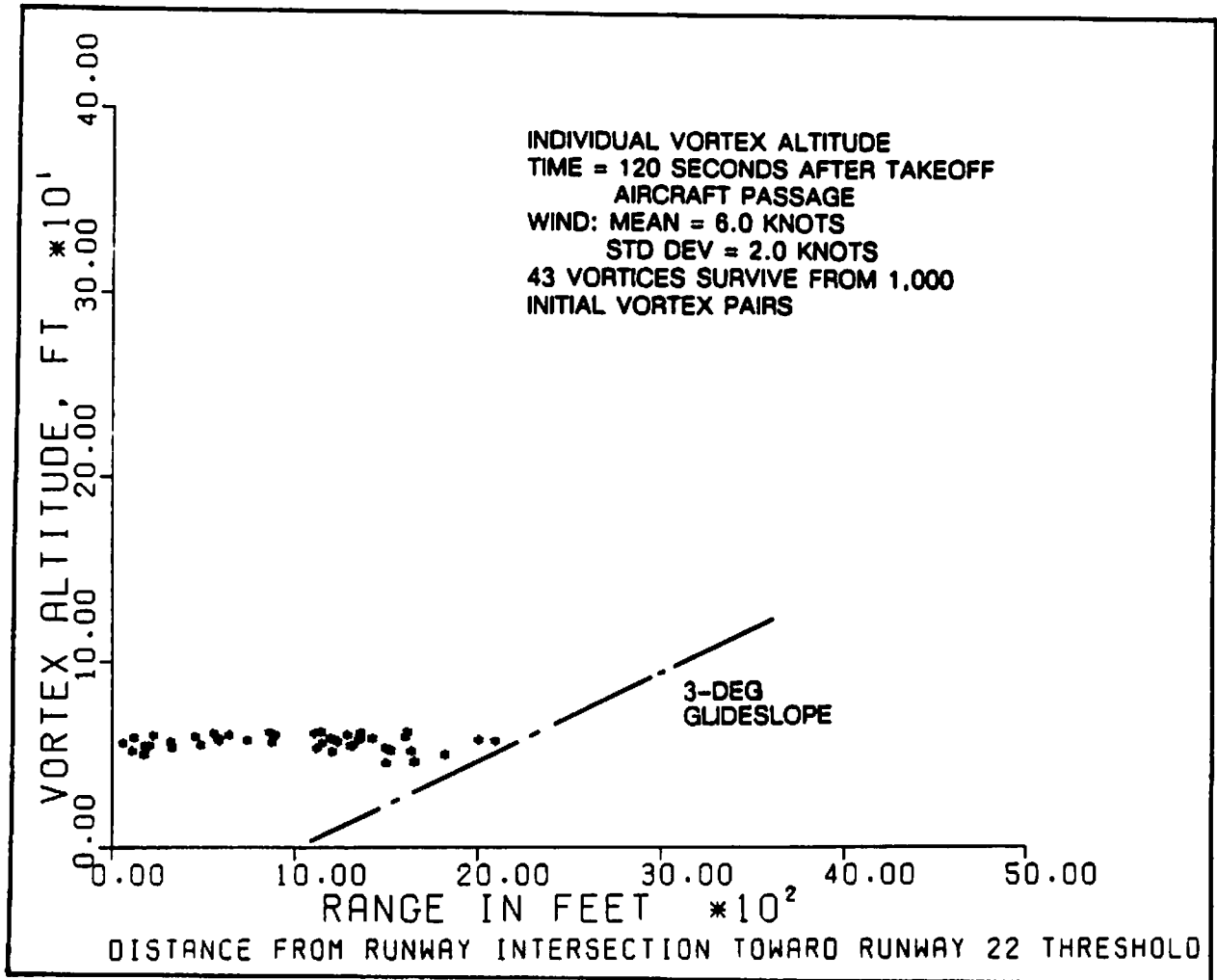
Figure 6. Scatter diagram of vortex position along Runway 22 at 120 seconds after take-off aircraft passage.
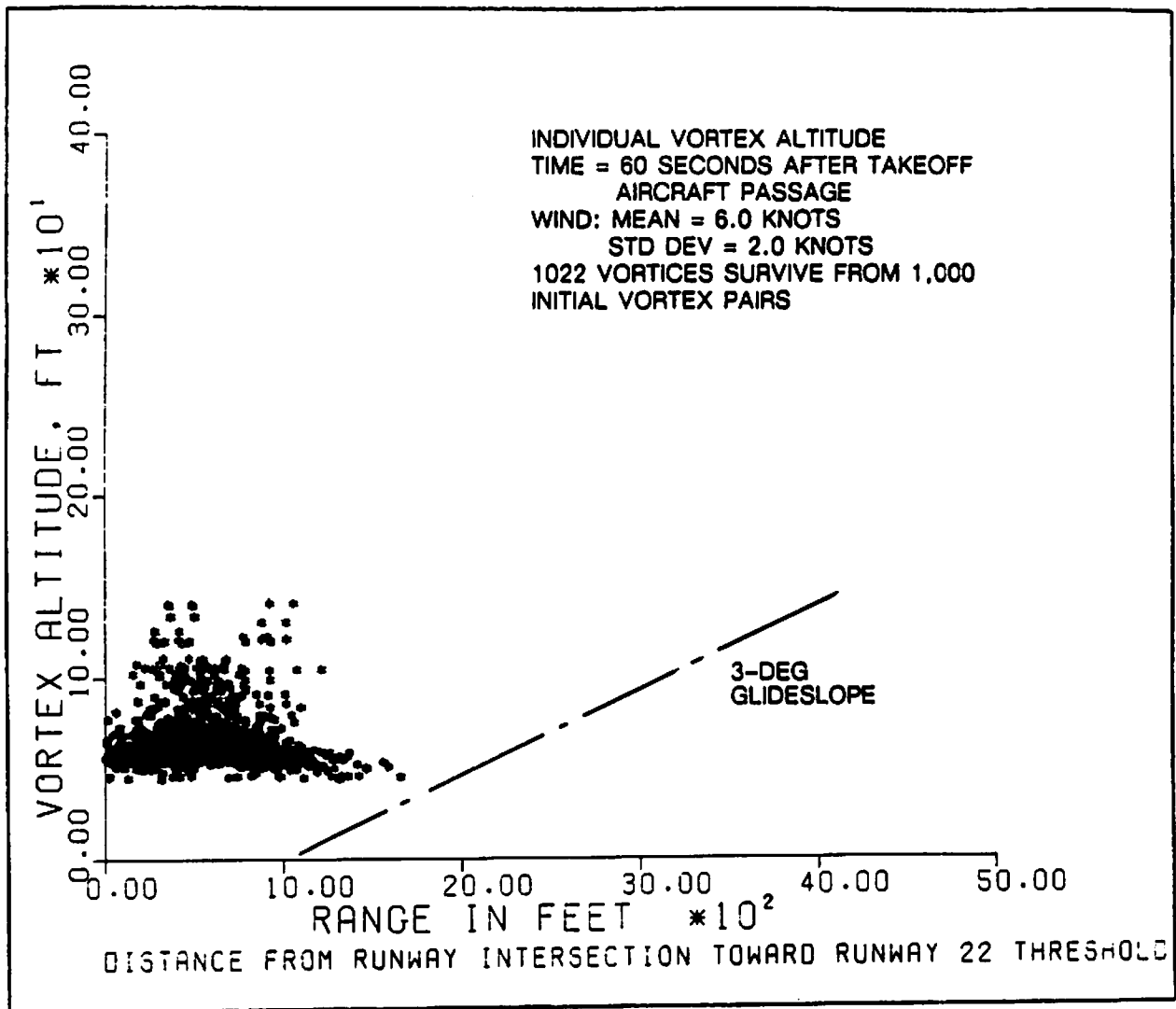
Figure 7. Scatter diagram of vortex position along Runway 22 at 60 seconds after take-off aircraft passage for heavy aircraft departures.
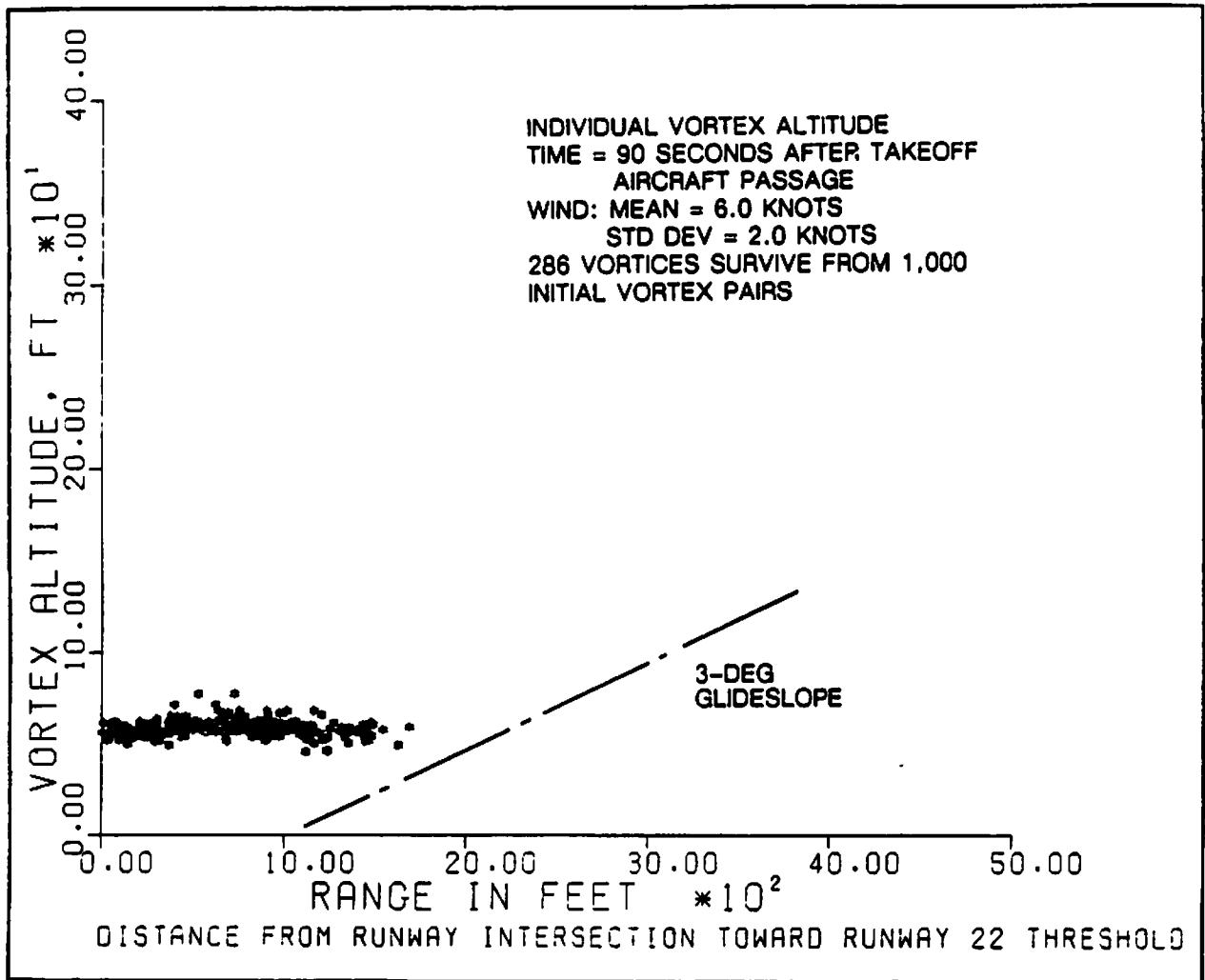
Figure 8. Scatter diagram of vortex position along Runway 22 at 90 seconds after take-off aircraft passage for heavy aircraft departures.
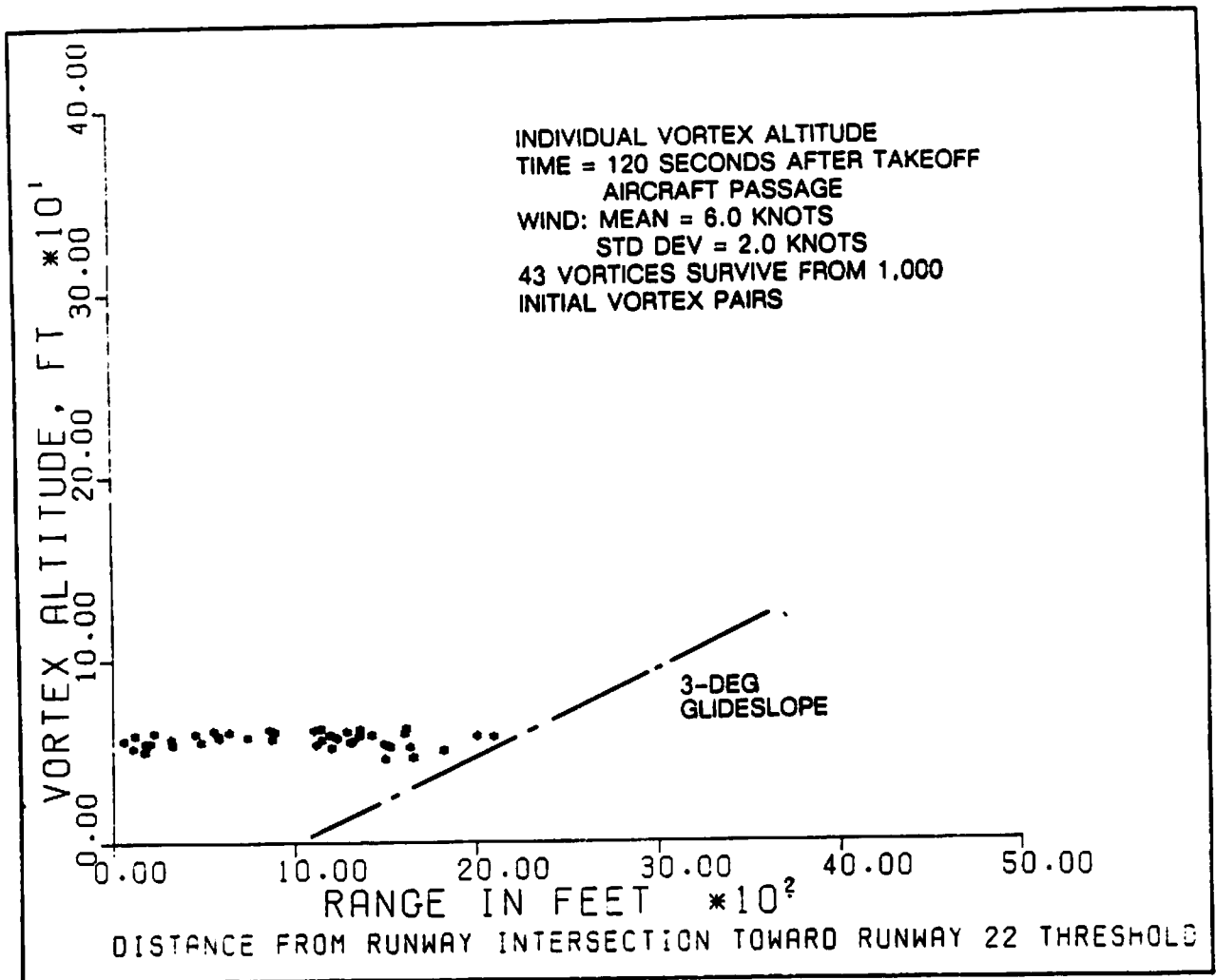
Figure 9. Scatter diagram of vortex position along Runway 22 at 120 seconds after take-off aircraft passage for heavy aircraft departures.
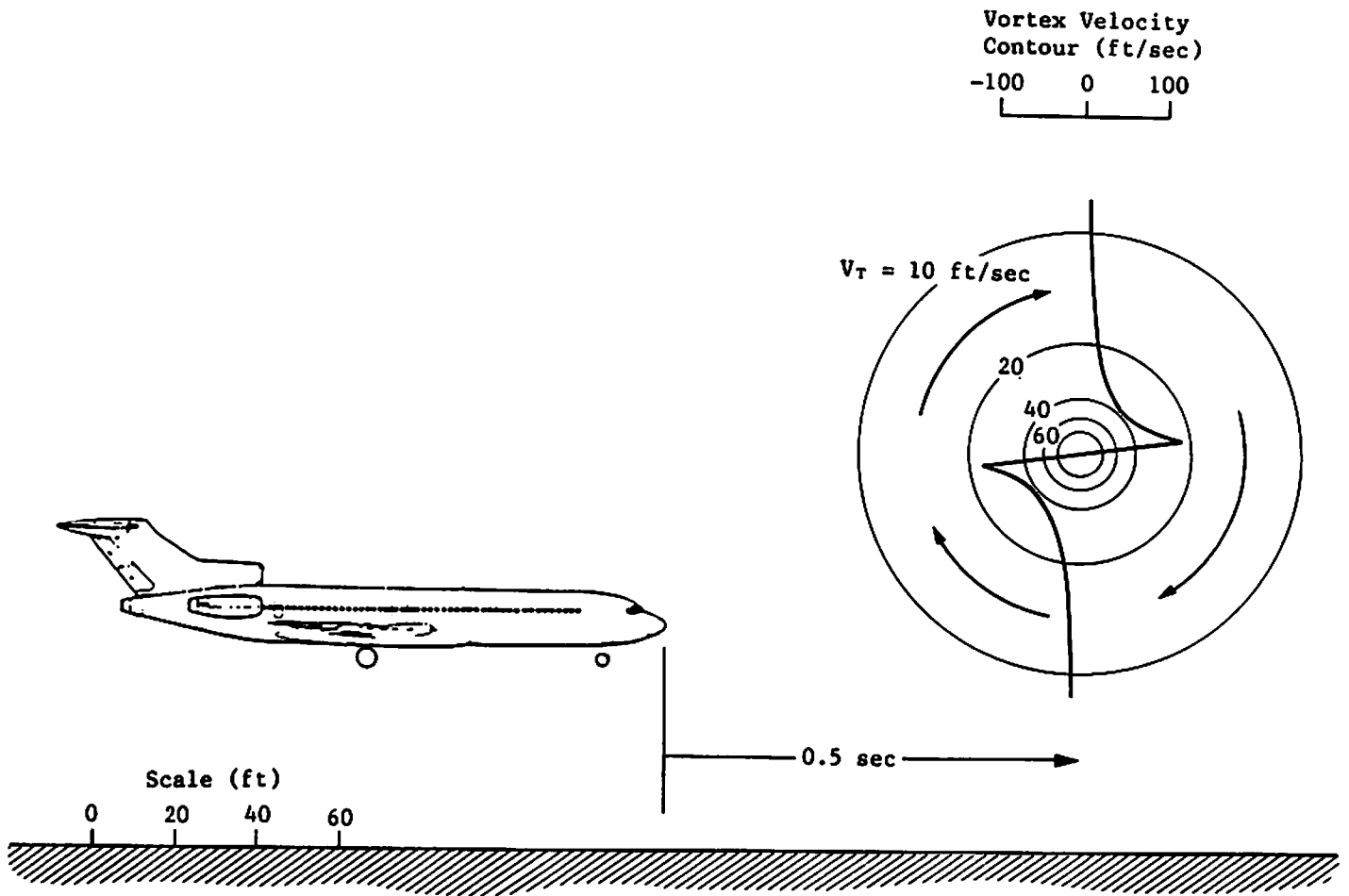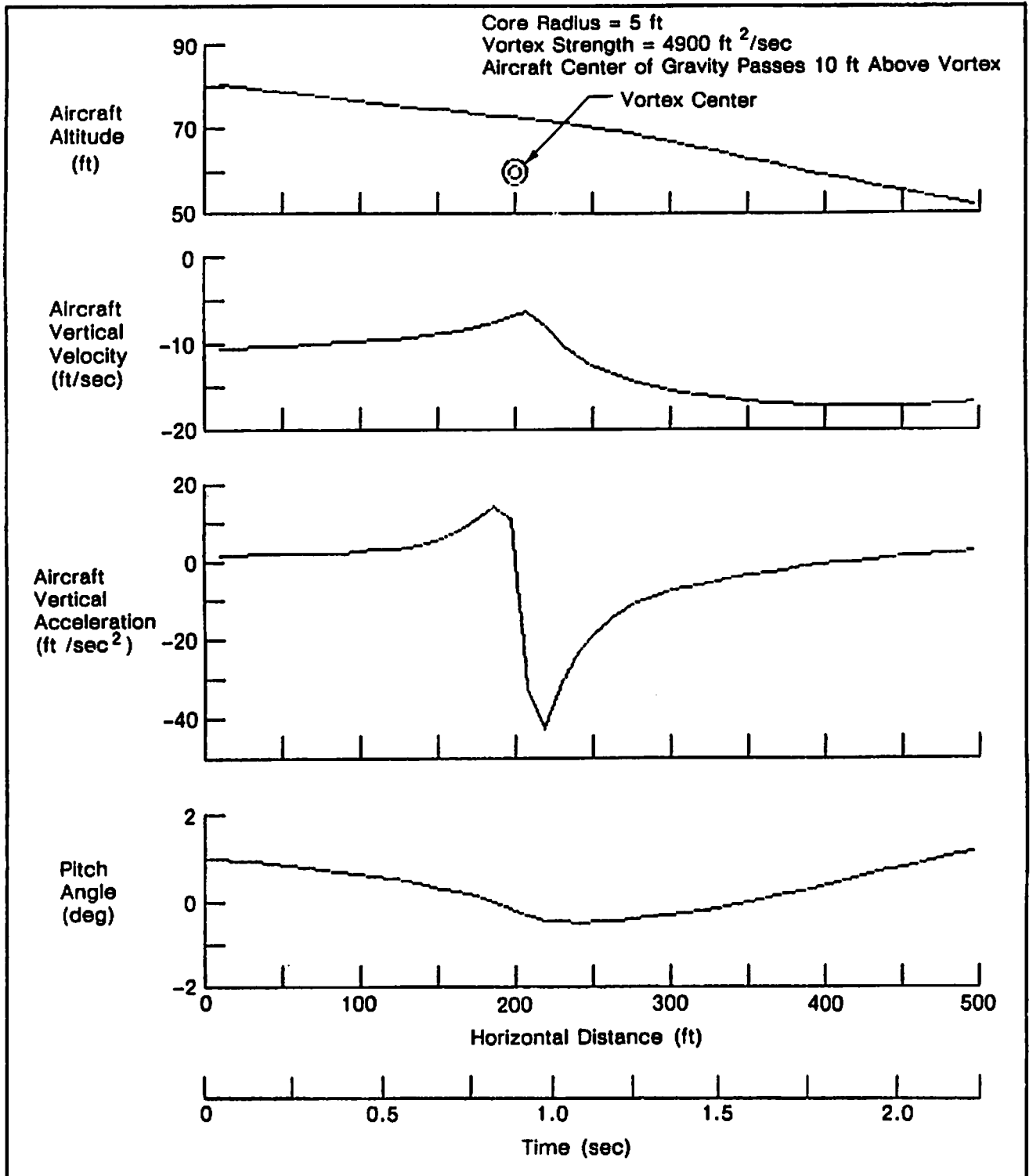
Figure 10. Geometry of cross-vortex encounter.

Figure 11. Response of a Boeing 727 to a cross-vortex encounter when the nominal aircraft flight path passes 10 feet above the vortex core.
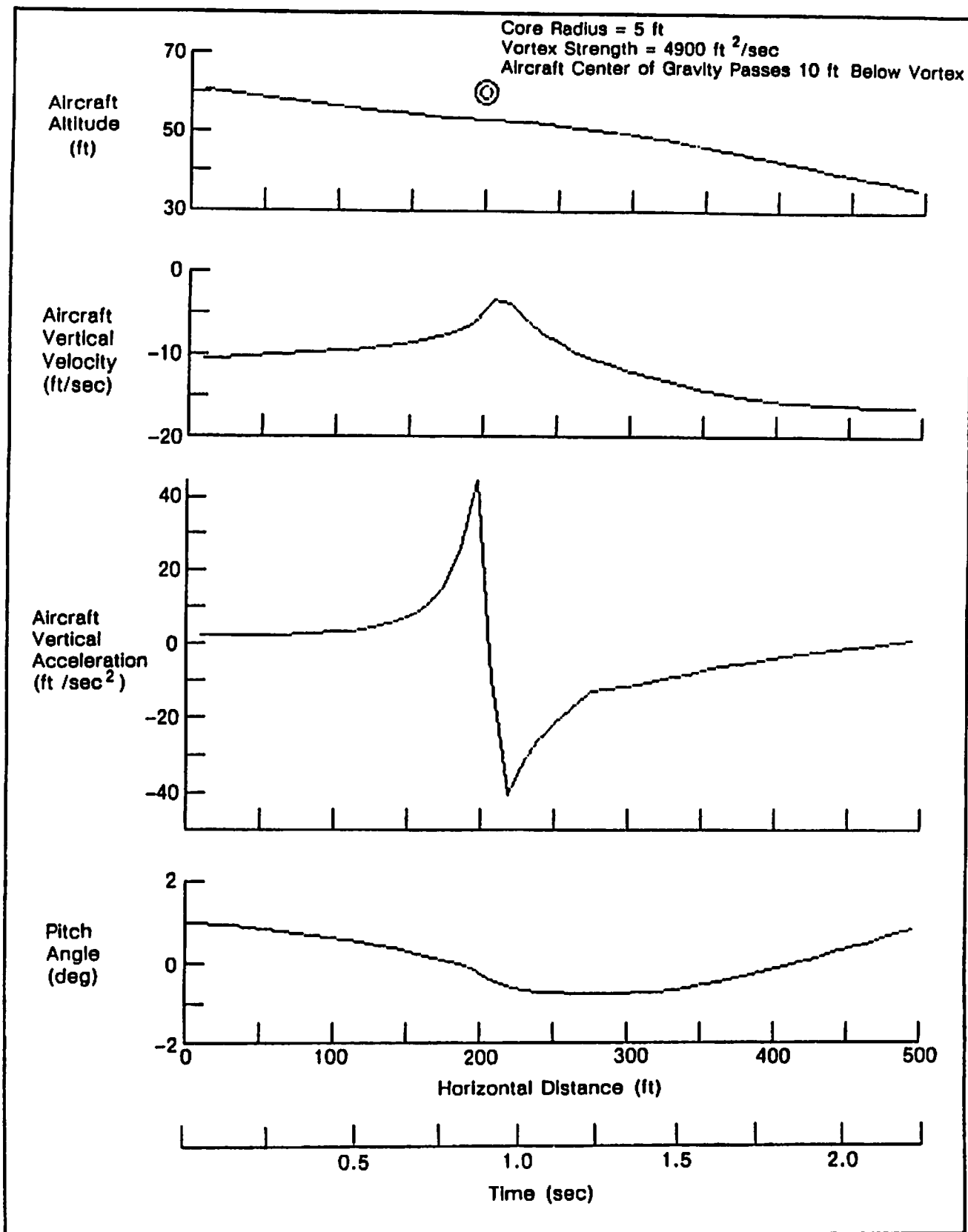
Figure 12. Response of a Boeing 727 to a cross-vortex encounter when the nominal aircraft flight path passes 10 feet below the vortex core.

Figure 13. Response of a Boeing 727 to a cross-vortex encounter when the nominal aircraft flight path passes 25 feet below the vortex core.

Figure 14. Maximum vertical acceleration during vortex encounter for a Boeing 727 aircraft.

DHC-7 CROSS-VORTEX ENCOUNTER

Core Radius = 5 ft
Vortex Strength = 4900 ft ^{2}/sec
Aircraft Center of Gravity Passes 10 ft Above Vortex

Vortex Center

Aircraft Altitude (ft)

Aircraft Vertical Velocity (ft/sec)

Aircraft Vertical Acceleration (ft /sec^2)

Pitch Angle (deg)

Horizontal Distance (ft)

Time (sec)

Figure 15. Response of a deHavilland DHC-7 to a cross-vortex encounter when the nominal aircraft flight path passes 10 feet above the vortex core.
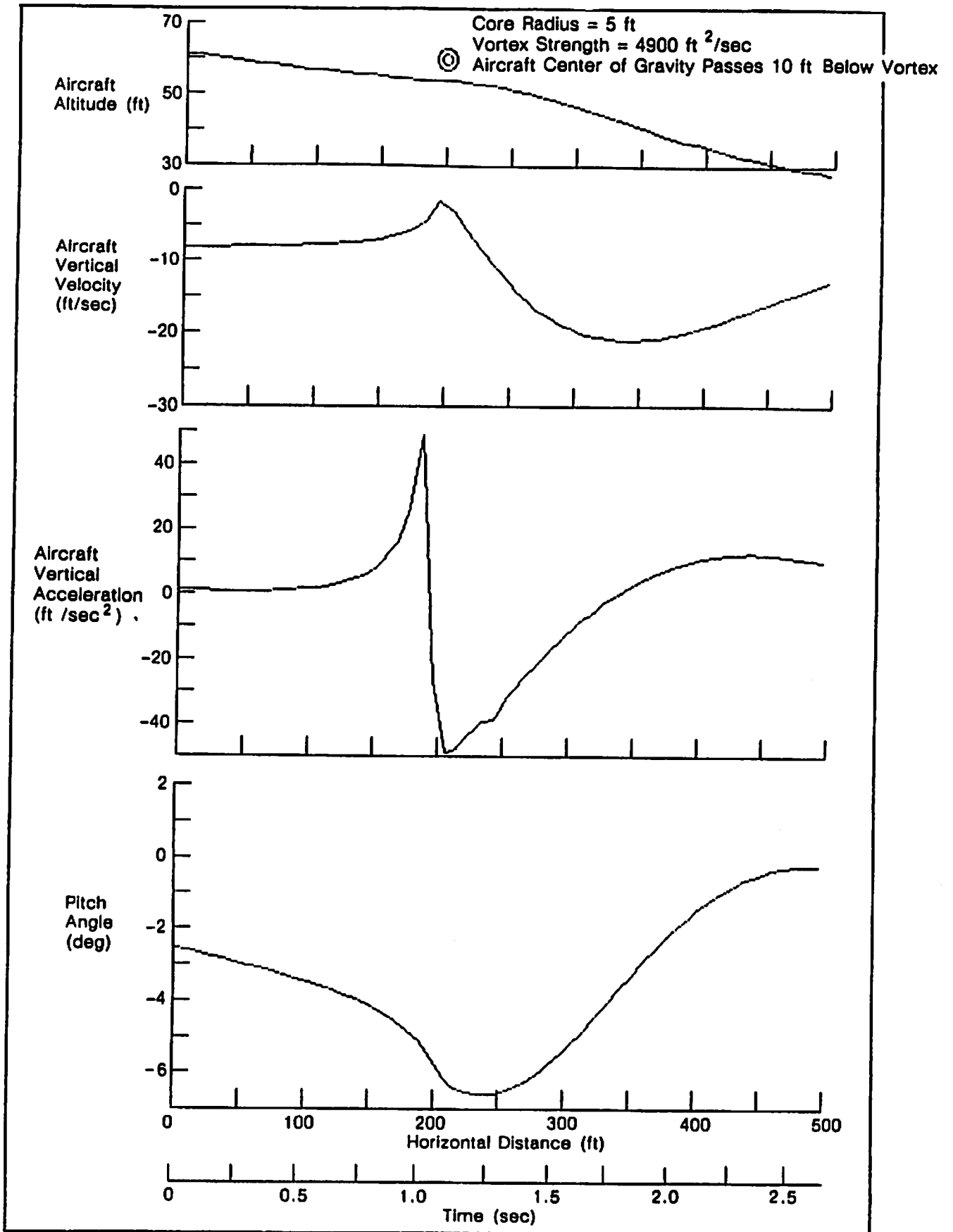
Figure 16. Response of a deHavilland DHC-7 to a cross-vortex encounter when the nominal aircraft flight path passes 10 feet below the vortex core.
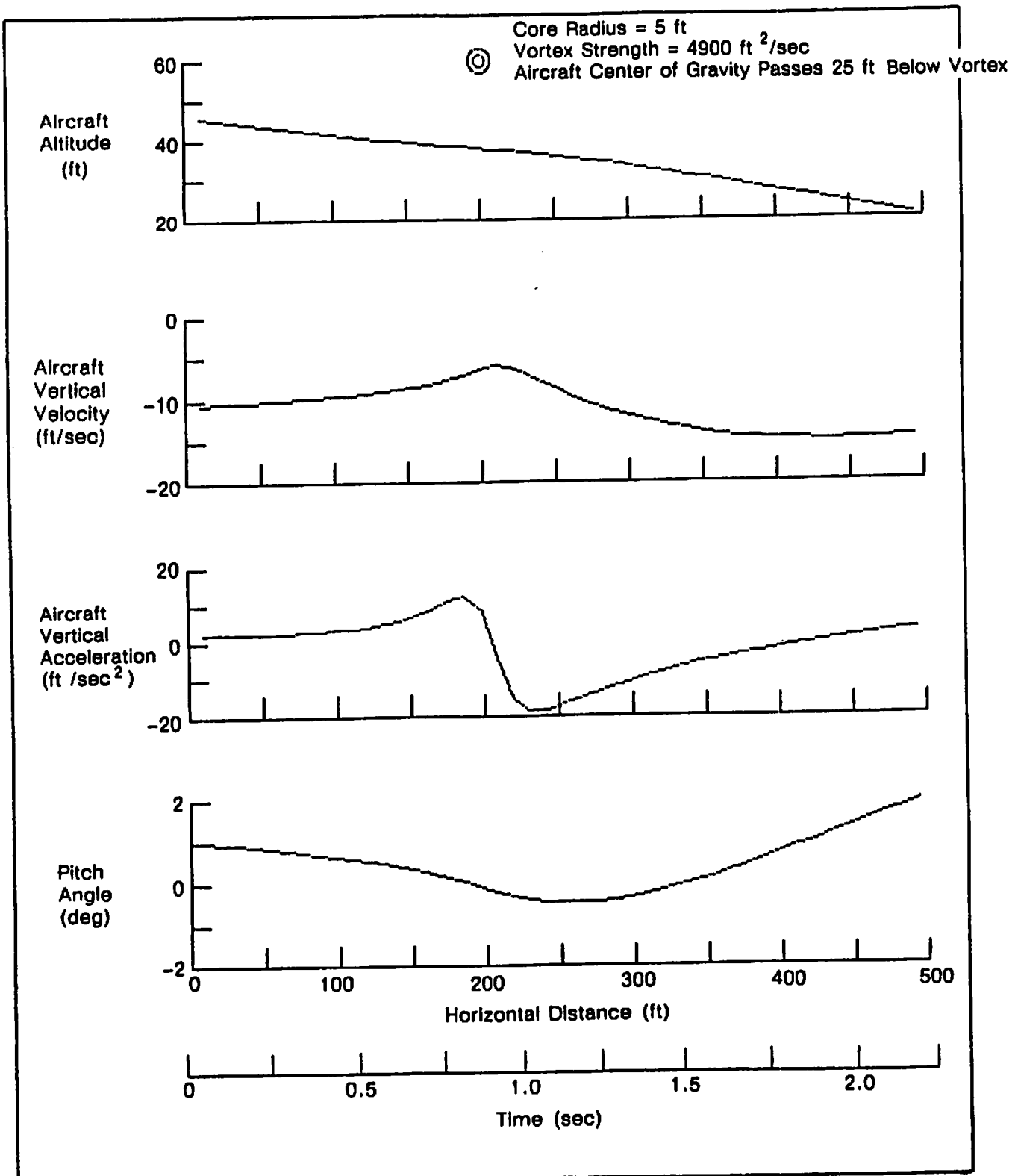
54-24
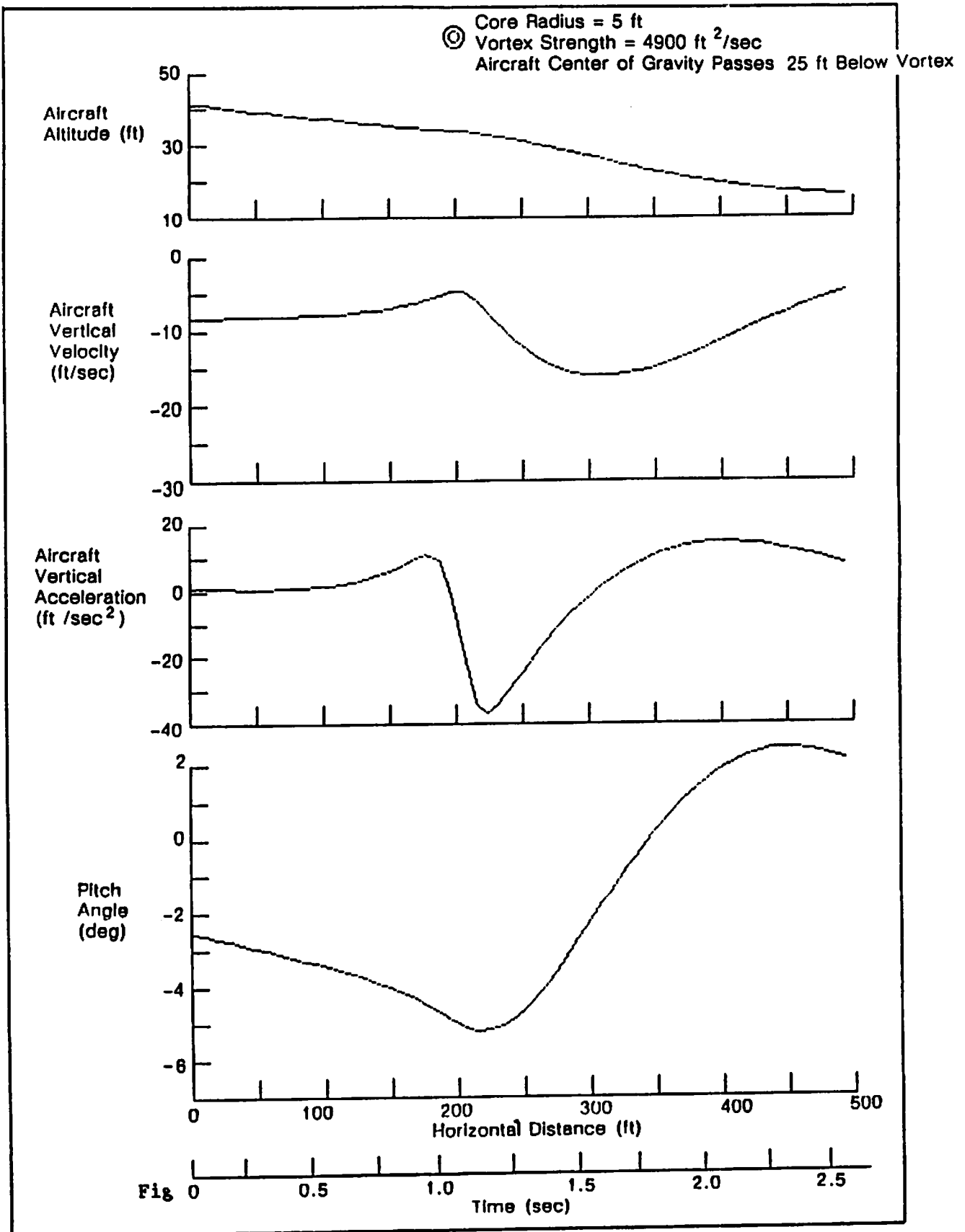
Figure 17. Response of a deHavilland DHC-7 to a cross-vortex encounter when the nominal aircraft flight path passes 25 feet below the vortex core.
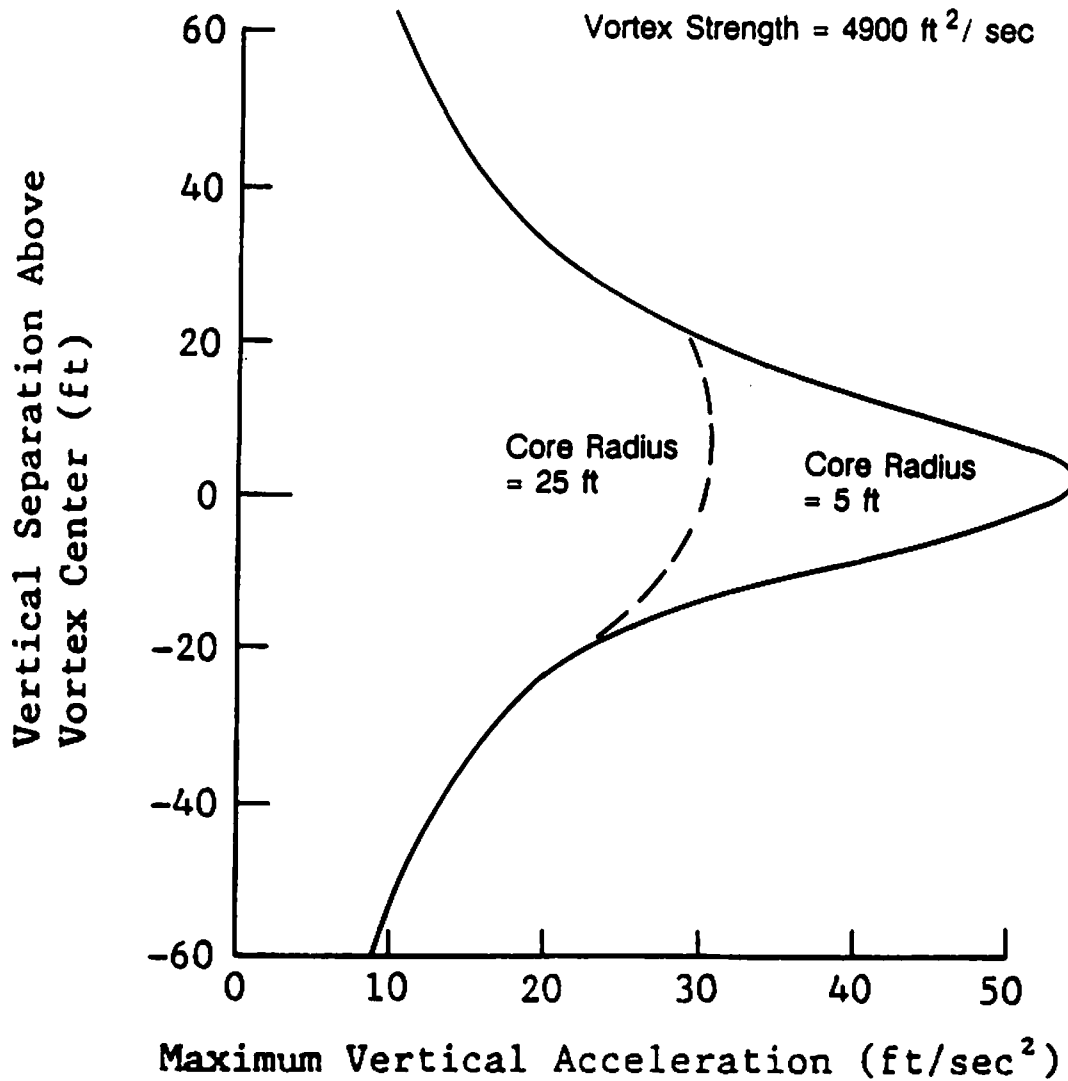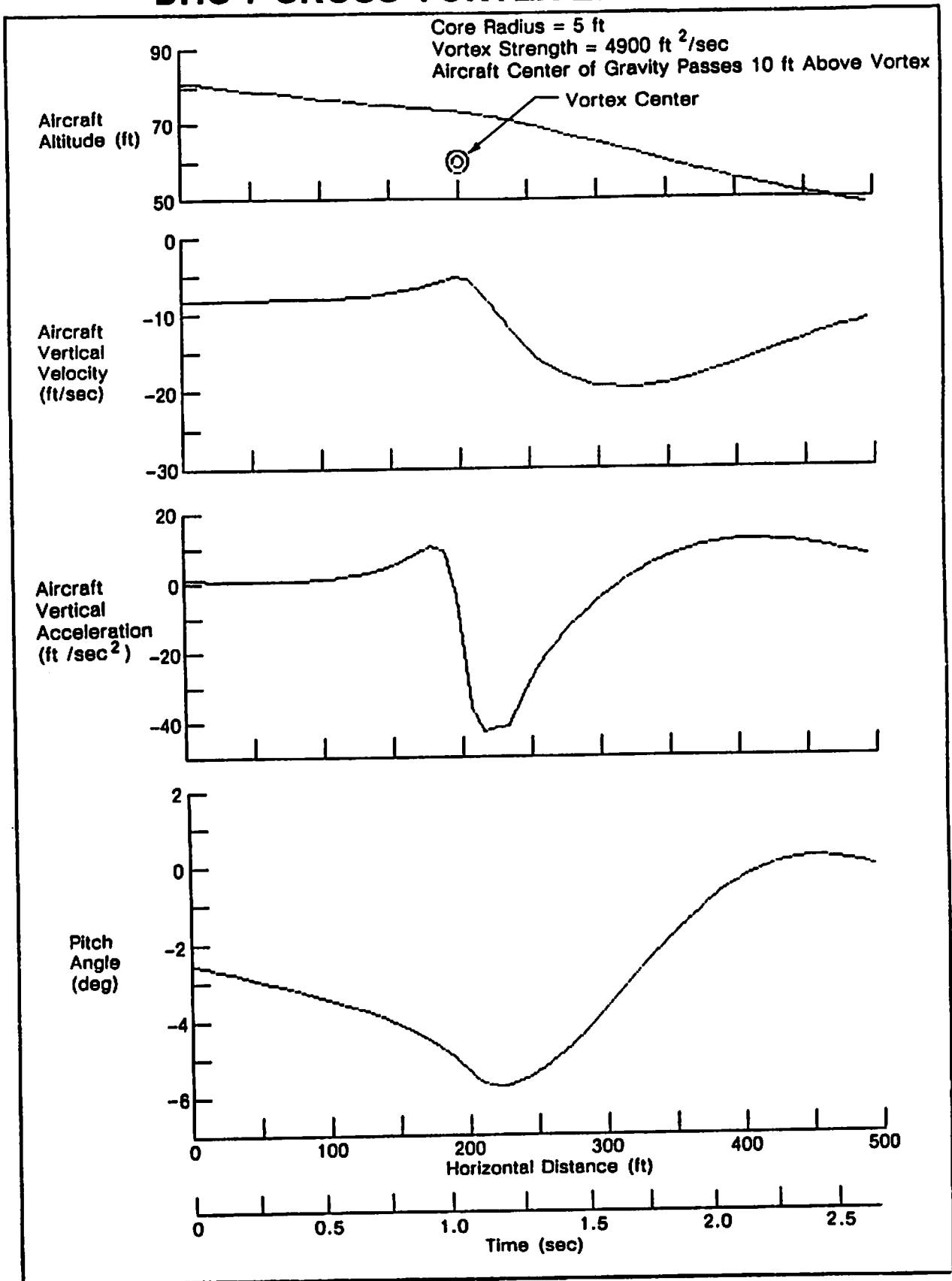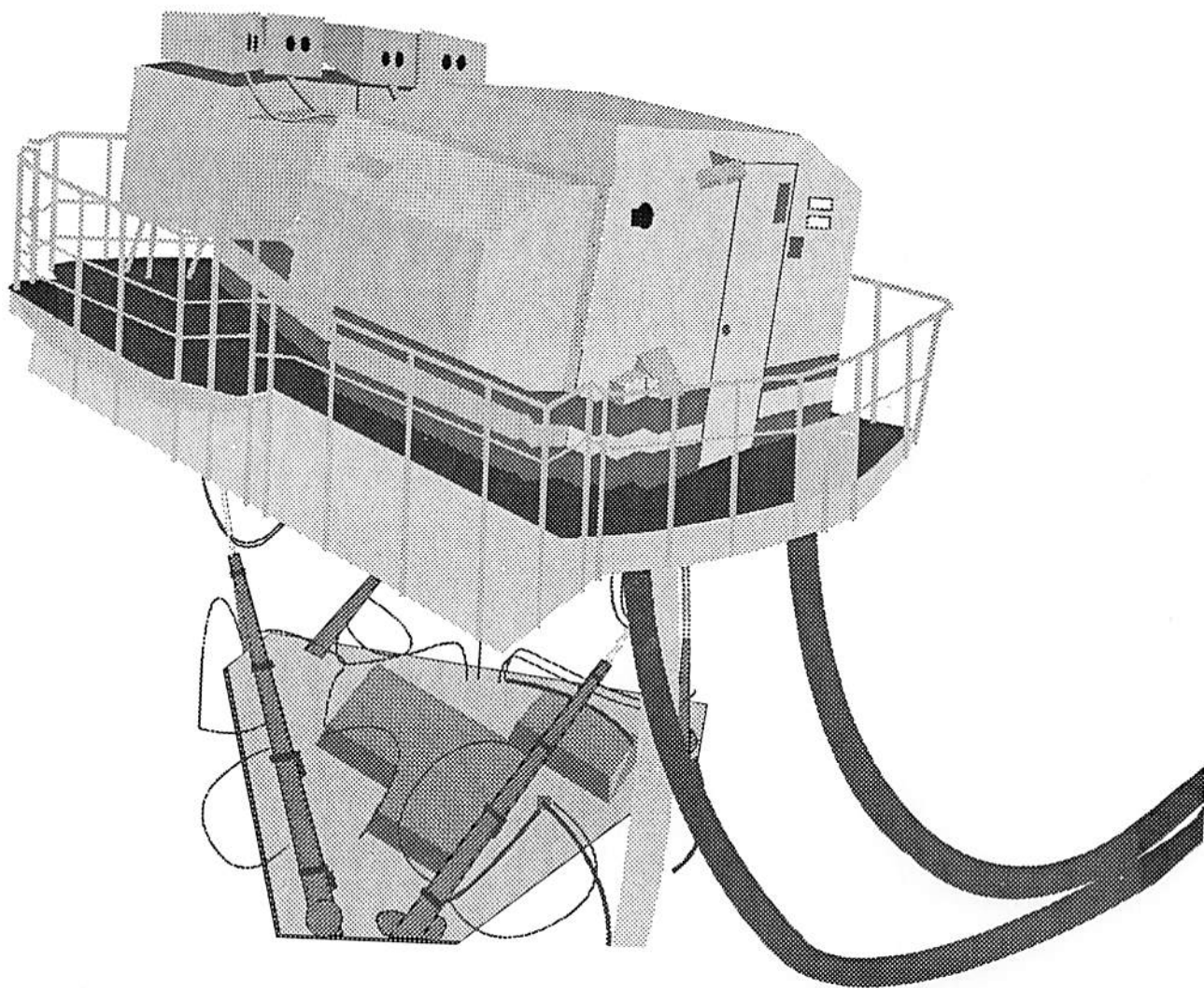
Figure 18. FAA Boeing 727 simulator to be used for pilot assessment of cross-vortex encounter.
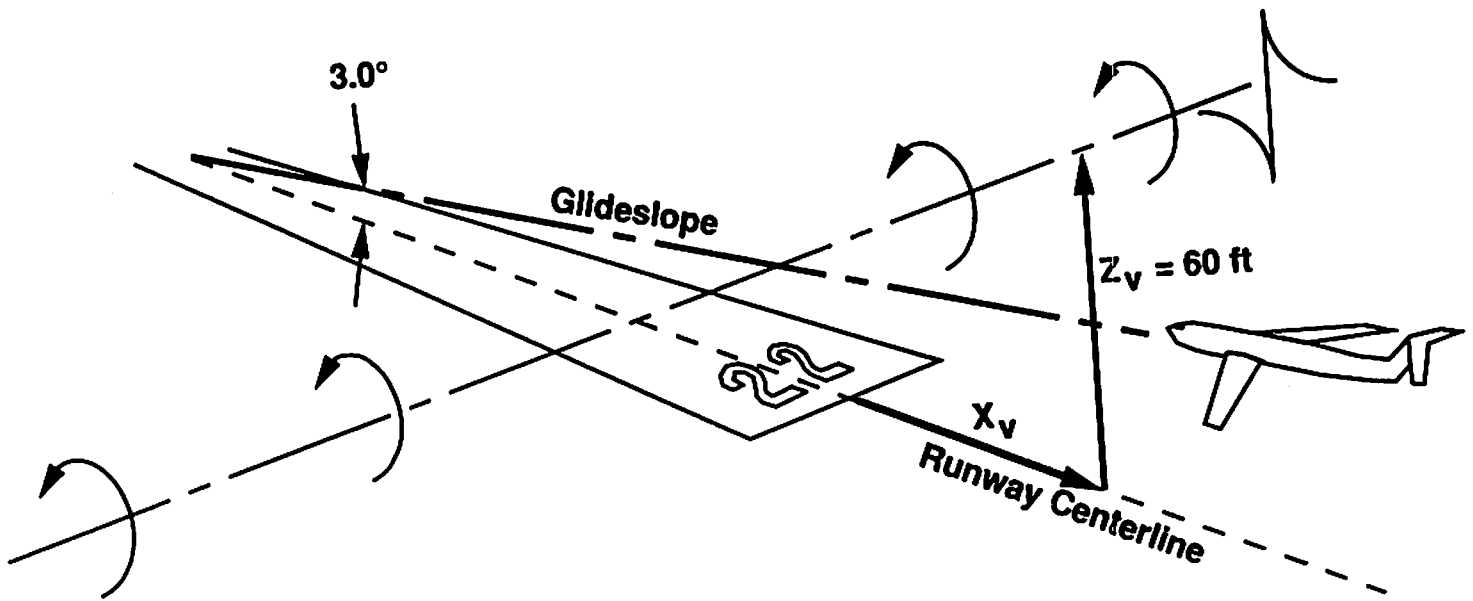
Figure 19. Landing configuration for moving base simulation studies of cross-vortex encounters.
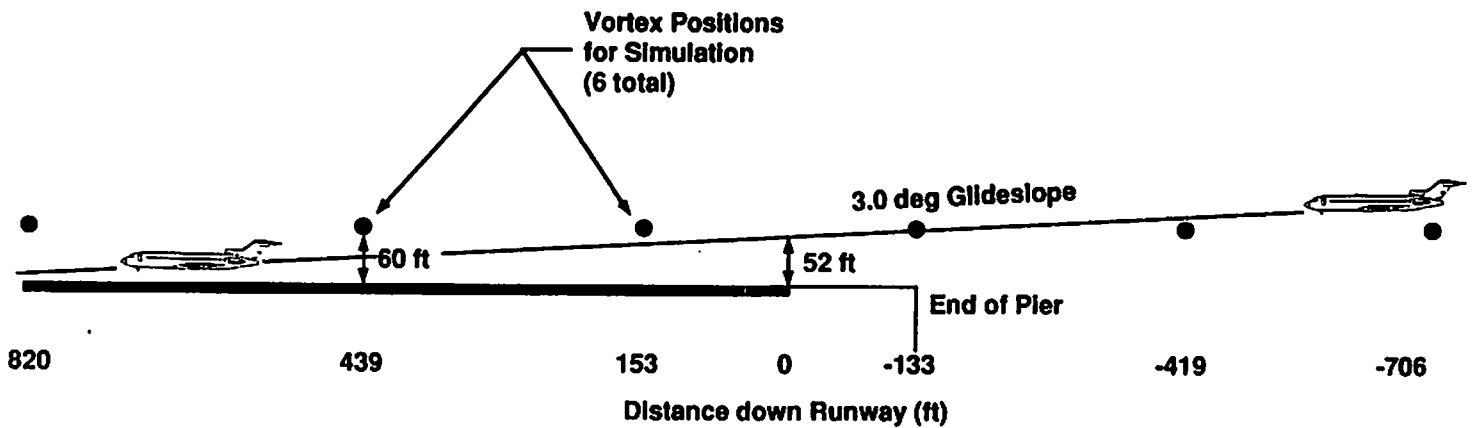
Figure 20. Locations of vortex axis for six different vortex positions for moving base simulation studies of cross-vortex encounters.

REFERENCES

1. Dunlay, W. J. and J. P. Muldoon, "Vortex Interactions at LaGuardia Airport," Federal Aviation Administration International Wake Vortex Symposium, Washington, DC, Oct., 1991.

2. Hallock, J. N., B. P. Winston, D. C. Burnham, T. E. Sullivan, I. G. McWilliams, and W. D. Wood, "Joint US/UK Vortex Tracking Program at Heathrow International Airport," FAA-RD-76-58-II, Vol. 2, Transportation Systems Center, Cambridge, MA, November 1977.

ONBOARD WAKE VORTEX AVOIDANCE: INSTRUMENTATION TO QUANTIFY VORTEX WAKE HAZARD

Alan J. Bilanin, Milton E. Teske and Howard C. Curtiss, Jr.
Continuum Dynamics, Inc.
P.O. Box 3073
Princeton, New Jersey 08543

ABSTRACT

An onboard vortex wake detection system using existing proven instrumentation such as a combination of accelerometers and angle of attack vanes may be technically feasible. This system might be incorporated into existing onboard systems (such as wind-shear detection systems) and might provide the pilot with the location of the vortex wake as well as a suggested evasive manuever. This system, if implemented, might permit a reduction of current landing separation, thereby reducing takeoff and departure delays.

This instrumentation may also have a short-term use in quantifying the magnitude of upset resulting from an aircraft encountering a vortex wake. Several onboard wake detection systems are discussed and limitations are identified. Their use as a wake hazard detector will also be discussed.

INTRODUCTION

The FAA is currently expending a great deal of effort in determining means that could lead to capacity and efficiency gains in the National Airspace System (NAS). Planned NAS modernization improvements will accommodate the projected traffic growth, but safety considerations may limit utilization of the economies anticipated by these improvements. Currently, the vortex wake hazard is a major safety consideration and may limit the NAS to accommodate future growth.

Current IFR separation standards depend on the generator/encounter aircraft combination. The FAA estimates significant traffic increases at most airports over the next twenty years, and IFR delays will get worse. The MITRE Corporation, in studies for the FAA (Ref. 1), has shown that if the vortex wake hazard could be eliminated, the NAS could accommodate separations of 2.5 nmi and greatly reduce this hazard. NASA has pursued aerodynamic

alleviation at the source to reduce the intensity of the vortices, while the FAA has pursued a ground-based detection and avoidance system.

The NASA program (Refs. 2-4) has demonstrated that aerodynamic alleviation is possible, but to date these concepts are only partially successful. When deployed on existing aircraft, these concepts have performance and/or efficiency penalties. In addition, they have been shown to be sensitive to small aerodynamic changes (such as extending landing gear, Refs. 5 and 6). Since no general alleviation concept has been developed, NASA has revised its program to emphasize vortex physics with the hope of developing alleviation concepts which may be factored into the design of the next generation of jetliners. In any event vortex alleviation at the source seems a long way off.

The second approach to reduce vortex wake hazard, under development by the FAA, is to monitor the position of vortices using ground-based sensors. A workshop, held in September of 1983 at NASA Langley, addressed Wake Vortex Detection Technology and identified several promising sensor technologies. These technologies were either land-based or airborne. The workshop concluded, however, that operational readiness of any system is at least ten years away.

The need for an interim system, which will allow pilots to close separations during IFR conditions, is immediate. Under VFR conditions, pilots voluntarily reduce spacings to 2 nmi or less. If an onboard vortex detection system could be developed which would be reliable and inexpensive, and give pilots a level of confidence against vortex encounter by giving a warning of an imminent encounter, as well as evasive action, aircraft separations under IFR conditions may be reduced. This paper investigates the feasibility of developing an interim onboard vortex avoidance system. *This system would use existing proven sensors such as angle-of-attack vanes, roll rate sensors and/or accelerometers* and might become part of an existing avoidance system such as a wind-shear detection system.

For any system of this type to work, the following questions must be addressed:

1) Using existing instrumentation, how far from vortex cores can a vortex signature be detected?

2) Can this signature be used to compute the location of a vortex wake?

3) How large is its signal to noise ratio?

4) Will this signal be adequate to provide detection and give sufficient evasion time?

5) Are there reasons why the proposed concept might not work?

These questions will be addressed one-by-one.

DETECTABILITY

Idealized Signal Strength

The wake of an aircraft is made up of two counter-rotating vortices known as a vortex pair. Figure 1 shows a schematic of an encountering aircraft about to interact with the wake of a generator aircraft during approach. The wake of the generator extends aft of the encountering aircraft, but in this schematic it is truncated at a transverse geometric plane located at the wing of the encountering aircraft. This plane will be used often to discuss vortex detection in the remainder of this paper. The wake shown schematically in this figure is not straight along the generator aircraft's landing trajectory but is shown distorted. This sinusoidal instability is one source of noise complicating the detection algorithm. Noise is a significant but surmountable problem in developing an onboard vortex detector system.

In the transverse or analysis plane, shown schmatically in Figure 2, the location of the vortex centers and location of an encountering aircraft relative to the vortex pair may be described. The strength of the vortex is quantified by the circulation Γ; the spacing between the vortices b is nominally about 2/3 the wingspan of the generating aircraft. The weight of the generating aircraft is related to the air density ρ and flight speed U by the expression $\rho U \Gamma b$. The product Γb is known as the dipole coefficient μ and to a good approximation determines the magnitude of the swirling velocity field for radial distances $R > b$ in the region where the encountering aircraft would first detect the presence of the vortex pair.

To good approximation the velocity field in this analysis plane may, for $R > b$, be given by

$$V = -\frac{\mu}{\pi} \frac{YZ}{R^4} \quad \text{and} \quad W = \frac{\mu}{2\pi} \frac{Y^2 - Z^2}{R^4} \tag{1}$$

A key observation is made that the swirling velocities (V,W) that characterize a wake flow field are to first approximation proportional to the dipole coefficient μ. Since all aircraft land at about the same speed (so as to maintain proper separation during approach) the dipole coefficient is related directly to the weight of the generating aircraft. This relationship between m and weight is tabulated in Table 1. From this table it may be seen that the dipole coefficient is about twice the weight of the aircraft in the units used. *Therefore, during landing approach the intensity of the vortex swirling velocity field is simply proportional to the weight of the generating aircraft.* The complex structure of this velocity field is shown in Figures 3 and 4. Here lines of constant V and W are shown for the wake of an aircraft weighing 550,000 lbs during landing approach. For this weight aircraft vertical velocities are of the order of 1.0 ft/sec at distances 400 ft lateral offset from the centerline of the wake, and drop off inversely as the square of the distance from the dipole center. This velocity field, or the response which it induces on an encountering aircraft, will be the signal with which a detection algorithm determines the relative location of an encountering aircraft from the wake center.

Existing Sensor Technology and Ideal Detection Distances

The sensors examined in this paper are summarized in Table 2. They have been chosen based upon prior or current use aboard aircraft, high reliability, and documented accuracy, sensitivity and threshold. The instruments are grouped into three categories based on which variables are sensed: fluid velocities in a plane perpendicular to the direction of motion of the encountering aircraft; rotary velocity or acceleration of the aircraft; or rectilinear velocity or acceleration of the aircraft. Certain sensors have been eliminated from consideration as a consequence of very slow response times (one such instrument is a rate-of-climb indicator). With these various instrument types, some simple estimates of ideal detection distances may now be made neglecting noise.

Detection Using Flow Angle Vanes

From Eq. (1) the velocity in the analysis plane Q divided by the encountering aircraft flight speed is given by

$$\frac{|Q|}{U} = \frac{\sqrt{W^2 + V^2}}{U} = \frac{\mu}{2\pi R^2 U} \tag{2}$$

and is the angle which would be measured on a flow angle vane mounted on an encountering aircraft. For the sake of discussion here and all subsequent discussions, it is assumed that the aircraft approach speed is 200 ft/sec. According to Rosemount Inc.'s Aerospace Division, angle-of-attack vanes can routinely be manufactured to detect angle changes as small as 0.25 deg and 0.5 deg although 0.5 deg is commonly quoted. Distances at which commercial jet transport can be first detected are given in Table 3. As expected, the heavier the generator aircraft the greater the distance at which detection is first ideally possible. The tabulated results can be summarized by characterizing aircraft by landing weight. Detection distances are shown as a function of weight in Figure 5.

Detection Using an Onboard Roll Rate Sensor

The most predominant response of aircraft to a vortex encounter is roll. Investigators have even proposed that the hazard associated with a vortex encounter should be determined by comparing the roll upset to the roll control authority of the aircraft (Refs. 8 and 9). A simple estimate of the ideal roll rate induced by the wake is to equate the roll rate $\dot{\phi}$ to the horizontal gradient of the vertical velocity $\partial W / \partial Y$ to give

$$\dot{\phi} = \frac{\partial W}{\partial Y} = \frac{\mu Y}{\pi} \frac{-Y^2 + 3Z^2}{R^6} \tag{3}$$

The ideal induced roll rate is now a complicated function of position. A detection estimate may be made by assuming a lateral encounter (Z = 0) at roll rate sensor thresholds. Figure 6 shows the lateral detection distance as a function of aircraft landing weight. The distance at which detection is first possible is comparable to using flow angle vanes (Figure 5).

Detection Using an Onboard Rectilinear Accelerometer

Rectilinear accelerations are produced onboard by changes in aerodynamic forces induced by the dipole flow field. Simple estimates of anticipated accelerations must be made using an aircraft dynamic model. A three-degree-of-freedom uncoupled model has been developed and coded to make these estimates. Roll ϕ, pitch θ and lateral and vertical accelerations $\ddot{y}$ and $\ddot{z}$ are computed using the conventions shown sketched below
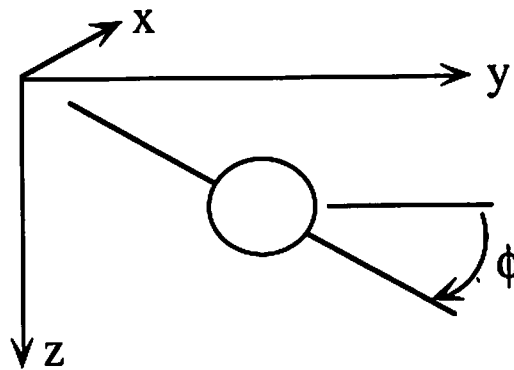
to give the equations

$$m\ddot{y} = C_L qS \sin \phi \tag{4}$$

$$m\ddot{z} = -C_L qS \cos \phi + mg(1 - \cos \phi) \tag{5}$$

$$I_{yy}\ddot{\theta} = \left[C_{m_\alpha}\alpha + C_{m_{\dot{\alpha}}}\frac{\dot{\alpha}c}{U} + C_{m_q}\frac{\dot{\theta}c}{U} \right] qSc \tag{6}$$

$$I_{xx}\ddot{\phi} = C_{l_p} qSb \frac{\dot{\phi}b}{2U} + \zeta_v \tag{7}$$

where

    a   -   angle of attack

    c   -   chord

C_{ℓ_p} — roll damping coefficient

C_L — lift coefficient

C_{m_α} — static pitching moment coefficient

$C_{m_{\dot\alpha}}$ — dynamic pitching moment coefficient

C_{m_q} — pitch damping coefficient

g — gravity

ζ_v — torque generated by the vortex pair

I_{xx} — moment of inertia about the x axis

I_{yy} — moment of inertia about the y axis

m — aircraft mass

q — dynamic pressure

S — aircraft planform area

For all dynamic simulations in this paper, the characteristics of the encountering aircraft are taken to be that of a Learjet, and the generator is taken to be that of a 550,000 lb aircraft with a separation distance between vortices of 140 ft.

A typical simulation is shown in Figure 7. The Learjet with controls locked is initially positioned at $Y = Z = 600$ ft and is trimmed to descend and move laterally toward $Y = Z = 0$ at 10 ft/sec. These data correspond to an intercept with the center of the vortex pair along a 3 deg angle. The upwash of the wake of the 550,000 lb aircraft alters the trajectory of the Learjet; it passes over the wake and out of the computational domain $|Y| \leq 600$ ft , $|Z| \leq 600$ ft in about 60 seconds. The Learjet is accelerated to the left during this simulation. This simulation is repeated many times with the Learjet positioned at other places along the computational boundary. Figure 8 shows the location within the computational domain where the magnitude of the lateral acceleration first exceeds $\ddot{y} > 0.1$ ft/sec^2 . Detecting this level of rectilinear acceleration is well within the state-of-the-art of existing accelerometers (Table 2).

Thus, existing sensors of the type routinely used on aircraft can detect vortex-induced signals several hundred feet away from the center of the wake. The heavier the generating aircraft, the more easily detectable the wake. A wake from a 500,000 lb aircraft is detectable at distances of nearly 500 ft from the wake centerline, while the wake of a

100,000 lb aircraft is detectable at a distance of approximately 200 ft from the wake centerline.

A DETECTOR ALGORITHM

The positioning of flow angle vanes on each wing tip permits the determination of lateral and vertical velocities as a function of time. From these measurements (assuming aircraft transverse motion can be neglected or has been removed from the signals) the following variables can be computed

$$V(t) = \frac{V_r(t) + V_l(t)}{2} \tag{8}$$

$$W(t) = \frac{W_r(t) + W_l(t)}{2} \tag{9}$$

$$\frac{\partial W(t)}{\partial Y} = \frac{W_r(t) - W_l(t)}{2S} \tag{10}$$

where V, W and $\partial W/\partial Y$ are the lateral velocity, vertical velocity and lateral gradient of vertical velocity at the encountering aircraft. The quantity $2S$ is the distance between the two wing-tip flow angle vanes, and subscript r and l denote right and left. The dipole approximations for V, W and $\partial W/\partial Y$ (Eqs. (1) and (3)) may then be solved for $Y(t)$, $Z(t)$ and μ. The position of the encountering aircraft relative to the center of the wake ($Y(t)$, $Z(t)$) is determined as a function of time, as well as the dipole coefficient or weight of the generating aircraft. The simplicity of this detector is illustrated by writing down the solution for $Y(t)$ and $Z(t)$

$$Y(t) = \frac{2W(t)}{\frac{\partial W(t)}{\partial Y}} \frac{(-1 + 3f^2)}{(1 - f^4)} \tag{11}$$

$$Z(t) = fY(t) \tag{12}$$

$$f = \frac{W(t)}{V(t)} \left[1 \pm \sqrt{1 + \left(\frac{V(t)}{W(t)}\right)^2} \right] \tag{13}$$

where the sign of f must be the sign of $-V(t)$. The most complicated operation required in this detector algorithm involves taking a square root and, therefore, this detector could easily be programmed into an onboard microprocessor and work in real time.

The accuracy of this detector may be evaluated in several ways. The first is to use the detector to predict the location of an aircraft moving in the wake flow field, and compare this prediction with the actual aircraft location. This comparison is shown in Figure 9

where the predicted positions using the detector are shown for an aircraft which is actually located on rays originating from the wake centerline $Y = Z = 0$. The flow field used in this study is the same field in the simulation shown in Figure 7. As the vortices are approached, the predicted positions differ from the actual position. This, of course, is a consequence of the fact that the detector is looking for a dipole. The excellent agreement at distances greater than about 100 ft from the wake centerline for such a simple detector algorithm is very encouraging.

A second comparison of detector accuracy can be made by recomputing the dynamic simulation of the Learjet with controls locked. Removing aircraft motion from the flow angle vane signal (which is easily done here, since aircraft absolute motion is computed) the actual and predicted trajectories are shown in Figure 10. Note that only as the Learjet position approaches the center of the vortex pair, at a distance of the order of the vortex separation, does the predicted trajectory differ from the actual trajectory. This result is also very encouraging.

Thus, it can be demonstrated that a relatively simple detector algorithm can be used to compute the relative position between an encountering aircraft and a vortex wake.

SIGNAL TO NOISE RATIO

Noise will enter the onboard vortex wake detection signal from four sources: atmospheric turbulence, sinusoidal instability of the wake, aircraft induced noise from structural flexibility and control surface motion, and electronic processing of the sensor output. That noise is removed by averaging over the signal. In this case detector accuracy would decrease with signal averaging. Specifically, the predicted aircraft position will be computed from

$$Y_a(t) = \frac{1}{T} \int_{t-T}^{t} Y(t)dt \tag{14}$$

$$Z_a(t) = \frac{1}{T} \int_{t-T}^{t} Z(t)dt \tag{15}$$

where T is the averaging time and Y_a and Z_a are the averaged predicted aircraft position. The simulation of the Learjet with controls locked as shown in Figures 7 and 10 may be repeated, and the detector position time histories $Y(t)$ and $Z(t)$ averaged for $T = 4$ and 10 seconds (Figures 11 and 12). A comparison of Figure 7 of actual Learjet position with that of Figures 11 and 12 suggests that four-second averaging of the detector signal results in errors over the simulation of 75 ft or less, and ten-second averaging results in errors of hundreds of feet, and is unacceptable. Near the end of the simulation lateral velocities are approaching 50 ft/sec, which represents an encounter angle with the wake of over 14 deg.

Therefore, it is concluded that with the detector algorithm and averaging times on the order of four seconds, acceptable predictions of relative positions between wake and aircraft are possible, even with the angle between the wake and encountering aircraft appreciably greater than 6 deg .

Atmospheric Turbulence

Under landing conditions several hundred feet above the ground, aircraft are operating in the atmospheric mixed layer. The thickness of this layer varies during the day heating cycle and is related to the degree of cloud cover, among other variables. What is relevant with regard to operating in a turbulent environment is that turbulent fluctuations are random (they have no mean when averaged), and turbulent eddies are only correlated over finite distances (over a turbulent integral scale length Λ).

It is also generally agreed that under most conditions in the earth's mixed layer the integral scale or coherence length of eddies may be estimated from

$$\Lambda \pounds 0.6h \tag{16}$$

where h is the distance above the ground. The averaging time for turbulent fluctuations from a signal becomes

$$T_t \approx \Lambda/U \tag{17}$$

where U is the flight speed. Approximately four seconds is available for signal averaging; thus, using a 200 ft/sec approach speed, noise from turbulence can be removed from the detector signal at altitudes between

$$0 \leq h \leq 1200 \text{ ft} \tag{18}$$

Since above this altitude a vortex encounter is not likely to be serious, it seems from this simple analysis that noise from atmospheric turbulence may not be an insurmountable issue.

Sinusoidal Instability of the Wake

The phenomenon of sinusoidal or Crow instability of a vortex wake is shown in Figure 13. The phenomenon has been extensively studied in the literature (Refs. 11-14). and an analysis by Bliss (Ref. 15) has shown how the phenomenon is forced by atmospheric turbulence. His analysis has shown that the most unstable wavelengths are of the order of 5 vortex spacings. The instability is shown schematically in Figure 14. To demonstrate that the noise introduced into the detector algorithm by sinusoidal instability can be averaged out, the three-degree-of-freedom simulation code velocity field was modified to allow the

Learjet to fly into the vortex velocity field of sinusoidally displaced vortices. Figure 15 shows the predicted aircraft trajectory from a detector signal averaged over four seconds, when the amplitude of the instability was taken to be 40 ft with a wavelength of 750 ft. All other conditions of the simulation are the same as the simulation shown in Figure 7. It appears again that if four-second averaging of the detector signal can be achieved in flight, the noise associated with sinusoidal instability can be successfully removed from the signal. This does not come as a surprise, since the typical time to average out the sinusoidal instability noise is

$$T_S = \lambda_S/U \tag{19}$$

or for the conditions used here $T_S \cong 3.75$ seconds .

A final comment on sinusoidal instability is relevant here. As turbulent intensity increases in the atmosphere, the time at which vortices link to form rings (as shown in Figure 13) decreases. Bliss (Ref. 15) has obtained an approximate expression to evaluate wake time, or time to link. The computed wake lifetimes for a Learjet and a B-747 aircraft are plotted in Figure 16. The ordinate is the root mean square vertical turbulent velocity in ft/sec. It is curious that although the detector will have to operate in a noisy turbulent environment, the more turbulent the atmosphere the less likely the wake is a hazard.

<p style="text-align:center">Aircraft Motion</p>

If sensors are mounted at the aircraft wing tips or in the aircraft fuselage as it flies through atmospheric turbulence, wing tip motion and fuselage accelerations will contribute noise to the detection signal. Reference 16 details a two-degree-of-freedom wing flapping model developed to analyze this possibility. The results from this model are summarized in Figures 17 and 18. Nondimensional accelerations of the fuselage (Figure 17) are maximum at a turbulence scale of less than 100 ft, with a value of

$$\frac{\bar{\ddot{z}}}{g} \cong 7 \frac{\overline{W_t}}{U} \tag{20}$$

where $\overline{W_t}$ is the root mean square vertical turbulent velocity. Using $\overline{W_t} = 1$ ft/sec to represent mild turbulence, $\bar{\ddot{z}} \cong 0.2$ ft/sec^2 is on the order of the threshold value of an accelerometer. This result suggests that the noise is on the order of the signal when detection begins. Since the scale at which this response occurs is so small, an averaging time of only 0.5 sec should be needed to remove the noise. A similar conclusion may be reached with regard to the root mean square tip velocity $\overline{c_A}$ (Figure 18).

Thus, at distances where the presence of a vortex should first be detected (several hundred feet), noise will be comparable to signal. Fortunately, noise can be removed from signal by a simple time average. Averaging times on the order of four seconds appear to be adequate.

DETECTION AND EVASION TIME

The last issue to be addressed concerns whether a wake can be detected, a warning given to a pilot and an evasive maneuver executed before a significant vortex upset occurs. This question can be addressed by example. The distance at which a detector must begin to detect a vortex may be approximated by the expression

$$R = \frac{b + b_f}{2} + V_e(T + T_e) \tag{21}$$

where

b_f - span of the encountering aircraft

V_e - lateral encounter velocity (10 ft/sec for a 3 deg encounter angle)

T - detector averaging time, approximately 4 seconds

T_e - pilot response time to execute an evasive maneuver after warning, approximately three seconds

For the assumptions

$$b = 75 \text{ ft}$$
$$b_f = 100 \text{ ft}$$
$$V_e = 20 \text{ ft/sec (a 6 deg encounter)}$$
$$T + T_e = 7 \text{ seconds}$$

the wake must first be detected at a distance R = 250 ft. In light of the detection distance estimates given above, this detection requirement seems achievable.

Thus, detectors using existing sensors appear to have sufficient thresholds and accuracy to detect a vortex and provide a pilot with a warning prior to significant vortex upset even with encounter angles of up to 6 deg . For encounter angles greater than   6 deg , it is shown in Ref. 16 that maximum induced roll rates are well below the roll control authority of the encountering aircraft.

OTHER PROPOSED CONCEPTS

To date, the authors have examined the effect of aileron deflection on flow angle vanes mounted on wing tips, finding the induced noise level to be small. There are no technical reasons why the proposed concept cannot work.

CONCLUSIONS

This paper examined the technical feasibility of developing an onboard vortex avoidance system which would utilize existing sensor and instrumentation technology. The following conclusions are reached:

1) Generating aircraft leave as a wake a dipole velocity field which can be detected using state-of-the-art instrumentation.

2) The dipole velocity field itself, or aircraft motions such as roll and/or acceleration, may be sensed to determine the position of the vortex wake relative to the aircraft.

3) A vortex wake of the large jumbo jet may be sensed at lateral distances on the order of 500 ft using existing state-of-the-art instrumentation.

4) Assuming lateral encounter velocities, corresponding to wake interception angles of up to 6 deg , sufficient time exists to detect the vortex wake, alert the pilot and undertake an evasive maneuver prior to encounter. For encountering angles greater than 6 deg induced roll rates are below the roll control authority of the aircraft.

5) Instrumentation noise will be an issue and will lead to detection false alarms if not properly included. All indications suggest that noise may be easily removed from the detection signal.

6) While no detection algorithm has been developed or proposed in the paper, it has been shown how two simple flow angle vanes may be used to determine the position of an aircraft relative to a vortex wake.

7) There appears at this time no technical reason why an onboard vortex avoidance system cannot be developed using state-of-the-art instrumentation.

ACKNOWLEDGEMENT

Table 1. Published Landing Weights and Computed Dipole Coefficients for Major Transport Aircraft (Ref. 7)

Generating Aircraft	Weight (lb) (max landing)	μ (ft^3/sec)	μ/Weight (ft^3/sec/lb)
B707	228,000	458,000	2.0
B727	154,333	308,000	2.0
B737	106,750	213,000	2.0
B747	552,000	969,000	1.8
B757	198,000	398,000	2.0
B767	282,667	523,000	1.9
L-1011	365,500	637,000	1.7
DC-8	229,333	417,000	1.8
DC-9	101,020	208,000	2.1
MD	131,375	269,000	2.1
DC-10	383,250	715,000	1.9

Table 2. Tabulation of Instrument Sensors Considered for Detecting a Vortex Wake

AERODYNAMIC ANGLES

Variable	Instrument	Range	Accuracy	Threshold	Response	Manufacturer	Aircraft
Angle of Attack	Vanes	±60 deg	±0.5 °(1)	±0.2- 0.3 °	(2)	Rosemount Inc Aerospace Div	727,737 757,767
Side Slip Aerospace Div.	Vanes	±60 deg	±0.5 °(1)	±0.2- 0.3 °	(2)	Rosemount Inc.	(3)

ROLL RATE/ACCELERATION

Variable	Instrument	Range	Accuracy	Threshold	Response	Manufacturer	Aircraft
Roll Rate	Rate Gyro	60 deg/sec	±0.15 deg/sec	0.01 deg/sec	28 Hz	US Time Corporation	Typical
Roll Rate	Laser Inertial Navigation	400 deg/sec	±0.1 deg/sec	±0.015 deg/sec	(2)	Honeywell Government & Aeronautical Products Div.	737-000 757,767
Roll Acceleration	Angular Accelerometer	5 rad/sec^2	$\pm0.0003 \text{ rad/sec}^2$	2µrad/sec	10 Hz	Systron Inertial Div.	(4)

VERTICAL VELOCITY/ACCELERATION

Variable	Instrument	Range	Accuracy	Threshold	Response	Manufacturer	Aircraft
Vertical Velocity	Rate of Climb	6000 ft/min	±200 ft/min	(2)	(2)	United Instruments	737,757
Vertical Velocity	Laser Inertial Navigation	(5)	(5)	(5)	(5)	Honeywell	777,757
Vertical Velocity	Linear	$\pm130 \text{ ft/sec}^2$	$\pm0.3 \text{ ft/sec}^2$(6)	0.03 ft/sec^2	(2)	Honeywell	737,757

(1) ±0.25 deg accuracy is possible on these instruments.
(2) Unknown.
(3) Most commercial aircraft use an on board computer to calculate the side slip angle from various instruments.
(4) Not installed on most commercial aircraft.
(5) This system integrates the velocity from the linear accelerometer. Accuracy depends on the air data computer.
(6) $\pm0.03 \text{ ft/sec}^2$ is available.

Table 3. Idealized Detection Distances R_1 and R_2 Assuming Flow Angle Vanes Can Detect Angle Changes of 0.5° and 0.25° deg, Respectively

Generating Aircraft	Weight (lb) (max landing)	μ (ft^3/sec)	R_1 (ft)	R_2 (ft)
B707	228,000	458,000	214	303
B727	154,333	308,000	175	248
B737	106,750	213,000	145	206
B747	552,000	969,000	310	440
B757	198,000	398,000	197	279
B767	282,667	523,000	228	323
L-1011	365,500	637,000	252	357
DC-8	229,333	417,000	204	289
DC-9	101,020	208,000	144	204
MD	131,375	269,000	164	232
DC-10	383,250	715,000	267	378
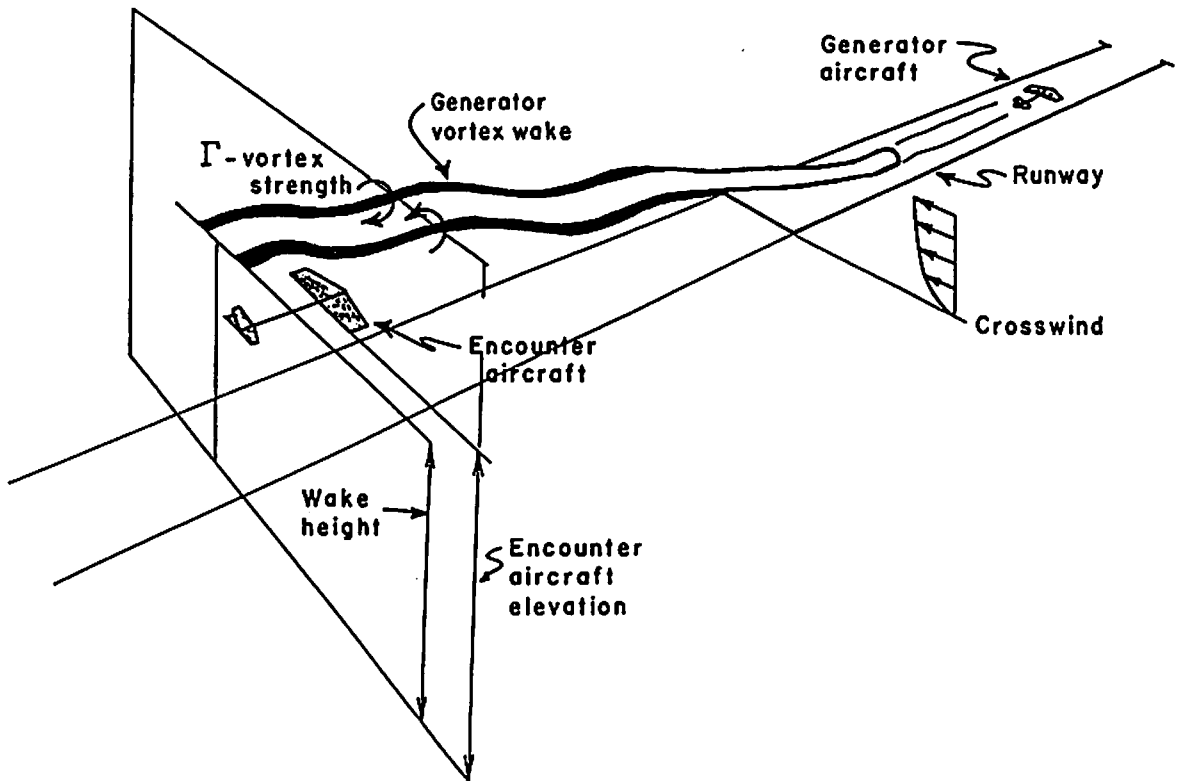
Figure 1. Schematic of a vortex wake encounter upon approach. Note that a crosswind advects the vortex pair and atmospheric turbulence results in a sinusoidal instability of the vortex.
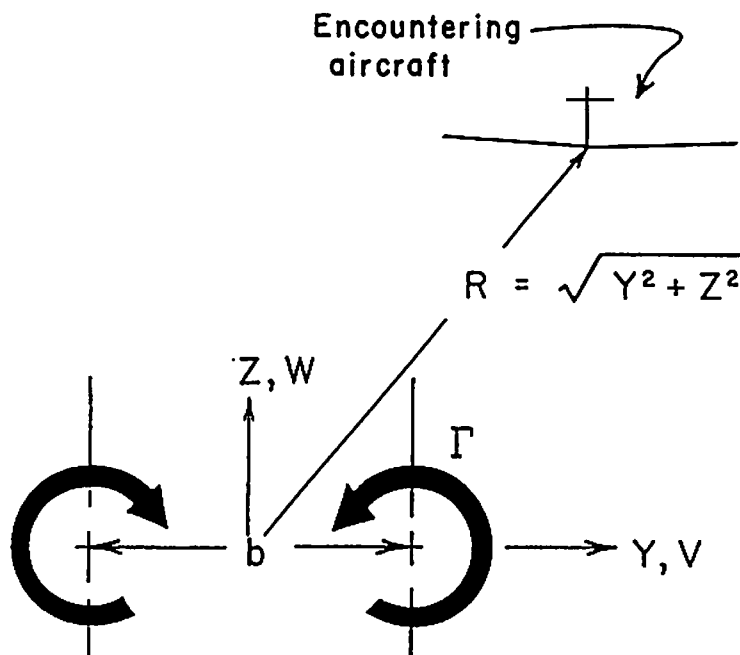

Figure 2. Schematic of an encountering aircraft in the vortex flow field of a generator. The Cartesian coordinate system (Y,Z) has corresponding velocity components (V,W).
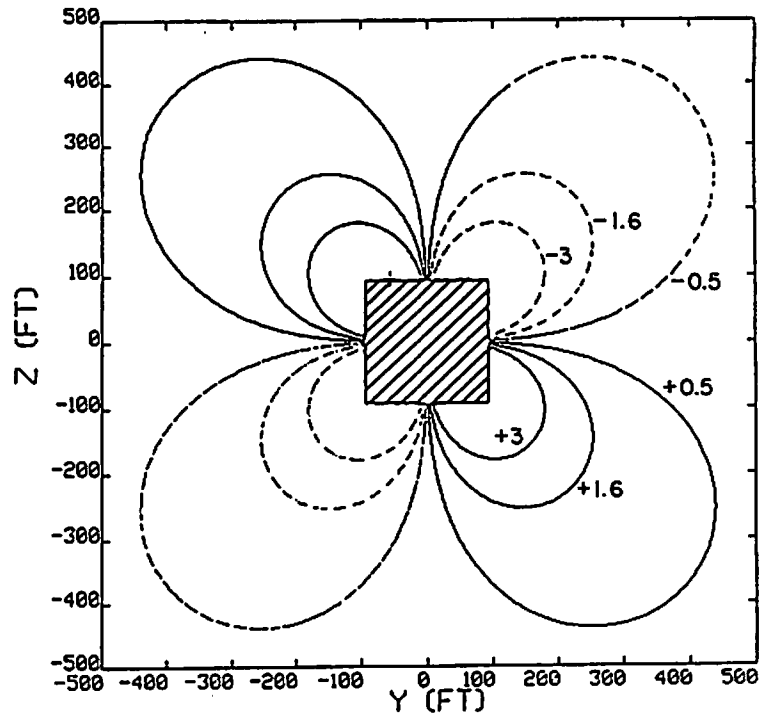
Figure 3. The horizontal velocity distribution V (ft/sec) in the wake of a 550,000 lb
aircraft during landing. Velocity isopleths are omitted near the aircraft
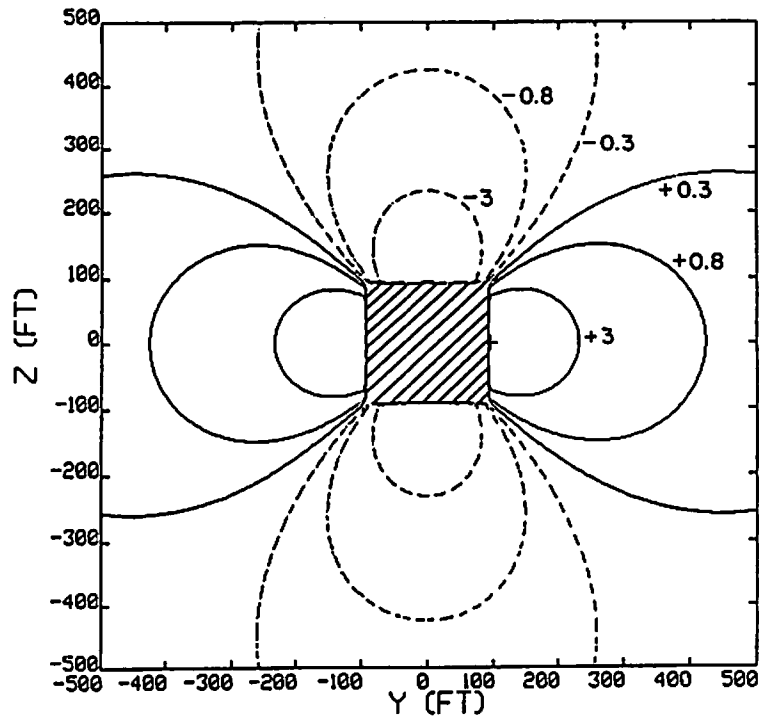where the dipole approximations is invalid.

Figure 4. The vertical velocity distribution W (ft/sec) in the wake of a
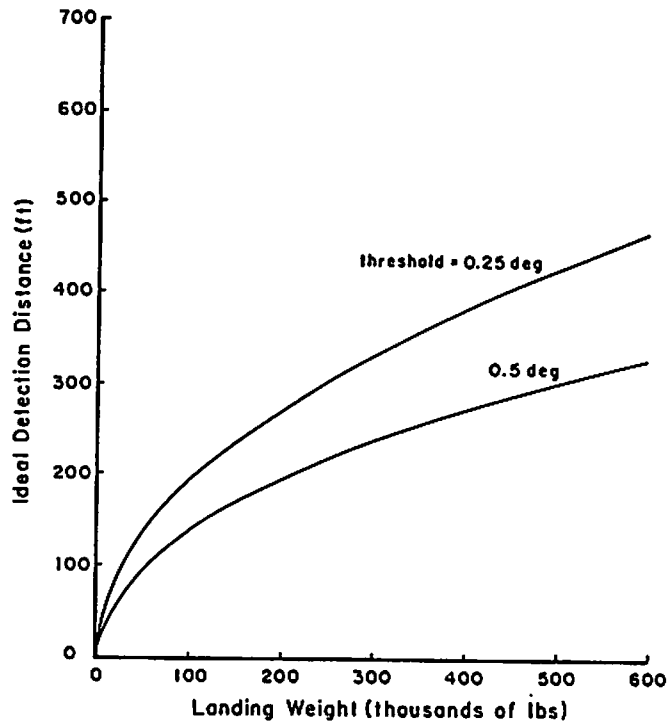550,000 lb aircraft during landing.

Figure 5. Detection distance using flow angle vanes as a function of aircraft landing weight and instrument threshold.
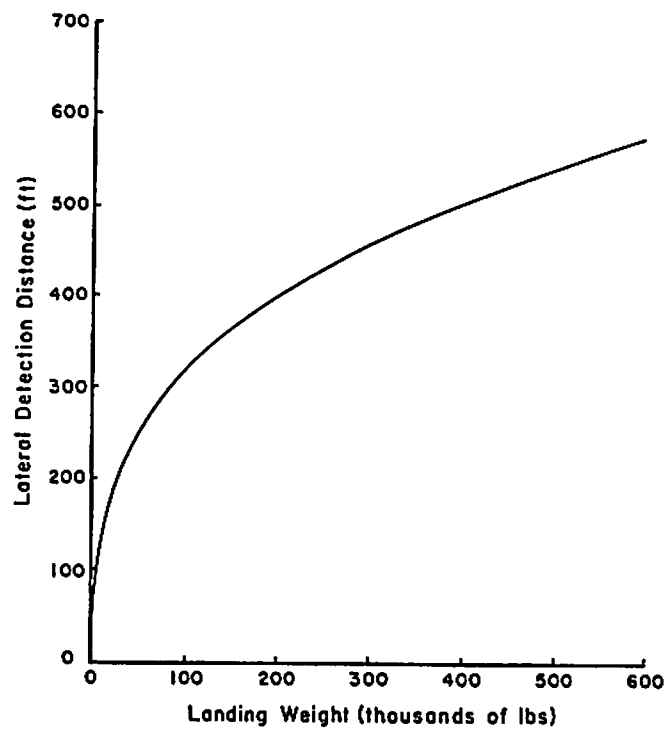

Figure 6. Lateral detection distance using roll rate sensors as a function of aircraft landing weight.
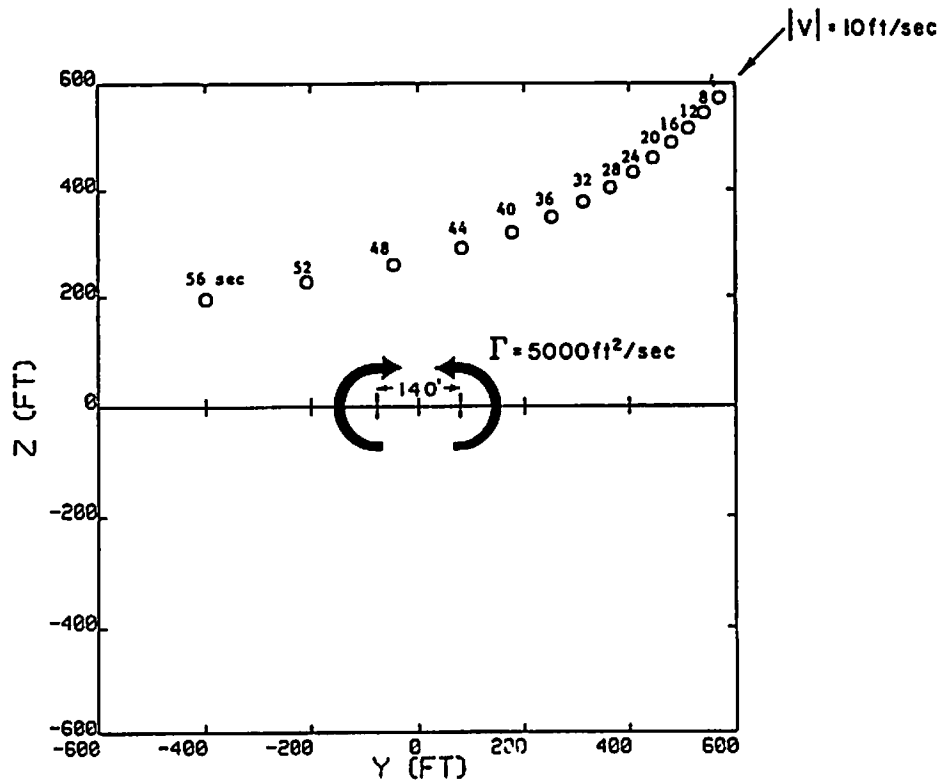
Figure 7. Three-degree-of-freedom simulation of predicted Learjet trajectory for controls locked.
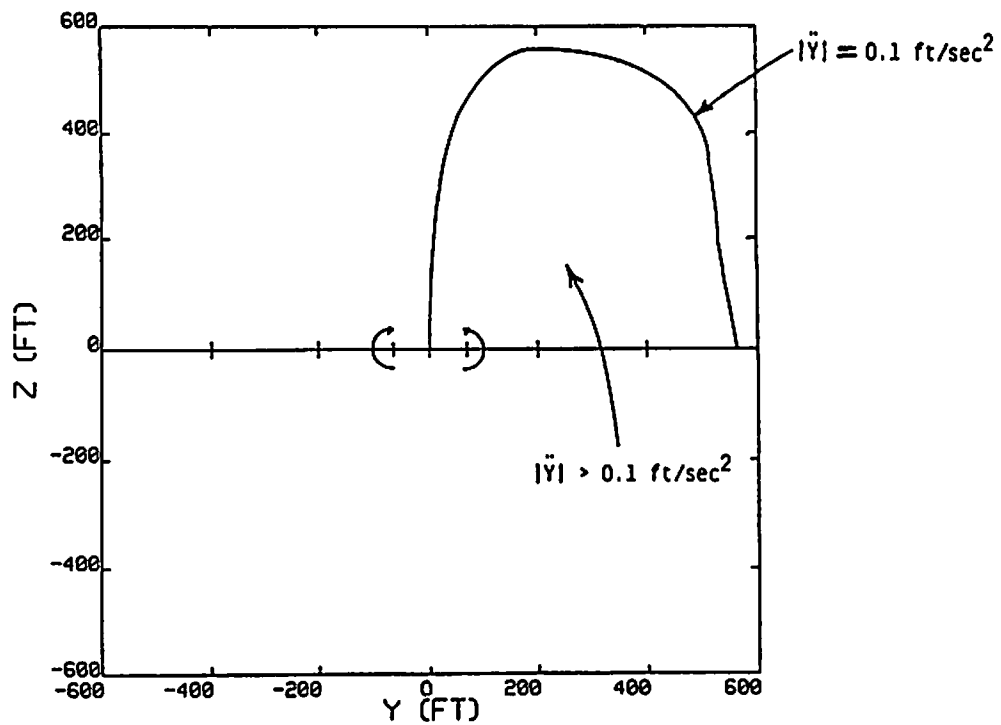

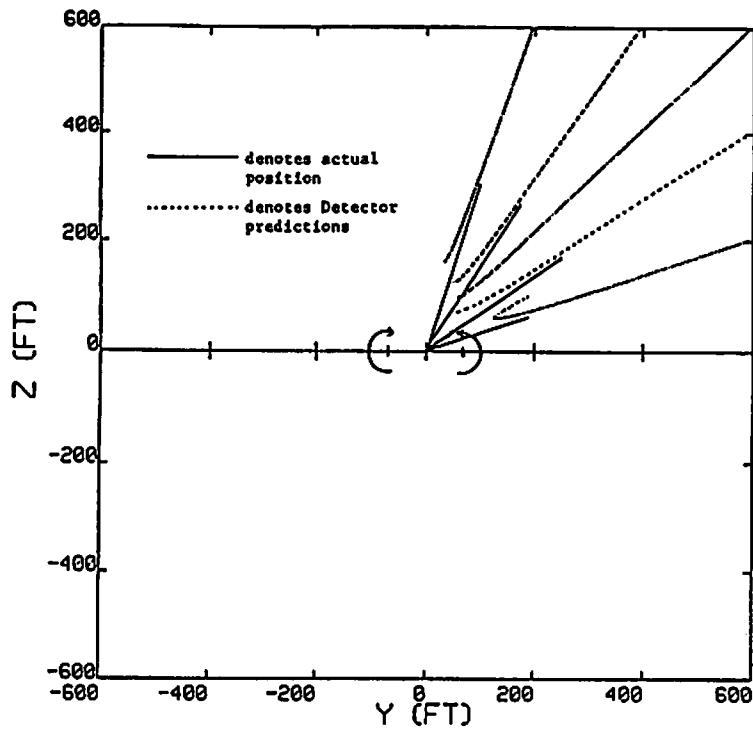**Figure 8. Detection distance using a lateral acceleration threshold of 0.1 ft/sec².**

Figure 9. Detector predicted and actual trajectories for an aircraft located on trajectories which are rays from the center (Y = Z = 0).
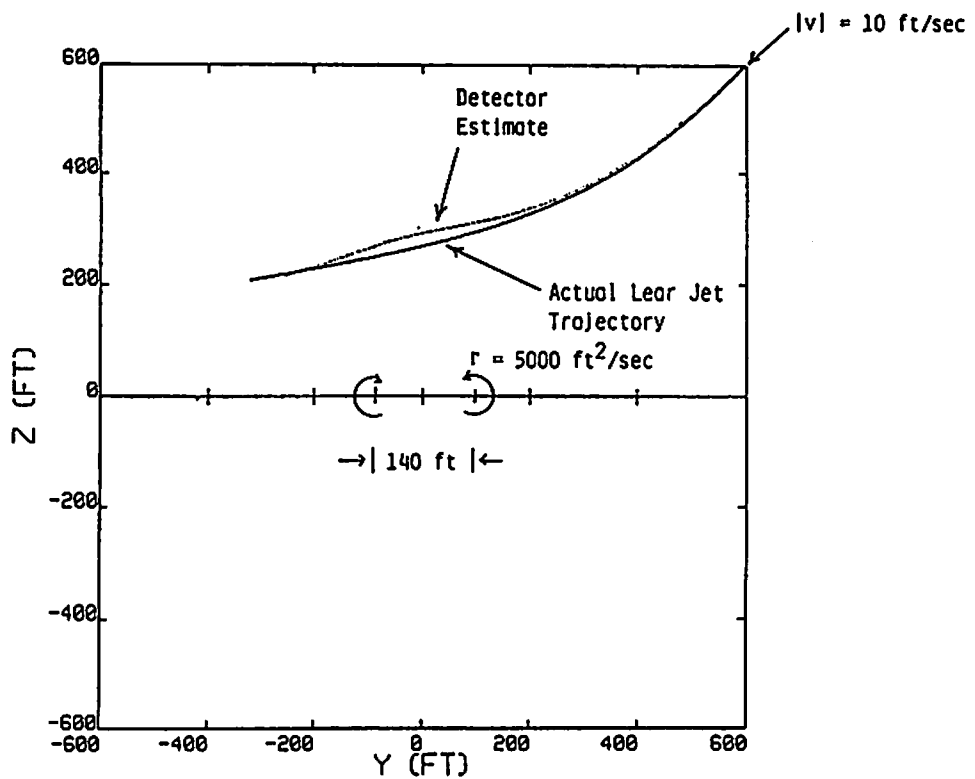

Figure 10. Three-degree-of-freedom simulation with Learjet controls locked.
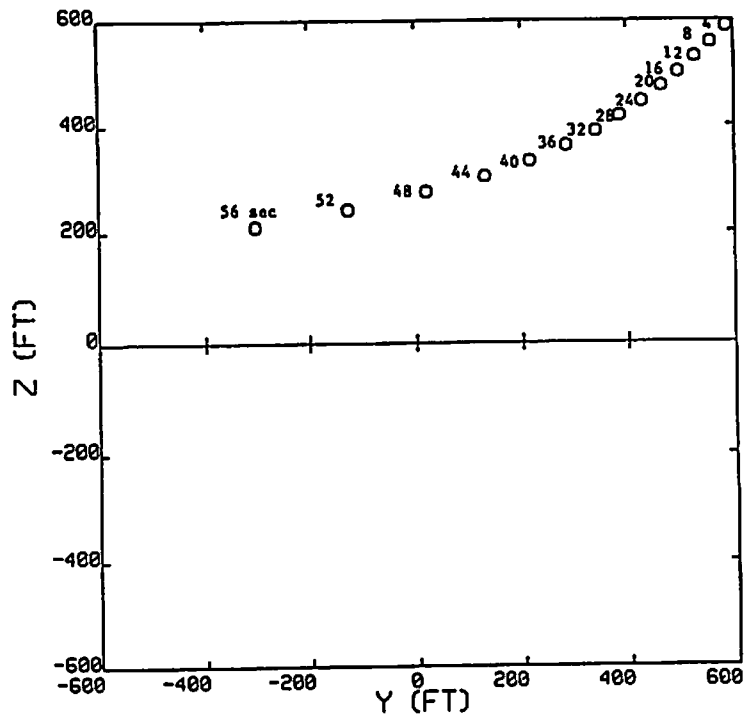
Figure 11. Three-degree-of-freedom simulation with Learjet controls locked with 4 second averaging.
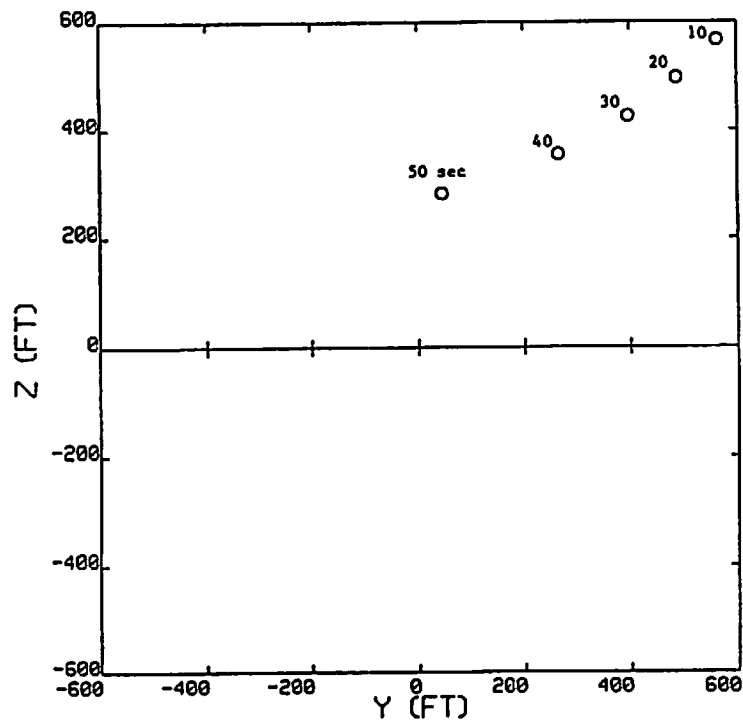
Figure 12. Three-degree-of-freedom simulation with Learjet controls locked with 10 second averaging.
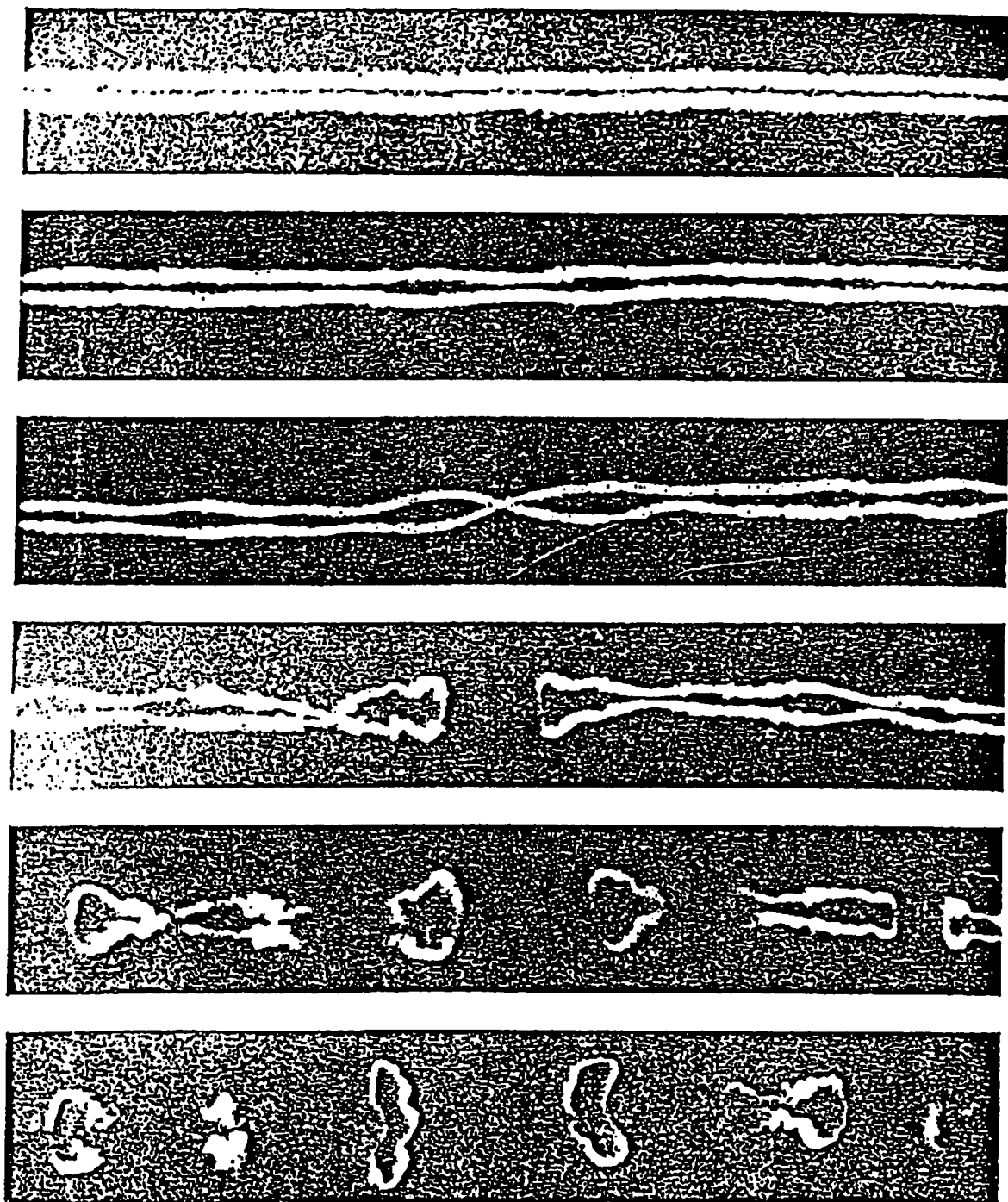
Figure 13. Instability of a pair of trailing vortices. The vortex trail of a B-47 aircraft
was photographed directly overhead at intervals of 15 s after its passage. The vortex
cores are made visible by condensation of moisture. They slowly recede and
draw together in a symmetrical nearly sinusoidal pattern until they connect
to form a train of vortex rings. The wake then quickly
disintegrates (Ref. 10).
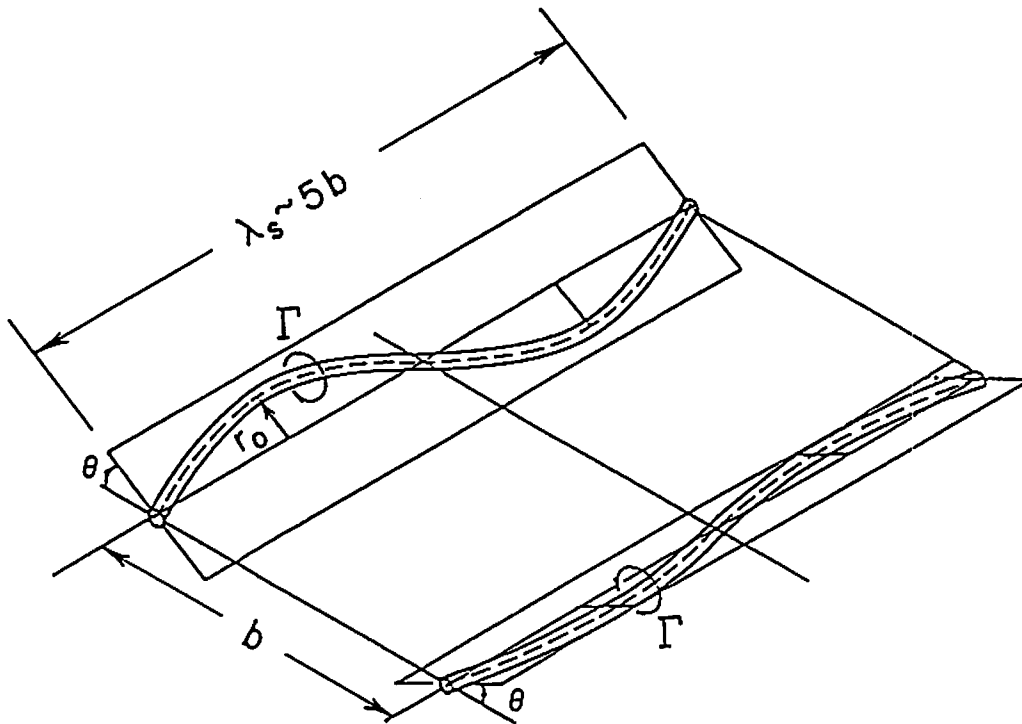
Figure 14. General features of the sinusoidal vortex pair instability. The amplitude of the instability is r_0 which grows with time until the vortices link and form crude rings.
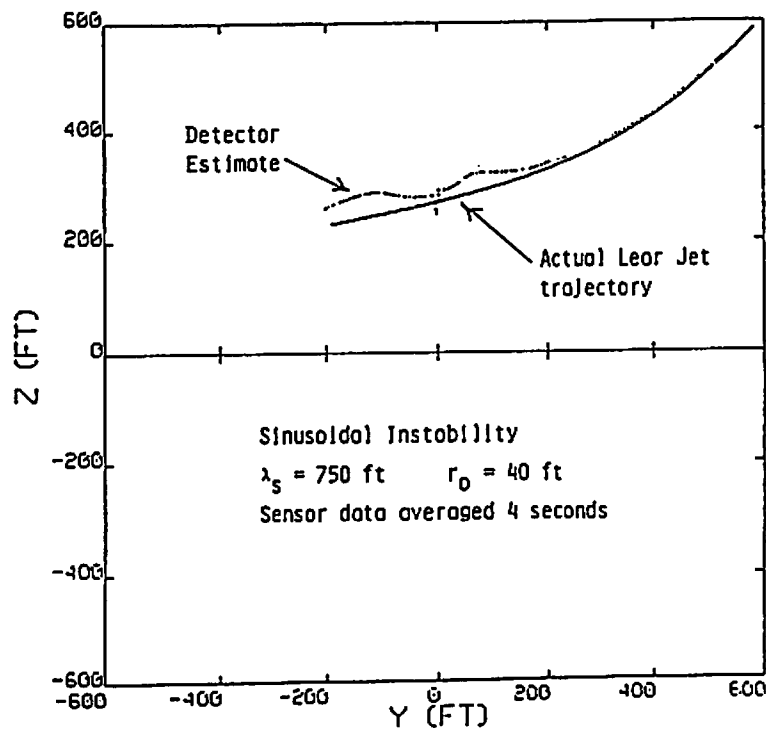
Figure 15. Three-degree-of-freedom simulation with Learjet controls locked.
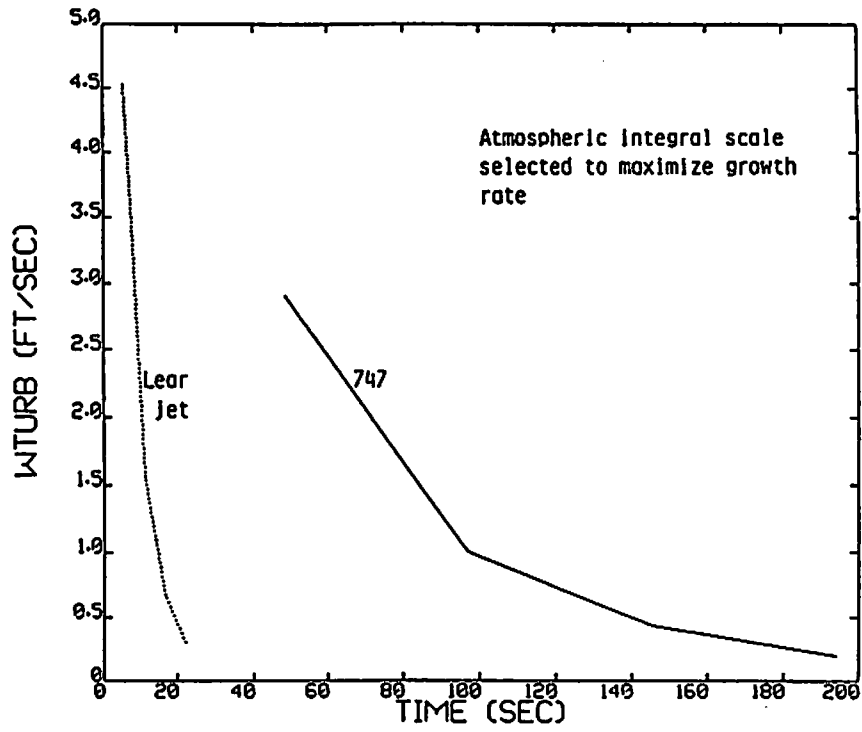
Figure 16. Wake lifetime in a turbulent atmospheric sinusoidal instability.

Figure 17. Vertical aircraft acceleration resulting from flying in a turbulent atmosphere.

Figure 18. Mean square wing tip velocity resulting from wing bending forced by atmospheric turbulence.

REFERENCES

1. Swedish, W. J., "Evaluation of the Potential for Reducing Longitudinal Spacing on Final Approach." Report No. FAA-EM-79-7, MITRE Corporation, August 1979.

2. Croom, D. R., "Low-Speed Wind-Tunnel Investigation of Various Segments of Flight Spoilers as Trailing-Vortex-Alleviation Devices on a Transport Aircraft Model." NASA Technical Note No. TN D-8182, March 1976.

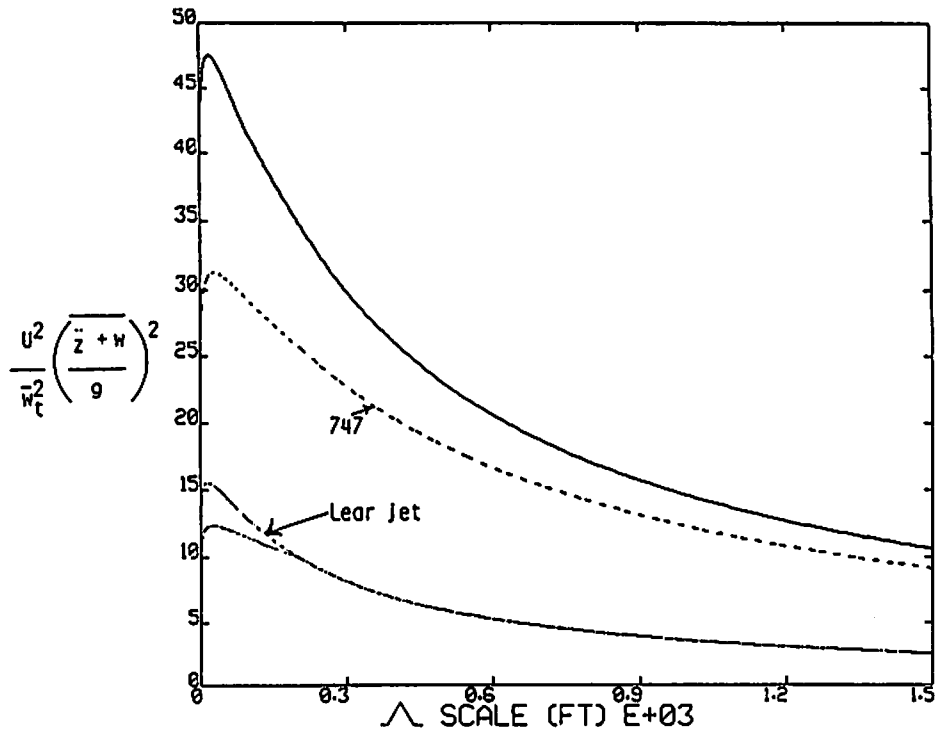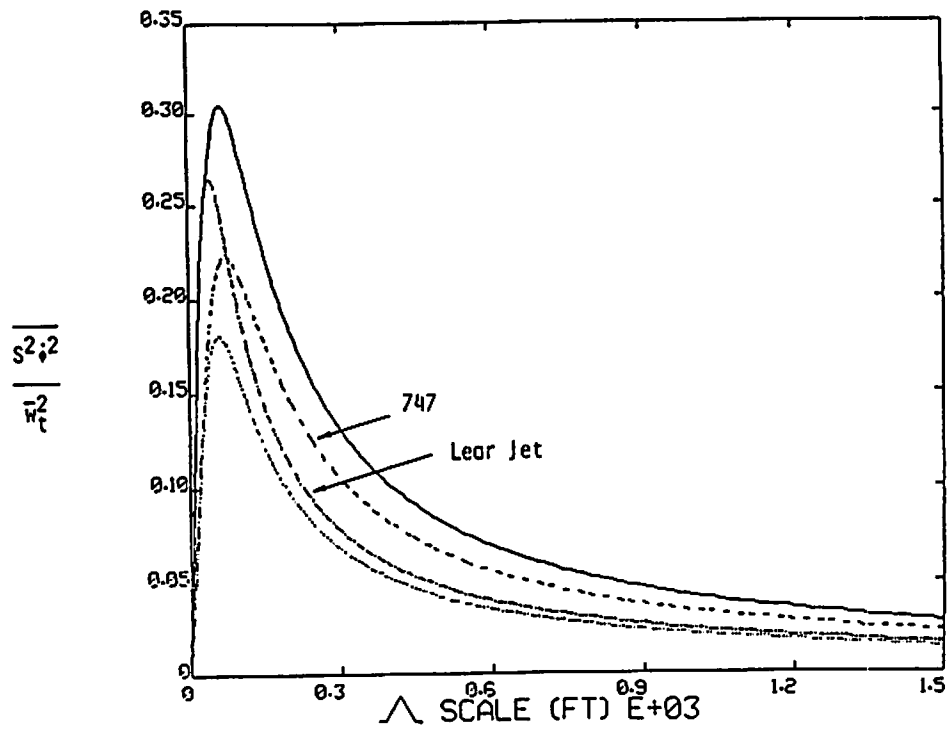3. Croom, D. R., "The Development and Use of Spoilers as Vortex Attenuators." NASA SP-409 Wake Vortex Minimization Symposium held in Washington, D.C., pp. 339-368, February 1976.

4. Patterson, J. C., Hastings, Jr., E. C. and Jordan, Jr., F. L., "Ground Development and Flight Correlation of the Vortex Attenuating Spline Device." NASA SP-409 Wake Vortex Minimization Symposium held in Washington, D.C., pp. 271-303, February 1976.

5. Ciffone, D. L. and Lonzo, Jr., C., "Flow Visualization of Vortex Interactions in Multiple Vortex Wakes Behind Aircraft." NASA Technical Memorandum No. TM X-62459, June 1975.

6. Corsiglia, V. R. and Dunham, R. E., "Aircraft Wake-Vortex Minimization by Use of Flaps." NASA SP-409 Wake Vortex Minimization Symposium held in Washington, D.C., pp. 305-338, February 1976.

7. Aviation Week and Space Technology, March 18, 1985, p. 148.

8. Hallock, J. N. and Eberle, W. R., "Aircraft Wake Vortices, A State-of-the-Art Review of the United States R&D Program." FAA Report No. FAA-RD-77-23, February 1977.

9. Holbrook, G. R., "Vortex Wake Hazard Analysis Including the Effect of the Encountering Wing on the Vortex." Master's Thesis, George Washington University, August 1985.

10. "An Album of Fluid Motion." Stanford University, Parabolic Press, 1982, p. 69.

11. Bilanin, A. J. and Widnall, S. E., "Aircraft Wake Dissipation by Sinusoidal Instability and Vortex Breakdown." AIAA Paper No. 73-107, presented at the 11th Aerospace Sciences Meeting, Washington, D.C., January 1973.

12. Crow, S. C., "Stability Theory for a Pair of Trailing Vortices." AIAA Journal 8, 2172-2179, December 1970.

13. Widnall, S. E., Bliss, D. B. and Zalay, A., "Theoretical and Experimental Study of the Stability of a Vortex Pair." Aircraft Wake Turbulence and Its Detection (Edited by

Olsen, J., Goldberg, A. and Rogers, M.), Plenum Press, New York, 1971, pp. 305-338.

14. Hackett, J. E. and Evans, P. F., "Numerical Studies of Three-Dimensional Breakdown in Trailing Vortex Wakes." Journal of Aircraft 14, November 1977.

15. Bliss, D. B., "Effect of Unsteady Forcing on the Sinusoidal Instability of Vortex Wakes." Journal of Aircraft 19, 713-721, September 1982.

16. Bilanin, A. J., Teske, M. E. and Curtiss, Jr., H. C., "Feasibility of an Onboard Wake Vortex Avoidance System." Continuum Dynamics, Inc. Report No. 87-02 prepared under Contract Number NAS1-17742 for NASA Langley and under Contract Number DTRS-57-85-C-000123 for Department of Transportation, April 1987.

APPENDIX A

RECOMMENDATIONS TO THE FAA

Presented on behalf of:

Thomas Bosco, Port Authority of New York and New Jersey
Jeff Fitch, Sea-Tac International Airport
Mary Rose Loney, City of Chicago Dept. of Aviation
Siegbert Poritzky, Airports Association Council Int'l - NA
William Cotton, United Airlines
John Ryan, Air Transport Association of America

We believe the Conference was valuable because it pointed up the prodigious amounts of research already done, which have corroborated the achieved safety of current operations, and made clear that the relief from the increased separation impact of wake vortices would produce major capacity gains at busy airports. We recognize that various studies reach differing conclusions on the actual capacity gains or instantaneous delay reductions to be achieved. The beneficial impact will vary widely for different airports under different conditions, but we believe the potential benefits of reduction of the serious negative impact of wake vortices far outweigh the costs. Work to at last provide beneficial results in the operating system needs to proceed rapidly.

On Tuesday, Administrator Busey asked for recommendations at the end of the symposium. In the U.S., nearly two decades of R&D have so far yielded no implemented improvements with respect to wake vortex alleviation, and FAA did not request any R&D funds for FY92 (although the Administrator has said some money would be "found" so as not to end all work).

The following are our recommendations to FAA and perhaps other administrations:

1. Establish stable management and leadership on the wake vortex issue in FAA, emphasizing early implementation of products.

2. Treat the wake vortex impact alleviation effort as a system issue, and actively pursue system integration with other efforts (TATCA, ASTA, TDWR, etc.) with special attention to acquisition and integration of dynamic windfield data in the airport area.

3. While energetically pursuing the system integration matters, concentrate also on things that can be done now or soon.

  e.g. - Eliminate restrictions when winds are such that wakes are swept away.

- Reduce separation standards as soon as data permits (e.g., LaGuardia cross-wake vortex encounters).

4. Make the development of a workable operations concept for use of better wake vortex information a high priority part of the R&D effort, working with ATC people.

5. Obtain up-to-date wake vortex signatures on all important aircraft types so as to make early wake-adaptive spacing possible.

6. Introduce, soon, the capability (TATCA, ASTA, TDWR, etc.) to present to controllers, in usable ways, the actual (between pairs) spacing requirements.

7. Airport-specific FAA-industry task forces should address the wake vortex alleviation issue and possible remedies as part of their efforts.

8. Fund the work at least $5 million/year and find at least $3 million this year (FY-92).

APPENDIX B

ATTENDEES AT THE FAA INTERNATIONAL WAKE VORTEX SYMPOSIUM
WASHINGTON, DC (OCTOBER 29-31, 1991)

H.P. Adamson
Turbulance Prediction Systems
3131 Indian Road
Boulder, CO 80301

James Allen
FAA AEA-260
Federal Building
JFK International Airport
Jamaica, NY 11430

Donald Altman
NW Research Assoc.
P.O. Box 3027
Bellevue, WA 98009

Chester W. Anderson
FAA AGL-507
2300 E. Devon Ave
Des Plaines, IL 60018

John W. Andrews
MIT Lincoln Lab.
244 Wood Street
Lexington, MA 02173

Ray Asay
United Parcel Service
NASC Bldg. #2
Flight Safety
Louisville, KY 40213

Robert Ash
Old Dominion Univ.
Dept. of Mechanical Engineering
241 KDH
Norfolk, VA 23529-0247

Claude Azibane
Accident Investigation Board of French Civil Aviation
246 Rue Le Courbe
75732 Paris, France

Bouglas Baart
FAA ACD-340
Technical Center
Atlantic City Int'l Airport
Atlantic City, NJ 08405

James Banks
ATCA
2300 Clarendon Blvd.
Suite 711
Arlington, VA 22201

Mark Baumgartner
Princeton Univ.
15 Dickinson Street, #32
Princeton, NJ 08540

Jonathan Beard
820 West End Ave, #B
New York, NY 10025

A.J. Bedard, Jr.
NOAA/ERL/WPL
325 Broadway
Boulder, CO 80303

Sergei M. Belotserkovsky
TsAGI, USSR
Zhukovsky
17 Radio Street, 107005
Moscow, USSR

Mark R. Bergstrom
Hughes Aircraft/EDSG
Building E-1
Mailstop B-131
P.O. Box 902
El Segundo, CA 90245

Bob Berluchhi
FAA ATM-100
800 Independence Ave, SW
Washington, DC 20591

Francois Bertin
Transports, France
Min. Des Transports et De L'Espace
246 Rue LeCourbe
75732 Paris, France

Jack Bertron
FAA AFS-450
800 Independence Ave., SW
Washington, DC 20591

Keith Biehl
FAA ACN-360
Atlantic City Int'l Airport
Atlantic City, NJ 08405

James C. Biggers
ARC Professional Services
8201 Corporate Drive
Suite 350
Landover, MD 20785

Alan J. Bilanin
Continuum Dynamics
P.O. Box 3073
Princeton, NJ 08542

Carl Borchers
U.S. DOT
FAA Trans. Safety Instit.
6500 S. MacArthur Blvd
Oklahoma City, OK 72125

Thomas Bosco
Port Authority of NY and NJ
1 World Trade Center, 65E
New York, NY 10048

Bernard Brooks
AGI, UK
Ebblake Industrial Estate
Verwood
Dorset, BH31 6BE England

Jon Brown
Loral Data Systems
6000 Fruitville Road
P.O. Box 3041
Sarasota, FL 34230

Gary L. Bryan
MITRE
7525 Colshire Dr.
M/S W852
McLean, VA 22102

Lewis Buckler
FAA ARD-300
800 Independence Ave., SW
Washington, DC 20591

David Burnham
SESI
P.O. Box 64
Orleans, MA 02653

James B. Busey IV
FAA AOA-1
Current Address: DOT S-2
Washington, DC 20590

Steven D. Campbell
MIT Lincoln Lab.
244 Wood Street
Lexington, MA 02173

Bruce Carmichael
NCAR
P.O. Box 3000
2555 55th Street
Boulder, CO 80301

Thomas Carmody
FAA AAI-40
800 Independence Ave., SW
Washington, DC 20591

Dean Chamberlain
Aviation Safety Magazine
FAA AFS-20
800 Independence Ave., SW
Washington, DC 20591

Jean-Pierre Chevallier
Thomson-CSF
18 Avenue M-Juin
92366 Meudon-la-Foret Cedex
Paris, France

Jim Chow
Stanford University
RAINS #740
Stanford, CA 94305

Paul Christianson
Boeing
P.O. Box 3707
MS 47-31
Seattle, WA 98124

Gary Church
Aviation Management
8752 Center Road
Springfield, VA 22152

Myron Clark
FAA AFS-406
800 Independence Ave., SW
Washington, DC 20591

Kirk Clawson
NOAA
1750 Foot Drive
Idaho Falls, ID 83402

William Colligan
SAIC
1710 Goodridge Drive
McLean, VA 22102

Steven T. Connolly
Applied Technologies
6395 Gunpark Drive
Unit E
Boulder, CO 80301

Declan Conroy
Inside DOT
627 National Press Bldg
Washington, DC 20045

Dan Cook
Air Safety Week
1900 L Street, NW
Washington, DC 20006

Robert Cook
Department of State
U.S. Mission
ICAO P.O. Box 847
Champlain, NY 12919

Victor Corsiglia
NASA HQ
600 Independence Ave
Washington, DC 20546

William B. Cotton
United Airlines
EXOVF
P.O. Box 66100
Chicago, IL 60666

Leonard Credeur
NASA Langley
Mail Stop 156A
Hampton, VA 23665-5225

J.B. Critchley
UK CAA
45-59 Kingsway
London, WC2B 6TE
England

Steven Crow
Univ. of Arizona
AME Dept.
Aero Building 16
Tuscon, AZ 85721

Patrick Curran
Sundstrand Aerospace
4747 Harrison Avenue
P.O. Box 7002
Rockford, IL 61125

H.C. Curtiss
Princeton Univ.
Dept. of Mechanical Engineering
Princeton, NJ 08544

Russ Davoren
FAA AAC-933E
P.O. Box 25082
Oklahoma City, OK 73125

Harvey De Graw
FAA AEA-630
JFK Int'l Airport
Fitzgerald Bldg.
Jamaica, NY 11430

Donald Delisi
NW Research Assoc.
P.O. Box 3027
Bellevue, WA 98009

Manhar Dhanak
Florida Atlantic University
Dept. of Ocean Eng.
Boca Raton, FL 33431

Archie Dillard
FAA AAC-950
P.O. Box 25082
Oklahoma City, OK 73125

Alain Donzier
Remtech
P.O. Box 2423
1044 Townley Circle
Longmont, CO 80502

John F. Dove
Dove Electronics
227 Liberty Plaza
Rome, NY 13440

Paul R. Drouilet
MIT Lincoln Lab.
244 Wood Street
Lexington, MA 02173-9108

Branimir Dulic
Transport Canada
330 Sparks Street
Area 7F
Ottawa, Ontario KIA ON8
Canada

Earl Dunham
NASA Langley
Mail Stop 260-1
Hampton, VA 23665

William Dunlay
PMG Peak Marwick
160 Bovet Road
Suite 300
San Mateo, CA 94402

William R. Eberle
Lockhead Missiles & Space Corp., Inc.
P.O. Box 070017
Huntsville, AL 35807

Eldon Elam
FAA AAI-110
800 Independence Ave., SW
Washington, DC 20591

John J. Elnitski
VEDA Inc.
1800 N. Beauregard Street
Alexandria, VA 22311

Donald D. Engen
AOPA Air Safety Foundation
421 Aviation Way
Fredrick, MD 21701

Paul J. Engstenberg
United Parcel Service
214 Winterberry Drive
Dover, DE 19901

Paul Erway
FAA ARD-30
800 Independence Ave., SW
Washington, DC 20591

James Evans
MIT Lincoln Lab.
244 Wood Street
Lexington, MA 02173

Alex Fisher
British Airways
Flt Tech Projects (S355)
P.O. Box 10 Hounslow
Middlesex, England TW62JA

Jeff Fitch
Port of Seattle
SEA-TAC Int'l Airport
P.O. Box 68727
Seattle, WA 98168

Rufus Forrest
Air National Guard
119th AREFG/SE
Forbes Field ANG
Topeka, KS 66619

J. Franke
Institut Fur Meterolgie
Univ. of Hannover
Herrenhauser Strasse 2
D-3000 Hannover 21,
Germany

Jerome Freedman
General Electric
Govt. Electronic Syst. Div.
Moorestown, NJ 08057

Xavier Fron
Centre Experimental Eurocontrol
BP-15
91222 Bretiguy Sur Orge Cedex
France

William Gallo
FAA AGC-400
800 Independence Ave., SW
Washington, DC 20591

Leo Garodz
Flight & Aviation Safety
517 Whitman Chocolates
Whitman Square
Turnersville, NJ 08012

Paul Gauthier
Canadian ATC Association
1100-400 Cumberland Street
Ottawa, Ontario KIN8X3
Canada

E. Michael Geyer
TASC
55 Walkers Brook Drive
Reading, MA 01867

Tom Gilbert
USAF
330 CFIS/DOP
Castle AFB, CA 95342-5000

William P. Gilbert
NASA Langley
Mailstop 246A
Hampton, VA 23665

Trevor J. Gilpin
CAA House
45-59 Kingsway
London, WC2B 6TB
England

Craig Goff
FAA ASE-400
800 Independence Ave., SW
Washington, DC 20591

Douglas Goldberg
Landrum & Brown
11279 Cornell Part Drive
Cincinatti, OH 45242

Joseph F. Golden
NOAA
Chief Scientist Office
1825 Connecticut Avenue
Washington, DC 20235

Herb Goldstein
FAA ARD-5
800 Independence Ave., SW
Washington, DC 20591

Peter Granitzny
Deutscher Wetterdienst
Frankfurter Strasse 135
Offenbach, D-6050
Germany

Sheldon Green
Univ. of British Columbia
2324 Main Mall
Vancouver, Canada V6T124

George Greene
NASA Langley
Mailstop 247
Hampton, VA 23665

Robert D. Grennan
Sundstrand
4747 Harrison Avenue
Rockford, IL 61125

Scott Griffith
Allied Pilots Assoc.
P.O. Box 5524
Arlington, TX 76005-5524

James N. Hallock
DOT/VNTSC DTS-67
Kendall Square
Cambridge, MA 02142

G.K. Hamilton
Cortana Corp.
520 N. Washington Street, #200
Falls Church, VA 22046

Charles H. Hawkins
FAA ACE-220A
601 E. 12th Street
Room 1664
Kansas City, MO 64106

Ronald Herbert
Precision Airlines
841 Galaxy Way
Manchester, NH 03103

Richard Heinrichs
MIT Lincoln Lab.
244 Wood Street
Room N-237
Lexington, MA 02173

Lynn Helms
International Consultant
5 Cooper Lane
Westport, CT 06880

Geoffrey C. Howell
UK CAA
45/59 Kingsway
London, WC2B 6TE
England

Jack Howell
FAA ACT-2
Atlantic City Int'l Airport
Atlantic City, NJ 08405

Carl T. Hsieh
Naval Surface Warfare Center
10901 New Hampshire Ave
Silver Spring, MD 20903-5000

Liu Hu
CAA Aircraft Airworth. Dept.
155 Dong Si Street, West
P.O. Box 644
Beijing, China 100710

Milton Huffaker
Coherent Technologies
3300 Mitchell Lane, #330
Boulder, CO 80301

G.M. Jefferson
UK NATS
CAA House
45/59 Kingsway
London, WC2B 6TE
England

Albert V. Jelalian
Raytheon
528 Boston Post Road
Sudbury, MA 01776

Richard Jesuroga
Forecast Systems Lab.
NOAA/ERL/FSL
FS5 325 Broadway
Boulder, CO 80303

Amanda Johnson
8 Columbia Avenue
Brunswick, ME 04011

David Johnson
Science & Technology
Corporate Headquarters
101 Research Dr.
Hampton, VA 23666

Stuart Jolley
Roke Manor
Romsey
Hampshire, SO51 OZN
England

William W. Joss
MIT Lincoln Lab.
244 Wood Street
Lexington, MA 02173

Osama A. Kandil
Old Dominion Univ.
Mechan. Engineering Dept.
Norfolk, VA 23529

Mehdi R. Khorrami
High Technology Corp.
C/O NASA Langley
MS-163
Hampton, VA 23665-5225

Larry Kline
SW Airline Pilots Assoc.
8036 Aviation Place
Lockbox #17
Leftfield, Dallas, TX 75235

Russel Knowles
SAA Pilots Assoc.
10 Blockhouse Street
Kempton Park
Johannesburg, South Africa

Friedrich Koepp
DLR, Germany
Institute of Optoelectronics
Oberpfaffenhofen, Germany

Barry Krasner
NATCA
Suite 845
444 North Capitol Street, NW
Washington, DC 20001

George Larson
Air and Space
370 L'Enfant Promenade, SW
10th Floor
Washington, DC 20224-2518

Pat Lavergne
FAA ACE-530
601 E. 12th Street
Kansas City, MO 64106

William G. Laynor
NTSB
490 E. L'Enfant Plaza
Washington, DC 20594

Christian Le Roux
Transport, France
L'Espace
246 Rue Lecourbe, 75732
Paris, France

Martin Lessen
Univ. of Rochester
12 Country Club Drive
Rochester, NY 14618

Arthur Levy
FAA ANR-150
1825 Connecticut Ave., NW
Washington, DC 20009

Dieter K. Lezius
Lockheed Missiles & Space Co.
3170 Porter Drive
Palo Alto, CA 94304

William Lindenmuth
David Taylor Research Ctr.
6916 All View Drive
Columbia, MD 21046

Vance Lineberger
USAF
HQ Office of Safety
Pentagon
Washington, DC 20330-1000

C.H. Liu
MS15E
NASA/Langley
Hampton, VA 23666-5225

Peter Liu
Quest Integrated, Inc.
21414-68th Avenue South
Kent, WA 98032

Jack Loewenstein
FAA ASE-2
800 Independence Ave., SW
Washington, DC 20591

Mary Rose Loney
Dept. of Aviation, Chicago
Chicago O'Hare Int'l Airport
P.O. Box 66142
Chicago, IL 60666

Steven Lowe
FAA AEU-500
American Embassy
APO, NY 09667

Robert Machol
FAA ASD-4
800 Independence Ave., SW
Washington, DC 20591

Bill Mahoney
NCAR
2555 55th Street
Boulder, CO 80301

Walter Manning
FAA AOR-200
800 Independence Ave., SW
Washington, DC 20591

Nick Martin
GEC Ferranti
Monks Way
Linford Wood
Milton Keynes, Bucks MK14 6LA
England

Manuel Martinez-Sanchez
MIT
Dept. of Aeronautics
Cambridge, MA 02139

Carol May
Cortana Corp.
520 N. Washington Street, #200
Falls Church, VA 22046

Lance McDonald
American Eagle
2340 River Road
Suite 104
Des Plaines, IL 60018

Al McDonough
FAA AEA-630
Fitzgerald Federal Bldg.
JFK International Airport
Jamaica, NY 11430

Gordon Merrit
Johns Hopkins Univ.
John Hopkins Road
Laurel, MD 20723

Bob Moeser
Airline Pilot Mag.
535 Herndon Parkway
P.O. Box 1169
Herndon, VA 22070

Helen Monk
FAA ACD-130
Atlantic City Int'l Airport
Atlantic City, NJ 08405

Anthony R. Moore
FAA ASQ-140
800 Independence Ave., SW
Washington, DC 20591

Kevin Moore
Embassy of Australia
1601 Massachusetts Ave., NW
Washington, DC 20036

Oscar Morgenstern
MITRE
7525 Colshire Drive
McLean, VA 22102

Anand Mundra
MITRE
7525 Colshire Drive
McLean, VA 22102

Hirotaka Nagahata
All Nippon Airways
1-6-6 Hanedo Airport
Ota-ku
Tokyo, Japan 144

Giora Nagid
ICAO
1000 Sherbrooke Street, West
Montreal
Quebec, H3A2R2 Canada

Robert Nelson
Univ. of Notre Dame
Hesserd Ctr. for Aerospace Res.
Bldg. 66
South Bend, IN 46556

Gerald Nespor
GE Aerospace
199 Borton Landing Road
Morristown, NJ 08057

Vojin Nikolic
Univ. of Notre Dame
Hesserd Center for Aerospace Res.
Bldg. 66
South Bend, IN 46556

Max Noori
Cortana Corp.
520 N. Washington Street, #200
Falls Church, VA 22046

Daniel Nosenchuck
Princeton Univ.
D-302
E-Quad
Princeton, NJ 08544

Richard Page
FAA ACD-340
Atlantic City Int'l Airport
Atlantic City, NJ 08405

Phillippe Papin
Thomson-CSF
18 Avenue M-Juin
92366 Meudon-La Foret Cedex
Paris, France

Kenneth Peppard
FAA ASC-203
800 Independence Ave. SW
Washington, DC 20591

Siegbert Portizky
AACI
1220 19th Street, NW
Suite 800
Washington, DC 20036

Todd R. Quackenbush
Continuum Dynamics
P.O. Box 3073
Princeton, NJ 08543

Robert Quirk
FAA ACE-220A
601 E. 12th Street
Kansas City, MO 64106

Johannes Reichmuth
DLR
Flughafen
D-3300 Braunschweig
Germany

Jeremy Richards
GEC Ferranti
Monks Way, Linford Wood
Milton Keynes, Bucks MK14 6LA
England

Jean-Pierre Robert
Airbus Industrie
1 Rond Point Maurice Bellonte
31707 Blagnac Cedex
France

Bob Robins
NW Research Assoc.
P.O. Box 3027
Bellevue, WA 98009

Theodore Robinson
FAA ANC-504
800 Independence Ave., SW
Washington, DC 20591

James Rogers
FAA ARD-300
800 Independence Ave., SW
Washington, DC 20591

Edwin P. Rood
Office of Naval Res. (1132F)
Fluid Dynamics Program
Arlington, VA 22217-5000

Vernon Rossow
NASA Ames
Fixed Wing Aerodynamic Branch
Mail Stop 247-2
Moffett Field, CA 94035-1000

Irving Roth
UNISYS
Defense Systems, Inc.
365 Lakeville Road
Great Neck, NY 11020

Robert Rovinsky
FAA AOR-200
800 Independence Ave., SW
Washington, DC 20591

William L. Rubin
166-47 15 Ave.
Whitestone
New York, NY 11357

Robert P. Rudis
DOT/VNTSC DTS-53
Kendall Square
Cambridge, MA 02142

John R. Ryan
ATA
1709 New York Ave., NW
Suite 500
Washington, DC 20006

Hiroaki Sakai
All Nippon Airways
1-6-6 Haneda Airport
Ota-Ku
Tokyo, Japan 144

Charles E. Schemm
Johns Hopkins Univ.
Johns Hopkins Road
Laurel, MD 20723

H.D. Schenk
DLR
Flughafen D-3300
Braunschweig, Germany

Jan Schumacher
Deutsche Airbus
Kreetslag 10
2003 Hanburg 95
Germany

Melvin B. Schwartz
United Airlines
San Francisco International Airport
San Francisco, CA 94128

Mei-Mei Shen
Seagull Technology
1310 Hollenbeck Ave.
Sunnyvale, CA 94087

S.R. Sherratt
UK NATS
45/59 Kingsway
London, WC2B 6TE
England

George Skaliotis
DOT/VNTC
DTS/53
Kendall Square
Cambridge, MA 02142

Jacqueline Smith
FAA AGL-2
2300 E. Devon Avenue
Des Plains, IL 60018

Evan Soffer
FAA APO-220
800 Independence Ave., SW
Washington, DC 20591

Frank Soloninka
FAA ATP-120
800 Independence Ave., SW
Washington, DC 20591

David Soreide
Boeing
P.O. Box 3999
M/S 7J-05
Seattle, WA 98124

Edward A. Spitzer
DOT/VNTSC DTS-53
Kendall Square
55 Broadway
Cambridge, MA 02142

Gene Stanton
FAA ASF-20
800 Independence Ave., SW
Washington, DC 20591

Lenard Starks
MITRE
7525 Colshire Drive
McLean, VA 22102

Jan Steenblik
AirLine Pilot Mag.
535 Herndon Pkwy
P.O. Box 1169
Herndon, VA 22070

Eric C. Stewart
NASA Langley
M/S 247
Hampton, VA 23665

Tom Stone
Airline Pilots Assoc.
535 Herndon Pkwy
Herndon, VA 22070

Claude Stouff
DGAC-SFACT E.
246 Rue Lecourbe
Paris Cedex 15,
France

Robert Striegel
Air Line Pilots Association
535 Herndon Parkway
Herndon, VA 22070

Timothy Styslinger
U.S. DOT
860 Beacon Street, #703
Boston, MA 02142

George Succi
Technology Integration
54 Midlesex Turnpike
Bedford, MA 01730

Peter Tait
GEC Marconi
West Hanningfield Road
Great Baddow
Chelmsford, Essex
England

Russell Targ
Lockheed
3251 Hanover Street
Orgn. 97-01 Bldg. 201
Palo Alto, CA 94304-1191

Steve Teager
FAA ACN-371
Atlantic City Int'l Airport
Atlantic City, NJ 08405

Scott Tento
SAIC
Suite 225, Market Pl. 1
2001 Western Ave.
Seattle, WA 98121

Milton E. Teske
Continuum Dynamics
P.O. Box 3073
Princeton, NJ 08543

G. Tetzlaff
Institut Fur Meterologie
University of Hannover
Herrenhauserstr 2
D-3000 Hannover 21, Germany

S.D. Thomas
FAA AFS-405
800 Independence Ave., SW
Washington, DC 20591

Alex Thomson
Coherent Technologies, Inc.
P.O. Box 7488
Boulder, CO 80301-7488

David Tuttle
FAA ARD-200
800 Independence Ave., SW
Washington, DC 20591

Joseph Tymczyszyn
29138 Oceanridge Drive
Rancho Palos Verdes, CA 90274

Robert Ulanch
FAA ACD-340
Atlantic City Int'l Airport
Atlantic City, NJ 08405

Brian Uzzle
FAA AOV-300
800 Independence Ave., SW
Washington, DC 20591

Walter O. Valarezo
Douglas Aircraft
3855 Lakewood Blvd.
MC 36-41
Long Beach, CA 90846

H.J. Van Woortman
NLR
P.O. Box 90502
1006 BM
Amsterdam, Netherlands

Charles Varnell
E-Systems, Inc.
Garland Division
14503 Faraday Drive
Rockville, MD 20853

Howard Vaughn
FAA AIA-110
800 Independence Ave., SW
Washington, DC 20591

Edward Vertatschitsch
Boeing
P.O. Box 3999
M/S 7J-65
Seattle, WA 98124

Dan Vicroy
NASA Langley
Flight Mgmt Division
MS-156A
Hampton, VA 23665

Jerry D. Welch
MIT Lincoln Laboratory
244 Wood Street
Lexington, MA 02173

Louis Williams
NASA Code RF
600 Independence Ave., SW
Washington, DC 20546

Heinz Winter
DLR
Flughafen
D-3300 Braunscheig,
Germany

Tin-Chee Wong
Old Dominion Univ.
MEM Dept.
Norfolk, VA 23529

Robert Woodhouse
IATA
2000 Peel Street
Montreal
Quebec, Canada

Peter Wroblewski
MITRE
Washington Center
1800 Dolley Madison Blvd.
McLean, VA 22102

Richard Young
FAA ATR-330
800 Independence Ave., SW
Washington, DC 20591

A.N. Zamyatin
Flight Research
140160 Zhukovsky
Moscow Region, USSR

Y.A. Zavershnev
Flight Research
140160 Zhukovsky
Moscow Region, USSR

Z. Zheng
Old Dominion Univ.
Norfolk, VA 23529-0247

Thomas Zierten
Boeing
Commercial Airplane Group
P.O. Box 3707 MS 6MWE
Seattle, WA 98124-2207

Greg Zilliac
NASA AMES
Mail Stop 260-1
Moffett Field, CA 94035